



Synthesis, characterization and applications of complexes involving redox-active ligands

Romain Kunert

► To cite this version:

Romain Kunert. Synthesis, characterization and applications of complexes involving redox-active ligands. Organic chemistry. Université Grenoble Alpes [2020-..]; Simon Fraser university (Burnaby, Canada), 2022. English. NNT : 2022GRALV045 . tel-03827384

HAL Id: tel-03827384

<https://theses.hal.science/tel-03827384>

Submitted on 24 Oct 2022

HAL is a multi-disciplinary open access archive for the deposit and dissemination of scientific research documents, whether they are published or not. The documents may come from teaching and research institutions in France or abroad, or from public or private research centers.

L'archive ouverte pluridisciplinaire **HAL**, est destinée au dépôt et à la diffusion de documents scientifiques de niveau recherche, publiés ou non, émanant des établissements d'enseignement et de recherche français ou étrangers, des laboratoires publics ou privés.

THÈSE

Pour obtenir le grade de

DOCTEUR DE L'UNIVERSITÉ GRENOBLE ALPES

**préparée dans le cadre d'une cotutelle entre l'Université
Grenoble Alpes et la Simon Fraser University**

Spécialité : Chimie inorganique et bioinorganique

-Vu l'arrêté du 6 janvier 2005 relatif à la cotutelle internationale de thèse
-Vu l'arrêté ministériel du 25 mai 2016 fixant le cadre national de la formation et les modalités conduisant à la délivrance du diplôme national de doctorant
-Vu la convention du 9 octobre 2019 visant à organiser la cotutelle internationale de thèse

Présentée par

Romain KUNERT

Thèse dirigée par **Olivier JARJAYES**
codirigée par **Tim STORR**

préparée au sein du **Département de Chimie Moléculaire**
dans l'**École Doctorale Chimie et Science du Vivant**
et au sein du **Storr Lab – Bioinorganic and Medicinal Chemistry**
dans le **Department of Chemistry / Faculty of Science**

Synthesis, characterization and applications of complexes involving redox-active ligands

Thèse soutenue publiquement le **08 juillet 2022**,
devant le jury composé de :

Madame Audrey AUFRANT

Directrice de Recherche, CNRS, Institut Polytechnique de Paris, Rapportrice

Monsieur Stéphane BELLEMIN-LAPONNAZ

Directeur de Recherche, CNRS, Université de Strasbourg, Rapporteur

Monsieur Cyrille TRAIN

Professeur des Universités, Université Grenoble Alpes, Président de jury

Monsieur Jeffrey WARREN

Professeur Associé à la Simon Fraser University, Examineur

Monsieur Daniel LEZNOFF

Professeur à la Simon Fraser University, Membre invité

Monsieur Fabrice THOMAS

Professeur des Universités, Université Grenoble Alpes, Membre invité

Monsieur Olivier JARJAYES

Maitre de Conférences à l'Université Grenoble Alpes, Directeur de thèse

Monsieur Tim STORR

Professeur à la Simon Fraser University, Codirecteur de thèse



Table of contents

List of acronyms	5
Preface	7
Chapter I. General introduction.....	9
1. Redox-active ligands	11
1.1. Radicals	11
1.1.1. Discovery of free radicals by Gomberg.....	11
1.1.2. Structure and reactivity of radicals.....	12
1.1.3. History and applications of radicals in chemistry	12
1.1.4. Radicals in biology	13
1.2. Main families of redox-active ligands.....	17
1.2.1. Tuning of the Lewis acidity of the metal.....	18
1.2.2. Reservoirs in electron transfer reactions	18
1.2.3. Chemical transformations on the redox-active ligand	20
1.3. Salen complexes	20
1.3.1. Structure and main applications	21
1.3.2. Redox-activity of the phenolate ring	24
1.3.3. Copper complexes as molecular models of GOase	27
1.3.4. Nickel complexes to probe the electronic structure of oxidized species	37
1.3.5. Manganese complexes presenting ligand-centered redox activity	43
2. Introduction of <i>N</i> -Heterocyclic Carbenes (NHCs).....	45
2.1. History and features of NHCs	45
2.1.1. Initial works and their legacy	45
2.1.2. Electronic properties.....	46
2.1.3. Experimental determination	48
2.2. Preparation	49
2.2.1. Ring closure by the amino groups	50
2.2.2. Ring closure from the backbone frame.....	52
2.2.3. Ring closure by the carbon center	52
2.3. Impact of NHCs on organometallic catalysis.....	54
2.3.1. Olefin metathesis	54
2.3.2. Palladium catalyzed cross-coupling reactions.....	54
2.3.3. Nickel catalyzed cross-coupling reactions	55
2.4. Redox-active NHCs.....	56
2.4.1. NHCs association with redox-active units.....	56
2.4.2. Metal complexes bearing NHC-phenolate ligands	58
3. Influence of redox-active ligands on nitrogen chemistry	64
3.1. Nitrogen fixation	64
3.2. Nitrogenase.....	65
3.2.1. Structure and activity of nitrogenase	65
3.2.2. Mechanistic insights	65

3.3. Molecular complexes for catalytic N ₂ reduction	68
3.3.1. Seminal Schrock discovery	68
3.3.2. Peters iron catalysts	69
3.3.3. Low-valent molybdenum Nishibayashi catalysts	70
3.4. Transition metal nitrides.....	73
3.4.1. Metal nitrides syntheses	73
3.4.2. Bonding considerations	77
3.4.3. Early-transition metal nitrides	79
3.4.4. Late-transition metal nitrides.....	79
3.4.5. Mid-transition metal nitrides	80
3.4.6. Redox activity with metal-nitrides	81
 Chapter II. Group 10 metal complexes	 83
1. Introduction	85
2. Synthesis of the Proligand and complexes	86
3. Structures of neutral complexes NiL^{C2O2} , PdL^{C2O2} and PtL^{C2O2}	87
4. Electrochemistry of the proligand and of the neutral complexes	88
5. Oxidation protocol.....	90
6. Crystal structure of [NiL^{C2O2}] ⁺	91
7. EPR spectroscopy of the oxidized complexes.....	92
8. UV-vis-NIR spectroscopy	94
9. Theoretical calculations.....	96
10. Formation of Nickel(III)-pyridine adducts	100
11. Conclusion.....	107
 Chapter III. Manganese complexes.....	 109
1. Formation of a transient nitrido species in manganese complexes	111
1.1. Introduction	111
1.2. Synthesis of Mn(III) precursor complexes.....	112
1.3. Structures of the Mn(III) precursors.....	114
1.4. UV-vis of the Mn(III) complexes.....	115
1.5. Synthetic assays to reach the nitrido MnL^{C2O2}(N) complex.....	115
1.6. Investigation of the N-inserted products	120
1.7. Isotopic labelling	124
1.8. Theoretical calculations.....	128
1.9. <i>In-situ</i> reactivity studies	137
1.10. Conclusion.....	138
2. Preliminary investigations of electrocatalytic ammonia oxidation	138
2.1. Introduction	138
2.2. Preliminary investigation in ammonia oxidation using MnL^{C2O2}Br	140
2.3. Conclusion.....	144
 Chapter IV. Nitridochromium complexes.....	 145
1. Introduction	147
2. Synthesis and characterization of the neutral CrL^{C2O2}(N) complex.....	148

2.1. Synthesis of $\text{CrL}^{\text{C2O2}}(\text{N})$	148
2.2. Structure of neutral $\text{CrL}^{\text{C2O2}}(\text{N})$	148
2.3. EPR and UV-vis-NIR spectroscopy	149
2.4. Theoretical calculations on the neutral complex.....	151
2.5. Electrochemistry of the neutral complex.	155
3. Oxidation of $\text{CrL}^{\text{C2O2}}(\text{N})$	156
3.1. One-electron oxidized $[\text{CrL}^{\text{C2O2}}(\text{N})]^+$ complex.....	156
3.2. Room temperature degradation products	162
3.2.1. Room temperature chemical oxidation.....	162
3.2.2. Evolution of $[\text{CrL}^{\text{C2O2}}(\text{N})]^+$ at room temperature	166
3.2.3. Electrochemical formation of $[\text{X}]^+$ at room temperature.....	168
3.2.4. Theoretical calculations.....	172
4. Conclusion.....	175
Chapter V. Distorted salen complexes	177
1. Introduction	179
2. Synthesis of the ligands and neutral copper complexes	180
3. Crystallographic structure of the ligands and neutral complexes	180
4. Electrochemistry.....	183
5. UV-vis-NIR and EPR spectroscopies of the neutral complexes	186
6. Oxidation protocol and structures of one-electron oxidized complexes	189
7. EPR and magnetic measurements of the cations.....	192
8. UV-vis-NIR investigation of the cations.....	192
9. Theoretical calculations.....	194
10. Catalysis.....	201
11. Conclusion.....	203
Chapter VI. Conclusion and perspectives	205
1. General conclusion.....	207
2. Perspectives	209
2.1. Nickel complexes	209
2.2. Manganese complexes.....	211
2.3. Chromium complexes	213
2.4. Distorted salen copper complexes.....	215
Chapter VII. Experimental section.....	217
1. Methods	219
1.1. Electron paramagnetic resonance (EPR) spectroscopy	219
1.2. Nuclear magnetic resonance (NMR) spectroscopy	219
1.3. Mass spectrometry (MS)	219
1.4. Microanalysis	219
1.5. Electrochemistry.....	219
1.6. Ultraviolet-visible and near-infrared spectroscopy (UV-vis-NIR)	219
1.7. Crystal structure analysis	220
1.8. Computational details.....	226

1.9. Catalysis (Chapter V)	227
2. Synthesis.....	228
2.1. Chapter II.....	228
2.2. Chapter III	232
2.3. Chapter IV	234
2.4. Chapter V	235
References	240

List of acronyms

AO	Ammonia oxidation	MO	Molecular orbital
BDFE	Bond-dissociation free energy	MS	Mass spectrometry
BSS	Broken-symmetry singlet	NBO	Natural bond order
CT	Charge transfer	NHC	<i>N</i> -heterocyclic carbene
CV	Cyclic voltammetry	NHE	Normal hydrogen electrode
DMF	Dimethylformamide	NIR	Near-infrared
DMSO	Dimethyl sulfoxide	NMR	Nuclear magnetic resonance
DNA	Deoxyribonucleic acid	NPA	Natural population analysis
EDTA	Ethylenediaminetetraacetic acid	Nuc	Nucleophilic substrate
Elec	Electrophilic substrate	OA	Oxidative addition
EPR	Electron paramagnetic resonance	PES	Potential energy surface
ESI	Electrospray ionization	RDE	Rotating disk electrode
EXAFS	Extended X-ray absorption fine structure	RE	Reductive elimination
Fc	Ferrocene	RNR	Ribonucleotide reductase
Fc ⁺	Ferrocenium	ROS	Reactive oxygen species
GC	Gas chromatography	SET	Single electron transfer
GOase	Galactose oxidase	SOPT	Second order perturbation theory
HAT	Hydrogen atom transfer	SOMO	Singly occupied molecular orbital
HFC	Hyperfine coupling constant	TBAP	Tetrabutylammonium perchlorate
HKR	Hydrolytic kinetic resolution	TBHP	<i>tert</i> -butyl hydroperoxide
HOMO	Highest occupied molecular orbital	TEMPO	(2,2,6,6-tetramethylpiperidin-1-yl)oxyl
HRMS	High-resolution mass spectrometry	TEP	Tolman electronic parameter
ILCT	Intraligand charge transfer	THF	Tetrahydrofuran
IR	Infrared	TOF	Turnover frequency
IVCT	Intervalence charge transfer	TON	Turnover number
LLCT	Ligand-to-ligand charge transfer	UV-vis	Ultraviolet-visible
LUMO	Lowest unoccupied molecular orbital	WT	Wild type
MLCT	Metal-to-ligand charge transfer	ZFS	Zero-field splitting

Preface

A wide range of efficient inorganic catalysts routinely used in the laboratory are based on noble, expensive and/or hazardous metals. This stems from the natural propensity of noble metals to transfer two-electrons at a single metal center. However, certain metalloenzymes are able to catalyze polyelectronic reactions with mononuclear abundant metal centers. For this purpose, they utilize pro-radical ligands coordinated to the metal that work in synergy to facilitate multielectron chemistry. This original metal-radical association, found in the active site of galactose oxidase, cytochrome P450 and glyoxal oxidase, is a formidable source of inspiration for the chemists, since it can confer to non-noble metals a “noble character”.

Many structural molecular models have been developed. Salen ligands, bearing two redox-active phenolate centers, have been one of the most popular classes of compound studied for its redox non-innocence. Their ease of synthesis, high modularity and ability to form stable complexes of a wide range of metallic ions, have made salen ligands one of the biggest staples in coordination chemistry as a whole.

On the other hand, *N*-Heterocyclic carbenes have been used in organometallic catalysis to form stable complexes with electron-rich metal ions but have also been reported in high-valent complexes more recently. The ability to accommodate both low and high oxidation states is sought in the development of catalysts to prevent the loss of metal in the turnover between oxidized and reduced states of the complex. We proposed to explore new types of redox-active ligands derived from salens, incorporating strong C-donors instead of iminic donors. We planned to investigate the electronic structure of this new ligand framework and to valorize its properties in challenging chemical transformations.

Chapter I of this thesis will consist of a general introduction on the history, development and most relevant applications of ligand non-innocence. We will generally explore the coordination chemistry of the salen structure in coordination chemistry and specifically detail their use as redox-active ligands in the biomimicry of galactose oxidase. We will also depict the history and features of *N*-heterocyclic carbenes, as well as their impact on organometallic chemistry. We will also highlight the most relevant reports of the association of NHC units in redox-active ligands and discuss the use of molecular complexes in the challenging area of research focused on nitrogen chemistry. We will finally detail the growing development of molecular models for the catalytic fixation of N₂ and the development of metal nitride complexes for N-atom transfer reactions.

Chapter II will present the synthesis of an original redox-active framework bearing two NHC units and two pro-radical phenolate centers. We will then discuss the synthesis and characterization of group 10 metal complexes and the electronic properties of the oxidized species.

Chapter III will focus on the development of manganese complexes in an attempt to form a nitride manganese complex to be used in amination reactions. We will detail different attempts to isolate and characterize the nitride complex and explain its reactive behavior.

Chap IV deals with the synthesis of nitridochromium complexes using the NHC-phenolate chelating framework. We will characterize the neutral complex and present its one-electron

oxidation. We will thoroughly investigate the electronic structure of the oxidized species and rationalize its evolution into different oxidation products.

Chapter V will present a last research area on distorted copper salen complexes. The oxidized complexes will be characterized and ultimately studied as molecular models of galactose oxidase in the aerobic oxidation of non-activated primary alcohols.

Chapter I.

General introduction

1. Redox-active ligands	11
1.1. Radicals	11
1.2. Main families of redox-active ligands	17
1.3. Salen complexes	20
2. Introduction of N-Heterocyclic Carbenes (NHCs)	45
2.1. History and features of NHCs	45
2.2. Preparation.....	49
2.3. Impact of NHCs on organometallic catalysis	54
2.3. Redox-active NHCs.....	56
3. Influence of redox-active ligands on nitrogen chemistry	64
3.1. Nitrogen fixation	64
3.2. Nitrogenase.....	65
3.3. Molecular complexes for catalytic N ₂ reduction	68
3.4. Transition metal nitrides.....	73

1. Redox-active ligands

1.1. Radicals

1.1.1. Discovery of free radicals by Gomberg

The idea of free organic radicals was first introduced in 1900 by Pr. Moses Gomberg.^[1] The groundbreaking discovery shattered the previously held ideas concerning the structure and reactivity of organic molecules. As many great breakthroughs in chemistry, the discovery of a free radical (R^\bullet) was purely serendipitous. Gomberg was initially trying to synthesize the hypothetical highly crowded hexaphenylethane (**Figure I.1**) by treating triphenylmethyl chloride with a metal. As the bright colored resulting solution appeared to be highly reactive towards oxygen and iodine, Gomberg postulated on the existence of the triphenylmethyl radical.

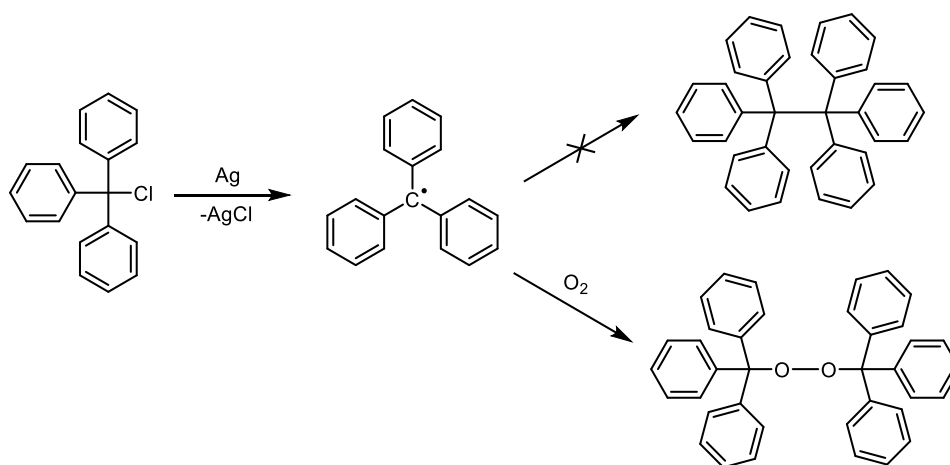


Figure I.1. Synthetic pathway for the discovery of the triphenylmethyl radical.

After having proven the existence of organic free radicals, Gomberg redefined our vision of the tetravalent carbon atom and ushered a new field of research in organic chemistry. In addition, the triphenylmethyl radical was extensively used to help in the development of Electron Paramagnetic Resonance (EPR) spectroscopy that is now one of the core tools used in assessing the electronic structure of a wide panel of chemical compounds.

Radicals are now widely studied and used in global industrial processes, with important use in the development of polymer chemistry, specifically in plastics and rubber manufacture. In addition, radicals have been shown to be ubiquitous in nature. They have proved to be a key component of the active site of certain enzymes but can also be responsible for certain types of cancers or acute illnesses and regulate the aging process in the body.^[2] All of these examples have made radicals a key target in the development of pharmaceuticals and in the field of biochemistry as a whole.

1.1.2. Structure and reactivity of radicals

Covalent bonding in chemistry is based on atoms sharing electrons from their outer electron shells (or valence shell) to form electron doublets, “linking” or bonding the atoms together to form a larger structure. As such, molecules tend to have an even number of electrons, such as was postulated in a larger sense in the “octet theory” of Irving Langmuir in 1919, that evolved over time to what is known today as the famous “octet rule”.^[3] However as one notable exception, free radicals are species that present one or more unpaired valence electrons. While being intrinsically stable from a thermodynamic standpoint, the presence of such unpaired electrons usually tends to make free radicals react readily in a number of ways (**Figure I.2**): reacting with themselves to dimerize (**A**), adding to another molecule (**B**) or finally giving or taking an electron from another molecule (**C**).

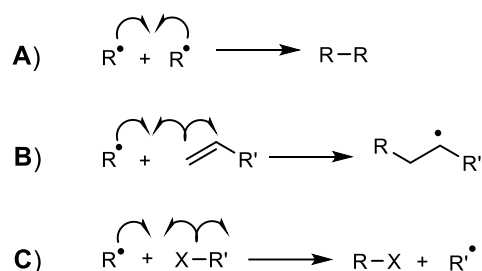


Figure I.2. Representations of the most common reactivities of free radicals.

While dimerization of a free radical shuts off further radical reactivity, reaction with another molecule leads to formation of new radical species, developing a chain reaction at the core of a large number of polymerization reactions. Such processes usually involve radicals with only one unpaired electron but reports of compounds with two or three single electrons (biradicals, triradicals, etc) have been developed as we will discuss later in this introduction.

1.1.3. History and applications of radicals in chemistry

The existence of free radicals, in the discovery of the triphenylmethyl (or trityl) radical, was questioned for about a decade before being admitted by the scientific community. They remained odd curiosities without much further developments in the field until reports in 1929 by Friedrich Paneth and Wilhelm Hofeditz of a transitory methyl $\bullet\text{CH}_3$ radical.^[4] This finding proved that radicals could be involved without our foresight in a wide panel of chemical reactions.

Their use as organic reagents was first reported by Morris Kharasch and Franck Mayo in radical addition reactions^[5] and was the beginning of the development of synthetic materials using radical polymerization.

Compared to conventional polymerization such as used in the production of nylon, radical polymerization was more versatile. It is able to handle harsher reaction conditions and to be tolerant of chemical impurities. It also proved to be capable of valorizing a wide panel of monomers. Free radicals are currently involved in the production of approximately half of the polymers that we use in everyday life, from paints and adhesives to plastics in food packaging and more.

1.1.4. Radicals in biology

Due to their reactive nature, free radicals were generally seen as toxic to living systems. A canonical example is the hydroxyl radical $\cdot\text{OH}$ that is one of the most potent reactive oxygen species (ROS).^[2] The hydroxyl radical readily reacts with lipids in cell membranes, triggering a chain reaction of lipid peroxidation, causing membrane damage. $\cdot\text{OH}$ is also known to add to and alter sugar groups and DNA bases, inducing the denaturation of the double-helix structure that can lead to mutations and cell death. As such, ROS need to be swiftly eliminated by the organism, with even more acute control for hydroxyl radicals.

However, the idea of the biological incompatibility of radicals was fundamentally altered in the light of a series of biochemical reports that demonstrated a wide panel of remarkably well controlled metabolic and biosynthetic reactions involving radical intermediate species. Since the 1970s, it has been established that stable radicals exist in enzymes and that they are critical to many biological processes. For example, ribonucleotide reductases (RNRs), essential for the synthesis of DNA, present cysteinyl radicals in RNR class I and II (**Figure I.3.B**),^[6] or glycyl species in class III anaerobic RNR (**Figure I.3.A**).^[7] Tryptophanyl radicals (**Figure I.3.C**) have also been extensively studied and can be found in cytochrome C peroxidases.^[8]

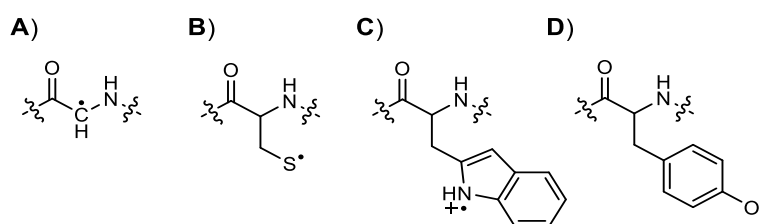


Figure I.3. Radicals present on amino acid chains: glycyl (A), cysteinyl (B), tryptophanyl (C) and tyrosinyl (D).

As another example, the cytochrome P450 enzyme superfamily is one of the most well-known proteins presenting a radical in its active site. Different forms of cytochrome P450 have been discovered in all eukaryotic organisms, animals, plants and fungi and some types of prokaryotes. In the human body, cytochrome P450 was estimated to be responsible for the phase I metabolism of 75% of known pharmaceuticals.^[9]

This family of hemoproteins catalyzes hydroxylation of hydrocarbons by utilizing the successive formation of radicals, generally known as the radical rebound mechanism.^[10] In the catalytic cycle of the enzyme (**Figure I.4.A**), an iron(IV) oxo species with a porphyrinyl radical $[(\text{Por})^{\bullet+}\text{Fe}^{\text{IV}}=\text{O}]$ acts as the hydroxylating species by hydrogen abstraction on the hydrocarbon substrate, generating a carbon radical intermediate ($\text{R-H} \rightarrow \text{R}^{\bullet}$) that in turn recombines with the hydroxyl to form the oxidized product ($\text{R}^{\bullet} \rightarrow \text{R-OH}$).

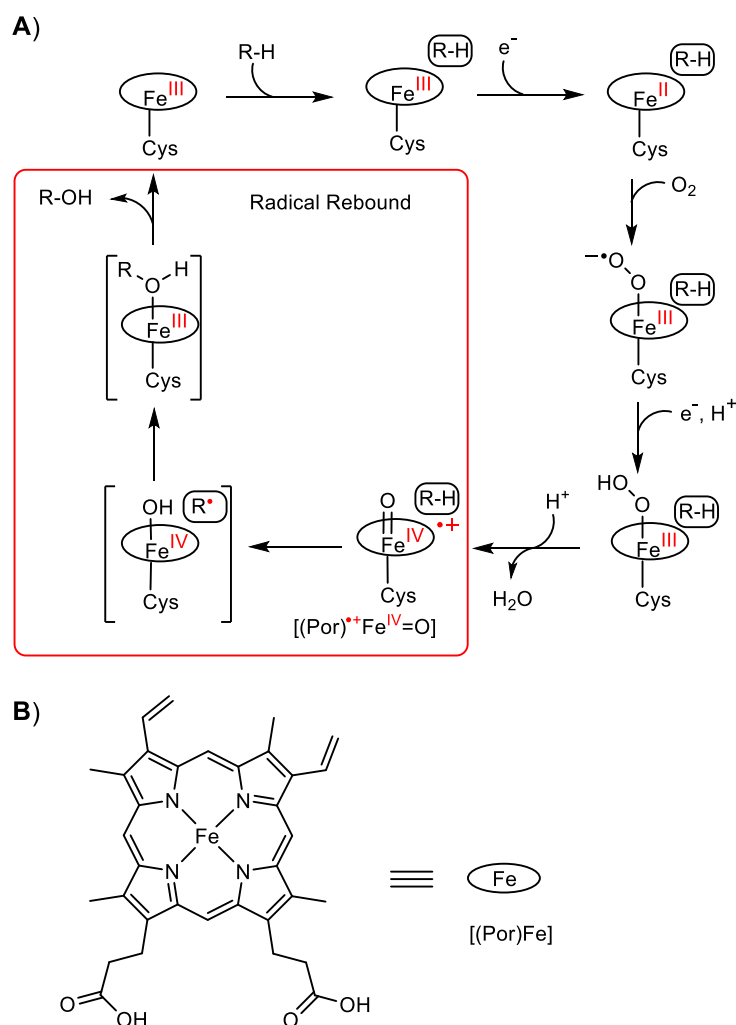


Figure I.4. Catalytic cycle of the cytochrome P450 hydroxylation of hydrocarbons, with the radical rebound mechanism circled in red (**A**). Structure of the protoporphyrin ring with bound iron metal center for the type-b heme (**B**).

In 1972, Reichard *et al.* showed that the phenol moiety in tyrosine amino acids could be mono-oxidized in some proteins to afford tyrosinyl radicals.^[11] They are known today to represent the largest assembly of biological free radicals and are encountered in a number of different proteins such as in photosystem II, galactose oxidase, glyoxal oxidase and more.^[12]

A decisive discovery in the understanding of biological radicals was the concerted effort to determine the structure of the active site of galactose oxidase (GOase) in the 1990s.^[13–15] In 1999, Whittaker *et al.* found that a tyrosinyl radical was directly coordinated to the mononuclear copper in glyoxal oxidase.^[16] GOase was later found to bear a similar tyrosinyl radical bound to the metal center of the enzyme. These discoveries shed new light on the coordination of the tyrosinyl radicals and their impact on enzymatic reactivity.

GOase is a fungal enzyme comprised of 639 amino acids (68.5 kDa) secreted by *Fusarium oxysporum*. It is the best-characterized member of a family of enzymes known as radical-copper oxidases that includes another fungal enzyme, glyoxal oxidase.^[17]

GOase catalyzes the aerobic two-electron oxidation of a large panel of primary alcohols (RCH_2OH) like sugars and polysaccharides, to their corresponding aldehydes (RCHO). The oxidation of alcohols is coupled with reduction of molecular oxygen to hydrogen peroxide in a ping-pong turnover mechanism (**Figure I.5**).

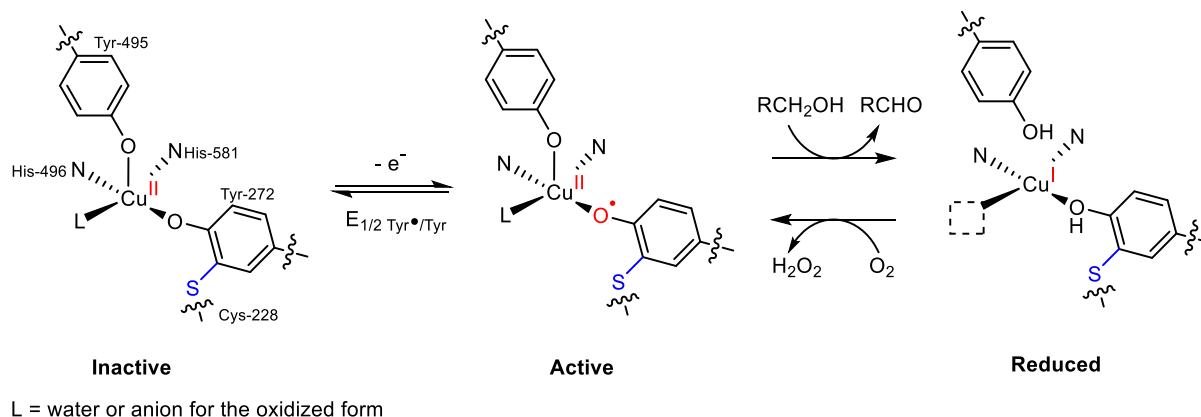


Figure I.5. Half-reactions catalyzed by GOase with the structure of the different forms of the active site of GOase. A unique Cys-Tyr cross-linkage in the active site of the enzyme is highlighted in blue.

The active site presents four amino acid side chains (Tyr-272, Tyr-495, His-496, and His-581) folded from remote regions of the polypeptide chain of the protein. They directly coordinate a mononuclear Cu center also bound by an exogenous ligand (L) to form a distorted five-coordinate square pyramidal metal complex (**Figure I.5**). The axial Tyr-495 acts as a base to activate the primary alcohol substrate by deprotonation (**Figure I.6.A**) before oxidation of the alkoxy ligand. The oxidation occurs by a combination of a single electron transfer (SET) to the Cu center and a hydrogen atom transfer (HAT) to the equatorial Tyr-272 radical. Through spectroscopic characterization and isotopic labeling experiments, the mechanism was determined to first involve the HAT as a rate-limiting step before reduction of the Cu center (**Figure I.6.B,C**).^[13] While the oxidation of the primary alcohols has been thoroughly explored, the distinct mechanism for the reduction of molecular oxygen remains obscure.

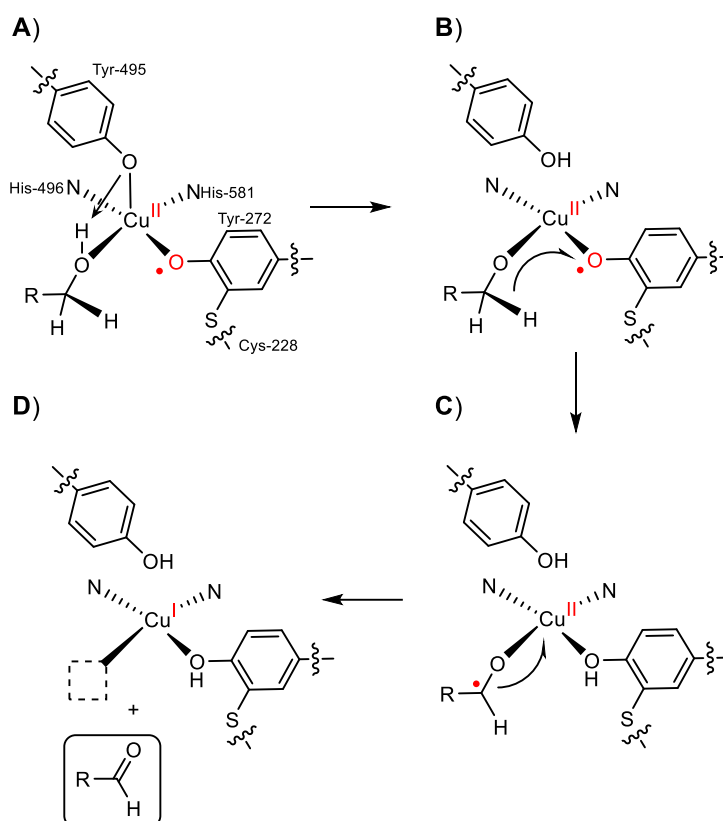


Figure I.6. Mechanistic steps in the oxidation of primary alcohols in GOase: Deprotonation of the alcohol substrate (**A**), hydrogen atom transfer, HAT (**B**), single electron transfer, SET (**C**) and release of the aldehyde product (**D**).

Another striking structural feature of the active site of the enzyme is a modified amino acid residue obtained from cross-linkage at the ortho position of Tyr-272 to the sulfur atom of the cysteine Cys-228 (**Figure I.5**). It has been shown that the post-translational modification likely occurs spontaneously in the presence of copper and dioxygen without any other cofactors.^[18] This cross-link is an essential feature of the enzyme for its redox activity as it is expected to lower its oxidation potential for activation to the active Cu(II)-tyrosyl form (**Figure I.5**). As we will discuss later, a number of groups have developed Cu(II)-phenolate complexes that can be oxidized to persistent Cu(II)-phenoxyl species. In those models, the introduction of a thioether substituent on the phenolate ring, mimicking the cross-link in wild type (WT) GOase, decreases the redox potential of the phenolate/phenoxyl couple by 200 to 500 mV.^[19–22] This behavior on model molecular compounds correlated nicely with the difference of redox potential observed in WT GOase ($E_{1/2} = +0.40$ V vs NHE) compared to a regular tyrosyl radical (+0.90 V vs NHE).

1.2. Main families of redox-active ligands

The use of metals to enhance the reactivity of a chemical reaction dates as far back as the 19th century. One of the earliest examples was the use, in a patent dating from 1831, of finely divided platinum in the synthesis of sulfuric acid.^[23] An overwhelming majority of chemicals manufactured today have relied on the use of metal catalysts in at least one step of their synthesis. Most catalysts used in research or in industrial processes are based on scarce and expensive “noble metals”. Rhodium, iridium and platinum are more valued for their propensity to undergo two electron redox processes, required for most bond making or breaking events such as oxidative addition (OA) or reductive elimination (RE). Due to their limited access and the continuous rise in the price of those metals, the development of catalysts from base metals, such as copper, iron or cobalt, have undergone a quick expansion in the past decades. Still, abundant metals usually undergo one electron processes. Two successive one electron redox changes could be seen as an adapted alternative to replicate two electron reactions. However, this process would afford radical intermediates after the first electron transfer, greatly increasing the potential for undesired side reactions to poison the catalyst. To mimic the properties of noble metals, chemists have taken inspiration from Nature. As shown previously, some metalloenzymes, such as Cytochrome P450 and Galactose Oxidase, are able to use radicals in their active site to contribute to the reactivity of the metal center. In chemical models, ligands able to act as redox centers are known as redox “active”. Redox activity of ligands in inorganic complexes was first suspected by Jørgenson in 1966. At the time, he classified ligands as ‘innocent’ or ‘non-innocent’ based on whether the oxidation state of the metal center could be determined.^[24] From simple energetic considerations, the ability of the ligand to participate in the redox activity of the complex depends on the relative ordering of metal (M) versus ligand (L) frontier orbitals (**Figure I.7**).

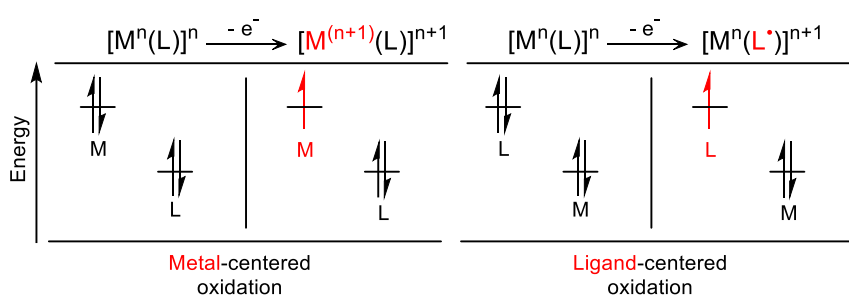


Figure I.7. Ordering of frontier orbitals for ligand-centered redox processes.

Redox-active ligands can act in several different ways to influence the overall reactivity and selectivity of a catalyst by tuning the Lewis acidity of the metal, acting as electron reservoirs for electron transfer reactions, or even directly forming or breaking bonds with substrates. It is important to note that most of the reactions involving redox-active ligands are governed by a mix of these different effects as they are intricately linked together.

1.2.1. Tuning of the Lewis acidity of the metal

The overall electronic structure of the catalyst modifies substrate bonding and activation through the Lewis acidity of the metal center. In conventional ligand design approaches, modification of the electronic structure is achieved by modulation of electron donating or withdrawing groups on the ligand. In the case of redox-active ligands, their oxidation state can directly impact the Lewis acidity of the metal without changing the steric environment of the complex. Such design was recently utilized in oxidation of H_2 by an iridium complex (**Figure I.8**).^[25]

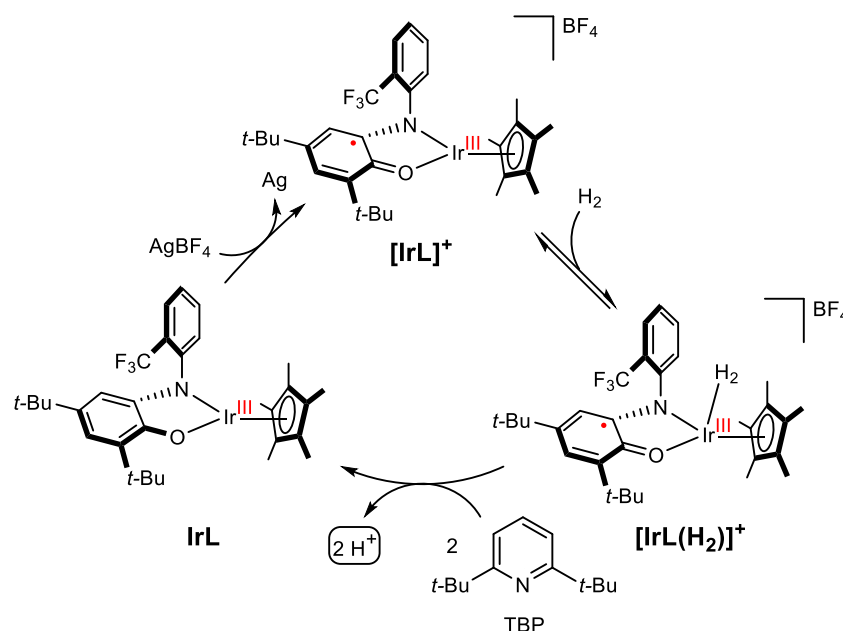


Figure I.8. Oxidation of H_2 by an Ir(III) catalyst utilizing a redox active ligand.

By oxidation of the ligand, the electronic hole on the organic framework in complex **[IrL]⁺** leads to an increased Lewis acidity of the metal center. The increased Lewis acidity of the Ir(III) ion allows H_2 to be bound and activated when it could not with the more electron rich complex **IrL**. The bound H_2 in **[IrL(H₂)]⁺** is subsequently oxidized to protons with the help of a non-coordinating base (2,6-di-*tert*-butyl-pyridine, TBP). As mentioned before, the ligand also acts as an electron reservoir in the reaction. In this case, electron transfer occurs on the ligand framework, allowing the iridium center to remain in a stable (+III) oxidation state.

1.2.2. Reservoirs in electron transfer reactions

The most prevalent use of redox active ligands is their ability to act as electron storage moieties to catalyze polyelectronic reactions. Binuclear ruthenium quinone catalysts have been utilized in water oxidation to accommodate the four electrons involved in the reaction (**Figure I.9.A**). Initially assumed to involve two $\text{Ru}^{\text{III}}/\text{Ru}^{\text{II}}$ and two ligand-centered quinone/semiquinone redox couples, further investigation suggested that all four oxidation steps might be centered on the quinoid ligands with a catalytic cycle involving exclusively Ru(II) species (**Figure I.9.B,C**).

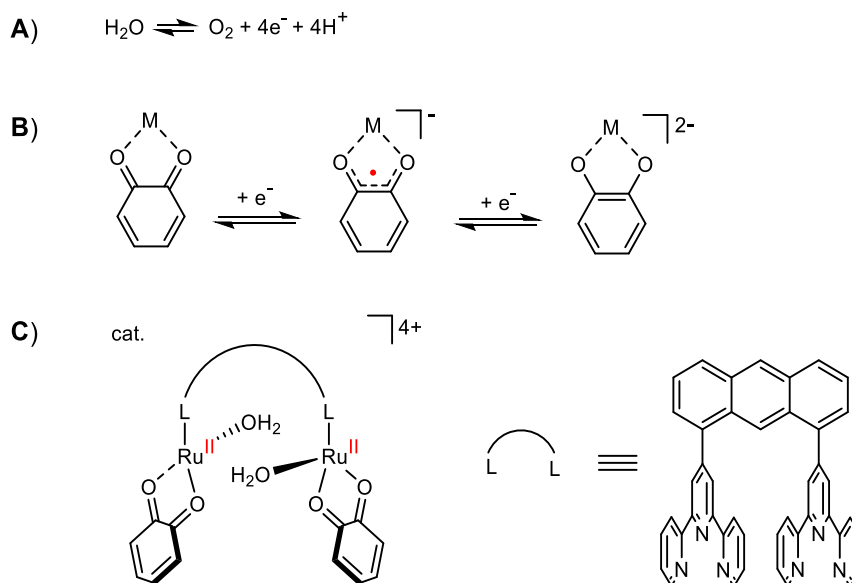


Figure I.9. Water oxidation by a binuclear Ru(II)-quinone catalyst: Water oxidation reaction (A), Structures of the different redox states of quinones bound to a metal (B) and structure of the Ruthenium catalyst (C).

One of the most elegant uses of a ligand-centered redox-activity in catalysis was highlighted by Chirik on challenging C-C coupling reactions. Using a pyridine-bis-imine framework, he developed an iron catalyst for the $[2\pi + 2\pi]$ cycloaddition of dienes.^[26]

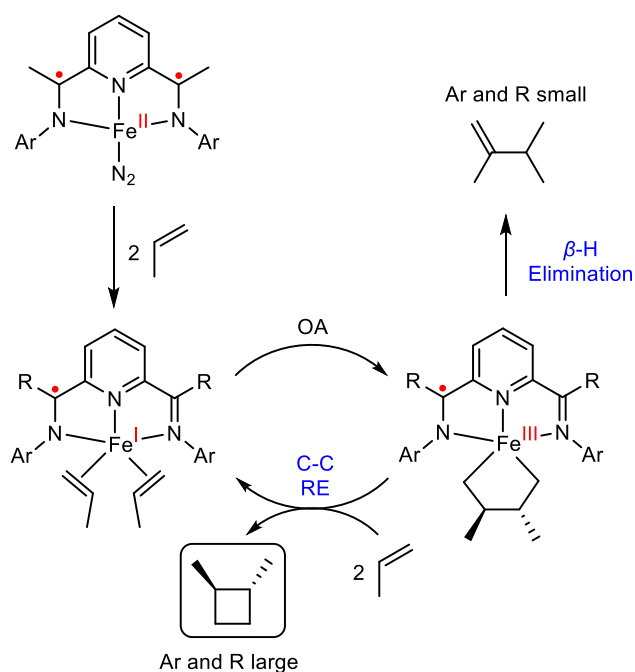


Figure I.10. Mechanism for the catalytic cyclobutane formation of propene by Chirik *et al.*

He later expanded the substrate scope to cyclobutane formation of unactivated alkenes (**Figure I.10**), even accessing allylic cyclobutanes.^[27] Additionally, the catalyst was further refined by ligand design to favor C-C reductive elimination over parasitic β -H elimination pathways by increasing steric hindrance at the coordination site (**Figure I.10**). Chirik and Sylvester also reported the hydrogen mediated reductive cyclization of 1,6-dienes and enynes.^[28]

1.2.3. Chemical transformations on the redox-active ligand

Some redox-active ligands can directly take part in the formation or breaking of bonds with substrates. A prime example would be the recent use of a nickel-dithiolene complex for purification of ethylene from gas mixtures. The ethylene gas is able to bind reversibly to the sulfur atoms in the dithiolene ligands depending on their redox state (**Figure I.11**).^[29–31] This ethylene capture strategy, that is likely involving thiyl radical intermediates, was also expanded on a rhenium complex with thiophosphine ligands.^[32,33]

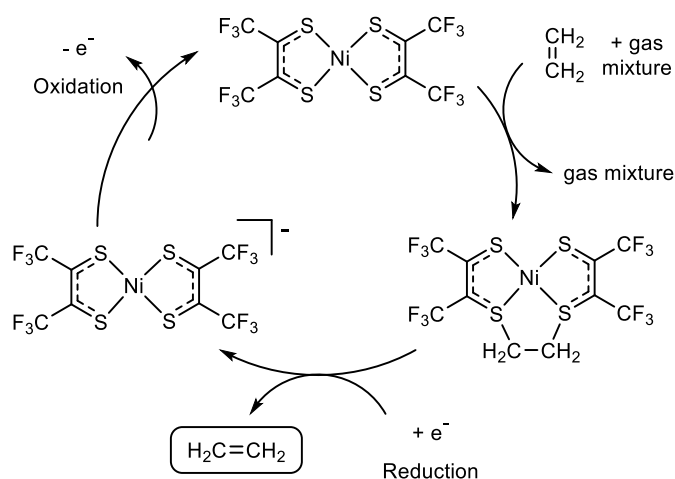


Figure I.11. Purification of ethylene gas by a Nickel complex utilizing a redox-active ligand.

GOase is another example of a redox-active ligand directly taking part in the bond breaking process on the substrates. As discussed before, the enzyme catalyzes the two-electron oxidation of primary alcohols by using a tyrosinyl radical as a redox cofactor to its mononuclear copper center. This reaction was shown to involve a H-atom abstraction from the tyrosinyl radical as the rate-limiting step in the catalytic cycle (**Figure I.6.B**). In order to better understand the interaction between the tyrosinyl radical and the Cu center in GOase, a great variety of copper-phenoxyl complexes were designed. Among others, the salen platform proved to be highly versatile and underwent significant development. We will focus in the next section on this specific family of complexes.

1.3. Salen complexes

Salen ligands are some of the most prominent ligands featuring redox-active phenolates. They are a fundamental class of ligands in coordination chemistry, now known for close to a century. They have been studied extensively with more than 1700 results using “salen complexes” keywords in Scifinder with more than 2500 compounds synthesized. Interest in these compounds intensified in the 1990s when the Jacobsen and Katsuki groups discovered that the enantioselective epoxidation of unfunctionalized alkenes could be catalyzed by chiral Mn(salen) complexes.^[34] Since that time, many reactions of extremely varied nature catalyzed by salen complexes have been described. This has greatly contributed to the increase in the number of these compounds in the literature. Since the elucidation of the electronic structure of the active form of GOase in the 1990s, they have also become one of the main ligand classes used to develop molecular models of the enzyme.

1.3.1. Structure and main applications

The first salen-type Schiff base complexes were synthesized by Pfeiffer in 1933 by a metal-assisted condensation of salicylaldehyde on an ethane-1,2-diamine, affording the *N,N'*-bis(salicylaldehyde)ethylenediimine ligand backbone.^[35] While this type of one-pot reaction of the metal favors formation of the diimine of the ligand backbone from the template effect, the ligands are generally prepared by themselves by condensation of two equivalents of salicylaldehyde derivatives with a diamine precursor (**Figure I.12.A**), usually in a polar protic solvent (MeOH/EtOH) and are easily isolated by precipitation.

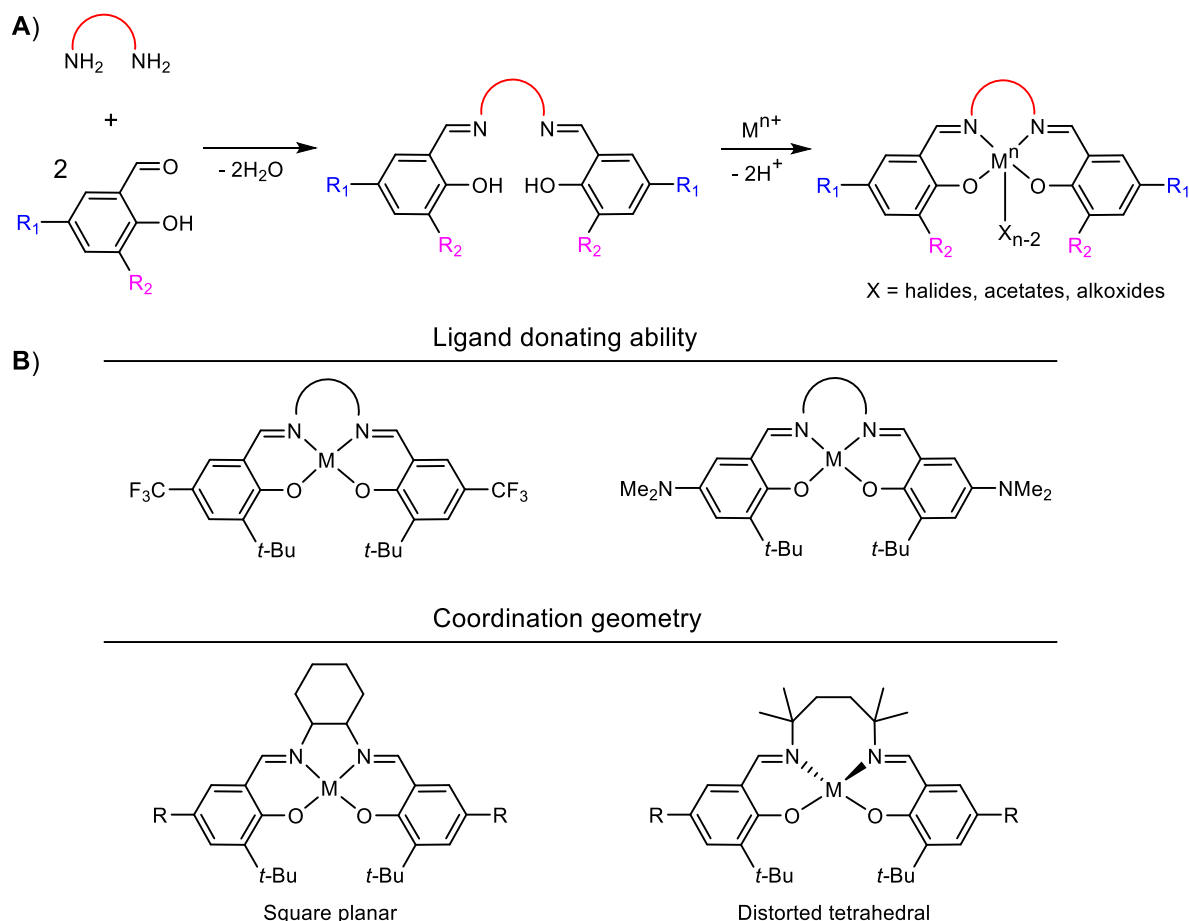


Figure I.12. Synthesis of salen ligands and metallo-salen complexes with highlights on the main modulation sites for the metal geometry (red) electronic properties (blue, purple) and steric protection (purple) (**A**). Examples of electronic and structural modulations of the salen framework (**B**).

Chiral versions of the ligands have been reported for different enantioselective reactions by using chiral diamine bridges such as in the widely popular *N,N'*-cyclohexanediamine ligand (**Figure I.13**, **Figure I.14**). Unsymmetrical ligands have also been developed by successively using one equivalent of two different salicylaldehyde derivatives. The salen framework presents a rich versatility to modify the geometrical properties and the electronic structure of the complexes (**Figure I.12.B**). Additionally, their ability to accommodate a wide number of metal ions has made salen complexes a true cornerstone in coordination chemistry.

Metallo-salen complexes are ubiquitous in a variety of research fields. One of their major uses is in enantioselective catalysis. Enantioselective reactions have long been a major struggle in organic synthesis, and enantiomers can display drastically different behaviors, for example in the intricate interactions of pharmaceuticals in the human body. The possible chiral environment of salen ligands have been valorized with different metal ions for a wide range of reactions (**Table I.1**) that keep expanding with frequent new reports. Additionally, a number of non-enantioselective reactions have also used the stability and versatility of metallo-salen compounds for racemic reactions or reactions on achiral compounds.

Table I.1. Reactions of metallo-salen catalysts with detailed metallic ions used in each case.

<p>Epoxide opening^[36]</p>	<p>Sulfoxidation^[37]</p>
<p>Hetero Dies-Alder^[38]</p>	<p>Sulfimide^[39]</p>
<p>Baeyer-Villiger^[40]</p>	<p>Alkene aziridination^[41]</p>
<p>Carbonyls 1,2-additions^[42–44]</p>	<p>Olefin cyclopropanation^[45,46]</p>
<p>Strecker reaction^[47]</p>	

The rise of interest in the now huge field of metallo-salen catalysts can be traced back to the ground-breaking report by Jacobsen of enantioselective epoxidations catalyzed by a chiral manganese salen complex.^[34]

While enantioselective epoxidations were already developed by Sharpless on allylic alcohols, the scope of the reaction was limited to simple alkenes. To bypass this issue, Jacobsen was able to use the stereogenic environment of the chiral *N,N'*-cyclohexanediamine ligand with a Mn(III) metal center.^[34] Bleach (NaOCl) was used as a readily available stoichiometric oxygen source for the reaction in dichloromethane. The catalytic cycle proved to be a ping-pong mechanism between the starting Mn(III) catalyst and a high-valent Mn(V)-oxo complex (**Figure I.13**).^[48] The axial ligand (L) proved to have slight effects on enantioselectivity, reaction rate and product yield.^[48]

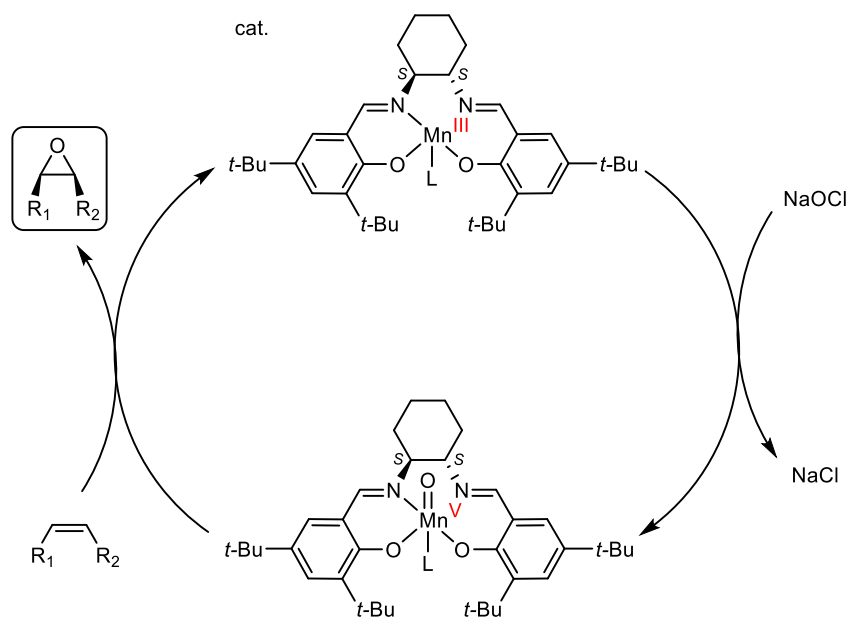
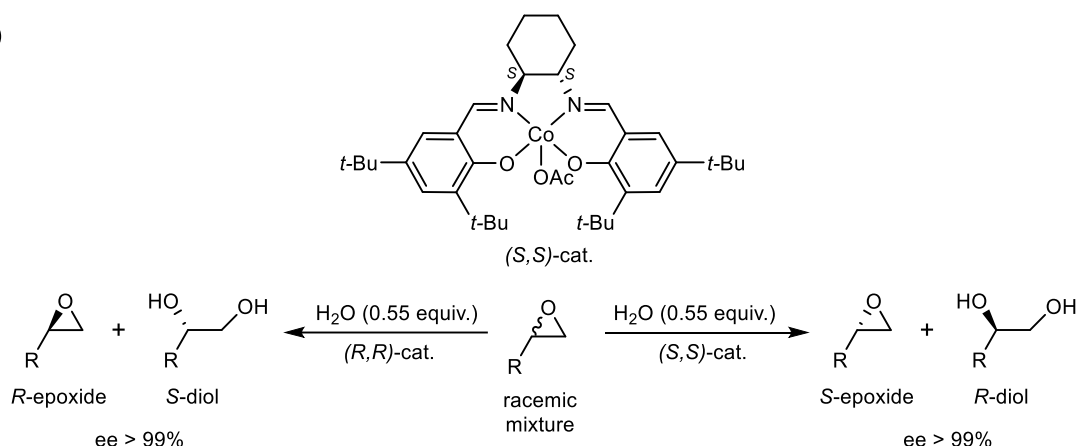


Figure I.13. Catalytic cycle of the Jacobsen epoxidation reaction.^[48]

Still to this day, the Jacobsen epoxidation reaction is used in the large scale synthesis of key pharmaceuticals^[49] such as Indinavir,^[50–52] an HIV protease inhibitor, or CDP840,^[53] a Phosphodiesterase IV inhibitor used in autoimmune diseases such as Alzheimer's disease, psoriasis, and rheumatoid arthritis.

Despite the breakthrough of the Jacobsen epoxidation methodology, this is not the major industrial process using metallo-salen catalysts. This honor belongs to another process developed by Jacobsen involving the same salen ligand: the hydrolytic kinetic resolution (HKR) method, discovered in 1997.^[54] Enantioselective epoxidation of terminal alkenes is still not reachable but the issue was resolved by enantiomeric enrichment of a racemic mixture using a cobalt-salen complex (**Figure I.14.A**). The electronic structure of the active catalyst has been questioned as either metal centered Co^{III}-salen or ligand-centered Co^{II}-(salen^{•+}) (**Figure I.14.B**) according to different reports with varying axial ligands.^[55–57]

A)



B)

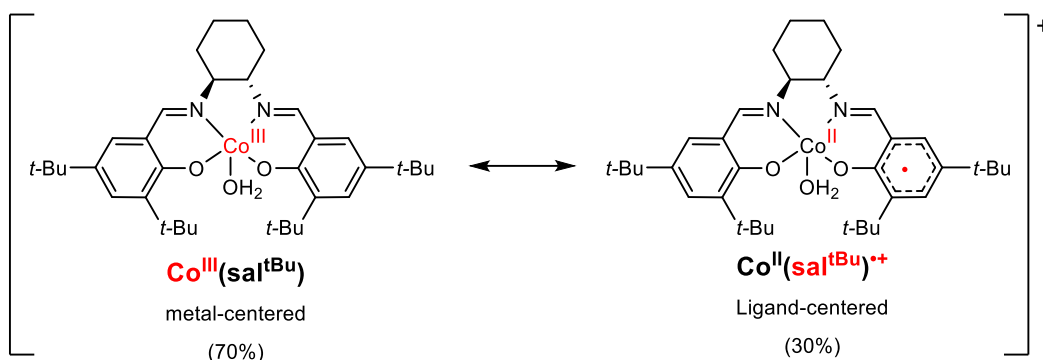


Figure I.14. Jacobsen hydrolytic kinetic resolution method^[54] (A) and canonical structures of the active form of the catalyst, with electronic contributions of each structure extracted from theoretical calculations.^[56]

This reaction has been applied in large scale industrial processes and is involved in the synthesis of different commercially available chiral synthons such as propylene oxide and propylene glycol^[58] or pharmaceuticals such as β -adrenergic blocking agents (commonly known as *beta*-blockers).^[59]

1.3.2. Redox-activity of the phenolate ring

The term "phenoxyl" radical was first introduced in 1914 by Pummerer to denote species involved in the oxidation of naphthols and phenantholes.^[60] However it is not until quite later in 1953, that the first stable phenoxyl radical was reported by Cook and Müller with the 2,4,6-tri-*tert*-butylphenoxyl species.^[61,62] Their characterization remained pretty challenging and the first EPR characterization of 2,4,6-tri-*tert*-butylphenoxyl was only reported in 1967.^[63] The first crystallographic structure of a phenoxyl radical was reported shortly after by Williams in 1968.^[64] However, it was only after four decades that a high-resolution X-ray crystal structure of the tri-*tert*-butylphenoxyl radical was published (in 2008).^[65] The difficulty to detect and characterize phenoxyl radicals was due to their general instability. Therefore, strategies were developed to increase their stability so that they could be analyzed by conventional techniques.

The stabilization of phenoxyl radicals relies on their electronic structure. The oxidation locus is generally represented as localized on the oxygen atom, with delocalization over the phenyl aromatic ring (**Figure I.15.A**). A significant portion of the electron density is located on the *ortho* and *para* phenolic positions hence substituents need to be introduced to protect those positions and prevent radical dimerization (**Figure I.2.A**).

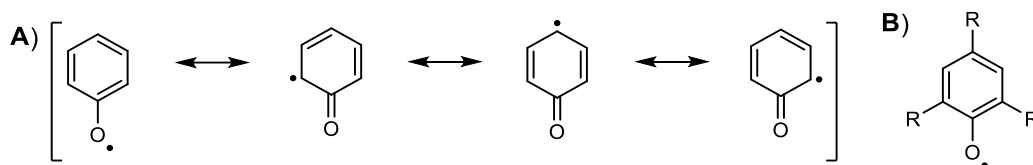


Figure I.15. Resonance forms of the phenoxyl radicals (**A**) and strategic *ortho* and *para* substitutions for their stabilization (**B**).

Substituents were also chosen to compensate the electronic deficiency of the radical. For this purpose, a number of mesomeric and/ or inductive donor groups were used such as heteroatomic substituents (-OR, -NR₂, -SR) or bulky alkyl substituents. The *tert*-butyl group is widely represented as it can be easily introduced from a large variety of organic synthon precursors in the ligand synthesis. In general, the more donating a substituent is, the more stable the radical is, even if some counterexamples are known.

- Electrochemistry

Phenoxyl radicals are obtained from oxidation of a phenol precursor. Oxidation of the free tri-*tert*-butylphenol occurs at a high potential of 1.07 V compared to the Ferrocenium/Ferrocene (Fc⁺/Fc) standard.^[66] This potential is drastically reduced to -0.68 V in the presence of a strong base such as NaOH.^[67] This is easily explained when considering that a deprotonated phenolate (pK_a = 12.2 in water for tri-*tert*-butylphenol) is more electron rich and therefore easier to oxidize.

Moreover, oxidation of a phenol involves additional chemical steps when compared to the straightforward oxidation of a phenolate (**Figure I.16.A**). The first step is the electron loss to afford a cationic phenoxyl radical. However, such species have drastically low pK_a values (pK_a ≈ -9.5 for tri-*tert*-butylphenol cationic radical)^[66] and can only be observed in strongly acidic media (12M H₂SO₄). They readily deprotonate to give the neutral phenoxyl radical. The radical is then reoxidized to a phenoxonium ion as it has a lower second oxidation potential ($E_{1/2}^2$) than the starting phenol ($E_{1/2}^3$). Overall, the general mechanism for oxidation of phenols implies two electron oxidations and one proton transfer reaction (**Figure I.16.B**).

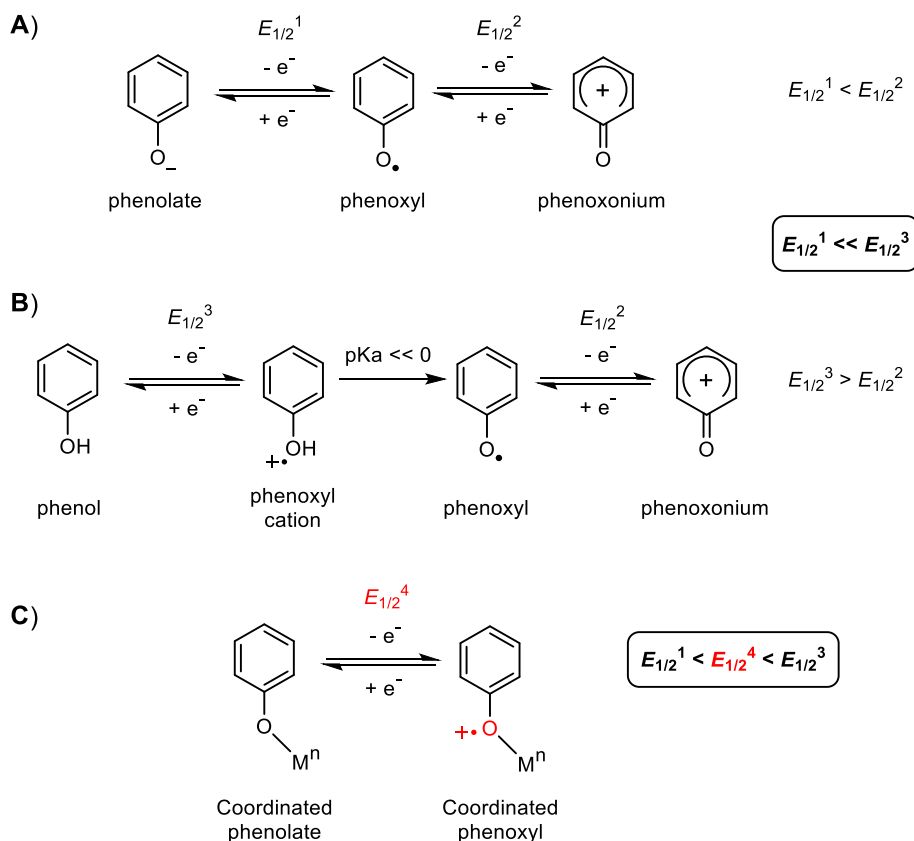


Figure I.16. Mechanistic steps for oxidation of a phenolate (**A**) a phenol (**B**) and a coordinated phenol (**C**).

The Lewis acidity of the metal drastically lowers the pKa of the phenols leading to easily reachable phenolate-metal complexes which are quite common in literature. The metal strongly influences the electron density of the phenolate moiety resulting in oxidation potentials between that of phenol and free phenolates. Most importantly, the oxidation of phenolates coordinated to metals occur through a simple electron transfer process (**Figure I.16.C**) distinct from the more intricate oxidation of uncoordinated phenols (**Figure I.16.B**).

- Electron paramagnetic resonance (EPR)

Phenoxyl radicals are paramagnetic ($S = 1/2$) species which can easily be characterized by EPR. The electronic structure of the radicals can be elucidated by the g tensor and the hyperfine coupling constants. Phenoxyl radicals usually display an isotropic signal at g values around 2.003. However, coordination to a metal center can strongly impact its spectroscopic signature. While remaining in a doublet state ($S = 1/2$) when coordinated to a diamagnetic metal center, partial delocalization of the spin to the metal can lead to anisotropic systems and a shifted g value. Additionally, in the presence of a paramagnetic metal center, a magnetic coupling can be observed between the spin of the organic radical and the spin of the metal. Additional tools such as magnetic measurements or theoretical calculations such as density functional theory (DFT) are usually required to probe the ground state of the complex.

The association of redox-active phenolates with redox active metals thus complicates the assessment of the correct electronic structure in oxidized salen species. In that case, the oxidation can either be centered on the metal ($[M^{(n+1)}\text{-phenolate}]^+$) or on the ligand backbone to afford a phenoxyl radical ($[M^{(n)}\text{-phenoxyl}]^{+\bullet}$) (**Figure I.17**).

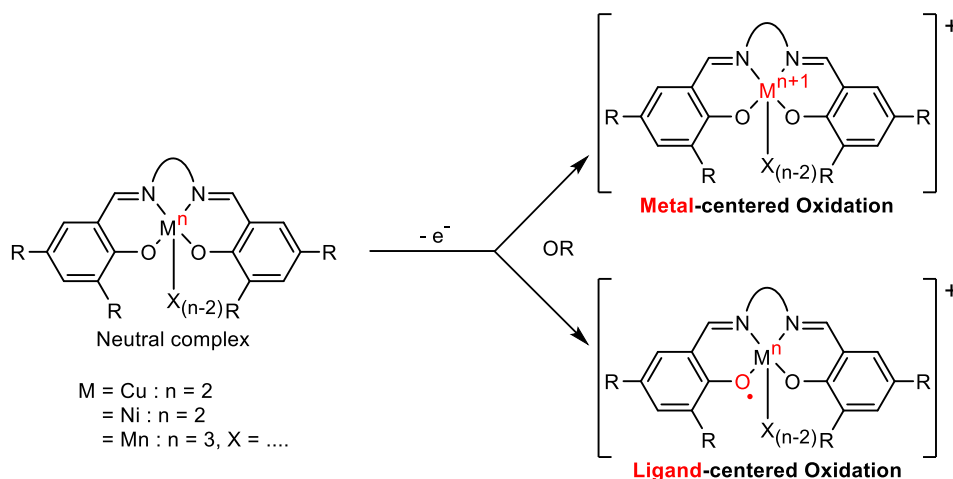


Figure I.17. Oxidation centers in metallo-salen complexes.

Pro-radical behavior has been shown on the salen ligands of a wide range of first-row transition metal complexes. We will be focusing on metals of interest for this thesis, namely copper, nickel and manganese complexes. No ligand-centered redox activity has been reported for chromium salen complexes and they will therefore not be detailed in this introduction.

1.3.3. Copper complexes as molecular models of GOase

- Biomimicry of GOase

Copper is a redox-active metal generally found in oxidation states (+I) d^{10} (+II) d^9 or (+III) d^8 . The three different oxidation states have been relevant in the biomimicry of the GOase enzyme. GOase presents a ping pong mechanism with two different redox-states. The oxidized form is active towards oxidation of primary alcohols and includes a Cu(II) mononuclear center with a coordinated tyrosinyl radical. The reduced form of the enzyme includes a Cu(I) center and is reactivated through reduction of molecular oxygen (see section 1.1.4., **Figure I.18**).

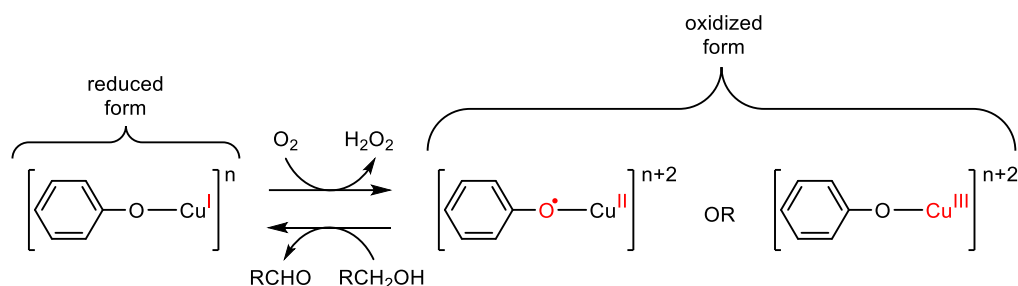


Figure I.18. Relevant forms for the biomimicry of GOase with copper-phenolate models.

Very few molecular models of the Cu(I) reduced form of GOase have been developed. Stack and coworkers postulated that the stabilization of the Cu(I) reduced state was a key factor to improve the activity of copper models of GOase for aerobic alcohol oxidation.^[68] As a d^{10} metal ion, Cu(I) complexes favor tetrahedral coordination as a more stable geometry by reducing steric clash between ligands. Hence, the first reports of copper-salen catalytic models were developed with a distorted metal coordination. For that purpose, Stack used a sterically hindered binaphthyl spacer to enforce a non-square planar coordination opposed to the planar geometry generally observed in salen complexes.^[68,69] Nevertheless and still to this day, no reduced copper(I)-salen complexes have been fully characterized. One of the issues of salen ligands for this purpose is the presence of two anionic phenolate ligands that are poorly suited to stabilize the copper(I) ion. As another model, the Tolman group used a series of ligands bearing one phenol arm attached to a triazole macrocycle. Using the distorted environment of the ligands and their softer coordination properties, they were able to isolate and crystalize Cu(I)-phenolate complexes (**Figure I.19**) and study its reactivity towards oxygen.^[70]

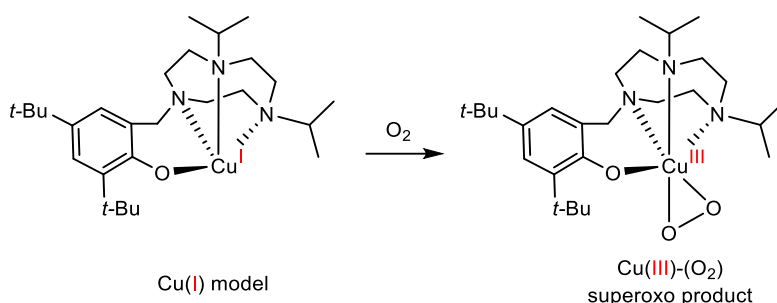


Figure I.19. Cu(I) complex and its reactivity with oxygen as a molecular model of GOase reduced state.^[70]

They showed the formation of a side-on superoxo adduct that was proposed as a possible intermediate in the GOase reduction of molecular oxygen. Nevertheless, they were not able to generate a Cu(II)-phenoxyl complex as a final product to mimic the active oxidized state of the enzyme.

Molecular models for the oxidized form of GOase have been more extensively investigated. Historically, because the GOase oxidized active form was EPR silent, its electronic structure was originally thought to be a Cu(III) high-valent center (**Figure I.18**).^[71] Hence an effort was made in the 1980s to develop molecular models to stabilize Cu(III) ion centers. The copper(III) d^8 ion is suited by compact square planar geometries^[72] and requires anionic ligands to stabilize its high-valent state. Treco and coworkers reported a series of copper complexes stabilized by tetradentate ligands bearing two anionic amidates.^[73] Two ligands with coordinating phenolates were developed (**Figure I.20**) and can be seen as an analogue structure of the salen ligand framework. They formally presented the complexes with high-valent Cu(III) centers, stabilized by the strong donating properties of the polyanionic ligands.

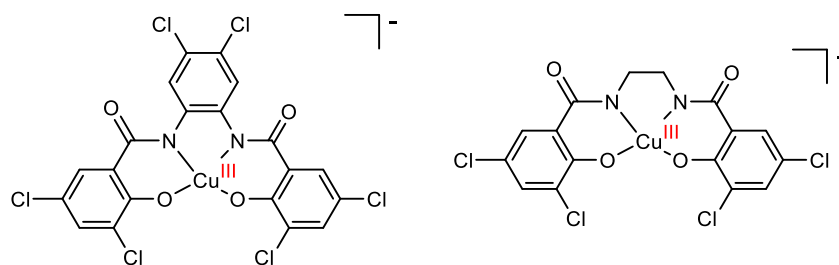


Figure I.20. Cu(III)-phenolate complexes stabilized by chelation of anionic amidates as reported by Treco.^[73]

Copper(II) d^9 ions are stabilized in similar square planar geometries to copper(III) centers. Hence, salen ligand systems appear suitable to stabilize both Cu(III)-phenolate or Cu(II)-phenoxyl valence tautomers (**Figure I.18**). However the dianionic nature of the salen ligand compared to the tetraanionic amidate analogue reported by Treco was thought to be a limitation to reach Cu(III) high-valent centers.

The copper(II)-phenoxyl electronic structure has proven to be the vastly more common form of one-electron oxidized copper salen complexes. The first reported salen compounds bearing radicals were, as a matter of fact, copper complexes.^[69] These complexes, published back in 1996, were developed with thio-ether ortho-substituents on the phenolate rings, in order to mimic the Tyr272-Cys228 crosslink in GOase. The oxidation of these complexes was assigned as a ligand oxidation $[\text{Cu}^{\text{II}}(\text{L})]^{\bullet+}$ rather than a metal centered oxidation $[\text{Cu}^{\text{III}}(\text{L})]^+$ according to EXAFS experiments.^[68]

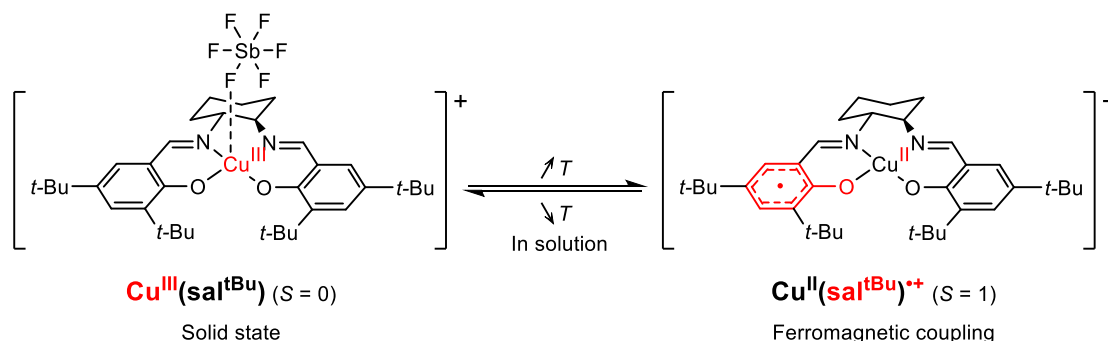


Figure I.21. Temperature dependent valence tautomerism between $[\text{Cu}^{\text{III}}(\text{sal}^{\text{tBu}})]^+$ and $[\text{Cu}^{\text{II}}(\text{sal}^{\text{tBu}})]^{\bullet+}$.

The complex $[\text{Cu}(\text{sal}^{\text{tBu}})]^+$ was also reported as copper(II)-phenoxyl compound and was the first example of UV-vis-NIR spectroscopy used as a means to characterize phenoxyl salen complexes.^[74] However, its crystallographic structure was later reported and showed the copper center to be a high-valent Cu(III) ion in the solid state.^[75] This assignment was corroborated by solid state magnetic susceptibility measurements. These results were rationalized considering a temperature dependent equilibrium in solution between $[\text{Cu}^{\text{II}}(\text{sal}^{\text{tBu}})]^{\bullet+}$ and $[\text{Cu}^{\text{III}}(\text{sal}^{\text{tBu}})]^+$ species. Both ^1H NMR and UV-vis-NIR absorption spectroscopy showed a reversible equilibrium between the Cu(III)-phenolate and the Cu(II)-phenoxyl redox states. The magnetic susceptibility of the oxidized complex was measured in solution via the Evan's method at varying temperatures. The solution became less paramagnetic when dropping in temperature from 295 to 178 K. Hence, it was proposed that the Cu(III)-phenolate form was more predominant at lower temperature (**Figure I.21**).

- EPR of copper-phenoxy complexes

Neutral Cu^{II} -salen complexes can be readily characterized by EPR spectroscopy as paramagnetic species (d^9 , $S = 1/2$). Frozen X-band EPR usually display axial or rhombic signals characteristic for nearly square-planar complexes with $d_{x^2-y^2}$ ground state. However, EPR of one-electron oxidized copper salen complexes is much less straightforward. Upon oxidation, the X-band EPR signal is generally quenched and can be interpreted in three different ways, by formation of:

- (i) A diamagnetic $\text{Cu}(\text{III})$ -phenolate (d^8 , $S = 0$) species.
- (ii) An antiferromagnetically coupled $\text{Cu}(\text{II})$ -phenoxy complex ($S = 0$).
- (iii) A ferromagnetically coupled $\text{Cu}(\text{II})$ -phenoxy complex ($S = 1$) with large zero-field splitting parameters.

In 2010, the Thomas group assigned the complex $[\text{Cu}^{\text{II}}(\text{sal}^{\text{OMe}})]^{+\bullet}$ as a ferromagnetically coupled $\text{Cu}(\text{II})$ -phenoxy species based on its X-ray structure and on theoretical calculations (**Figure I.23.B**).^[76] They calculated a zero-field splitting parameter (ZFS) of $D = 0.722 \text{ cm}^{-1}$. This result was consistent with the X-band EPR silence observed for $[\text{Cu}^{\text{II}}(\text{sal}^{\text{OMe}})]^{+\bullet}$ as the operating microwave frequency for low temperature X-band experiments is typically of lower energy ($\approx 0.3 \text{ cm}^{-1}$).^[77] In 2012, Shimazaki used low-temperature Q-band EPR to gain more insight on the ZFS parameters of salen copper(II)-phenoxy complex $[\text{Cu}(\text{1,3-sal})]^{+\bullet}$ (**Figure I.22**). The Q-band has a higher frequency ($\nu \approx 34 \text{ GHz}$) and is more energetic in comparison to X-band ($\approx 1 \text{ cm}^{-1}$). Therefore, Q-band is more useful to investigate paramagnetic systems with larger ZFS parameters.

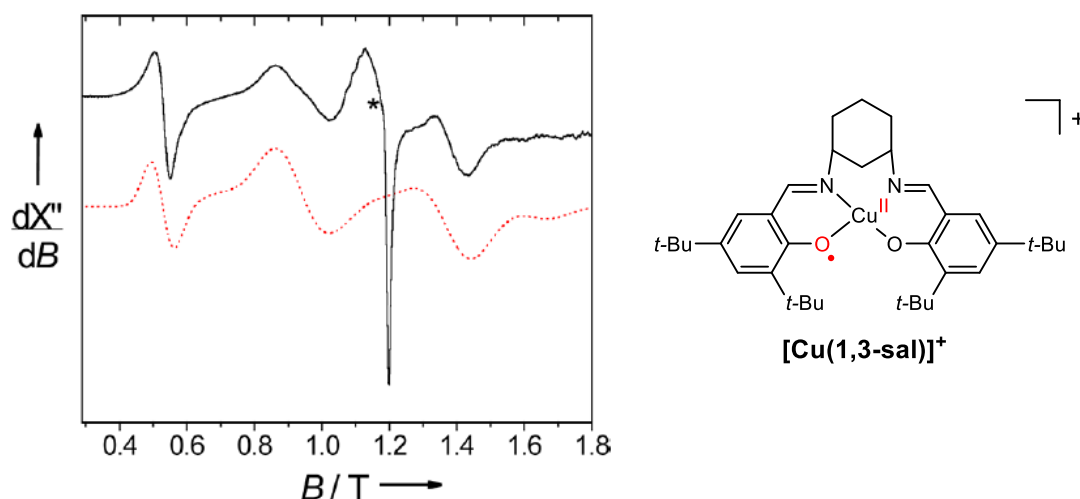


Figure I.22. Experimental (black) and simulated (dotted red line) Q-band EPR spectra of $\text{Cu}(\text{II})$ -phenoxy complex $[\text{Cu}(\text{1,3-sal})]^{+\bullet}$. $T = 12 \text{ K}$. The asterisk indicates a mononuclear $\text{Cu}(\text{II})$ ($S = 1/2$) impurity that was present in the sample.

The Q-band spectrum showed two contributions: a two-line pattern centered at $g = 2.06$ and a half-field transition at $g = 4$. The half-field signal is characteristic of a $\Delta M_s = \pm 2$ transition and confirmed the existence of a triplet system.^[78] The spectrum was simulated (dotted red line, **Figure I.22**) and gave a ZFS parameter of $D = 0.470 \text{ cm}^{-1}$ and $g_{\text{iso}} = 2.06$. This was the first time a triplet state was evidenced experimentally for a $\text{Cu}(\text{II})$ -phenoxy complex.

Nevertheless, because drastically different spin configurations can all result in EPR silence, standard X-band EPR experiments need to be critically analyzed. Other additional means of information, including magnetic susceptibility measurements or theoretical calculations, are required to better determine the electronic structure of oxidized copper salen complexes.

- Crystal structures of copper-phenoxyl complexes

X-ray diffraction is a powerful tool to assess the redox state in copper salen species. The first crystal structure of an unambiguous copper(II)-phenoxyl radical salen compound was reported in 2010 by Thomas and coworkers.^[79] The radical was characterized by an increased Cu-O1 coordination bond (+0.09 Å compared to neutral **Cu^{II}(sal^{OMe})**) due to the weaker donating properties of the phenoxyl ligand.

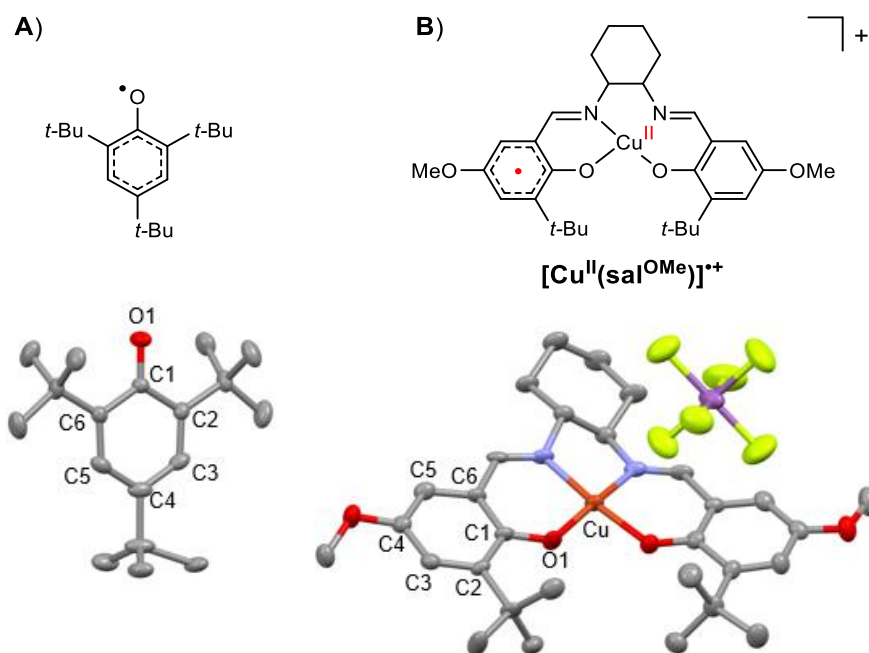


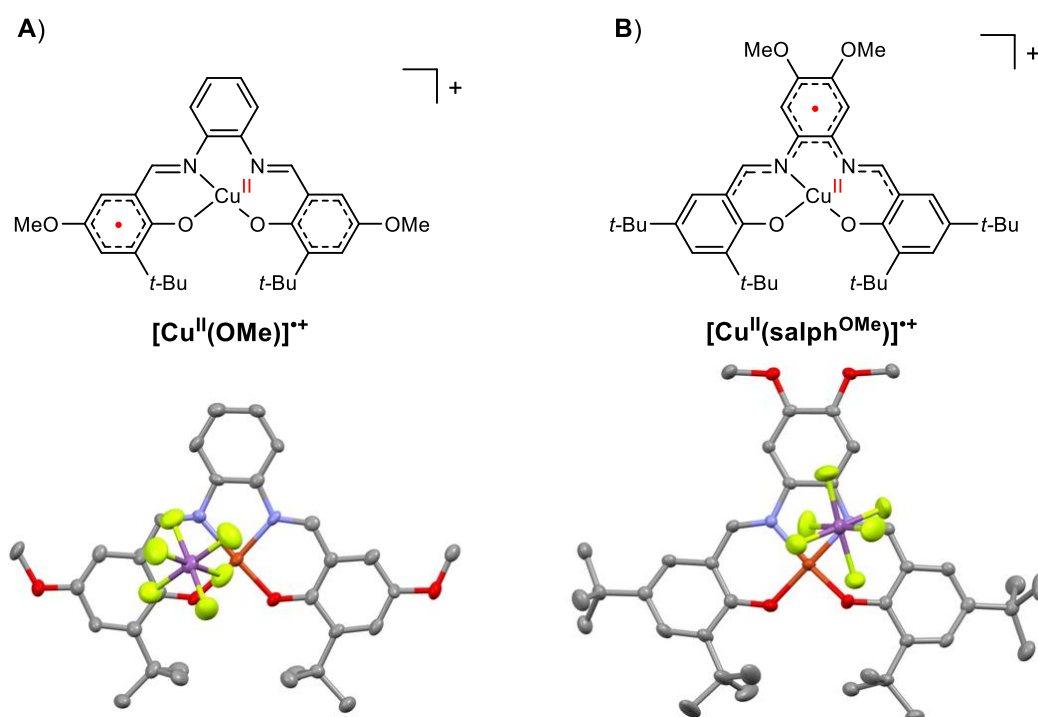
Figure I.23. Free 2,4,6-tri-*tert*-butylphenoxyl radical and its crystal structure (A) and first crystalized Cu(II)-phenoxyl salen complex [Cu^{II}(sal^{OMe})]^{•+} (B).^[76] The atom numbering used in the text is depicted on the X-ray structures.

[Cu^{II}(sal^{OMe})]^{•+} also displayed quinoid alternance of bond lengths in one aromatic ring that unambiguously showed the radical character of the complex. O1-C1, C2-C3, and C5-C6 (**Figure I.23**) shortened by 0.063, 0.025 and 0.039 Å respectively when compared to neutral **Cu^{II}(sal^{OMe})**. This phenoxyl ring in the complex did correlate closely with the crystal structure of the free 2,4,6-tri-*tert*-butylphenoxyl radical (**Table I.2**).

Table I.2. Selected bond lengths in phenoxyl rings of 2,4,6-tri-*tert*-butylphenoxyl and in oxidized $[\text{Cu}^{\text{II}}(\text{sal}^{\text{OMe}})]^{+\bullet}$. Comparison with phenolate rings of neutral $\text{Cu}^{\text{II}}(\text{sal}^{\text{OMe}})$.

compounds	$(t\text{-Bu})_3\text{ArO}^\bullet$	$[\text{Cu}^{\text{II}}(\text{sal}^{\text{OMe}})]^{+\bullet}$ phenoxyl ring	$\text{Cu}^{\text{II}}(\text{sal}^{\text{OMe}})$
O1-C1	1.246(2)	1.251(5)	1.314(2)
C1-C2	1.471(1)	1.468(5)	1.437(3)
C2-C3	1.367(2)	1.354(6)	1.379(3)
C3-C4	1.407(2)	1.420(5)	1.400(3)
C4-C5	1.407(2)	1.393(6)	1.366(3)
C5-C6	1.367(2)	1.369(6)	1.408(3)
C6-C1	1.471(1)	1.461(5)	1.407(3)

The salophen copper complex $[\text{Cu}^{\text{II}}(\text{OMe})]^{+\bullet}$ was also crystallized (**Figure I.24.A**) and did present similar quinoid deformations indicating the presence of a phenoxyl radical. However, when the aromatic spacer was electron enriched by introduction of methoxy donating groups ($[\text{Cu}(\text{salph}^{\text{OMe}})]^{+\bullet}$, **Figure I.24.B**), a drastically different behavior emerged. In that case, the X-ray structure showed a quinoid distribution of bonds within the electron-rich aromatic spacer rather than on the phenolate rings. This was the first example of a redox-active bridge in copper salen complexes.

**Figure I.24.** Different oxidation centers in copper(II)-radical salenophen: phenolate ring in $[\text{Cu}^{\text{II}}(\text{OMe})]^{+\bullet}$ (A)^[80] and aromatic bridge in $[\text{Cu}(\text{salph}^{\text{OMe}})]^{+\bullet}$ (B).^[81]

In that case, theoretical studies also showed that the Cu(III) redox state was almost isoenergetic with the Cu(II)-radical form. This shows that the Cu(III) state could also be reachable with this electron-rich spacer.

- Robin-Day classification of Cu(II)-phenoxyl complexes

The salen ligand system bears two redox-active phenolates. Accordingly, in mono-oxidized phenoxyl salen species $[\text{Cu}^{\text{II}}(\text{L})]^+$, each phenolate ring can host the electron hole. The degree of interaction between two redox centers was used to classify the compounds. Hence, three classes of mixed-valent systems were proposed according to Robin and Day (**Figure I.25.A**).^[82] In a class I system, an unpaired electron is completely localized on one redox site and has negligible electronic coupling with the other redox unit. At the opposite, a class III system is completely delocalized and presents a strong electronic coupling between the two redox sites. Finally, a class II system has a weak coupling and can be seen as a partially localized radical. The Marcus theory of electron transfer reactions was presented back in 1956.^[83] In 1967, Hush adapted the theory to provide a theoretical model for unravelling the Robin-Day classification of mixed-valent systems based on their intervalence charge transfers.^[84] (**Figure I.25.B**).

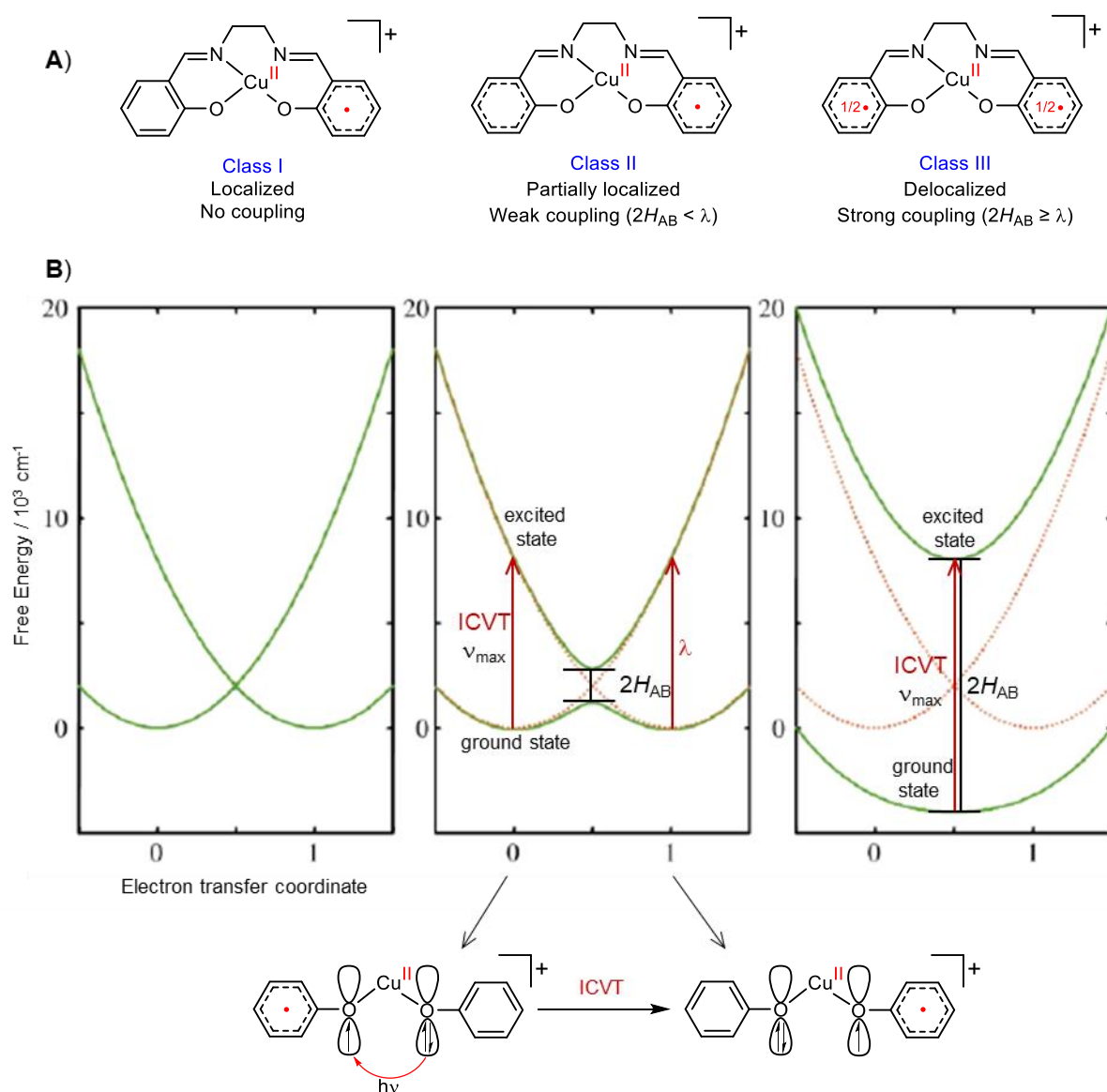


Figure I.25. Robin-Day classification of mixed-valent systems (A) and their respective Marcus-Hush models (B) applied to symmetric Cu(II)-phenoxyl salen complexes.

In the Marcus-Hush model, the localization of an unpaired electron on one redox moiety or the other can be represented by two harmonic functions representing molecular vibrations. In localized systems (Class I and II, **Figure I.25**), each harmonic function defines a ground state of minimum energy for localization of the electron on either redox moiety (0 or 1 on the electron transfer coordinate). In class II systems, the coupling of the two harmonic functions forms an energy surface with a transition state that defines the electronic coupling H_{AB} between the two redox units. In strongly coupled systems (Class III) the energy surface has a single minimum of energy corresponding to the completely delocalized unpaired electron. The electron transfer is also accompanied by a structural change with a reorganizational energy λ .

In class II systems, an intervalence charge transfer (IVCT) corresponds to the transition of the unpaired electron from one redox site to the other. In symmetric systems, the reorganization energy λ corresponds to the energy of the maximum absorbance of the IVCT transition (ν_{\max} , **Figure I.25**) and is related to the shape of the IVCT band (ϵ_{\max} , $\Delta\nu_{1/2}$). In the case of IVCT transitions, the absorption bandwidth is expected to increase with ν_{\max} and its theoretical value (calcd. $\Delta\nu_{1/2}$) is given by equation (1). Furthermore, H_{AB} can be experimentally calculated based on the band-shape parameters and an estimate of the electron transfer distance r_{CT} according to the Hush equation (2).

$$(1) \quad \text{calcd. } \Delta\nu_{1/2} = \sqrt{16 \ln 2 RT \nu_{\max}} = \sqrt{2310 \nu_{\max}}$$

$$(2) \quad H_{AB} = 2.06 \times 10^{-2} \times \frac{\sqrt{\epsilon_{\max} \cdot \Delta\nu_{1/2} \cdot \nu_{\max}}}{r_{CT}}$$

In the case of salen phenoxyl complexes, IVCT bands correspond to a phenolate to phenoxyl ligand-ligand charge transfer (LLCT) (**Figure I.25**). Class III mixed-valent phenoxyl systems are fully delocalized and display sharp and intense IVCT transitions ($\Delta\nu_{1/2} \approx \text{calcd. } \Delta\nu_{1/2}$). A Class II mixed-valent compound is a partially localized radical that displays broader and weaker IVCT transitions ($\Delta\nu_{1/2} > \text{calcd. } \Delta\nu_{1/2}$). The ratio between the electronic coupling H_{AB} and the reorganization energy λ has been used to categorize mixed-valent species. Class II partially localized systems have a threshold ratio $2H_{AB}/\lambda < 0.7$ and Class III delocalized systems have a $2H_{AB}/\lambda$ value close to 1.^[85] A borderline class II/III system with moderate coupling is considered for $0.7 < 2H_{AB}/\lambda < 1$.

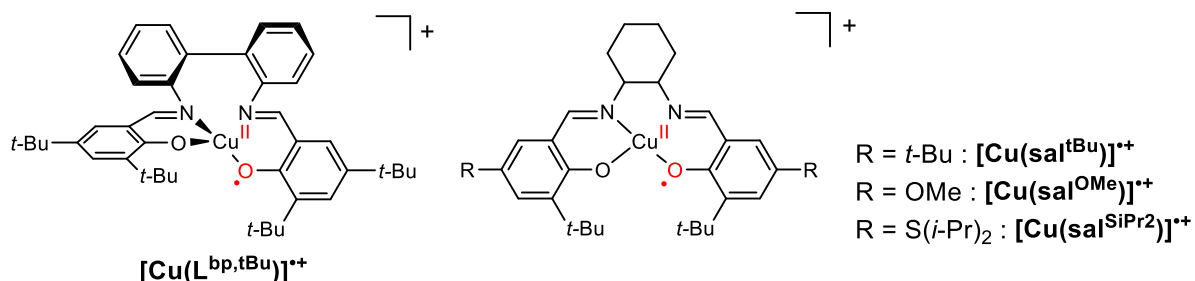


Figure I.26. Different Cu(II)-phenoxyl complexes with reported Marcus-Hush analysis of the IVCT band-shape parameters.^[86,87]

Most copper-salen phenoxyl complexes reported to date have been categorized as class II systems. However, more distorted systems appear to present lower electronic coupling H_{AB} and ϵ_{\max} values. This suggests a lower probability for intervalence electron transfer (**Table I.3**).^[86]

More electron-donating *para*-substituents also generally tend to localize the phenoxyl radical (Table I.3).^[87]

Table I.3. IVCT band-shape analysis of different one-electron oxidized Cu-salen complexes.

complex	ν_{\max} [cm ⁻¹]	ϵ [M ⁻¹ .cm ⁻¹]	$\Delta\nu_{1/2}$ [cm ⁻¹]	H_{AB}	$2H_{AB}/\lambda$
[Cu(L ^{bp,tBu})] ^{•+} ^a	6600	630	6300	1100	0.39
[Cu(sal ^{tBu})] ^{•+} ^b	5700	2900	5600	2300	0.81
[Cu(sal ^{OMe})] ^{•+} ^b	7800	1400	6200	2000	0.51
[Cu(sal ^{SiPr2})] ^{•+} ^b	10200	1300	6200	2200	0.43

^a Adapted from reference ^[86]. ^b Adapted from reference ^[87].

- Catalytic aerobic oxidation of alcohols

Copper salen complexes have been investigated for the aerobic oxidation of alcohols based on the activity of the wild-type enzyme GOase to oxidize a wide range of primary alcohols. The first report of a catalytic oxidation using copper radical salen complexes was published by Wang and Stack in 1996.^[69]

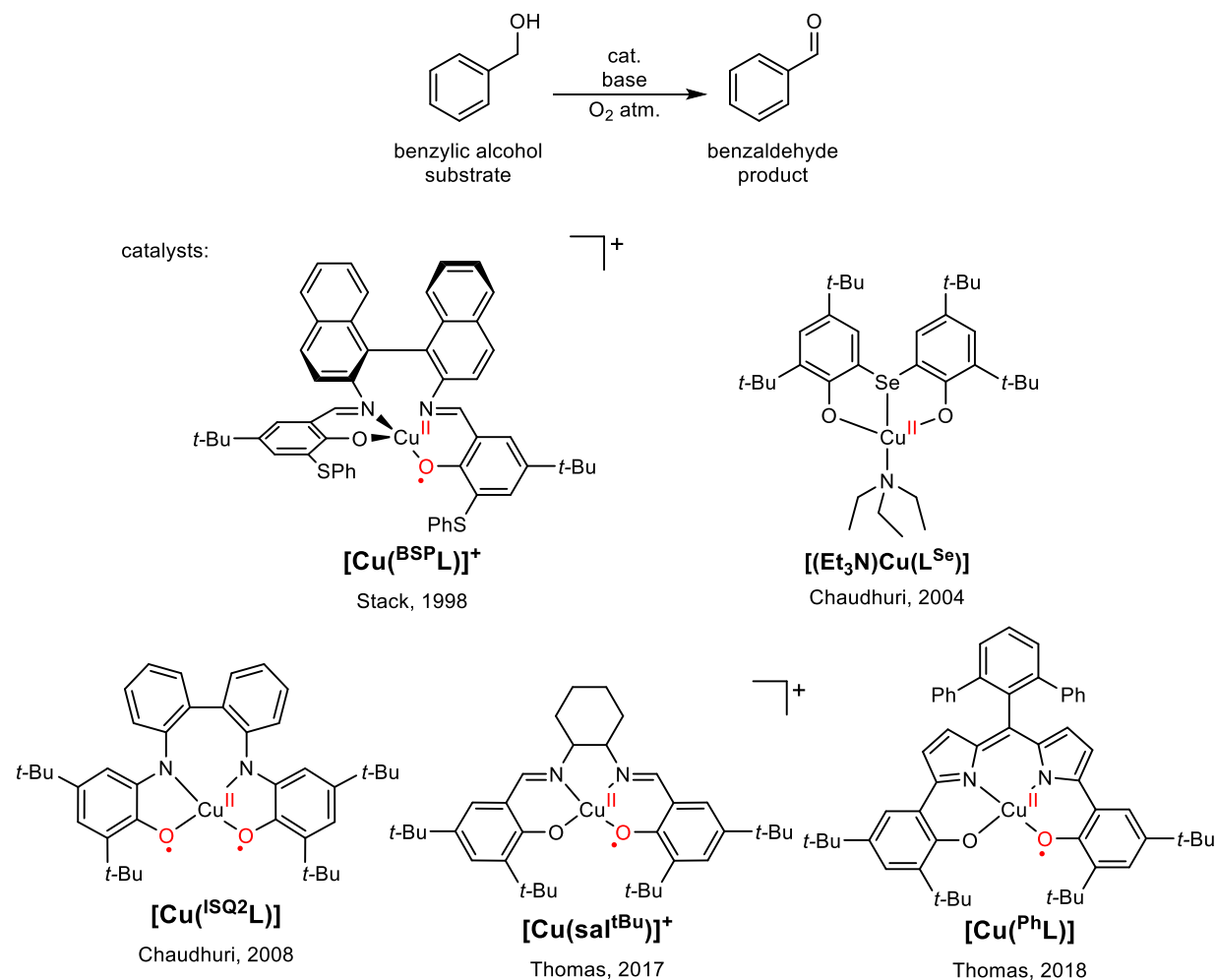


Figure I.27. Aerobic oxidation of a primary alcohol using copper-phenoxyl complexes as mimics of GOase.^[68,88–91]

They used benzyl alcohol as a primary alcohol model substrate. They directly solubilized neutral copper(II) salen complexes in benzyl alcohol and oxidized the complexes using a chemical oxidant. In presence of a strong base (nBuLi), complex $[\text{Cu}^{\text{BSP}}\text{L}]$ showed catalytic formation of benzaldehyde with up to 10 turnovers.^[69] They proposed that distortion at the copper center was necessary for catalytic activity to stabilize copper(I) reduced intermediates in the proposed catalytic cycle. Additionally, they hypothesized that both *ortho* and *para*-substitution of the phenolate rings were required for catalytic activity to prevent radical dimerization of the oxidized phenoxyl complexes. They later expanded their system to work under 1 atmosphere of O_2 to better mimic the activity of GOase and only used a catalytic amount of base. They showed an increase of activity with the same catalyst with up to 1300 equivalents of benzaldehyde produced at room temperature ($[\text{Cu}^{\text{BSP}}\text{L}]^+$, **Figure I.27**).^[68] Other oxidized copper-phenolate model complexes have been tested for aerobic oxidation of benzyl alcohol and their activity are summarized in **Table I.I.4**.

Table I.I.4. Aerobic oxidation of benzyl alcohol by copper-phenoxyl models of GOase.

TON (after 24h)	cat. mol%	base	catalyst
1300	0.01	2% sodium alkoxide	$[\text{Cu}^{\text{BSP}}\text{L}]^+$ ^[68]
95	0.125	4% MeONBu ₄	$[(\text{Et}_3\text{N})\text{Cu}(\text{L}^{\text{Se}})]$ ^[88]
65	1	0.9 equiv. NBu ₄ OH	$[\text{Cu}^{\text{ISQ}^2}\text{L}]$ ^[89]
63	0.08	1.2 equiv. <i>t</i> -BuOK	$[\text{Cu}(\text{sal}^{\text{tBu}})]^+$ ^[90]
300	0.08	1.2 equiv. <i>t</i> -BuOK	$[\text{Cu}^{\text{Ph}}\text{L}]$ ^[91]

All reports have shown that the use of a base is required to improve the reactivity of the oxidation (**Table I.I.4**). This behavior highlights the necessity to reach the deprotonated alkoxide form of the substrate before its oxidation to form the aldehyde product.

Other alcohols were tested as substrates to gain more insight on the aerobic oxidation mechanism using copper-phenoxyl catalysts. Notably, Stack observed a competitive kinetic-isotope effect when comparing PhCH_2O^- and deuterated substrate PhCD_2O^- .^[68] This observation showed that cleavage of the benzylic C α -H is involved in the rate-limiting step of the catalytic cycle. Given the radical nature of the oxidized phenoxyl ligands and their proximity to the benzylic H-atoms of the alcohol substrate, H-atom abstraction was proposed as a reasonable mechanism. In accordance, oxidation of unactivated allylic substrates proved more difficult than benzylic substrates and fewer reports are present in literature.^[86,89,90,92,93] This lower activity on alkyl alcohols is also observed in GOase, where reaction rates are more than 10^3 slower than for benzylic substrates.^[71] These results show that different copper-phenoxyl complexes, including salen species, are valuable models to mimic the activity of GOase for aerobic oxidation of primary alcohols.

1.3.4. Nickel complexes to probe the electronic structure of oxidized species

In salen complexes featuring paramagnetic metal centers the assignment of the oxidation site between metal or ligand-centered can be difficult due to magnetic coupling. It is usually a combination of different techniques, including EPR, near-infrared (NIR) spectroscopy and X-ray diffraction, that is required to unambiguously assign the redox state of the oxidized complexes.

On the other hand, the nickel(II) ion is diamagnetic in the square planar environment present in most salen complexes. Accordingly, one-electron oxidations generate ($S = 1/2$) spin systems that allows for a straightforward analysis by EPR spectroscopy. Contribution of the metal center to the singly occupied molecular orbital (SOMO) can be assessed from the anisotropy and shift of the g tensor of the systems. Additionally, delocalization of the ligand radical in Ni(II)-phenoxyl cations can be readily probed by NIR spectroscopy. This has elevated nickel-salen complexes as the most convenient candidates to probe the electronic structure of one-electron oxidized salen complexes. Modulations of the ligand frameworks were inspected, including phenolate substituents and metal geometry. The impact of different experimental conditions on the electronic structure was also investigated, including solvents, introduction of exogenous ligands or temperature.

- Ni(III)-phenolate or Ni(II)-phenoxyl

The nickel ion exists in either Ni(II) or Ni(III) oxidation states in most salen complexes. Mono-oxidation of Ni(II)-salen complexes was initially believed to be metal-centered, affording Ni(III) cations. Freire and Castro were the first to deeply investigate the oxidation of Ni(II)-salen in coordinating solvents (DMF, DMSO, pyridine) in the 1990s.^[94,95] Different coordinating species can form Ni(III)-salen complexes after oxidation, ranging from weakly coordinating solvents like methanol to strongly σ -donating ligands like pyridine.^[96,97] The Ni(III) character in coordinating solvents can be identified by anisotropic rhombic systems with g_{average} values typically higher than 2.15. In the case of pyridine adducts, the EPR spectra display additional features from hyperfine interaction between the ^{14}N nucleus of the pyridine ligands ($I_N = 1$) and the unpaired electron of the nickel(III) ion (**Figure I.28**). The unpaired electron lies in a d_{z^2} orbital in Ni(III) complexes in square pyramidal or elongated octahedral geometries. Therefore, the hyperfine coupling interaction indicates that oxidation of square planar Ni(II) salens is coupled with the coordination of solvent molecules in axial positions.

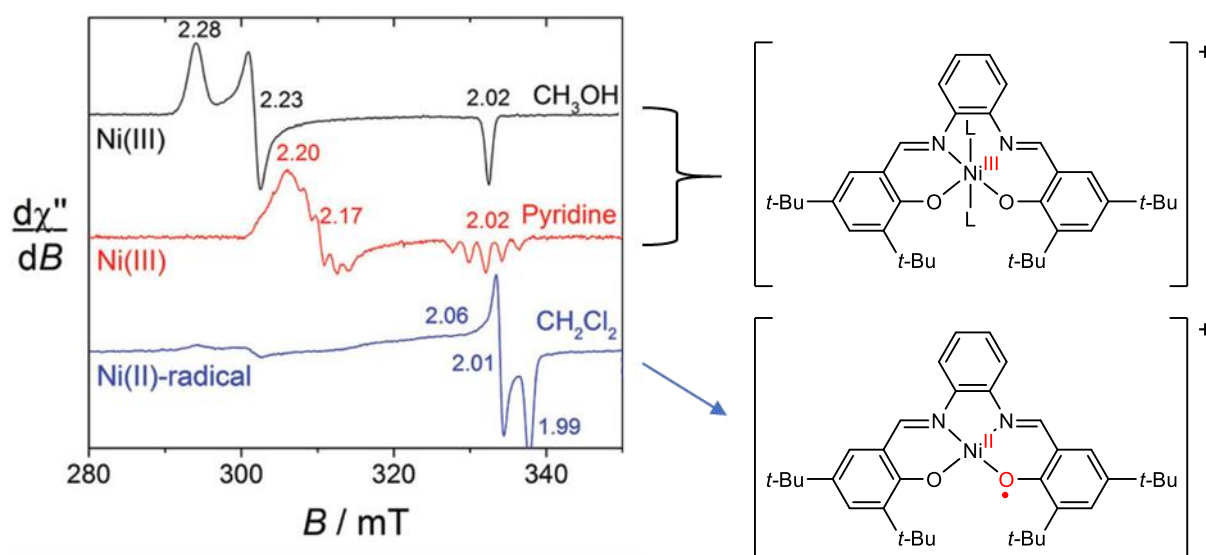


Figure I.28. EPR spectra of a one-electron oxidized nickel-salophen complex in different solvents^[98] with detailed g values. L = solvents (methanol, pyridine) in the Ni(III) structures. $T = 100$ K.

When working in non-coordinating solvents, EPR of oxidized Ni-salen complexes usually display a weaker anisotropy and lower g values that have been attributed to phenoxyl radical species ($g_{\text{average}} \approx 2.0$, **Figure I.28**). Historically, the Ni(II)-phenoxyl forms of oxidized nickel salen compounds were first dismissed as over-oxidized species or degradation products of Ni(III) parent species in the 1990s. However, the elusive Ni(II)-radical form was re-examined by Yamauchi and coworkers in 2003.^[99] In this publication, they reported a temperature-dependent Ni(II)-phenoxyl \leftrightarrow Ni(III)-phenolate valence tautomerism for a one-electron oxidized nickel salen complex $[\text{Ni}(\text{sal}^{\text{tBu}})]^+$ (**Figure I.29**).

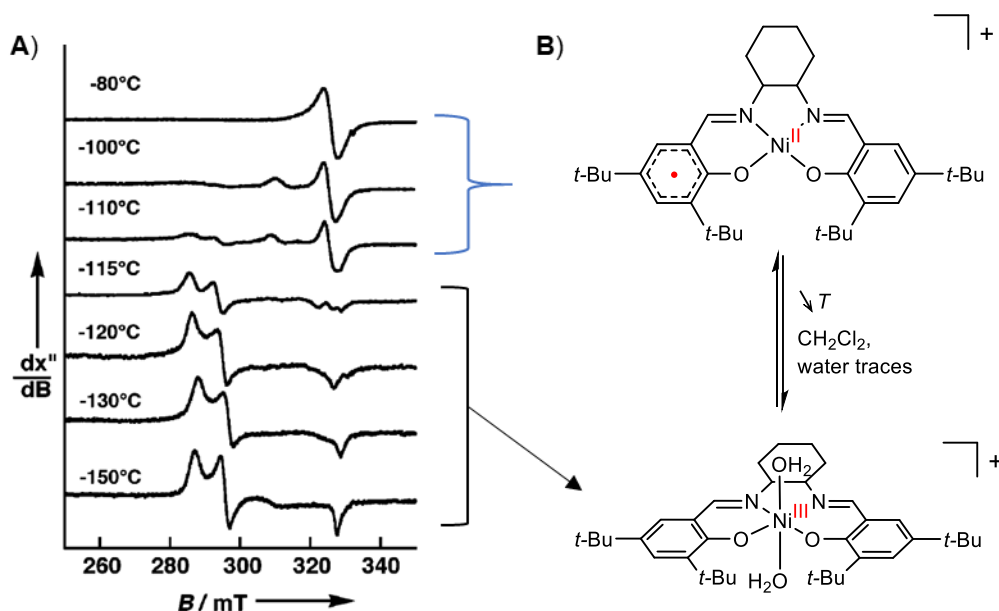


Figure I.29. Valence tautomerism between Ni(II)-phenoxyl and Ni(III)-phenolate forms depending on temperature.^[99] Solution X-band EPR spectra of $[\text{Ni}(\text{sal}^{\text{tBu}})]^+$ at different temperatures (A) and corresponding main valence tautomers (B).

When working in non-coordinating CH_2Cl_2 , they observed an isotropic signal characteristic of the Ni(II)-phenoxyl form ($g \approx 2.04$) at -40°C . Nevertheless, when dropping in temperature, the EPR spectra completely changed to a highly anisotropic rhombic signature with higher g values ($g_1 = 2.30$, $g_2 = 2.23$, $g_3 = 2.02$ and $g_{\text{av}} = 2.18$), characteristic of a Ni(III) ion. The spectral change proved to be fully reversible, evidencing the equilibrium between the two redox states. In this case, adventitious water in the dichloromethane solvent was proposed as the cause for the valence-tautomerism.^[97,100] When dropping in temperature, the nickel ion increases its affinity to water traces and evolves towards an octahedral Ni(III) complex with two weakly bound exogenous water molecules (**Figure I.29**). The role of innocuous solvent coordination in Ni(II)-phenoxyl \leftrightarrow Ni(III)-phenolate valence tautomerism was evidenced in solid state powder EPR experiments.^[101] In the solid state, $[\text{Ni}(\text{sal}^t\text{Bu})]^+$ displayed the same spectroscopic signature, attributed to the phenoxyl radical form, no matter the change in temperature. In the same year, the crystallographic structure of $[\text{Ni}(\text{sal}^t\text{Bu})]^+$ was reported and definitely confirmed the Ni(II)-phenoxyl redox state.^[100]

- Impact of phenolate *para*-substituents

The electronic structure of oxidized nickel-salen species was shown to be heavily influenced by modulation of the *para*-substituents of the phenolate rings. A series of oxidized Ni(II)-phenoxyl salophen complexes was developed with different substituents ($\text{R} = \text{NMe}_2$, OMe, *t*-Bu, **Figure I.30**).^[97] Logically, more electron-donating groups gave rise to more easily oxidizable complexes ($E_{1/2(\text{phenoxyl/phenolate})} = -0.24$, 0.22 and 0.37 V for $\text{R} = \text{NMe}_2$, OMe and *t*-Bu respectively).

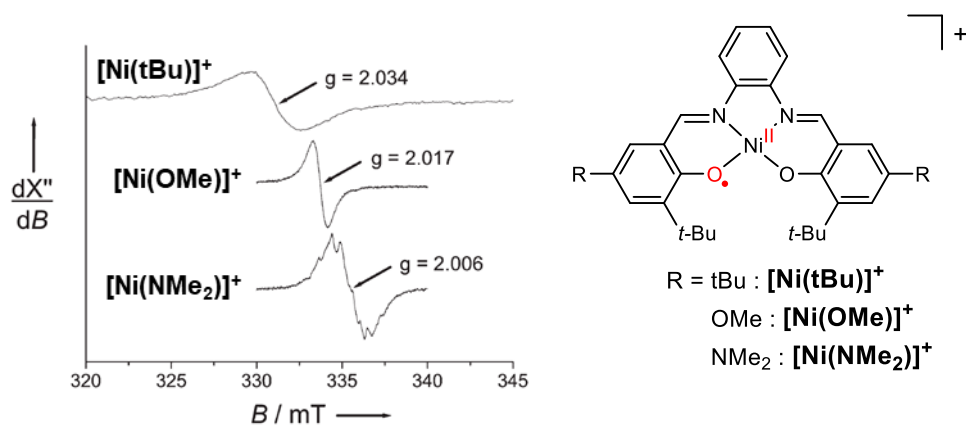


Figure I.30. X-band EPR spectra of one-electron oxidized nickel-salophen complexes with different phenolate *para*-substituents.^[97] Anhydrous CH_2Cl_2 solutions, $T = 233$ K.

Interestingly, the contribution of the nickel center to the SOMO was also impacted. Solution EPR experiments showed that the complex with the most donating substituent $[\text{Ni}(\text{NMe}_2)]^+$ presented the lowest g_{iso} value of 2.006. The intermediate OMe substituent gave a g_{iso} value of 2.017 for $[\text{Ni}(\text{OMe})]^+$. $[\text{Ni}(\text{tBu})]^+$ had the highest g_{iso} value of 2.034 with the weakest electron donating group (**Figure I.30**). The more electron-donating groups are therefore able to compensate for the electronic deficiency of the phenoxyl ring and reduces the contribution of the nickel center. This is also seen in the molecular orbitals of the oxidized complexes. More electron donating groups results in SOMOs with stronger radical characters (g_{iso} closer to 2.005 of genuine free phenoxyl radicals). In contrast, the least electron-donor group (*t*-Bu) cannot

sufficiently compensate the electronic hole and stronger contribution of the *d* orbitals of the nickel ion is required. The resulting SOMO presents a stronger metallic character with a higher g_{iso} value (**Figure I.31**).

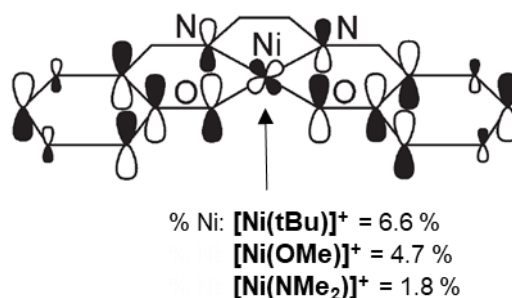


Figure I.31. SOMO of a mixed-valent Ni(II)-radical salen complex^[98] and calculated contribution of the nickel ion to the total spin density in oxidized nickel(II)-phenoxyl salophen complexes.^[97] DFT calculations at the B3LYP level.

This behavior is supported by theoretical calculations of the spin densities of the oxidized complexes. The complex with the weakest electron-donating group $[\text{Ni}(\text{tBu})]^+$ presented the highest spin density on the nickel center (6.6 %). In comparison, contribution of the metal was minimal for the more electron-rich $[\text{Ni}(\text{NMe}_2)]^+$, with only 1.8 % of electronic density on the nickel ion. Once again, $[\text{Ni}(\text{OMe})]^+$ presented an intermediate behavior with 4.7 % nickel electronic density.

- Radical delocalization

A correlation was also demonstrated between the localization of the radical and the electron-donating power of the *para*-substituents of the phenolates. The first crystallographic structure of a Ni(II)-radical complex was reported in 2007 for $[\text{Ni}(\text{sal}^{\text{tBu}})]^+$.^[100] The structure presented a symmetrical coordination sphere of the nickel ion. Oxidation was accompanied by a contraction of the coordination sphere by 0.02 and 0.03 Å for the Ni–O and Ni–N bond lengths respectively when compared to the neutral parent complex. This contraction is consistent with removal of an electron from a ligand-based antibonding orbital. Interestingly, this behavior is opposite to the elongation of the Cu–O bond observed in most copper-salen analogues. It is important to note that the organic framework did not display any substantial structural change upon oxidation and no clear quinoid form of a phenoxyl radical could be observed. This indicates a complete delocalization of the ligand radical between the two redox-active rings, making $[\text{Ni}(\text{sal}^{\text{tBu}})]^+$ a class III mixed-valent radical following the Robin-Day classification.

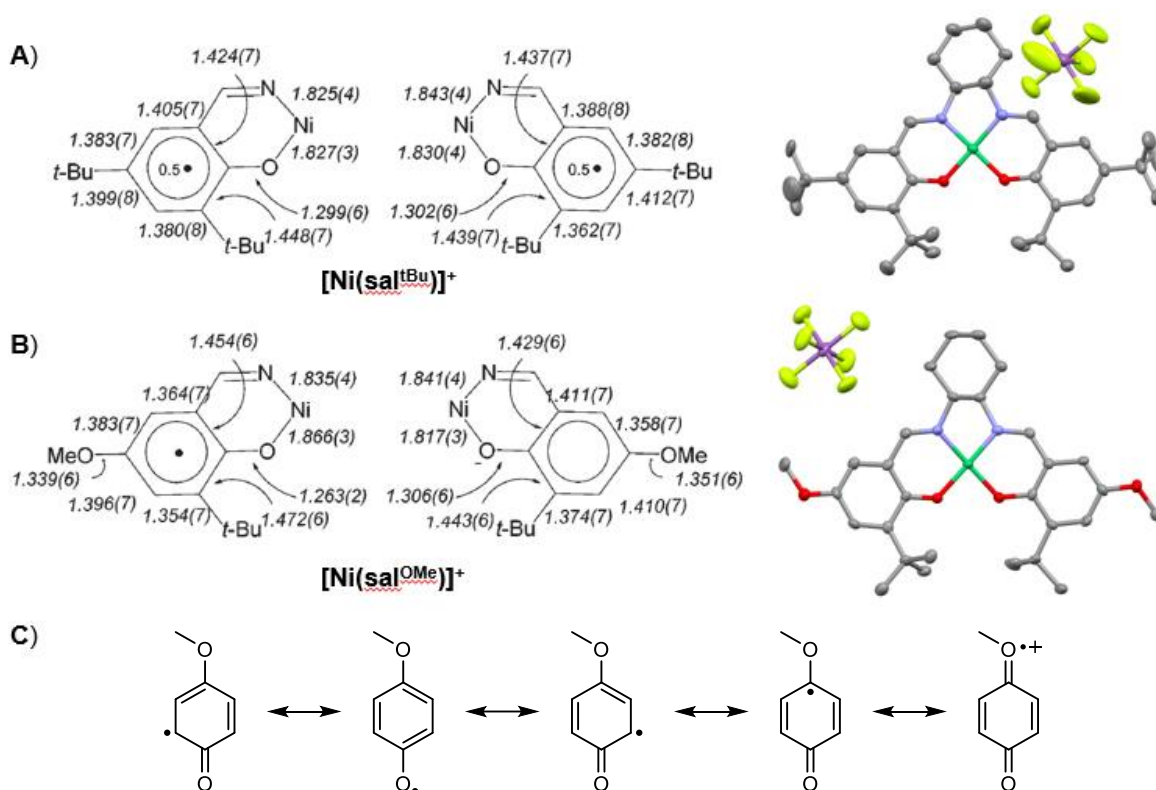


Figure I.32. Crystallographic structure and selected bond lengths^[98] of [Ni(sal^{tBu})]⁺ (A)^[100] and [Ni(sal^{OMe})]⁺ (B).^[79] Canonical structures of a methoxyphenoxyl radical (C).

This assignment is also supported by NIR spectroscopy with the observation of a sharp and intense IVCT band at low energy (**Figure I.33.A, Table I.5**).^[102] The assignment as an IVCT was confirmed in theoretical calculations as a ligand to ligand charge transfer from β -HOMO to β -LUMO. Noticeably, the orbitals involved in the transition were shown to be fully delocalized over the two redox-active rings. The calculated electron density was completely symmetrical as well (**Figure I.33.B**). All those theoretical results are strongly consistent with experimental results to assign [Ni(sal^{tBu})]⁺ as a fully delocalized class III mixed-valent radical.

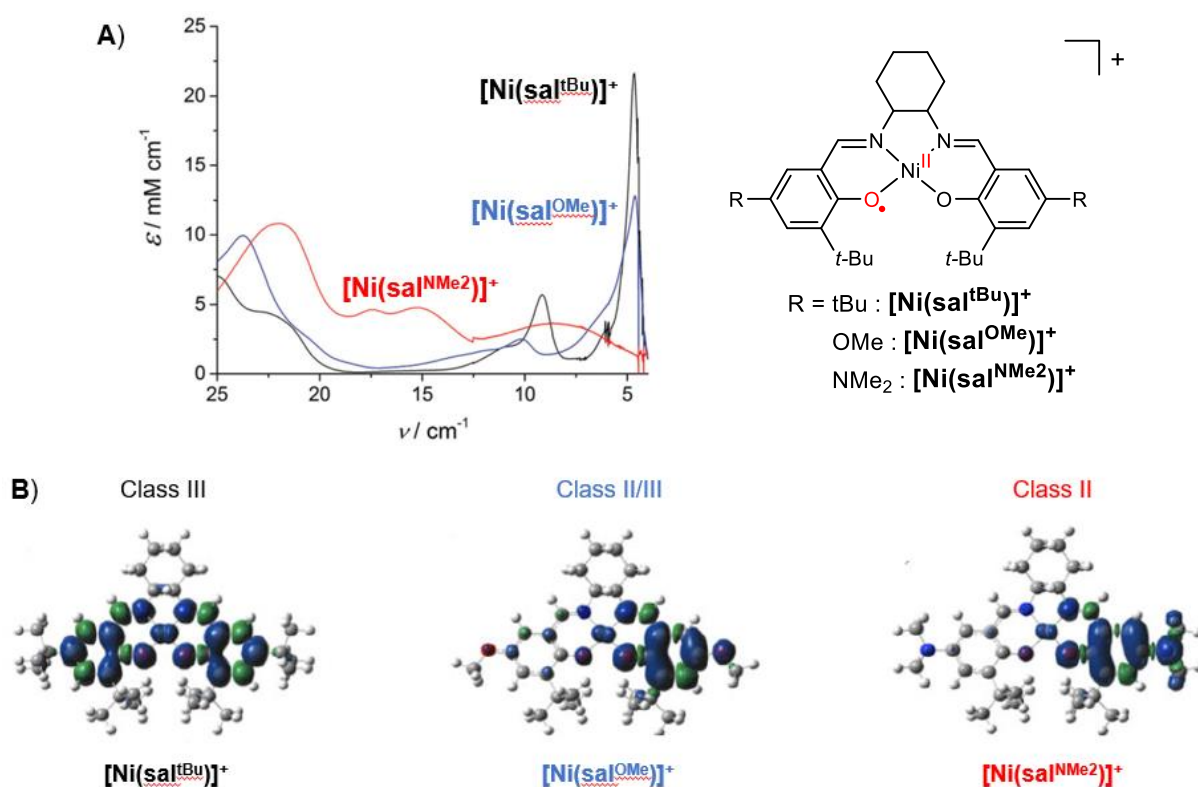


Figure I.33. UV-vis-NIR spectra of one-electron oxidized $[\text{Ni}(\text{sal}^{\text{tBu}})]^+$, $[\text{Ni}(\text{sal}^{\text{OMe}})]^+$ and $[\text{Ni}(\text{sal}^{\text{NMe}_2})]^+$ complexes (A) and their calculated spin density (B). DFT calculations at the CAM-B3LYP level.

The methoxy derivative $[\text{Ni}(\text{sal}^{\text{OMe}})]^+$ was also prepared and crystallized.^[79] In that case, the crystal structure displayed a localized radical in the solid-state. Quinoid distortions expected for methoxyphenoxyl radicals were observed in one half of the ligand. The other half did not present significant structural changes after oxidation. The IVCT band observed for $[\text{Ni}(\text{sal}^{\text{OMe}})]^+$ in the NIR region was also less intense and sharp than for $[\text{Ni}(\text{sal}^{\text{tBu}})]^+$ (Table I.5). This corroborated with a partial radical localization in solution as well. Theoretical calculations were also consistent and displayed an unsymmetrical electron density mostly localized on one side of the ligand (Figure I.33.B). The NIR band-shape parameters of the IVCT band still shows a significant communication between the two-redox rings and $[\text{Ni}(\text{sal}^{\text{OMe}})]^+$ was assigned as a borderline class II/III radical.

Table I.5. Analysis of IVCT bands displayed by a series of one-electron oxidized Ni-salen complexes.

complex	$\nu_{\text{max}} [\text{cm}^{-1}]$	$\epsilon [\text{M}^{-1} \cdot \text{cm}^{-1}]$	$\Delta\nu_{1/2} [\text{cm}^{-1}]$
$[\text{Ni}(\text{sal}^{\text{CF}_3})]^{+a}$	4900	16200	-
$[\text{Ni}(\text{sal}^{\text{tBu}})]^{+b}$	4700	21600	660
$[\text{Ni}(\text{sal}^{\text{OMe}})]^{+b}$	4600	12700	1250
$[\text{Ni}(\text{sal}^{\text{NMe}_2})]^{+b}$	8500	3600	6650

^a Adapted from reference ^[103]. ^b Adapted from reference ^[98].

The $[\text{Ni}(\text{sal}^{\text{NMe}_2})]^+$ complex was also prepared to investigate the impact of an even stronger electron-donating *para*-substituent,^[102] as well as $[\text{Ni}(\text{sal}^{\text{CF}_3})]^+$ for comparison with an electron-withdrawing group.^[103] Neither could be crystallized but their NIR spectroscopy gave some great insight on the delocalization of the phenoxyl radical. $[\text{Ni}(\text{sal}^{\text{NMe}_2})]^+$ displayed the least intense and broadest IVCT band of the series (**Figure I.33.A**), indicative of a strong localization of the radical that was also observed in DFT calculations (**Figure I.33.B**). The transition was also of higher energy and significantly blue-shifted compared to the rest of the series. Hence, $[\text{Ni}(\text{sal}^{\text{NMe}_2})]^+$ was assigned as a class II mixed-valent system. On the other hand, $[\text{Ni}(\text{sal}^{\text{CF}_3})]^+$ presented a sharp and intense IVCT band akin to $[\text{Ni}(\text{sal}^{\text{tBu}})]^+$ (**Table I.5**) showing that $[\text{Ni}(\text{sal}^{\text{CF}_3})]^+$ also holds strong delocalization of the ligand radical, with significant Ni contribution to the SOMO.

1.3.5. Manganese complexes presenting ligand-centered redox activity

The number of reports of ligand redox activity in manganese-salen complexes is comparatively much lower than for copper or nickel compounds. The manganese ion generally adopts redox states ranging from +II, +III, +IV up to +V within salen complexes. The most stable oxidation state is manganese(III) with the most common geometry being a square pyramidal coordination with the counterion (often a halide or acetate ligand) coordinated in apical position. Back in 2011, Fuji *et al.* reported a series of symmetric and dissymmetric Mn(III)-salen complexes and investigated their redox activity.^[104] They showed that the oxidations were strictly ligand-centered and led to radical $[\text{Mn}^{\text{III}}\text{L}]^+$ phenoxyl complexes.

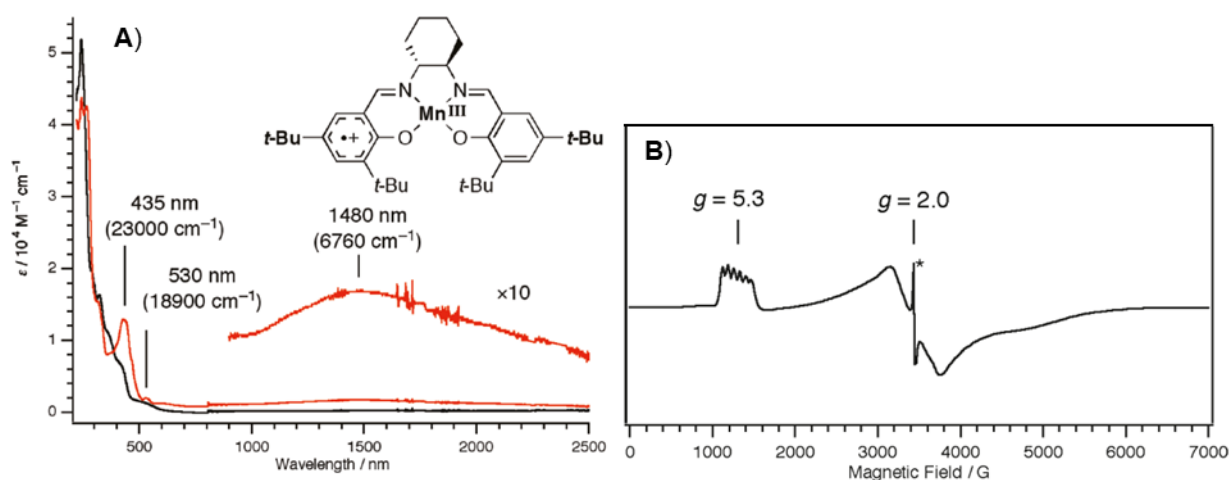


Figure I.34. UV-vis-NIR (**A**) and X-band EPR spectra (**B**) of oxidized $[\text{Mn}^{\text{III}}(\text{sal}^{\text{tBu}})(\text{SbF}_6)]^+$ complex, Figure adapted from reference^[104].

X-band EPR of oxidized complexes $[\text{Mn}^{\text{III}}(\text{sal}^{\text{Ph/tBu/OMe}})(\text{SbF}_6)]^+$ all displayed two separate signatures (**Figure I.34.B**). A low-field component was observed at $g = 5.3$ – 5.7 with a six-line hyperfine coupling pattern arising from the ^{55}Mn nucleus ($I = 5/2$). Another broad component was observed at $g \approx 2$. Those two sets of broad $g \approx 2$ and $g \approx 5$ signals have been assigned to a rhombic $S = 3/2$ system which was confirmed with magnetic susceptibility experiments. This demonstrated an antiferromagnetic coupling between a high-spin Mn(III) (d^4 , $S = 2$) center and a phenoxyl organic radical ($S = 1/2$). An additional sharp signal was also observed at $g = 2.0$ for $[\text{Mn}^{\text{III}}(\text{sal}^{\text{Ph}})(\text{SbF}_6)]^+$ and $[\text{Mn}^{\text{III}}(\text{sal}^{\text{tBu}})(\text{SbF}_6)]^+$ and was proposed to arise from free ligand radicals not magnetically coupled to manganese ions.



Figure I.35. TD-DFT calculated NIR transition in a model $[\text{Mn}^{\text{III}}\text{L}]^{*+}$ one-electron oxidized complex.^[105]

The oxidized complexes also displayed broad and weak absorption bands in the NIR region (**Figure I.34.A**) that were attributed to ICVT transitions of the ligand phenoxyl radical. Band-shape analysis of the IVCT bands depicted oxidized $[\text{Mn}^{\text{III}}(\text{sal})]^{*+}$ complexes as class II mixed-valent phenoxyl radicals in the Robin-Day classification. These assignments were also corroborated by theoretical calculations that presented highly localized and unsymmetrical molecular orbitals involved in the transition (**Figure I.35**).^[105] Surprisingly, the analogous nickel complex $[\text{Ni}(\text{sal}^{\text{tBu}})]^{*+}$ was shown to be a class III mixed-valent system (see discussion of **Figure I.33** and **Table I.5**). This difference in behavior was investigated by theoretical calculations and was attributed to the formal charge of the Mn(III) center in $[\text{Mn}^{\text{III}}(\text{sal}^{\text{tBu}})]^{*+}$.^[105] Electronic communication between the two redox active rings goes through metal orbitals. In the case of the Mn(III) ion, there is a strong energy gap between the redox active orbitals of the metal and of the ligand. This difference in energy leads to less efficient electronic coupling between the two redox-active rings resulting in class II mixed-valence.

More recently, the Storr group has also investigated the redox activity of a series of Mn(V)salen complexes bearing a nitrido (N^{3-}) ligand.^[106] They reported ligand or metal-centered redox activity depending on the *para*-substituents of the phenolate rings. Furthermore, the oxidized species depicted a drastic difference in reactivity of the nitrido ligand depending on the center of oxidation. This report will be discussed in the later part of this introduction that focuses on metal nitride complexes (Chap I.3.4.6.).

2. Introduction of *N*-Heterocyclic Carbenes (NHCs)

2.1. History and features of NHCs

2.1.1. Initial works and their legacy

A carbene center is formally defined as a neutral divalent carbon atom with a lone pair of electrons. This elusive form of the familiar carbon atom had long been a subject of interest and chemists had tried to isolate carbenes as far back as 1835 with the first experiments of Dumas.^[107] In his pioneering work, he tried to form the core carbene methylene unit :CH_2 by reacting methanol with dehydrating agents. Despite a joint effort with many other chemists, no one was able to successfully characterize free carbenes at the time. They were thus thought as mere curiosities: reactive, fleeting species.

Wanzlick was the first to investigate the reactivity and stability of what is known today as *N*-heterocyclic carbenes (NHCs) in the early 1960s. He tried to generate a free carbene through elimination of chloroform in an imidazolidine compound but could only isolate a dimeric “hidden carbene” species (**Figure I.36.A**).^[108] Shortly after, Wanzlick and Öfele independently reported the first metallic complexes bearing NHC ligands.^[109,110] Both of them used imidazolium salt precursor and directly reached the metallic complexes by their deprotonation. However, they did not try to isolate the free NHC itself.

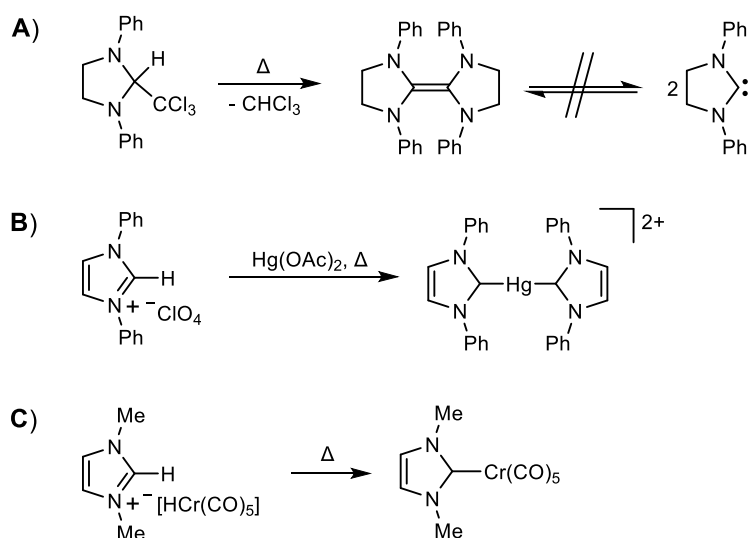


Figure I.36. Key historic syntheses in NHC chemistry: First study of the reactivity of NHC-type molecules by Wanzlick (A) and first reports of carbene-metal complexes by Wanzlick (B) and Öfele (C).

These metallic complexes did not strike a huge interest in the coordination chemistry of NHC at the time. The real pioneering report in the field of NHC chemistry was the publication by Arduengo in 1991 of the incredible stability of a free NHC with its crystallographic structure (**Figure I.37**).^[111] The free NHC was obtained by simple deprotonation of an imidazolium salt precursor based on previous investigations by Wanzlick. This first example of a “bottleable” free NHC completely opened a field of research on this class of compounds and that have now become a major staple in chemistry as a whole.

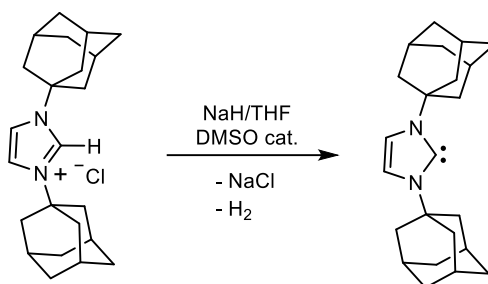


Figure I.37. Report of a stable free carbene by Arduengo.^[111]

While catalytic applications remain the most prominent use of NHC compounds, the sheer number of articles and reviews published every year in all fields of chemistry is quite impressive, with more than 1000 yearly publications since 2011 for the keyword “NHC” in Scifinder. This is a great testimony to the huge popularity of this relatively new class of molecules.

2.1.2. Electronic properties

Carbene properties can widely differ depending on their geometry. They can either be bent or linear, with separate electronic configurations for each case. The linear configuration presents sp hybridization with two degenerate p_π orbitals to accommodate the two non-bonding electrons in a triplet ground state (**Figure I.38**). However, the linear configuration remains an extreme case and most carbenes are bent, making the carbon a sp^2 center (**Figure I.38**). In that case, the frontier orbital p_x acquires some s character and will be called σ while the p_y orbital remains mostly unmixed and is labelled p_π . Depending on their structure and electronic properties, carbenes can either be seen as a diradical triplet $\sigma^1 p_\pi^1$ species, or a more stable singlet σ^2 with a donating lone pair (**Figure I.38**).

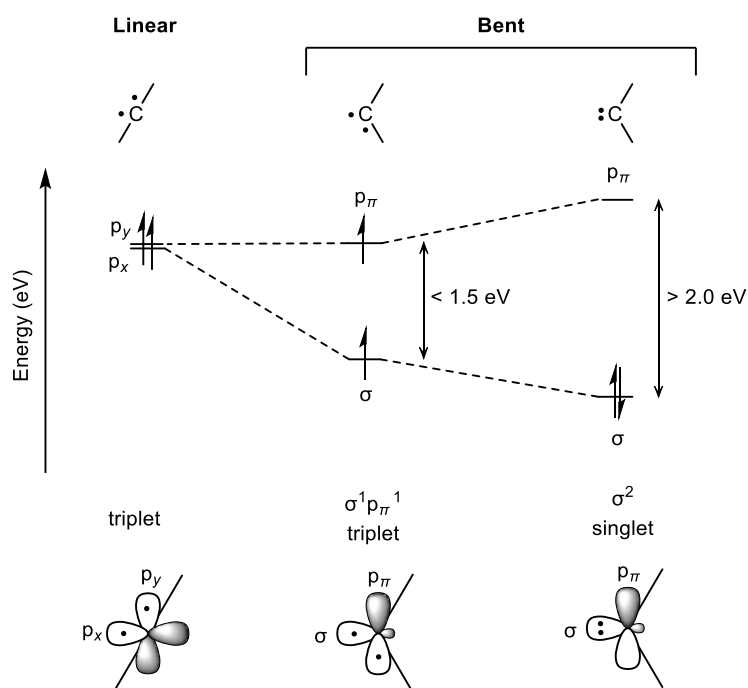


Figure I.38. Impact on geometry on the frontier orbitals and different electronic configurations of a carbene.

Given those configurations, one can easily anticipate that the electronic configuration can drastically impact the reactivity of the carbene centers. Singlet σ^2 carbenes should present both nucleophilic and electrophilic properties (ambiphilic reactivity) as they possess both a filled and an empty orbital. On the other hand, triplet carbenes can be seen as highly reactive diradical moieties. The energy gap between the frontier orbitals σ and p_π directly dictates the ground state of the carbene and can be regarded similarly as the crystal field theory for high spin and low spin configurations for metal complexes. From theoretical calculations, the difference between the singlet and the triplet forms was calculated to be only 0.5 eV (**Figure I.38**).^[112] As such, by simple electronic effects, the substituents on the carbene center can directly dictate its ground state and therefore, its reactivity.

Inductive effects directly impact the σ frontier orbital, with stabilization by electronegative substituents. This increases the energy gap between σ and p_π orbitals, favoring a singlet ground state (**Figure I.39.A**). Although they can impact the spin multiplicity of the carbene, inductive effects have a minor contribution when compared to mesomeric effects. Mesomeric electron donating groups (including halides, amines, phosphates, ethers, thiols and more) destabilize the p_π orbital of the carbene by interaction with their own appropriate filled p orbitals (**Figure I.39.C**) thus favoring the singlet carbenes once again. Conversely, π -accepting substituents (carboxyl derivatives, cyanides, trifluoromethyl groups, etc.) tend to favor triplet carbenes.

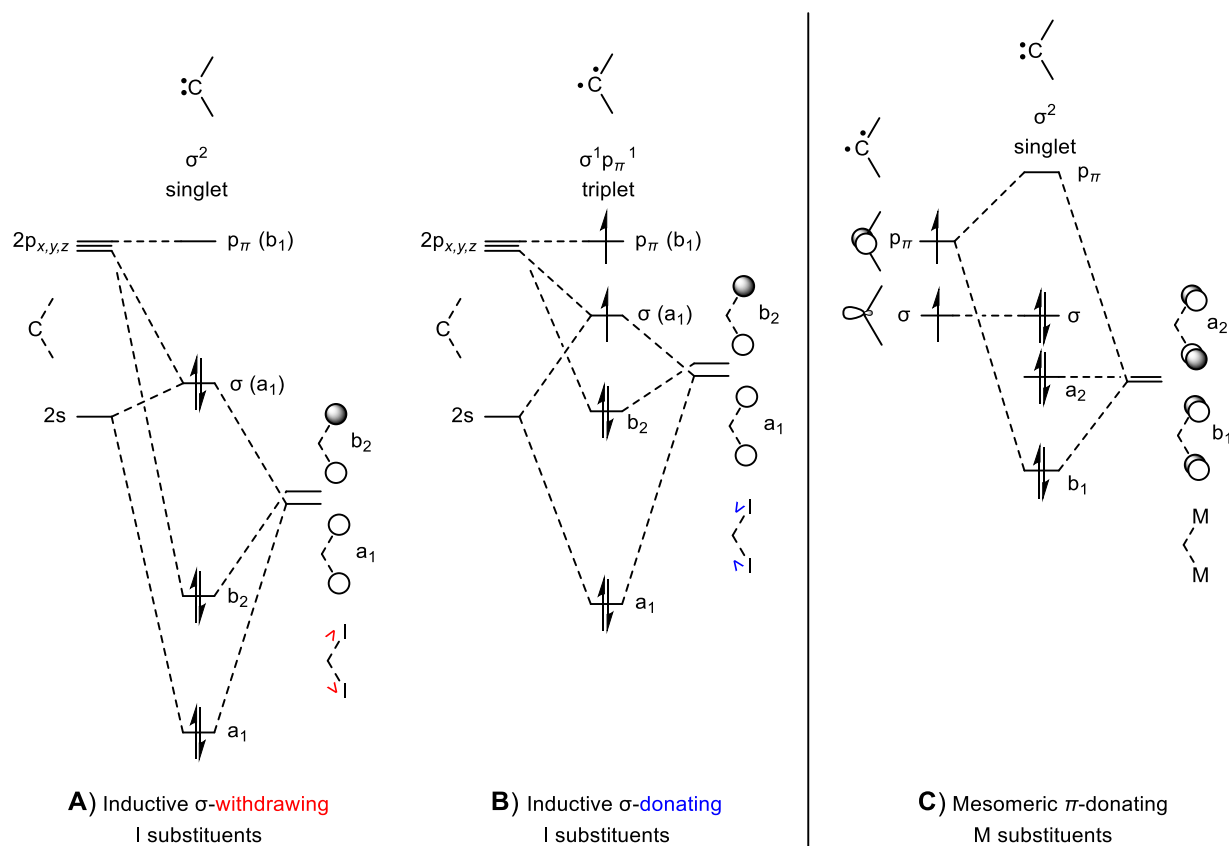


Figure I.39. Perturbation orbital diagram depicting the impact of inductive effects on the ground state of carbenes (**A,B**) and stabilization of a carbene by donating mesomeric substituents (**C**).

Diaminocarbenes or NHCs, possess both the inductive withdrawing and mesomeric donating properties and can be considered as singlet carbenes. These unique electronic properties have made NHCs some of the most versatile and ubiquitous carbene species.

Singlet carbenes form a synergetic metal-carbon bond by carbene σ -donation to the metal and π -accepting backdonation from the metal center, as described in the Dewar-Chatt-Duncanson model.^[113] The different electronic contributions involved in the metal-NHC bonds are represented below (**Figure I.40**). NHCs are generally considered as poor π -accepting ligands with a weaker retrodonation from the metal center as the carbenic center is already stabilized by the strong π -donation of the two amines.

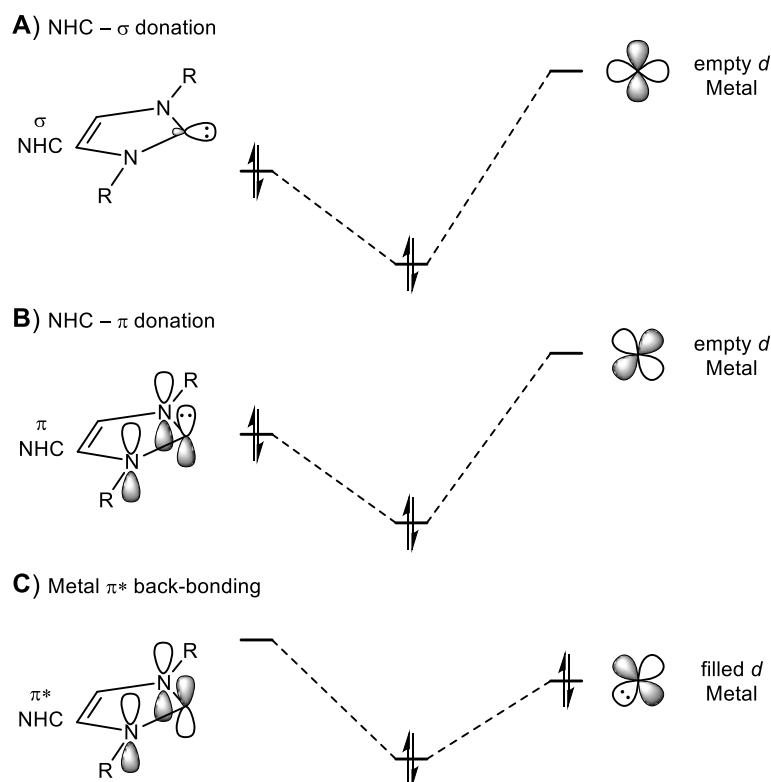


Figure I.40. Different orbital contributions in the Metal-NHC bond.

2.1.3. Experimental determination

For a long time, NHCs had only been thought of as phosphines' new cousin as neutral, two-electron donor ligands. However, they are now useful alternatives that bind more strongly to the metallic center in organometallic chemistry. Furthermore, they are more versatile, both in terms of electronic and steric properties due to the number of modulation sites they offer. To assess the binding properties of NHCs, different experimental methodologies have been used to compare them with their phosphine homologues.

One of the most straightforward tools to assess the donating properties of a ligand is the use of Tolman electronic parameters (TEP). This method was originally developed to describe tertiary phosphine ligands, relying on the infrared stretching frequency of the CO bonds in tetrahedral $\text{Ni}(\text{CO})_3\text{L}$ (L = phosphine) complexes.^[114] The CO stretching frequency is impacted by the electron density at the metal center: with a more electron rich metal center, the degree of π -

backbonding on the π^* antibonding orbital of the CO ligands is increased (**Figure I.41**). This results in a weakened carbon–oxygen triple bond and a lower ν_{CO} stretching frequency.

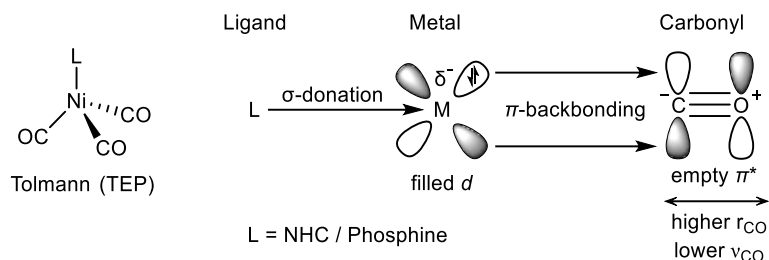


Figure I.41. Influence of the electron donation of a ligand L to the π -backbonding of carbonyls in the Tolman model.

The σ -donating properties of NHC ligands are thus inferred from lower stretching frequencies in the IR spectrum as a result of stronger electronic donation. The TEP of phosphine ligands typically ranges from 2050 to 2200 cm^{-1} from strongly donating phosphines, such as $\text{P}(t\text{-Bu})_3$ (2056.1 cm^{-1}), to halide-phosphines such as PF_3 (2110.8 cm^{-1}) compared to 2143 cm^{-1} for free carbon monoxide. On the extreme end of the scale, NHC ligands have shown TEP values as low as 2030 cm^{-1} . However, the use of TEP presents different limitations, including the toxicity of the carbonyl complexes, the impact of the solvent system in the IR experiment or steric effects that are less reliable to predict compared to phosphines. To address this issue, other types of metrics have been developed to quantify the donating properties of the NHC, such as rhodium(I) and iridium(I)-NHC probes.^[115]

Additionally, but not limited to, nuclear magnetic resonance (NMR) experiments of Bertrand's ^{31}P and Ganter's ^{77}Se scales have been used to rationalize the π -accepting properties in NHC complexes.^[115] The NMR shifts are highly dependent on the amount of π -back-bonding to the carbene center, which leads to a deshielding (shift to lower field) of the NMR signals. These studies have shown that NHCs are overall poor π -accepting ligands and behave more as π -donating ligands even if there is still some debate on this topic.

2.2. Preparation

NHC ligands have been used extensively for a wide range of applications, most specifically in organometallic catalysis^[116–118] and more recently as nucleophilic organocatalysts^[119,120] in their own right. Their success mainly lies on their high modularity. Variations on both the NHC backbone and the different associations of NHCs with other coordinating ligands are basically limitless due to the number of ways to build them. Back in 2011, Bellemin-Laponnaz and César published a thorough review^[121] on the different strategic methods to reach the many different protonated salts widely used as precursors for free NHCs and metal complexes alike.

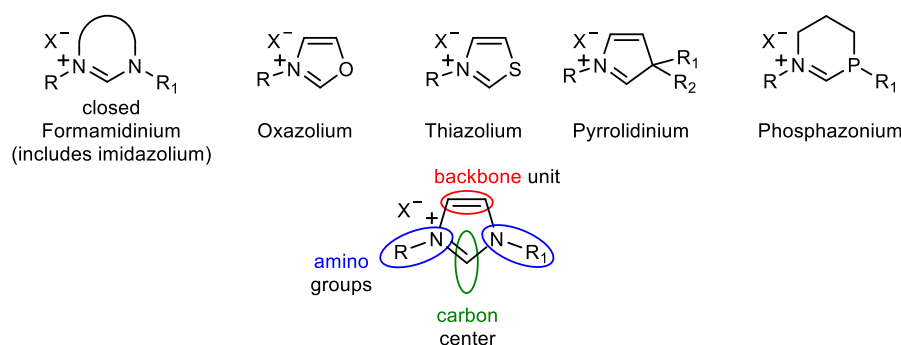


Figure I.42. Salt precursors of *N*-Heterocyclic structures covered from review^[121] and key units in an imidazolium NHC precursor.

A number of NHCs have been developed that showed unusual coordination modes (**Figure I.43**) and other NHCs derivatives with only one amino donor or mixed systems with π -donating substituents (**Figure I.42**) have been reported. However, the most commonly used carbenes are derived from an imidazole ring. This is due to the various convenient and reliable synthetic pathways to the imidazolium precursors. As imidazolium NHC precursors have been the center of my research, I will focus more specifically on their key synthetic routes.

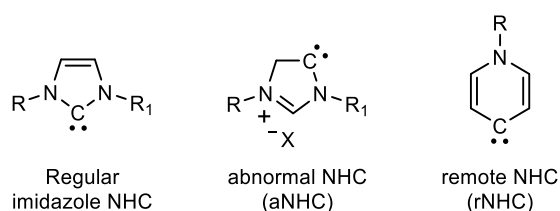


Figure I.43. Different coordination modes in unusual NHCs.

The structure of an NHC can be separated into three key moieties: an ammonium unit, a precarbenic carbon center and a backbone framework (**Figure I.42**). Accordingly, three different general synthetic pathways have been used to access NHC salt precursors:

- Ring closure by introduction of the amino moiety.
- Ring closure by introduction of the carbon center.
- Ring closure from the backbone unit.

2.2.1. Ring closure by the amino groups

Final introduction of the amino moiety has been the least explored pathway. It has been mostly developed by Fürstner *et al.* for the synthesis of unsymmetrical NHC precursors (**Figure I.44**).^[122,123] This methodology has then been expanded to the synthesis of triazolium salts by condensation with hydrazine derivatives by Lassaletta *et al.*^[124] but remains a more niche synthetic route compared to the other two.

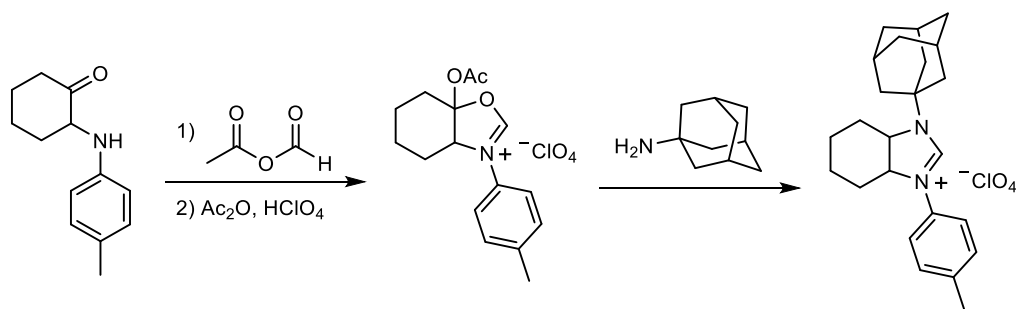


Figure I.44. Fürstner *et al.* synthesis of unsymmetrical imidazolium salts.

2.2.2. Ring closure from the backbone frame

On the other hand, ring closure from the backbone framework or by the precarbenic carbon atom are closely related. They often involve reactions with the same reactants, just in a different order. More specifically, formation of the N-C-N precarbenic center involves the use of similar carbon electrophiles. The general method is to react a bis-electrophile backbone unit, generally a bis-halide derivative, on a previously formed formamidine already containing the N-C-N precarbenic unit (**Figure I.45**). One main advantage of the backbone ring closure is the superior versatility of the route to craft more intricate and complex backbones in the NHCs. Variation of the size of the NHC ring, introduction of conjugated π -systems or inorganic backbones can all be achieved using this method (**Figure I.45**).

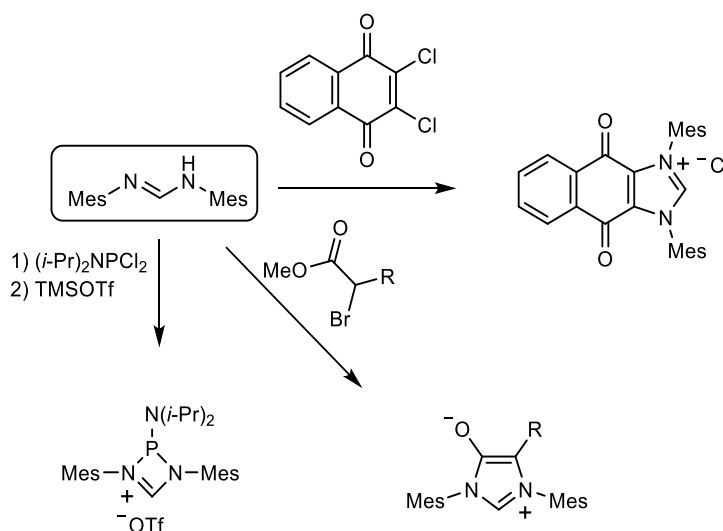


Figure I.45. Representative examples of the variety of NHC salts obtained by the backbone closure pathway on the same formamidine unit.^[121]

2.2.3. Ring closure by the carbon center

The most widespread synthetic method is the final introduction of the precarbenic carbon atom, both for its convenience and the overall high efficiency. Either a diimine or a diamine can be reacted with different carbon electrophiles to afford the final NHC salts. A large panel of carbon electrophile reagents have been used but the most widely reported are triethylorthoformate HC(OEt)_3 and paraformaldehyde. Other 1,1-bis(electrophile) alkylating agents are more scarcely used but have been valorized in more delicate reactions (**Figure I.46**).^[121]

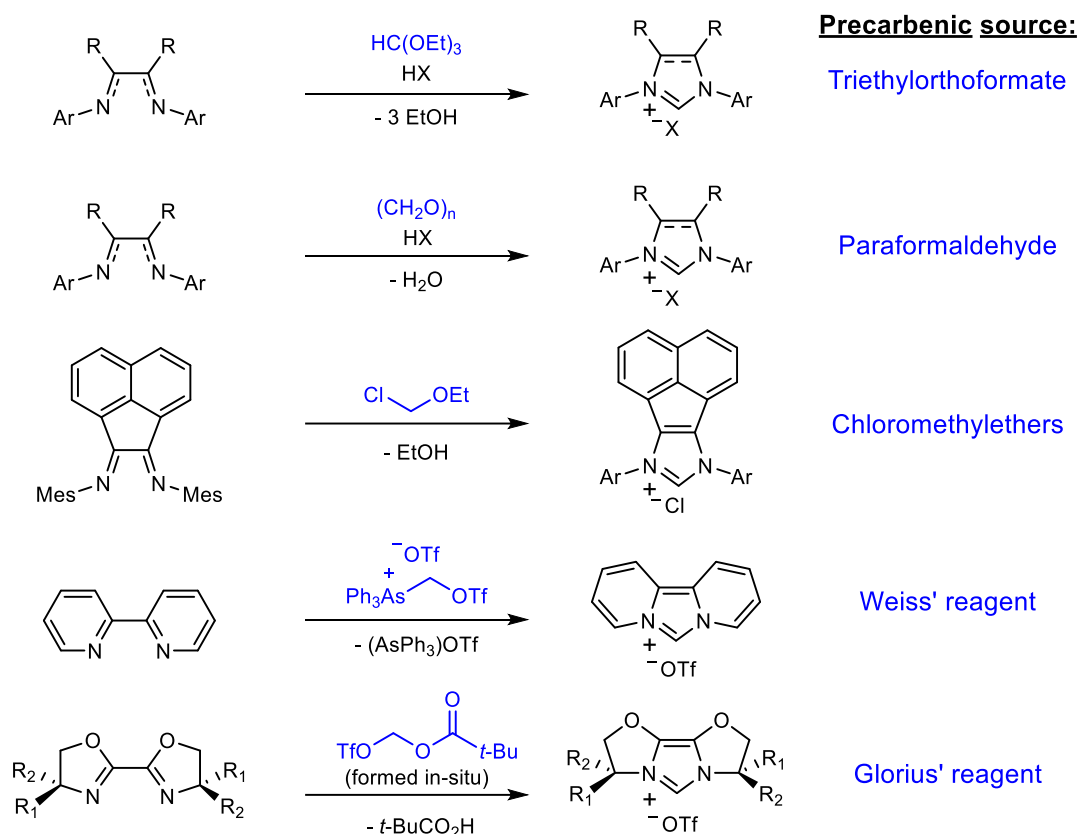


Figure I.46. Representative syntheses of NHC salts using the precarbenic center closing pathway.^[121]

Finally, different types of one-pot syntheses have been developed to introduce the three NHC building blocks together. One of the most useful and straightforward is the synthesis patented by Arduengo in 1991 using a primary amine, formaldehyde and glyoxal.^[125] This process was adapted to form neutral imidazole rings using one equivalent of primary amine, with ammonium chloride as the secondary nitrogen atom source. These imidazole rings can then be alkylated to form unsymmetrical monodentate NHCs or can be condensed to form a bidentate ligand with two NHCs by using a bis-electrophilic alkylating agent (**Figure I.47**).

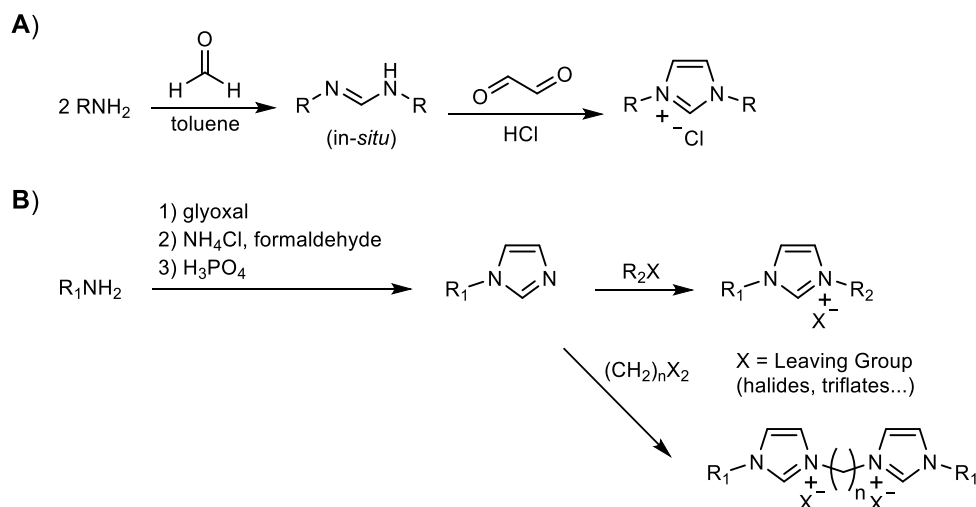


Figure I.47. Arduengo one-pot synthesis (**A**) and adapted methodology for unsymmetrical and bidentate NHC salts (**B**).

2.3. Impact of NHCs on organometallic catalysis

NHCs, also called Arduengo carbenes after his groundbreaking report in 1991, have become more and more ubiquitous over the years. NHCs were initially viewed as more unstable analogues of the phosphine ligands that had an uncontested supremacy over the field of organometallic chemistry. However, they were gradually shown to present enhanced donating properties, form stronger bonds with the metal centers and possess a greater versatility to modulate both the electronic and the steric properties of the ligand framework.

2.3.1. Olefin metathesis

One of the best examples for the rise of popularity for NHCs in comparison to phosphine ligands is the development of the Grubbs' catalysts for olefin metathesis. Olefin metathesis is a very rich research field, that culminated in the 2005 Nobel Prize to Chauvin, Schrock and Grubbs. The development of tolerant, reactive metal complexes to control the C-C bond formations was the key to the successful development of new catalysts and the introduction of the NHCs as ligands is widely considered to be a major breakthrough in the field.

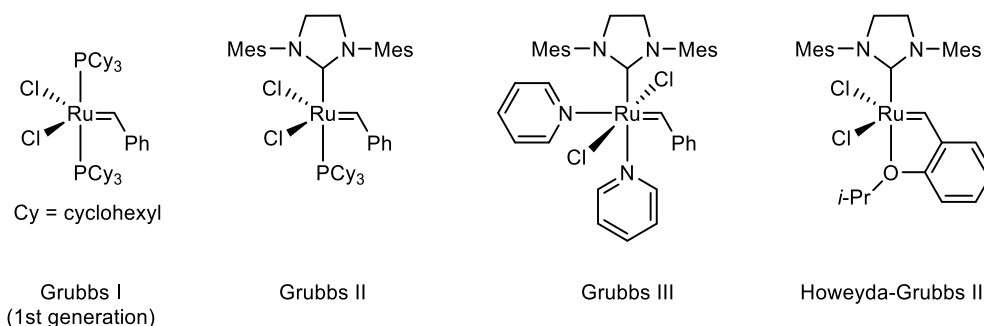


Figure I.48. Different generations of Grubbs catalysts.

Initially developed using phosphines (Grubbs I), the next generations of the Grubbs catalysts replaced one phosphine ligand in favor of a simple NHC with now complete removal of phosphines in the latest and most active catalysts to date (**Figure I.48**). The most crucial improvement of these new NHC compounds was their vastly greater stability compared to the first-generation. The catalysts proved more tolerant to oxygen and moisture and greatly facilitated their handling. The difference of stability was attributed to the lower propensity of the NHC to dissociate from the metal. Moreover, the 2nd generation and higher proved to be more reactive than the phosphine complexes, allowing a decrease of the reaction temperatures that further lowered the decomposition of the catalysts. Finally, the scope of the substrates with NHC catalysts increased and with it, new types of reactions that the first Grubbs compound could not reach.

2.3.2. Palladium catalyzed cross-coupling reactions

Palladium-catalyzed cross-coupling reactions are also a major field of research that revolutionized the way in which chemists handled formation of carbon-carbon bonds. Their development awarded Heck, Negishi and Suzuki the Nobel Prize in Chemistry in 2010. The very common activation of a Pd precatalyst through reductive elimination and/or ligand displacement (**Figure I.49**) has limited the use of complex design of ligands. Additionally,

nowadays, a large amount of catalysis are heterogenous rather homogeneous, with a wide development of Pd nanoparticles or surface supported Pd catalysts.

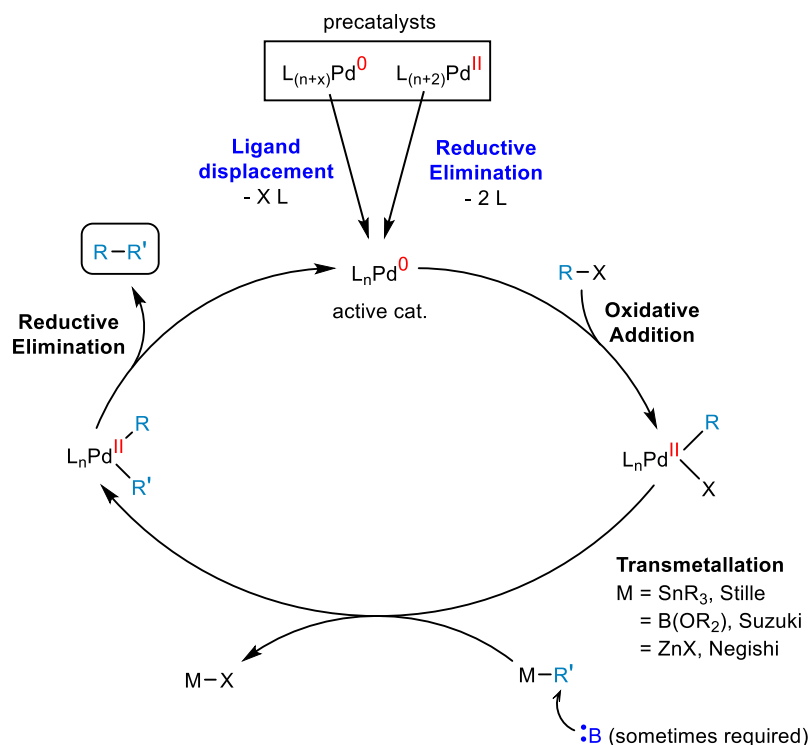


Figure I.49. General catalytic cycle for Pd-catalyzed cross-coupling reactions.

Still, NHCs were successful in palladium cross-coupling reactions allowing for the use of milder conditions^[126] and showing strong activity for many different processes with high tolerance towards functional groups.^[127] Interestingly, in most cases, the NHCs have been introduced as their protonated imidazolium precursors (NHC-HCl) directly in solution alongside with a palladium salt (**Figure I.50**). Many reactions carried out also did not involve any base, neither to help the coordination of the NHC, nor to help the transmetalation step, that often requires activation of the $M-R'$ coupling partner (**Figure I.49**).

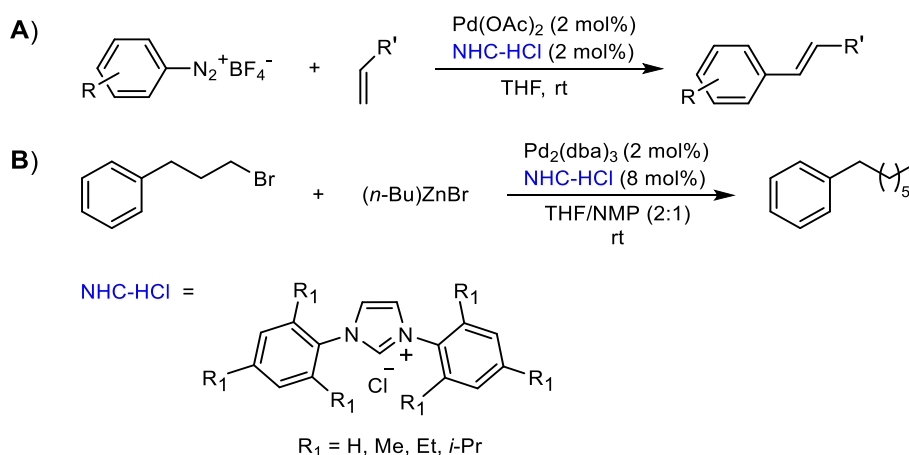


Figure I.50. Use of imidazolium NHC precursors in the Heck^[126] (A) and Negishi^[127] (B) Pd-catalyzed cross-coupling reactions.

2.3.3. Nickel catalyzed cross-coupling reactions

The high cost associated with the use of a scarce noble metals has driven research towards alternative catalysts using base metals. In this purpose, Böhm and Herrmann utilized the properties of NHC ligands on nickel catalysts to couple aryl Grignards to aryl fluorides in the Kumada-Tamao-Corriu (KTC) reaction.^[128] Much in a similar way than with palladium catalysis, high yields were obtained by mixing the nickel salt with a protonated NHC precursor.

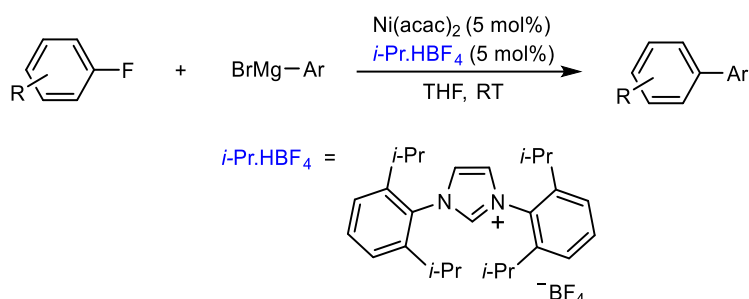


Figure I.51. Seminal KTC coupling catalysis using an in-situ generated Ni(NHC) catalyst by Herrmann and coworkers.^[128]

Since then, a plethora of Ni(NHC) catalysts have emerged, ranging from simple monodentate NHC complexes to multidentate complexes with smart redox-active ligand design (**Figure I.52**). The nickel ion is rather unique and peculiar as it is able to catalyze reactions involving a “traditional” (Ni(0)/Ni(II)) catalytic cycle but also through a (Ni(I)/Ni(III)) or even a proposed (Ni(II)/Ni(IV)) mechanism.^[129] As such, the unique propensity of the NHC ligands to accommodate both electron rich centers and high valent metals through their strong σ -donation has made them ideal partners to form robust active Ni catalysts. The catalytic applications of Ni(NHC) systems is a quickly expanding field, including C–C cross-couplings, C–S couplings, functionalization and activation of C–H and C–F bonds, oxidation of secondary alcohols and more.^[129]

A large number of NHC complexes other than Ru, Pd or Ni-NHC catalysts are currently developed. NHC research in organometallic chemistry is now a more mature science after 30 rapid years of expansion and more and more clever ligand designs are emerging.^[130] Still, a lot of ground remains to be explored, particularly in the field of redox-active ligands.

2.4. Redox-active NHCs

2.4.1. NHCs association with redox-active units

The strong electronic density on NHCs prevents their reduction and no redox activity has been reported in classical NHCs. However, there has been a few examples of modified NHCs to introduce redox-active moieties, either directly on the NHC backbone or on the amino arms. For example, the π -aromaticity of a quinone-annulated NHC was used to modulate the donating properties of the carbene between the neutral and reduced forms of a nickel catalyst (**Figure I.52**). The neutral catalyst presented an interesting reactivity in catalytic cross-coupling reactions while the reduced complex had a drastically lower activity.^[131]

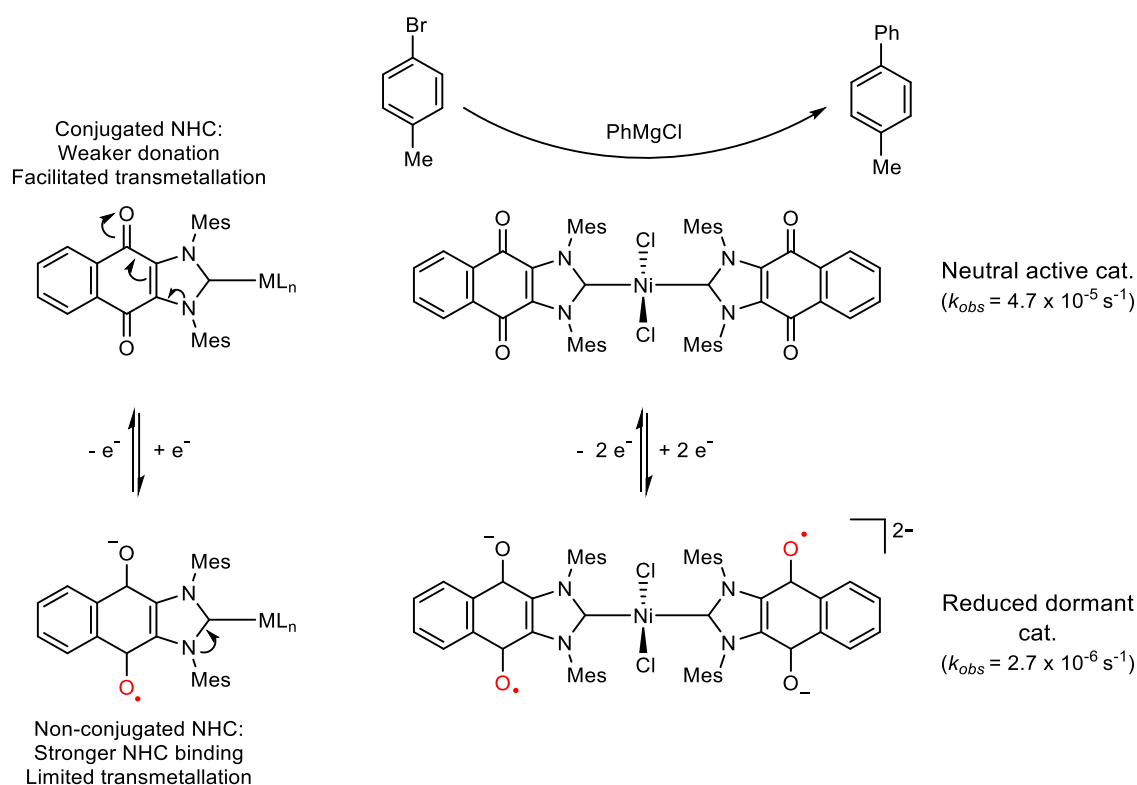


Figure I.52. Redox states modulating the donating properties of a quinoline annulated NHC ligand and its influence on the catalytic properties of a Ni(II) catalyst for Kumada cross-coupling reactions.

The distinct reactivities of the neutral and reduced forms was rationalized by the loss of aromaticity in the reduced complex. The loss of electronic delocalization on the quinone backbone results in stronger donation from the NHC ligand, forming a stronger NHC-Metal bond in the reduced unconjugated form. This stronger bond was proposed to be an inhibiting factor for the transmetallation step in the cross-coupling catalytic cycle and would explain the lower catalytic activity of the reduced complex.

In another redox switch, a ruthenium NHC analogue from the Hoveyda-Grubbs catalyst for olefin metathesis, utilized ferrocenyl (Fc) units as redox centers. By oxidation of the ferrocene unit, the catalyst could be precipitated out of solution to stop its catalytic activity.^[132] Noteworthy, the process proved reversible as the catalyst could be fully restored by collection and reduction back to the neutral form.

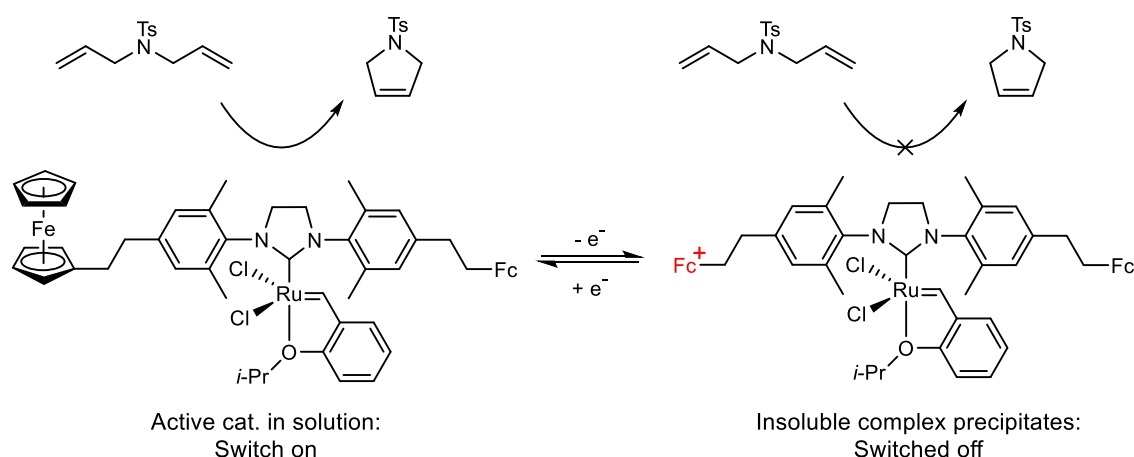


Figure I.53. Redox switchable catalyst for the olefin metathesis reaction.

Other complexes involving similar ligand design strategies have been reviewed recently by Peris.^[130] The electronic hole in the oxidized products was nevertheless not centered on the carbenic position in NHC compounds but on redox sites remote from the coordination sphere. Hence, the aim of these new types of compounds is mostly to associate the strong donating properties and the modularity of the NHC unit with the redox assistance provided to the metal center by the redox-active unit.

2.4.2. Metal complexes bearing NHC-phenolate ligands

The coupling of NHCs with aryloxides was first reported in 2003 by the Kawaguchi group^[133] as a key in stabilizing early transition metals in high oxidation states. The strong donating properties of the NHC as well as the hard anionic phenolate moiety sufficiently stabilized group 4 metal complexes (M = Ti, Zr, Hf). The titanium(IV) complex was used as an ethylene polymerization catalyst under standard methyl aluminoxane (MAO) activation and showed an activity of $290 \text{ kg} \cdot \text{mol}_{\text{cat}}^{-1} \cdot \text{h}^{-1} \cdot \text{bar}^{-1}$.

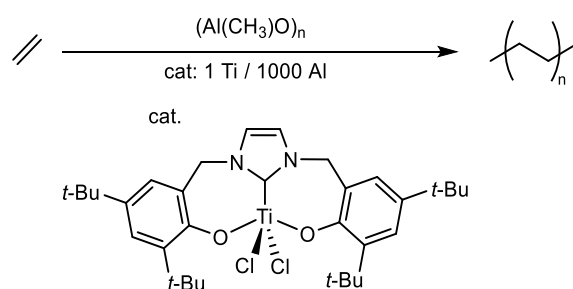


Figure I.54. First complex reported with a multidentate ligand coupling the two NHC and phenolate units and its use in ethylene polymerization catalysis.

A bidentate derivative synthesized by the same authors, and initially used as a chelate for magnesium ions, was chelated to a Ni(II) center (**Figure I.55**). This nickel(II) complex showed activity in polymerization of norbornene ($100 \text{ kg} \cdot \text{mol}_{\text{cat}}^{-1} \cdot \text{h}^{-1} \cdot \text{bar}^{-1}$). However, both the bidentate and tridentate ligands appeared to be prone to 1,2-rearrangements after deprotonation when handled at room temperature (**Figure I.55**).

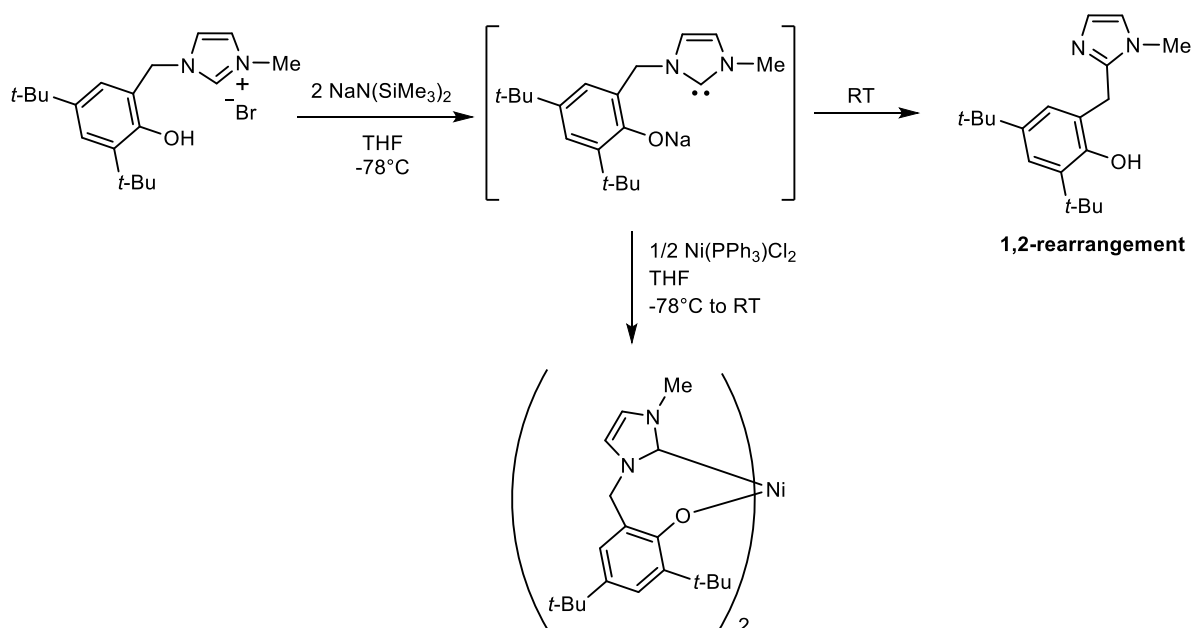


Figure I.55. Synthesis of a Ni(II) complex for the polymerization of norbornene and the degradation of the NHC-phenolate bidentate ligand at room temperature.

Waltman and Grubbs developed a bidentate ligand associating a phenolate group directly functionalized on the amino group of an NHC (labelled **L^{CO}** in this thesis, **Figure I.56**).^[134] The original aim to develop this new class of ligand was to “expand the current repertoire of available carbene ligands”. This new ligand design was proposed as an analogue to the popular salicylidene chelating pattern, widely used in coordination and organometallic chemistry.^[135,136]

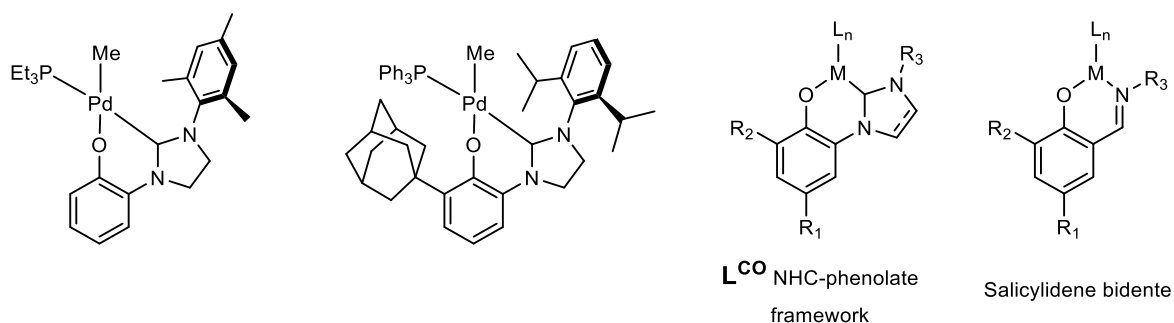


Figure I.56. First reported complexes bearing an NHC-phenolate ligand and comparison with the salicylaldehyde ligand.

However, the synthesis of NHC compounds was not yet a mature science at this period and access to this new ligand class was challenging and time-consuming. This has limited the expansion of this class of NHC ligands even with contribution by Ren *et al.* for a more straightforward synthetic route. By reaction of N-substituted imidazoles on 4-bromo-2,4,6-tri-*tert*-butyl-2,5-cyclohexadien-1-one, they were able to prepare the NHC imidazolium salt precursors (**Figure I.57**) They next formed the Pd(II) allylic complexes that proved to be reactive catalysts for simple Suzuki couplings.^[137]

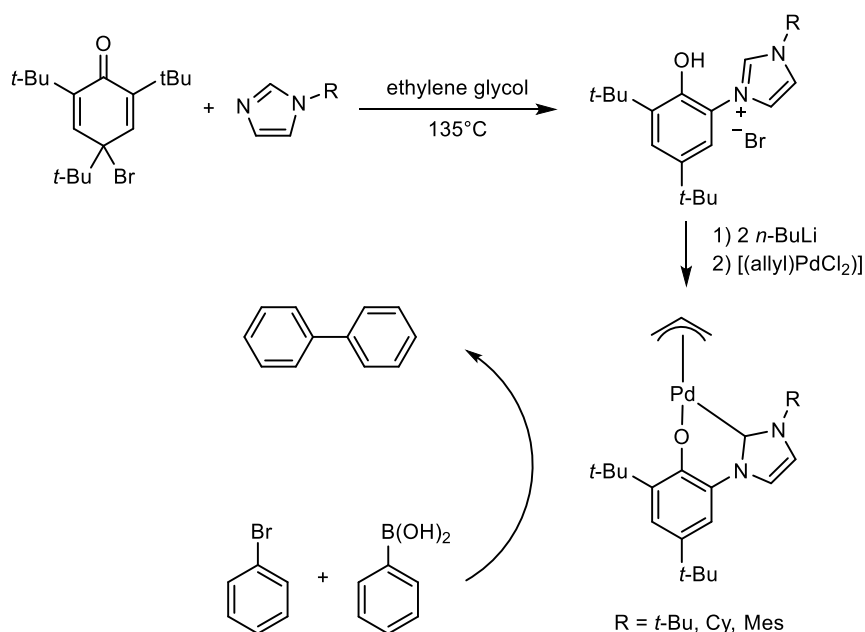


Figure I.57. Facile synthesis for HL^{CO} imidazolium salts by Ren *et al.* and their complexation to form $[\text{Pd}(\text{allyl})\text{L}^{\text{CO}}]$ complexes for Suzuki coupling reactions.

Later, these ligands were also used to form Zr(IV) and Ti(IV) octahedral complexes but showed limited reactivity for ethylene polymerization catalysis (only up to $76 \text{ kg} \cdot \text{mol}_{\text{cat}}^{-1} \cdot \text{h}^{-1} \cdot \text{bar}^{-1}$) with MAO activation.^[138] More recently, Au(I), Rh(III) and Ni(II) complexes were also reported.^[139] Another convenient synthetic route was reported by Wang and coworkers in 2015 with a catalytic C-N coupling.^[140] They were able to cross-couple 2-iodo-phenol derivatives to imidazole by a copper-catalyzed reaction with cesium carbonate (**Figure I.58**). The imidazolium NHC precursors were then obtained by N-alkylation and developed Ru(III)-NHC complexes.

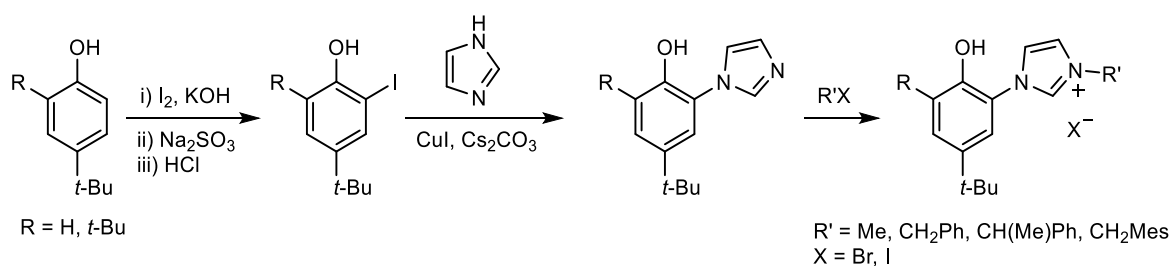


Figure I.58. Synthetic route to imidazolium-phenol proligands as reported by Wang and coworkers.^[140]

To obtain a more robust alternative than the ligand developed by Kawaguchi, Bellemin-Laponnaz *et al.* later reported a new tripodal “pincer” ligand L^{OCO} with the triethylorthoformate synthesis detailed in **Figure I.46**.^[141] Interestingly, the pincer ligand was highly suitable to stabilize high-valent metal centers scarcely reported in literature such as vanadium(V) species or Mn(III)-NHC complexes. Once again, Group 4 metal complexes were developed and used for different catalytic purposes such as the stereoselective ring opening polymerization (ROP) of racemic lactide^[142] or copolymerization of CO₂ with cyclohexene-oxide (**Figure I.59**).^[143]

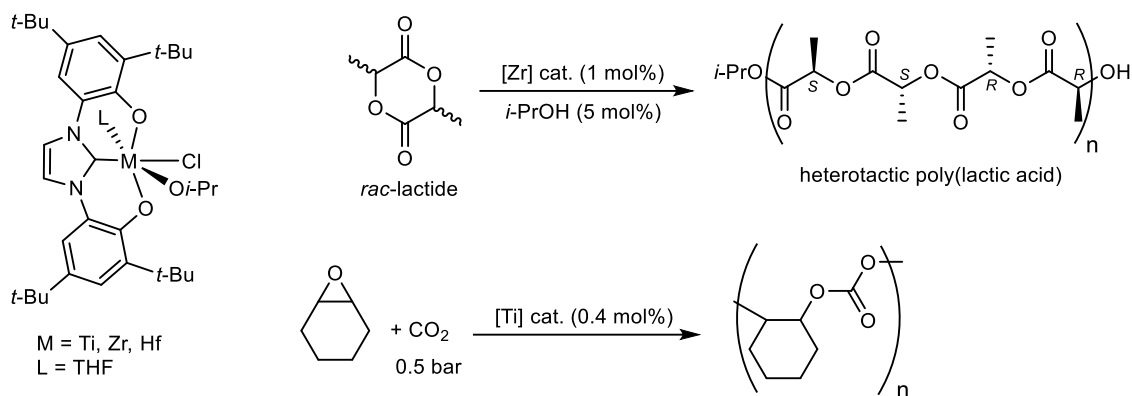


Figure I.59. Group 4 complexes of the pincer L^{OCO} ligand and some of their catalytic applications.

The Bellemin-Lapponnaz group also used this new ligand to investigate the luminescent properties of group 10 complexes (M = Ni, Pd, Pt).^[144] The aim in that case was to utilize the rigid structure of the ligand to disfavor non-radiative deactivation of the phosphorescent complexes by structural distortion.

However, the redox activity of this class of ligands was only demonstrated in 2014, 5 years after the initial reports of the manganese and vanadium complexes. Using an excess of triethylamine (Et₃N), an organic base widely used for the chelation of phenolate moieties, Romain *et al.* synthesized homoleptic octahedral complexes of the group 4 metal ions (**Figure I.60.A**).^[145] The complexes showed comparable electrochemical behaviors with at least two monoelectronic oxidation events in cyclic voltammetry (CV) that were attributed to successive oxidations to form phenoxyl radicals. The nature of the oxidation was confirmed by EPR spectroscopy on the mono-oxidized electrogenerated species. The oxidation products indeed showed broad isotropic signals at $g \approx 2.00$, close to genuine free phenoxyl radicals.

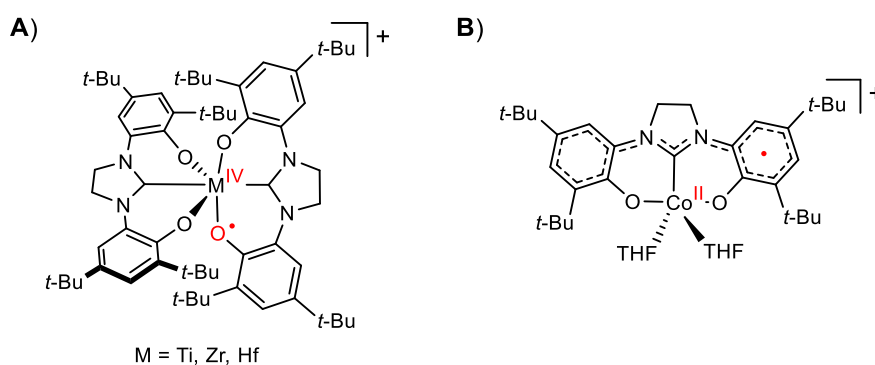


Figure I.60. Mono-oxidized $[ML^{OCO}]^+$ complexes displaying phenoxyl radical centers by Romain *et al.* (A) and Harris *et al.* (B).

A more complete picture of the electronic structure of oxidized compounds using the pincer ligand was published recently on cobalt complexes (**Figure I.60.B**).^[146] In this work, a combination of magnetic susceptibility measurements, EPR experiments and theoretical calculations were used to discriminate between different possible ground states for the oxidized compounds:

- (i) Low-spin Co(II) antiferromagnetically coupled to a ligand radical ($S = 0$).
- (ii) Intermediate-spin Co(III) center ($S = 1$).
- (iii) Low-spin Co(II) ferromagnetically coupled to a phenoxyl radical ($S = 1$).
- (iv) High-spin Co(II) antiferromagnetically coupled to a ligand radical ($S = 1$).

The general conclusion pointed towards formation of a phenoxyl radical upon oxidation with a strong ferromagnetic coupling to the Co(II) center (case iii).

Finally, the Thomas group reported on the electronic properties of two nickel complexes with pincer ligands and a pyridine coligand (**Figure I.61**).^[147] They were able to chemically oxidize one of the two complexes using silver and successfully crystallized the oxidation product. The oxidation proved to be mainly ligand-centered on the two phenolate rings (Class II/III intervalence, see section 1.3.3.) with a partial delocalization on the nickel ion as demonstrated by X-Ray diffraction, EPR and UV-vis-NIR spectroscopies.

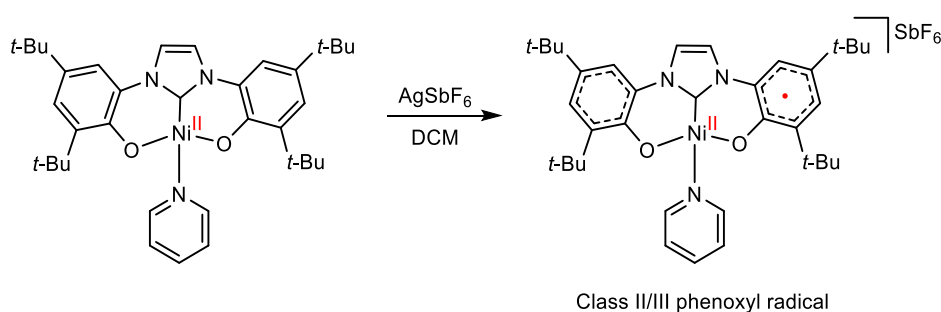


Figure I.61. Neutral $\text{Ni}^{\text{II}}\text{L}^{\text{OCO}}\cdot\text{pyr}$ complex and its chemical oxidation to a $[\text{Ni}^{\text{II}}\text{L}^{\text{OCO}}\cdot\text{pyr}]^{+\bullet}$ delocalized phenoxyl radical.^[147]

Finally, a tetradentate ligand combining two NHC moieties and two phenolates was also developed and coordinated to a nickel(II) ion and used in catalysis for C-C and C-N bond formations (**Figure I.62.A**).^[148] Other analogues were also developed and used on Platinum(II) complexes as blue fluorophores with promising quantum yields (**Figure I.62.B**).^[149] The redox activity of the ligand was yet to be demonstrated.

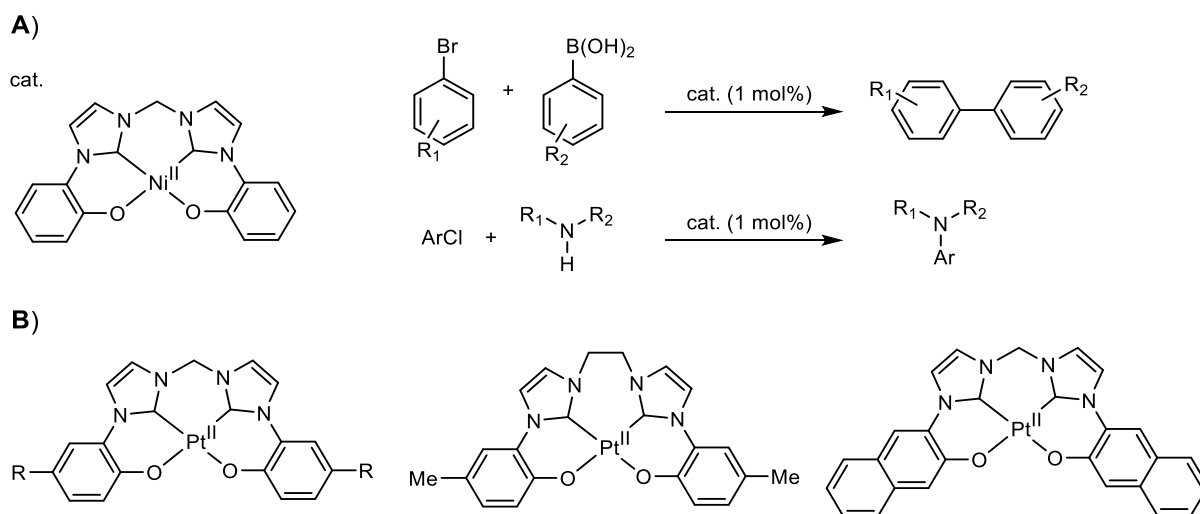


Figure I.62. Tetradentate complexes bearing two phenol and two NHC units: Reactions of a Ni(II) catalyst (**A**) and Pt(II) complexes for light emission (**B**).

Other ligand designs have also incorporated both NHC and phenol subunits but remain scarce. Most examples include other group 4 or group 10 catalysts^[150,151] and one recent publication reported their use as an inverse crown ether to trap magnesium-oxo species.^[152]

Finally but nonetheless, the Meyer group, has also inserted some phenol subunits in their famous tripodal NHC ligand designed a few years ago.^[153] Well-known in the field of research on nitride chemistry, they have reported the first evidence of a cobalt-nitrido intermediate that they characterized using low temperature EPR following irradiation of an azido Co(II) precursor (**Figure I.63**).^[154]

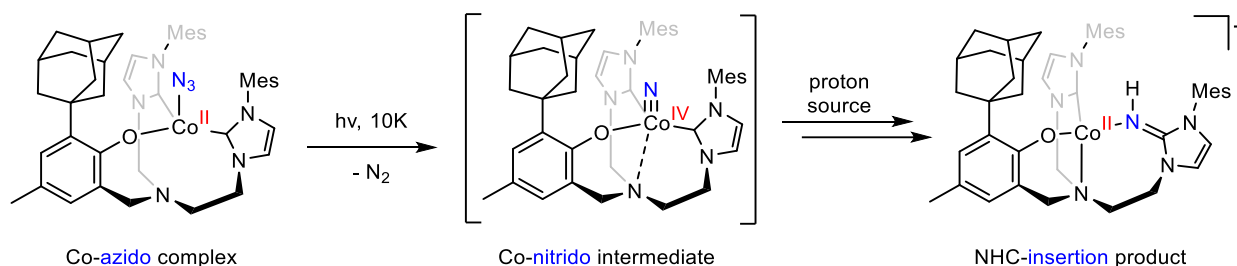


Figure I.63. First evidence of a Co-nitrido species by the Meyer group, supported by a bis-NHC phenolate tripodal ligand.

When warmed back to room temperature, the intermediate readily evolved to form an insertion product on the carbenic position of an NHC (**Figure I.63**). Such insertion reactions have been known for some time now (**Figure I.55**), specifically in the case of high valent metal centers.^[155]

Although, there is an increasing number of ligands combining phenolate and NHCs in the literature, very little effort has been made to valorize the redox-activity of these new classes of ligands. As such, the research of my thesis was focused on obtaining a deeper understanding of their electronic structure as well as its impact on the coordination and activation of small molecules, specifically the chemistry of nitrogen activation.

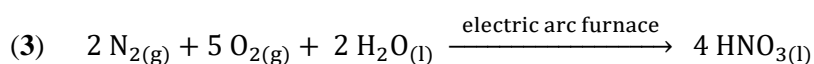
3. Influence of redox-active ligands on nitrogen chemistry

3.1. Nitrogen fixation

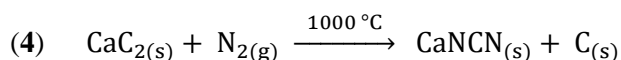
The nitrogen element (N) has historically been a key molecular piece for production of fertilizers. Additionally, our modern society has become dependent on a wide cast of nitrogen-containing molecules playing irreplaceable roles in diverse fields such as pharmaceuticals, polymers, propellants, dyes and catalysts. However, at the end of the 19th century, as natural reserves of nitrogen compounds started to deplete, the need for alternative sources to produce nitrogen-containing chemicals became dire. The key to answer that issue appeared to be clear: nitrogen (N₂). Constituting 78% of the Earth's atmosphere, nitrogen appears to be a readily available and abundant feedstock for production of nitrogen-containing compounds. However, due to its extreme inertness, N₂ has to be first activated, or "fixed", into suitable forms to be efficiently used in large scale applications.

Three different processes were based on this idea. The Birkeland-Eyde process used electric discharges into an oxygen-nitrogen mixture to produce nitric acid (**3**). However, the electric arc furnace required proved to be too expensive and made it obsolete. The Franck-Caro cyanamide process uses calcium carbide (CaC₂) to react with nitrogen at high temperature to form CaNCN (**4**). Finally, the most prominent Haber-Bosch process was developed using nitrogen and three equivalents of hydrogen gas (H₂) on an iron metal-catalyst to produce ammonia (NH₃) (**5**). While being thermodynamically favored, the process requires particularly harsh conditions such as high pressures and temperatures to favor ammonia production.

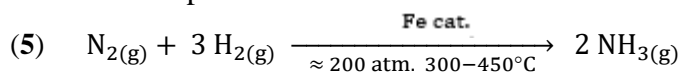
Birkeland-Eyde process:



Franck-Caro cyanamide process:



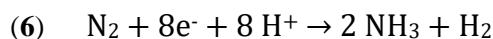
Haber-Bosch process:



Still, this major breakthrough to afford an economically viable production of ammonia led to two Nobel prizes. Fritz Haber was awarded in 1918 to demonstrate the reaction at a laboratory scale and Carl Bosch in 1931 for its adaptation into an industrial scale process. The Haber-Bosch process is still the long-standing major option for nitrogen fixation since its development in the first decade of the 20th century. However, due to the different factors explained previously, the process represents close to 2% of the entire world energy consumption. Additionally, the process requires methane to form the hydrogen required in the reaction, in a time where carbon-based feedstocks pose a major threat as greenhouse gases in the global warming crisis. As such, the development of alternative means of nitrogen fixation under milder conditions has become one of the most crucial and challenging problems in chemistry.

3.2. Nitrogenase

Nitrogenase is the enzyme that catalyzes biological N_2 reduction to NH_3 , achieving an impressive rate enhancement over the uncatalyzed reaction, according to the following general reaction:



Still to this day, a high demand remains for N_2 fixation to support food and chemical production. The heavy reliance of the industrial Haber–Bosch nitrogen fixation reaction on fossil fuels, presents major worldwide energy concerns. Therefore, more than ever, there is a strong need to elucidate how nitrogenase achieves this challenging reaction under mild conditions.

3.2.1. Structure and activity of nitrogenase

There are three forms of nitrogenase: the molybdenum-dependent Mo-nitrogenase, vanadium-dependent V-nitrogenase, and iron-only Fe-nitrogenase.^[156] The Mo-nitrogenase is the most common in nature. The expression of the different forms appears to be controlled by metal regulation. If no Mo is available or cannot be deftly transported, one of the two other forms will be expressed.^[157]

The structure of Fe-nitrogenase has still not been resolved but the Mo and V-nitrogenases present similar quaternary structures.^[158,159] The protein can be separated in two components: the catalytic active component MFe protein ($\text{M} = \text{Mo}, \text{V}, \text{Fe}$) and two Fe proteins responsible for the electron input to the active site, using ATP hydrolysis. The MoFe protein is separated in two halves. Each half is host to a cofactor, called respectively FeMo-co, FeV-co and FeFe-co, which is the active site of N_2 reduction. Electrons from the Fe protein are transferred through the MoFe protein by iron-sulfur clusters [8Fe-7S], labeled P-clusters (**Figure I.64**).

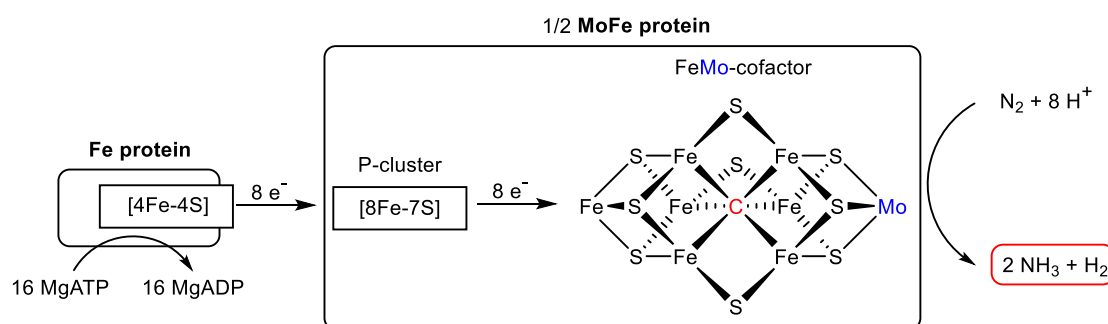


Figure I.64. General structure of half of a Mo-nitrogenase enzyme and its catalytic activity for N_2 reduction.

3.2.2. Mechanistic insights

It is key to note that contrary to the Haber-Bosch process, protons are consumed in the reaction rather than dihydrogen. Furthermore, a mole of H_2 is produced for two moles of ammonia (**Figure I.64**), requiring 8 electrons in the overall reaction instead of the 6 required to reduce dinitrogen itself as presented in Equation (6). Extensive studies into the mechanism of the nitrogen reduction at the FeMo-co active site has led to the development of the Lowe-Thorneley model, (**Figure I.65.A**).^[160] The FeMo-co site was labeled and separated into 8 different states from E_0 to E_8 corresponding to sequential additions of electron and protons.

To explain the release of the dihydrogen molecule, models involving metal-bound hydrides were proposed.^[161] Before N_2 can be incorporated, 4 protons are inserted and reduced (E_{0-4}), ending up in a transition state ($E_4(4H)$) presenting two reduced hydrides, **Figure I.65.B**).^[162] This key intermediate state was labeled by the roman god of transitions, Janus. It is the starting point for nitrogen evolution in the catalytic cycle but is also keen to “fall back” to the starting state E_0 by elimination of two dihydrogen molecules (**Figure I.65.A**).^[163]

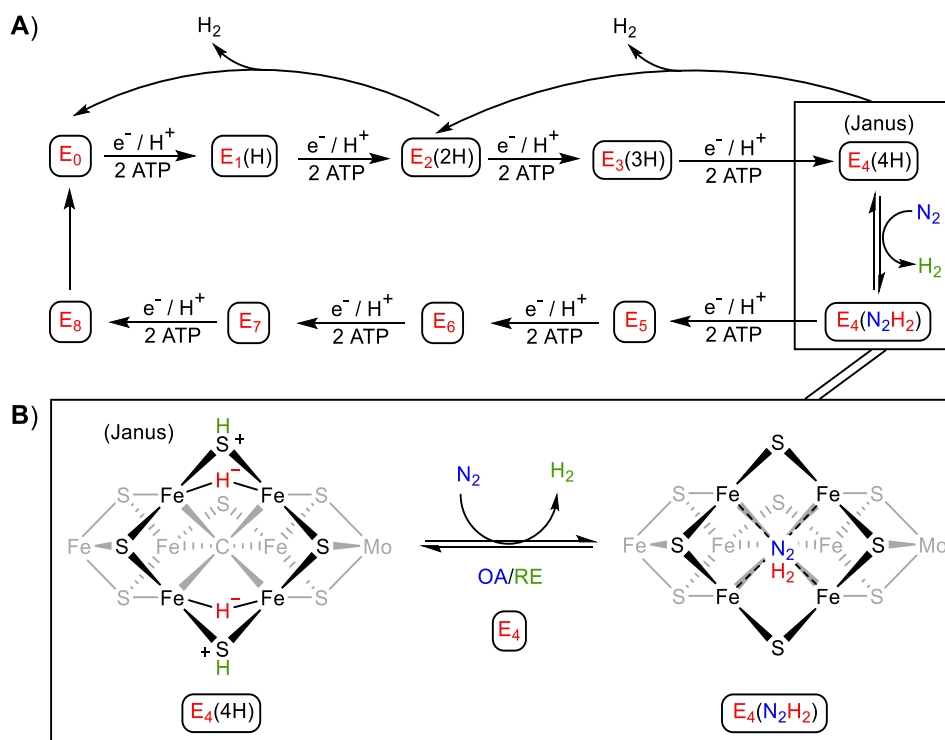


Figure I.65. Generalized Lowe-Thorneley model for the $8(e^-/H^+)$ reduction of dinitrogen in the FeMo-co active site (**A**) and schematic representation of the coupled OA/RE process for N_2 insertion and release of H_2 from the Janus intermediate (**B**).

From the Janus intermediate, N_2 would be incorporated by oxidative addition (OA) while the H_2 molecule produced in the catalytic cycle is collaterally released by reductive elimination (RE) (**Figure I.65.B**).^[162] This starting state $E_4(N_2H_2)$ for the evolution of nitrogen has still not been structurally characterized. Additionally, the mechanistic pathway for the release of the two NH_3 molecules in Eq. (6) has not been clearly enlightened. As such, two reduction pathways have been proposed: an alternating and a distal pathway (**Figure I.66**).

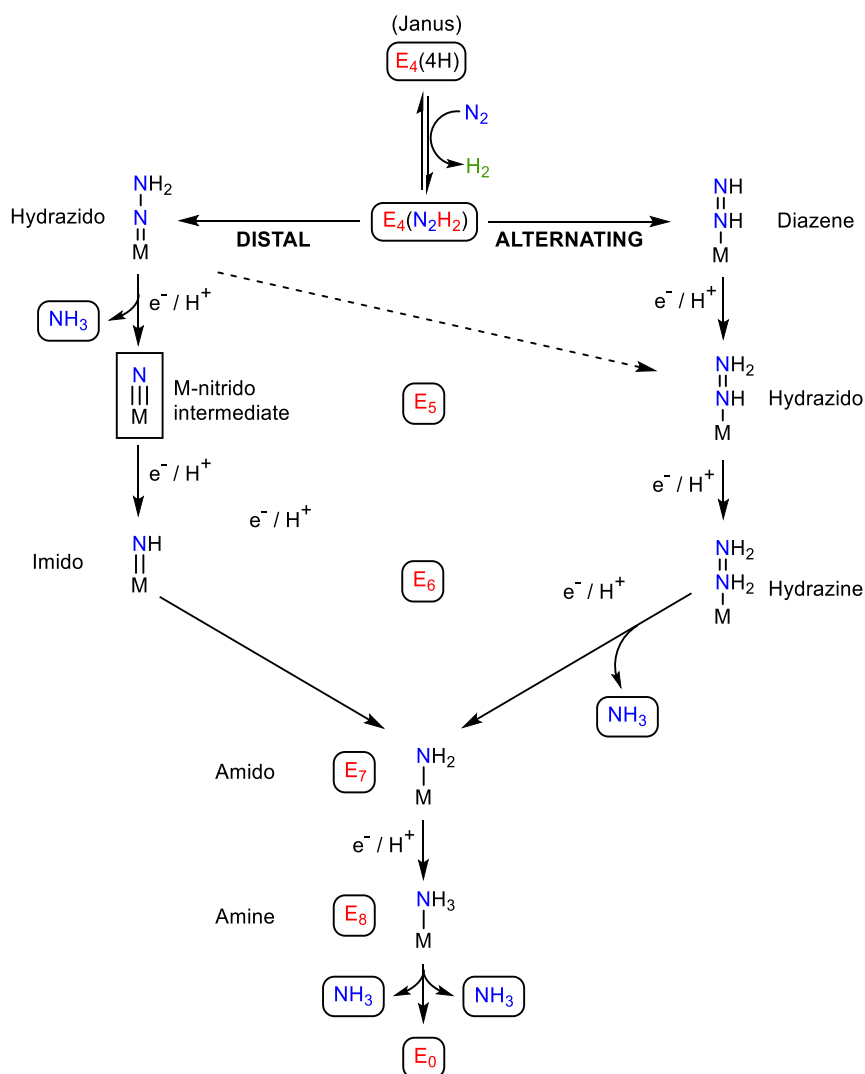


Figure I.66. Proposed distal and alternating pathways for the reduction of N_2 with credible intermediates. M represents the active site of the FeMo-cofactor. A hybrid pathway is presented by a dashed-arrow.

In the case of the alternating evolution, the two N atoms are hydrogenated in parallel, affording a hydrazine intermediate (E_6) before successive release of the two ammonia molecules in the last two reaction steps. On the other hand, the distal pathway is proposed to follow complete hydrogenation of each N atom, forming a $M \equiv N$ nitrido intermediate (E_5) after release of the first NH_3 .

The discrimination of one pathway over another is still a matter of debate but some insight from publications point towards the alternating pathway. Specifically, it has been shown that hydrazine is a product of N_2 in V-nitrogenase.^[164] To note, vanadium nitrogenase presents the same quaternary structure as Mo-nitrogenase and OA/RE coupled mechanism for incorporation of N_2 and is therefore believed to operate in a similar fashion. Additionally, Mo-nitrogenase was proved to produce hydrazine when submitted to acidic or basic quenching during N_2 reduction.^[160,165] As the presence of hydrazine as a product would be prevented in the distal pathway, these results point towards the alternating reduction of dinitrogen. More recently, Peters and coworkers also theorized on a hybrid explanation that would be consistent with those observations. The mechanism would follow hydrogenation of a hydrazido(2^-) ligand in the

distal pathway ($E_4(N_2H_2)$) to form the hydrazido(1^-) compound in the E_5 state of the alternating pathway (**Figure I.66**, dashed arrow).^[166]

The exact binding and mechanism for the nitrogen reduction remains not entirely clear. However, the reports of the crystallographic structures for both the Fe-protein and the MoFe-protein has given some important information to inspire chemists for new molecular models of nitrogenase to mimic its activity. At this crucial interface between biology and chemistry, dinitrogen biological fixation and chemical N_2 reduction using transition metal complexes remain tightly bound together.

3.3. Molecular complexes for catalytic N_2 reduction

3.3.1. Seminal Schrock discovery

Activating molecular nitrogen by soluble metal complexes is a longstanding challenge in inorganic chemistry. This simple, readily available small molecule is notoriously unreactive and generally resists coordination unless specific conditions are met. As such, the discovery of the first N_2 coordination complex by Senoff in 1965^[167] was initially met with strong skepticism as dinitrogen was believed to have too weak donating properties to be considered as an isolable ligand. However, a definitive proof of the nature of the complex was obtained from its crystal structure in the following year.^[168] This discovery boosted the development of hundreds of N_2 complexes ranging all across the transition metals series. This field arose in the hope of developing well-defined abiological catalytic reduction of nitrogen, using ambient reaction conditions of temperature and pressure with protons and electrons as is the case in the nitrogenase enzymes. Still, very few reports of catalytic formation of NH_3 from nitrogen were published^[169–173] and no system could give much insight on the N_2 reduction mechanism until Schrock reported the seminal “Catalytic Reduction of Dinitrogen to Ammonia at a single Molybdenum Center”^[174] in 2003. In his paper, Schrock isolated and characterized a mononuclear complex of molybdenum with a triamidoamine ligand HIPT and dinitrogen ($Mo(N_2)$), as well as a number of different reduced intermediates including diazene ($Mo-N=N$), hydrazine ($Mo=N-NH_2$), nitride ($Mo\equiv N$), and ammonia ($Mo(NH_3)$) derivatives (**Figure I.67**). From those different intermediates, Schrock suggested a distal reduction pathway of nitrogen, in opposition with the alternating pathway generally proposed in the nitrogenase enzymes (Chap I.3.2.2.).

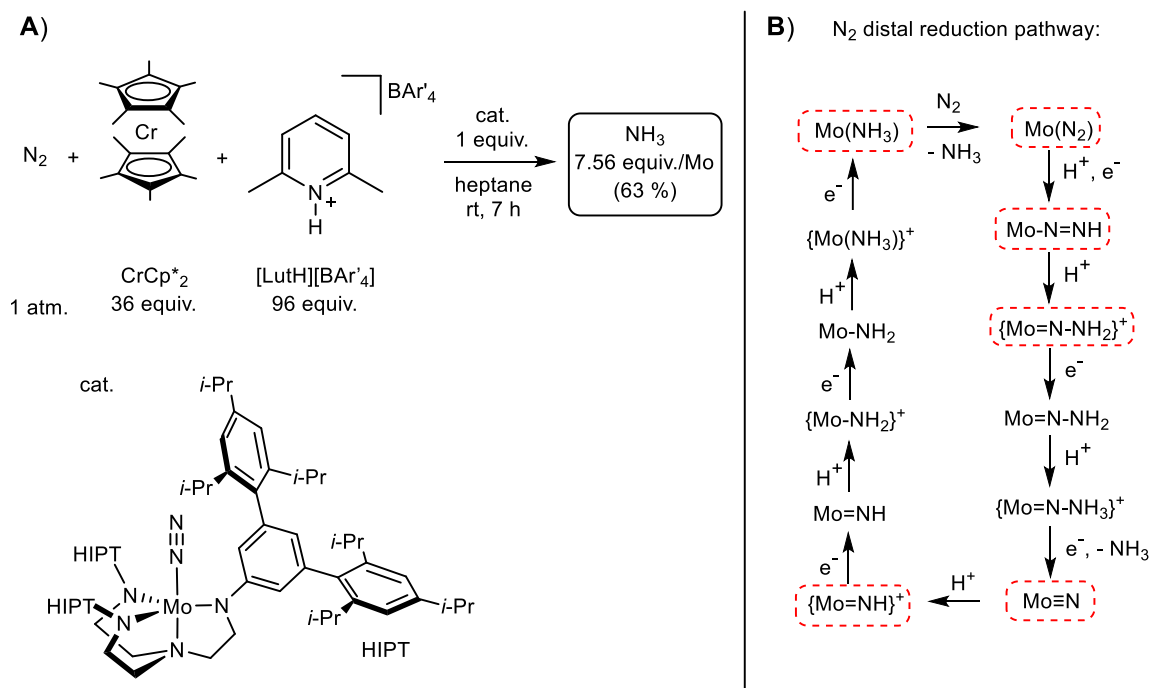


Figure I.67. Seminal report of catalytic formation of ammonia from dinitrogen gas by Schrock^[174] (**A**) and proposed distal pathway for N_2 reduction in the catalytic cycle (**B**). The intermediates synthesized and characterized by Schrock in the report are highlighted in red.

With his catalyst, he used a large excess of a proton source and of a strong reducing agent, a lutidinium salt $[LutH][BAr'_4]$ and decamethylchromocene $CrCp^*_2$ respectively, under atmospheric pressure of N_2 at room temperature. He was able to achieve up to 4 turnovers, forming 8 equivalents of ammonia per molybdenum center.

This publication ushered a new era of research for molecular models for dinitrogen fixation with a number of different groups competing to improve the catalytic efficiency of the reaction. While various transition metals have been shown to activate N_2 for different reactions^[175] iron and molybdenum have been mostly used for this specific purpose as they are part of the most studied FeMo cofactor in the nitrogenase enzymes.^[176]

3.3.2. Peters iron catalysts

Notably, the Peters group developed a range of iron catalysts as models, using a family of trisphosphino ligand with an ancillary light atom center ($E = Si, C, B$).^[177–179] The ligands were designed to mimic the peculiar environment at the putative Fe binding site for N_2 in the FeMo cofactor, displaying an interstitial carbide that had its identity proven only recently (highlighted in red, **Figure I.64**).^[180–183] Using excess proton and electron sources once again, with an etherate salt and potassium graphite (KC_8) respectively, Peters and coworkers obtained up to 64 equivalents of NH_3 formed per Fe center (**Figure I.68**).

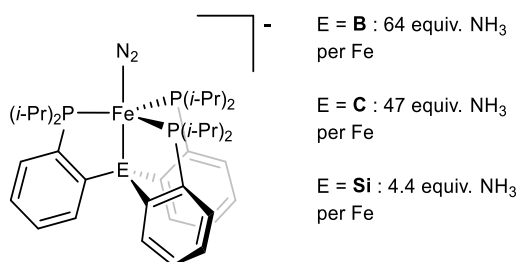


Figure I.68. Series of catalysts for nitrogen reduction reported by Peters and coworkers.

3.3.3. Low-valent molybdenum Nishibayashi catalysts

Meanwhile, the Nishibayashi group investigated low-valent Molybdenum-phosphine catalysts. Their initial report in 2010 described the synthesis of a dinuclear Mo(0) system $[\text{Mo}_2(\text{N}_2)_4(\text{PNP})_2(\mu\text{-N}_2)]$ with a bridged N_2 ligand using a pincer PNP-based ligand where PNP = 2,6-bis(di-*tert*-butylphosphinomethyl)pyridine). $[\text{Mo}_2(\text{N}_2)_4(\text{PNP})_2(\mu\text{-N}_2)]$ was obtained from the reduction of a mononuclear $[\text{Mo}^{\text{III}}(\text{PNP})\text{Cl}_3]$ complex with a Na-Hg amalgam under N_2 atmosphere (**Figure I.69**). The dimer displayed limited but promising reactivity with up to 11.6 equivalents of ammonia produced per Mo center.^[184]

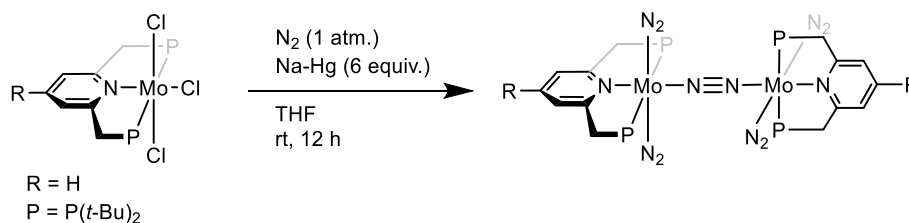


Figure I.69. Synthesis of the first catalyst for nitrogen reduction reported by Nishibayashi.

Nishibayashi expanded this research on the PNP ligand system, tuning coordination at the phosphine site through modification of its substituents^[185] ($\text{P} = \text{P}(\text{i-Pr})_2$, $\text{P}(\text{t-Bu})_2$, PPh_2 , PAd_2). The phosphine substituents proved to be critical as neither the iso-propyl nor the adamantyl substituted complexes allowed for the formation of the Mo(0) dimeric systems. The electronic effects of the para position of the pyridine ring were also investigated ($\text{R} = \text{H}$, Ph , Me_3Si , t-Bu , Me , MeO). The electron donating properties of the Mo center proved to deeply affect the reactivity of the catalyst. Indeed, the more electron-rich catalyst ($\text{R} = \text{OMe}$) was able to form more ammonia than the original catalyst ($\text{R} = \text{H}$) with 34 and 23 equivalents of ammonia per Mo center respectively.

The mechanism of nitrogen reduction was further investigated using density functional theory where a monomeric molybdenum nitride species $[\text{Mo}(\text{OTf})\text{N}(\text{PNP})]$ was proposed as a key intermediate in the reaction (**Figure I.70**).^[186]

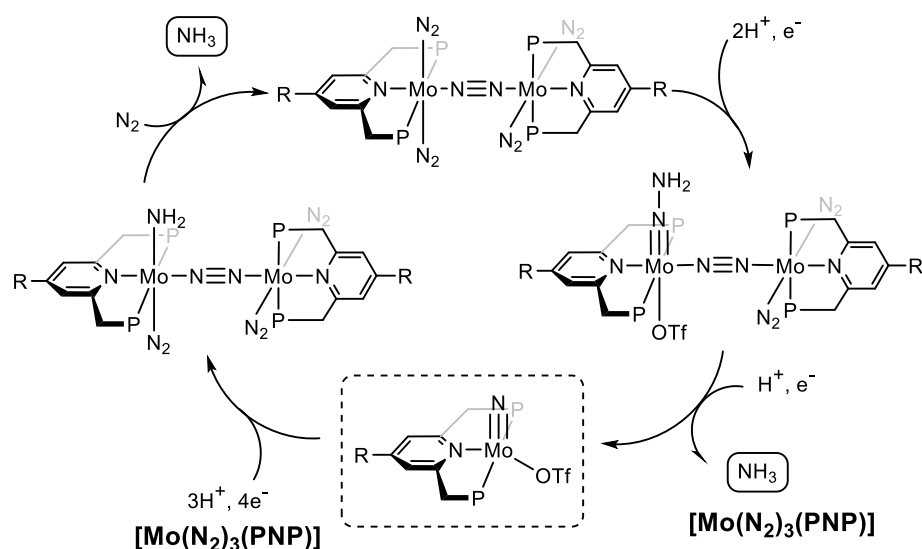


Figure I.70. Proposed catalytic cycle of formation of ammonia from dinitrogen with Nishibayashi dimer catalysts. A key molybdenum nitride intermediate is highlighted in a dashed box.

Following this hypothesis, Tanaka et al. explored the activity of mononuclear molybdenum nitride species on the reduction of N_2 . The mononuclear nitride complexes showed to be catalytically active with comparable formation of ammonia in comparison to the dimer $[\text{Mo}_2(\text{N}_2)_4(\text{PNP})_2(\mu\text{-N}_2)]$.^[187]

Introduction of redox-active subunits in the ligand design was also probed, integrating ferrocene and ruthenocene groups as R para substituents.^[188] While the incorporation of the metallocenes was found to have a negligible impact on N_2 activation through infrared (IR) spectroscopy, the catalyst displayed increased formation of ammonia (37 equivalents, R = Fc) when compared against the parent catalyst (23 equivalents, R = H). This difference was rationalized in DFT calculations in terms of reduction of the hydrazinium intermediate $[\text{Mo}(\text{NNH}_3)]^+$. The introduction of the redox-active subunit allowed for an easier reduction, leading to an improved release of NH_3 . Furthermore, the effect was limited when a longer linker was introduced between the metallocene and the pyridine ring. This highlighted the impact of the electronic communication between the metallocene and the pyridine on the activity of the catalyst.

In 2017, Eizawa et al. also studied alternative type of PCP pincer ligands, introducing NHC ligands in place of the traditional pyridine rings (**Figure I.71**).^[189] They exploited the impressive electron-donating properties of NHC ligands to design more effective catalysts. Additionally, the propensity of NHCs to form highly stable and electron-rich complexes was hypothesized as a way to prevent dissociation of the pincer ligand during catalytic turnovers. The NHC complex proved indeed to be more effective than the seminal PNP catalyst under similar reaction conditions, forming 17.6 and 12.2 equivalents of ammonia respectively.

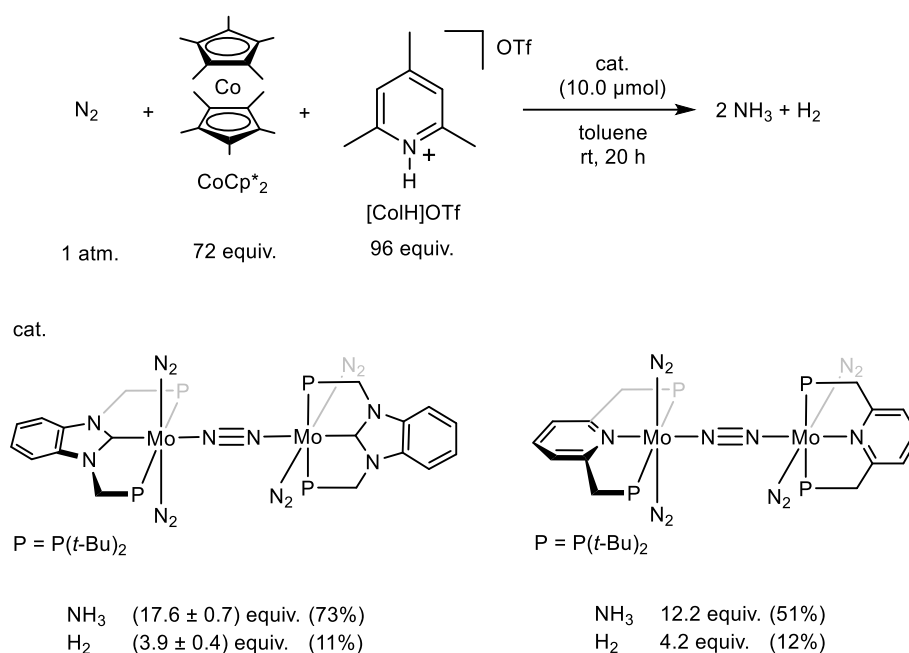


Figure I.71. Catalytic formation of ammonia from dinitrogen gas using NHC or pyridine-based catalysts.

Additionally, the nature and amounts of both the proton source and the reductant were investigated by Nishibayashi and coworkers. They concluded that the lutidinium triflate salts $[LutH]OTf$, which were used as a weak acid ($pK_a = 6.77$) were the best alternative over picolinium or collidinium derivatives. The decamethylchromocene $CrCp^*_2$ was used as the reducing agent ($E_{1/2} = -1.35V$ vs Ag^+/Ag) and proved to be more suitable than the cobaltocene analogues. Furthermore, increased loading of the two reagents showed a drastic increase of formation of ammonia, even with decreased catalytic loadings. As such the use of 1440 equivalents of $CrCp^*_2$ and 1920 equivalents $[LutH]OTf$ in the presence of 10.0 μ mol of NHC-based catalyst afforded up to 200 equivalents of NH_3 , compared to 17.6 equivalents of ammonia with the catalytic conditions depicted in **Figure I.71**.

Still, the use of such reducing agents and proton sources dampened the vision of a viable process with these molecular models as they remained expensive and non-readily available reagents. To answer this ongoing issue in the field, Ashida et al. recently valorized the use of samarium iodide SmI_2 as a reducing agent that can be used in tandem with polar, protic proton donors such as water or alcohols.^[190] This creative approach led to remarkable results with up to 4350 equivalents of ammonia formed at a high turnover frequency (TOF) of 117 min^{-1} comparable to the TOF of nitrogenase enzymes ($40\text{--}120 \text{ min}^{-1}$)^[191] using a NHC Mo precatalyst (**Figure I.72**).

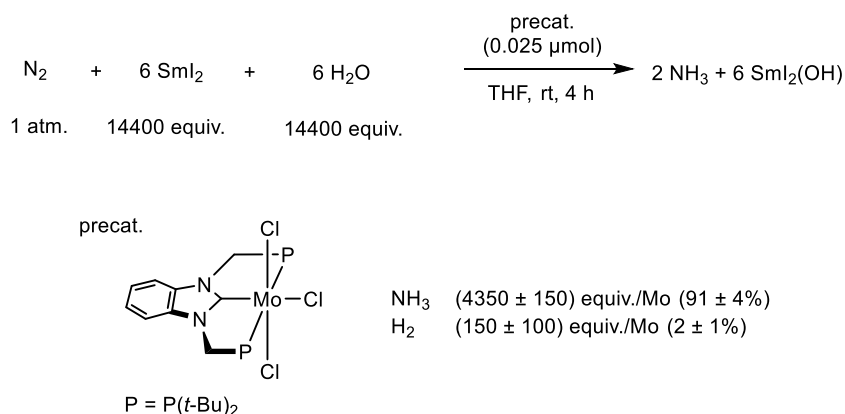


Figure I.72. Catalytic formation of ammonia from dinitrogen gas using a molybdenum precatalyst.

3.4. Transition metal nitrides

As we discussed above, metal nitride complexes can be intermediates in the catalytic process towards nitrogen reduction towards ammonia.^[192] Thus, the study of their properties and reactivity keep providing valuable insight into the mechanistic details of N₂ activation. On the other hand, their role as potential reactive synthons in organic chemistry has been considered more recently.^[193,194] Indeed, the vast majority of metal nitride complexes are unreactive at the nitride, and thus the ability to generate a reactive nitride fragment remains of major interest.^[195] Transition metal complexes bearing terminal nitride (N³⁻) ligands have been known for over 170 years. The electronic structure and bonding of metal-nitrogen multiple bonds has since been a long-standing topic of interest. Overall, the kinetic and thermodynamic stability of nitride-containing compounds has made them attractive candidates for use in thermo and piezoelectric materials for energy harvesting and thin films. Nitride bonds to main group elements, such as boron nitrides, represent an extremely robust and versatile class of materials (sometimes harder than diamond) which are traditionally used as components in high-temperature equipment.

3.4.1. Metal nitrides syntheses

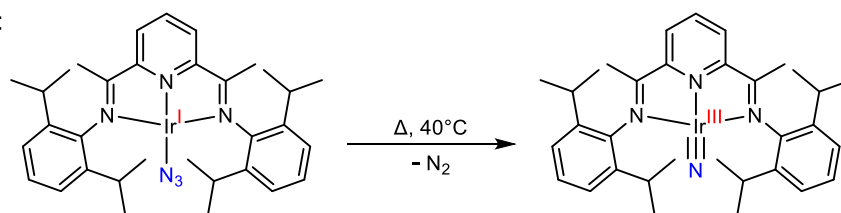
Many different routes to obtain metal complexes with terminal nitride ligands that have been extensively reviewed. For the most common syntheses, four different strategies can be distinguished:

- (i) Decomposition of azide precursors.
- (ii) Oxidation of ammonia.
- (iii) Nitrogen atom transfers.
- (iv) Cleavage of “N-E” bonds.

- Decomposition of azide precursors

One of the most convenient and widely used pathways to obtain terminal nitrides is to develop azide precursors. These complexes can then be photochemically excited or undergo thermolysis in the solid state to eject dinitrogen,^[196] affording the oxidized metal-nitride final product. While being the most prominent synthetic route, there are only few mechanistic insights on the decomposition pathway from the azide compound to the terminal nitride complex.

A) Thermolysis:



B) Photolysis:

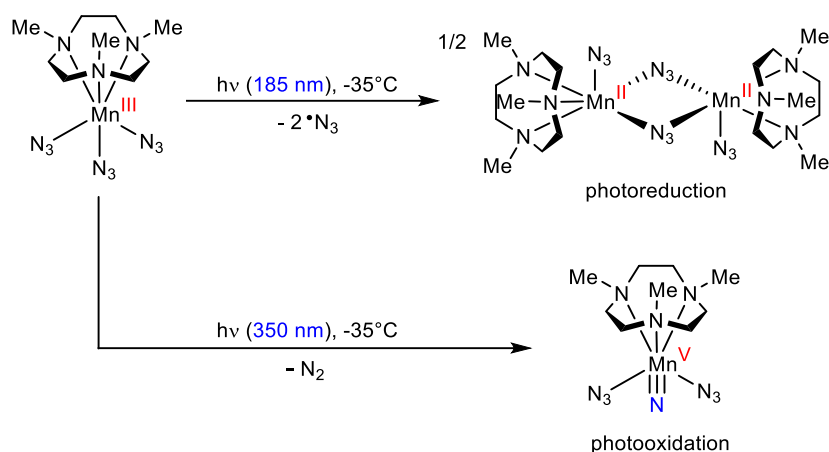


Figure I.73. Formation of metal nitride complexes by solid-state thermolysis (A) and photolysis with different behaviors depending on the irradiation wavelength (B).

Different tweaks to the general methods have been used to enhance the yields of the reactions. For thermolysis, the reaction has shown to be enhanced by activation using a Lewis acid.^[197] On the other hand, for photochemical decomposition, formation of the nitride can also be strongly dependent on the selection of the irradiation wavelength (**Figure I.73.B**).^[198,199] Higher energy light tends to afford faster reactions with better yields and hence UV-light is commonly used. However, irradiation at frequencies corresponding to $N_3 \rightarrow$ Metal charge transfers have been proposed to lead to photoreduction and ejection of a N_3 radical instead. In order to address this issue, photolysis in frozen solution has also been used in different cases.^[154,200] The theoretical reduced mobility of the ejected azide radical would make the photoreduction partially reversible, increasing the yield for the oxidized metal-nitride desired product.

- Ammonia oxidation

Ammonia has also been used as the core N atom donating reagent when coupled to an oxidizing agent. This synthesis has been specifically used on a number of Mn(V)nitride salen complexes, utilizing ammonium hydroxide and bleach as inexpensive, readily available reagents.^[201,202] While the sturdiness of the salen framework can withstand this protocol, the harsh oxidizing conditions prevents the use of this method in case of more delicate compounds.

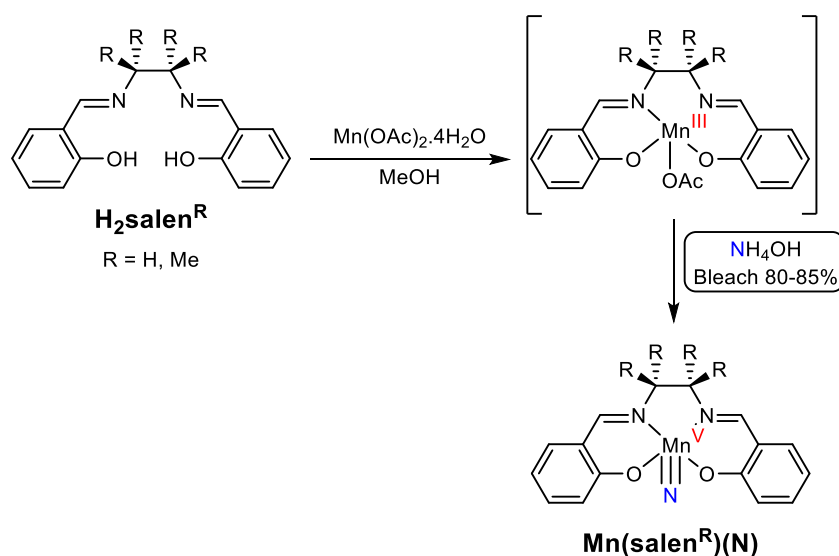


Figure I.74. Synthesis of Mn(V) salen nitride complexes developed by Carreira and coworkers.^[201]

- Nitrogen atom transfer

The versatility of the salens to form stable complexes in a wide range of oxidation states has also been used to develop nitride transfer reagents. Manganese salen nitride complexes have shown intermetal reactivity to exchange the nitrido moiety with another exogenous ligand from a different metal complex (**Figure I.75**). The reaction can be driven by the difference of solubility between the two different forms of the Mn-salen complexes.

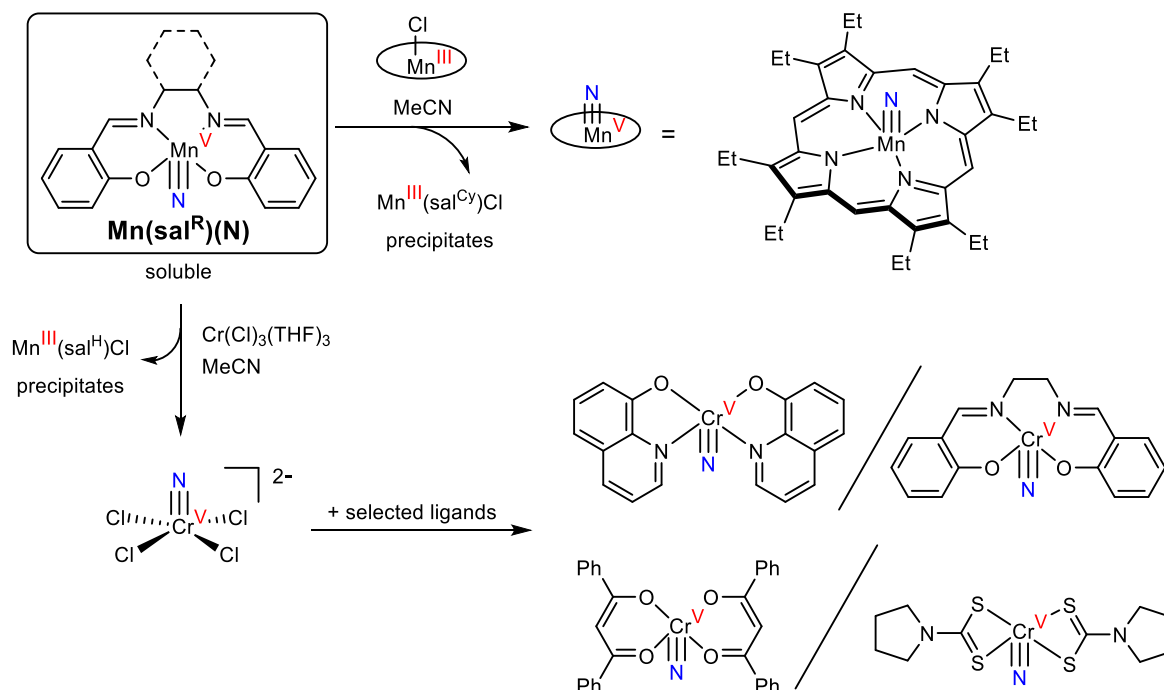


Figure I.75. Use of manganese salen nitrido complexes as nitride transfer agents: direct formation of Mn(N) complexes (top)^[203] and two-step formation of Cr(N) species (bottom).^[204]

The use of such metal salen nitride transfer reagents present a number of benefits, as these are air-stable compounds that can be prepared on a large scale from the previously described ammonia oxidation route. This method was also refined to obtain a simple [Cr(N)Cl₄]²⁻ metal

nitride compound that can be directly chelated in-situ with the desired ligand framework (**Figure I.75**).

Other compounds were used to deliver the nitride ligand. The chromium complex $(\text{N})\text{Cr}(\text{t-BuO})_3$ was also used to transfer its nitride to afford a $\text{V}^{\text{V}}(\text{N})$ complex.^[205] Organic reagents were also developed: 2-methylaziridine was used on a tungsten complex to afford the $(\text{t-BuSiO})_3\text{W}(\text{N})$ complex, though in a relatively poor yield (22%).^[206] The more versatile deprotonated 2,3:5,6-dibenzo-7-azabicyclo[2.2.1]hepta-2,5-diene was developed by the Cummins group,^[207] and is now generally called the Cummins' reagent. This nitride transfer agent has found a wider use due to the soft conditions of the reaction and its convenient purification, with only anthracene and simple lithium salts as the byproducts.

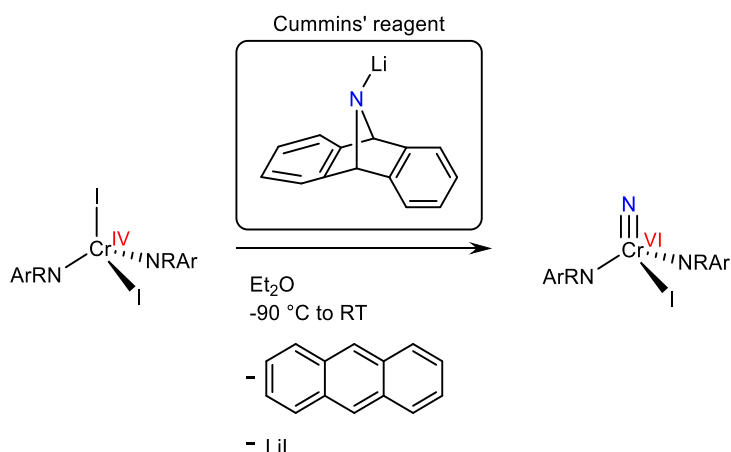


Figure I.76. First report of the use of the Cummins' reagent for the synthesis of a Cr(N) complex.^[207]

- Cleavage of “N-E” bonds

Akin to the nitrogen atom transfer reagents, a number of substituted nitrogen groups have been transferred on metal nitride complexes as a kind of “hidden” nitrides. Terminal nitrides are obtained from oxidative cleavage from a wide range of “N-E” chemical functions (**Figure I.77**). However, these reactions are usually quite system-specific and have rarely been used as a general process.

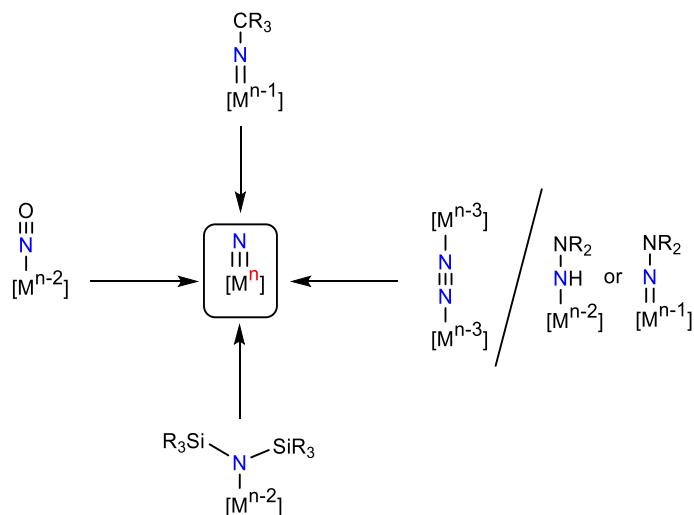


Figure I.77. General pathways to obtain metal-nitrides from bond cleavage of N-E bonds.

For example, cleavage of dinitrogen has been reported for early transition metals when coupled with a strong reducing agent.^[208] This reactivity, related to the nitrogen fixation process, faces the same hurdles. Accordingly, this synthetic route has remained sparse and is rarely seen as a reliable pathway to afford terminal nitride compounds.

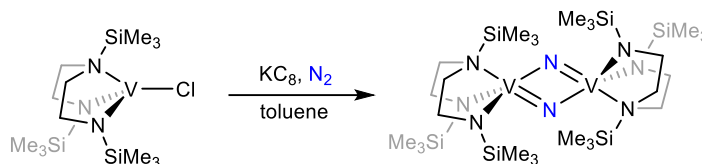


Figure I.78. Synthesis of a bis(μ -N)vanadium dimer through cleavage of dinitrogen.^[208]

Related to the alternative activation pathway of dinitrogen proposed in nitrogenase, anionic hydrazine ligands (hydrazido(1-) or (2-)) (**Figure I.77**) have been used to reach mid transition metal nitrides. High valent technetium Tc(V/VII),^[209,210] rhenium Re(V/VII),^[211] molybdenum Mo(IV),^[212] tungsten W(IV),^[213] and ruthenium Ru(VI)^[214] nitrides have been developed using this method.

Cleavage of N-Si bonds has been mostly developed using $\text{N}(\text{SiMe}_3)_3$ as a cheap N atom source on high valent metal complexes bearing multiple chloride ligands. The reaction usually engaged heavier metal centers with no reports from first row transition ions.^[215] In this case, the driving force behind the reaction was proposed to be formation of strong Si-Cl and $\text{M}\equiv\text{N}$ bonds.

Finally, decarbonylation of isocyanate ($\text{N}=\text{C}=\text{O}$) by Cummins^[216] or deoxygenation of nitrosyl (NO) ligands^[217] has also been published alongside other peculiar bond cleavage reactions. Although intriguing, these results remained confined as niche reports that have not been built upon. As such, these reactions were not given more thought in the context of this thesis.

3.4.2. Bonding considerations

Some insight on the behavior of metal nitride complexes can be gained from simple bonding considerations. The molecular orbital (MO) diagram for the interaction of a single terminal nitride unit with an arbitrary d^0 early transition metal is depicted in **Figure I.79**, with four coplanar σ -donating ligands.^[218] The coordination environment represented here is akin to that of salen complexes discussed previously. The M-N interaction contains a σ bond formed from the favorable overlap of a filled nitride sp_z hybrid with the empty d_{z^2} orbital. The interaction is also predicted to exhibit two π bonds formed by the overlap of filled p_x and p_y orbitals on the nitride with empty d orbitals of correct symmetry on the metal center. The strong σ and π donating ability of the nitride ligand confers an exceptionally strong *trans* effect that results in the stabilization of lower coordination numbers. Indeed, square pyramidal geometries are commonly observed, with the nitride at the apical position.

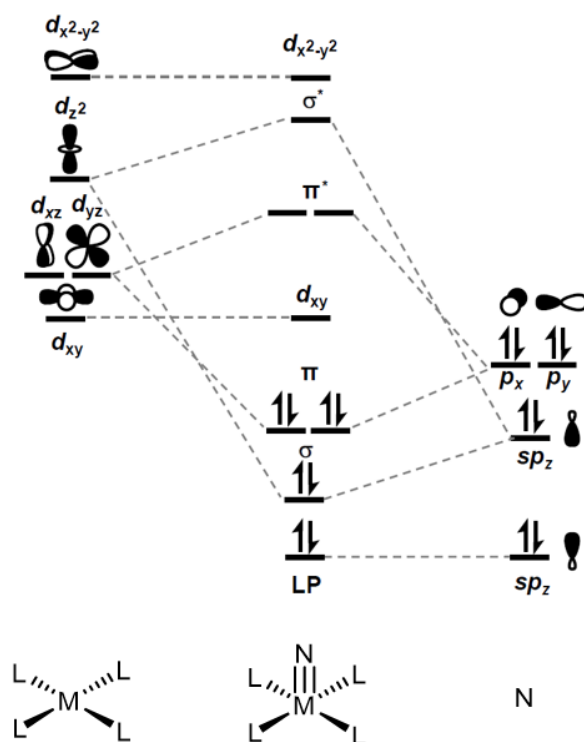


Figure I.79. Partial MO diagram for a d^0 transition metal nitride complex in square pyramidal geometry, considering the metal d -orbitals and nitride atomic orbitals.^[218]

Since it is a very strong σ and π donor, one might consider the nitride ligand to act with a simple nucleophilic character. However, considering the bonding scheme of the nitride ligand depicted above, its reactivity can be rationalized from the relative energies of the metal and nitride orbitals. A simple model involving two extreme cases can be considered (**Figure I.80**).^[195]

On one hand, the metal d -orbitals are located above the nitride atomic orbitals, which leads to predominantly nitride-based bonding orbitals. Following this thought, the nitride fragment is expected to behave as a nucleophile. On the other hand, when the d -orbitals are lower in energy, the antibonding MOs will be mostly ligand centered, and the nitride ligand is predicted to be electrophilic. In situations where the π^* orbitals contain similar metal and nitride character, ambiphilic reactivity is observed.^[219,220] This typically occurs for mid-transition metal nitride complexes.

From these energetic considerations, early transition metal nitrides are expected to be nucleophilic, while late metal nitrides are expected to be electrophilic. Furthermore, the nucleophilicity of the nitride is expected to increase with the metal oxidation state due to the destabilization of the metal d orbitals.

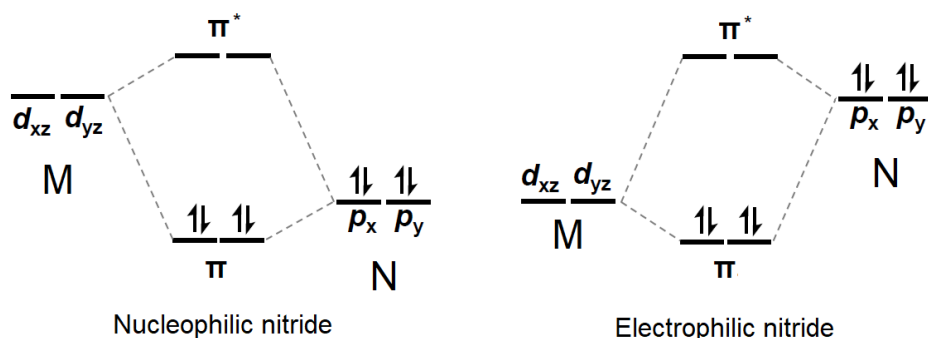


Figure I.80. Simplified MO diagrams of the π interactions of nitride p and metal d orbitals.^[195]

3.4.3. Early-transition metal nitrides

Following the previous discussion, early transition metal nitrides behave as nucleophiles and can react with electrophilic substrates such as alkylating agents^[219,221–227] and boranes^[228–230] to afford adducts. Formation of an adduct usually occurs without a change in oxidation state and the resulting imido species $M\equiv N-R$ retains sp hybridization in most cases, affording linear bonding patterns. As illustrated below, the Mo tetraphenylporphyrin nitride complex reacts with boron trifluoride to form the corresponding imido complex. Bent sp^2 hybridized imido complexes are scarcer ($M=N-Elec$), and can occur with additional competing π -basicity from ancillary ligands.^[231,232]

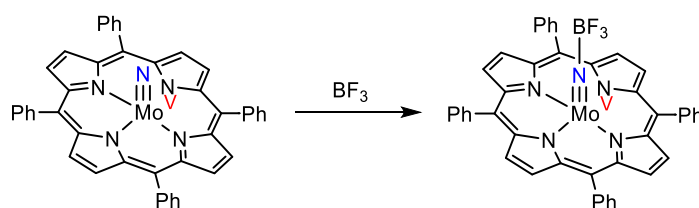


Figure I.81. Nucleophilic behavior of a Mo-nitride porphyrin complex.^[219]

3.4.4. Late-transition metal nitrides

Contrary to early transition metals, late transition metal nitrides are electrophilic and significantly less stable. This is due to the lack of empty d orbitals of appropriate energy and symmetry to accommodate nitride π electron density.^[233] Highly reactive complexes of group 9-10 metals have been reported and are susceptible to rapid decomposition via intramolecular ligand insertion reactions.^[154,196,234,235]

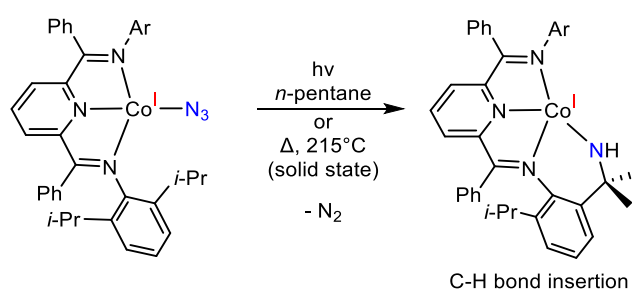


Figure I.82. Intramolecular C-H bond insertion reaction in a cobalt complex by Chirik and coworkers.^[235]

The electrophilicity of late-transition metal nitrides can be illustrated by the reactivity of a transient Ni nitride complex described by the Van der Vlugt group.^[236] Theoretical calculations predicted the formation of a nitrido species upon photolysis of an azide precursor in benzene before the nitrido moiety is intramolecularly ‘trapped’ by nucleophilic attack from a nearby phosphine ligand. The final iminophosphorane ligand product was obtained after C-H activation of benzene used as solvent (**Figure I.83**).

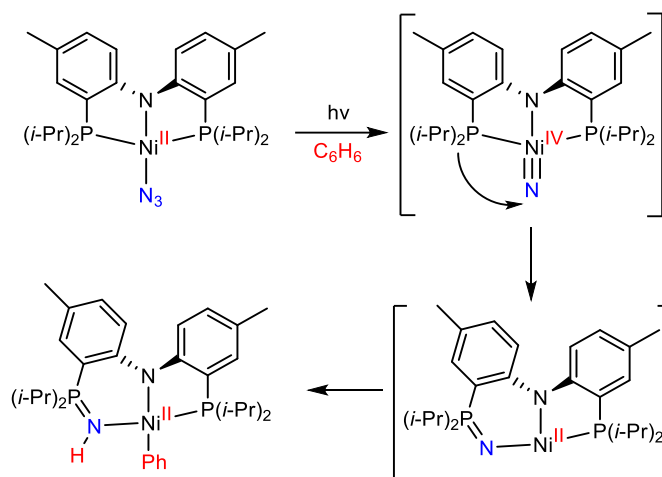


Figure I.83. Proposed intramolecular nitride insertion after activation of a Ni-azide complex.^[236]

3.4.5. Mid-transition metal nitrides

Mid-transition metals of group 7-8 exhibit reactivity intermediate between early and late transition metal analogues. Group 8 nitrides such as Fe are appealing due to their involvement in several model reactions relevant to nitrogen fixation and frequently exhibit electrophilic behavior.^[177,179,237–248] The reaction with nucleophiles (Nuc) results in a reduction at the metal center, resulting in a decrease of the metal-nitride bond order from population of π^* antibonding MO (see **Figure I.79**).^[249,250] Reactivity with phosphines is most commonly observed for group 8 metals and results in the formation of a iminophosphorane ligand ($\text{N}=\text{PR}_3$).^[251–254] In rare cases, complete N-atom transfer to the nucleophilic substrate can occur.^[239,248] Additionally, ambiphilic reactivity can arise where the nitride is regarded as both nucleophilic and electrophilic. For example, an Os nitride supported by a P–N–P type pincer ligand prepared by the Schneider group reacted with both bromotrimethylsilane (electrophile) and trimethylphosphine (nucleophile) to form the respective adducts (**Figure I.84**).^[255]

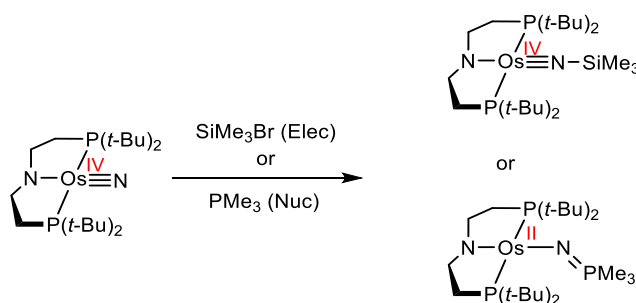


Figure I.84. Ambiphilic Os-nitride complex displaying both electrophilic and nucleophilic behavior.^[255]

On the other hand, group 7 metals such as manganese nitrides display a more distinct nucleophilic behavior and have been valorized as nitrogen atom transfer reagents.^[256–261] The reactivity of analogous metal oxo complexes for O atom transfer is well established,^[262,263] but the utility of nitride complexes in this regard is significantly less explored. Pioneering work by Groves and co-workers features a Mn nitride porphyrin complex that inserts into the C–C double bond of cyclooctene, and is the first reported case of olefin aziridination by a metal nitride complex.^[264] The addition of a Lewis acid such as trifluoroacetic anhydride (TFAA) was necessary to drive reactivity as it converts the nitride into a transient imide species that is active towards group transfer (**Figure I.85.A**).^[265] This was later expanded to include amination of styrenes and silyl enol ethers using salen ancillary ligands^[266,267] as well as other mid-transition metals such as Ru (**Figure I.85.C**).^[268,269] In the absence of substrate, the reactive imido species is susceptible to N–N coupling (**Figure I.85.B**).^[270]

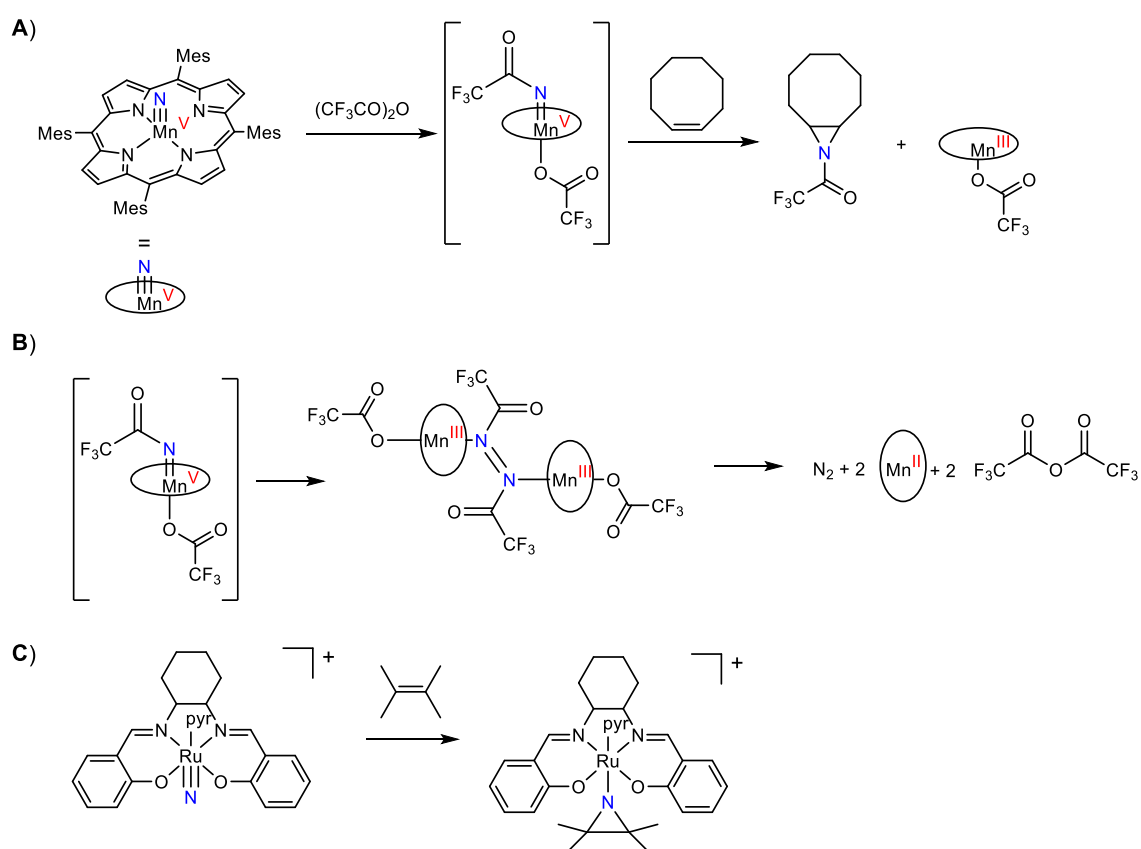


Figure I.85. Select examples of N-transfer reactions upon activation of the nitride: Aziridination of cyclooctene using a Mn complex^[264] (**A**), homocoupling of a Mn(V) imido complex^[270] (**B**) and aziridination of tetramethylethylene with a Ru complex^[269] (**C**).

3.4.6. Redox activity with metal-nitrides

While bonding considerations offer us some insight onto the reactivity of different nitride complexes, the nitride ligand has been shown to be non-innocent in some cases, making the coordination of the nitride ligand more complex to gauge. Indirect evidence for nitride redox activity was first reported for Cr(V) nitride complexes and their imido adducts after reaction with different Lewis acids.^[227] Specifically, the uncharacteristic increase of ¹⁴N hyperfine coupling constants in these complexes with increasing Cr–N bond length was attributed to contribution of a Cr(III)–N[–] resonance structure of the usual Cr(V)≡N^{3–} form. Strong

experimental and theoretical evidences was also given on the existence of unpaired electron density on the nitride ligand in a square planar Ir(IV) nitride complex **(PNP)Ir(N)**, where PNP: [N(CHCHP(*t*-Bu)₂)₂] (**Figure I.86**).^[271] This nitridyl radical resonance structure was proposed as a key component for the homocoupling of nitride complexes to form [M-N≡N-M] dimers.

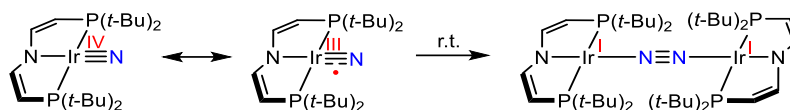


Figure I.86. Proposed mechanistic pathway for homocoupling of an Iridium nitride complex through a nitridyl radical species.^[272]

The reactive behavior of the nitride fragment has also been shown to be influenced by the redox activity of other ancillary ligands. Namely, the Storr group has recently investigated the effect of *para*-R substituent electronic tuning on metal nitride chemistry in salen manganese complexes.^[273] Complexes with mildly electron-donating (*R* = *t*-Bu) and strongly withdrawing groups (*R* = CF₃) resulted in metal-based oxidation (**Figure I.87.A**). They exhibited a highly reactive Mn(VI)–nitride unit that rapidly decayed via N–N coupling to afford N₂ and a Mn(III) decay product. The rate of coupling was found to be dependent on the electron-withdrawing ability of the *R* group, with the CF₃ substituent affording a faster coupling rate compared to the *t*-Bu derivative. In contrast, oxidation of the Mn(V) nitride bearing a strongly electron-donating *para*-R substituent (*R* = NMe₂) resulted in ligand-based oxidation. The resulting phenoxyl ligand radical proved quite stable and remarkably resistant to the homocoupling pathway (**Figure I.87.B**).

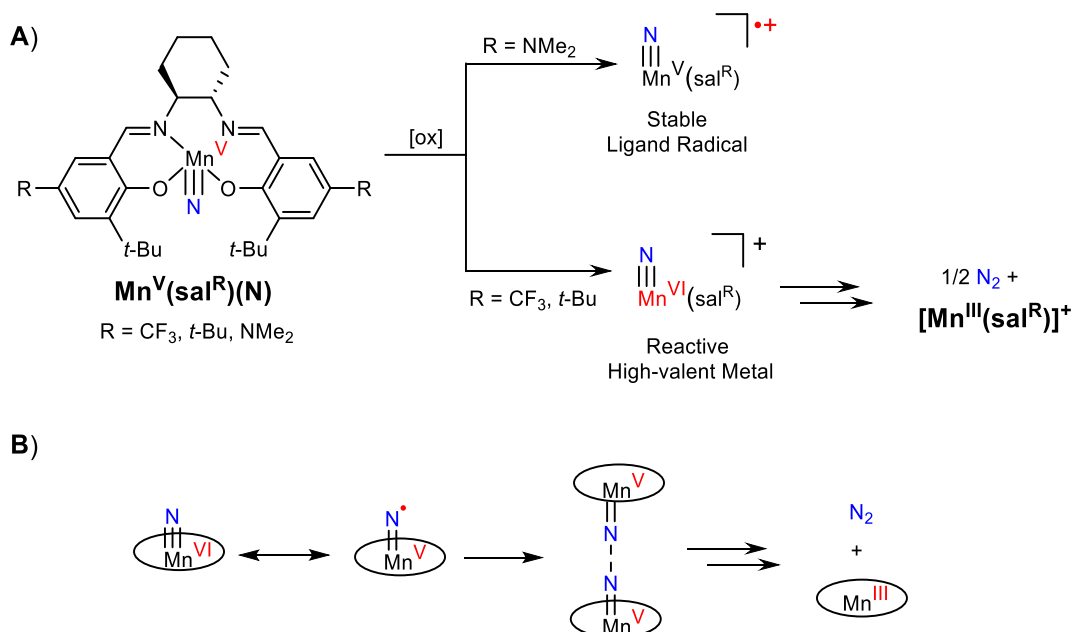


Figure I.87. Oxidation of Mn(V) nitride salen complexes with different reactive behavior depending on *para*-R electronics (**A**)^[273] and proposed homocoupling pathway for the evolution of the high-valent Mn(VI) oxidized complexes (**B**).

Chapter II.

Group 10 metal complexes

1. Introduction	85
2. Synthesis of the Proligand and complexes	86
3. Structures of neutral complexes NiL ^{C2O2} , PdL ^{C2O2} and PtL ^{C2O2}	87
4. Electrochemistry of the proligand and of the neutral complexes	88
5. Oxidation protocol.....	90
6. Crystal structure of [NiL ^{C2O2}] ⁺	91
7. EPR spectroscopy of the oxidized complexes.....	92
8. UV-vis-NIR spectroscopy	94
9. Theoretical calculations.....	96
10. Formation of Ni(III)-pyridine adducts	100
11. Conclusion.....	107

Stable M(II)-Radicals and Ni(III) Complexes of a Bis(phenol) *N*-Heterocyclic Carbene Chelated to Group 10 Metal Ions.^[274]

1. Introduction

Phenolate units have been used extensively as redox active moieties to design model compounds of galactose oxidase. Salen complexes are the most represented complexes in that regard but, despite their ubiquity, salen ligands present some limited coordination properties. While they are able to accommodate high-valent copper(III) centers in some rare instances,^[75] no reports of persistent low-valent Cu(I) salen complexes are known. To overcome this issue, we recently focused on *N*-Heterocyclic carbenes (NHCs) in our ligand designs. NHCs are widely used in organometallic catalysts to accommodate electron-rich metals. But, more recently, NHCs have also shown to be able to bind high-valent metal centers, including Cu(III),^[155] Co(IV)^[275] and more.^[141,276] Furthermore, NHCs are unique strong σ -donating ligands, able to form stronger metal-ligand bonds than other neutral functions, including imines found in salen species. This propensity to form stable complexes over a wide range of redox states has prompted us to incorporate NHCs alongside phenolates in our design of redox-active ligands.

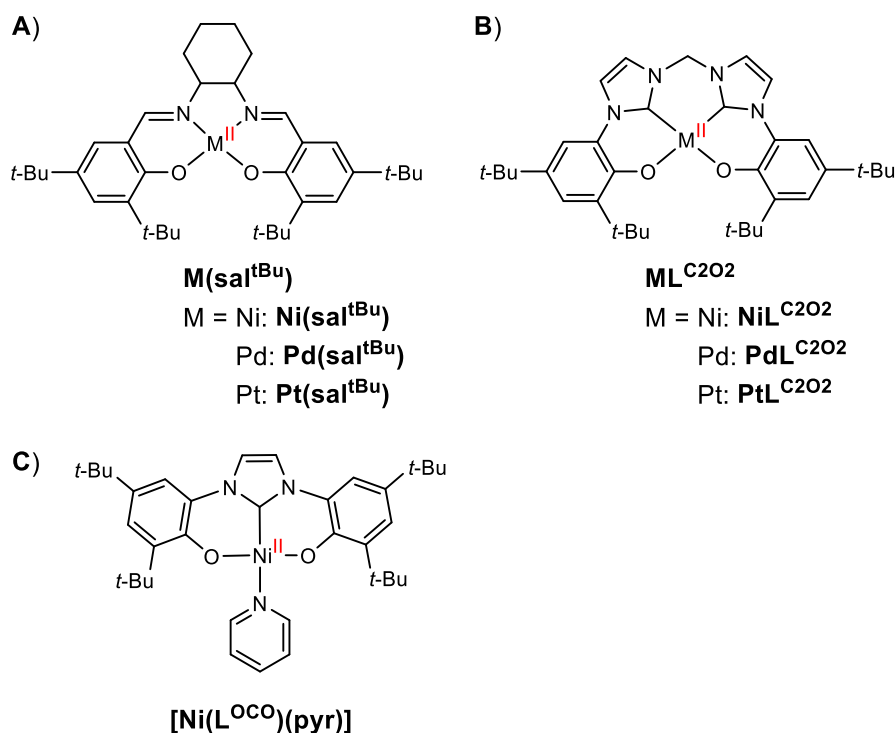


Figure II.1. Relevant group 10 complexes for the study of the redox activity of bis(phenol) ligands: $M(\text{sal}^t\text{Bu})$ complexes (A),^[277] ML^{C202} complexes discussed in this chapter (B) and nickel pincer complex $[\text{Ni}(\text{L}^{\text{OCO}})(\text{pyr})]$ (C).^[147]

Ligands incorporating both NHC and phenolate groups have already been reported in the literature but not much attention has been given to their redox activity. The most representative ligand of this family is the tridentate pincer L^{OCO} . It has been coordinated to different metal centers and its catalytic activity has been explored in different polymerization reactions.^[142,143] Its redox activity has also been investigated in the case of cobalt^[146] and nickel complexes

$[\text{Ni}(\text{L}^{\text{OCO}})(\text{pyr})]$, **Figure II.1.C**).^[147] Tetradentate ligands coupling two phenol and two NHC units have also been reported but are limited to a nickel catalyst^[148] and a series of platinum fluorophores.^[149] Therefore, we developed a new tetradentate proligand **H₄L^{C2O2}Br₂** as a C₂O₂ chelate analogue to the classic salen structure (**Figure II.1.A**) and developed its group 10 metal complexes (**Figure II.1.B**). The inherent diamagnetic properties of the group 10 metals in the (+II) oxidation state were used to probe the electronic structure of complexes after oxidation.

2. Synthesis of the Proligand and complexes

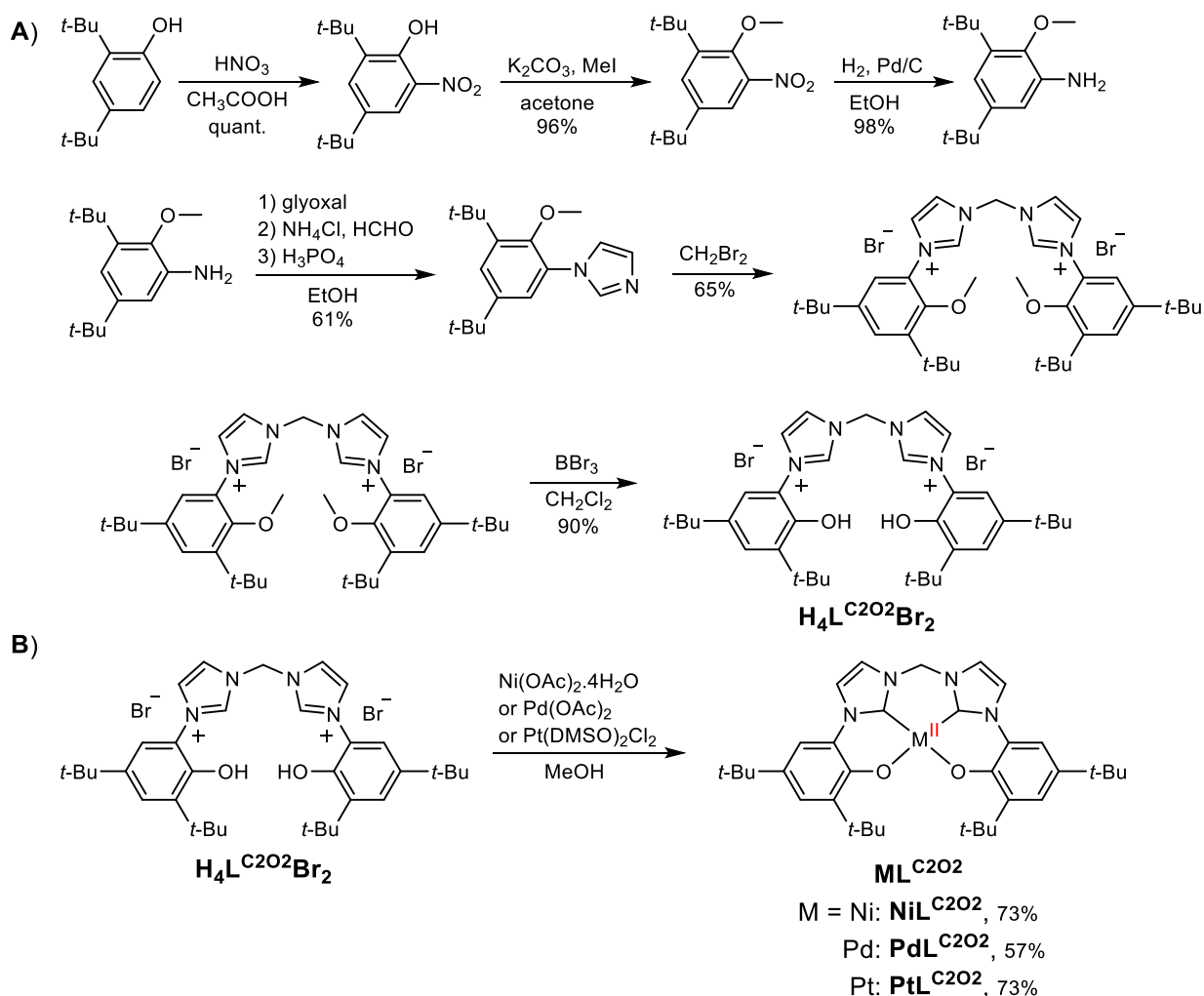


Figure II.2. Synthesis of proligand **H₄L^{C2O2}Br₂** (A) and **ML^{C2O2}** complexes (B).

Proligand **H₄L^{C2O2}Br₂** was prepared in a six-step synthesis, starting from commercially available 2,4-di-*tert*-butylphenol, in an overall yield of 33% (**Figure II.2**). 2,4-di-*tert*-butylphenol was first quantitatively nitrated in a HNO₃/CH₃COOH medium. Then, the phenol group was protected by reaction with MeI under basic (K₂CO₃) conditions. The imidazole ring was built following a procedure reported by van der Donk *et al.*^[278] by a treatment with glyoxal, ammonium chloride, formaldehyde, and concentrated phosphoric acid. The two aryl-substituted imidazoles were then coupled in refluxing dibromomethane to afford the bis(imidazolium) salt. The deprotection of the phenol groups was finally performed using tribromoborane to obtain the targeted proligand **H₄L^{C2O2}Br₂**. The nickel complex **NiL^{C2O2}** was synthesized by mixing equimolar amounts of the proligand **H₄L^{C2O2}Br₂** and Ni(OAc)₂·4H₂O in the presence of 4

equivalents of Et₃N in refluxing ethanol under an argon atmosphere. The palladium **PdL**^{C2O2} and platinum **PtL**^{C2O2} complexes were obtained following the same protocol, except for the use of different metal salts, Pd(OAc)₂ or Pt(DMSO)₂Cl₂, respectively.

3. Structures of neutral complexes **NiL**^{C2O2}, **PdL**^{C2O2} and **PtL**^{C2O2}

Single crystals suitable for X-ray diffraction were obtained by slow evaporation of concentrated methanol, DMF and DMSO solutions of **NiL**^{C2O2}, **PdL**^{C2O2} and **PtL**^{C2O2}, respectively. The three complexes are isostructural and the metal centers are mostly square planar, coordinated by two phenolate oxygens (O1/O1*) and two carbons of both NHC rings (C7/C7*).

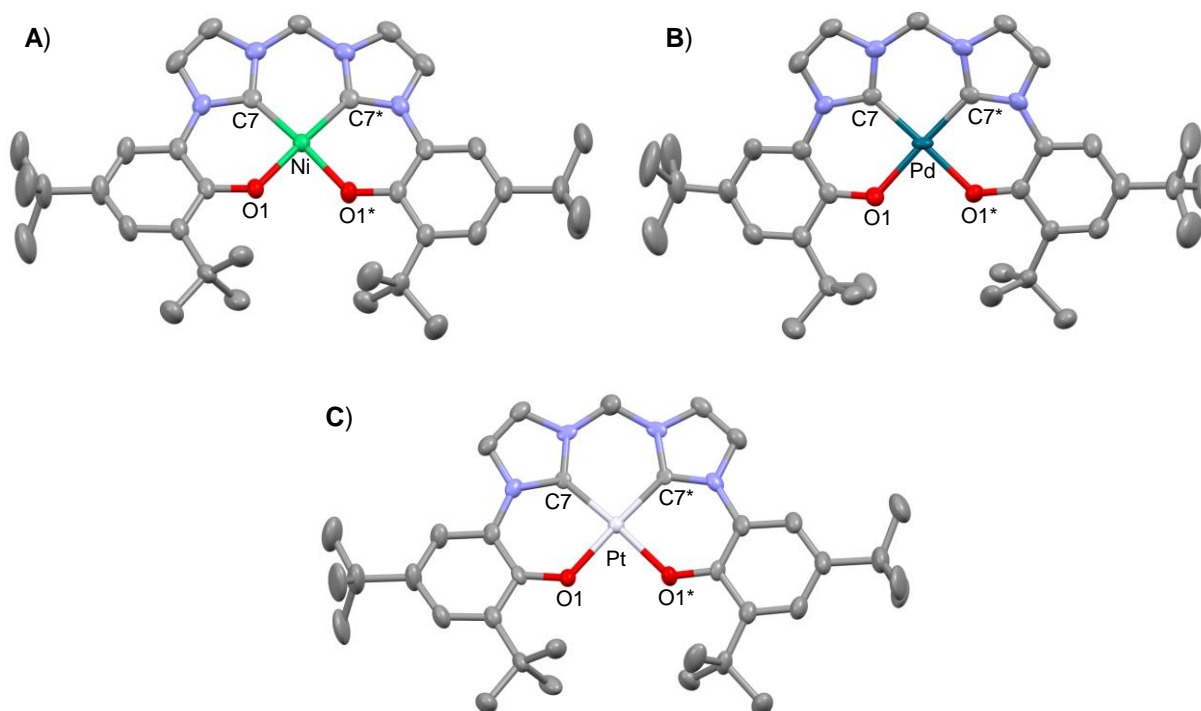


Figure II.3. X-ray crystal structures of the neutral complexes: **NiL**^{C2O2} (A) **PdL**^{C2O2} (B) and **PtL**^{C2O2} (C). The hydrogen atoms are omitted for clarity.

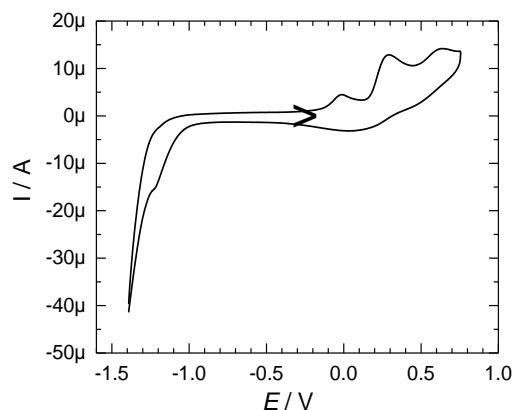
Tetrahedral distortion is minimal in all complexes with the angles between the opposite mean planes O1-M-C7 and O1*-M-C7* of 5, 5 and 3° for **NiL**^{C2O2}, **PdL**^{C2O2} and **PtL**^{C2O2} respectively. The ligand is essentially planar in all complexes as well, with the two NHC units being coplanar within 3° for all three complexes. The phenolate rings are also coplanar within 9, 9 and 7° with the connecting NHC units for **NiL**^{C2O2}, **PdL**^{C2O2} and **PtL**^{C2O2} respectively. The coordination bonds for **NiL**^{C2O2} are 1.881 Å for M-O1 and 1.843 Å for M-C7. The bond lengths increase to 2.021 and 1.927 Å respectively in **PdL**^{C2O2} and 2.028 and 1.918 Å in **PtL**^{C2O2}. This change along the group 10 series is due to the increase of ion radii in palladium and platinum centers.

Table II.1. Coordination bond distances in the neutral complexes and $[\text{NiL}^{\text{C2O2}}]^+$ monocation (\AA).

complex	M-O1	M-O2	M-C7	M-C17
NiL^{C2O2}	1.881(2)	-	1.843(2)	-
PdL^{C2O2}	2.021(2)	-	1.927(3)	-
PtL^{C2O2}	2.028(5)	-	1.918(7)	-
$[\text{NiL}^{\text{C2O2}}]^+$	1.840(5)	1.854(5)	1.847(8)	1.850(8)

4. Electrochemistry of the proligand and of the neutral complexes

The electrochemical properties of the proligand **H₄L^{C2O2}Br₂** and its complexes **NiL^{C2O2}**, **PdL^{C2O2}** and **PtL^{C2O2}** were investigated by cyclic voltammetry (CV) in CH_2Cl_2 solutions containing 0.1 M tetrabutylammonium perchlorate (TBAP) as supporting electrolyte. The proligand displayed irreversible oxidation waves at substantially low potentials of 0.30 and 0.64 V vs the Fc^+/Fc reference (**Figure II.4**).

**Figure II.4.** CV curve of 0.5 mM CH_2Cl_2 solution of **H₄L^{C2O2}Br₂**. $T = 298\text{ K}$, vitreous carbon electrode. Potentials given versus the Fc^+/Fc reference.

The irreversibility of the redox waves prevents a detailed assignment of the redox event. However, it is tempting to assume that they belong to successive phenol oxidations. An additional oxidation event was observed at a negative potential of -0.02 V but its nature was not investigated.

The three neutral complexes displayed two well-defined reversible oxidation waves (**Figure II.5**). These redox processes were confirmed to be monoelectronic according to rotating-disk electrode voltammetry and coulometric analysis during bulk electrolysis experiments. The reversibility of the redox events indicated that the oxidized products were stable on the CV time-scale and that the structural reorganization was small upon oxidation. The oxidation potentials were not drastically impacted by the nature of the metal center (**Table II.2**). All of these combined features strongly argue for successive ligand-centered oxidations to produce phenoxyl radical species.

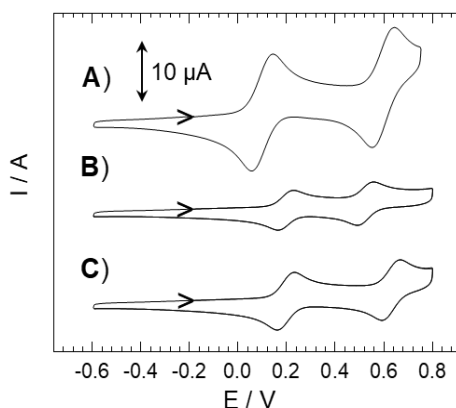


Figure II.5. CV curves of 0.50 mM CH_2Cl_2 solution of $\text{NiL}^{\text{C}2\text{O}2}$ (A) 0.20 mM $\text{PdL}^{\text{C}2\text{O}2}$ (B) and 0.28 mM $\text{PtL}^{\text{C}2\text{O}2}$ (C) (for solubility reasons). $T = 293$ K, vitreous carbon electrode. Potentials given versus the Fc^+/Fc reference.

The oxidation potentials were globally lower than for group 10 metal(II) salen complexes using the N,N' -bis(3,5-di-*tert*-butylsalicylidene)-1,2-cyclohexanediamine ligand ($\text{M}(\text{sal}^{\text{tBu}})$, **Figure II.1.A**). This is indicative of an increased thermodynamic stabilization of high oxidation states with this $\text{L}^{\text{C}2\text{O}2}$ ligand, likely due to the strong σ -donating properties of the NHC units.

Table II.2. Electrochemical data for group 10 neutral M(II)-phenolate complexes.^a

complex	$E_{1/2}^1$	ΔE_p^1	$E_{1/2}^2$	ΔE_p^2	$\Delta E_{1/2}$
$\text{NiL}^{\text{C}2\text{O}2^b}$	0.11	0.09	0.60	0.09	0.49
$\text{PdL}^{\text{C}2\text{O}2^b}$	0.21	0.06	0.55	0.07	0.34
$\text{PtL}^{\text{C}2\text{O}2^b}$	0.21	0.06	0.65	0.08	0.44
$\text{Ni}(\text{sal}^{\text{tBu}})^c$	0.37	-	0.85	-	0.48
$\text{Pd}(\text{sal}^{\text{tBu}})^c$	0.45	-	0.80	-	0.35
$\text{Pt}(\text{sal}^{\text{tBu}})^c$	0.35	-	0.94	-	0.59

^aThe potentials are given at 293 K and referenced to the Fc^+/Fc redox couple (0.19 V vs Ag/AgNO_3 0.01 M and $\Delta E_p = 0.08$ V under our experimental conditions). ^bIn CH_2Cl_2 (+ 0.1 M TBAP). ^cAs reported in reference [277]: 1mM complex, 0.1M TBAP, scan rate 100mV/s, CH_2Cl_2 , 230 K).

The CV experiments allowed us to probe the degree of electronic coupling between the two redox-active phenolate rings. The difference in oxidation potentials ($\Delta E_{1/2} = E_{1/2}^2 - E_{1/2}^1$) is indicative of the electrochemical communication between the two phenolates.^[279] A higher $\Delta E_{1/2}$ is usually representative of a stronger electronic coupling, while a lower $\Delta E_{1/2}$ depicts weaker communication between the two redox-active centers and a more localized phenoxyl radical upon oxidation. Therefore, the palladium complex $\text{PdL}^{\text{C}2\text{O}2}$ appears to have the weakest electronic communication amongst our series. The palladium salen complex $\text{Pd}(\text{sal}^{\text{tBu}})$ also shows the weakest coupling in its group 10 series (**Table II.2**). This highlights a characteristic behavior of the palladium ion to partially localize the phenoxyl radical in these mixed-valence systems. The $\Delta E_{1/2}$ of $\text{NiL}^{\text{C}2\text{O}2}$ and its $\text{Ni}(\text{sal}^{\text{tBu}})$ salen analogue were similar (0.49 vs 0.48 V) as well as with $\text{PdL}^{\text{C}2\text{O}2}$ and $\text{Pd}(\text{sal}^{\text{tBu}})$ (0.34 vs 0.35 V). This shows that the electronic properties of the spacer in these tetradentate ligands have minimal influence on the electronic

coupling between the phenolates. On the other hand, the nickel complex of the tridentate pincer ligand $[\text{Ni}(\text{L}^{\text{OCO}})(\text{pyr})]$ has a substantially different $\Delta E_{1/2}$ compared to NiL^{C2O2} (0.60 vs 0.49 V). This suggests that the orientation of the phenolates significantly impacts the electronic coupling.

5. Oxidation protocol

Mono-oxidized species were generated quantitatively either by coulometry-controlled bulk electrolysis at +0.25 V at low temperature (233 K) or by chemical oxidation using a slight excess of silver hexafluoroantimonate oxidant added to CH_2Cl_2 solutions of the neutral complexes. Both methods afforded the same results, and successful oxidation was demonstrated by the apparition of a dark green color. Chemically generated mono-cations $[\text{NiL}^{\text{C2O2}}]^+$ and $[\text{PtL}^{\text{C2O2}}]^+$ are remarkably stable in CH_2Cl_2 solutions, with no decomposition observed after two weeks. Single crystals of $[\text{NiL}^{\text{C2O2}}]^+$ were obtained by slow diffusion of pentane in a concentrated dichloromethane solution. $[\text{PtL}^{\text{C2O2}}]^+$ was also crystallized by slow evaporation of a saturated dichloromethane solution but no single crystals suitable for X-ray diffraction could be obtained. $[\text{PdL}^{\text{C2O2}}]^+$ could not be crystallized as the solution evolved over the span of a few hours. The lower stability of palladium complexes bearing phenoxyl radicals compared to their nickel analogs has already been reported in mono-oxidized salen compounds.^[101] Hence, the different behavior is assigned as a particular reactivity of the phenoxyl-Pd pattern rather than an effect from NHC coordination.

We were able to reach two-electron-oxidized species using coulometry-controlled bulk electrolysis at +0.7-0.75 V at low temperature (213 K). Surprisingly, in that case, the palladium dication species $[\text{PdL}^{\text{C2O2}}]^{2+}$ appeared to be the most stable of the three, with no change in the solution observed after a couple days, even at room temperature. On the other hand, both $[\text{NiL}^{\text{C2O2}}]^{2+}$ and $[\text{PtL}^{\text{C2O2}}]^{2+}$ rapidly evolved even at low temperatures.

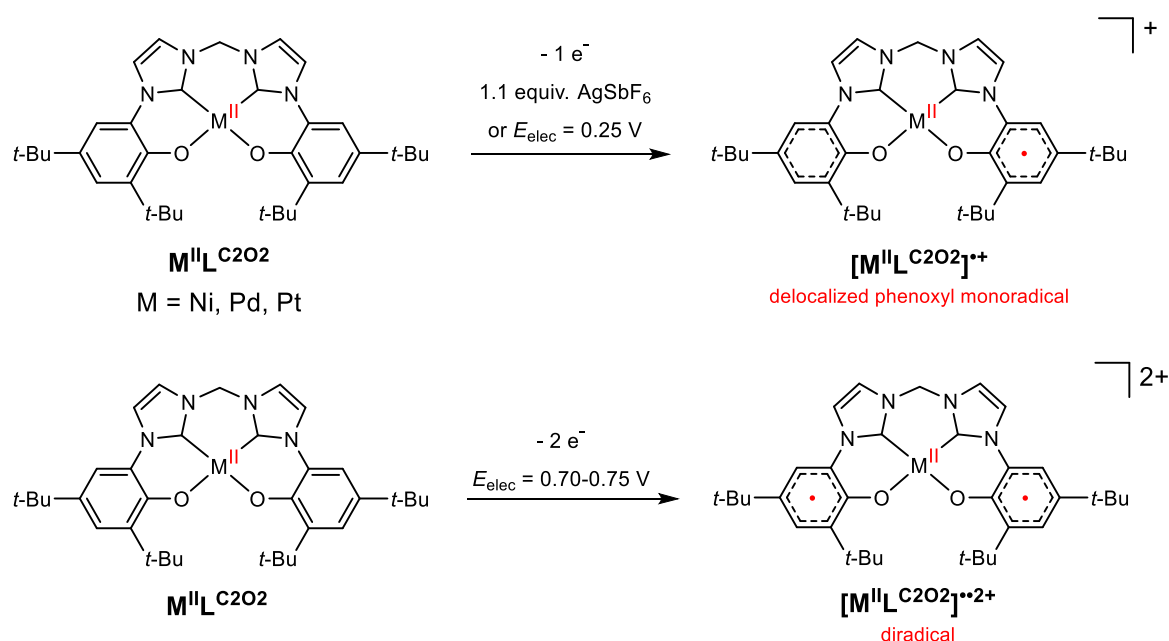


Figure II.6. One and two-electron oxidations of neutral $\text{M}^{\text{II}}\text{L}^{\text{C2O2}}$ complexes.

6. Crystal structure of $[\text{NiL}^{\text{C2O2}}]^+$

Chemically generated $[\text{NiL}^{\text{C2O2}}]^+(\text{SbF}_6)^-$ was obtained as single crystals suitable for X-ray diffraction analysis. Its one-electron oxidized state was demonstrated by the presence of a single SbF_6^- anion in the unit cell of the complex (**Figure II.7**).

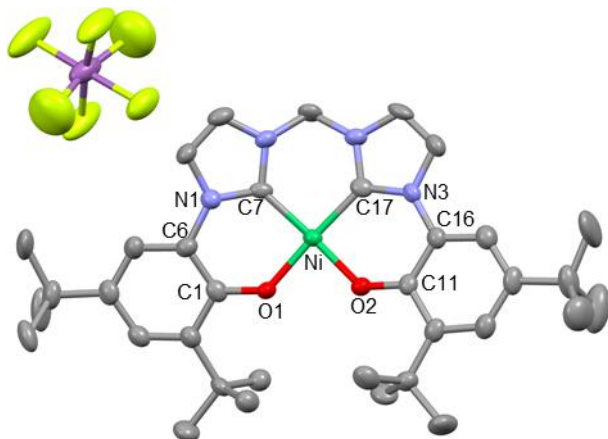


Figure II.7. X-ray crystal structure of $[\text{NiL}^{\text{C2O2}}]^+(\text{SbF}_6)^-$. The hydrogen atoms are omitted for clarity.

The nickel ion lies in a slightly dissymmetric square planar environment. A contraction of the coordination sphere was observed upon oxidation with shorter Ni-O1, Ni-O2 bonds (-0.041 and -0.027 Å respectively) in comparison to the neutral precursor NiL^{C2O2} (**Figure II.8**). This behavior is also observed in oxidized nickel(II) radical salen complexes^[100] and is indicative of the removal of an electron from a ligand-based antibonding orbital upon oxidation, resulting in an increased back-donation from the ligand. This was supported by theoretical calculations, whom will be detailed in section 9. . The HOMO of the neutral precursor NiL^{C2O2} was indeed calculated to be delocalized over both phenolic rings of the ligand and to be antibonding in nature. The dihedral angle between the mean planes O1-Ni-C7 and O2-Ni-C17 is 9°, which indicates a main square planar geometry as for NiL^{C2O2} . Notably, the phenolato ring comprising the O2 atom is coplanar with its neighboring NHC units (holding the C17 carbene center). The opposite phenolate and NHC units (including the coordinating atoms O1 and C7) are distorted in respect to each other by a 20° angle. The N-C bond connecting the NHC and phenolate rings is also shorter (C16-N3 = 1.402 Å vs C6-N1 = 1.427 Å, **Figure II.7**) in comparison to the neutral precursor. This structural feature suggests the presence of an extended conjugation between the two coplanar rings, at least in the solid state. While the coordination sphere appears to be mainly symmetric, the structural features of the two phenolic rings of $[\text{NiL}^{\text{C2O2}}]^+$ are sensibly different.

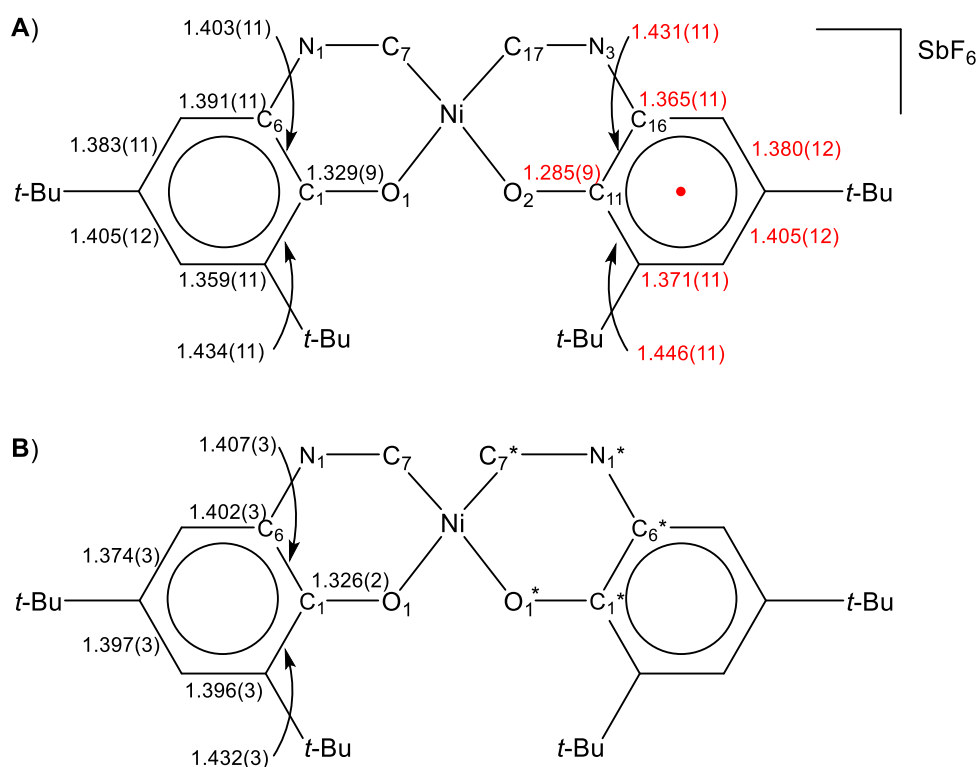


Figure II.8. Phenolic bond distances in $[\text{NiL}^{\text{C2O2}}]^+(\text{SbF}_6)^-$ (A) and comparison with the neutral precursor NiL^{C2O2} (B). The bond distances are given in Å. Partial localization of the phenoxyl radical is highlighted in red in (A).

Notably, the O1-C1 bond in $[\text{NiL}^{\text{C2O2}}]^+$ compares well with the neutral precursor NiL^{C2O2} at 1.329(9) and 1.326(2) respectively Å. The opposite phenolic bond O2-C11 is markedly shorter at 1.285(9) Å, which is a characteristic shortening observed in phenoxyl radical rings. A significant quinoidal distribution of the bond distances is also present on the ring holding the O2 atom, whereas the opposite phenolate is significantly less affected after oxidation. The fact that the Ni-O1 and Ni-O2 bonds are mostly comparable, whereas the phenolate rings of the ligand are distinctly dissymmetric suggests that $[\text{NiL}^{\text{C2O2}}]^+$ holds a partially located radical in the solid state. Hence, the cation can be classified as a borderline class II/III mixed-valent $\text{Ni(II)(phenoxyl)(phenolate)}$ according to the Robin-Day classification.

7. EPR spectroscopy of the oxidized complexes

Group 10 metals in +II oxidation states have a diamagnetic d^8 ($S = 0$) ground state. This electronic property is particularly useful to analyze the electronic structure of one-electron oxidized species using EPR. Chemically generated $[\text{NiL}^{\text{C2O2}}]^+$ presented a single unresolved resonance at $g = 2.033$, indicative of a ($S = 1/2$) system. The large peak-to-peak line width (5.55 mT) pointed towards an unresolved anisotropy, as already reported for $[\text{Ni}(\text{L}^{\text{OCO}})(\text{pyr})]^+$.^[147] The presence of 0.1 M TBAP in the solution of the electrochemically generated $[\text{NiL}^{\text{C2O2}}]^+$ resolved the anisotropy, presenting a rhombic system with g values of 2.087, 2.016 and 1.992 ($g_{\text{average}} = 2.032$). Line-broadening of the low-field g -tensor made for the simulation less precise in this region (Figure II.9.A). Both for chemically or electrochemically generated $[\text{NiL}^{\text{C2O2}}]^+$, the g_{average} values supported the presence of a phenoxyl radical species. Nevertheless, the anisotropy and g_{average} exceeded the reported values of

genuine phenoxyl radicals species ($g_{iso} = 2.005$).^[63] This reveals a partial contribution of the nickel metal center on the SOMO as was evidenced in theoretical calculations (**Figure II.11**).

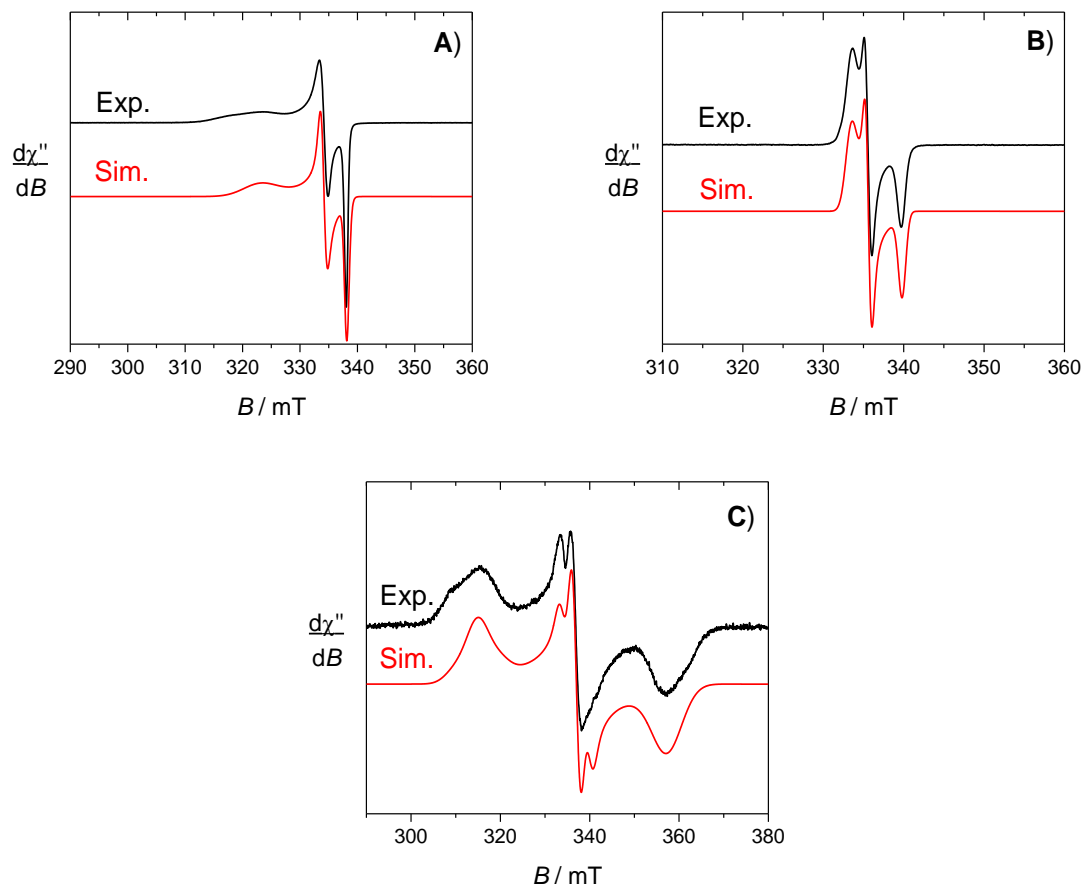


Figure II.9. X-band EPR spectra of electrochemically generated $[\text{NiL}^{\text{C2O2}}]^+$ (0.5 mM) (A), $[\text{PdL}^{\text{C2O2}}]^+$ (0.28 mM) (B) and $[\text{PtL}^{\text{C2O2}}]^+$ (0.21 mM) (C) (for solubility reasons). Experimental spectra (black) and simulated (red) using parameters given in **Table II.3**. Microwave frequency 9.43 GHz, power 1.1 mW (A and B) or 2.2 mW (C); mod. frequency 100 kHz, amp. 0.3 mT; $T = 100$ K.

The electrochemically generated $[\text{PdL}^{\text{C2O2}}]^+$ displayed a rhombic system with g values of 2.021, 2.008 and 1.983 ($g_{\text{average}} = 2.004$). This is once again indicative of a phenoxyl radical as the g_{average} value is well below typically observed Pd(III) complexes ($g_{\perp} < 2.1$).^[280–282] The g_{average} value is lower than for the nickel complex, which was already reported in salen and semiquinone compounds. The theoretical g values were also in good agreement with the experiments (**Table II.3**). Electrochemically generated $[\text{PtL}^{\text{C2O2}}]^+$ was deconvoluted into two subspectra depending on isotopic distribution. One subspectrum was simulated by considering the ^{195}Pt isotope in its natural abundance (34%) that holds a nuclear spin of 1/2, hence producing a hyperfine splitting. The other contribution was attributed to the combined other abundant Pt isotopes with no nuclear spins (^{192}Pt , ^{194}Pt , ^{196}Pt and ^{198}Pt , 66%). The g values obtained from the simulated spectra after deconvolution were 2.140, 1.999 and 1.885 ($g_{\text{average}} = 2.008$) with hyperfine coupling constants (HFC) of 280, 160 and 150 MHz respectively. Once again, the g_{average} value close to $g = 2$ points out the main phenoxyl radical character in the complex. This observation is also corroborated by the HFC values that are comparatively smaller than those of Pt(III) complexes.^[283–285]

Table II.3. EPR parameters of the monocations.^a

complex	<i>g</i> -tensor	<i>g</i> _{average}	<i>A</i> -tensor
[NiL ^{C2O2}] ⁺	2.087, 2.016, 1.992	2.032	
[NiL ^{C2O2}] ⁺ ^b	2.054, 2.018, 1.991	2.021	
[PdL ^{C2O2}] ⁺	2.021, 2.008, 1.983	2.004	
[PdL ^{C2O2}] ⁺ ^b	2.013, 1.999, 1.992	2.001	
[PtL ^{C2O2}] ⁺	2.140, 1.999, 1.885	2.008	280, 160, 150 ^c

^aElectrochemically generated in CH₂Cl₂ solutions containing 0.1 M TBAP. Values extracted from spectral simulations. ^bCalculated by DFT (B3LYP-D3BJ, TZVP basis set for C, H, O, N and CP(PPP) for metal ion). ^cSimulated with 34% ¹⁹⁵Pt isotope (*I* = 1/2) and 66% isotopes with no nuclear spin.

8. UV-vis-NIR spectroscopy

The nature of the oxidized cations and dications was further investigated using UV-vis-NIR spectroscopy. In mixed-valence systems with two redox-active units, intervalence charge transfers (IVCTs) can be observed depending on the electronic coupling between the two redox moieties. Furthermore, the shape of the IVCT band gives insight into the degree of electronic coupling according to the Marcus-Hush analysis (Chap I.1.3.3.).

In salen nickel complexes, one electron-oxidation in non-coordinating solvents usually produce radical species which feature an IVCT band. It corresponds to a phenolate to phenoxyl ligand to ligand charge transfer (LLCT). Fully delocalized class III mixed-valent and borderline class II/III species (according to the Robin Day classification) usually present sharp and intense IVCT transitions at low energy. The mono-oxidized cations displayed rich Vis-NIR spectrum, with predominant features at 2396 nm (4174 cm⁻¹), 2600 nm (broad, 3850 cm⁻¹), and 2294 nm (4359 cm⁻¹) for [NiL^{C2O2}]⁺, [PdL^{C2O2}]⁺ and [PtL^{C2O2}]⁺ respectively (**Table II.4**).

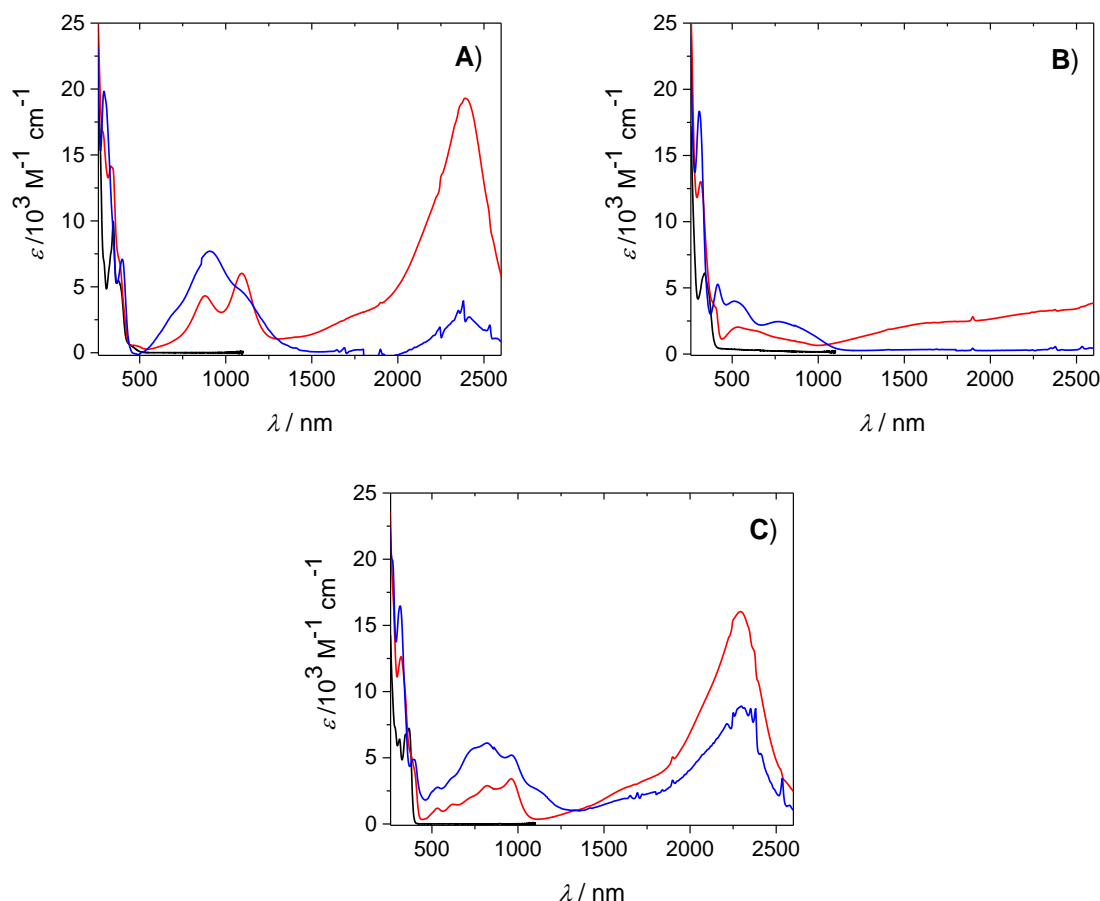


Figure II.10. UV-vis-NIR spectra of neutral (black) mono-oxidized (red) and bis-oxidized (blue) complexes: $[\text{NiL}^{\text{C2O2}}]^{0-2+}$ (0.5 mM) (A) $[\text{PdL}^{\text{C2O2}}]^{0-2+}$ (0.28 mM) (B) and $[\text{PtL}^{\text{C2O2}}]^{0-2+}$ (0.21 mM) (C) (for solubility reasons). CH_2Cl_2 solutions containing 0.1 M TBAP. $T = 298$ K (neutral and mono-oxidized) and 253 K (bis-oxidized).

Table II.4. UV-Vis-NIR data of the group 10 complexes.^a

complex	λ_{max} [nm] (ϵ [$\text{M}^{-1} \cdot \text{cm}^{-1}$])
NiL^{C2O2}	348 (9788), 377 (5451), 460 (446, br)
$[\text{NiL}^{\text{C2O2}}]^+$	332 (14146), 881 (4308), 1094 (6014), 2390 (19291)
$[\text{NiL}^{\text{C2O2}}]^{2+}$ ^b	291 (19810), 309 (18397), 399 (7088), 708 (3185, sh), 906 (7700), 1107 (4485, sh), 2388 (2595)
PdL^{C2O2}	341 (6100), 360 (4939, sh)
$[\text{PdL}^{\text{C2O2}}]^+$	318 (13017), 395 (3642, sh), 410 (3271, sh), 528 (2029), 1700 (2366, sh), 2600 (2930, br)
$[\text{PdL}^{\text{C2O2}}]^{2+}$	310 (18339), 416 (5266), 516 (3985), 766 (2449)
PtL^{C2O2}	312 (6396), 348 (6766), 367 (7214)
$[\text{PtL}^{\text{C2O2}}]^+$	322 (12635), 400 (3968, sh), 532 (1185), 622 (1479), 822 (2888), 962 (3404), 2294 (16037)

^aIn CH_2Cl_2 solutions containing 0.1 M TBAP. br: broad; sh: shoulder. ^bThe degradation of $[\text{NiL}^{\text{C2O2}}]^{2+}$ led to the formation of a $[\text{NiL}^{\text{C2O2}}]^+$ contaminant characterized by the band around 2400 nm (ca. 15%). Molar extinction coefficients were calculated from the concentration of complex before electrolysis.

Band shape analysis of the charge transfers were conducted according to the Marcus-Hush equation (2) (Table II.5). In the case of $[\text{NiL}^{\text{C2O2}}]^+$ and $[\text{PtL}^{\text{C2O2}}]^+$, the theoretical bandwidths (calcd. $\Delta\nu_{1/2}$) calculated from equation (1), are larger than the experimental values (exp $\Delta\nu_{1/2}$).

These sharp and intense bands are indicative of a strong delocalization of the electronic hole over the two redox active rings. Both cations also presented strong electronic coupling H_{AB} values and $2H_{\text{AB}}/\lambda$ ratios close to 1 (Table II.5). These results support a strong delocalization of the phenoxyl radical and both $[\text{NiL}^{\text{C2O2}}]^+$ and $[\text{PtL}^{\text{C2O2}}]^+$ were assigned as borderline class II/III mixed-valent radicals according to the Robin Day classification. $[\text{PdL}^{\text{C2O2}}]^+$ displayed the broadest and least intense NIR feature of the mono-oxidized complexes (Figure II.10.B) and we could not conduct a band shape analysis. This suggests that $[\text{PdL}^{\text{C2O2}}]^+$ is the complex with the least delocalized radical of the series and it was assigned as a class II radical species. This is consistent with the electrochemical results that presents a weaker electronic communication between the phenolate rings in the palladium complex.

Table II.5. Band-shape analysis of the prominent NIR transition of the mono-oxidized complexes.^a

complex	$\lambda = \nu_{\text{max}}$ [cm ⁻¹]	ϵ [M ⁻¹ .cm ⁻¹]	calcd. $\Delta\nu_{1/2}$ [cm ⁻¹]	exp $\Delta\nu_{1/2}$ [cm ⁻¹]	H_{AB} [cm ⁻¹]	$2H_{\text{AB}}/\lambda$
$[\text{NiL}^{\text{C2O2}}]^+$	4184	19291	3109	2778	1915 ^b	0.916
$[\text{PdL}^{\text{C2O2}}]^+$			n.d. ^c			
$[\text{PtL}^{\text{C2O2}}]^+$	4359	16037	3173	2835	1764 ^d	0.809

^aElectrochemically generated in CH₂Cl₂ solutions containing 0.1 M TBAP. ^bWith $r_{\text{CT}} = r_{\text{O1-O2}}$ distance (2.527 Å) from X-ray structure of $[\text{NiL}^{\text{C2O2}}]^+$. ^cUnable to determine due to the broadness of the NIR feature of $[\text{PdL}^{\text{C2O2}}]^+$. ^dWith $r_{\text{CT}} = r_{\text{O1-O2}}$ distance (2.762 Å) from X-ray structure of PtL^{C2O2} .

The dications $[\text{NiL}^{\text{C2O2}}]^{2+}$ and $[\text{PdL}^{\text{C2O2}}]^{2+}$ were stable enough at 253 K to undertake spectroscopic characterization (blue spectra, Figure II.10). Oxidation from the monocations to the corresponding $[\text{NiL}^{\text{C2O2}}]^{2+}$ and $[\text{PdL}^{\text{C2O2}}]^{2+}$ dications is correlated to a strong quenching of the low energy NIR features displayed above 2000 nm. $[\text{PdL}^{\text{C2O2}}]^{2+}$ remained stable over the span of multiple hours while the spectra of $[\text{NiL}^{\text{C2O2}}]^{2+}$ degraded back to the NIR signature of the monocation. Quenching of the NIR band was also observed for $[\text{PtL}^{\text{C2O2}}]^{2+}$ but the degradation back to the monooxidized complex was too rapid, even at 253 K, and prevented further spectroscopic investigation. The quenching of the NIR feature is consistent with formation of a diradical species in the two-electron oxidized complexes. Indeed, the formation of a second radical prevents any intervalence charge transfer.

9. Theoretical calculations

The electronic structures of the oxidized complexes were investigated by DFT. Different functionals were used to determine the best fit with the experimental data. The popular hybrid B3LYP functional was previously used to a great extent for $[\text{Ni}(\text{L}^{\text{OCO}})(\text{pyr})]^+$. The B3LYP-D3 and CAM-B3LYP functionals, which both include corrections for long-range dispersion interactions, were also investigated. The B3LYP-D3 functional afforded the best agreement with the crystallographic structure of $[\text{NiL}^{\text{C2O2}}]^+$. The 6-31G* basis set was used on all atoms for the nickel complexes. The heavier metal centers in the palladium and platinum complexes

were calculated using the LanL2DZ ECP functional that uses only effective core potentials. This afforded a more accurate simulation of the spectroscopic signature of the oxidized palladium and platinum complexes.

Table II.6. Crystallographic and theoretical bond distances in the neutral complexes and $[\text{NiL}^{\text{C2O2}}]^+$ (Å).

complex	NiL^{C2O2} crystal. ^a	NiL^{C2O2} simul. ^b	PdL^{C2O2} crystal. ^a	PdL^{C2O2} simul. ^c	PtL^{C2O2} crystal. ^a	PtL^{C2O2} simul. ^c	$[\text{NiL}^{\text{C2O2}}]^+$ crystal. ^a	$[\text{NiL}^{\text{C2O2}}]^+$ simul. ^b
M-O1	1.881(2)	1.868	2.021(2)	2.061	2.028(5)	2.058	1.840(5)	1.840
M-O2	1.881(2)	1.878	2.021(2)	2.049	2.028(5)	2.051	1.854(5)	1.851
M-C7	1.843(2)	1.844	1.927(3)	1.948	1.918(7)	1.935	1.847(8)	1.848
M-C17	1.843(2)	1.843	1.927(3)	1.951	1.918(7)	1.936	1.850(8)	1.844

^aFrom the respective crystallographic structures.

^bFrom B3LYP-D3 calculation with 6-31G* basis set on all atoms.

^cFrom B3LYP-D3 calculation with 6-31G* basis set on C, H, N and O atoms and LanL2DZ ECP on the metal center.

The B3LYP-D3 optimized structure of $[\text{NiL}^{\text{C2O2}}]^+$ is slightly dissymmetric, with a Ni-O1 bond 0.011 Å shorter than the Ni-O2 bond. The contraction of the coordination sphere upon oxidation from neutral NiL^{C2O2} to $[\text{NiL}^{\text{C2O2}}]^+$ is also nicely predicted. The spin density for all three monocations was mostly centered on the peripheral phenyl rings, namely the O and both *C_{ortho}* and *C_{para}* atoms. The NHC carbene rings did not show any significant electron density. This confirms the main phenoxyl radical character of the one-electron oxidized species. The degree of delocalization of the electronic hole appeared to be highly influenced by the functional used in the calculations. Both B3LYP and B3LYP-D3 showed large delocalization of the electronic hole over both peripheral rings, whereas CAM-B3LYP predicts localization with a dissymmetric spin population. As both $[\text{NiL}^{\text{C2O2}}]^+$ and $[\text{PtL}^{\text{C2O2}}]^+$ present high delocalization of the phenoxyl radical in NIR spectroscopy characterization, B3LYP-D3 was validated as the most appropriate functional to describe our complexes.

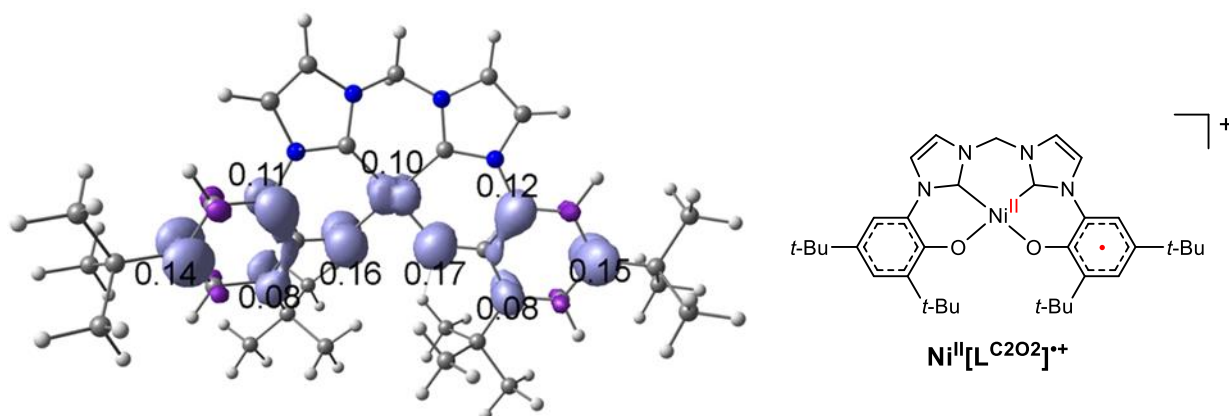


Figure II.11. Spin density plot of $[\text{NiL}^{\text{C2O2}}]^+$ with the main Mulliken spin populations (B3LYP-D3/6-31G*).

Interestingly, the Mulliken spin population on the metal centers was not negligible, with 10% of the spin density located on the nickel center in $[\text{NiL}^{\text{C2O2}}]^+$ (Figure II.11). Calculations using

the LanL2DZ ECP basis set on all metal centers also presented a partial metallic character, with 7, 4 and 7% electron density for $[\text{NiL}^{\text{C2O2}}]^+$, $[\text{PdL}^{\text{C2O2}}]^+$ and $[\text{PtL}^{\text{C2O2}}]^+$ respectively. These results are consistent with the experimental EPR spectra, that all showed significant contributions of the metal centers with highly anisotropic systems with high g -values. The dications $[\text{NiL}^{\text{C2O2}}]^{2+}$ and $[\text{PdL}^{\text{C2O2}}]^{2+}$ were also simulated. An elongation of the M-O bonds of ca. 0.04 Å is predicted when going from the mono to the dications. The coordination sphere remains slightly dissymmetric with Ni-O1 and Ni-O2 bonds of 1.894 and 1.877 Å respectively in $[\text{NiL}^{\text{C2O2}}]^{2+}$. The energetic analysis showed that the dications have a broken-symmetry (BS) singlet ground-state (**Figure II.12**). The triplet state was 226 cm^{-1} higher in energy and the genuine singlet even higher by 3100 cm^{-1} . These energy values are comparable with another bis-oxidized nickel salen complex reported by the Storr group.^[286] The singlet solution also showed internal instability and collapsed to the broken symmetry solution.

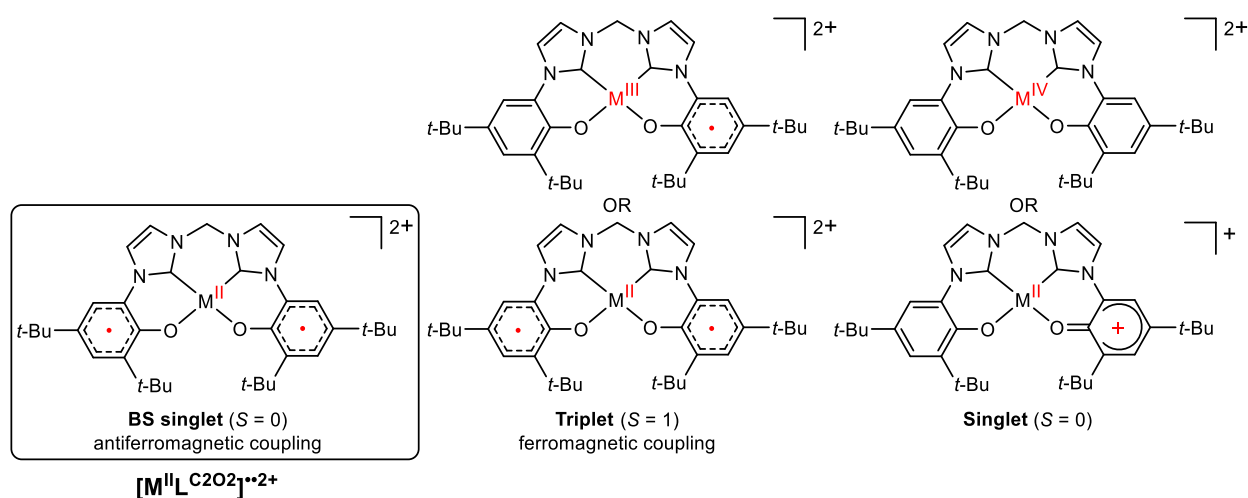


Figure II.12. Possible electronic structures for the dicationic complexes.

The localization of the spin density on the broken symmetry singlet was mostly similar in comparison to the monocations but was twice as large in magnitude, with one positive phenoxyl ring and a negative opposite ring (**Figure II.13**). In other words, the dications are antiferromagnetically exchange coupled bis(phenoxyl) diradical species.

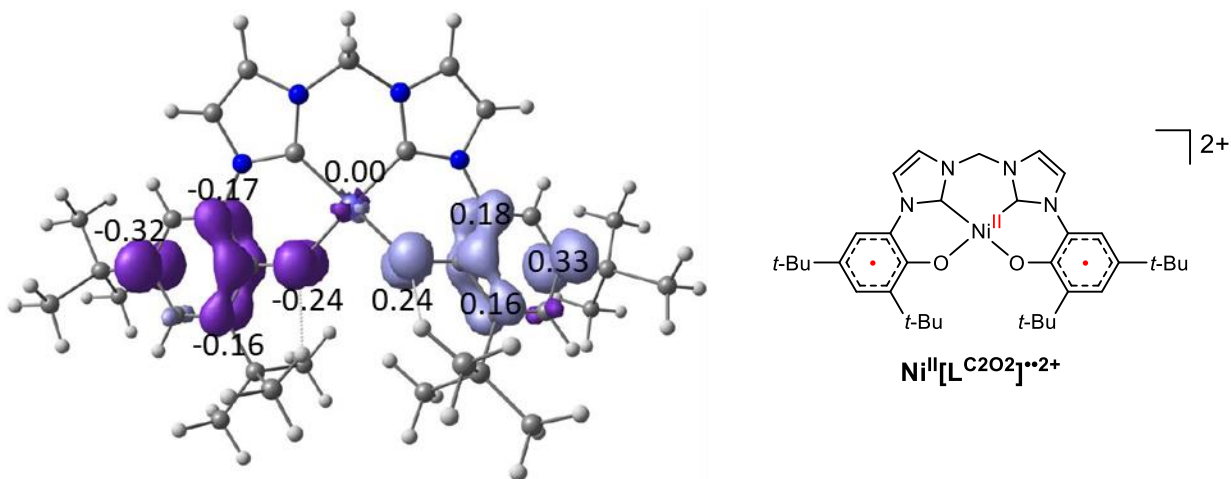


Figure II.13. Spin density plot of $[\text{NiL}^{\text{C2O2}}]^{2+}$ with the main Mulliken spin populations (B3LYP-D3/6-31G*).

The magnetic couplings were calculated as -215 and -102 cm⁻¹ for [NiL^{C2O2}]²⁺ and [PdL^{C2O2}]²⁺ respectively, according to the Yamaguchi formula.^[287] These relatively strong antiferromagnetic couplings are consistent with the EPR silence observed for the dications and are comparable to other diradical bis(phenoxyl)^[286] or bis(iminosemiquinone)^[288] systems in literature.

To gain more insight into the electronic transitions, Time-Dependent-DFT (TD-DFT) calculations were conducted. The B3LYP-D3 functional predicted an intense NIR band in the 4281-5081 cm⁻¹ region for all three monocations, in good agreement with the NIR transitions observed experimentally. These transitions corresponded to β -HOMO \rightarrow β -LUMO excitations with the two orbitals developed over both peripheral rings of the ligand framework (**Figure II.14**). They were thus assigned as IVCT phenolate \rightarrow phenoxyl transitions.

Table II.7. TD-DFT assignments of the low energy transitions in the mono-oxidized complexes.^a

complex ^a	main transitions	assignment	calcd.	exp.	f_{osc}
[NiL ^{C2O2}] ⁺	β -HOMO \rightarrow β -LUMO	LLCT (IVCT)	5081	4184	0.916
	^b	MLCT/LLCT	10482	9141	0.0728
	^b	MLCT/LLCT	12019	11351	0.0368
[PdL ^{C2O2}] ⁺	β -HOMO \rightarrow β -LUMO	LLCT (IVCT)	4281	3846	0.1887
	β -HOMO-5 \rightarrow β -LUMO	MLCT/LLCT	16287	18940	0.0359
[PtL ^{C2O2}] ⁺	β -HOMO \rightarrow β -LUMO	LLCT (ICVT)	4998	4359	0.2068
	β -HOMO-1 \rightarrow β -LUMO	MLCT/LLCT	11353	10395	0.045
	β -HOMO-2 \rightarrow β -LUMO	MLCT/LLCT	12723	12165	0.0247

^aB3LYP-D3/TZVP except for Pd and Pt (LanL2DZ ECP)/PCM. ^bExtracted from natural transition orbital (NTO) analysis.

Consistently with the experimental results, the calculations also predicted two electronic excitations of lower intensity in the 800-1100 nm region (9000 – 12500 cm⁻¹) for [NiL^{C2O2}]⁺ and [PtL^{C2O2}]⁺ (**Table II.7**). For [PdL^{C2O2}]⁺, these transitions are drastically blue-shifted and only one excitation could be assigned in the frame of the TD-DFT calculations. In the case of [NiL^{C2O2}]⁺, a natural orbital analysis was required to describe the two donor orbitals. The analysis showed that those two excitations are mixed metal-to-ligand and ligand-to-ligand charge transfers (MLCT/LLCT). Indeed, the two donor orbitals involved both *d* orbitals of the nickel center and ligand orbitals delocalized over the whole ligand framework (**Figure II.14**). The same behavior was observed in [PtL^{C2O2}]⁺ where the donor orbitals (β -HOMO-1 and β -HOMO-2, **Table II.7**) were localized on both the metal center and the ligand backbone.

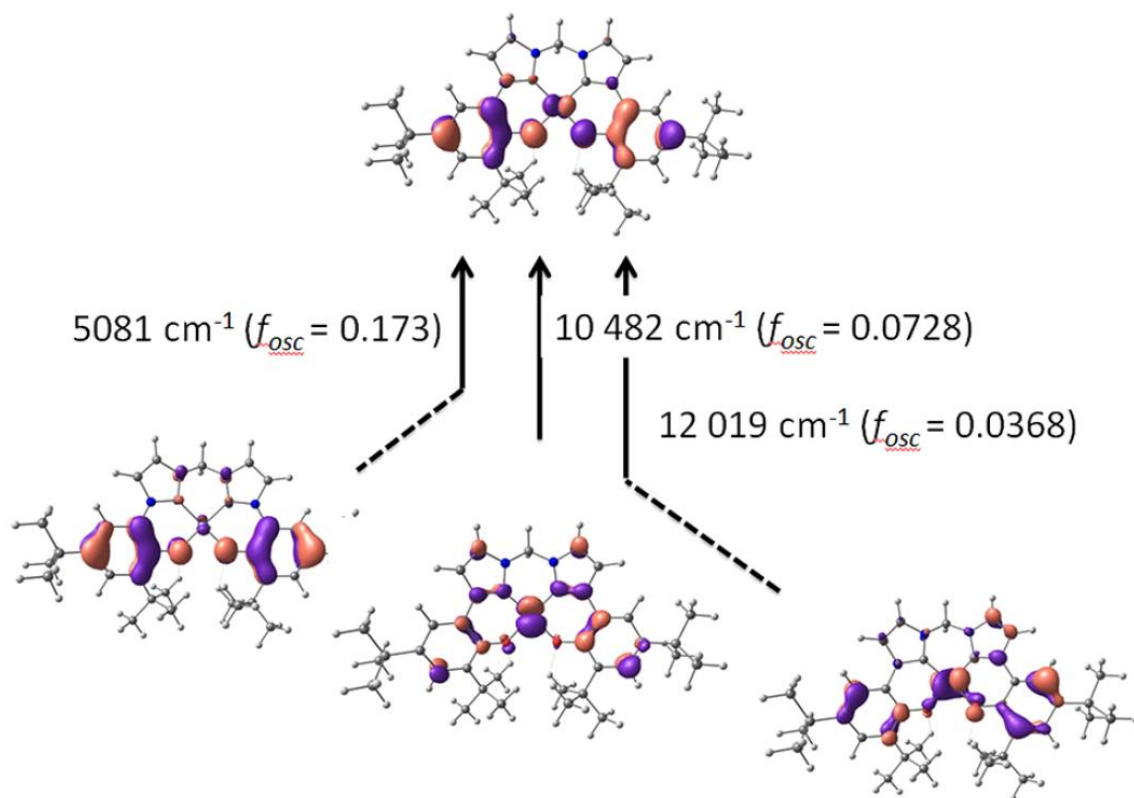


Figure II.14. TD-DFT calculated excitations for $[\text{NiL}^{\text{C202}}]^+$ (B3LYP-D3/TZVP/PCM).

10. Formation of Nickel(III)-pyridine adducts

The ground-state of oxidized Ni(II)-radical species is known to be sensible to axial solvent coordination. In early investigations, Freire and de Castro demonstrated that the electronic structure of oxidized nickel salophen complexes produces Ni(III) adducts.^[289] Further investigation has shown that Ni(II)-phenoxyl radical complexes can be converted into Ni(III) high-valent complexes by axial ligation of a number of different ligands.^[95–97] Hence, we investigated the sensitivity of our cations towards pyridine. The UV-vis-NIR spectrum of $[\text{NiL}^{\text{C202}}]^+$ was shown to be impacted by addition of pyridine. Titration experiments were conducted in order to investigate pyridine affinity. A clean isosbestic point was seen for the first additions up to 250 equivalents of pyridine. Both the bands in the 800–1200 nm region and the intervalence band at 2390 nm decreased in intensity, while new bands appeared around 1700 and 700 nm. Other features were also observed around 400 nm. After addition of pyridine up to a 2500-fold excess (0.4 M pyridine), all NIR transitions were completely quenched. Two intense transitions remained at 341 and 395 nm, as well as a weak band around 700 nm. Investigation of the spectra over time showed that the putative pyridine adducts remained stable over the span of a few hours at 298 K.

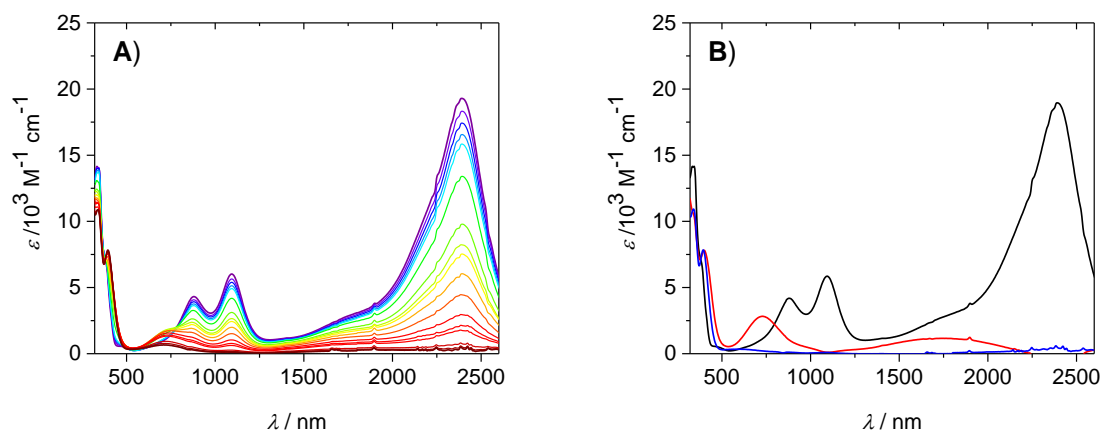


Figure II.15. Evolution of the UV-vis-NIR spectra of $[\text{NiL}^{\text{C2O2}}]^+$ (0.5 mM in CH_2Cl_2 with 0.1 M TBAP) upon addition of pyridine (0 to 0.4 M): (A) Experimental spectra and (B) simulated spectra for $[\text{NiL}^{\text{C2O2}}]^+$ (black) and pyridine adducts $[\text{NiL}^{\text{C2O2.pyr}}]^+$ (red) and $[\text{NiL}^{\text{C2O2.2pyr}}]^+$ (blue). $T = 298 \text{ K}$.

The UV-vis-NIR titration data were fitted using the Specfit software to determine the binding constants of $[\text{NiL}^{\text{C2O2}}]^+$ with pyridine. Two equilibria were considered: First, the formation of a monopyridine adduct $[\text{NiL}^{\text{C2O2.pyr}}]^+$, then followed by the formation of the dipyridine species $[\text{NiL}^{\text{C2O2.2pyr}}]^+$ (Figure II.16.A). We calculated respective affinity constants of $\log \beta = 1.3$ and 2.2 M^{-1} at 298 K. The pyridine affinities were shown to be temperature dependent. At 233 K, the $\log \beta$ values increased to 2.5 and 3.8 M^{-1} for the formation of mono and dipyridine adducts respectively. This behavior was also reported for mono-oxidized Ni(II)-salophen complexes.^[96,97] The pyridine binding affinities are notably lower with our $[\text{NiL}^{\text{C2O2}}]^+$ complex when comparing to the nickel salophen analogue (Figure II.16.B).^[96] We interpreted this difference by the strong donating properties of the NHC carbene units in $[\text{NiL}^{\text{C2O2}}]^+$, which would disfavor the binding of additional donating ligands like pyridine. This behavior is also corroborated by the low pyridine affinities reported for another nickel complex bearing strongly donating amidate ligands (Figure II.16.C).^[97]

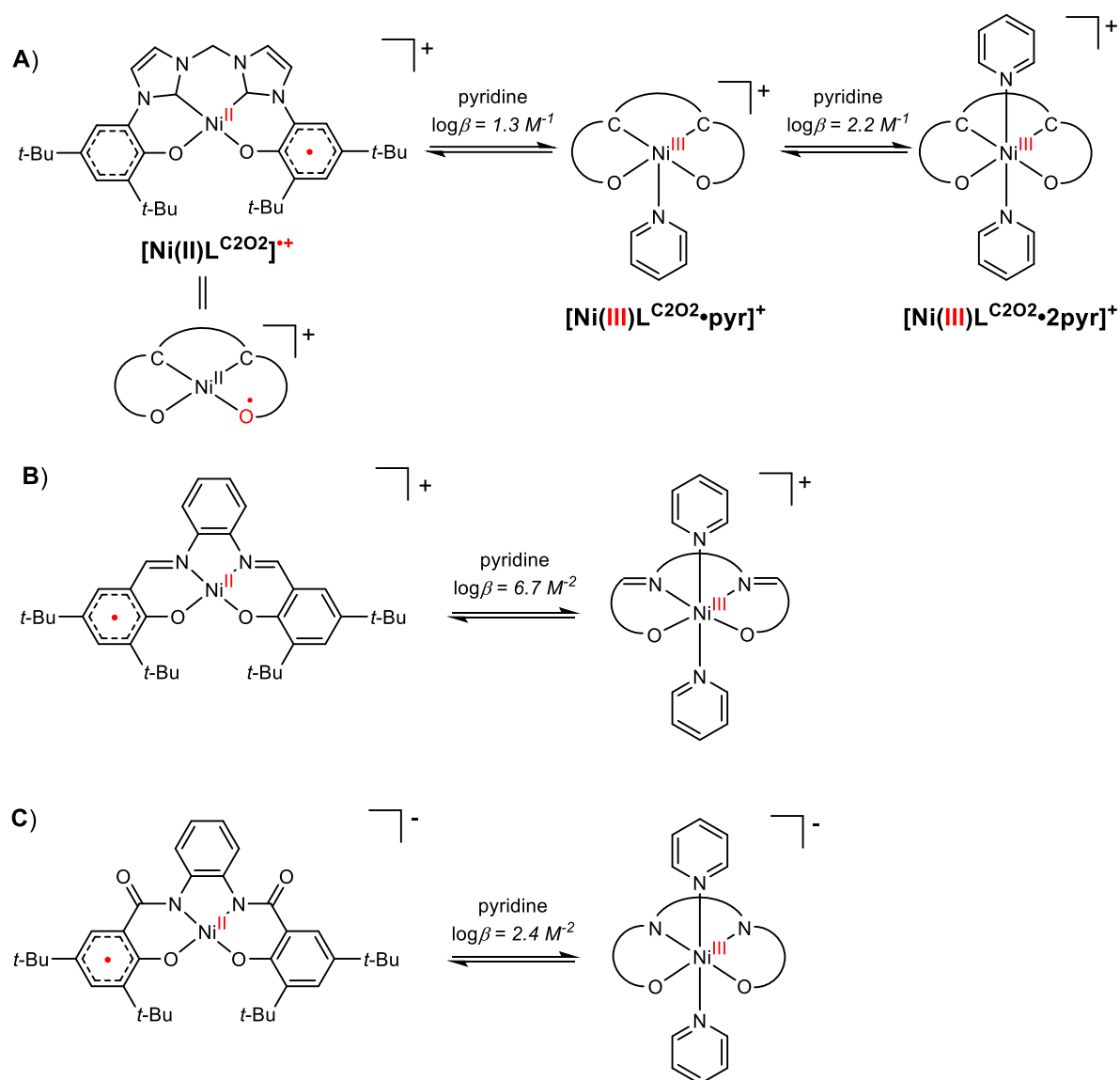


Figure II.16. Comparison of the pyridine binding constants for different Ni(II)-phenoxyl complexes: $[\text{NiL}^{\text{C2O2}}]^+$ (A), a nickel salophen analogue (B)^[96] and a nickel complex with amidate donors (C).^[97] The $\log\beta$ values given are for $T = 298$ K.

The deconvoluted spectra for $[\text{NiL}^{\text{C2O2}}.\text{pyr}]^+$ and $[\text{NiL}^{\text{C2O2}}.2\text{pyr}]^+$ were extracted (**Figure II.15.B**) and their spectroscopic signature is reported in **Table II.8**.

Table II.8. UV-vis-NIR signature of $[\text{NiL}^{\text{C2O2}}]^+$ and its pyridine adducts.

complex	λ_{max} [nm] (ϵ [$\text{M}^{-1}.\text{cm}^{-1}$])
$[\text{NiL}^{\text{C2O2}}]^{+a}$	332 (14146), 881 (4308), 1094 (6014), 2390 (19291)
$[\text{NiL}^{\text{C2O2}}.\text{pyr}]^{+b}$	401 (7807), 728 (2820), 1775 (1149)
$[\text{NiL}^{\text{C2O2}}.2\text{pyr}]^{+c}$	341 (10873), 395 (7832), 707 (657)

^aIn CH_2Cl_2 solutions containing 0.1 M TBAP. Molar extinction coefficients were calculated from the concentration of NiL^{C2O2} before electrolysis. ^bData extracted from the fitted spectrum presented in **Figure II.15.B**. ^cTaken from spectrum recorded with 0.4 M pyridine in **Figure II.15.A**.

Theoretical calculations were conducted to confirm the electronic structure of the pyridine adducts. The simulated structure of $[\text{NiL}^{\text{C2O2}}\cdot\text{pyr}]^+$ present a nickel center lying in a square pyramidal geometry, with the pyridine bound in the apical position. The dipyridine adduct $[\text{NiL}^{\text{C2O2}}\cdot 2\text{pyr}]^+$ showed an elongated octahedral geometry with two pyridines coordinated in axial positions. The ligand adopted an umbrella shape and the two pyridines were tilted by ca. 90° to minimize steric clashes. Both mono and dipyridine adducts were calculated with a metal d_z^2 SOMO. The Mulliken spin populations on the nickel ions were 0.81 and 0.87 for $[\text{NiL}^{\text{C2O2}}\cdot\text{pyr}]^+$ and $[\text{NiL}^{\text{C2O2}}\cdot 2\text{pyr}]^+$ respectively. The binding of both one and two pyridine molecules is therefore predicted to promote an intramolecular electron transfer that ultimately affords Ni(III) complexes in either case.

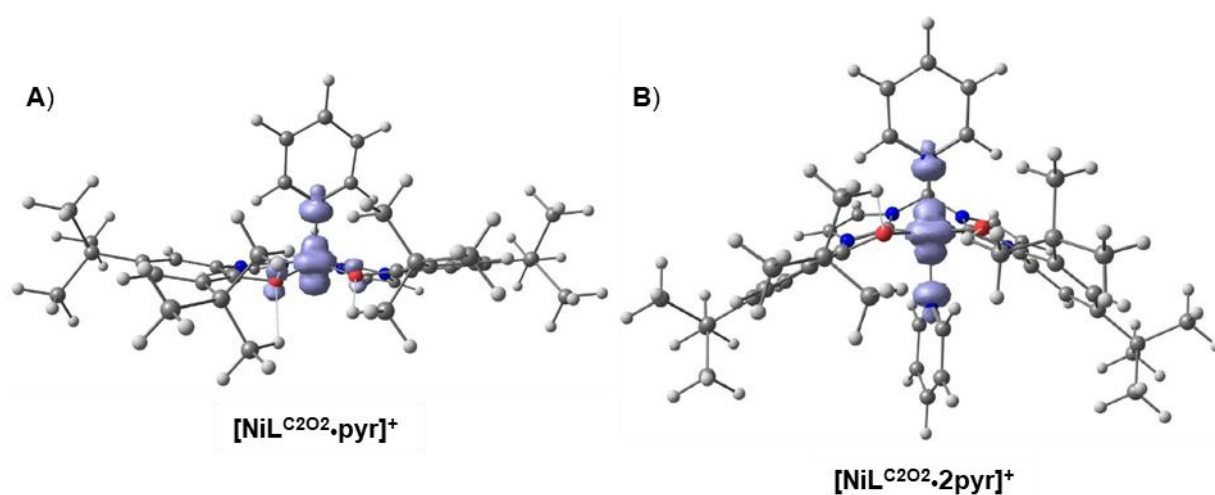


Figure II.17. Spin density plots of the nickel(III)-pyridine adducts: $[\text{NiL}^{\text{C2O2}}\cdot\text{pyr}]^+$ (A) and $[\text{NiL}^{\text{C2O2}}\cdot 2\text{pyr}]^+$ (B) (B3LYP-D3/6-31G*).

TD-DFT calculations were also conducted to assign the transitions deconvoluted from the titration experiments. For $[\text{NiL}^{\text{C2O2}}\cdot\text{pyr}]^+$, two LMCT transitions were predicted at 612 and 1254 nm ($f_{\text{osc}} = 0.0431$ and 0.0341). They reasonably matched the intense transition at 728 nm and the NIR trail at 1775 nm that were deconvoluted from the titration experiment (**Table II.8**). Calculations on $[\text{NiL}^{\text{C2O2}}\cdot 2\text{pyr}]^+$ correctly predicted the absence of NIR features observed experimentally. An intense transition ($f_{\text{osc}} = 0.0736$, mostly LMCT) was predicted at 377 nm and was assigned as the band observed at 395 nm in the UV-vis-NIR experiment.

To confirm the electronic structure of pyridine adducts, we conducted EPR experiments on $[\text{NiL}^{\text{C2O2}}\cdot\text{pyr}]^+$ in the presence of increasing amounts of pyridine. When a stoichiometric amount of pyridine was introduced, a rhombic signal was observed with a strong anisotropy with g values of 2.223, 2.199 and 2.003 ($g_{\text{average}} = 2.145$), obtained from spectrum simulation (**Figure II.18.B**). This signature is characteristic of Ni(III) ions and most importantly, a distinct three-line pattern hyperfine interaction was observed in the high-field component. This indicates that the unpaired electron is residing in the metal d_{z^2} orbital and is interacting in axial position with a single ^{14}N nucleus ($I_N = 1$). This result correlates with the spin density observed on the pyridine ligand in theoretical calculations for $[\text{NiL}^{\text{C2O2}}\cdot\text{pyr}]^+$ (**Figure II.17.A**). This also corroborates nicely with a square pyramidal coordination geometry with an axially bound pyridine, as was presented in theoretical calculations.

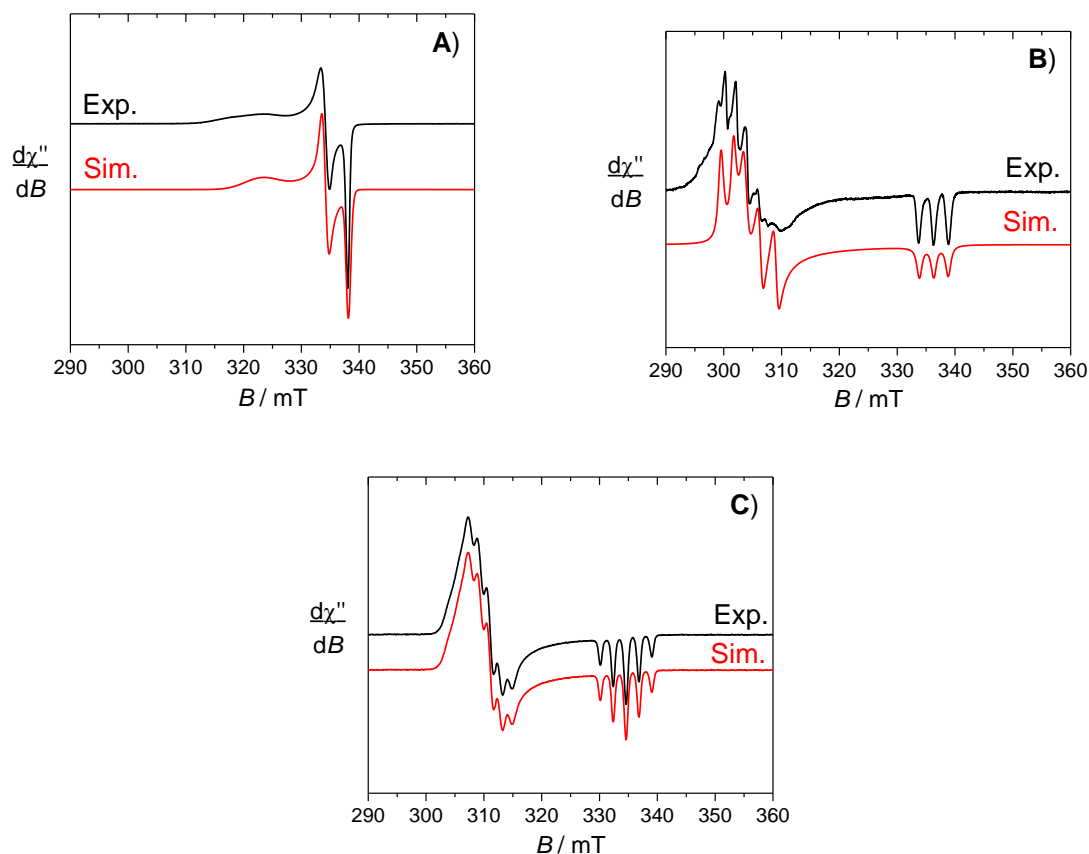


Figure II.18. X-band EPR spectra $[\text{NiL}^{\text{C2O2}}]^+$ (A) and of pyridine adducts $[\text{NiL}^{\text{C2O2}}\cdot\text{pyr}]^+$ (in presence of 0.5 mM pyridine, the contribution of $[\text{NiL}^{\text{C2O2}}]^+$ was subtracted from the experimental spectra) (B) and $[\text{NiL}^{\text{C2O2}}\cdot 2\text{pyr}]^+$ (0.4 M pyridine) (C). CH_2Cl_2 solutions (+ 0.1 M TBAP). Experimental spectra (black) and simulated (red) using parameters given in **Table II.9**. Microwave frequency 9.43 GHz, power 1.1 mW; mod. frequency 100 kHz, amp. 0.3 mT; $T = 100$ K.

In the presence of an excess of pyridine (0.4 M), $[\text{NiL}^{\text{C2O2}}]^+$ displayed a rhombic signal with a high anisotropy with g values of 2.191, 2.165 and 2.013 ($g_{\text{average}} = 2.123$), once again characteristic of a Ni(III) species (**Figure II.18.C**). The g values are different from those simulated for $[\text{NiL}^{\text{C2O2}}\cdot\text{pyr}]^+$ and showed the formation of a different adduct. Notably, five-line pattern hyperfine interactions were observed for all three g components. This pattern discloses the interaction of the electron spin with two equivalent ^{14}N nuclei, in accordance with an octahedral nickel geometry with pyridine ligands bound in the two axial positions. The lower HFC constants of 50–64 MHz when comparing to the monopyridine adduct (68–83 MHz, **Table II.9**) are also consistent with an elongated octahedral geometry. Indeed, an elongated octahedral geometry is expected to lower the interaction of the unpaired spin with the two ^{14}N nuclei in comparison to a square pyramidal geometry observed in the monopyridine adduct.

Table II.9. EPR parameters of the nickel monocations.^a

complex	g-tensor	g_{average}	A-tensor (MHz)
$[\text{NiL}^{\text{C2O2}}]^+$	2.087, 2.016, 1.992	2.032	-
$[\text{NiL}^{\text{C2O2}}]^+{}^b$	2.054, 2.018, 1.991	2.021	-
$[\text{NiL}^{\text{C2O2}}\cdot\text{pyr}]^+{}^c$	2.233, 2.199, 2.003	2.145	68, 83, 70
$[\text{NiL}^{\text{C2O2}}\cdot\text{pyr}]^+{}^b$	2.174, 2.142, 2.020	2.112	59, 61, 77
$[\text{NiL}^{\text{C2O2}}\cdot 2\text{pyr}]^+{}^c$	2.191, 2.165, 2.013	2.123	50, 50, 64
$[\text{NiL}^{\text{C2O2}}\cdot 2\text{pyr}]^+{}^b$	2.140, 2.127, 2.020	2.096	47, 48, 61

^aElectrochemically generated in CH_2Cl_2 solutions containing 0.1 M TBAP. Values extracted from spectral simulations. ^bFrom DFT calculations (B3LYP-D3BJ calculation with TZVP basis set on C, H, N and O atoms and CP(PPP) for the metal center. ^cIn the presence of 2.1 mM pyridine for $[\text{NiL}^{\text{C2O2}}\cdot\text{pyr}]^+$ or 0.4 M pyridine for $[\text{NiL}^{\text{C2O2}}\cdot 2\text{pyr}]^+$.

The EPR parameters of the nickel cation and its pyridine adducts were also simulated using DFT calculations. The calculated spin parameters were in reasonable agreement with the experimental values, as shown in **Table II.9**. The anisotropy and g_{average} values were slightly underestimated but this behavior is consistent with the propensity of DFT calculations to overestimate the covalency of coordination bonds. Nevertheless, the global trends of anisotropy, g_{average} and hyperfine coupling values were predicted along the series of $[\text{NiL}^{\text{C2O2}}]^+$ and its two pyridine adducts. Thus, both experimental and theoretical results corroborate the successive formation of mono and dipyridine adducts and confirmed their assignment as Ni(III) complexes.

The sensitivity towards pyridine was also investigated on the palladium and platinum cations. When adding increasing amount of pyridine on $[\text{PdL}^{\text{C2O2}}]^+$, its NIR features are gradually quenched in absorption spectroscopy. However, the bleaching of the IVCT band also appeared to further continue over time, indicating that the species in solution were not stable in the presence of pyridine. This likely indicates reduction of the phenoxyl radical, which is common in the field of porphyrin chemistry. This interpretation was also consistent with EPR investigations. The X-band EPR signature of $[\text{PdL}^{\text{C2O2}}]^+$ in presence of pyridine did not depict a Pd(III) species. Instead, in excess pyridine (10-500 equiv.) the spectrum evolved towards a completely isotropic signal (**Figure II.19.B**), without significant change of g_{iso} (2.001, identical to g_{average} of the rhombic signal of $[\text{PdL}^{\text{C2O2}}]^+$). This proved that the complex retained its Pd(II)-phenoxyl electronic structure in the pyridine medium. With an equimolar amount of pyridine, the spectrum was deconvoluted in two different signatures: 90% of the spectra was from the isotropic signal, and 10% originated from the rhombic signal observed in absence of pyridine.

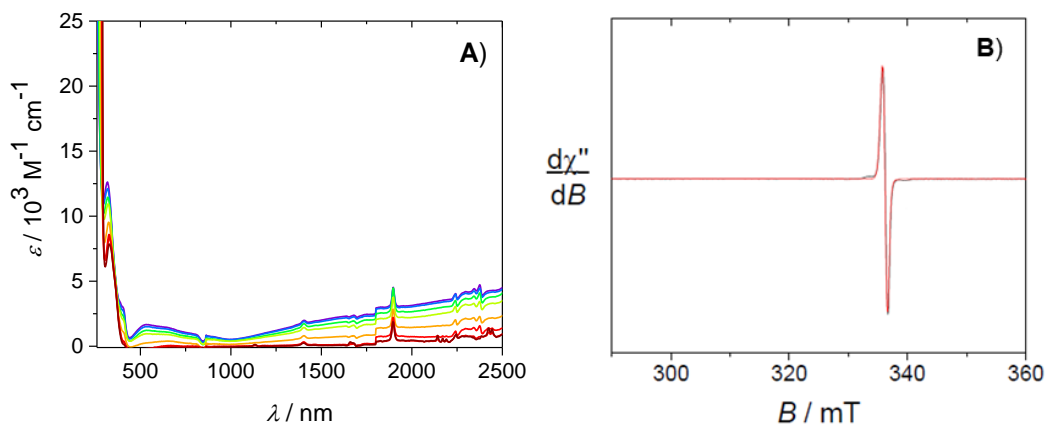


Figure II.19. Evolution of $[\text{PdL}^{\text{C2O2}}]^+$ (0.28 mM in CH_2Cl_2 with 0.1 M TBAP) upon addition of pyridine: Room temperature UV-vis-NIR spectra in presence of 0 (purple) to 500 molar equiv. (brown) of pyridine (A) X-band EPR spectra in presence of 10 molar equiv. of pyridine. Microwave frequency 9.43 GHz, power 1.1 mW; mod. frequency 100 kHz, amp. 0.3 mT; $T = 100$ K (B).

Pyridine adducts of $[\text{PdL}^{\text{C2O2}}]^+$ were also simulated by DFT calculations. Analysis of the spin density showed that the monopyridine adduct was a genuine radical phenoxyl species. On the other hand, the dipyridine adduct showed an intermediate Pd(III)/Pd(II)-phenoxyl character.

The platinum cation appeared even more sensitive to pyridine. Features of the phenoxyl radical were quenched rapidly in both EPR and NIR absorption experiments of $[\text{PtL}^{\text{C2O2}}]^+$ when in presence of pyridine. The rapid reduction of the radical prevented detailed spectroscopic investigations. To gain more insight, we conducted CV experiments on the neutral complex PtL^{C2O2} in presence of pyridine.

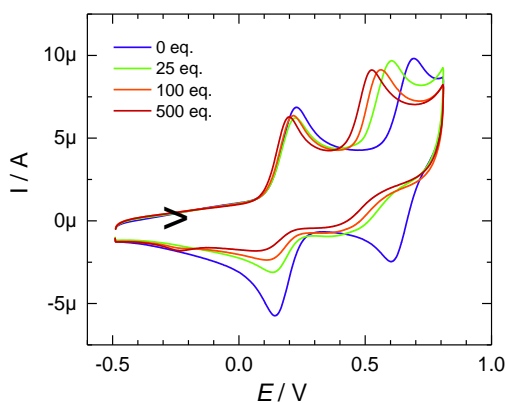


Figure II.20. CV curves of CH_2Cl_2 solutions (+ 0.1 M TBAP) of PtL^{C2O2} (0.28 mM) upon addition of pyridine. The number of molar equivalents of pyridine are indicated in caption. $T = 293$ K, vitreous carbon electrode. Potentials given versus the Fc^+/Fc reference.

The reversibility of the two oxidation events, that correspond to the formation of the phenoxyl radicals, decreases significantly upon addition of pyridine and is consistent with the rapid degradation of the radical observed in spectroscopic titration experiments (see above).

11. Conclusion

In summary, we synthesized a new proligand $\text{H}_4\text{L}^{\text{C}2\text{O}2}\text{Br}_2$ and developed its group 10 $\text{M}^{\text{II}}\text{L}^{\text{C}2\text{O}2}$ complexes, that presented a planar C_2O_2 coordination set involving two NHC and two phenolate units. The complexes could be readily oxidized to stable cations at particularly low potentials. The nickel and platinum cations displayed an intense intervalence charge transfer band in the NIR region that reflected their delocalized phenoxyl radical nature. They were categorized as class (II/III) mixed valent radical species. The palladium cation showed a more localized radical character with a less intense IVCT band. The nickel cation $[\text{NiL}^{\text{C}2\text{O}2}]^+$ was crystalized and consistently showed a mostly symmetrical coordination sphere and characteristic structural features of a phenoxyl radical. Addition of pyridine to $[\text{NiL}^{\text{C}2\text{O}2}]^+$ induced an intramolecular electron transfer to afford two Ni(III)-pyridine adducts. The Ni(III) center presented either a square pyramidal or an octahedral geometry depending on the number of pyridine molecules bound. To the best of our knowledge, this is the first report of a Ni(III) complex with NHC donors. We were also able to oxidize the complexes by two electrons and the $[\text{NiL}^{\text{C}2\text{O}2}]^{2+}$ and $[\text{PdL}^{\text{C}2\text{O}2}]^{2+}$ dications were shown to be stable enough at low temperature to be characterized spectroscopically. Both dications exhibited quenching of the inter-valence feature in NIR spectroscopy that was indicative of a diradical character. This assignment was further confirmed in theoretical calculations that depicted the dications as strongly antiferromagnetically-coupled diradical species.

We showed that the NHC ligand, while well known to stabilize low-valent metal ions could also accommodate Ni(III) high-valent centers when coupled with di-*tert*-butylphenolates or even reach two-electron oxidized radical complexes. Both species are rather elusive and have rarely been described and could open perspectives for new types of catalytic reactions.^[290]

Chapter III.

Manganese complexes

1. Formation of a transient nitrido species in manganese complexes.....	111
1.1. Introduction	111
1.2. Synthesis of Mn(III) precursor complexes	112
1.3. Srtucture of the Mn(III) precursors	114
1.4. UV-vis of the Mn(III) complexes	115
1.5. Synthetic assays to reach the nitrido MnL^{C2O2}(N) complex	115
1.6. Investigation of the N-inserted products	120
1.7. Isotopic labelling	124
1.8. Theoretical calculations	128
1.9. <i>In-situ</i> reactivity studies.....	137
1.10. Conclusion	138
2. Preliminary investigations of electrocatalytic ammonia oxidation.....	138
2.1. Introduction	138
2.2. Preliminary investigation in ammonia oxidation using MnL^{C2O2}Br	140
2.3. Conclusion	144

1. Formation of a transient nitrido species in manganese complexes

1.1. Introduction

We developed a bis(phenol) NHC platform as a counterpart of the classical salen framework and investigated its coordinating properties towards group 10 metals. The ligand displayed strong electron donating properties and allowed us to reach two electron oxidized species. As such we were interested to valorize the ligand to develop transition metal nitride complexes. The first metal of interest in our research was manganese. Manganese nitride complexes usually present one of the richest reactivity of the abundant first row transition metals. In these compounds, the nitrido ligand was shown to be able to act both as a nucleophilic and an electrophilic unit. One of the most interesting development of manganese nitride complexes is in their use as nitrogen atom transfer reagents for aziridination reactions. Despite their huge potential as key reagents in organic chemistry, nitrogen atom-transfer reagents are far less studied than their metal oxo counterparts which are used regularly in epoxidation reactions. One of the main reasons for the scarcity of nitrogen atom-transfer reagents is their relative lack of modularity. N-insertion reactions using metal nitride complexes have been largely limited to electron-rich olefin substrates. Furthermore, nitrogen atom-transfer reagents generally need to be preemptively activated by electrophiles, such as trifluoroacetic anhydride, to show N-insertion reactivity (**Figure III.1**).^[264,266]

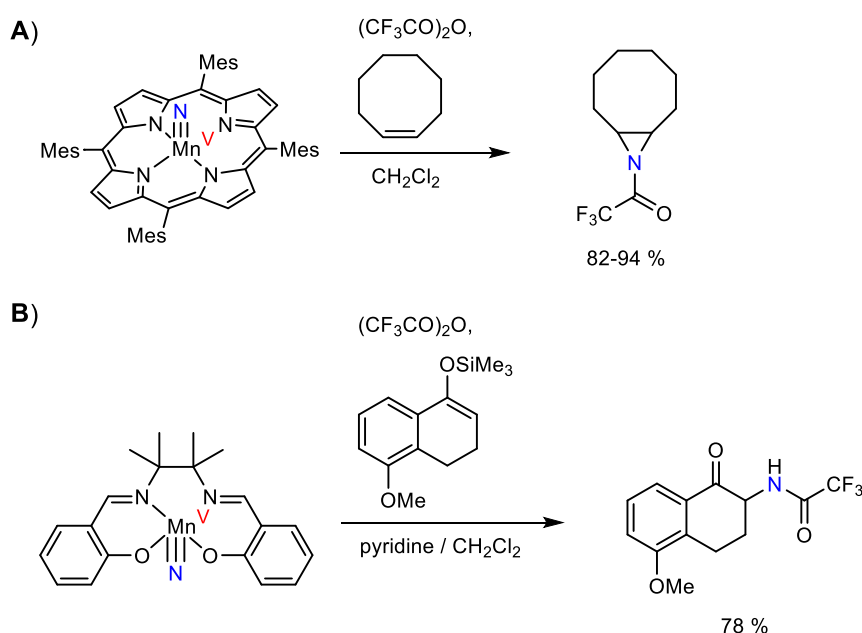


Figure III.1. Select examples of N-transfer reactions upon activation of the nitride: Aziridination of cyclooctene using a Mn(V) porphyrin compound^[264] (A) and amination of silyl enol ethers by a Mn(V)salen complex^[266] (B).

We therefore planned to generate and characterize a $\text{Mn}^{\text{V}}\text{L}^{\text{C202}}(\text{N})$ nitride complex using the electron-rich scaffold of the L^{C202} ligand and investigate its reactivity towards different substrates, including electron-poor olefins in aziridination reactions (**Figure III.2**).

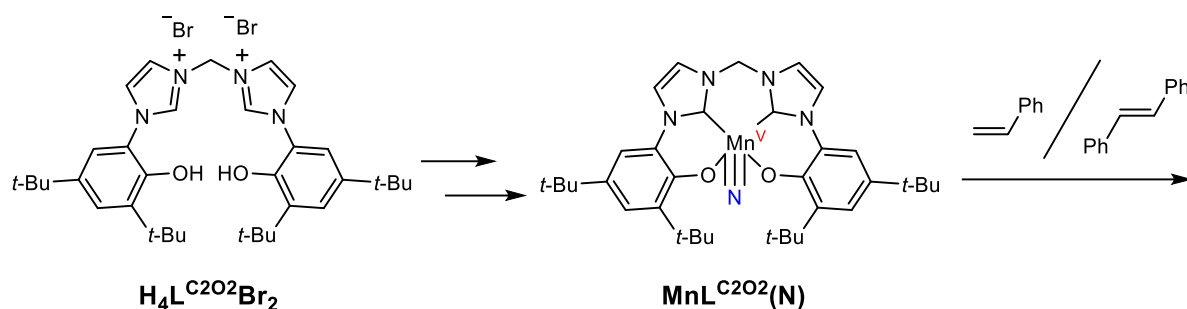


Figure III.2. Envisioned investigation of a $\text{MnL}^{\text{C}2\text{O}2}(\text{N})$ nitride complex for N-transfer reactions on electron-poor olefins.

1.2. Synthesis of Mn(III) precursor complexes

A number of synthetic pathways have been used to develop metal nitride complexes with a large number of transition metals. All of synthetic routes to the Mn(V) nitride species go through a Mn(III) precursor. Hence, we developed two Mn(III) precursors: a bromide Mn(III) complex $\text{MnL}^{\text{C}2\text{O}2}\text{Br}$ to be used in direct nitrogen exchange reactions (**Figure III.3.A,B**); and an azide complex $\text{MnL}^{\text{C}2\text{O}2}(\text{N}_3)$ for azide decomposition reactions (**Figure III.3.D**).

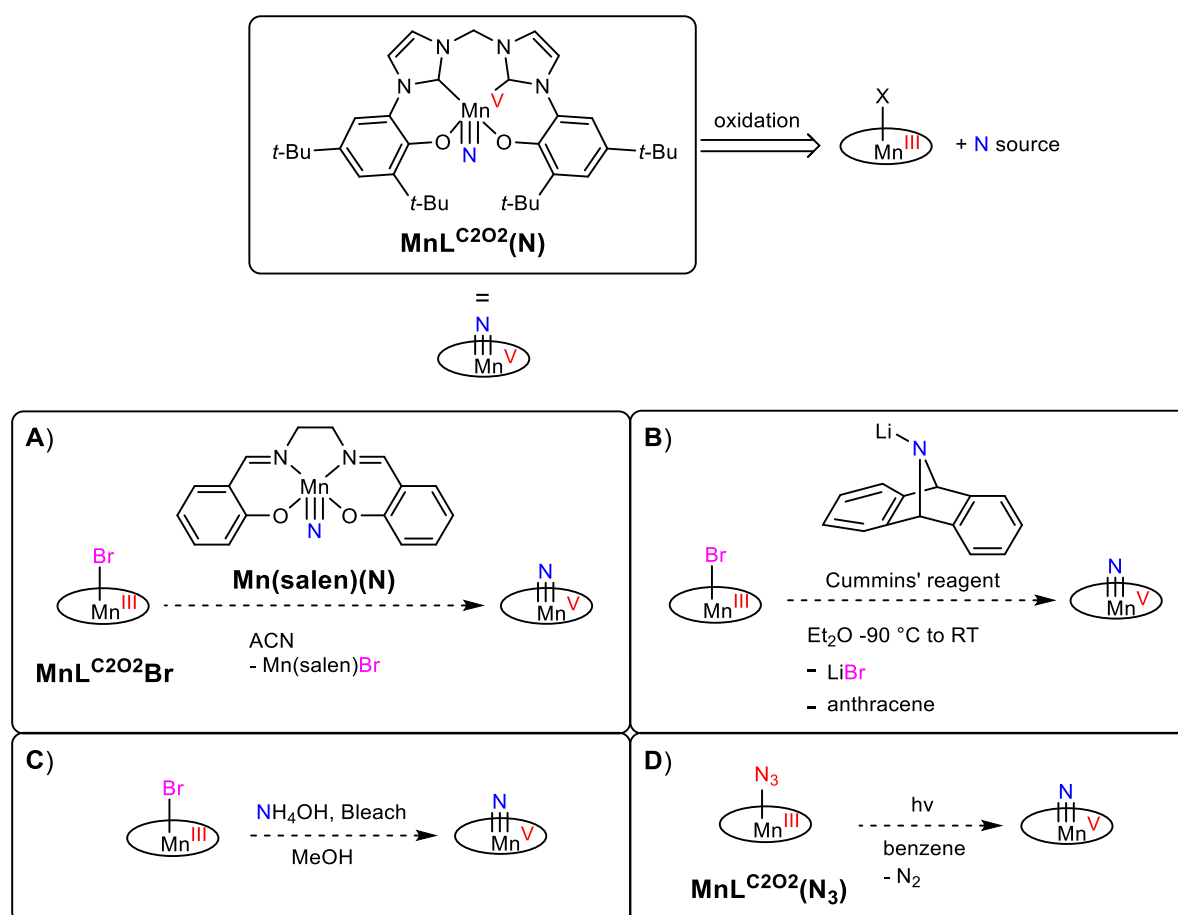


Figure III.3. Envisioned synthetic routes towards the manganese nitride complex $\text{MnL}^{\text{C}2\text{O}2}(\text{N})$: Nitride exchange derived from Gross^[203] (A), nitrogen exchange using Cummins' reagent^[207] (B), ammonia oxidation inspired from Carreira *et al.*^[266] (C) and decomposition of an azide precursor (D).

The proligand **H₄L^{C202}Br₂** was prepared following a six-step synthesis detailed in Chapter II. As detailed above, we avoided the use of nucleophilic solvents such as methanol and ethanol, classically used in complexation reactions. Indeed, preliminary attempts to use ethanol in the complexation demonstrated ligand degradation. We used electrospray ionization mass spectrometry (ESI-MS) to gain insight into the different species formed. The solvent likely promotes a nucleophilic attack at the methylene position between the two NHC rings, with different species isolated pointing towards cleavage at the methylene unit between the two NHC rings. This was verified by identification of the ether adduct from ethanol (MS: $m/z = 331.36$ $[M]^+$) and the elimination product 2,4-di-*tert*-butyl-6-imidazol-phenol (MS: $m/z = 273.27$ $[M + H]^+$) in the ESI-MS spectrum (**Figure III.4**).

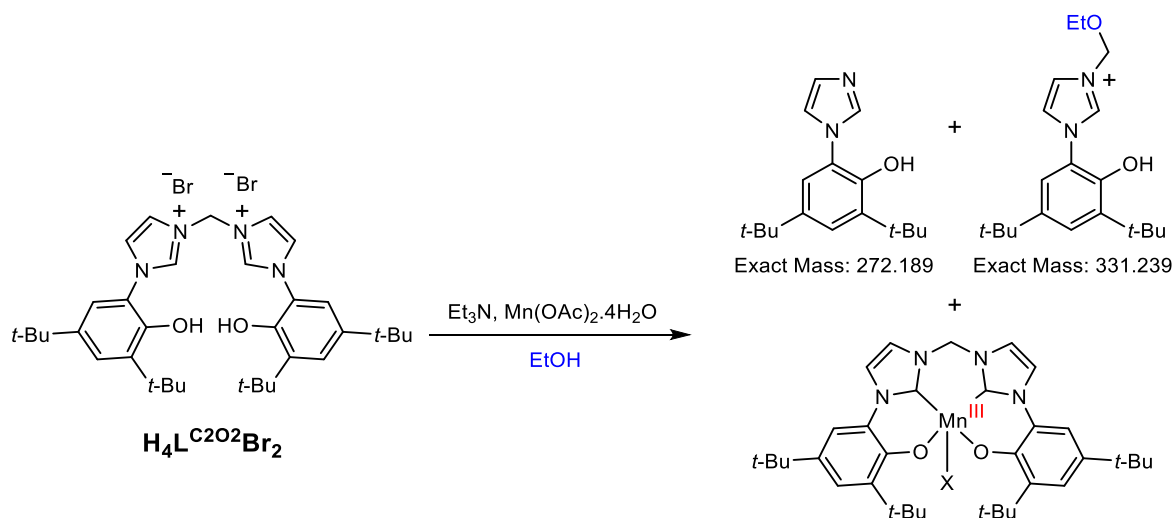


Figure III.4. $\text{Mn}^{\text{III}}\text{L}^{\text{C202}}$ synthesis attempt and its degradation products from ethanol.

The desired $\text{Mn}^{\text{III}}\text{L}^{\text{C202}}$ complex was also detected ($m/z = 609.44$ $[\text{Mn}^{\text{III}}\text{L}^{\text{C202}}]^+$) within the mixture but could not be isolated. The ligand cleavage is likely facilitated by the strong Lewis acidity of the Mn(III) ion which would lead to the activation of the bridging methylene unit. It subsequently acts as an electrophilic center. The results prompted us to handle in less nucleophilic solvents, such as dichloromethane or acetonitrile.

Complex $\text{MnL}^{\text{C202}}\text{Br}$ was therefore obtained by suspending an equimolar amount of proligand and manganese(II) acetate tetrahydrate in acetonitrile and adding four equivalents of triethylamine. The reaction mixture was refluxed under air until the proligand was fully consumed. Salt impurities and byproducts were eliminated by filtration over celite in toluene to afford the complex in 89% yield. The azido complex $\text{MnL}^{\text{C202}}(\text{N}_3)$ was prepared by ligand metathesis of $\text{MnL}^{\text{C202}}\text{Br}$. A concentrated acetonitrile solution of $\text{MnL}^{\text{C202}}\text{Br}$ was treated with a 1.5 equivalents of sodium azide solution in H_2O . Upon addition, the sodium azide reagent precipitated and H_2O was added dropwise until complete solubilization. A large spatula of sodium sulfate desiccant was added before the volatiles were removed under vacuum. The excess of sodium azide was then removed by filtration over celite in CH_2Cl_2 to afford $\text{MnL}^{\text{C202}}(\text{N}_3)$ in a 95% yield. The nature of the azide complex was confirmed by IR spectroscopy where $\text{MnL}^{\text{C202}}(\text{N}_3)$ displayed a characteristic sharp azide stretch at $\nu = 2040\text{ cm}^{-1}$.

1.3. Structures of the Mn(III) precursors

Single crystals suitable for X-Ray diffraction were obtained for both **MnL^{C2O2}Br** and **MnL^{C2O2}(N₃)** by slow evaporation of concentrated CH₂Cl₂ and acetonitrile solutions respectively.

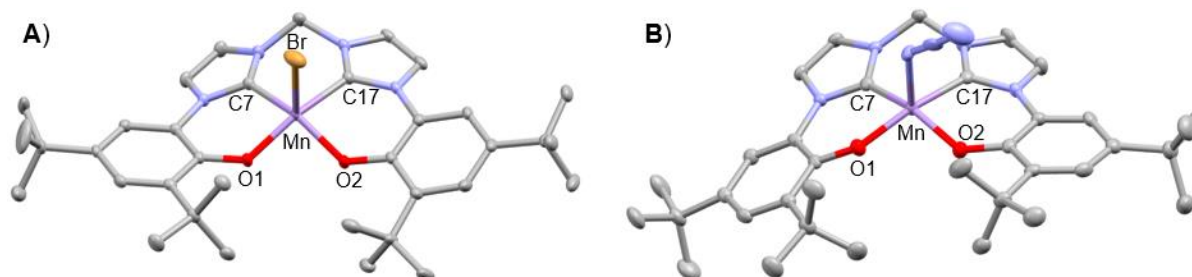


Figure III.5. X-Ray crystal structures of **MnL^{C2O2}Br** (A) and **MnL^{C2O2}(N₃)** (B).

In both complexes the metal ion lies in a distorted square pyramidal geometry with the manganese center coordinated by two phenolate oxygens (O1/O2) and two carbons of the NHC units (C7/C17) in equatorial positions. The anionic bromide or azide ligands are bound in the axial position, shifting the manganese ion slightly out of the O1-O2-C17-C7 plane. The Mn-phenolate and Mn-NHC coordination lengths are similar within the accuracy of the structures in both complexes. The variable out of plane distortion of the metal ion suggests a significant flexibility of the tetradentate ligand. In **MnL^{C2O2}Br**, the NHC rings are angled with the phenolate rings by 25 and 28°. The ligand also adopts a slight umbrella shape with a distortion between the two NHC rings of 32°. This shape is also present in **MnL^{C2O2}(N₃)**, with the two NHC planes defining a similar 33° angle. However, the NHC rings are more planar with their connected phenolates with 9 and 14° angles.

Table III.1. Coordination bond distances in the Mn(III) complexes (Å).

complex	MnL^{C2O2}Br	MnL^{C2O2}(N₃)
Mn-O1	1.8808(13)	1.8835(17)
Mn-O2	1.8975(14)	1.8898(18)
Mn-C7	2.0260(19)	2.021(3)
Mn-C17	2.0276(19)	2.025(3)
Mn-X ^a	2.5498(4)	2.147(2)

^aX = Br in **MnL^{C2O2}Br**, X = N₃ in **MnL^{C2O2}(N₃)**.

1.4. UV-vis of the Mn(III) complexes

Both Mn(III) complexes presented a similar characteristic brownish color and their absorption spectra are detailed below in **Figure III.6** and **Table III.2**. The two complexes displayed two broad absorption shoulders in similar regions of the visible region. **MnL^{C2O2}(N₃)** was slightly red-shifted by approximately 800 cm⁻¹ when compared to **MnL^{C2O2}Br**. This likely indicates the involvement of apical ligand orbitals in the transitions.

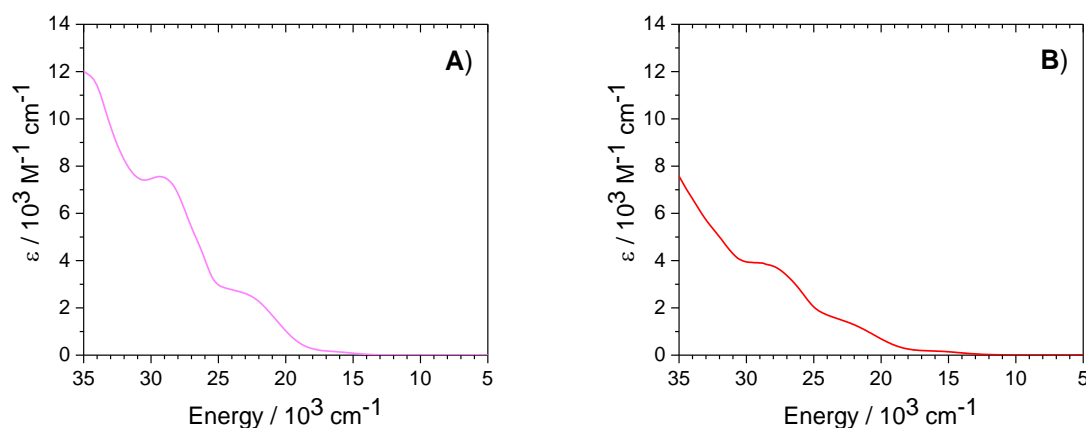


Figure III.6. UV-vis-NIR spectra of **MnL^{C2O2}Br** (A) and **MnL^{C2O2}(N₃)** (B) in CH₂Cl₂; *T* = 298 K.

Table III.2. UV-vis-NIR data for the Mn(III) complexes.^a

complex	λ_{max} [cm ⁻¹] (ϵ [M ⁻¹ cm ⁻¹])
MnL^{C2O2}Br	34200 (11660, sh), 29200 (7550), 22600 (2510, sh)
MnL^{C2O2}(N₃)	28400 (3830, sh), 21900 (1270, sh)

^aIn CH₂Cl₂ solution. sh: shoulder

1.5. Synthetic assays to reach the nitrido **MnL^{C2O2}(N)** complex

As detailed previously, we were required to use specific experimental conditions, including non-nucleophilic solvents, to avoid the degradation of our manganese complexes. Hence, our attempts to reach the nitride **MnL^{C2O2}(N)** complex were focused on the photolysis of the azide precursor **MnL^{C2O2}(N₃)** (**Figure III.3.A**) or the nitride exchange with the bromide complex **MnL^{C2O2}Br** (**Figure III.3.C**) that could both be conducted under mild conditions.

- Azide photolysis

A benzene solution of **MnL^{C2O2}(N₃)** was irradiated at $\lambda = 312$ nm (32 100 cm⁻¹) using UV lamps following a standard procedure for Mn(V) salen nitride complexes developed in the Storr group.^[291] The color of the solution gradually changed, consistent with evolution of the complex. However, no means of characterization was able to clearly indicate the formation of a nitride complex. Mn(V) nitride salen complexes are known to be low spin diamagnetic systems (d^2 , $S = 0$) that can be readily purified using silica chromatography and characterized by NMR and ESI-MS.^[291] In our case, both ¹H NMR and ESI-MS analyses of the crude

mixtures after photolysis displayed a complex mixture of compounds without a distinct signature of the putative Mn(V) nitride complex.

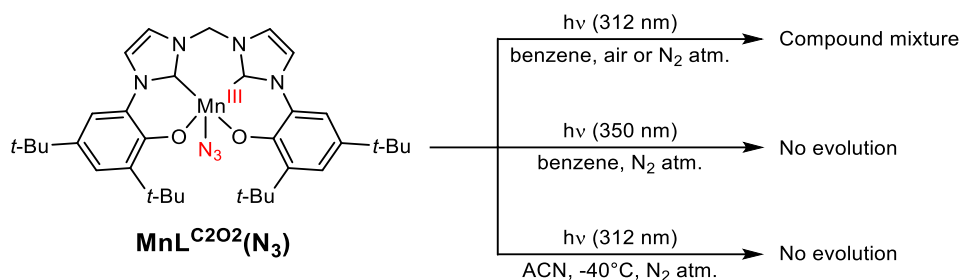


Figure III.7. Summary of the different photolysis trials on the azido $\text{MnL}^{\text{C2O2}}(\text{N}_3)$ complex.

As discussed above, the ligand framework appeared to be sensitive to the Lewis acidity of the metal center. Therefore, the expected high valent Mn(V) nitrido species may be too reactive to be characterized or isolated under such reaction conditions. Milder conditions were thus explored. Firstly, freshly dried solvents were used and irradiation was conducted under inert atmosphere to prevent moisture impact. Additionally, while convenient, the photoactivation of azide complexes is known to have a limited selectivity. Irradiation in the UV region likely excites the NHC phenolate ligand framework, alongside with the azide moiety, which may lead to decomposition products. The poor solubility of the $\text{H}_4\text{L}^{\text{C2O2}}\text{Br}_2$ proligand in the usual solvents for irradiation processes prevented us to run background experiments to check this hypothesis. Irradiation at lower energy ($\lambda = 350 \text{ nm}$, 28600 cm^{-1}) was conducted but unfortunately, no change was observed in multiple trials with UV-vis control experiments. Irradiation was also performed in acetonitrile at -35°C but once again the starting $\text{MnL}^{\text{C2O2}}(\text{N}_3)$ azide complex did not evolve. Overall, all efforts to prepare a Mn(V) nitride complex using this procedure were unsuccessful, either displaying degradation behavior or no evolution of the starting material.

- Nitride exchange with Mn(V) salen nitride complex

To address the issues observed in photolysis reactions, we used a nitride exchange reagent to substitute the bromide ligand in $\text{MnL}^{\text{C2O2}}\text{Br}$ by a nitride. Purely organic nitride donors, such as the Cummins' reagent (**Figure III.3.B**) are often used in nitride exchange reactions because they allow a simple purification. However, preparation of the Cummins' reagent requires a time-consuming multi-step synthesis. Hence, our interest focused on an inorganic nitrido donor: a Mn(V) salen nitride complex (**Figure III.3.A**). This complex is indeed known to exchange nitrides to Mn(III) complexes (see Chap I.3.4.1.). The Mn(V) salen nitride reagent was readily prepared in a two-step synthesis from inexpensive, commercially available reagents. Moreover, the nitride exchange reaction could easily be conducted in neat conditions in a glovebox under N_2 atmosphere (**Figure III.8**).

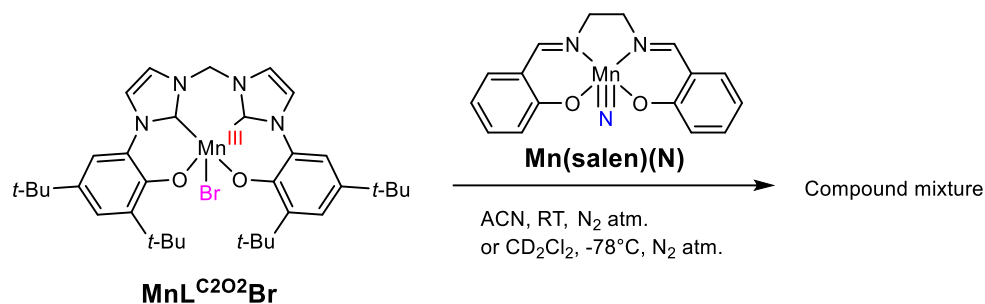


Figure III.8. Nitride exchange reactions on the **MnL^{C2O2}Br** bromide complex.

We conducted the experiment by mixing an acetonitrile solution of **MnL^{C2O2}Br** with 1 molar equivalent of the nitride exchange reagent. Consumption of the nitride exchange reagent was monitored by formation of a brown precipitate that was identified by ESI-MS ($m/z = 321.04$ [**Mn^{III}salen**]⁺) as the Mn(III)Br salen side-product of the reaction (**Figure III.3.A**). The side product was eliminated by filtration over celite and the filtrate was analyzed using ESI-MS. A peak could be detected at $m/z = 624.310$ (29%) that could correspond to the desired nitride **MnL^{C2O2}(N)**, but could also be interpreted as a nitrogen-inserted manganese complex (circled in blue in **Figure III.9**). Other peaks were observed at $m/z < 300$ which are assigned as cleavage fragments of the ligand. Another peak at $m/z = 570.381$ (26%) was attributed to a N-inserted ligand (compound **1** in **Figure III.9**). This experiment demonstrates that a nitrido complex likely forms under our experimental conditions but its instability prevents straightforward isolation. Nevertheless, one must be careful by interpreting those results since mass spectrometry experiments remain denaturing by nature. More specifically, ESI experiments usually require strongly polar solvents coupled with acidic additives as carrier eluants. As such, more conclusive evidence was required to confirm the nature of the reaction products.

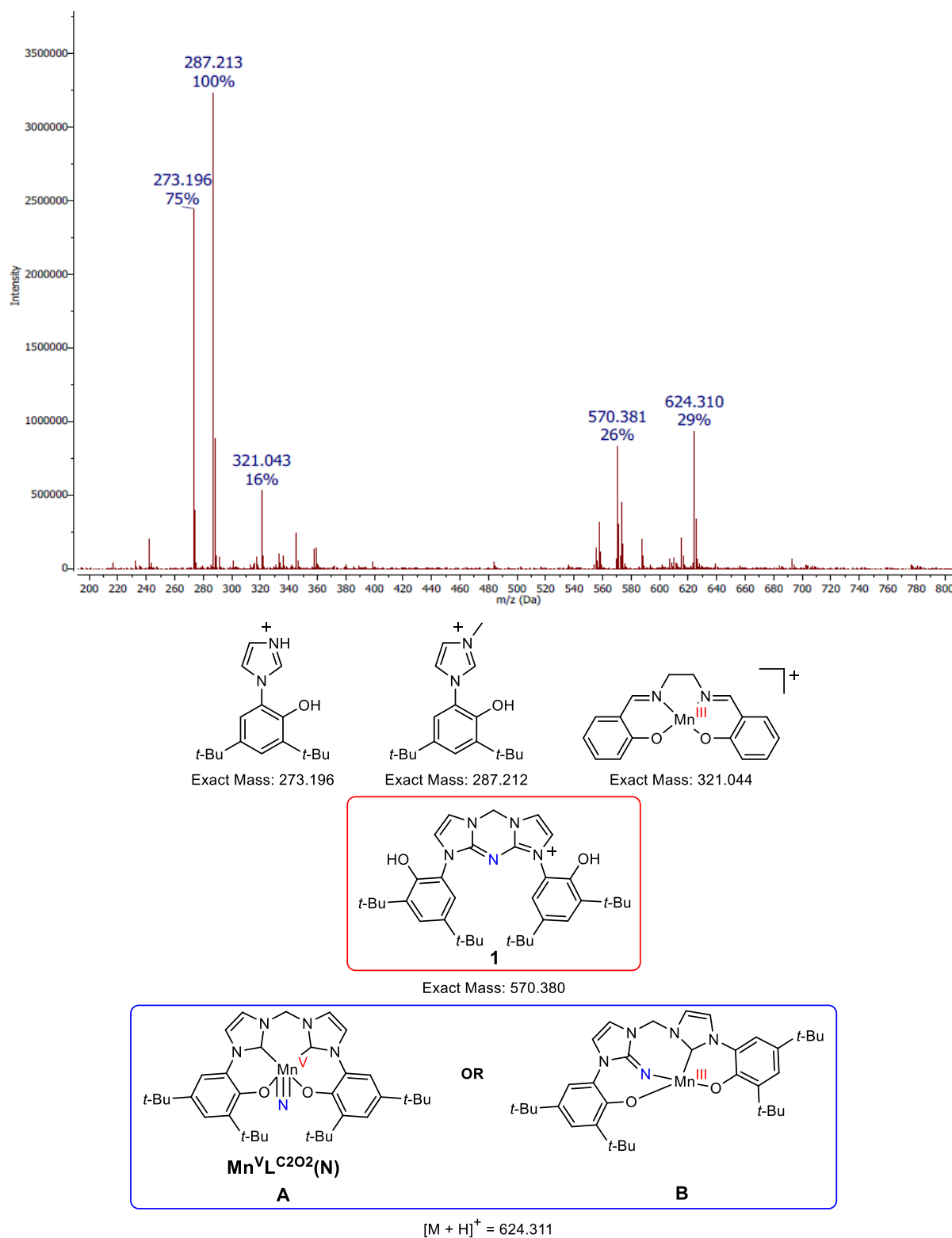


Figure III.9. Positive mode ESI-HRMS analysis of the nitride exchange reaction in acetonitrile and proposed species formed.

Low temperature (-78°C using dry ice baths) nitride exchange experiments were conducted in deuterated dichloromethane to limit decomposition. We attempted to characterize the putative nitride complex using low-temperature ^1H NMR. Unfortunately, no distinct NMR signature of the desired nitrido complex could be obtained. $\text{Mn}(\text{V})$ nitride complexes are known to be robust, stable species, with no reports of ligand N-insertion products. Nevertheless, reactions to obtain

the nitride complex showed an uncharacteristic behavior from reported Mn(V) nitride species. Nitrido ligands have been reported to undergo intramolecular N-insertion on the ligand backbone of electron-rich late-transition metal complexes (**Figure III.10.A,B**).^[154,235,236] NHC ligands are also known to be hosts to atom-insertion reactions on the carbenic center. Most relevant to our case, the Meyer group has recently reported the existence of a transient Co(IV)≡N nitride in the formation of a N-inserted NHC ligand (**Figure III.10.C**).

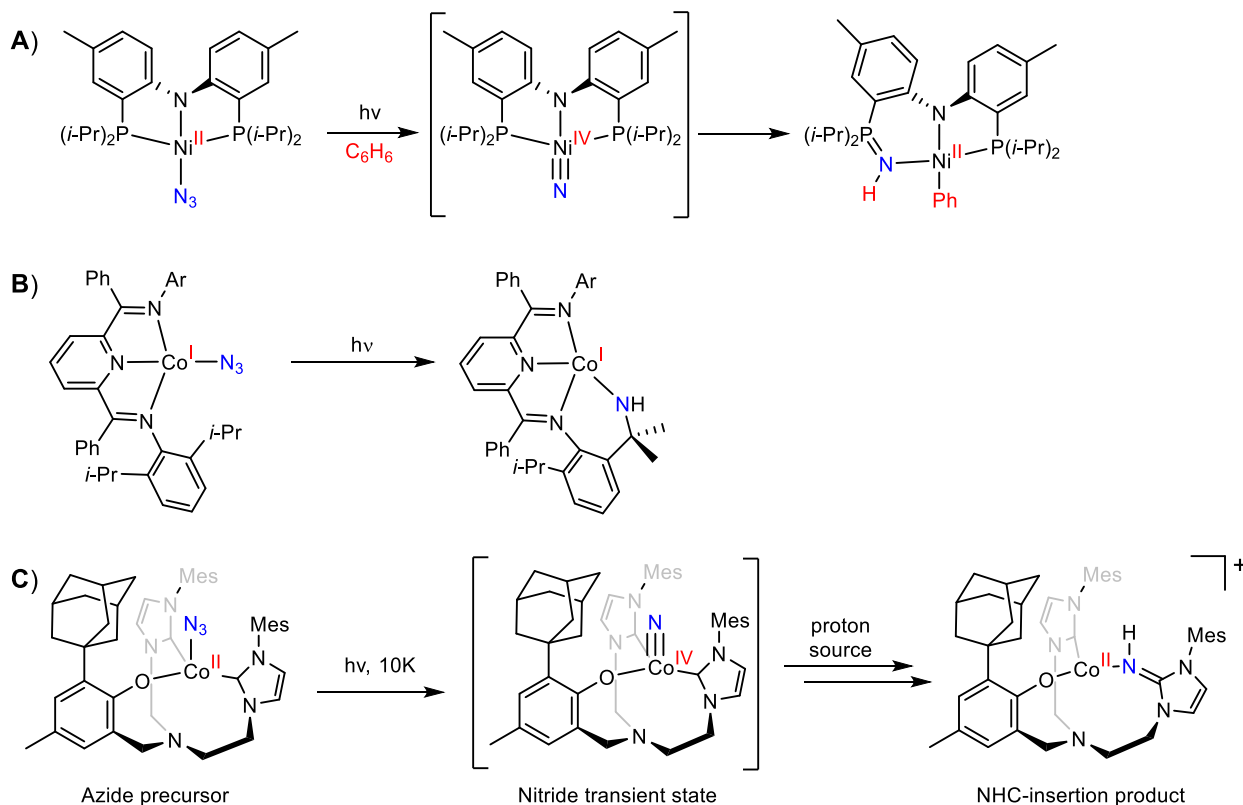


Figure III.10. Select examples of intramolecular nitride insertion reactions in a nickel species^[236] (**A**) and in a cobalt complex^[235] (**B**). Insertion of a transient nitride into a NHC ligand in a cobalt complex^[154] (**C**).

Hence, we proposed the formation of a transient $\text{Mn}^{\text{V}}\text{L}^{\text{C2O2}}(\text{N})$ nitride complex and its degradation through nitride-insertion reactions on the NHC ligand backbone and investigated the nature of these insertion products.

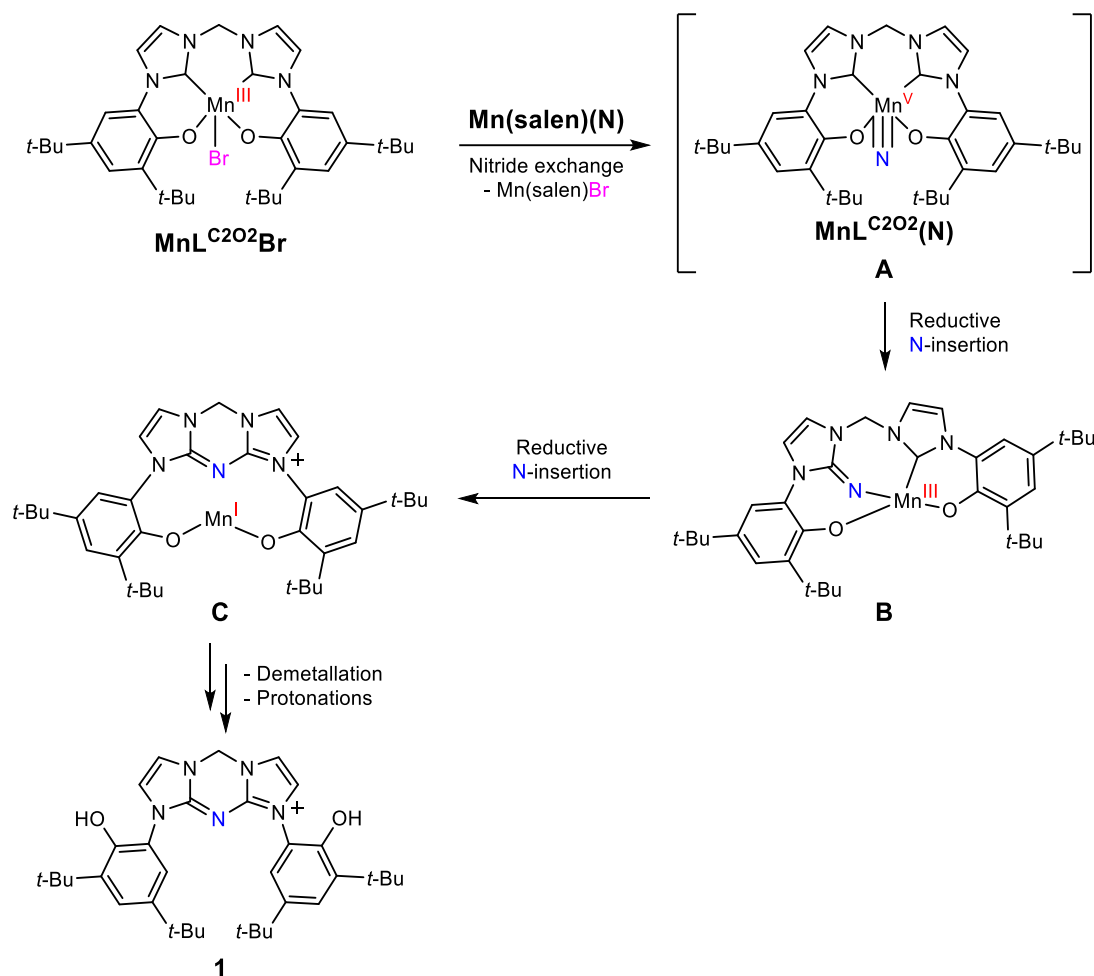


Figure III.11. Proposed pathway for the formation of a transient $\text{MnL}^{\text{C2O2}}(\text{N})$ nitride complex and its evolution through intramolecular N-insertion reactions.

1.6. Investigation of the N-inserted products

- Manganese complexes

Despite extensive efforts of purification, including recrystallizations, silica, alumina and size-exclusion chromatographies, we could not isolate nor characterize any manganese complexes after photolysis or nitride exchange reactions. Preliminary magnetic measurements using Evans' method showed that the crude photolysis reaction mixture had a magnetic susceptibility of $\mu_{\text{eff}} = 4.15$, which would correspond to 3.26 unpaired electrons. This is coherent with the absence of a ^1H NMR signature that was expected for a diamagnetic Mn(V) nitride complex.^[291] The high magnetic susceptibility points towards the plausible presence of high-spin manganese species, like N-inserted Mn(III) (d^4 , $S = 2$) or Mn(I) (d^6 , $S = 2$) species depicted above in **Figure III.11**. Nevertheless, due to the different possible degradation products, no definitive statement can be made about the true nature of species present in solution. X-band EPR measurements were also conducted to investigate the spectroscopic signature of the putative manganese species but no signal was observed. These results do not prove the absence of manganese complexes however, as both Mn(III) precursors $\text{MnL}^{\text{C2O2}}\text{Br}$ and $\text{MnL}^{\text{C2O2}}(\text{N}_3)$ were also EPR silent in both parallel and perpendicular modes. This is likely due to the strong field of the L^{C2O2} ligand.

- Insertion product 1

As we were unable to characterize manganese degradation products, we then focused on the characterization of the organic insertion product **1**. A hydrochloric acid solution was used in successive washings of the crude mixtures from either photolysis or nitride exchange reactions followed by successive washings with a saturated tetrasodium EDTA solution to remove metal ions from the solution. The procedure allowed us to remove the ion at $m/z = 624.31$ in the nitride exchange reactions, consistent with a demetallation from a putative N-inserted manganese species. A minor peak was identified ($m/z = 557.41$ (20%), **Figure III.12**) in the ESI-MS spectrum, which was assigned to the ionic form of the free **H₄L^{C202}** ligand.

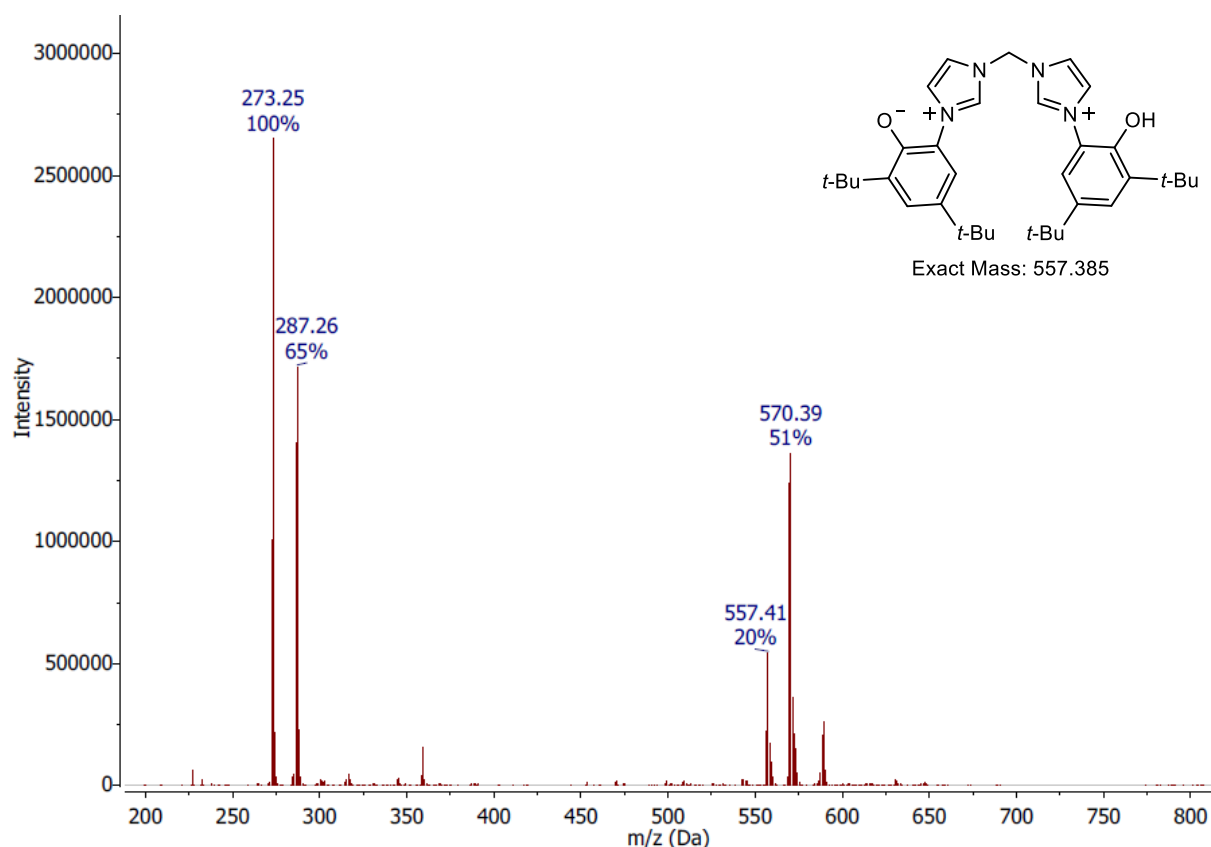


Figure III.12. Positive mode ESI-MS analysis of a nitride exchange reaction after HCl and EDTA washing procedures and structure of an ion of the free **L^{C202}** ligand.

The N-insertion product **1** ($m/z = 570.39$ in **Figure III.12**) was further purified by successive washings of an acetonitrile solution by hexanes. It was finally recrystallized by slow evaporation of a mixture of acetonitrile and dichloromethane that afforded single crystals suitable for X-ray diffraction.

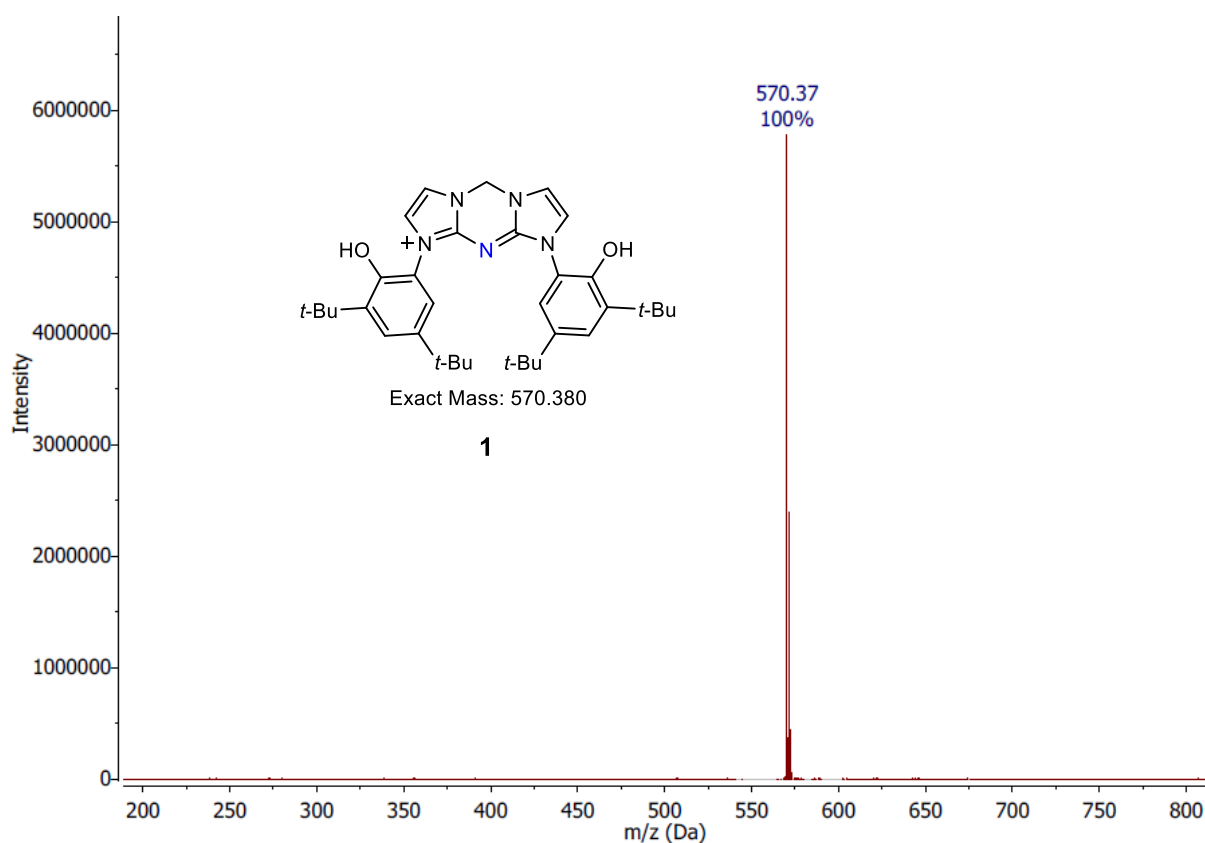


Figure III.13. Positive mode ESI-MS analysis of the N-insertion product **1** after recrystallization.

Species **1** is a cation, as demonstrated by the presence of a chloride counterion in the crystal cell. A single N atom (N1) is connected to the two C7 and C17 carbons (**Figure III.14**), forming three fused rings with two imidazoles and one central triazone pattern. Noteworthy, the inserted nitrogen N5 present similar short bond lengths with carbons C7/C17, which were the carbenic centers in the NHC precursors (N1-C7 and N1-C17: 1.335 and 1.334 Å respectively). The three fused rings are mostly planar, with an 11.0° angle between the planes of the two imidazole rings. All these features point towards the presence of a conjugated π system located on the N2-C7-N1-C17-N5 atoms (**Figure III.14**).

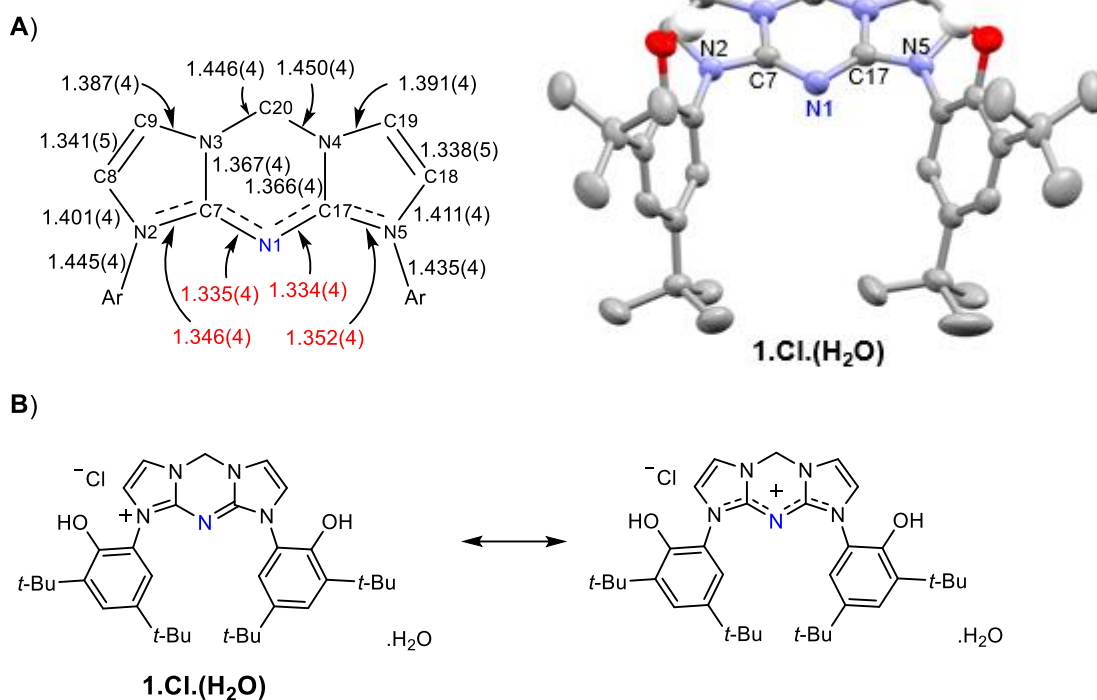


Figure III.14. Crystal structure of N-inserted product **1** and selected bond lengths (Å) (**A**). Resonance forms displaying the conjugated π system in the triazonium compound.

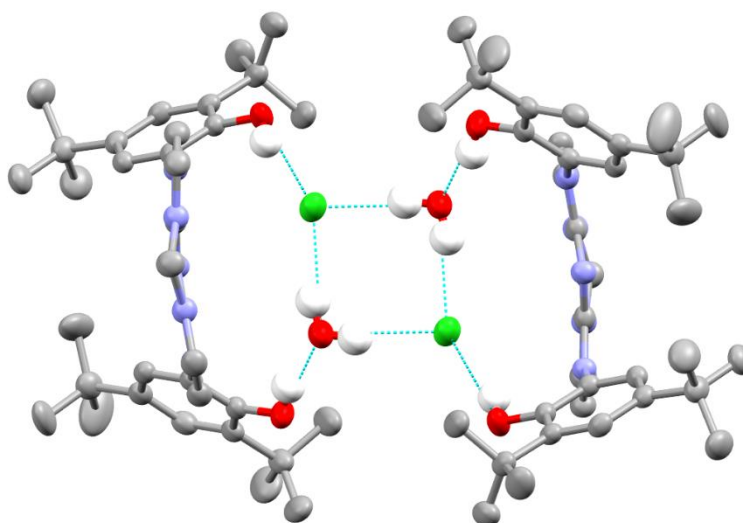


Figure III.15. Representation of the H-bond network in the crystallographic structure of **1**. Hydrogens not involved in H-bonds were omitted for clarity.

The chloride anion is involved in a H-bond network involving the phenol groups and exogenous water molecules present in the crystal cell (**Figure III.15**). Solvent molecules of dichloromethane and acetonitrile were also present in the crystal cell.

The ^1H NMR spectrum of **1** shows the compound to be symmetric in solution: ^1H NMR (600 MHz, CDCl_3) δ 8.72 (s, 2H), 7.32 (d, $J = 2.2$ Hz, 2H), 6.91 (s, 2H), 6.89 (s, 2H), 6.52 (s, 2H), 1.29 (s, 18H), 1.25 (s, 18H).

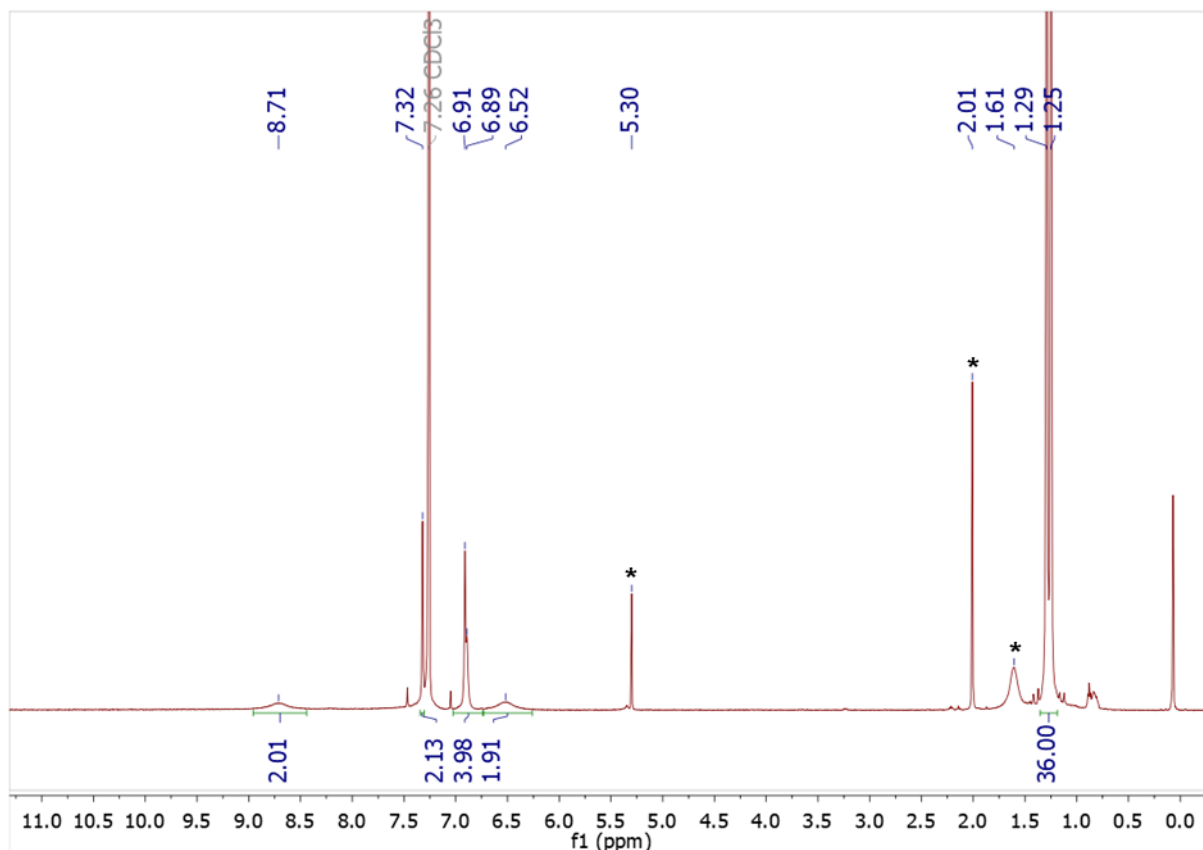


Figure III.16. ^1H NMR spectrum of N-insertion product **1**. Residual solvent traces from the crystallization process are showed with asterisks.

Overall, the insertion product **1** was obtained in a 30% yield based on the nitride exchange reaction after three extraction procedures (HCl / EDTA / hexanes). This considerable product yield precludes it from being only a minor impurity. Product **1** could also be obtained after purification of the photolysis reactions described previously, although in lower yields (11-15%). This can be explained from the previous discussion, where we discussed that the photoactivation of the $\text{L}^{\text{C}2\text{O}2}$ ligand backbone was a possible degradation factor.

1.7. Isotopic labelling

To confirm the origin of the N-atom insertion into the ligand backbone, we prepared the ^{15}N -labelled nitride exchange reagent $\text{Mn}(\text{salen})(^{15}\text{N})$. It was readily obtained using a ^{15}N -ammonium hydroxide solution as starting material according to **Figure III.17**.

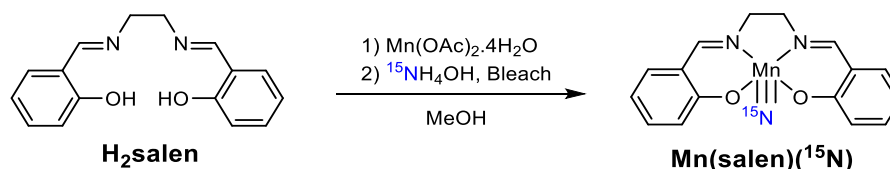


Figure III.17. Synthesis of the ^{15}N -labelled nitride exchange reagent $\text{Mn}(\text{salen})(^{15}\text{N})$.

The labelled precursor was then used in nitride exchange reactions and the reaction mixture was analyzed by ESI-HRMS (**Figure III.18**). An increase of m/z shift by one Dalton was observed for two ions ($m/z = 571.376$, 100% and $m/z = 625.305$, 20%) discriminating them as

^{15}N -labelled. These results indicated that the nitrogen atom inserted into the ligand (N5, **Figure III.14**) does indeed originate from a nitride insertion reaction.

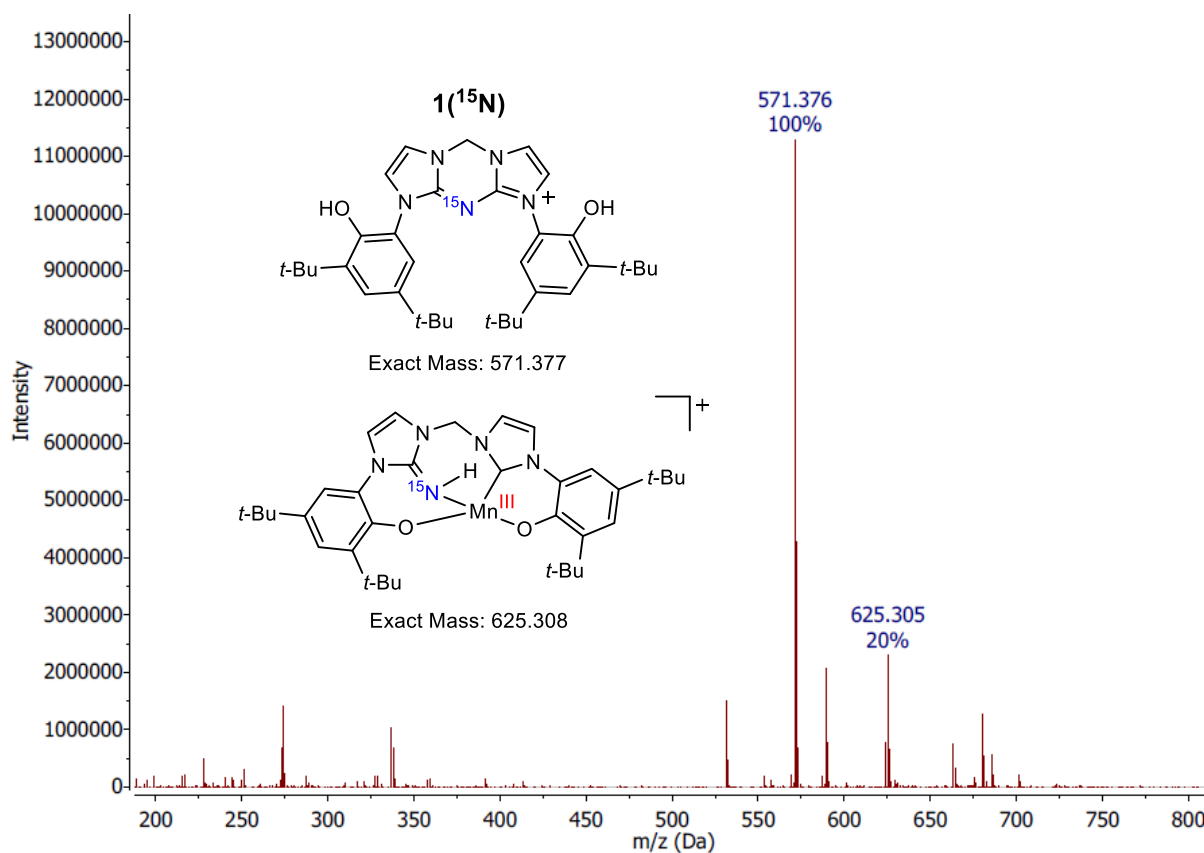


Figure III.18. ESI-HRMS analysis of the crude mixture of the nitride exchange reaction with the ^{15}N labelled nitride exchange reagent and ^{15}N -labelled ions of interest.

The ^{15}N -inserted product **1(^{15}N)** could be purified following the same washing procedures described above for compound **1**, albeit with a lower yield ($\rho = 21\%$). We were unable to obtain the ^{15}N NMR spectrum of compound **1(^{15}N)** for a more thorough characterization.

We still needed to verify that the N-insertion is the result of an intramolecular nitride-NHC coupling from a transient $\text{MnL}^{\text{C}2\text{O}2}(\text{N})$ nitride complex, rather than an intermolecular insertion from the salen nitride exchange reagent. Thus, we also investigated the photolysis reaction of a terminally ^{15}N -labelled azide precursor $\text{MnL}^{\text{C}2\text{O}2}(^{15}\text{N}=\text{N}_2)$. The terminally ^{15}N -labelled azide complex was prepared following the same procedure as compound $\text{MnL}^{\text{C}2\text{O}2}(\text{N}_3)$ but with a ^{15}N -labelled sodium azide-1- ^{15}N reagent.

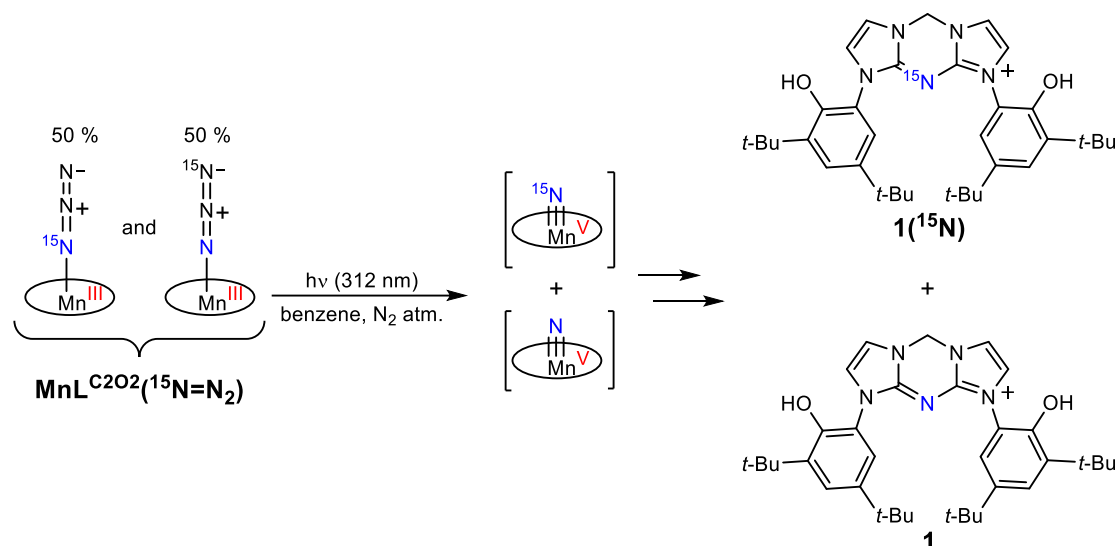


Figure III.19. Photolysis of a terminally ^{15}N -labelled azide complex $\text{MnL}^{\text{C2O2}}(^{15}\text{N}=\text{N}_2)$ and its resulting N-insertion products.

After purification following the washing procedures described for compound **1**, the photolysis of $\text{MnL}^{\text{C2O2}}(^{15}\text{N}=\text{N}_2)$ afforded a mix of ^{15}N -labelled and non-labelled N-insertion products, compounds $\mathbf{1}(^{15}\text{N})$ and **1** (Figure III.20). Other contaminating side-products were evidenced in the ESI-MS spectrum of the reaction and we were unable to obtain a clean ^1H -NMR spectrum. Nevertheless, we simulated the theoretical isotopic pattern for an equal mixture of labelled and un-labelled insertion products (50% $\mathbf{1}(^{15}\text{N})$ + 50 % **1**) that correlated closely with the experimental ESI-MS spectrum.

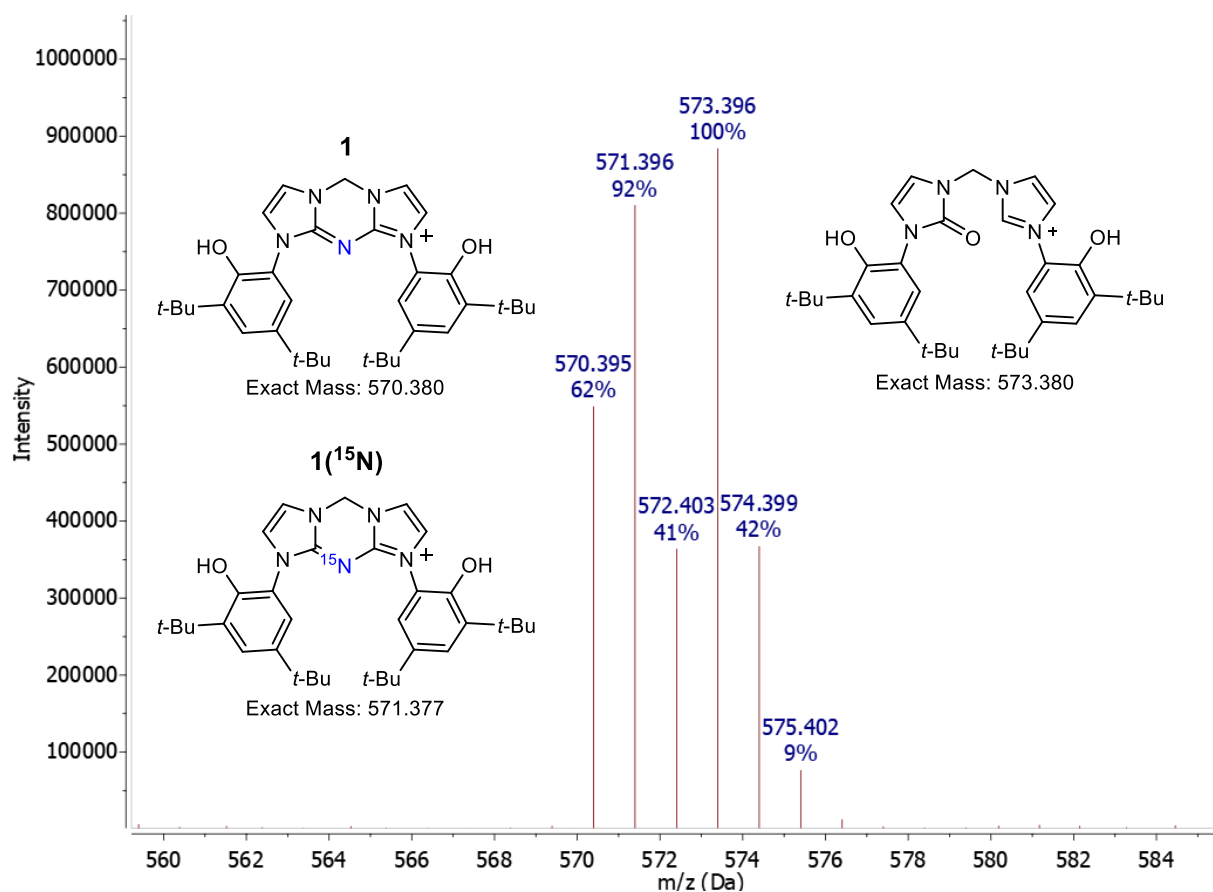


Figure III.20. Positive mode ESI-MS analysis of the photolysis of the ¹⁵N-labelled azide manganese complex and ions of interest.

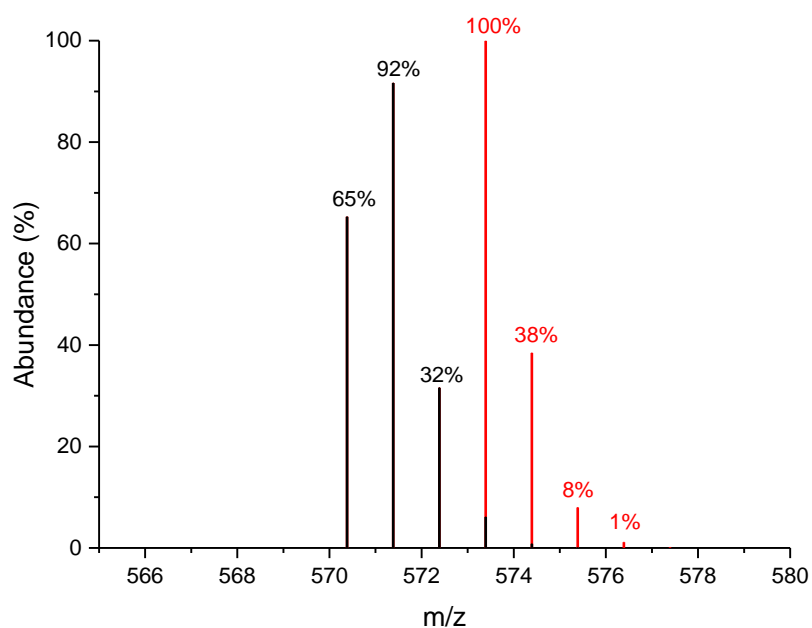


Figure III.21. Adjusted theoretical isotopic pattern for a 50% **1**(¹⁵N) + 50 % **1** compound mixture (black), with the added isotopic pattern of a putative oxygen-inserted ligand contaminant (red).

The equal distribution of compounds **1**(¹⁵N) and **1** showed a plausible formation of two different intermediate nitride complexes resulting from the two possible binding modes of the ¹⁵N-labelled azide in complex **MnL**^{C2O2}(¹⁵N=N₂) (**Figure III.19**). Overall, the different isotopic labelling experiments evidenced that the formation of N-inserted compound **1** most likely goes through the formation of a transient **MnL**^{C2O2}(N) nitride intermediate.

1.8. Theoretical calculations

To gain further knowledge into the ligand insertion process, we conducted DFT calculations. Nitride insertions on NHC ligands have been reported to be accompanied by a two-electron reduction of the metal center. This type of reactivity has been formally assigned as reductive eliminations of the nitride and NHC ligands.^[292] Therefore, we investigated the theoretical degradation of a transient **Mn(V)L**^{C2O2}(N) nitride complex towards the triazonium compound **1**. We envisioned a series of two reductive elimination reactions for the bis-insertion of the nitride ligand on the two NHC centers. Thus, we calculated the theoretical structure of a **Mn(V)** nitride complex and of different evolution products, including mono-inserted **Mn(III)**-guanidine derivatives and double-insertion **Mn(I)**-triazonium species (species **A**, **B**, **C**, respectively in **Figure III.22**). The structures were optimized using the BP86 functional (6-31G* basis set and SCRF(CH₂Cl₂) solvent model). It was chosen for consistency, based on theoretical calculations conducted on an analogue chromium nitride species **CrL**^{C2O2}(N) that will be later discussed in this thesis (Chapter IV).

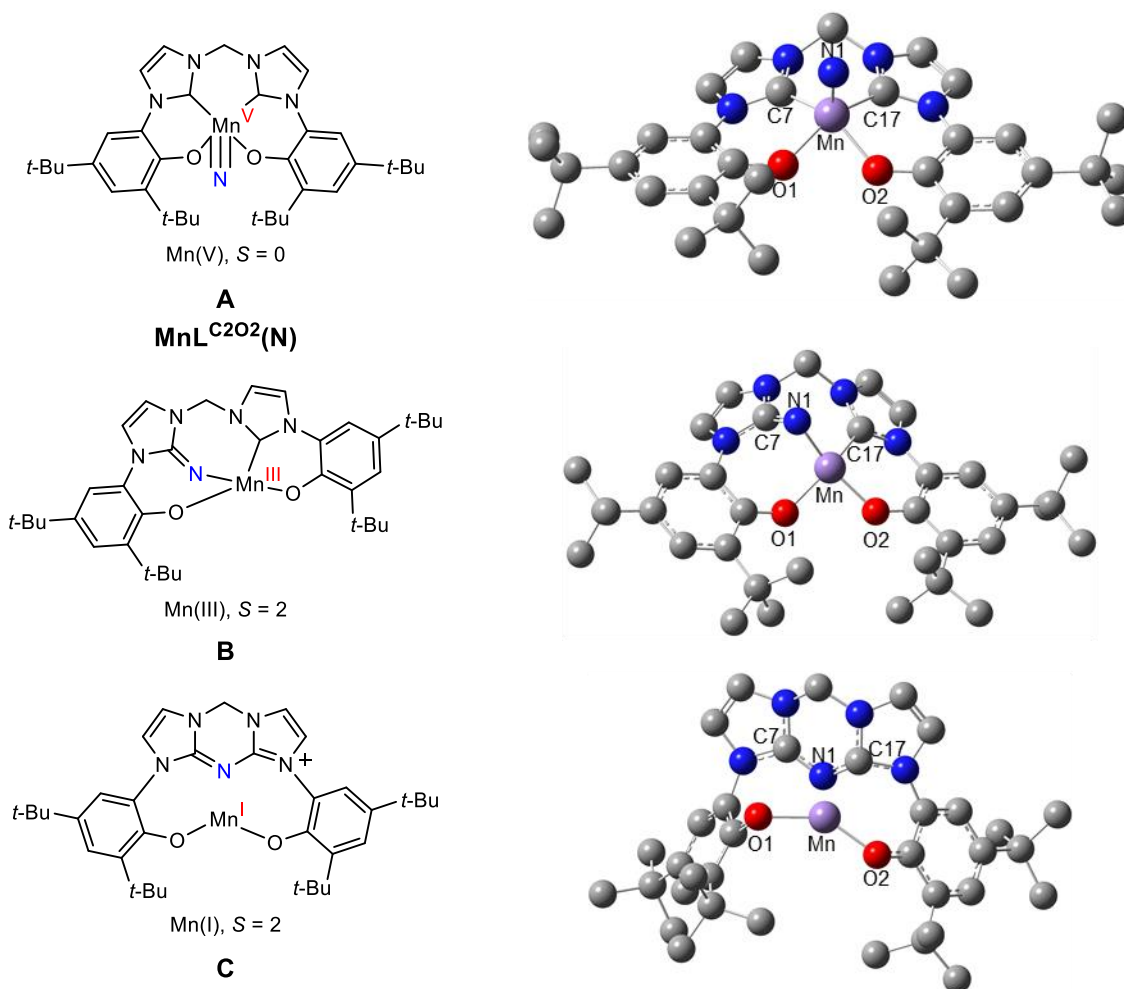


Figure III.22. Optimized structures for the proposed **A**, **B** and **C** intermediates in the nitride-NHC coupling reactions to form triazonium compound **1** (BP86/6-31G*/SCRF(CH₂Cl₂)).

The electronic structure of each theoretical species was investigated. Single-point energy calculations were conducted with the B3LYP functional (TZVP basis set and SCRF(CH₂Cl₂) solvent model). It was chosen as the functional that could best describe the formation of triazonium compound **1** observed experimentally. The Mn(V) nitride species (**A**) was predicted to be a low-spin singlet species (d^2 , $S = 0$). The mono N-inserted Mn(III) (**B**) and bis N-inserted Mn(I) (**C**) complexes were predicted to be high-spin quintet species (d^4 , $S = 2$ and d^6 , $S = 2$; respectively). The relative energies of the different spin states are given in **Table III.3**.

Table III.3. Energetic analysis of the Mn complexes of interest for the formation of compound **1**.^a

Spin state	Singlet ($S = 0$) (kcal.mol ⁻¹) ^b	Triplet ($S = 1$) (kcal.mol ⁻¹) ^b	Quintet ($S = 2$) (kcal.mol ⁻¹) ^b
A	0	+ 27.6	-
B	+54.8	- ^c	0
C	+ 61.0	- ^c	0

^aStructures optimized using BP86/6-31G*/SCRF(CH₂Cl₂). ^bRelative single-point energies from B3LYP/TZVP/SCRF(CH₂Cl₂) calculations. ^cFailed to optimize.

We probed the relative energy of each reductive coupling from compounds **A** to **B** to **C** for the mono and bis nitride-NHC insertions. The first nitride insertion (**A** \rightarrow **B**) appeared to be highly favorable with a downhill ΔE value of $-33.4 \text{ kcal.mol}^{-1}$. The second ligand coupling (**B** \rightarrow **C**) was calculated as an endothermic reaction by an uphill energy of $14.3 \text{ kcal.mol}^{-1}$ (**Figure III.23**).

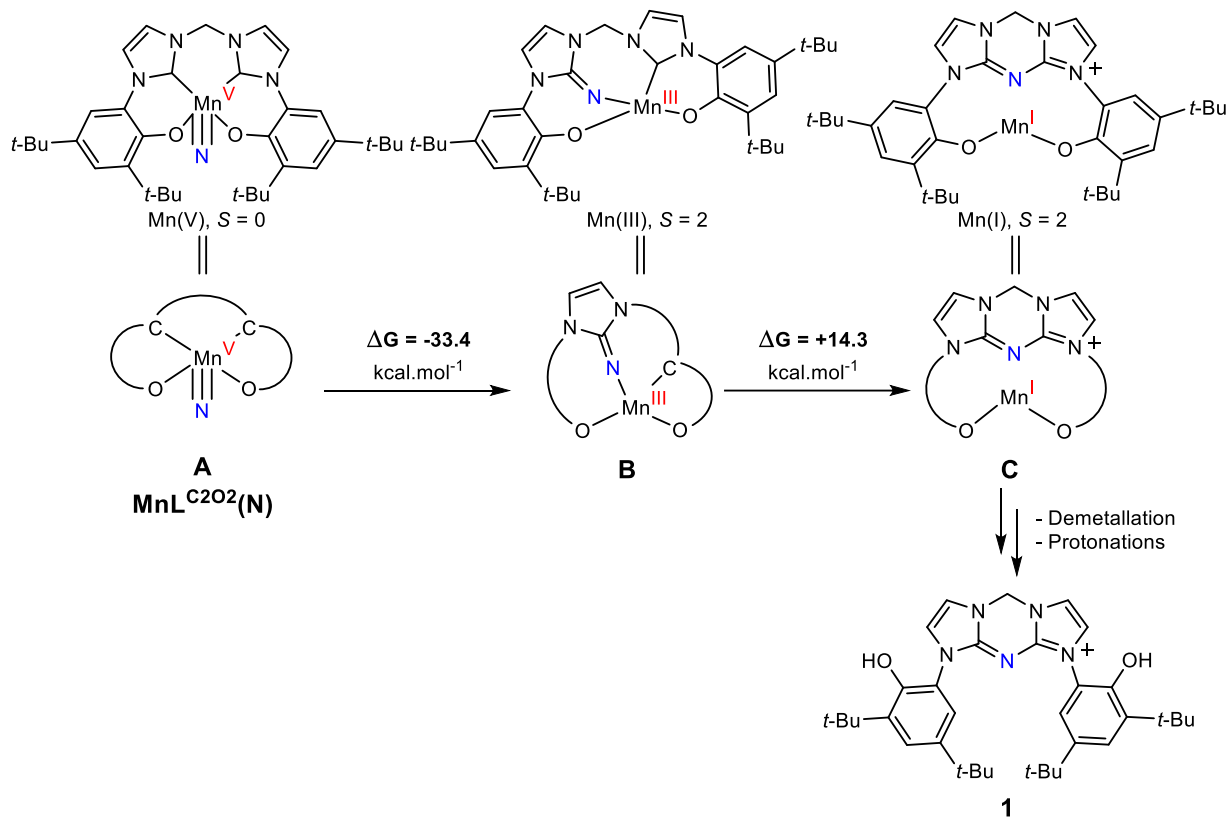


Figure III.23. Theoretical species investigated for the formation of compound **1**: transient Mn(V) nitrido (**A**), mono N-inserted Mn(III) (**B**) and bis N-inserted Mn(I) (**C**) species. Relative free energies from single-point calculations (B3LYP/TZVP/SCRF(CH_2Cl_2)).

This pathway underlines compound **B** as a potentially stable Mn(III)-guanidine intermediate in the evolution process to reach the triazonium **1**. However, we cannot yet discriminate the possibility of a concerted double reductive nitride-NHC coupling on the transient nitride to directly afford triazonium compounds (**A** \rightarrow **C**: $\Delta E = -19.1 \text{ kcal.mol}^{-1}$). The formation of either **B** or **C** N-inserted species would correlate with experimental ESI-HRMS analysis of crude nitride exchange reactions that showed the presence of a putative nitride-inserted manganese complex (**Figure III.9**: $m/z = 624.310 [\text{MnL}^{\text{C2O2}} + \text{N} + \text{H}]^+$ and **Figure III.18**: $m/z = 625.305 [\text{MnL}^{\text{C2O2}} + {}^{15}\text{N} + \text{H}]^+$). The presence of paramagnetic Mn(III) or Mn(I) complexes would also be consistent with the high magnetic susceptibility observed in crude mixtures of azide photolysis reactions. Furthermore, we could not obtain NMR signatures to show the presence of a diamagnetic Mn(V)-nitride complex.

We also calculated the protonated derivatives of the proposed **A**, **B** and **C** species relevant in the formation of triazonium **1**. We assessed the impact of the protonations to reach triazonium compounds based on their energetic analysis. Hydrochloric acid was chosen as the proton source in our calculations based on the washing procedures used to purify compound **1** (**Figure III.24**).

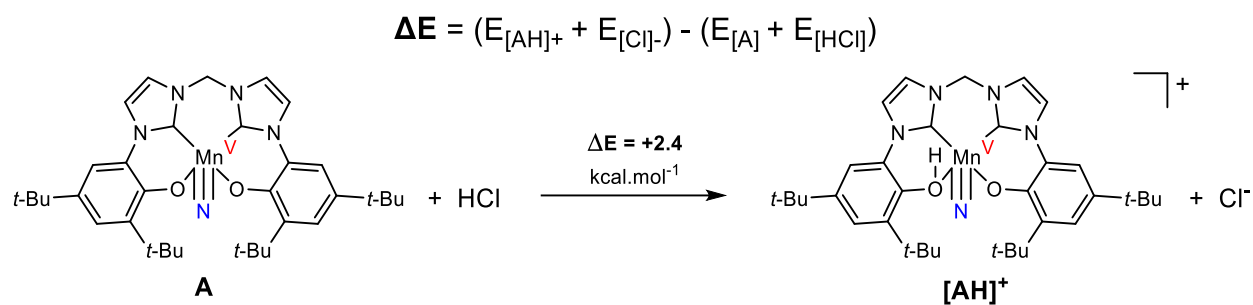


Figure III.24. Details of the energetic analysis for the protonation reactions of the manganese complexes. Structures optimized using BP86/6-31G*/SCRF(CH₂Cl₂). Relative free energies from single-point calculations (B3LYP/TZVP/SCRF(CH₂Cl₂)).

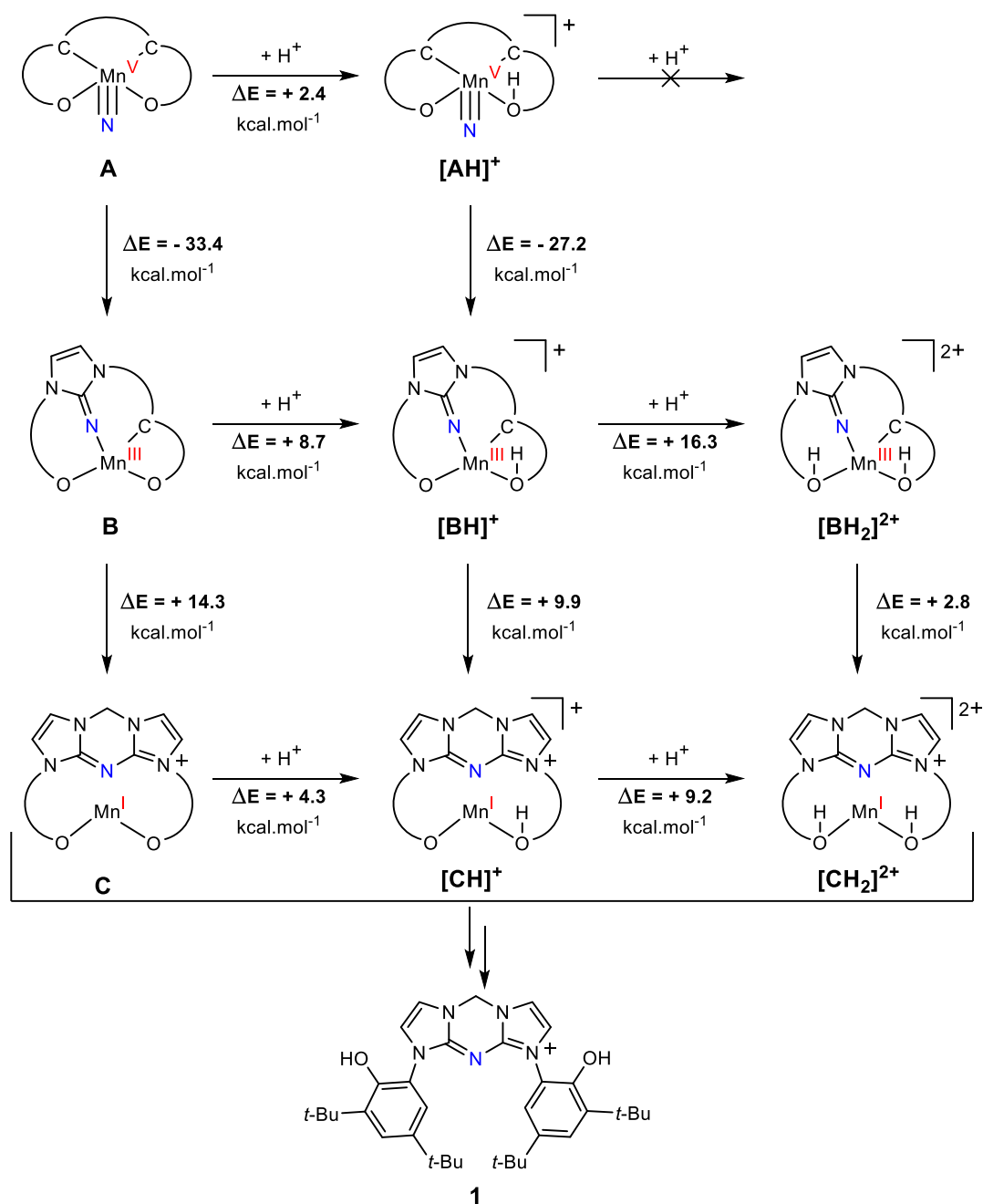


Figure III.25. Proposed reaction pathways to generate triazonium species. Computed free energy changes for reductive coupling reactions from top to bottom and protonation steps from left to right.

The different protonation and reductive coupling pathways to reach triazonium species are represented in **Figure III.25**. The results show that a more thermodynamically accessible pathway arises with the protonation of mono-inserted Mn(III) complex (**B** \rightarrow [**BH**]⁺) with an uphill energy change of 8.7 kcal.mol⁻¹ compared to the second reductive coupling reaction (**B** \rightarrow **C** : $\Delta E = + 14.3$ kcal.mol⁻¹). More extensive calculations, coupled with experimental evidence, are required to better understand the nitride insertion pathway. Specifically, investigation of the transition state of the different reductive coupling and protonation reactions would give us more complete insight into the kinetic limitations of each reaction. Nevertheless, these calculations show that compound **1** can reasonably be accessed from a transient Mn(V) nitride complex **A** by a succession of reductive nitride-NHC couplings and protonation reactions.

We also investigated the mechanism of the nitride-NHC coupling in the transient Mn(V) nitride complex **A**. Different reactions can be considered for a nitride insertion on an NHC ligand: reaction of an electrophilic nitride with a filled NHC orbital, or a nucleophilic nitride reacting with empty antibonding orbitals of the NHC ligand. Using simple bonding considerations in the putative **MnL**^{C202}(N) nitride complex **A**, we can expect different systems of interacting orbitals to be involved in the reaction (**Figure III.26**).

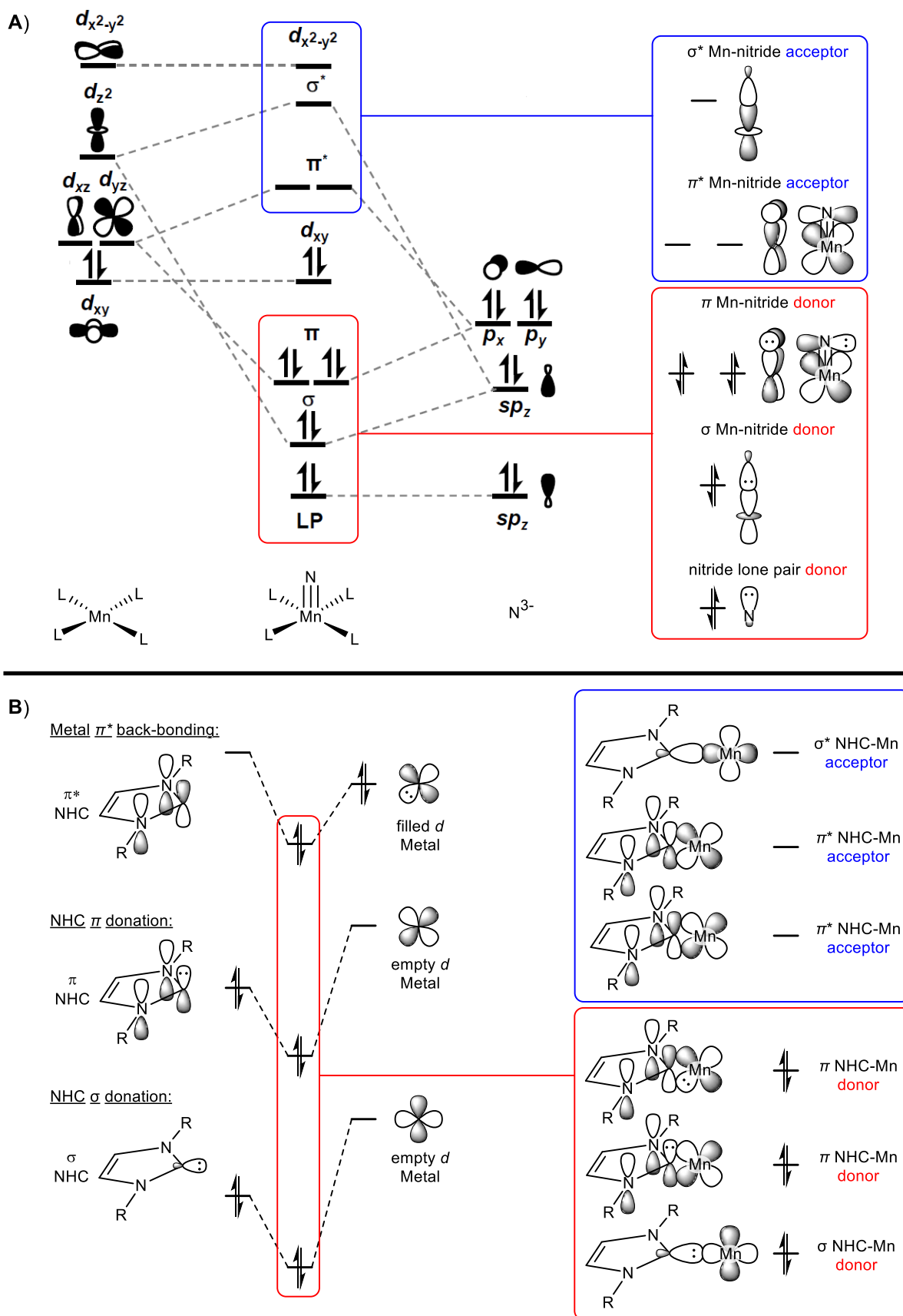


Figure III.26. Bonding considerations for a nitride insertion on an NHC ligand in a complex: partial MO diagram for a d^2 Mn(V) nitride complex in square pyramidal geometry (**A**) and orbitals involved in metal-NHC bonds (**B**). The different donating or accepting orbitals likely to interact in a nitride-NHC insertion are highlighted in red and blue, respectively.

Chapter III. Manganese complexes

Natural bond order (NBO) calculations were used to extract the orbitals to discriminate between the possible mechanisms. NBO analysis forms orthonormal sets of “maximum occupancy” orbitals using the wavefunction generated in geometry optimization calculations.^[293] This results in a Lewis-like set of orbitals and provides a means to interpret specific interactions through more traditional chemical bonding concepts.

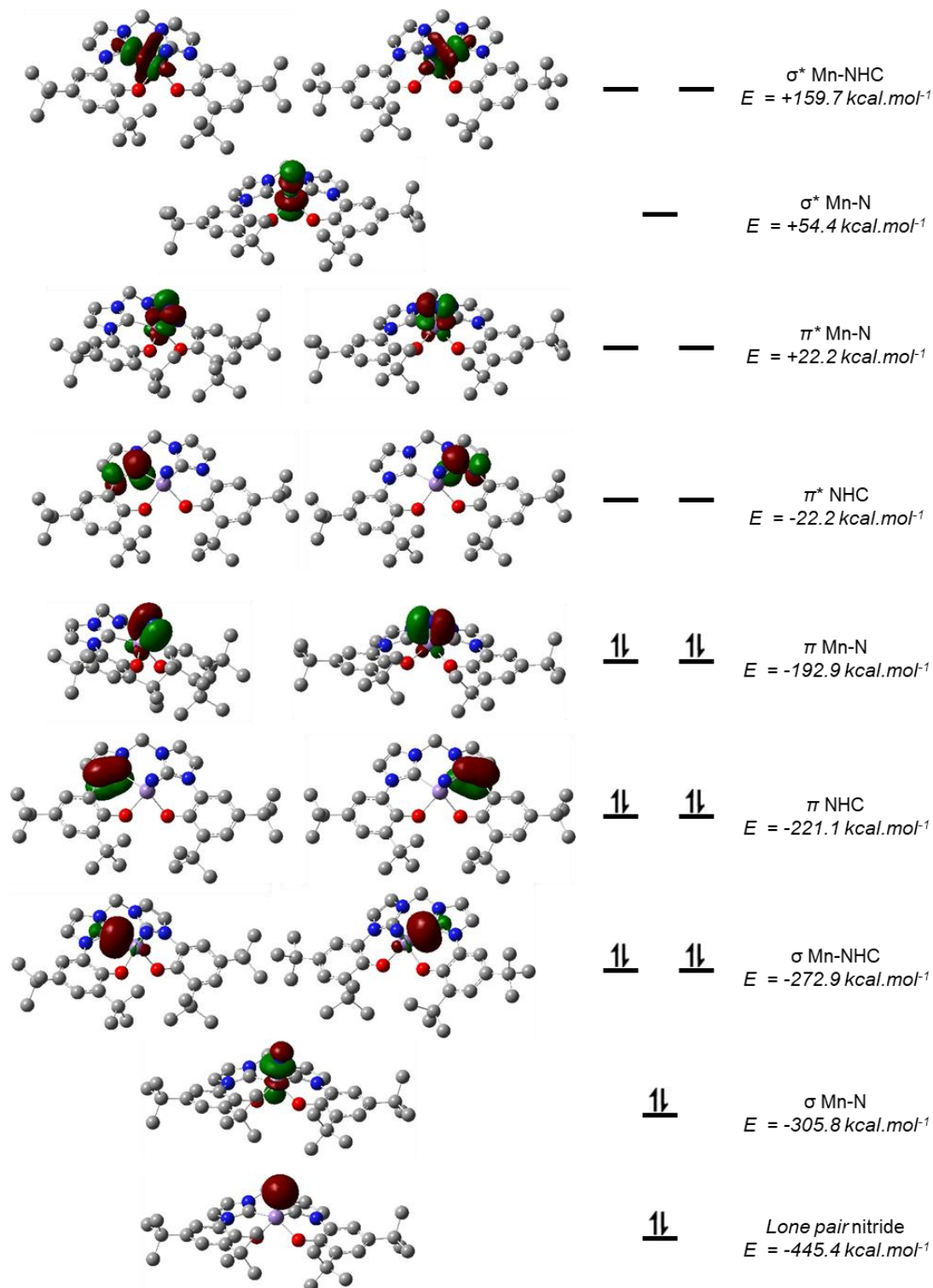


Figure III.27. Plots of the NBO orbitals examined for the nitride-NHC insertion reaction in calculated complex $\text{MnL}^{\text{C202}}(\text{N})$ (B3LYP/TZVP/SCRF(CH_2Cl_2)). The hydrogen atoms are omitted for clarity. Isoval = 0.05.

The different potential donor orbitals, from either the nitride or the NHC ligand, were extracted and are represented in **Figure III.27**. They include the nitride lone pair, the occupied Mn≡N triple bond orbitals and the σ NHC-Mn bond. The NBO depicted a π aromatic system in the NHC ligand that was also investigated. However, the calculations did not predict any π -bonding between the NHC ligand and the manganese center. In the same way, the potential unoccupied acceptor orbitals were investigated. They include the NHC π^* system, the Mn≡N π^* and σ^* orbitals and the NHC-Mn antibonding σ^* orbitals. The selected donating and accepting orbitals were further investigated with second order perturbation theory (SOPT) analysis of the NBO calculations. SOPT can be used to estimate the interaction between occupied (i) and unoccupied (j) NBO orbitals from the stabilization energy of their interaction.^[294]

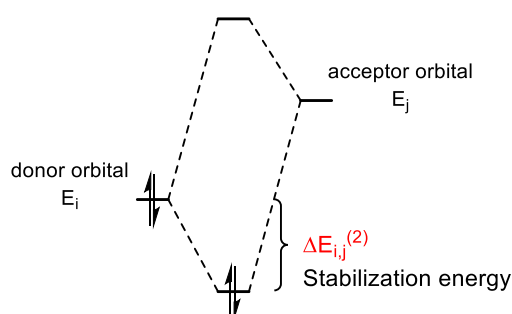


Figure III.28. Representation of the stabilizing interaction between a filled donor (i) and empty acceptor (j) orbitals in second-order perturbative analysis of NBO calculations.^[294]

The stabilizing energy, commonly referenced as $E^{(2)}$, is formulated as follows:

$$(7) \quad E^{(2)} = \Delta E_{ij}^{(2)} = q_i \frac{F_{ij}^2}{E_i - E_j}$$

where q_i is the electron occupancy of the donating orbital, E_i and E_j are the energy of the NBO donor and acceptor orbitals, respectively, and F_{ij} is the Fock matrix element between the donating and accepting orbitals. It is largely accepted that the larger the stabilizing energy, the stronger the interaction is between the donor and acceptor orbitals. The stabilization energy of the different donor-acceptor interactions for the nitride-NHC insertion are given in **Table III.4**.

Table III.4. Possible donor-acceptor interactions for the nitride-NHC insertion in the putative **MnL^{C202}(N)** complex.^a

Reactivity	Donor → Acceptor interaction	$E^{(2)}$ (kcal.mol ⁻¹)
Donating nitride → NHC acceptor	Mn≡N ^b → σ^* Mn-NHC	27.0
	Mn≡N ^b → NHC π^*	7.1
	nitride LP → σ^* Mn-NHC	3.8
	nitride LP → NHC π^*	< 0.50
Donating NHC → nitride acceptor	σ Mn-NHC → Mn≡N* ^c	12.1
	NHC π → Mn≡N* ^c	< 0.50

^aFrom DFT NBO calculations (B3LYP/TZVP/SCRF(CH₂Cl₂)). ^bSet of three donating orbitals: σ Mn-N and two π Mn=N (**Figure III.27**). ^cSet of three accepting antibonding orbitals: σ^* Mn-N and two π^* Mn=N (**Figure III.27**).

The most prevalent interaction corresponds to the donation of the $\text{Mn}\equiv\text{N}$ triple bond into the antibonding orbital of the Mn-NHC coordination bond ($E^{(2)} = 27.0 \text{ kcal.mol}^{-1}$). The opposite interaction is also observed from the bonding σ Mn-NHC orbital to the empty $\text{Mn}\equiv\text{N}^*$ antibonding system, but to a lesser extent ($E^{(2)} = 12.1 \text{ kcal.mol}^{-1}$). These results predict that the reaction of a nucleophilic nitride on an electrophilic NHC center is the most likely mechanism for the nitride-NHC insertion reaction.

This assignment is also supported by charge distribution analysis of the nitride and NHC centers of the $\text{Mn}^{\text{V}}\text{L}^{\text{C202}}(\text{N})$ complex using natural population analysis (NPA). NPA is the charge distribution analysis from the natural atomic orbitals constructed in NBO calculations. Mulliken charges are traditionally given to depict the atomic charge in theoretical calculations. However, the accuracy of Mulliken charges to depict reliable chemical phenomena has been questioned.^[293] It has notably shown to be highly sensitive to the basis set used and to be poorly suited for compounds with significant ionic character. Natural population analysis has been proposed as a more reliable and accurate description.^[295] In complex $\text{Mn}^{\text{V}}\text{L}^{\text{C202}}(\text{N})$, both Mulliken and NPA charges depict a negatively charged nitride (N1) and carbenic atoms (C7 and C17) with non-negligible positive charges (**Table III.5**).

Table III.5. Charge distribution analysis in the calculated $\text{Mn}(\text{V})\text{L}^{\text{C202}}(\text{N})$ complex.^a

Atoms ^b	NPA charges ^c	Mulliken charges ^a
Mn	+0.59	+0.97
O1	-0.67	-0.65
O2	-0.67	-0.65
C7	+0.21	+0.17
C17	+0.21	+0.17
N1	-0.19	-0.42

^aBP86/6-31G*/SCRF(CH_2Cl_2). ^bNumbering used depicted in **Figure III.22**.

^cFrom DFT NBO calculations (B3LYP/TZVP/SCRF(CH_2Cl_2)).

Overall, these theoretical calculations point towards insertion of a nucleophilic nitride on the two electrophilic NHC centers via a transient Mn(V) nitrido complex. This nucleophilic attack of the nitride is a rational first step in the decomposition of the manganese nitrido compound to afford organic compound **1** as a final product in the reaction.

This type of nucleophilic insertion on NHC ligands is known in the literature but was exclusively reported in strongly nucleophilic cobalt nitrido complexes (**Figure III.10.C,D**).^[154,235] Nitride insertion on NHC ligands in iron nitrido complexes was also reported by the Meyer group.^[296,297] However, in that case the proposed mechanism was the opposite, as a nucleophilic attack from the NHC ligand on an electrophilic nitride. They calculated that the π^* antibonding system of the $\text{Fe}\equiv\text{N}$ bond was energetically accessible and that the nitride would therefore act as an electrophile. The nucleophilic partner in the reaction was assessed to be the lone pair of the NHC ligand as is summarized in **Figure III.29**.^[297]

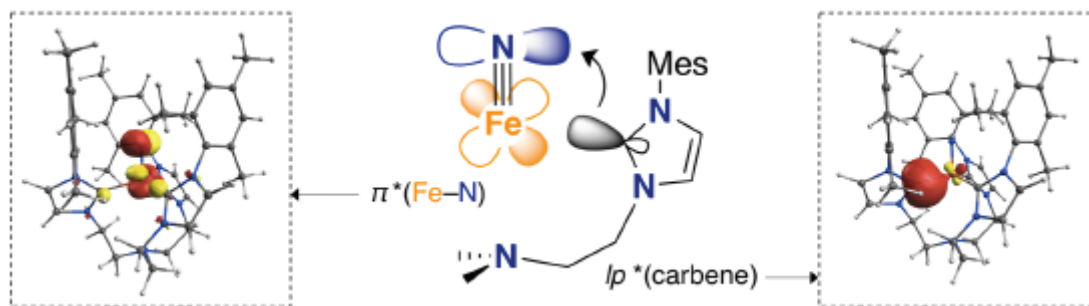


Figure III.29. Graphical representation of the relevant orbital interactions in the nitride insertion process in Iron complexes from the Meyer group.^[297]

A nitride intramolecular insertion product has recently been reported in a manganese complex. However, the insertion product was on a phosphine ligand, indicating the electrophilic character of the transient nitride.^[298] As such, our system appears to be the first mechanism of intramolecular nitride insertion that would showcase a nucleophilic nitride in a manganese complex.

1.9. *In-situ* reactivity studies

Different experimental procedures were envisioned to investigate the nucleophilic behavior of the putative transient nitride. Different procedures were tested to “trap” the transient nitride species. To be sure of the origin of the N atom in theoretical transfer reactions, our efforts focused on photolysis of the azide $\text{MnL}^{\text{C2O2}}(\text{N}_3)$ precursor, rather than nitride exchange reactions. $\text{MnL}^{\text{C2O2}}(\text{N}_3)$ was irradiated at 312 nm in presence of either styrene or trans-stilbene to probe the reactivity of the transient nitride in aziridination reactions. Unfortunately, no aziridine products could be characterized. Rather, the same intramolecular ligand insertion product **1** was observed in MS analysis of the crude mixtures in both cases. Varying concentrations of the alkene substrates were tested in an effort to favor intermolecular reactions but to no avail.

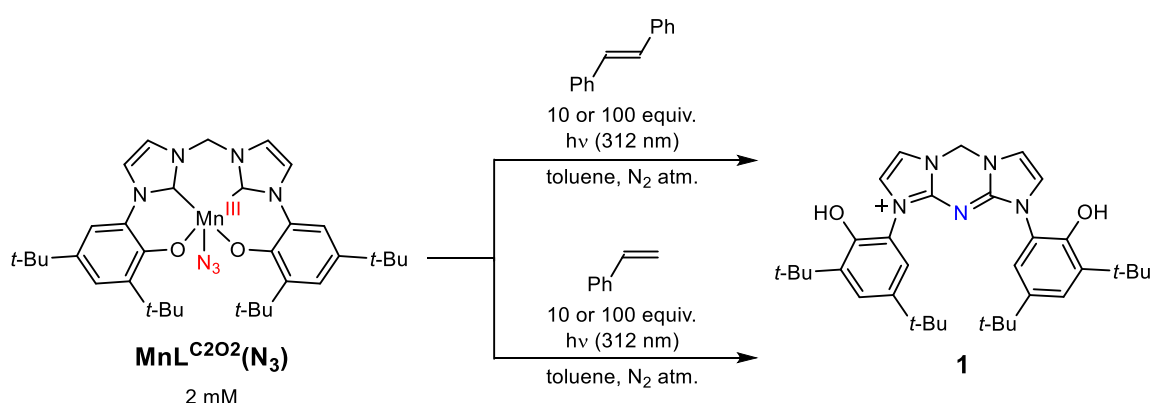


Figure III.30. Trial reactions for N-atom transfer reactivity on alkene substrates.

1.10. Conclusion

We attempted to synthesize a $\text{MnL}^{\text{C2O2}}(\text{N})$ nitride species and observed the formation of a doubly N-inserted compound **1** that presented a pattern of three fused heteroaromatic rings. Through isotopic labelling experiments and theoretical calculations, we assessed that compound **1** likely forms from the evolution of a transient $\text{MnL}^{\text{C2O2}}(\text{N})$ nitride compound. The manganese nitride complex appears to evolve through reductive nitride-NHC couplings involving a nucleophilic nitride reacting on an electrophilic NHC center. Experimental studies to scavenge the nitride intermediate with electron-poor olefin substrates were unsuccessful. Nevertheless, the reactive nature of the transient $\text{MnL}^{\text{C2O2}}(\text{N})$ nitride species underlines the long-term potential of this type of ligand system in challenging N-atom transfer reactions. A rational ligand design is required to harness the reactivity of the nucleophilic nitride towards substrates rather than intramolecular insertions. Because the nitride-NHC insertion appears to involve an electrophilic NHC center, alternative designs to increase the electron-density of the carbenic atom could be a promising path to explore. Alternative metal geometries, such as square planar complexes, could also displace the nitride moiety away from the NHC ligands to prevent intramolecular insertions, whilst enhancing the accessibility of potential exogenous substrates.

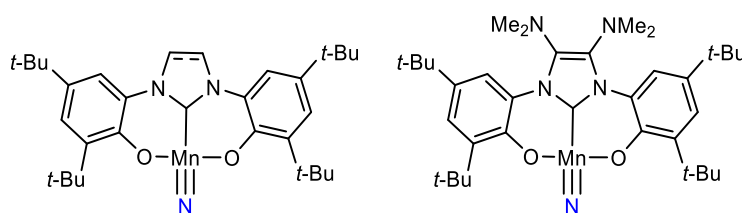
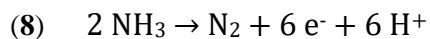


Figure III.31. Proposed manganese nitride alternative complexes utilizing NHC and phenolate ligands.

2. Preliminary investigations of electrocatalytic ammonia oxidation

2.1. Introduction

Ammonia production by the Haber-Bosch process is one of the largest industrial processes worldwide. NH_3 is used primarily as a key synthetic precursor in nitrogen-based fertilizers. More recently, its use as a carbon-free energy vector has gained a lot of interest. Liquid NH_3 can be readily distributed at modest pressures and has a 1.5 to 4 times higher energy density delivery than regular gas.^[299] To garner its energy, ammonia needs to be cleanly converted to N_2 in an ammonia oxidation (AO) reaction (**8**).



The field of AO research has attracted a growing interest in the last two decades, which is partially explained by the need to understand the mechanism of the opposite nitrogen fixation process (see Chap I.3). One of the greatest challenges to catalytically convert NH_3 to N_2 is the great thermodynamic sturdiness of its N-H bonds, with a high bond dissociation free energy ($\text{BDFE}_{\text{N-H}}$) of 99.4 kcal/mol.^[300] AO catalysts have been thoroughly studied in heterogenous systems, such as electrocatalysis^[301] and solid catalysis.^[302] On the other hand, molecular catalytic systems have only been reported recently, in 2019.^[303] The first systems were based on ruthenium catalysts and showed limited TON in both chemical oxidations and

Chapter III. Manganese complexes

electrocatalytic reactions. The Nishibayashi group optimized a system, using ammonium triflate NH_4OTf as a solid source of ammonia; the base 2,4,6-collidine was required to initiate the reaction and Magic blue was used as a chemical oxidant ($E_{1/2} = 0.67$ V vs Fc^+/Fc in acetonitrile).^[304] The catalyst reached up to 11.9 equivalents of N_2 produced per ruthenium atom of the catalysts (**Figure III.32**). On their side, the Smith group used saturated solutions of ammonia in THF solutions in bulk electrolysis experiments. They were able to form less than 2.1 N_2 molecules per equivalent of catalyst with an 86% faradaic efficiency.

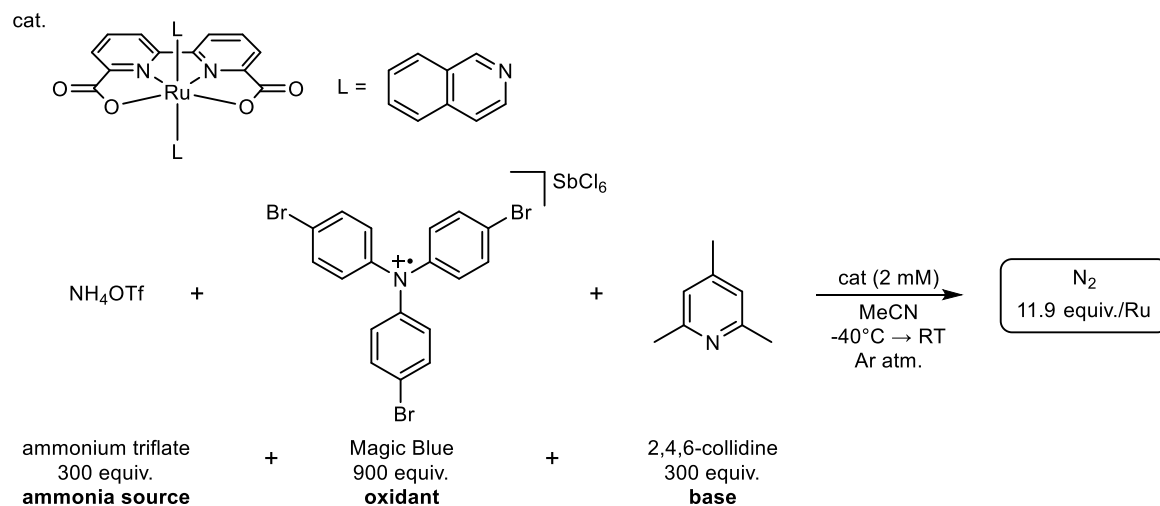


Figure III.32. Homogeneous catalytic oxidation of ammonia to nitrogen using a ruthenium catalyst as reported by Nishibayashi and coworkers.^[304]

More recently, the Peters group used a tripodal iron complex as a homogeneous electrocatalyst with ammonia acetonitrile solutions (**Figure III.33**). Ammonium triflate was used as a supporting electrolyte in the reaction and they showed that ammonia also acted as the activating base in the system. They were able to generate up to 149 equivalents of N_2 after 48 hours. While very promising, their system relied on a relatively high potential bias of +0.85 V vs the ferrocenium couple.

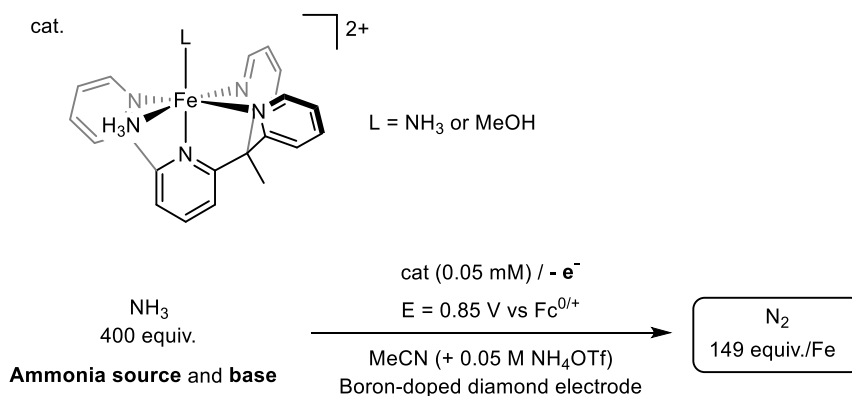


Figure III.33. Electrocatalytic oxidation of ammonia to nitrogen using an iron catalyst as reported by Peters and coworkers.^[305]

Very recently, the Nishibayashi group focused on manganese catalysts and showed that the Jacobsen complex was able to oxidize ammonia into nitrogen both chemically and electrochemically.^[306] However, the salen complex showed limited reactivity with 17 equivalents of N₂ produced by chemical oxidation and up to 6 by bulk electrolysis experiments. Similarly to the Peters group, they used a high oxidizing potential (+0.86 V vs Fc^{0/+}).

2.2. Preliminary investigation in ammonia oxidation using **MnL^{C2O2}Br**

- Attempts with ammonium triflate and 2,4,6-collidine

We conducted electrochemical preliminary experiments using the manganese(III) **MnL^{C2O2}Br** complex. We first used a system derived from the Nishibayashi reports which contained ammonium triflate and 2,4,6-collidine.

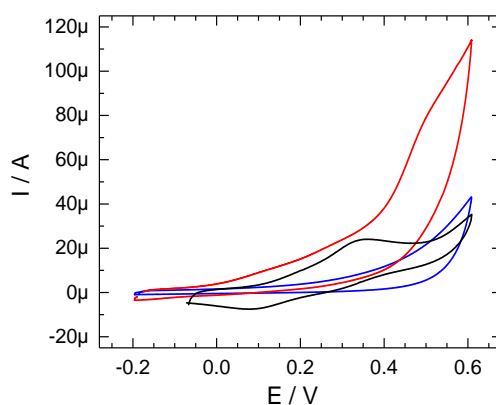


Figure III.34. CV curves of complex **MnL^{C2O2}Br** (1.0 mM) (black), NH₄OTf (0.6 M) and 2,4,6-collidine (0.6 M) (blue) and **MnL^{C2O2}Br** (1.0 mM) with NH₄OTf (0.6 M) and 2,4,6-collidine (0.6 M) (red). CH₃CN solutions containing 0.1 M [NBu₄][PF₆] as supporting electrolyte; *T* = 298 K, vitreous carbon working electrode. Potentials given versus the Fc^{+/0} reference.

In CH₃CN solutions (+0.1 M [NBu₄][PF₆]), the CV of complex **MnL^{C2O2}Br** alone displayed a broad non-reversible oxidation event at $E_p^a = 0.35$ V that was coupled with a reduction wave at $E_p^c = 0.08$ V (**Figure III.34**). This system was attributed to oxidation of the Mn(III) ion center to a Mn(IV) complex. The large potential gap between the oxidation and reduction waves ($\Delta E_p = 0.27$ V) as well as their broadness indicate an important structural reorganization of the complex upon oxidation. The oxidation wave progressively loses its intensity when cycling multiple times, underlining a likely EC coupled chemical transformation. Background oxidation of ammonia was assessed by mixing ammonium triflate and 2,4,6-collidine. When ammonium triflate, 2,4,6-collidine and **MnL^{C2O2}Br** were present simultaneously, a non-negligible increase in catalytic current was observed ($I_{cat} = 114$ μA at $E = 0.65$ V compared to 43 μA for the background oxidation without catalyst). These results suggest that the manganese complex is a potential catalyst for NH₃ oxidation.

Bulk electrolysis experiments were conducted next under argon atmosphere using a glassy carbon disk as a working electrode at an applied potential of 0.5 V vs Fc^{+/0} in CH₃CN solutions containing 0.1 M tetrabutylammonium hexafluorophosphate as supporting electrolyte. However, a rapid passivation was observed at the surface of the electrode, resulting

in a sharp drop of current (**Figure III.35**). The working carbon disk electrode was polished and cleaned before another bulk electrolysis was conducted. The activity was regained but rapid passivation was again observed, leading to a rapid current decrease.

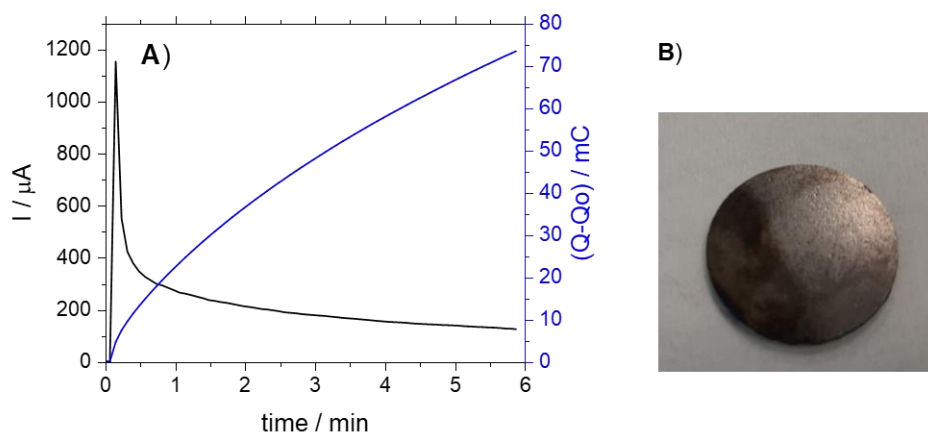


Figure III.35. Evolution of electrolysis current (black line) and coulometry (blue line) (**A**) and picture of the passivation of the carbon disk working electrode (**B**). Bulk electrolysis experiments: $\text{MnL}^{\text{C}2\text{O}2}\text{Br}$ (1 mM) with ammonium triflate (0.6 M) and 2,4,6-collidine (0.6 M) in MeCN solution containing 0.1 M $[\text{NBu}_4][\text{PF}_6]$ as supporting electrolyte; $T = 298 \text{ K}$.

A CV was recorded with a clean vitreous carbon electrode after the electrolysis was stopped. The system was controlled after stopping the electrolysis using CV experiments with clean vitreous carbon electrodes. The system did not appear to evolve and no drop in catalytic current was observed attesting to a relative stability of the manganese complex in the electrolytic medium (**Figure III.36**). However, the theoretical coulometry only reached 22% of one equivalent of $\text{MnL}^{\text{C}2\text{O}2}\text{Br}$ complex in solution.

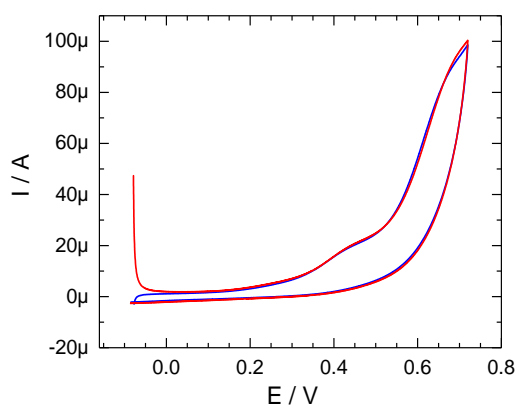


Figure III.36. CV curves of the bulk electrolysis experiments: before electrolysis (blue) and control after both bulk electrolysis (total coulometry = 107 mC) (red). $T = 298 \text{ K}$, vitreous carbon electrode. Potentials given versus the Fc^+/Fc reference.

The nature of the amorphous passivation product could not be assessed. A possible candidate would be insoluble 2,4,6-collidinium salts. The base is most likely the first recipient of the protons from the N-H bonds breaking in the ammonia molecule. The resulting protonated 2,4,6-collidine could precipitate out of solution or deposit on the electrode and dampen the electrocatalytic activity. Simple solubility tests will be conducted in the future to verify this hypothesis.

- Attempts using ammonium / ammonia solutions

We additionally investigated our Mn complex for NH_3 oxidation in ammonium / ammonia acetonitrile solutions of ammonia, derived from reports from the Peters group.^[307] Once again, the electrochemical behavior of the $\text{MnL}^{\text{C2O2}}\text{Br}$ complex was first probed using CV experiments (**Figure III.37**). The background ammonia oxidation was assessed using 50 mM NH_4OTf in 250 mM NH_3 acetonitrile solutions (diluted from saturated NH_3 in acetonitrile). Addition of the complex in the ammonia / ammonium triflate medium led to a strong increase in catalytic current once again. An additional precatalytic feature appeared when comparing to the CV experiments of the previous set-up but its nature was not investigated. Despite lower reagent concentrations, the relative increase in catalytic current proved greater than in the first system ($I_{\text{cat}} = 79 \mu\text{A}$ at $E = 0.65 \text{ V}$ compared to $15 \mu\text{A}$ for the background oxidation without complex).

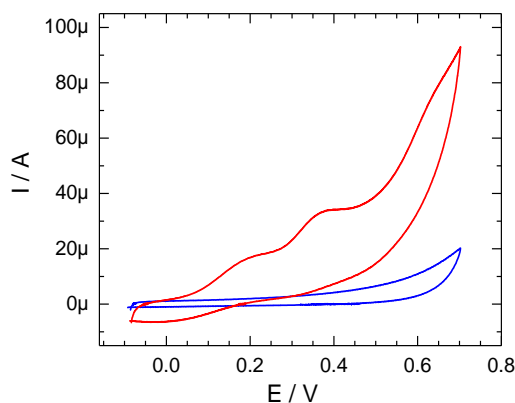


Figure III.37. CV curves of background ammonia oxidation: NH_4OTf (50 mM) and NH_3 (250 mM) (blue) and after addition of complex $\text{MnL}^{\text{C2O2}}\text{Br}$ (1.0 mM) (red). MeCN solutions containing 0.1 M $[\text{NBu}_4][\text{PF}_6]$ as supporting electrolyte; $T = 298 \text{ K}$, vitreous carbon electrode. Potentials given versus the Fc^+/Fc reference.

Bulk electrolysis experiments were again conducted at an applied potential of 0.50 V to assess the potential of this system in catalytic conditions. Passivation of the electrode was observed but the current decreased more slowly over time (**Figure III.38**). A control CV revealed a non-negligible loss of catalytic current after 338 mC was injected (70% of the theoretical coulometry for one equivalent of $\text{MnL}^{\text{C2O2}}\text{Br}$ complex in solution).

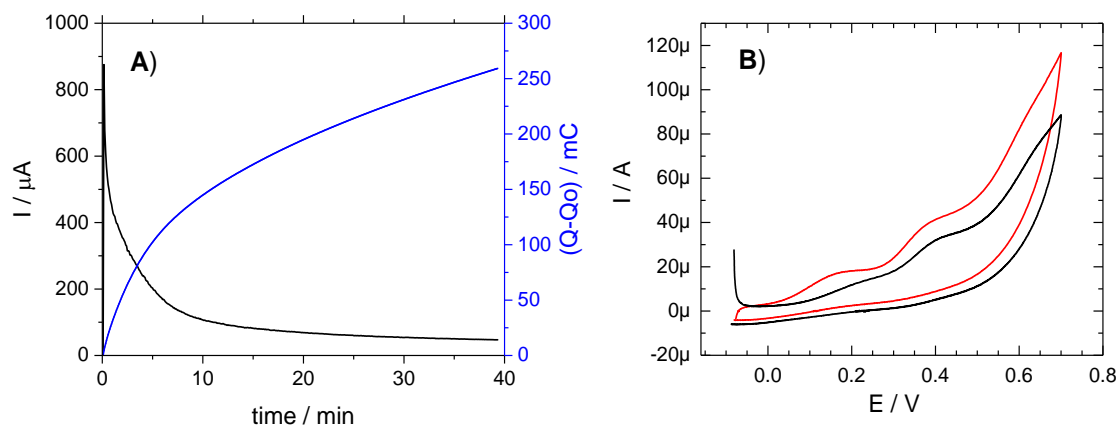


Figure III.38. Evolution of electrolysis current (black line) and coulometry (blue line) (A) and CV controls of the electrolysis: before electrolysis (red) and after 338 mC (black) (B). Bulk electrolysis experiments: $\text{MnL}^{\text{C}202}\text{Br}$ (1 mM) with ammonium triflate (50 mM) and ammonia (200 mM) in MeCN solution containing 0.1 M $[\text{NBu}_4][\text{PF}_6]$ as supporting electrolyte; carbon disk used as the working electrode. The CV controls were performed with clean vitreous carbon electrodes, Potentials given versus the Fc^+/Fc reference. $T = 298\text{ K}$.

While the passivation appeared more limited, a peculiar green deposit formed at the connection with the metal clip holding the carbon disk electrode in the electrolysis set-up (Figure III.39.A). The solution took a similar green color and X-band EPR experiments revealed a characteristic signature for a copper(II) species (Figure III.39.B). Another faint signal was superposed that was attributed to Mn(II) species.^[308] Additionally, parallel mode EPR analysis revealed a typical Mn(III) species (Figure III.40).^[308] Before electrolysis no such Mn(III) signature from the $\text{MnL}^{\text{C}202}\text{Br}$ complex could be observed, suggesting a change in the structure of the complex upon electrolysis.

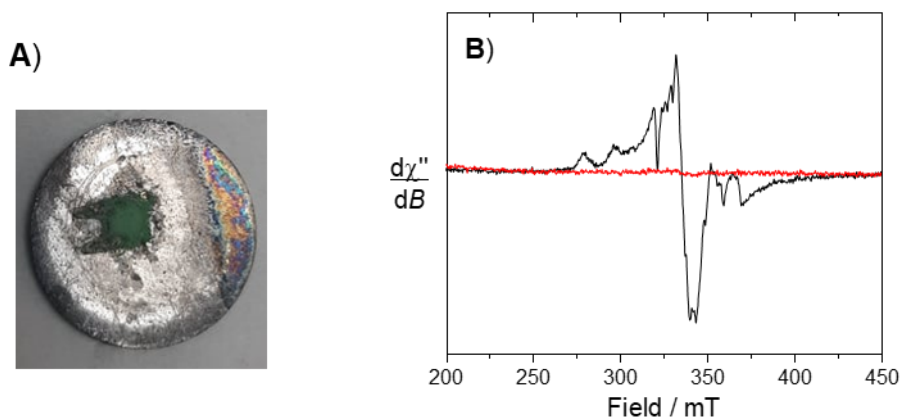


Figure III.39. Picture of the working carbon disk electrode (A) and X-Band EPR spectra of the solution before (red) and after (black) the bulk electrolysis experiment (B). Microwave frequency 9.64 GHz, power 6.5 mW; mod. frequency 100 kHz, amp. 0.5 mT; $T = 22\text{ K}$.

Overall, the EPR experiments pointed towards the green deposit being an oxidized product from the copper wire connection of the metal clip. This was rationalized from the action of gaseous ammonia escaping from solution.

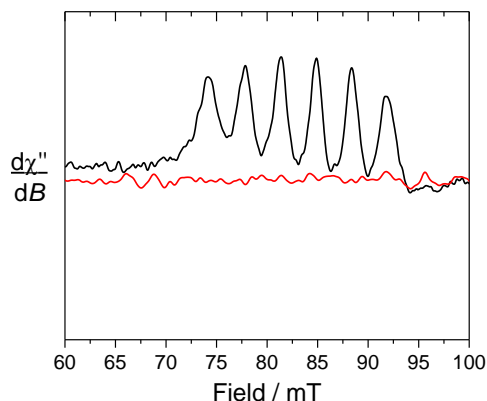


Figure III.40. Parallel mode X-Band EPR spectra of the solution before (red) and after (black) the bulk electrolysis experiment. Microwave frequency 9.39 GHz, power 21 mW; mod. frequency 100 kHz, amp. 0.5 mT; $T = 22$ K.

The rapid loss of catalytic current unfortunately shows that long bulk electrolysis experiments are not yet possible. Furthermore, the yield of oxidized NH_3 would be too low to use gas chromatography (GC) to confirm production of N_2 or side products like hydrazine derivatives.

2.3. Conclusion

Each report on homogeneous electrocatalytic ammonia oxidation has presented a different electrocatalytic medium, preventing direct comparison between each system and with our own. Still, the increase of catalytic current observed in our CV experiments appeared at considerably low potentials bias with strong intensities when pitted against the literature. This highlights the interesting potential of the $\text{MnL}^{\text{C202}}\text{Br}$ complex in electrocatalytic AO if proof of formation of N_2 can be made in future experiments. While possible, minute refinements on the electrocatalysis system would require a lot of time and resources. As such, other means will be needed to verify the putative AO catalytic activity of our $\text{MnL}^{\text{C202}}\text{Br}$ complex. Chemical oxidation reactions followed by gas chromatography (GC) analysis would offer us an alternative to unravel the AO activity of our complex. As such, they have been envisaged as the first follow-up experiments to continue on this research.

Chapter IV.

Nitridochromium complexes

1. Introduction	147
2. Synthesis and characterization of the neutral $\text{CrL}^{\text{C}2\text{O}2}(\text{N})$ complex.....	148
2.1. Synthesis of $\text{CrL}^{\text{C}2\text{O}2}(\text{N})$	148
2.2. Structure of neutral $\text{CrL}^{\text{C}2\text{O}2}(\text{N})$	148
2.3. EPR and UV-vis-NIR spectroscopy	149
2.4. Theoretical calculations on the neutral complex	151
2.5. Electrochemistry of the neutral complex	155
3. Oxidation of $\text{CrL}^{\text{C}2\text{O}2}(\text{N})$	156
3.1. One-electron oxidized $[\text{CrL}^{\text{C}2\text{O}2}(\text{N})]^+$ complex	156
3.2. Room temperature degradation products.....	162
3.2.1 Room temperature chemical oxidation	162
3.2.2 Evolution of $[\text{CrL}^{\text{C}2\text{O}2}(\text{N})]^+$ at room temperature	166
3.2.3 Electrochemical formation of $[\text{X}]^+$ at room temperature	168
3.2.4 Theoretical calculations	172
4. Conclusion.....	175

1. Introduction

The manganese complex $\text{MnL}^{\text{C}2\text{O}2}(\text{N})$ appeared to be prone to intramolecular nitride-NHC coupling reactions. Thus, we changed the metal ion in favor of a chromium center. We hypothesized that the $\text{CrL}^{\text{C}2\text{O}2}(\text{N})$ complex would be more easily isolated than its manganese analogue based on the stability generally observed for early transition metal nitride complexes (see Chap I.3.4.). As part of an exchange research program in the Thomas group, the graduate student Diego Martelino developed the initial synthesis of the $\text{CrL}^{\text{C}2\text{O}2}(\text{N})$ complex and obtained its crystallographic structure. He also conducted preliminary electrochemical and spectroscopic investigations on the neutral and one-electron oxidized complexes.

The redox properties of Cr complexes bearing redox-active phenoxyl ligands have scarcely been studied.^[309,310] Yet, the Storr group reported that the electronic structures in oxidized metal nitrido complexes had a drastic impact on their reactivity. In nitridomanganese salen complexes, high-valent Mn(VI) oxidized species showed to be highly prone to homocoupling reactivity to release an N_2 molecule.^[106] In contrast, an electron-rich complex with strongly donating NMe_2 phenolate substituents afforded a phenoxyl radical ligand upon oxidation that was remarkably stable and inert to homocoupling evolution. These results were extended towards nitridochromium salen analogues by Diego Martelino in his thesis for his Master's degree at the Simon Fraser University.^[311] He notably worked on the nucleophilic reactivity of the nitridochromium complexes with an electrophilic partner (tris(pentafluorophenyl)borane), depending on the oxidation state and the electronic structure of the complexes (**Figure IV.1**).

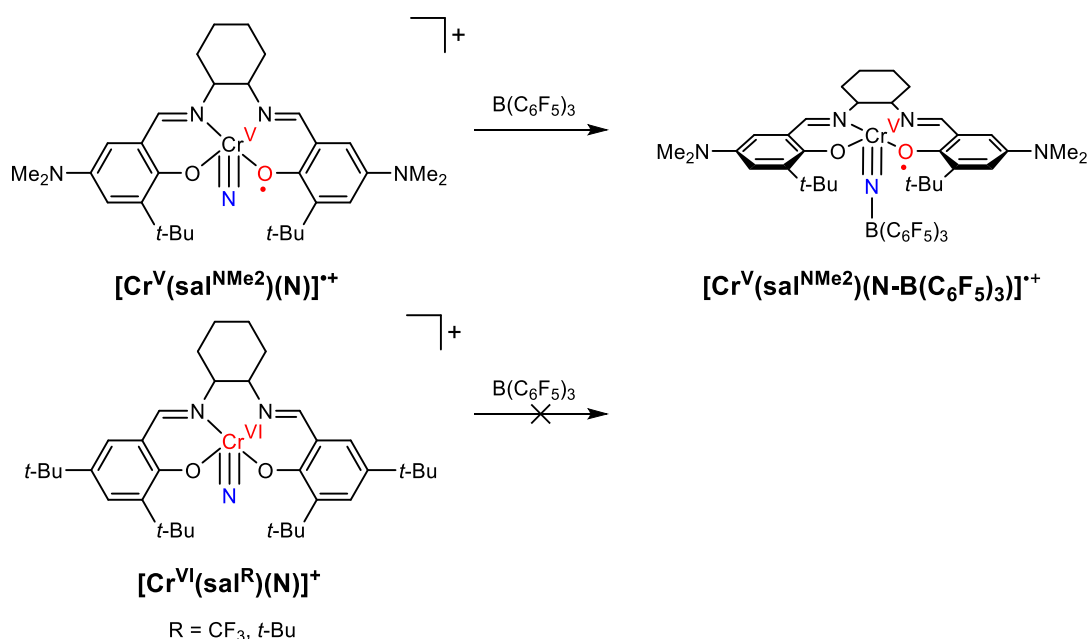


Figure IV.1. Different nucleophilic behavior of oxidized nitridochromium salen complexes depending on their electronic structure.^[311]

Thus, we developed the nitridochromium complex $\text{CrL}^{\text{C}2\text{O}2}(\text{N})$ to explore the impact of the strong electron donating properties of the $\text{L}^{\text{C}2\text{O}2}$ framework on the behavior of the nitride ligand. We also studied its electrochemical properties and explored the difference of reactivity between the transient manganese $\text{MnL}^{\text{C}2\text{O}2}(\text{N})$ complex and its Cr analogue. We finally investigated the electronic structure of the complex after oxidation and probed the nature of different oxidation products.

2. Synthesis and characterization of the neutral $\text{CrL}^{\text{C2O2}}(\text{N})$ complex

2.1. Synthesis of $\text{CrL}^{\text{C2O2}}(\text{N})$

The proligand $\text{H}_4\text{L}^{\text{C2O2}}\text{Br}_2$ was prepared following a six-step synthesis detailed in Chapter II. Complex $\text{CrL}^{\text{C2O2}}(\text{N})$ was prepared by chelation of a $[\text{Cr}(\text{N})\text{Cl}_4]^{2-}$ metal nitride complex using the $\text{H}_4\text{L}^{\text{C2O2}}\text{Br}_2$ proligand in basic medium, adapted from a procedure by Birk and Bendix.^[204]

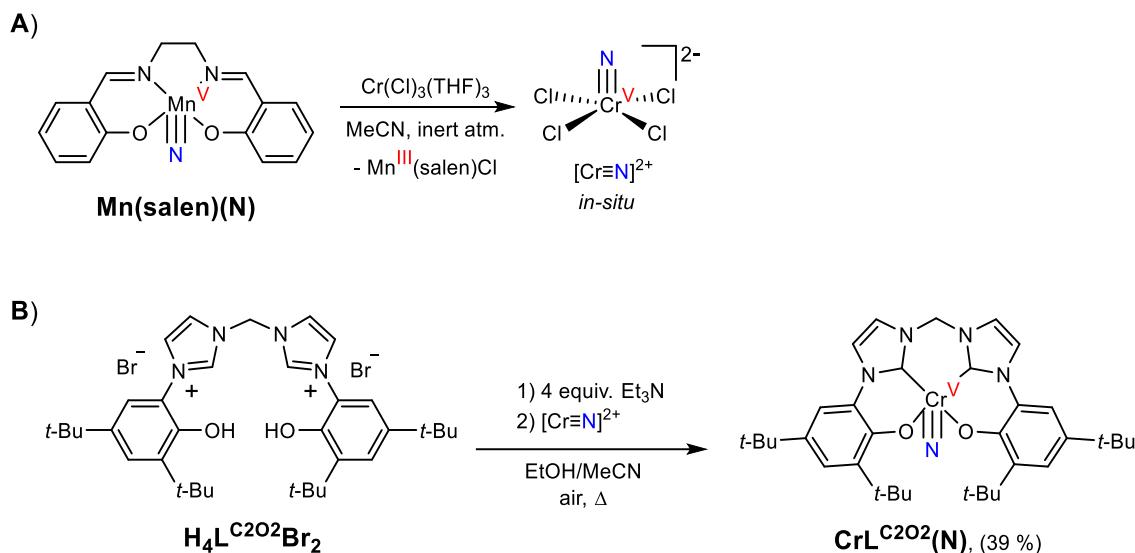


Figure IV.2. Synthesis of nitridochromium complex $\text{CrL}^{\text{C2O2}}(\text{N})$.

The $\text{Mn}(\text{salen})(\text{N})$ nitride exchange reagent used in Chapter III was added to an equimolar solution of chromium(III) chloride tetrahydrofuran complex (1:3) in dry acetonitrile under inert atmosphere in a glovebox. The Mn(III) salen side-product of the nitride exchange reaction was eliminated in the glovebox by filtration over celite to afford an acetonitrile solution of $[\text{Cr}(\text{N})\text{Cl}_4]^{2-}$ (**Figure IV.2.A**). Outside the glovebox, proligand $\text{H}_4\text{L}^{\text{C2O2}}\text{Br}_2$ was solubilized in ethanol with addition of triethylamine, resulting in a clear yellow solution. The acetonitrile solution of $[\text{Cr}(\text{N})\text{Cl}_4]^{2-}$ was added and the resulting mixture was heated under air, progressively turning bright orange. Volatiles were removed under vacuum and $\text{CrL}^{\text{C2O2}}(\text{N})$ was suspended and collected using methanol, with an overall yield of 39 % (**Figure IV.2.B**).

2.2. Structure of neutral $\text{CrL}^{\text{C2O2}}(\text{N})$.

Single crystals suitable for X-ray diffraction were obtained by slow evaporation of a dichloromethane/acetonitrile solution of $\text{CrL}^{\text{C2O2}}(\text{N})$.

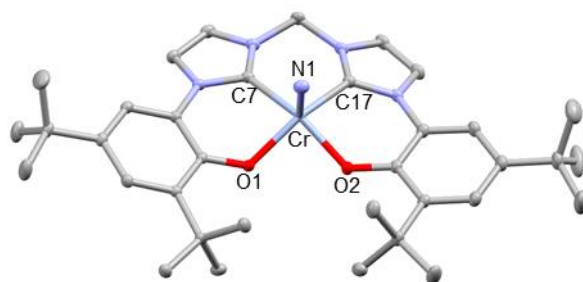


Figure IV.3. X-Ray crystal structure of $\text{CrL}^{\text{C2O2}}(\text{N})$. The hydrogen atoms are omitted for clarity.

The coordination bond distances of **CrL^{C202}(N)** are reported in **Table IV.1**. The chromium ion is in a distorted square pyramidal geometry with the chromium center coordinated by two phenolate oxygens (O1/O2) and two carbons of the NHC units (C7/C17) in equatorial positions (**Figure IV.3**). The nitrido ligand is bound in the axial position and shifts the chromium ion slightly out of the O1-O2-C17-C7 plane by ≈ 0.56 Å. This pyramidalization is slightly more pronounced than for most five-coordinate Cr(V) nitride complexes (**Table IV.2**).^[204] The short Cr-nitride (Cr-N1) bond length of 1.558 Å falls within the range of other five-coordinate Cr(V) nitride complexes previously reported (**Table IV.2**).^[217,312,313] It is indicative of the triple bond character of the chromium-nitride bond.

Table IV.1. Coordination bond distances in the neutral chromium nitride complex (Å).

complex	CrL^{C202}(N)
Cr-O1	1.935(1)
Cr-O2	1.919(1)
Cr-C7	2.058(1)
Cr-C17	2.062(1)
Cr-N1	1.558(1)

Table IV.2. Structurally characterized five-coordinate Cr(V) nitride complexes (Å).

complex	Cr-N ^a	Cr out of plane ^b (Å)	ref
CrL^{C202}(N)	1.558(1)	0.557(1)	-
[Cr(N)(salen)]	1.544(3)	0.499(3)	[314]
Cr(N)(quin) ₂	1.555(1)	0.519(1)	[204]
Cr(N)(dbm) ₂	1.549(1)	0.465(1)	[204]
Cr(N)(S ₂ CNC ₄ H ₈) ₂	1.549(1)	0.725(1)	[204]
[Cr(N)(ttp)]	1.565(6)	0.42	[264]
[Cr(N)(bpb)]	1.560(2)	0.51	[315]

^aCr-N1 for **CrL^{C202}(N)**. ^bDistance between the Cr ion and the mean equatorial plane (O1-O2-C17-C7) for **CrL^{C202}(N)**.

2.3. EPR and UV-vis-NIR spectroscopy

The electronic ground state of **CrL^{C202}(N)** was investigated by X-band EPR spectroscopy. 100 K frozen solution EPR experiments displayed an axial system indicative of a paramagnetic Cr(V) d^1 ($S = 1/2$) complex. This result confirmed that the complex was mononuclear in solution and behaved as an isolated spin system. On top of the main resonance, additional weak satellite features were observed arising from the hyperfine coupling with the ⁵³Cr isotope (9.5%, $I = 3/2$). The EPR parameters were extracted from spectra simulation and are reported in **Table IV.3**. All parameters lie in range of data previously reported for Cr(V) nitride complexes.^[204]

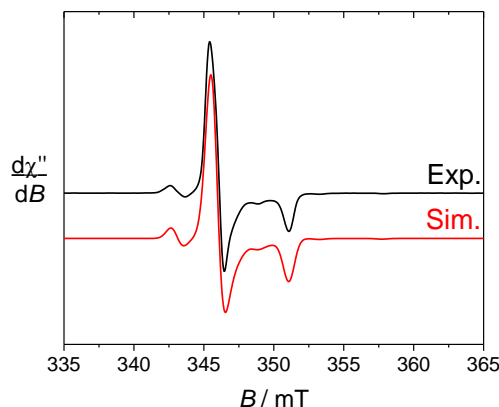


Figure IV.4. X-band EPR spectra of the neutral $\text{CrL}^{\text{C2O2}}(\text{N})$ complex in 0.5mM CH_2Cl_2 solutions (+ 0.1 M TBAP). Experimental (black) and simulated spectra (red) using parameters given in **Table IV.3**. Microwave frequency 9.42 GHz, power 1.1 mW; mod. frequency 100 kHz, amp. 0.3 mT; $T = 100$ K.

Table IV.3. Spin Hamiltonian parameters of the neutral chromium nitride complexes.^a

complex	g_{\perp}, g_{\parallel}	g_{average}	A_{\perp}, A_{\parallel} (MHz)
$\text{CrL}^{\text{C2O2}}(\text{N})$	1.991, 1.961	1.981	49, 121
$\text{Cr}(\text{sal}^{\text{R}})(\text{N})^b$	1.992, 1.950	1.978	53, 130

^aIn CH_2Cl_2 solutions containing 0.1 M TBAP. Values extracted from spectral simulations. ^bAdapted from reference [311].

The UV-vis absorption spectrum of $\text{CrL}^{\text{C2O2}}(\text{N})$ was also recorded (**Figure IV.5**). The complex displayed typical features of a d^1 Cr(V) species in square pyramidal geometry.^[315,316] An intense band is observed at high energy (30770 cm^{-1}) and was attributed to a LMCT transition. A weak transition ($\epsilon < 300 \text{ M}^{-1} \cdot \text{cm}^{-1}$) is observed at a lower energy (20880 cm^{-1}). This is consistent with a Laporte forbidden $d \rightarrow d$ transition from a non-bonding d_{xy} to the empty π^* $\text{Cr}\equiv\text{N}$ orbitals^[312] (d_{xz} or $d_{yz} \pi^*$, Chap I.3.4.2.).

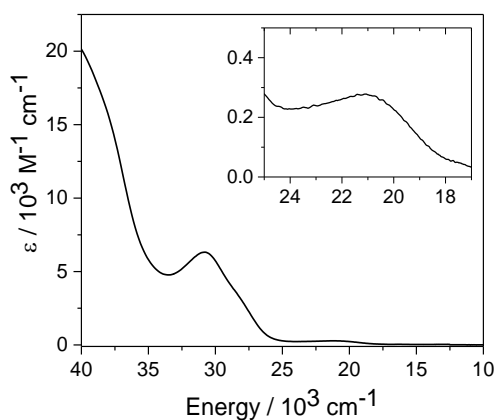


Figure IV.5. UV-vis-NIR spectra of CH_2Cl_2 solutions of $\text{CrL}^{\text{C2O2}}(\text{N})$. $T = 298$ K. The observable $d \rightarrow d$ transition is highlighted in the inset.

2.4. Theoretical calculations on the neutral complex.

- Electronic structure determination

The electronic structure of the neutral $\text{CrL}^{\text{C2O2}}(\text{N})$ complex was further investigated by DFT calculations. Different functionals were tested to obtain the best fit with the experimental crystal structure of $\text{CrL}^{\text{C2O2}}(\text{N})$. The BP86 optimized structure was the most accurate to predict the coordination sphere of the complex within 0.021 Å, with coordination bonds of 1.944 and 1.940 Å for Cr-O bonds and 2.051 and 2.055 Å for Cr-NHC bonds (**Table IV.4**). It also presented the most valid match with the experimental chromium nitride $\text{Cr}\equiv\text{N}$ bond (1.550 vs 1.558(1) in the crystal structure). The distorted square pyramidal geometry of the metal was accurately predicted, with a Cr ion out of the O1-O2-C17-C7 plane by 0.586 Å.

Table IV.4. Crystallographic and theoretical bond distances in the $\text{CrL}^{\text{C2O2}}(\text{N})$ complex (Å).

complex	$\text{CrL}^{\text{C2O2}}(\text{N})$ crystal. ^a	B3LYP theo. ^b	B3LYP-D3 theo. ^b	CAMB3LYP theo. ^b	BP86 theo. ^b	B3P86 theo. ^b
Cr-O1	1.935(1)	1.942	1.928	1.923	1.944	1.925
Cr-O2	1.919(1)	1.940	1.922	1.917	1.940	1.919
Cr-C7	2.058(1)	2.074	2.073	2.065	2.051	2.049
Cr-C17	2.062(1)	2.076	2.079	2.070	2.055	2.053
Cr-N1	1.558(1)	1.529	1.529	1.511	1.550	1.520

^aFrom X-ray crystal structure of $\text{CrL}^{\text{C2O2}}(\text{N})$.

^bFrom calculations with designated functional, 6-31G* basis set on all atoms with SCRF calculation using a dichloromethane solvent system.

The electronic ground spin-state of $\text{CrL}^{\text{C2O2}}(\text{N})$ was visualized through the SOMO of the complex and its spin density plot. The SOMO showed a predominant d_{xy} metallic nature and was non-bonding with respect to the nitride ligand (**Figure IV.6.A**). The spin density plot predicted significant spin localization on the Cr center (*i.e.* 1.13) and a degree of negative spin on the nitride (*i.e.* -0.20). The nitride spin density can be rationalized by considering the contribution of a nitridyl radical $\text{Cr}(\text{IV})=\text{N}\cdot$ ($S_{\text{N}} = 1/2$) resonance form to the $\text{Cr}(\text{V})\equiv\text{N}$ bond.^[291]

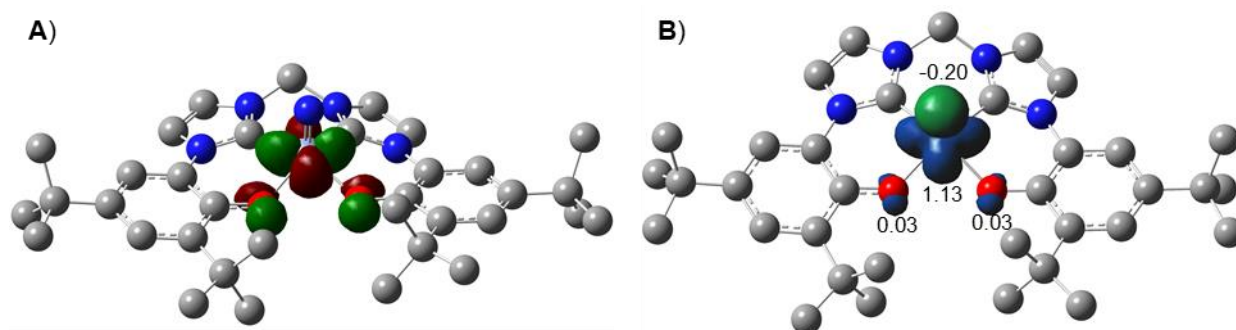


Figure IV.6. Theoretical analysis of the electronic structure of the neutral $\text{CrL}^{\text{C2O2}}(\text{N})$ complex: SOMO d_{xy} orbital (A) and spin density plot (including the main Mulliken spin populations) (B). From BP86/6-31g*/SCRF(CH_2Cl_2) calculations, isoval = 0.05 and 0.005, respectively. The hydrogen atoms are omitted for clarity.

- Reactivity differences between $\text{CrL}^{\text{C2O2}}(\text{N})$ and the transient $\text{MnL}^{\text{C2O2}}(\text{N})$ complex

The chromium complex $\text{CrL}^{\text{C2O2}}(\text{N})$ was prepared and characterized while its manganese analogue $\text{MnL}^{\text{C2O2}}(\text{N})$ was never isolated. $\text{MnL}^{\text{C2O2}}(\text{N})$ appeared to be a transient complex that readily reacted through intramolecular reductive couplings of the nitride with the NHC ligand backbone (see Chapter III). Thus, we used theoretical calculations to investigate the difference of reactivity between the chromium and manganese species.

In Chapter III, we calculated different intermediates in reductive nitride-NHC coupling reactions, starting from a Mn(V) nitride complex (**A**) to mono N-inserted Mn(III) (**B**) and bis N-inserted Mn(I) (**C**) proposed species (**Figure IV.7**, left). Hence, we calculated chromium analogues (**A'**, **B'** and **C'** respectively) and compared their energetic accessibility in nitride-NHC reductive coupling reactions (**Figure IV.7**, right). For the sake of consistency with the energetic analysis of the manganese species (Chap III.1.8.), we chose the B3LYP functional for single-point energy calculations (6-31G* basis set, CH_2Cl_2 solvent model).

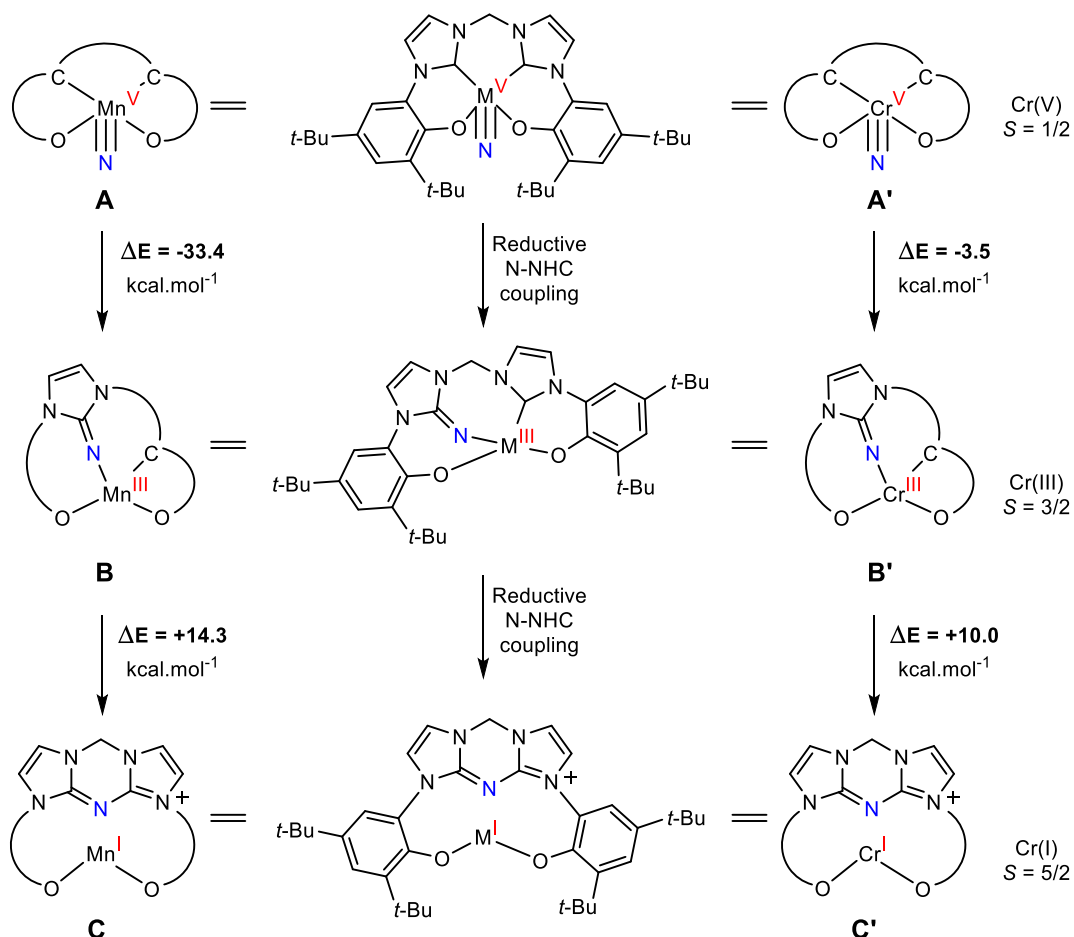


Figure IV.7. Energetic analysis of the nitride-NHC insertion in manganese (left) and chromium complexes (right). Relative free energies from single-point calculations (B3LYP/TZVP/SCRF(CH_2Cl_2)). The spin state of each theoretical species was investigated and lowest-energy state is represented.

The first nitride insertion was significantly less favored for the chromium complex, with a ΔE value of $-3.5 \text{ kcal.mol}^{-1}$ ($\text{A}' \rightarrow \text{B}'$) when compared to the reaction of the manganese species ($\text{A} \rightarrow \text{B}$: $\Delta E = -33.4 \text{ kcal.mol}^{-1}$). In the chromium complexes, the complete bis N-insertion

reaction was also unfavored by 6.5 kcal.mol⁻¹ (**A'** → **C'**) when it was calculated to be exothermic overall for the manganese species (**A** → **C** : $\Delta E = -20.7$ kcal.mol⁻¹). These results predict a clearly distinct behavior between the complexes of the two different metals and correlate with the general stability observed experimentally for **CrL**^{C2O2}(**N**) when **MnL**^{C2O2}(**N**) could not be isolated.

In the putative complex **MnL**^{C2O2}(**N**), the nitride insertion mechanism was investigated through second-order perturbation theory (SOPT) in NBO calculations. We analyzed the stabilizing energy $E^{(2)}$ between different donating (filled) and accepting (empty) orbitals involved in Mn-nitride and Mn-NHC bonds in **MnL**^{C2O2}(**N**). A significant interaction between the two donating π Mn-N orbitals and the empty σ^* Mn-NHC orbital was predicted. Thus, we concluded that the nitride insertion likely involved a nucleophilic nitride moiety reacting with electrophilic NHC centers (see Chapter III).

We conducted the same SOPT analysis on the chromium nitride complex (**CrL**^{C2O2}(**N**), **A'**) to further probe the difference in reactivity with the transient manganese complex (**MnL**^{C2O2}(**N**), **A**). The results are summarized in **Table IV.5**.

Table IV.5. SOPT analysis for nitride insertion reactivity in **MnL**^{C2O2}(**N**) and **CrL**^{C2O2}(**N**) complexes.^a

Reactivity	Donor → Acceptor interaction	$E^{(2)}$ (kcal.mol ⁻¹)	
		MnL ^{C2O2} (N)	CrL ^{C2O2} (N)
Donating nitride → NHC acceptor	$M\equiv N^b \rightarrow \sigma^* M-NHC$	27.0	15.3
	$M\equiv N^b \rightarrow NHC \pi^*$	7.1	5.8
	nitride LP → $\sigma^* M-NHC$	3.8	2.0
	nitride LP → $NHC \pi^*$	< 0.50	< 0.50
Donating NHC → nitride acceptor	$\sigma M-NHC \rightarrow M\equiv N^{*c}$	12.1	7.6
	$NHC \pi \rightarrow M\equiv N^{*c}$	< 0.50	< 0.50

^aFrom DFT NBO calculations (B3LYP/6-31G*/SCRF). M = Mn: **MnL**^{C2O2}(**N**), M = Cr: **CrL**^{C2O2}(**N**).

^bSet of three donating orbitals: σ M-N and two π M=N. ^cSet of three accepting antibonding orbitals: σ^* M-N and two π^* M=N.

In both complexes, the most prevalent interaction corresponded to the donation of the metal-nitride triple bond into the antibonding orbital of the metal-NHC coordination bond. However, the stabilizing energy $E^{(2)}$ was significantly lower in the chromium species, with 15.3 kcal.mol⁻¹ compared to 27.0 kcal.mol⁻¹ in the manganese compound. Furthermore, other donating-accepting interactions were all decreased in **CrL**^{C2O2}(**N**) when compared to **MnL**^{C2O2}(**N**). These results show an overall weaker nitride-NHC interaction in **CrL**^{C2O2}(**N**), which can explain its inertness towards nitride-NHC insertions.

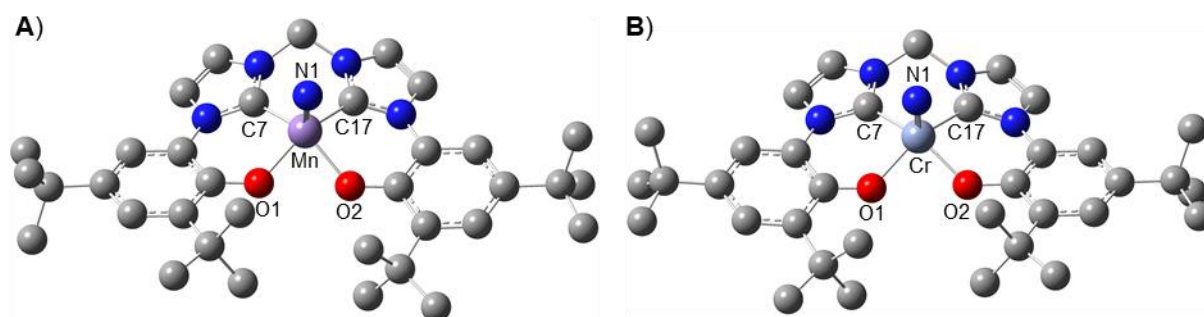
- Structural comparison between Mn and Cr complexes

Figure IV.8. Optimized theoretical structures of the metal nitride complexes: $\text{MnL}^{\text{C2O2}}(\text{N})$ ($S = 0$) (A) and $\text{CrL}^{\text{C2O2}}(\text{N})$ ($S = 1/2$) (B) with the numbering used in **Table IV.6**. The hydrogen atoms are not depicted for clarity. BP86/6-31G*/SCRF(CH_2Cl_2) optimization calculations.

We compared the calculated structures of $\text{MnL}^{\text{C2O2}}(\text{N})$ and $\text{CrL}^{\text{C2O2}}(\text{N})$ to rationalize the differences observed between the two complexes (**Figure IV.8**). The results are summarized in **Table IV.6**. With the BP86 functional, both complexes presented a distorted square pyramidal geometry with an axially-bound nitride ligand. However, $\text{MnL}^{\text{C2O2}}(\text{N})$ presented a less distorted pyramidal geometry with a metallic ion 0.548 Å out of the equatorial plane (0.586 Å in $\text{CrL}^{\text{C2O2}}(\text{N})$). The metal-nitride bond length was also shorter by 0.025 Å in the manganese complex (1.525 Å compared to 1.550 Å in the chromium analogue). These two different structural features have been shown experimentally when comparing chromium and manganese nitride salen complexes.^[248,311] Finally, $\text{MnL}^{\text{C2O2}}(\text{N})$ was calculated to have significantly shorter metal-NHC bonds, with Mn-C7 and Mn-C17 of 1.956 and 1.958 Å, respectively (Cr-C7 and Cr-C17 of 2.051 and 2.055 Å in $\text{CrL}^{\text{C2O2}}(\text{N})$).

Table IV.6. Structural analysis of the optimized structures of $\text{MnL}^{\text{C2O2}}(\text{N})$ and $\text{CrL}^{\text{C2O2}}(\text{N})$ (Å).^{a,b}

complex	$\text{MnL}^{\text{C2O2}}(\text{N})$	$\text{CrL}^{\text{C2O2}}(\text{N})$
M-O1	1.950	1.944
M-O2	1.951	1.940
M-C7	1.956	2.051
M-C17	1.958	2.055
M-N1	1.525	1.550
M out of plane (Å) ^c	0.548	0.586
N1-C7	2.727	2.794
N1-C17	2.674	2.859

^aBP86/6-31g*/SCRF(CH_2Cl_2). M = Mn: $\text{MnL}^{\text{C2O2}}(\text{N})$, M = Cr: $\text{CrL}^{\text{C2O2}}(\text{N})$.

^cDistance between the metal center and the mean equatorial plane O1-O2-C17-C7.

These structural differences result in a closer proximity between the nitride and the NHC carbenic centers in the manganese complex, with nitride-NHC distances of 2.674 and 2.727 Å, compared to 2.794 and 2.859 Å in the chromium complex. The shorter nitride-NHC distances in $\text{MnL}^{\text{C2O2}}(\text{N})$ can at least partially explain the stronger nitride-NHC interactions discussed

previously in SOPT NBO calculations. These results also correlate with the instability of the $\text{MnL}^{\text{C2O2}}(\text{N})$ complex and the relative inertness of its chromium analogue.

2.5. Electrochemistry of the neutral complex.

The electronic properties of $\text{CrL}^{\text{C2O2}}(\text{N})$ were investigated by cyclic voltammetry (**Figure IV.9**) and the electrochemical data are reported in **Table IV.12**. The complex displayed a reversible oxidation wave at a low potential ($E_{1/2} = 0.15$ V vs Fc^+/Fc). The redox process was confirmed to be monoelectronic according to rotating-disk electrode voltammetry and coulometric analysis during bulk electrolysis experiments. Analysis of the scan-rate dependence of the oxidation does not suggest a coupled chemical reaction and the oxidized species appeared to be stable on the CV time-scale.

The oxidation potential of $\text{CrL}^{\text{C2O2}}(\text{N})$ is significantly lower than the Cr(V) salen nitride complex $\text{Cr}(\text{sal}^{\text{tBu}})(\text{N})$ ($E_{1/2} = 0.61$ V vs Fc^+/Fc).^[311] This highlights once again the strong electron-donating properties of the L^{C2O2} ligand.

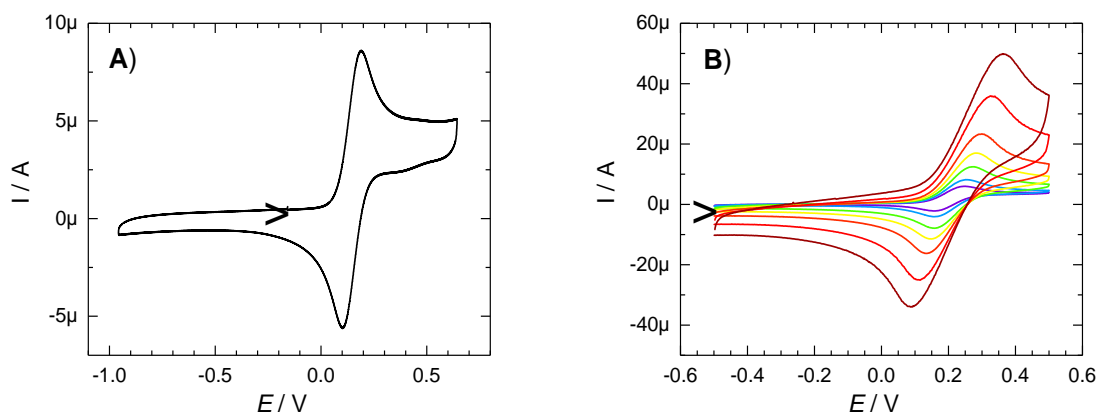


Figure IV.9. CV curve 0.5 mM $\text{CrL}^{\text{C2O2}}(\text{N})$ in a CH_2Cl_2 solution (**A**) and scan-rate dependence of the oxidation wave. Conditions: 1 mM $\text{CrL}^{\text{C2O2}}(\text{N})$, from 10 $\text{mV}\cdot\text{s}^{-1}$ (purple) to 1000 $\text{mV}\cdot\text{s}^{-1}$ (brown) (**B**). Supporting electrolyte = 0.1 M TBAP, $T = 298$ K, vitreous carbon working electrode. Potentials given versus the Fc^+/Fc reference.

The electron-rich chromium $\text{Cr}(\text{sal}^{\text{NMe2}})(\text{N})$ nitride complex have shown two close one-electron oxidation waves ($\Delta E_{1/2} = 0.16$ V) that were attributed to successive formations of phenoxyl radicals. This electrochemical behavior was also reported for the manganese analogue $\text{Mn}(\text{sal}^{\text{NMe2}})(\text{N})$.^[106] In the case of less electron-rich salen complexes $\text{Cr}(\text{sal}^{\text{CF3}})(\text{N})$ and $\text{Cr}(\text{sal}^{\text{tBu}})(\text{N})$, only one mono-oxidation process was observed and was assigned to metal-centered oxidations to reach Cr(VI) species, $[\text{Cr}^{\text{VI}}(\text{sal}^{\text{CF3}})(\text{N})]^+$ and $[\text{Cr}^{\text{VI}}(\text{sal}^{\text{tBu}})(\text{N})]^+$ respectively.^[311] This was also the case for the $\text{Mn}(\text{sal}^{\text{CF3}})(\text{N})$ and $\text{Mn}(\text{sal}^{\text{tBu}})(\text{N})$ manganese species.^[106]

$\text{CrL}^{\text{C2O2}}(\text{N})$ displayed a comparable CV with only one mono-oxidation process. Scans to potentials over 1.0 V vs Fc^+/Fc were irreversible and showed a degradation of the complex. This likely suggests that the redox event is a metal-centered oxidation to afford a $[\text{Cr}^{\text{VI}}\text{L}^{\text{C2O2}}(\text{N})]^+$ cation, rather than a ligand-centered oxidation. A metal-centered oxidation is also consistent with the metallic d_{xy} SOMO previously detailed for $\text{CrL}^{\text{C2O2}}(\text{N})$ in theoretical calculations (see section 2.4.).

3. Oxidation of $\text{CrL}^{\text{C}2\text{O}2}(\text{N})$

3.1. One-electron oxidized $[\text{CrL}^{\text{C}2\text{O}2}(\text{N})]^+$ complex

- UV-vis-NIR

The oxidation of $\text{CrL}^{\text{C}2\text{O}2}(\text{N})$ was first conducted at low temperature using a chemical oxidant and was monitored via UV-vis-NIR spectroscopy to obtain the spectroscopic signature of the cation. Titration experiments were conducted at 235 K following a procedure developed in the Storr group using tris(2,4-dibromophenyl)aminium hexafluoroantimonate (Magic Green: $[\text{N}(\text{C}_6\text{H}_3\text{Br}_2)_3]^+[\text{SbF}_6]^-$) as a chemical oxidant in a dichloromethane solution ($E_{1/2} = 1.1$ V vs Fc^+/Fc).^[317] The low-temperature oxidation of $\text{CrL}^{\text{C}2\text{O}2}(\text{N})$ is shown in **Figure IV.10**, where the complex was titrated with a saturated solution of oxidant until 1 equivalent was added.

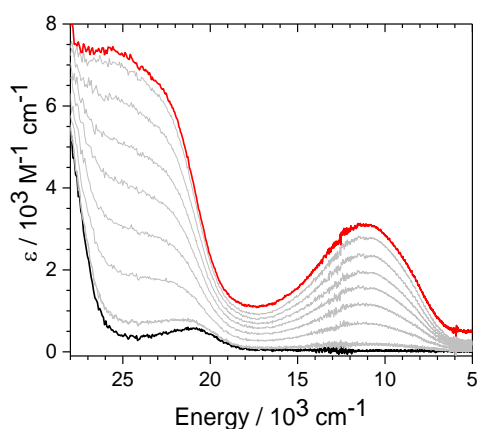


Figure IV.10. UV-vis-NIR signature of the chemical oxidation of $\text{CrL}^{\text{C}2\text{O}2}(\text{N})$ (0.45 mM) using $([\text{N}(\text{C}_6\text{H}_3\text{Br}_2)_3]^+[\text{SbF}_6]^-)$ in CH_2Cl_2 . Black: neutral, red: oxidized. Intermediate grey lines correspond to increasing aliquots of oxidant until 1 equivalent was reached. $T = 235$ K, inert N_2 atmosphere.

The oxidized complex displayed a low-energy NIR transition at $11\,160\text{ cm}^{-1}$ ($\epsilon = 3090\text{ M}^{-1}\cdot\text{cm}^{-1}$). This spectral signature is akin with metal-centered oxidations observed in nitridoCr(VI) and nitridoMn(VI) salen complexes (**Table IV.7**).^[291] In cations $[\text{Cr}^{\text{VI}}(\text{sal}^{\text{tBu}})(\text{N})]^+$ and $[\text{Cr}^{\text{VI}}(\text{sal}^{\text{CF}_3})(\text{N})]^+$ (**Figure IV.11.B**), similar transitions were assigned to a ligand-to-metal charge transfer (LMCT) excitation into the unoccupied d_{xy} orbital of a chromium(VI) ion.^[311]

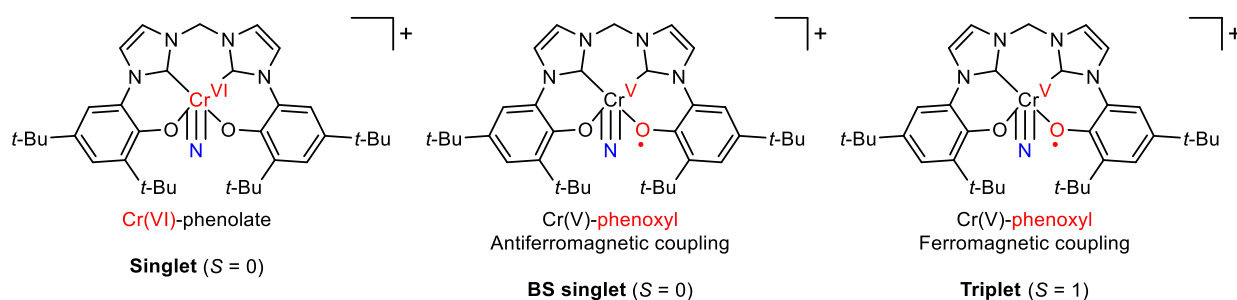
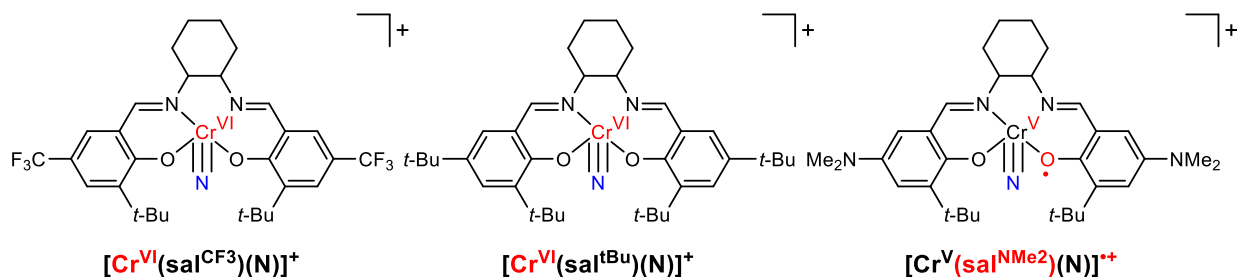
A) $[\text{CrL}^{\text{C}2\text{O}2}(\text{N})]^+$ B) $[\text{Cr}(\text{sal}^{\text{R}})(\text{N})]^+$ 

Figure IV.11. Possible electronic structures for the $[\text{CrL}^{\text{C}2\text{O}2}(\text{N})]^+$ cation (A) and relevant oxidized nitridochromium salen complexes (B).^[311]

Table IV.7. UV-vis-NIR data of the relevant chromium complexes.^a

complex	λ_{max} [cm^{-1}] (ϵ [$\text{M}^{-1} \cdot \text{cm}^{-1}$])
$\text{CrL}^{\text{C}2\text{O}2}(\text{N})$	30770 (6310), 27900 (2900, sh), 20880 (270)
$[\text{CrL}^{\text{C}2\text{O}2}(\text{N})]^{+b}$	23300 (6700, sh), 11100 (3110)
$[\text{Cr}^{\text{VI}}(\text{sal}^{\text{CF}_3})(\text{N})]^{+c}$	23000 (5800), 11000 (2200)
$[\text{Cr}^{\text{VI}}(\text{sal}^{\text{tBu}})(\text{N})]^{+c}$	21900 (5000), 8100 (4150)
$[\text{Cr}^{\text{V}}(\text{sal}^{\text{NMe}_2})(\text{N})]^{++c}$	21300 (6800), 18800 (6800), 11500 (1000)

^aIn CH_2Cl_2 solutions. br: broad; sh: shoulder

^bChemically generated in a CH_2Cl_2 solution using oxidant $([\text{N}(\text{C}_6\text{H}_3\text{Br}_2)_3]^{++}[\text{SbF}_6]^-)$ at $T = 235$ K.

^cAs reported in reference ^[311]. Conditions: Chemically generated in a CH_2Cl_2 solution using oxidant $([\text{N}(\text{C}_6\text{H}_3\text{Br}_2)_3]^{++}[\text{SbF}_6]^-)$ at $T = 233$ K.

As we have seen before in Chapter I and II, low-energy transitions can also arise in class II or class III delocalized mixed-valent systems with phenoxyl radicals. Band-shape analysis of the prominent NIR band in $[\text{CrL}^{\text{C}2\text{O}2}(\text{N})]^+$ does meet the criteria for a borderline class II/III mixed-valent system, with a relatively high $2H_{\text{AB}}/\lambda$ ratio of 0.67. This result shows that a Cr(V) complex with a partially localized phenoxyl radical remains a rational electronic structure for the $[\text{CrL}^{\text{C}2\text{O}2}(\text{N})]^+$ cation.

Table IV.8. Marcus-Hush band shape analysis of the prominent NIR transition in $[\text{CrL}^{\text{C}202}(\text{N})]^+$.

complex ^a	$\lambda = \nu_{\text{max}}$ [cm ⁻¹]	ϵ_{max} [M ⁻¹ .cm ⁻¹]	calcd. $\Delta\nu_{1/2}$ ^b [cm ⁻¹]	exp $\Delta\nu_{1/2}$ [cm ⁻¹]	H_{AB} ^c [cm ⁻¹]	$2H_{\text{AB}}/\lambda$
$[\text{CrL}^{\text{C}202}(\text{N})]^+$	11100	3110	5100	6900	3750	0.67

^aChemically generated in a CH_2Cl_2 solution using oxidant $([\text{N}(\text{C}_6\text{H}_3\text{Br}_2)_3]^+[\text{SbF}_6]^-)$ at $T = 235$ K.

^bAccording to $\text{calcd. } \Delta\nu_{1/2} = \sqrt{16 \ln 2 RT \nu_{\text{max}}} = \sqrt{2310 \nu_{\text{max}}}$

^cAccording to $H_{\text{AB}} = 2.06 \times 10^{-2} \times \frac{\sqrt{\epsilon_{\text{max}} \cdot \Delta\nu_{1/2} \cdot \nu_{\text{max}}}}{r_{\text{CT}}}$, with $r_{\text{CT}} = r_{\text{O1-O2}}$ distance (2.689 Å) from the X-ray structure of $\text{CrL}^{\text{C}202}(\text{N})$.

- Electrochemistry and EPR spectroscopy

To probe the electrochemical properties of $[\text{CrL}^{\text{C}202}(\text{N})]^+$, we conducted the one-electron oxidation of $\text{CrL}^{\text{C}202}(\text{N})$ at 235 K ($E_{\text{elec}} = 0.35$ V vs Fc^+/Fc). The oxidation was monitored by coulometry, Rotating disk electrode (RDE) and CV experiments. Low-temperature RDE showed a complete oxidation and we recorded the same CV signature in comparison to $\text{CrL}^{\text{C}202}(\text{N})$, with a reversible oxidation wave at 0.15 V vs Fc^+/Fc (**Figure IV.12**). This result confirmed that the low-temperature oxidation product was the cation $[\text{CrL}^{\text{C}202}(\text{N})]^+$ and that it was stable at 235 K.

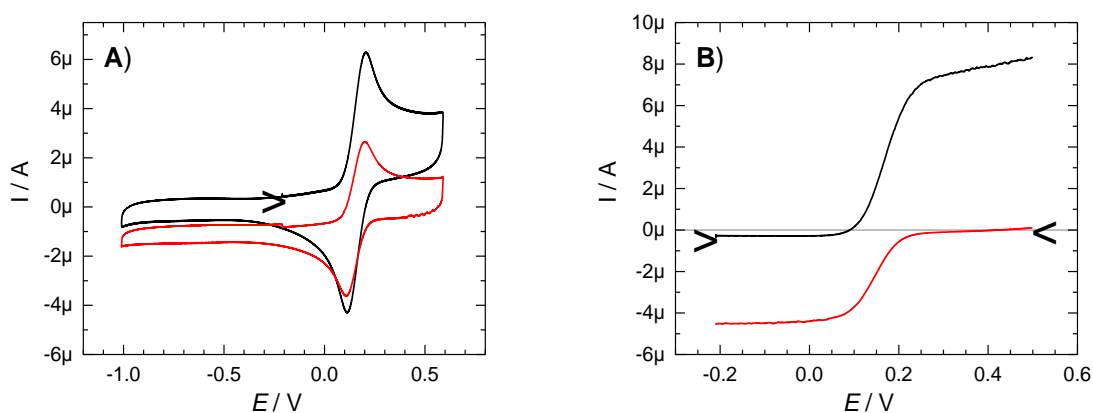


Figure IV.12. Low-temperature electrochemical oxidation of $\text{CrL}^{\text{C}202}(\text{N})$: CV curves (A) and RDE curves (B) of $\text{CrL}^{\text{C}202}(\text{N})$ before (black) and after one-electron oxidation (red). $T = 235$ K, argon atmosphere, 0.45 mM $\text{CrL}^{\text{C}202}(\text{N})$ in CH_2Cl_2 (+0.1 M TBAP) before oxidation. Vitreous carbon working electrode, scan rate: 100 mV.s⁻¹. Potentials given versus the Fc^+/Fc reference.

The electronic structure of $[\text{CrL}^{\text{C}202}(\text{N})]^+$ was also probed using X-band EPR spectroscopy at 100 K. The electrochemically generated monocation at low-temperature showed quenching of the EPR signature of $\text{CrL}^{\text{C}202}(\text{N})$. Integration of the EPR signals showed that the oxidation was more than 97% complete, with the 3% remaining signal attributed to unoxidized $\text{CrL}^{\text{C}202}(\text{N})$ (inset, **Figure IV.13**).

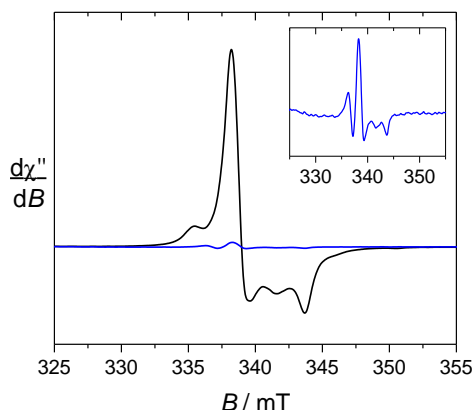


Figure IV.13. X-band EPR spectrum of $\text{CrL}^{\text{C2O2}}(\text{N})$ before (black) and after one-electron oxidation at low temperature ($T = 235$ K) (blue). Conditions: Argon atmosphere, 0.45 mM $\text{CrL}^{\text{C2O2}}(\text{N})$ CH_2Cl_2 solution before oxidation (+ 0.1 M TBAP). Microwave frequency 9.43 GHz, power 22.0 mW; mod. frequency 100 kHz, amp. 0.5 mT; $T = 100$ K.

As discussed before, a metal-centered oxidation to reach $[\text{Cr}^{\text{VI}}\text{L}^{\text{C2O2}}(\text{N})]^+$ (Cr(VI) , d^0 , singlet) can be expected and would result in EPR silence. However, a Cr(V) complex with a ligand-centered oxidation $[\text{Cr}^{\text{V}}\text{L}^{\text{C2O2}}(\text{N})]^+$ can also quench the EPR signal with either a ferromagnetic (triplet) or antiferromagnetic coupling (broken-symmetry singlet) with strong zero-field splitting. More insight was therefore required to definitely assess the electronic structure of the $[\text{CrL}^{\text{C2O2}}(\text{N})]^+$ cation.

- Theoretical calculations

As discussed previously, different possible electronic structures can be rationally expected for the $[\text{CrL}^{\text{C2O2}}(\text{N})]^+$ cation (**Figure IV.14**).

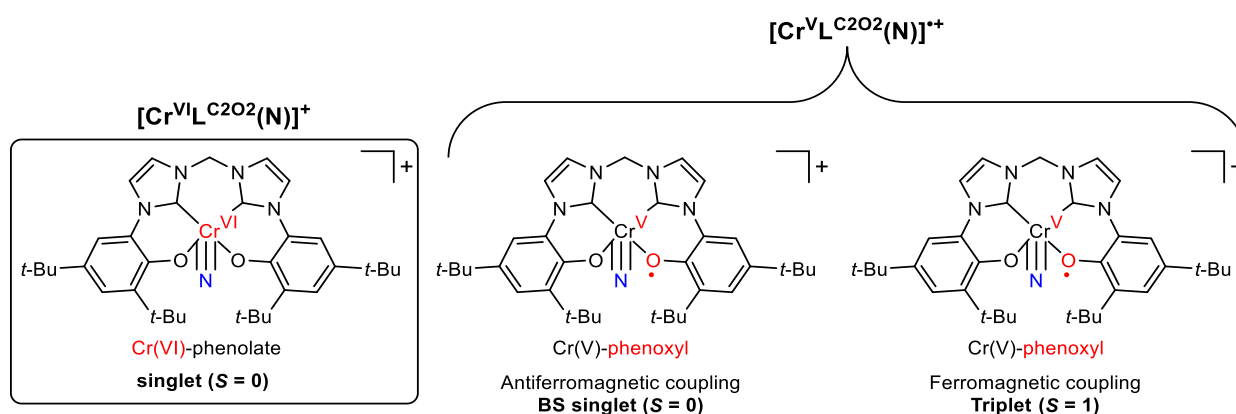


Figure IV.14. Possible electronic structures for one-electron oxidized complex $[\text{CrL}^{\text{C2O2}}(\text{N})]^+$.

The electrochemical behavior of $\text{CrL}^{\text{C2O2}}(\text{N})$ suggested a metal-centered oxidation to obtain a Cr(VI) , d^0 , singlet species $[\text{Cr}^{\text{VI}}\text{L}^{\text{C2O2}}(\text{N})]^+$ after oxidation. However, ligand-based oxidations were not discredited in UV-vis-NIR or EPR spectroscopy experiments. We therefore investigated the ground state of $[\text{CrL}^{\text{C2O2}}(\text{N})]^+$ by energetic analysis of the singlet, broken-symmetry singlet and triplet solutions. Different standard functionals were used to calculate the single point energies of the different structures. The results of the calculations are presented in **Table IV.9**.

Table IV.9. Energetic analysis of the possible electronic structures of oxidized $[\text{CrL}^{\text{C2O2}}(\text{N})]^+$.^a

single-point functional	Singlet (kcal.mol ⁻¹) ^b	BS singlet (kcal.mol ⁻¹) ^b	Triplet (kcal.mol ⁻¹) ^b
B3LYP	+0.5	0	+0.4
B3LYP-D3	+0.6	0	+0.4
CAMB3LYP	+3.1	0	+4.6
BP86	0	+9.7	+10.9
B3P86	0	+1.7	+2.1

^aOptimized structures using BP86/6-31G*/SCRF(CH₂Cl₂) calculations. ^bRelative energies from single point calculations using the respective functional with TZVP/SCRF(CH₂Cl₂) system.

The results appeared to be heavily dependent on the functional used. On one hand, the metal-oxidized Cr(VI) singlet $[\text{Cr}^{\text{VI}}\text{L}^{\text{C2O2}}(\text{N})]^+$ species was projected as the most stable solution using the BP86 or B3P86 functionals. On the other hand, the ligand-oxidized $[\text{Cr}^{\text{V}}(\text{sal}^{\text{NMe2}})(\text{N})]^+$ broken-symmetry singlet solution was depicted as the ground state using B3LYP, B3LYP-D3 and CAMB3LYP.

Experimentally, $[\text{CrL}^{\text{C2O2}}(\text{N})]^+$ displayed a low energy transition (11 100 cm⁻¹) of moderate intensity ($\epsilon \approx 3000 \text{ M}^{-1}.\text{cm}^{-1}$) in UV-vis-NIR spectroscopy. Thus, we conducted TD-DFT calculations of the different theoretical electronic structures to further discriminate between the possible ground-states. The results are reported in **Table IV.10**.

Table IV.10. TD-DFT investigation of the possible electronic structures of $[\text{CrL}^{\text{C2O2}}(\text{N})]^+$.^a

complex ^a	main transitions	assignment	calcd.	f_{osc}
Singlet	HOMO → LUMO	LMCT	10686	0.0101
BS singlet	α -HOMO → α -LUMO	LLCT (IVCT)	3486	0.1449
	α -HOMO-1 → α -LUMO	LLCT / MLCT	8064	0.0074
	α -HOMO-2 → α -LUMO	LLCT / MLCT	10445	0.0121
Triplet	β -HOMO → β -LUMO	LLCT (IVCT)	3480	0.1476
	β -HOMO-1 → β -LUMO	LLCT	10323	0.0109

^aB3LYP/TZVP/SCRF(CH₂Cl₂).

All three solutions were computed to have an electronic excitation around 11 000 cm⁻¹ that could match the experimental absorption spectra of $[\text{CrL}^{\text{C2O2}}(\text{N})]^+$. Nevertheless, the calculated ligand-centered oxidation products (broken-symmetry singlet and triplet species) also presented an additional intervalence charge transfer (IVCT) excitation around 3500 cm⁻¹, with a larger oscillator strength (higher f_{osc}). Considering the lack of striking NIR features below 11 000 cm⁻¹ in the UV-vis-NIR spectrum of $[\text{CrL}^{\text{C2O2}}(\text{N})]^+$, it was assigned as a Cr(VI) (singlet) $[\text{Cr}^{\text{VI}}\text{L}^{\text{C2O2}}(\text{N})]^+$ cation.

The excitation observed experimentally was therefore assigned as a ligand-to-metal charge transfer (LMCT) HOMO \rightarrow LUMO excitation based on the TD-DFT results (**Table IV.10**). The donor orbital is developed over both phenolate rings of the complex and the LUMO showed a main metallic character and was attributed to the unoccupied d_{xy} orbital of the Cr(VI) center (**Figure IV.15**).

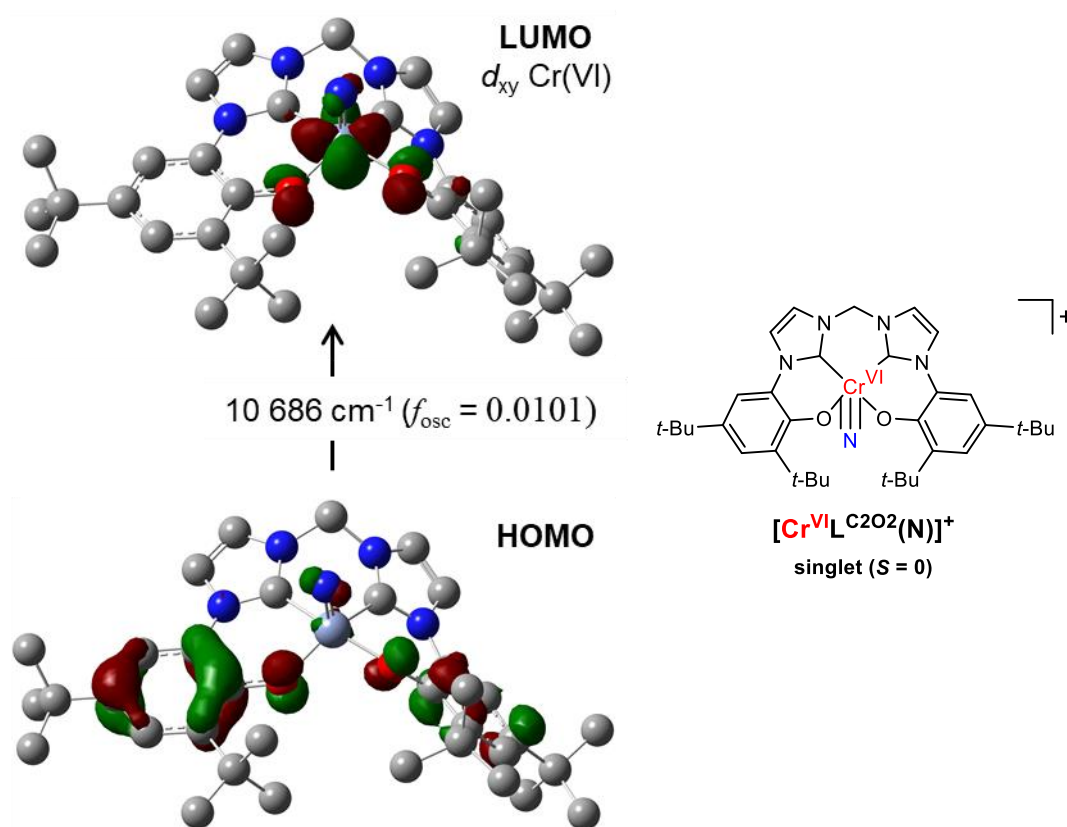


Figure IV.15. TD-DFT calculated low-energy excitation of the singlet $[\text{Cr}^{\text{VI}}\text{L}^{\text{C2O2}}(\text{N})]^+$ cation (B3LYP/TZVP/SCRF(CH_2Cl_2)).

3.2. Room temperature degradation products

3.2.1. Room temperature chemical oxidation

- UV-vis-NIR evolution

$[\text{CrL}^{\text{C2O2}}(\text{N})]^+$ appeared stable at low temperature over the span of a couple hours. However, it rapidly changed color when the solution was warmed back to room temperature. To investigate this degradation, we oxidized $\text{CrL}^{\text{C2O2}}(\text{N})$ at room temperature by introduction of one equivalent of oxidant ($[\text{N}(\text{C}_6\text{H}_3\text{Br}_2)_3]^+[\text{SbF}_6]^-$) and followed the evolution of the UV-vis-NIR signature of the medium over time (**Figure IV.16**).

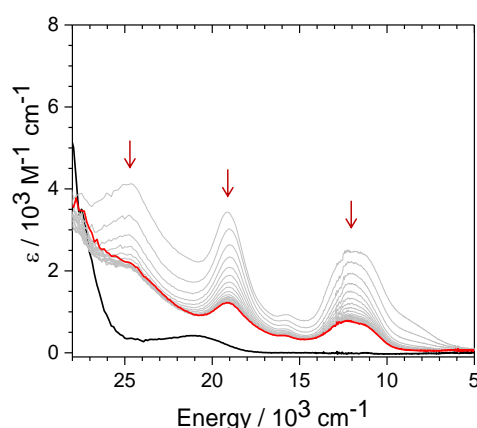


Figure IV.16. Room temperature oxidation of $\text{CrL}^{\text{C2O2}}(\text{N})$ and its evolution: neutral $\text{CrL}^{\text{C2O2}}(\text{N})$ (black) and after addition of 1 equivalent of oxidant ($[\text{N}(\text{C}_6\text{H}_3\text{Br}_2)_3]^+[\text{SbF}_6]^-$); from 10 minutes to 3 hours of reaction (red). CH_2Cl_2 solutions: 2.55 mM $\text{CrL}^{\text{C2O2}}(\text{N})$ before oxidation, 2.16 mM medium after addition of the solution of oxidant, $T = 298\text{ K}$, N_2 atmosphere.

Different spectral features appeared in the room temperature oxidation of $\text{CrL}^{\text{C2O2}}(\text{N})$ compared to the UV-vis-NIR signature of $[\text{CrL}^{\text{C2O2}}(\text{N})]^+$ at 235 K. A low energy transition around 11500 cm^{-1} was reminiscent of the low-temperature oxidation but other features around 8000 , 15500 , 19000 and 24500 cm^{-1} were observed that were gradually quenched over time. The evolution of the UV-vis-NIR spectra reached a plateau after 3 hours of reaction. For simplicity purposes in this text, the unknown resulting product of the room temperature oxidation of $\text{CrL}^{\text{C2O2}}(\text{N})$ will be labelled $[\text{X}]^+$. The UV-vis-NIR signature after reaction is reported in **Table IV.7**.

- Mass spectrometry and magnetic susceptibility investigation

The nature of the oxidation products at room temperature was also investigated using mass spectrometry. We conducted the one-electron oxidation of $\text{CrL}^{\text{C2O2}}(\text{N})$ in dry dichloromethane (2.45 mM) using an equimolar amount of silver hexafluoroantimonate (AgSbF_6) oxidant in dry dichloromethane. The reaction was stirred for 20 hours at room temperature ($T = 298\text{ K}$) under N_2 atmosphere in a glovebox then was then filtered over celite to remove colloidal silver. The solution was diluted in dichloromethane and analyzed using positive mode ESI-MS.

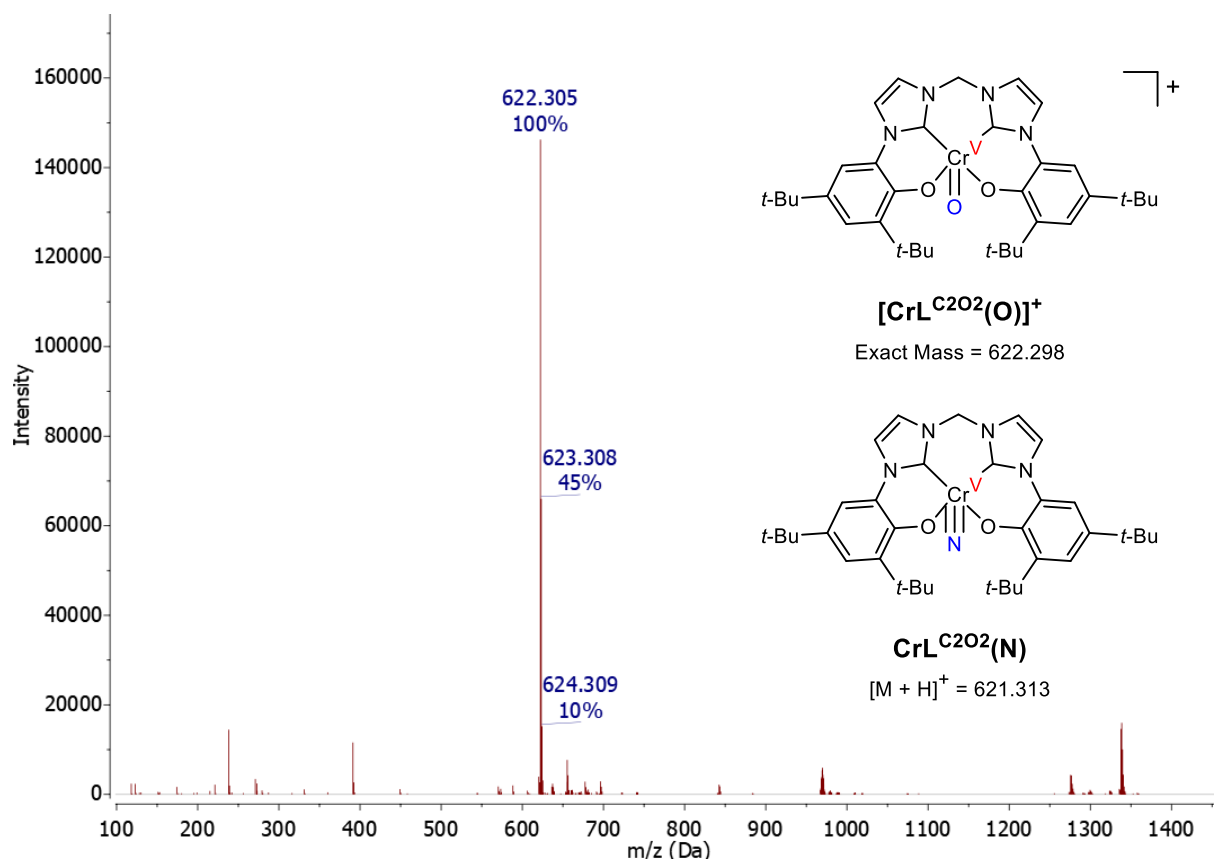


Figure IV.17. Positive mode ESI-MS analysis of the crude mixture of the room-temperature one-electron oxidation of $\text{CrL}^{\text{C2O2}}(\text{N})$ using the AgSbF_6 oxidant. Species of interests are depicted.

An increase of m/z shift by one Dalton was observed after the reaction. This new species was attributed to the formation of a new oxo chromium complex $\text{CrL}^{\text{C2O2}}(\text{O})$ with loss of the nitride ligand (**Figure IV.17**). The oxidation reaction was conducted under neat conditions without any potential oxygen atom donors. Thus, the oxygen atom likely originated from the denaturing conditions of the ESI-MS experiments that we discussed previously in Chapter III. Therefore, the $\text{CrL}^{\text{C2O2}}(\text{O})$ complex likely formed from the degradation of the unknown product $[\text{X}]^+$ present in inert conditions at room temperature, that itself evolved from $[\text{CrL}^{\text{C2O2}}(\text{N})]^+$, which appeared stable at $T = 235$ K. Hence, the mechanism for the evolution of these different oxidation products remains unclear.

The oxidation state of the $\text{CrL}^{\text{C2O2}}(\text{O})$ complex was also uncertain. It can rationally be explained as a cationic $[\text{Cr}^{\text{V}}\text{L}^{\text{C2O2}}(\text{O})]^+$ complex as depicted in **Figure IV.17** but also a neutral Cr(IV) complex that oxidizes in the ESI-MS conditions.^[318] To probe the electronic structure of the oxo product, we conducted magnetic susceptibility measurements using Evan's method. After evaporation of the crude mixture, 3.3 mg of product were solubilized in 1000 μL of deuterated dichloromethane and a sealed capillary of CD_2Cl_2 was used as internal reference. A paramagnetic shift of 0.0688 ppm was observed in ^1H NMR. To calculate the magnetic moment (μ_{eff}) of the oxo compound, both the neutral complex $\text{Cr}^{\text{IV}}\text{L}^{\text{C2O2}}(\text{O})$ and the cationic $[\text{Cr}^{\text{V}}\text{L}^{\text{C2O2}}(\text{O})]^+(\text{SbF}_6)^-$ species were considered (**Figure IV.18**).

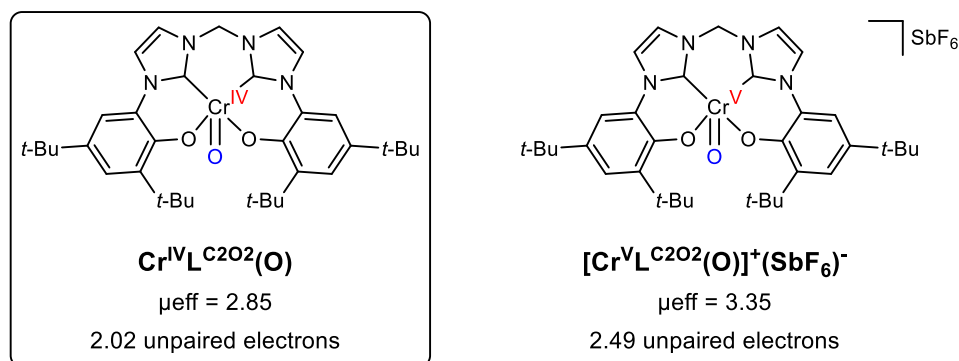


Figure IV.18. Structures considered for the oxo complex observed in ESI-MS experiments and their corresponding magnetic susceptibility using Evan's method analysis.

The calculated μ_{eff} value was only coherent when considering the neutral $\text{Cr}^{\text{IV}}\text{L}^{\text{C}2\text{O}2}(\text{O})$ complex. The magnetic susceptibility of 2.85 would correspond to 2.02 unpaired electrons and point towards the presence of a d^2 high-spin ($S = 1$) Cr(IV) complex. If considering the $[\text{Cr}^{\text{V}}\text{L}^{\text{C}2\text{O}2}(\text{O})]^+(\text{SbF}_6)^-$ species, the calculated μ_{eff} value of 3.35 would correspond to 2.49 unpaired electrons, which does not make sense for a d^1 Cr(V) ion.

The UV-vis-NIR signature of the crude oxo complex was also recorded. It exhibited no distinct excitations but absorbed light over the entire visible and NIR spectral window (**Figure IV.19**). The signature of the $\text{CrL}^{\text{C}2\text{O}2}(\text{O})$ compound appeared clearly distinct from the spectra recorded for the room temperature oxidation of $\text{CrL}^{\text{C}2\text{O}2}(\text{N})$ in neat conditions (**Figure IV.16**). This result was once again consistent with the observation that the oxo complex was likely not the oxidation product $[\text{X}]^+$ itself, but rather a result of its degradation in non-inert conditions.

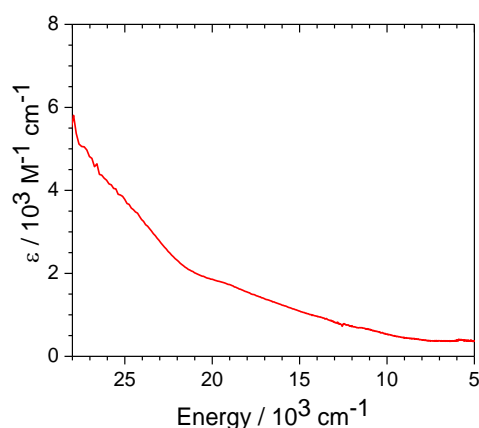


Figure IV.19. UV-vis-NIR spectrum of the crude $\text{CrL}^{\text{C}2\text{O}2}(\text{O})$ complex (2.45 mM) in a CH_2Cl_2 solution.

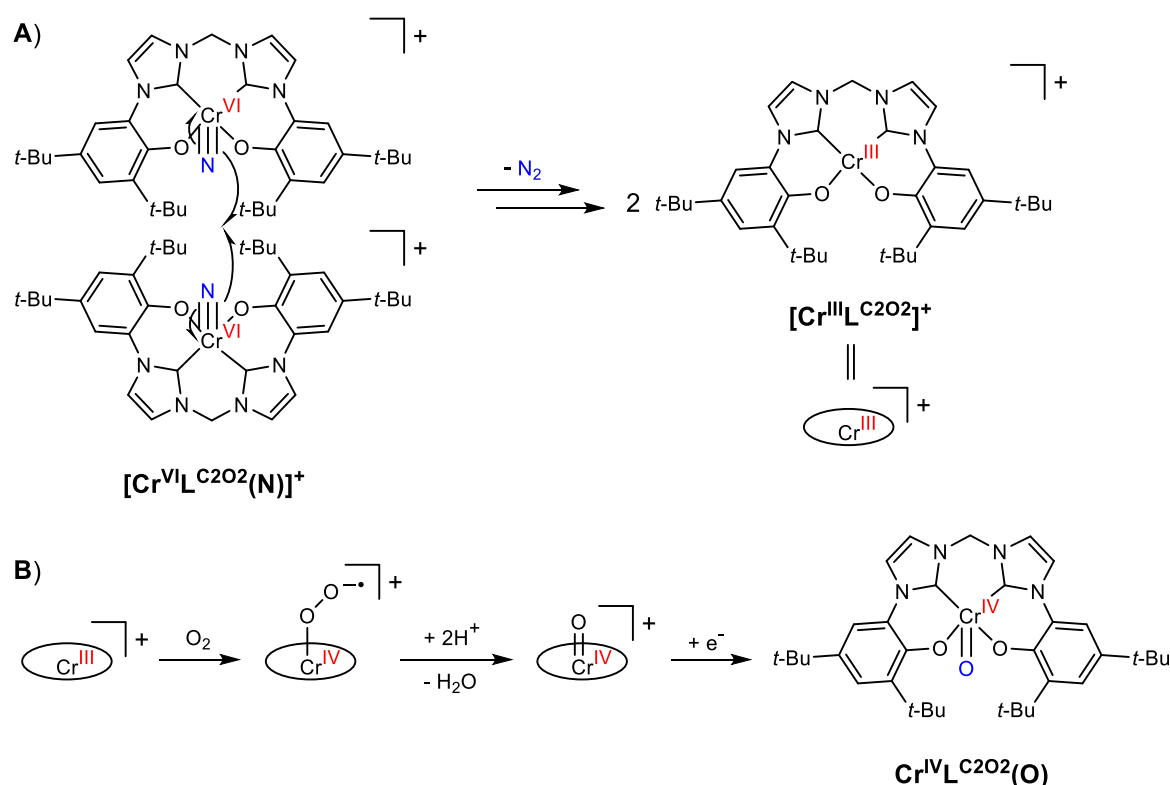
Due to a lack of time and material, the putative $\text{CrL}^{\text{C}2\text{O}2}(\text{O})$ complex was not further characterized. We therefore planned to focus on its preparation and isolation for further investigation.

Table IV.11. UV-vis-NIR data of the oxidation products of $\text{CrL}^{\text{C2O2}}(\text{N})$.^a

complex	λ_{max} [cm^{-1}] (ϵ [$\text{M}^{-1}.\text{cm}^{-1}$])
$[\text{CrL}^{\text{C2O2}}(\text{N})]^{+b}$	23300 (6700, sh), 11100 (3110)
$[\text{X}]^{+c}$	24700 (2200, sh), 19100 (1220), 15700 (410), 12300 (780), 11100 (640, sh)
$\text{CrL}^{\text{C2O2}}(\text{O})^d$	19100 (1730, sh), 11100 (650, sh), 5800 (390, br)

^aIn CH_2Cl_2 solutions. br: broad; sh: shoulder^bChemically generated using $([\text{N}(\text{C}_6\text{H}_3\text{Br}_2)_3]^{+}[\text{SbF}_6]^{-})$ at $T = 235$ K (N_2 atm., dry CH_2Cl_2 solution).^cChemically generated using $([\text{N}(\text{C}_6\text{H}_3\text{Br}_2)_3]^{+}[\text{SbF}_6]^{-})$ at $T = 298$ K (N_2 atm., dry CH_2Cl_2 solution).^dChemically generated using AgSbF_6 at $T = 298$ K (N_2 atm., dry CH_2Cl_2 solution) then being exposed to non-inert conditions.

The mechanism of formation for a $\text{Cr}^{\text{IV}}\text{L}^{\text{C2O2}}(\text{O})$ complex remains unclear. One hypothesis would be a first elimination of the nitride ligand in $[\text{CrL}^{\text{C2O2}}(\text{N})]^{+}$ through homocoupling reactivity and elimination of a N_2 molecule (**Figure IV.20.A**). This behavior was observed in a number of metal nitrido complexes and specifically in oxidized Mn(VI) nitrido salen complexes.^[106] The resulting $[\text{Cr}^{\text{III}}\text{L}^{\text{C2O2}}]^{+}$ complex could then form the oxo $\text{Cr}^{\text{IV}}\text{L}^{\text{C2O2}}(\text{O})$ complex through activation of an oxygen donor, such as O_2 or innocuous H_2O (**Figure IV.20.B**).

**Figure IV.20.** Proposed pathway for the formation of complex $\text{Cr}^{\text{IV}}\text{L}^{\text{C2O2}}(\text{O})$: Loss of nitride ligand through homocoupling reactivity (**A**) and activation of oxygen (**B**).

We conducted preliminary experiments to verify the formation and loss of a N_2 molecule in homocoupling reactivity. An isotopically labelled nitride complex $CrL^{C2O2}(^{15}N)$ was prepared in the same manner as complex $CrL^{C2O2}(N)$ but using the isotopically labelled nitride exchange reagent $Mn(salen)(^{15}N)$, for an overall yield of 35%. $CrL^{C2O2}(^{15}N)$ was then chemically oxidized at room temperature under argon atmosphere in a sealed vial, using an equimolar amount of $AgSbF_6$ in a dry CH_2Cl_2 solution. A sample of the reaction atmosphere was then taken and analyzed in gas chromatography-mass spectrometry (GC-MS) to detect formation of $^{15}N_2$. Unfortunately, we did not detect $^{15}N_2$ gas in the reaction. The homocoupling process might require activation by coordination of a donating exogenous ligand that would explain the absence of $^{15}N_2$ in the current conditions. Thus, for future experiments, we propose to introduce exogenous molecules, such as MeCN or H_2O , in the sealed reaction vial after chemical oxidation and observe their impact on the formation of $^{15}N_2$.

3.2.2. Evolution of $[CrL^{C2O2}(N)]^+$ at room temperature

- Electrochemistry

We conducted different electrochemical oxidations of $CrL^{C2O2}(N)$ to gain some insight into the formation of unknown product $[X]^+$ after oxidation. We first investigated the evolution of $[CrL^{C2O2}(N)]^+$ when it was warmed back to room temperature. $[CrL^{C2O2}(N)]^+$ was oxidized by bulk electrolysis of $CrL^{C2O2}(N)$ at 235 K ($E_{elec} = 0.35$ V vs Fc^+/Fc). The oxidation was monitored by coulometry, RDE and CV experiments as we detailed in section 3.1. (**Figure IV.12**). The electrolyzed solution was then warmed back to room temperature and we recorded the CV spectra of the medium over time. The reversible oxidation wave of $[CrL^{C2O2}(N)]^+$ progressively disappeared and a new oxidation event appeared at $E_{ox} \approx 0.39$ V. Poorly defined reduction processes also appeared below $E = -0.5$ V (**Figure IV.21**). The CV signature stabilized after 1 hour at 298 K.

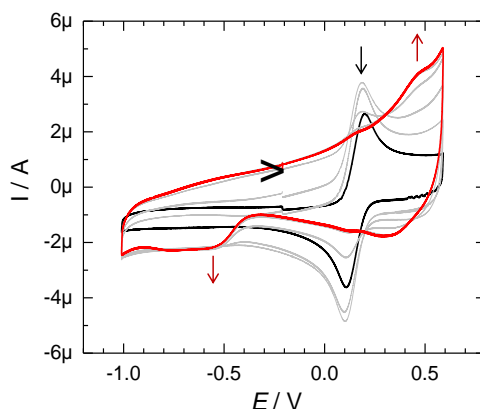


Figure IV.21. Evolution of the CV signature of $[CrL^{C2O2}(N)]^+$ ($T = 235$ K, black) after 90 min at room temperature ($T = 298$ K, red). Grey lines correspond to intermediate CV monitoring of the reaction. Conditions: Argon atmosphere, 0.45 mM $CrL^{C2O2}(N)$ in CH_2Cl_2 (+0.1 M TBAP) before oxidation. Vitreous carbon working electrode, scan rate: $100\text{ mV}\cdot\text{s}^{-1}$. Potentials given versus the Fc^+/Fc reference.

- X-band EPR

In a similar fashion, an EPR sample of $[\text{CrL}^{\text{C}2\text{O}2}(\text{N})]^+$ generated by bulk electrolysis at 235 K was warmed back to room temperature for 90 minutes. The EPR signature evolved, showing an anisotropic signal centered at $g \approx 1.98$ and two low-field components at $g \approx 2.53$ and g in the range 5.00-5.61 (Figure IV.22).

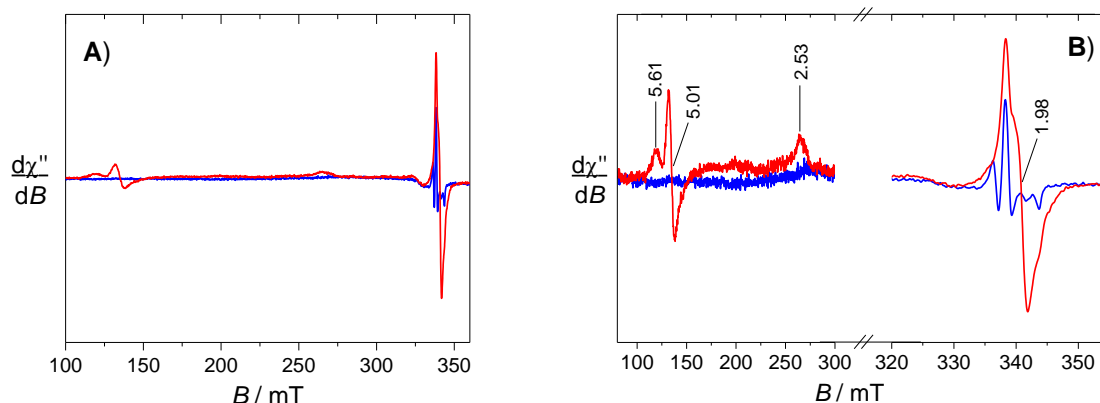


Figure IV.22. X-band EPR spectrum of $[\text{CrL}^{\text{C}2\text{O}2}(\text{N})]^+$ at low temperature ($T = 235$ K) (blue) and after being warmed to room temperature ($T = 298$ K, 90 min) (red). Full spectra (A) and zooms (B). Conditions: 0.45 mM $[\text{CrL}^{\text{C}2\text{O}2}(\text{N})]^+$ CH_2Cl_2 solution (+ 0.1 M TBAP). Microwave frequency 9.43 GHz, power 22.0 mW; mod. frequency 100 kHz, amp. 0.5 mT; $T = 100$ K.

The low-field component at $g \approx 5$ was attributed to a forbidden half-field transition $\Delta M_S = \pm 2$ and the broad component at $g \approx 2.50$ to one of the allowed $\Delta M_S = \pm 1$ transition in a triplet system ($S = 1$) (Figure IV.23.B). The $g \approx 1.98$ signal was attributed to a Cr(V) (d^1 , $S = 1/2$) contaminant with a poorly resolved anisotropy. The g_{iso} value is indeed comparable with g_{average} values of nitridochromium(V) complexes (Table IV.3)^[311] or Cr(V)-oxo species.^[319]

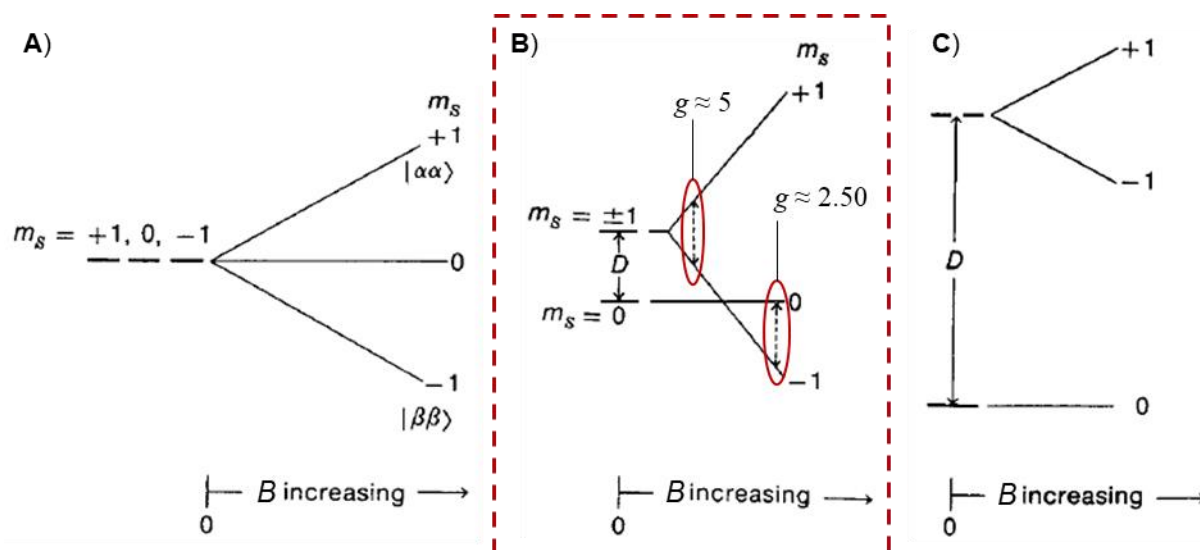


Figure IV.23. Zero-field splitting impact on the EPR transitions in triplet species: No zero-field effects (A). Moderate zero-field splittings. The circled dashed arrows represent the transitions observed experimentally in our X-band EPR experiments (B). Large zero-field effects (C). Adapted from reference ^[320].

3.2.3. Electrochemical formation of $[\mathbf{X}]^+$ at room temperature- Electrochemistry

We also investigated the electrochemical oxidation of $\text{CrL}^{\text{C2O2}}(\text{N})$ conducted at room temperature ($E_{\text{elec}} = 0.35 \text{ V}$ vs Fc^+/Fc , $T = 298 \text{ K}$) to compare with the evolution of $[\text{CrL}^{\text{C2O2}}(\text{N})]^+$. The bulk electrolysis was controlled by coulometry and we recorded the CV of the medium after one-electron oxidation. The CV signature of the starting neutral complex $\text{CrL}^{\text{C2O2}}(\text{N})$ was completely quenched and a new quasi-reversible oxidation process appeared at $E_{1/2} = 0.39 \text{ V}$ ($\Delta E_p = 0.15 \text{ V}$). An irreversible reduction process is also recorded at $E_p^{\text{red}} = -0.63 \text{ V}$ (**Figure IV.24**).

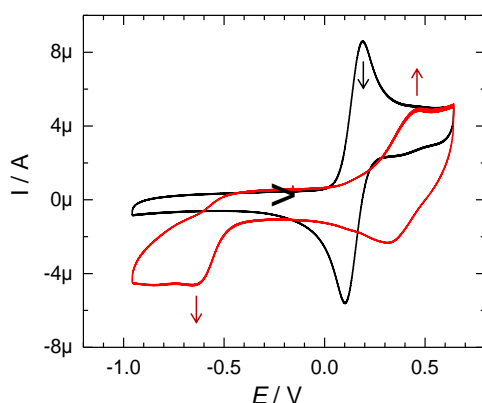


Figure IV.24. Room-temperature electrochemical oxidation of $\text{CrL}^{\text{C2O2}}(\text{N})$: CV curves of $\text{CrL}^{\text{C2O2}}(\text{N})$ before (black) and after one-electron oxidation (red). Conditions: $T = 298 \text{ K}$, argon atmosphere, 0.50 mM $\text{CrL}^{\text{C2O2}}(\text{N})$ in CH_2Cl_2 (+ 0.1 M TBAP) before oxidation. Vitreous carbon working electrode, scan rate: $100 \text{ mV}\cdot\text{s}^{-1}$. Potentials given versus the Fc^+/Fc reference.

The CV spectra of the room temperature oxidation of $\text{CrL}^{\text{C2O2}}(\text{N})$ appeared comparable to the room-temperature evolution of $[\text{CrL}^{\text{C2O2}}(\text{N})]^+$ generated at 235 K (**Figure IV.21**). This result shows that both pathways likely result in the same oxidation product $[\mathbf{X}]^+$.

Table IV.12. Electrochemical data of the relevant chromium complexes.^a

complex	E_p^{red}	$E_{1/2}^{\text{ox1}}$ (ΔE)	$E_{1/2}^{\text{ox2}}$ (ΔE)	$\Delta E_{1/2}^{\text{ox}}$
$\text{CrL}^{\text{C2O2}}(\text{N})$	-	0.15 (0.09)	-	-
$[\text{CrL}^{\text{C2O2}}(\text{N})]^{+b}$	-	0.15 (0.09)	-	-
$[\mathbf{X}]^{+c}$	-0.63^d	0.39 (0.15)	-	-
$\text{Cr}(\text{sal}^{\text{CF3}})(\text{N})^e$	-	0.61 (0.19)	-	-
$\text{Cr}(\text{sal}^{\text{tBu}})(\text{N})^e$	-	0.87 (0.23)	-	-
$\text{Cr}(\text{sal}^{\text{NMe2}})(\text{N})^e$	-	-0.04 (0.17)	0.12 (0.17)	0.16

^aGlassy carbon working electrode, potentials are referenced to the Fc^+/Fc redox couple (0.10 V vs Ag/AgNO_3 0.01 M and $\Delta E_p = 0.08 \text{ V}$ under our experimental conditions). In CH_2Cl_2 solutions (+ 0.1 M TBAP); scan rate: 100 mV/s . ^bRecorded at $T = 235 \text{ K}$. ^cRecorded at $T = 298 \text{ K}$. ^dIrreversible process.

^eAs reported in reference [311], Conditions: 1.0 mM complex in CH_2Cl_2 solutions (+ 0.1 M TBAP); scan rate: 100 mV/s . $T = 298 \text{ K}$.

- X-band EPR

The room-temperature oxidation of $\text{CrL}^{\text{C202}}(\text{N})$ was also investigated by EPR (**Figure IV.25**). An aliquot was taken after one electron was removed by bulk electrolysis at $T = 298$ K. We observed the appearance of an isotropic signal centered at $g \approx 1.98$ and two low-field components around $g \approx 2.54$ and g in the range 5.03-5.40 (**Figure IV.25.B**). The low temperature X-band EPR of the sample displayed a comparable signature with the room-temperature evolution of $[\text{CrL}^{\text{C202}}(\text{N})]^+$ generated at 235 K (**Figure IV.22**). Once again, this supports the hypothesis that both oxidation pathways lead to the formation of $[\text{X}]^+$ at room temperature.

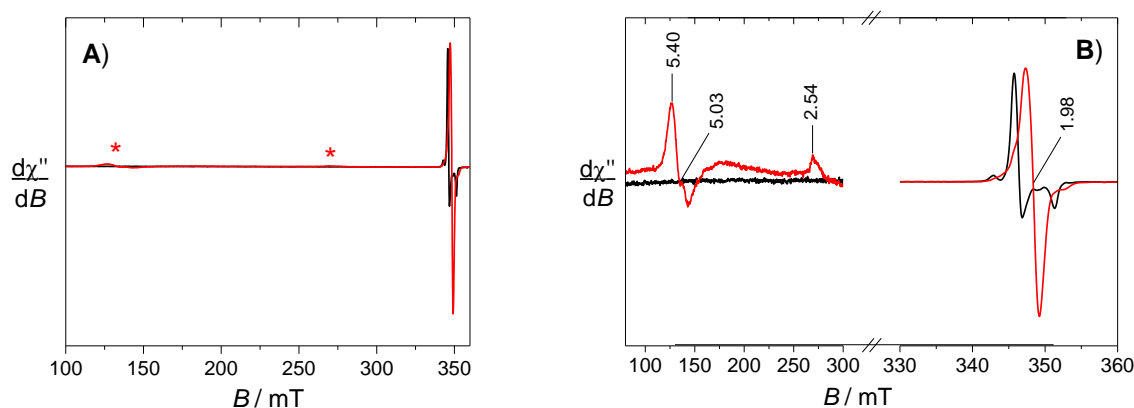


Figure IV.25. X-band EPR spectrum of $\text{CrL}^{\text{C202}}(\text{N})$ before (black) and after one-electron oxidation at room-temperature ($T = 298$ K) (red). Full spectra (**A**) and zooms (**B**). Conditions: Argon atmosphere, 0.5 mM $\text{CrL}^{\text{C202}}(\text{N})$ CH_2Cl_2 solution before oxidation (+ 0.1 M TBAP). Microwave frequency 9.64 GHz, power 6.5 mW; mod. frequency 100 kHz, amp. 0.5 mT; $T = 22$ K. The low-field components of $[\text{X}]^+$ are depicted by asterisks in the full spectrum.

- Variable temperature EPR

We conducted variable temperature EPR experiments to investigate the ground-state of the low-field component at $g > 5$ in X-band EPR. The temperature dependence of the EPR signal allows to probe the electronic structure of a magnetically coupled system. Indeed, the intensity of the EPR signal of a ground-state is expected to correlate with $1/T$.^[321] Investigation in the 6-32 K range showed that the intensity of the low-field component in $[\text{X}]^+$ deviated from linearity, thus revealing an excited state for the triplet (**Figure IV.26.A**). The spins would therefore be antiferromagnetically coupled with a diamagnetic ground-state.

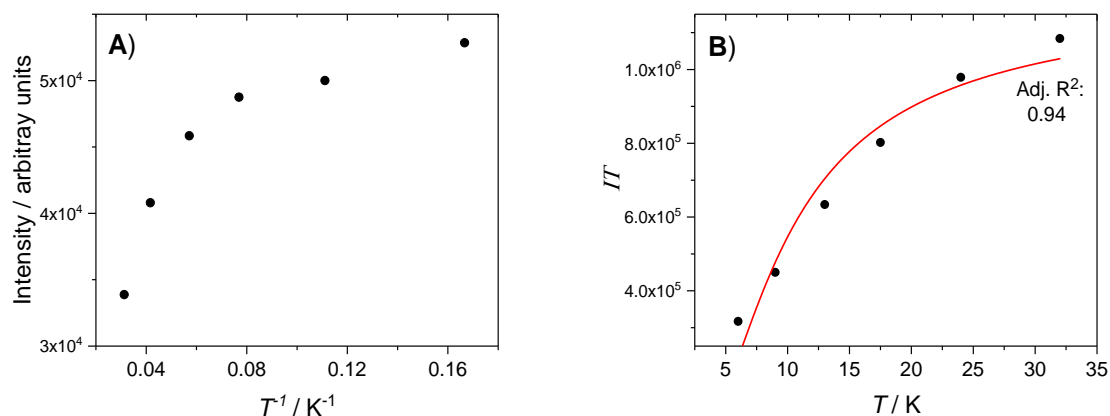


Figure IV.26. X-band EPR temperature dependence of $[X]^+$ at varying temperature ($T = 6$ to 32 K): Intensity of the low-field component ($g > 5$) as function of $1/T$ (A). IT as a function of T and best fit using parameters given in text (B). Conditions: Argon atmosphere, 0.5 mM $\text{CrL}^{\text{C}2\text{O}2}(\text{N})$ CH_2Cl_2 solution before oxidation (+ 0.1 M TBAP). Microwave frequency 9.64 GHz, power 3.3 mW; mod. frequency 100 kHz, amp. 0.5 mT.

The temperature dependence of the magnetic susceptibility of two interacting $S = 1/2$ spin systems was described by Bleaney and Bowers.^[322] The magnetic coupling J was calculated using the fit of IT as a function of T using equation (9), derived from the Bleaney-Bowers equation:

$$(9) \quad IT = C \exp(2J/kT)/(1 + 3\exp(2J/kT))$$

Where C is the Curie constant of the magnetic susceptibility of the compound (expressed in kelvins) and k is the Boltzmann constant ($0.695 \text{ cm}^{-1} \cdot \text{K}^{-1}$). We obtained a J coupling of $-6.2 \pm 1 \text{ cm}^{-1}$ after fitting, in agreement with a very weak antiferromagnetic coupling (Figure IV.26.B).

- Pulsed-EPR

We also investigated the EPR triplet signature of $[X]^+$ using pulsed-EPR experiments. Electron-spin-echo detected field-sweep experiments showed the presence of multiple broad components in the 200 - 550 mT range. They were assigned to the allowed $\Delta M_S = \pm 1$ transitions in a triplet state. The half-field transition $\Delta M_S = \pm 2$ was still observed around 130 mT. A sharp signal was observed at $B = 347$ mT and was once again assigned as a Cr(V) ($S = 1/2$) contaminant species (Figure IV.27.B). It is less easily observed in pulsed EPR, which is intrinsically due to the technique and its sensitivity.

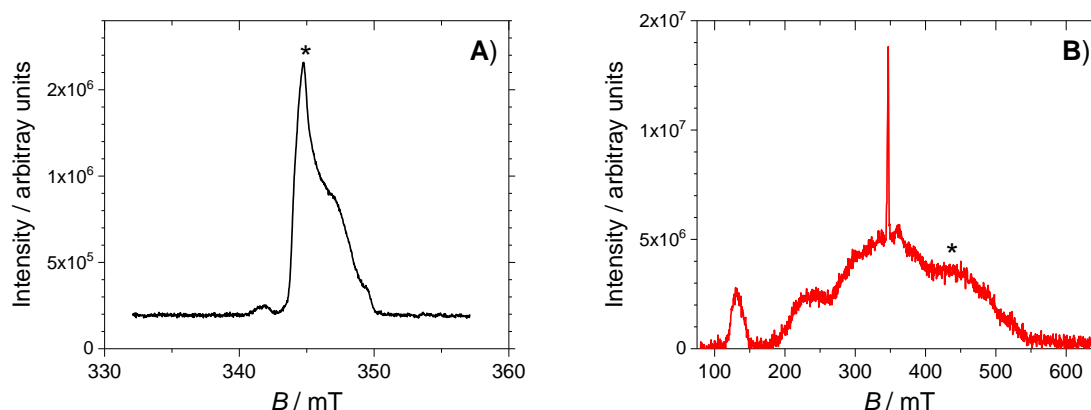


Figure IV.27. X-band electron-spin-echo detected field sweeps of $\text{CrL}^{\text{C202}}(\text{N})$ before (A) and after one-electron oxidation at room-temperature ($[\text{X}]^+$, $T = 298 \text{ K}$) (B). $T = 10 \text{ K}$. The B fields selected for nutation experiments (Figure IV.28) are highlighted by asterisks.

Electron-spin transient nutation (ETSN) measurements were also conducted. ETSN is based on the fact that a magnetic moment precesses with a specific nutation frequency (ω_n) depending on its spin multiplicity.^[323] In a static magnetic field, the nutation frequency (ω_n) for an allowed transition $|S, M_S\rangle \leftrightarrow |S, M_S-1\rangle$ is given by equation (10):

$$(10) \quad \omega_n = \sqrt{S(S+1) - M_S(M_S-1)} \omega_1$$

Where ω_1 is the nutation frequency of a reference doublet ($S=1/2$) species. ETSN can therefore allow to probe the spin S of an unknown compound in solution. Equation (10) gives a theoretical ratio of $\omega_n = \sqrt{2} \omega_1$ for an allowed $\Delta M_S = \pm 1$ transition in a triplet species ($|1, 0\rangle \leftrightarrow |1, \pm 1\rangle$, Figure IV.23)

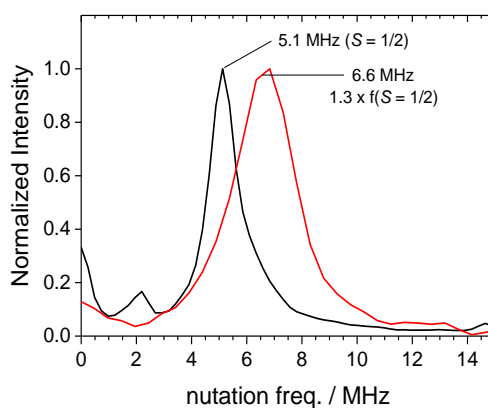


Figure IV.28. X-band EPR nutation experiments on $\text{CrL}^{\text{C202}}(\text{N})$ (black, $B = 3447 \text{ G}$) and $[\text{X}]^+$ (red, $B = 4300 \text{ G}$). $T = 10 \text{ K}$. Power attenuation 10 dB.

Nutation experiments on $[\text{X}]^+$ at 430 mT in the expected $\Delta M_S = \pm 1$ transitions of the triplet state revealed a nutation frequency of 6.6 MHz. This frequency was approximately 1.3 times higher than the nutation frequency recorded for $\text{CrL}^{\text{C202}}(\text{N})$ at 345 mT, which was our reference for a $S = 1/2$ system (Figure IV.27). The nutation frequency ratio of $\omega_n = 1.3 \omega_1$ is inferior to the theoretical ratio 1.42. These results still point towards the likely presence of a triplet state in the

unknown product $[\mathbf{X}]^+$. Additional nutation experiments using Q-band pulsed-EPR are currently undergoing to further confirm this statement.

3.2.4. Theoretical calculations

The possible species for the unknown product $[\mathbf{X}]^+$ were finally probed using DFT calculations. As discussed before in EPR experiments, $[\mathbf{X}]^+$ showed an excited triplet state populated from a diamagnetic ground-state with a very weak antiferromagnetic coupling of $J = -6.2 \pm 1 \text{ cm}^{-1}$. Thus, we envisioned different species that could evolve from $[\text{CrL}^{\text{C2O2}}(\text{N})]^+$ that could fit this description. For the sake of consistency, the structures of the theoretical species were optimized using the BP86 functional, with a 6-31G* basis set on all atoms and a SCRF dichloromethane solvent model.

The ligand-centered oxidation of $\text{CrL}^{\text{C2O2}}(\text{N})$ ($[\text{Cr}^{\text{VL}}\text{L}^{\text{C2O2}}(\text{N})]^+$, **Figure IV.14**) was investigated as a possible solution. As detailed in the theoretical energetic analysis of **Table IV.13**, the triplet solution is almost isoenergetic (functionals B3LYP, B3LYP-D3 and CAMB3LYP) with the singlet $[\text{Cr}^{\text{VL}}\text{L}^{\text{C2O2}}(\text{N})]^+$ species we attributed for the cation $[\text{CrL}^{\text{C2O2}}(\text{N})]^+$ at low temperature. Therefore, an electron transfer to reach the triplet $[\text{Cr}^{\text{VL}}\text{L}^{\text{C2O2}}(\text{N})]^+$ species could rationally happen when warming $[\text{Cr}^{\text{VL}}\text{L}^{\text{C2O2}}(\text{N})]^+$ to room temperature.

Table IV.13. Energetic analysis of the possible electronic structures of oxidized $[\text{CrL}^{\text{C2O2}}(\text{N})]^+$.^a

single-point functional	Singlet (kcal.mol ⁻¹) ^b	BS singlet (kcal.mol ⁻¹) ^b	Triplet (kcal.mol ⁻¹) ^b	$\langle S^2 \rangle_{\text{triplet}}$	$\langle S^2 \rangle_{\text{BSS}}$	$J \text{ (cm}^{-1}\text{)}$ ^c
B3LYP	+0.5	0	+0.4	2.0719	1.0937	-144
B3LYP-D3	+0.6	0	+0.4	2.0719	1.0937	-144
CAMB3LYP	+3.1	0	+4.6	2.1448	1.1828	-1668
BP86	0	+9.7	+10.9	2.0184	0.7975	-317
B3P86	0	+1.7	+2.1	2.0721	1.0949	-158

^aOptimized structures using BP86/6-31G*/SCRF(CH₂Cl₂) calculations. ^bRelative energies from single point calculations using the respective functional with TZVP/SCRF(CH₂Cl₂) system.

^cCalculated according to the Yamaguchi formula: $J = -(E_{\text{triplet}} - E_{\text{BSS}}) / (\langle S^2 \rangle_{\text{triplet}} - \langle S^2 \rangle_{\text{BSS}})$ where BSS = broken-symmetry singlet.

This type of valence tautomerism has been reported before in a Cu(III)phenolate ($S = 0$, lower T) \leftrightarrow Cu(II)-phenoxyl ($S = 1$, higher T) equilibrium in a copper salen complex (Chap I.3.3.). However, the evolution of $[\text{Cr}^{\text{VL}}\text{L}^{\text{C2O2}}(\text{N})]^+$ has shown to be irreversible. This indicates that the formation of the room temperature product $[\mathbf{X}]^+$ involves a chemical transformation of $[\text{Cr}^{\text{VL}}\text{L}^{\text{C2O2}}(\text{N})]^+$ and discredits a simple valence-tautomerism as a possible solution.

As discussed previously in this chapter, metal-nitrido complexes are known to be prone to homocoupling reactions to form N₂. In certain cases, the N₂ molecule was even observed to be “trapped” as a bridging ligand in dimeric complexes.^[272] This type of homocoupling reactivity could produce a Cr(V)=N-N=Cr(V) dimeric species with magnetic coupling between two Cr(V) d^1 metallic centers (**Figure IV.29**).

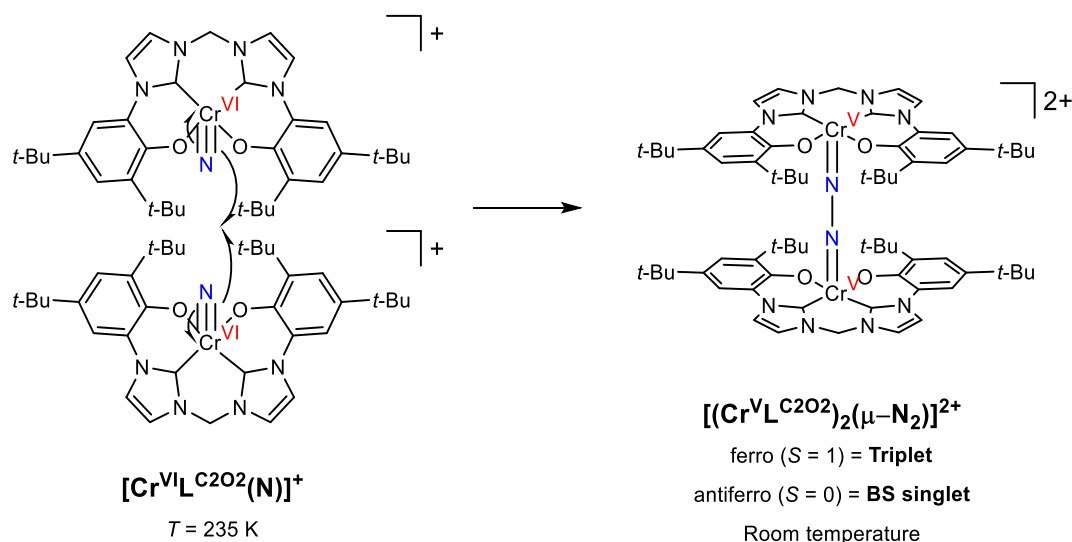


Figure IV.29. Proposed evolution of the $[\text{Cr}^{\text{VI}}\text{L}^{\text{C2O2}}(\text{N})]^+$ cation towards a dimeric $[(\text{Cr}^{\text{V}}\text{L}^{\text{C2O2}})_2(\mu\text{-N}_2)]^{2+}$ complex through homocoupling reactivity.

The theoretical structure of the $[(\text{Cr}^{\text{V}}\text{L}^{\text{C2O2}})_2(\mu\text{-N}_2)]^{2+}$ dimeric complex could only be optimized using the B3LYP functional (6-31G* basis set and CH_2Cl_2 solvent model) compared to other species detailed with the BP86 functional. Analysis of the spin density plot of the triplet and broken-symmetry singlet solutions of the dimer confirmed the presence of two Cr(V) centers, either ferro or antiferromagnetically coupled (**Figure IV.30**). Some significant spin density was calculated on the bridging N atoms. This can be rationalized by the contribution of a resonance form $\text{Cr}(\text{IV})\text{-N}=\text{N}\text{-Cr}(\text{IV})$ to the proposed $\text{Cr}(\text{V})=\text{N}=\text{N}=\text{Cr}(\text{V})$ electronic structure. This statement is supported by the elongated Cr-N bonds (1.818 Å) and short N-N bridging bond (1.16 Å) in the optimized structure.

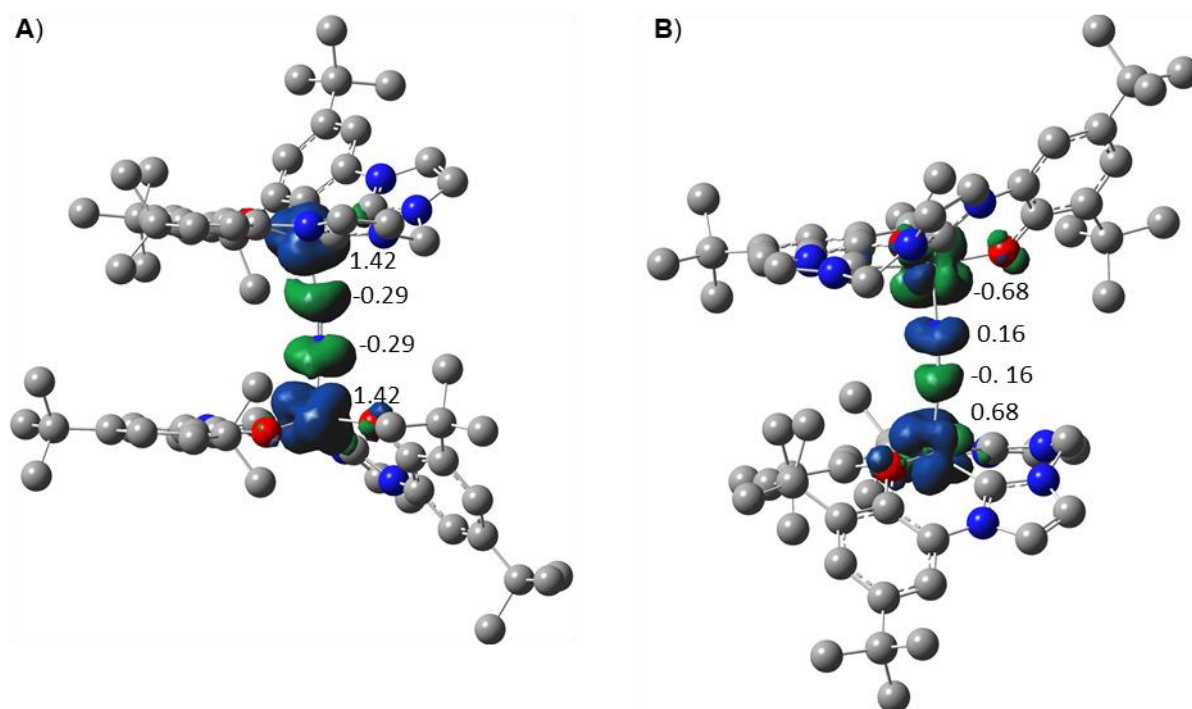


Figure IV.30. Spin density plots (including the main Mulliken spin populations) of the $[(\text{Cr}^{\text{V}}\text{L}^{\text{C2O2}})_2(\mu\text{-N}_2)]^{2+}$ dimer: triplet (A) and broken-symmetry singlet (B) states. From B3LYP/6-31G*/SCRF(CH_2Cl_2) calculations, isoval = 0.005. Hydrogen atoms are omitted for clarity.

We conducted the energetic analysis of the triplet and broken-symmetry singlet solutions to investigate the ground-state of the $[(\text{Cr}^{\text{V}}\text{L}^{\text{C2O2}})_2(\mu\text{-N}_2)]^{2+}$ dimer. The magnetic couplings J were calculated using the Yamaguchi formula.^[287] The results are reported in **Table IV.14**.

Table IV.14. Analysis of the possible electronic structures of the $[(\text{Cr}^{\text{V}}\text{L}^{\text{C2O2}})_2(\mu\text{-N}_2)]^{2+}$ dimer.^a

single point functional	Triplet (kcal.mol ⁻¹) ^b	BS singlet (kcal.mol ⁻¹) ^b	$\langle S^2 \rangle_{\text{triplet}}$	$\langle S^2 \rangle_{\text{BSS}}$	J (cm ⁻¹) ^c
B3LYP	0	+8.1	2.6071	1.3407	+2233
B3LYP-D3	0	+8.1	2.6071	1.3407	+2233
CAMB3LYP	0	+6.8	2.7787	1.6433	+2084
BP86	0	+5.7	2.1897	1.0433	+1725
B3P86	0	+8.0	2.6204	1.4064	+2317

^aOptimized structures using B3LYP/6-31G*/SCRF(CH₂Cl₂) calculations. Unable to converge a singlet solution. ^bRelative energies from single point calculations using the respective functional with TZVP/SCRF(CH₂Cl₂) system. ^cCalculated according to the Yamaguchi formula: $J = -(E_{\text{triplet}} - E_{\text{BSS}}) / (\langle S^2 \rangle_{\text{triplet}} - \langle S^2 \rangle_{\text{BSS}})$ where BSS = broken-symmetry singlet.

The triplet was consistently found to be the ground-state solution across the different functionals used for the single point calculations. The energy gap between the ferro and antiferromagnetically coupled species was also significant (> 5 kcal.mol⁻¹). As a result, a strong ferromagnetic coupling was calculated at approximately +2000 cm⁻¹. These results are inconsistent with the magnetic coupling calculated from variable temperature EPR experiments ($J \approx -6$ cm⁻¹). Thus, even if the $[(\text{Cr}^{\text{V}}\text{L}^{\text{C2O2}})_2(\mu\text{-N}_2)]^{2+}$ dimer might form in solution, it is likely not responsible for the EPR signature of the unknown product $[\text{X}]^+$.

We have previously seen the formation of a putative $\text{Cr}^{\text{IV}}\text{L}^{\text{C2O2}}(\text{O})$ complex that showed to be a triplet at room temperature. We therefore investigated its electronic structure in DFT calculations. We optimized structures for the high-spin (triplet) and low-spin (singlet) state of the $\text{Cr}^{\text{IV}}\text{L}^{\text{C2O2}}(\text{O})$ complex. The energetic analysis of the two solutions showed that the triplet species was the ground-state solution in all cases (**Table IV.15**).

Table IV.15. Energetic analysis of the possible electronic structures of the $\text{CrL}^{\text{C2O2}}(\text{O})$ complex.^a

single-point functional	Triplet (kcal.mol ⁻¹) ^b	Singlet (kcal.mol ⁻¹) ^b
B3LYP	0	+4.6
B3LYP-D3	0	+4.1
CAMB3LYP	0	+5.5
BP86	0	+0.8
B3P86	0	+4.1

^aOptimized structures using BP86/6-31G*/SCRF(CH₂Cl₂) calculations. Broken-symmetry singlets converge to the singlet state. ^bRelative energies from single-point calculations using the respective functional with TZVP/SCRF(CH₂Cl₂) system.

Analysis of the spin-density plot of the triplet state showed the metallic center to bear most of the unpaired electrons (*i.e.* 1.68), thus confirming the presence of a Cr(IV) center in a high-spin configuration (**Figure IV.31**).

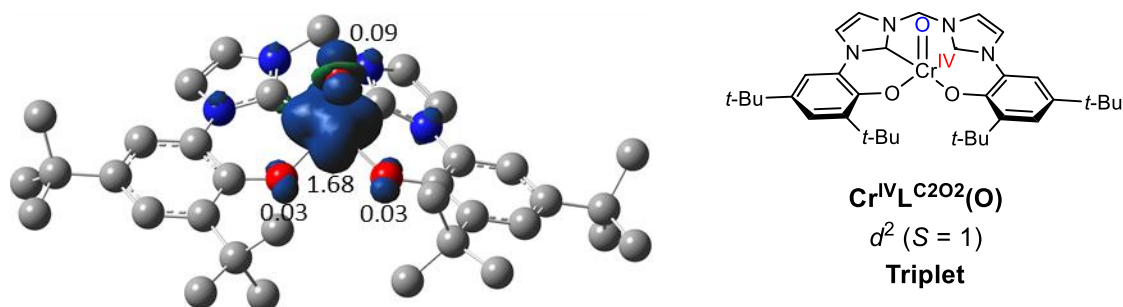


Figure IV.31. Spin density plot of $\text{Cr}^{\text{IV}}\text{L}^{\text{C2O2}}(\text{O})$ with the main Mulliken spin populations (BP86/6-31G*/SCRF(CH_2Cl_2)).

However, the magnetic ground-state is once again incorrect in comparison to our variable temperature EPR experiment. We will therefore require to experimentally characterize the oxo $\text{CrL}^{\text{C2O2}}(\text{O})$ complex after preparation to compare its spectroscopic signature with the UV-vis-NIR and X-band EPR of the unknown product $[\text{X}]^+$.

Other species can be proposed as possible solutions for $[\text{X}]^+$, like other type of oxo or nitrido dimeric complexes resulting from the $[\text{Cr}^{\text{VI}}\text{L}^{\text{C2O2}}(\text{N})]^+$ cation. Nevertheless, any proposed species would require more experimental evidence before theoretical analysis and will thus be investigated in future research.

4. Conclusion

We synthesized a nitridochromium(V) complex $\text{CrL}^{\text{C2O2}}(\text{N})$ that displayed a distorted square pyramidal geometry with a nitrido ligand bound in the apical position. The complex was remarkably stable and did not present intramolecular nitride-NHC coupling reactivity like the manganese $\text{MnL}^{\text{C2O2}}(\text{N})$ analogue. The difference of behavior was probed in theoretical calculations. The nitride-NHC coupling reactions were less energetically accessible and overall endothermic in the chromium complexes. Natural bond order calculations also showed a weaker interaction between the nitrido ligand and the carbenic centers in $\text{CrL}^{\text{C2O2}}(\text{N})$. This difference was partially attributed to the structural differences observed between the manganese and chromium species. The predicted structure of the $\text{MnL}^{\text{C2O2}}(\text{N})$ complex displayed a more compact coordination sphere. This difference resulted in a closer spatial proximity between the nitride and NHC centers in the manganese complex. These theoretical results were all consistent with a more inert chromium complex, as was observed experimentally.

We then investigated the electronic properties of $\text{CrL}^{\text{C2O2}}(\text{N})$ where the complex was shown to exhibit a low and accessible oxidation potential. The one-electron oxidized $[\text{CrL}^{\text{C2O2}}(\text{N})]^+$ cation was obtained chemically and electrochemically at low-temperature. It was assigned as a high-valent Cr(VI) species based on a combination of its electrochemical properties, spectroscopic signatures in X-band EPR and UV-vis-NIR and different theoretical investigations. $[\text{CrL}^{\text{C2O2}}(\text{N})]^+$ evolved irreversibly at room temperature to an unknown product that we labelled as $[\text{X}]^+$. In X-band EPR, $[\text{X}]^+$ showed the signature of an excited triplet state

($S = 1$) populated at room temperature from a singlet ground state with a weak antiferromagnetic coupling of $J \approx -6 \text{ cm}^{-1}$. In non-inert conditions, we observed the formation of an oxo **CrL^{C2O2}(O)** compound based on mass spectrometry experiments. It was assigned as a neutral Cr(IV) complex in high-spin configuration using magnetic susceptibility measurements using Evan's method.

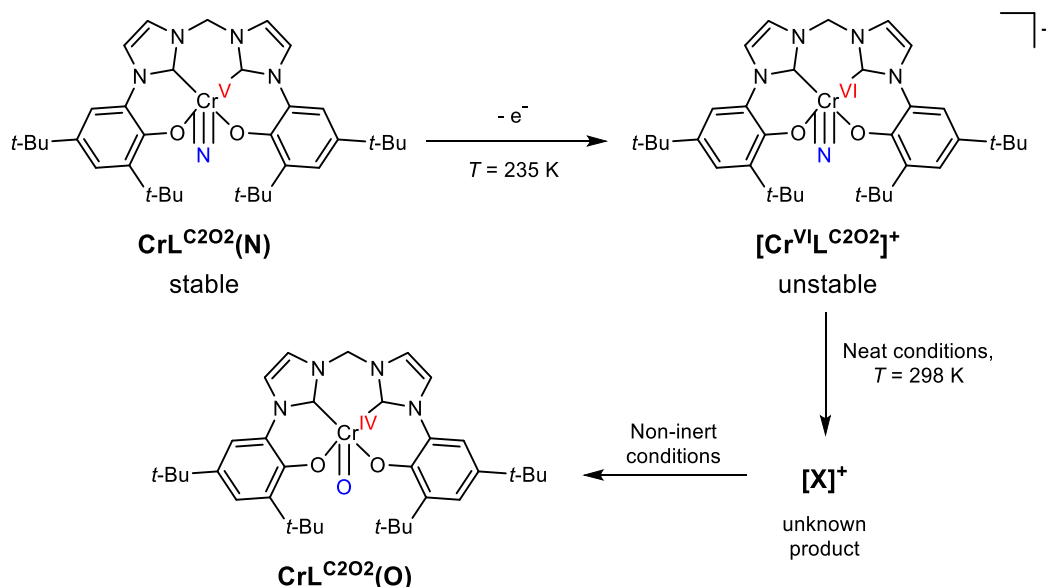


Figure IV.32. Oxidation of the **CrL^{C2O2}(N)** complex and overall evolution of the oxidation products.

The pathway of formation of the **Cr^{IV}L^{C2O2}(O)** compound as well as the nature of the intermediate oxidation product **[X]⁺** are still unknown and will be the subject of further investigations.

Due to limited time, we were unable to investigate the reactivity of neutral **CrL^{C2O2}(N)** and oxidized **[CrL^{C2O2}(N)]⁺** complexes in N-atom transfer reactivity. We postulated previously that the electron-density of the **L^{C2O2}** ligand should improve the nucleophilicity of the nitride moiety when compared to salen frameworks. Preliminary NBO calculations appear to support that statement and our first reactivity investigations will thus focus on different electrophilic partners, including tris(pentafluorophenyl)borane, the trityl cation, or electron-poor olefin substrates.

Chapter V.

Distorted copper salen complexes

1. Introduction	179
2. Synthesis of the ligands and neutral copper complexes	180
3. Crystallographic structure of the ligands and neutral complexes	180
4. Electrochemistry.....	183
5. UV-vis-NIR and EPR spectroscopies of the neutral complexes	186
6. Oxidation protocol and structures of one-electron oxidized complexes	189
7. EPR and magnetic measurements of the cations.....	192
8. UV-vis-NIR investigation of the cations.....	192
9. Theoretical calculations.....	194
10. Catalysis	201
11. Conclusion.....	203

Distorted copper(II) radicals with sterically hindered salens: electronic structure and aerobic oxidation of alcohols.^[86]

1. Introduction

Galactose oxidase (GOase) is an enzyme able to use an organic tyrosinyl radical, in tandem with a mononuclear copper center, to perform two electron oxidation reactions of primary alcohols (**Figure V.1**). The peculiarity of this interplay between metal and redox-active ligand, coupled with the growing need to develop clean oxidation catalysts,^[324] has pushed the design of a number of molecular models to mimic the active site of galactose oxidase and its reactivity.

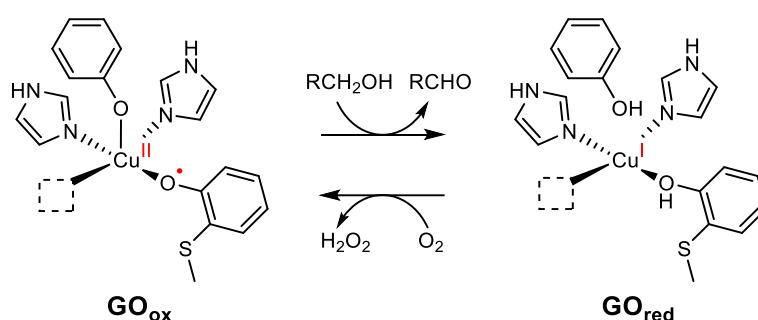


Figure V.1. Aerobic oxidation of primary alcohols by galactose oxidase.

Copper salen complexes are one of the most representative class of mimics and have been explored for their GOase-like reactivity since the late 1990s.^[68,69] Since then, different key factors have been proposed to enhance the reactivity of the copper catalysts. A strong effort has been made to reach low oxidation potentials to facilitate the formation of the active radical species, which was achieved by tuning the electronics of the phenolate *para* substituents.^[76,87] Back in 1996 and the first report of catalytic oxidation of alcohols by copper salen complexes, Stack and coworkers also postulated that the stabilization of the Cu(I) reduced state could have a determining impact on the activity of copper models of GOase.^[69] Indeed a minimal structural reorganization is required to have an efficient shuttling between the copper(II)-radical oxidized and the copper(I) reduced states in the catalytic cycle. An effort was thus made to stabilize the copper ion in strongly distorted tetracoordinated geometries based on the copper tendency to adopt a tetrahedral geometry in its (+I) oxidation state. While other classes of ligands used to develop GOase models can naturally propose a distorted coordination to the copper ion, the salen framework usually favors a square planar geometry, more suited to stabilize copper(II) complexes. This planar structure is favored in the reference salen complexes featuring ethylene or cyclohexylidene spacers due to planar 5-membered [CuNCCN] chelate rings (**Figure V.2.A**).

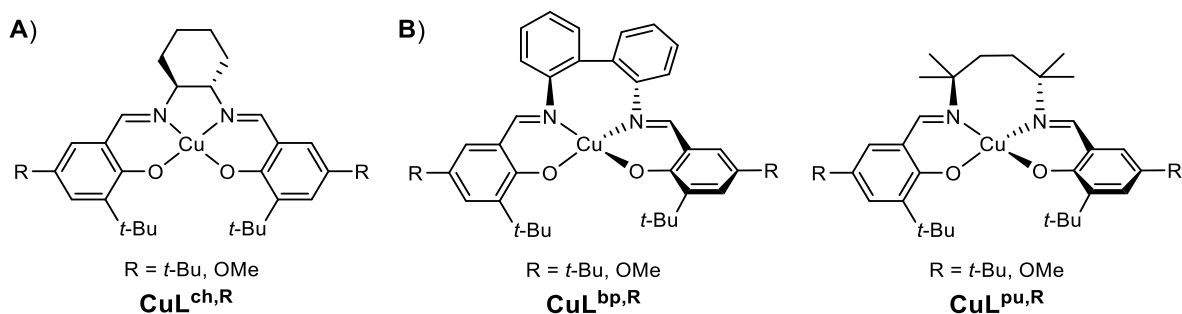


Figure V.2. Representative copper salen models of galactose oxidase: reference salen complexes $\text{CuL}^{\text{ch},\text{R}}$ (A) and structures of the distorted copper complexes $\text{CuL}^{\text{bp},\text{R}}$ and $\text{CuL}^{\text{pu},\text{R}}$ discussed in this chapter (B).

To enforce a distortion of the metal center, we developed two new series of ligands bearing putrescine or biphenyl diamine linkers connected to sterically hindered and electron rich salicylidene peripheral rings. We synthesized the respective copper complexes and studied their one-electron oxidized species. We finally investigated their reactivity towards aerobic oxidation of different alcohol substrates.

2. Synthesis of the ligands and neutral copper complexes

The synthesis of ligand $\text{H}_2\text{L}^{\text{bp},t\text{Bu}}$, alongside its copper complex, were previously reported by Wang *et al.* in 2014.^[325] The other ligands were obtained by a classical Schiff base condensation of either diamine bridge with 2 molar equivalents of the relevant salicylaldehyde derivative. The ligands were chelated to the copper(II) salt by mixing a dichloromethane solution of the salen ligand (1 equiv.) with a methanol solution of copper(II) acetate monohydrate (1.1 equiv.) in the presence of triethylamine (2 equiv.). The solutions were stirred under reflux for a couple hours and then concentrated under reduced pressure. The neutral copper complexes were finally obtained after recrystallization at low temperature.

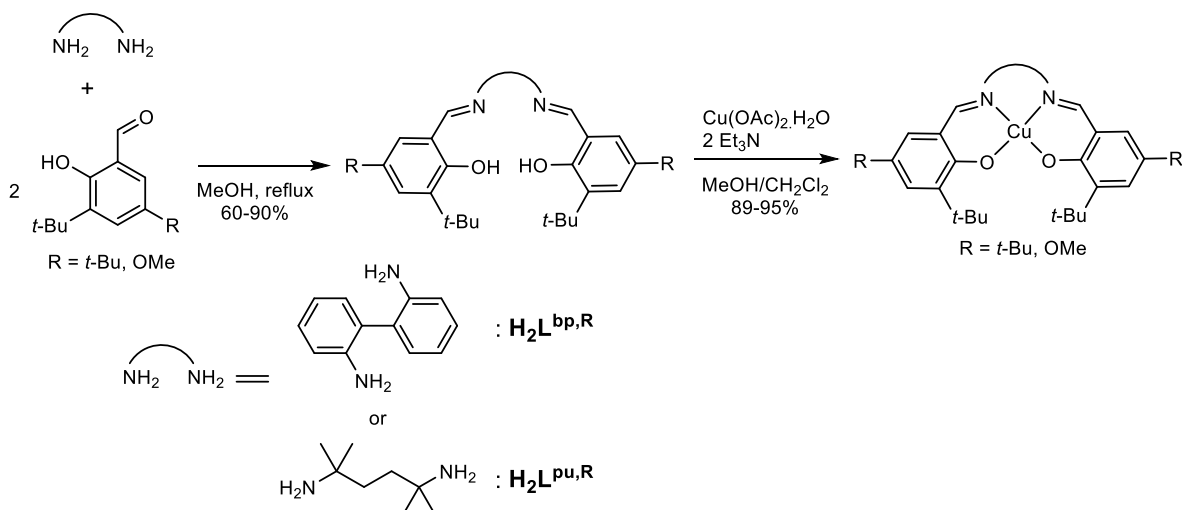


Figure V.3. General synthesis of the salen ligands and their copper complexes.

3. Crystallographic structure of the ligands and neutral complexes

Single crystals suitable for X-Ray diffraction were obtained for ligands $\text{H}_2\text{L}^{\text{bp},\text{OMe}}$ and $\text{H}_2\text{L}^{\text{pu},t\text{Bu}}$ by slow evaporation of saturated methanol solutions. In each crystallographic structure, the

phenolic protons form hydrogen bonds with the adjacent imine N atom, with short O...N distances from 2.534 to 2.581 Å. The bridge of each ligand strongly influences the orientation of the phenolic arms. In the case of **H₂L^{bp,OMe}**, the biphenyl spacer is largely distorted, with a dihedral angle of 62° between its two aromatic rings, due to steric clash of the *ortho* aromatic hydrogens. Due to the extended conjugation of the salicylidene groups, the two phenol moieties are positioned close to each other, with a 4.27 Å distance between their centroids. They also engage in weak intramolecular pi-stacking interactions at the solid state, as can be judged by a small angle of 19° between the two phenolic planes. In the case of **H₂L^{pu,tBu}**, the flexibility of the putrescine bridge allows for a linear structure in the solid state to minimize steric clash. The two peripheral rings are maximally separated by a distance of 13.5 Å between their centroids.

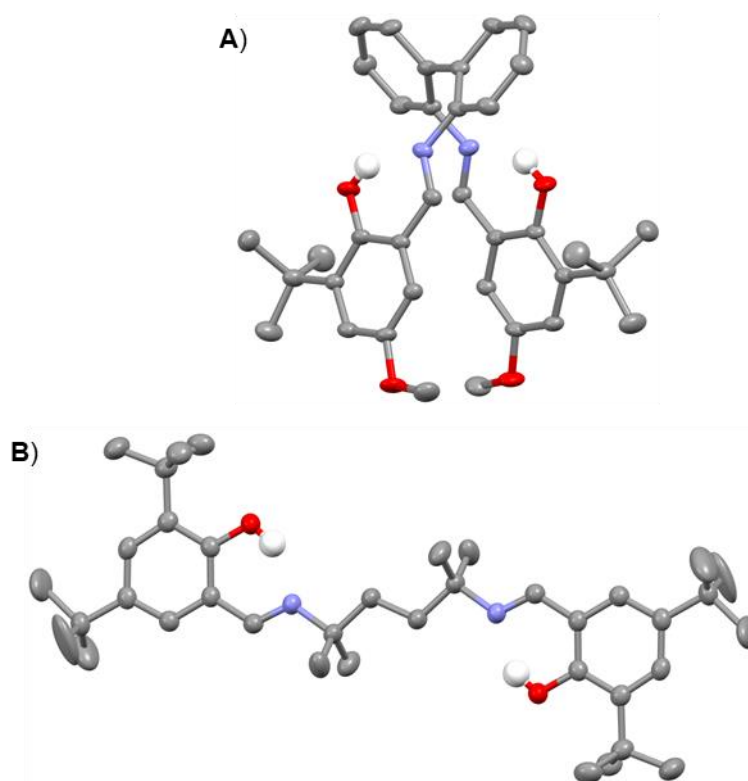


Figure V.4. X-ray crystal structures of the ligands: **H₂L^{bp,OMe}** (A) and **H₂L^{pu,tBu}** (B). The hydrogen atoms apart of the phenolic protons are omitted for clarity.

Single crystals suitable for X-ray diffraction were obtained for all four neutral copper(II) salen complexes. The complexes **CuL^{pu,tBu}** and **CuL^{pu,OMe}** of the putrescine spacer series were obtained by slow evaporation of saturated methanol solutions. Complexes of the biphenyl diamine spacer series were crystalized by slow evaporation of concentrated pentane and dichloromethane solutions for **CuL^{bp,tBu}** and **CuL^{bp,OMe}** respectively. In all complexes, the copper ion is coordinated by two oxygen atoms (O1 and O2) of the phenolate arms and the nitrogen atoms (N1 and N2) of the two imine groups.

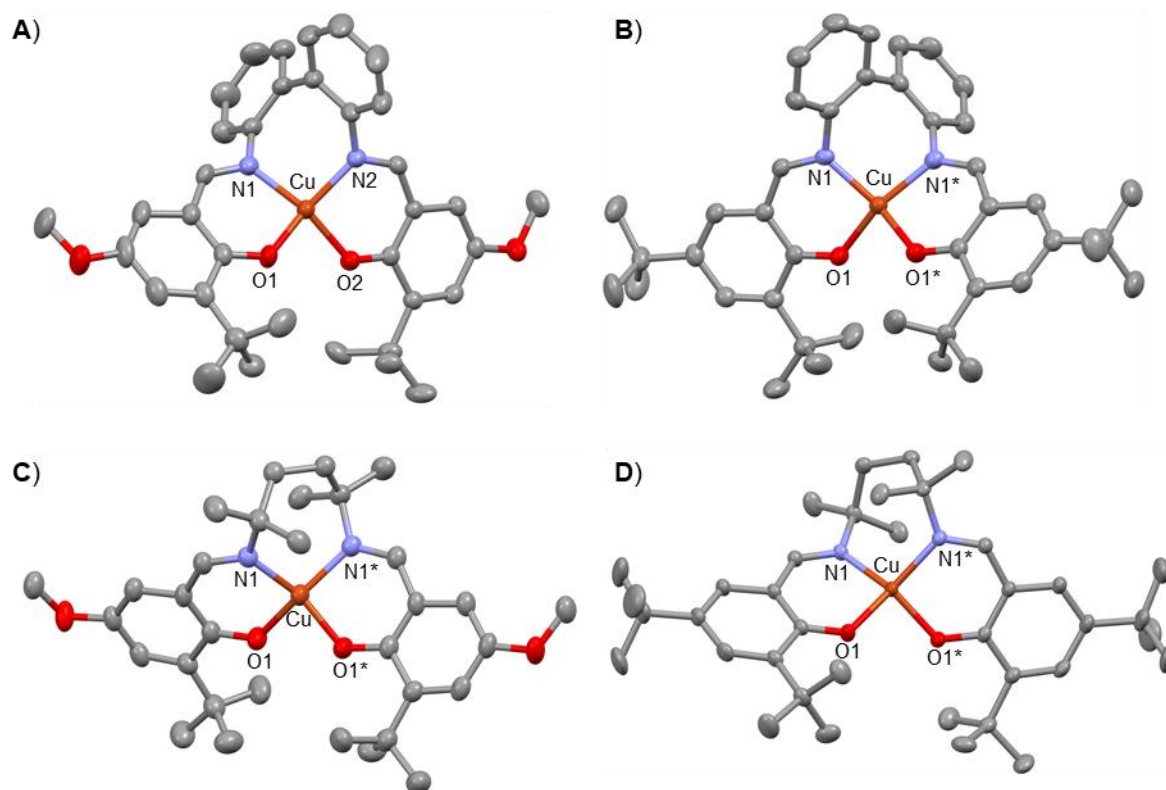


Figure V.5. Structures of the neutral copper complexes: **CuL^{bp,tBu}** (A) **CuL^{bp,OMe}** (B) **CuL^{pu,tBu}** (C) and **CuL^{pu,OMe}** (D). The hydrogen atoms are omitted for clarity.

The coordination sphere of the metal appears to be barely affected by the phenolate *para* substituents along the pair of complexes of the same bridge (putrescine or biphenyl diamine). Both the coordination bond distances and the geometry of the copper ions are reported in **Table V.1**. They are highly similar between complexes of the same series.

Table V.1. Coordination distances and geometry of the neutral complexes.^a

complex	Cu-O1	Cu-O2	Cu-N1	Cu-N2	τ_4
CuL^{bp,OMe}	1.895(3)	1.880(3)	1.946(5)	1.953(4)	0.37
CuL^{bp,tBu}	1.885(2)	1.894(2)	1.959(3)	1.951(3)	0.40
CuL^{pu,OMe}	1.892(2)	1.892(2)	1.972(3)	1.972(3)	0.46
CuL^{pu,tBu}	1.896(1)	1.896(1)	1.958(1)	1.958(1)	0.54
[CuL^{bp,OMe}] ⁺	1.926(2)	1.926(2)	1.965(3)	1.965(3)	0.22
[CuL^{pu,OMe}] ⁺	1.911(3)	1.904(3)	1.957(3)	1.954(3)	0.44

^aBond distances in Å. $\tau_4 = \frac{360^\circ - (\alpha + \beta)}{141^\circ}$ where α and β are the two greatest angles of coordination.

CuL^{bp,OMe} is slightly dissymmetric with coordination bond distances Cu-O1, Cu-N1, Cu-O2 and Cu-N2 of 1.895, 1.880, 1.946 and 1.953 Å respectively. **CuL^{bp,tBu}** has fairly comparable coordination sphere with Cu-O1, Cu-N1, Cu-O2 and Cu-N2 of 1.885, 1.894, 1.959 and 1.951 Å respectively. The dihedral angle between the two aromatic rings of the biphenyl spacer is 59 and 58° for **CuL^{bp,tBu}** and **CuL^{bp,OMe}** respectively. This distortion of the biphenyl bridge is similar to that observed for the **H₂L^{bp,OMe}** free ligand (62°). This shows that the distorted copper

coordination is directly impacted by the linker.^[326] The geometry of copper ions in a four coordinate complex can be estimated by the structural index τ_4 , first proposed by Houser in 2007.^[327] τ_4 is defined by equation (11) where α and β are the two greatest angles of coordination:

$$(11) \quad \tau_4 = \frac{360^\circ - (\alpha + \beta)}{141^\circ}$$

A perfect square planar geometry is defined by a τ_4 of 0, whereas a perfect tetrahedral coordination has a τ_4 of 1. Complexes **CuL^{bp,OMe}** and **CuL^{bp,tBu}** have a τ_4 index of 0.37 and 0.40 respectively, which shows a significantly larger distortion in comparison to the reference copper salen complexes featuring ethylene ($\tau_4 = 0.05$)^[328] and cyclohexylidene ($\tau_4 = 0.04$ -0.10) spacers.^[76,328] The τ_4 indexes are even higher than other copper complexes using sterically hindered or elongated spacers like binaphthyl ($\tau_4 = 0.30$)^[68] or propylidene ($\tau_4 = 0.31$)^[329] linkers. They are nevertheless pretty close to that reported for the copper complex with unsubstituted phenols with the same biphenyl spacer ($\tau_4 = 0.38$).^[326] This is once again indicative that the phenolate *para* substituents have a limited structural impact when compared to the large influence of the bridging unit.

In the putrescine bridge series, both **CuL^{pu,tBu}** and **CuL^{pu,OMe}** are centrosymmetric at the copper center. The coordination bond distances compares well between the two complexes, with Cu-O1* and Cu-N1* bonds of 1.896 and 1.958 Å for **CuL^{pu,tBu}** and 1.892 and 1.972 Å for **CuL^{pu,OMe}**. The two compounds present an even higher tetrahedral distortion than the complexes using the biphenyl bridge, with τ_4 indexes of 0.54 and 0.47 for **CuL^{pu,tBu}** and **CuL^{pu,OMe}** respectively. Nevertheless, their geometry is only slightly more distorted than a complex featuring an unsubstituted 4-atom linker ($\tau_4 = 0.44$).^[330] This suggests that the methylene substituted groups of the putrescine bridge has only a marginal structural impact, and that the tetrahedral distortion is mainly imposed by the elongation of the linker chain.

Overall, X-ray diffraction of all four complexes show that the copper(II) ion adopts a desired intermediate geometry between square planar and tetrahedral in every case.

4. Electrochemistry

The electronic properties of the ligands and of copper(II) complexes were investigated by cyclic voltammetry using CH₂Cl₂ solutions containing 0.1 M tetrabutylammonium perchlorate as supporting electrolyte. Both **H₂L^{pu,OMe}** and **H₂L^{pu,tBu}** ligands displayed a monoelectronic quasi reversible oxidation wave (**Figure V.7.A**). This redox system was assigned as a phenoxyl-iminium/phenol-imine redox couple, which is an oxidation coupled with a proton transfer (**Figure V.6**).^[328] **H₂L^{pu,tBu}** presented a significantly higher potential at $E_{1/2} = 0.52$ V vs Fc⁺/Fc (compared to 0.32 V for **H₂L^{pu,OMe}**) as can be expected by the weaker electron-donating properties of the *tert*-butyl group compared to the methoxy substituent.

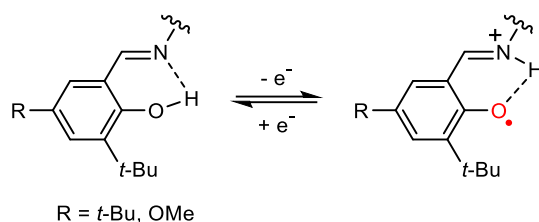


Figure V.6. Oxidation of a hydrogen bonded phenol in the salicylidene pattern.

The redox waves of the biphenyl derivatives **H₂L^{bp,OMe}** and **H₂L^{bp,tBu}** were further anodically shifted compared to the putrescine species and presented only poorly reversible or irreversible oxidation systems (**Figure V.7**). This was once again rationalized by the weaker electron-donating properties of the aromatic biphenyl diamine linker compared to the putrescine bridge. Both the high oxidation potentials and irreversibility of the redox systems show that the free biphenyl ligands are not sufficiently electron-rich to stabilize the phenoxyl radical after oxidation.

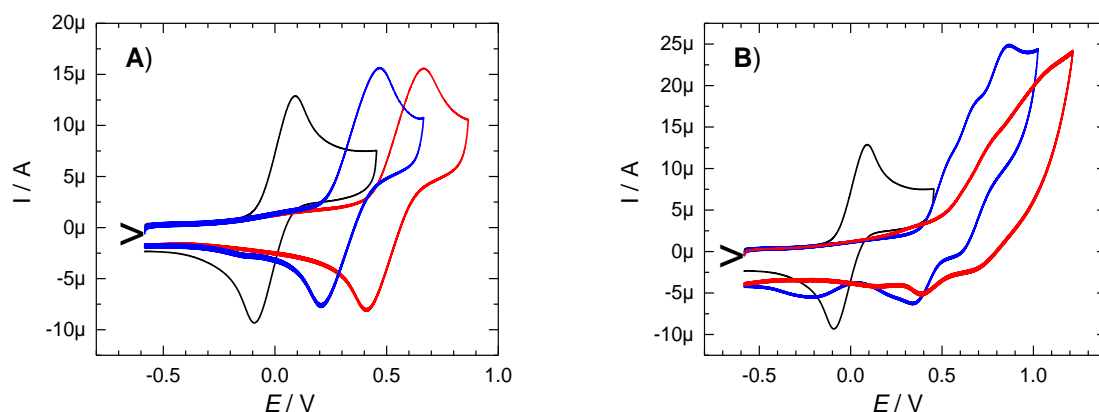


Figure V.7. CV curves of 0.44 mM CH_2Cl_2 solutions (containing 0.1 M TBAP as supporting electrolyte). Ligands of the putrescine series: **H₂L^{pu,OMe}** (blue) **H₂L^{pu,tBu}** (red) and ferrocene (black) (**A**). Ligands of the biphenyl diamine series: **H₂L^{bp,OMe}** (blue) **H₂L^{bp,tBu}** (red) and ferrocene (black) (**B**). $T = 298\text{ K}$, vitreous carbon electrode, scan rate: 100 mV/s. Potentials given versus the Fc^+/Fc reference.

The electrochemical data of the neutral copper(II) complexes are reported in **Table V.2**. Complex **CuL^{bp,OMe}** presented two quasi-reversible oxidation waves at $E_{1/2}^{\text{ox1}} = 0.34$ and $E_{1/2}^{\text{ox2}} = 0.53\text{ V}$ versus the ferrocene reference (**Figure V.8.A**). The two redox systems were both attributed to ligand-centered oxidations to form phenoxyl radicals. Interestingly, the complex also displayed a quasi-reversible reduction wave at -1.50 V , which was assigned to the $\text{Cu(II)}/\text{Cu(I)}$ redox couple.^[331] The **CuL^{bp,tBu}** derivative showed a similar oxidation behavior than its methoxy counterpart but with anodically shifted waves, in accordance with the weaker electron-donating properties of the *tert*-butyl group (**Figure V.8.B**). Its reduction wave was pretty comparable to the one of **CuL^{bp,OMe}** at $E_{1/2}^{\text{red}} = -1.55\text{ V}$. This indicates that this redox couple is only marginally impacted by the electronic properties of the ligand and further supports its assignment as a metal-centered reduction process.

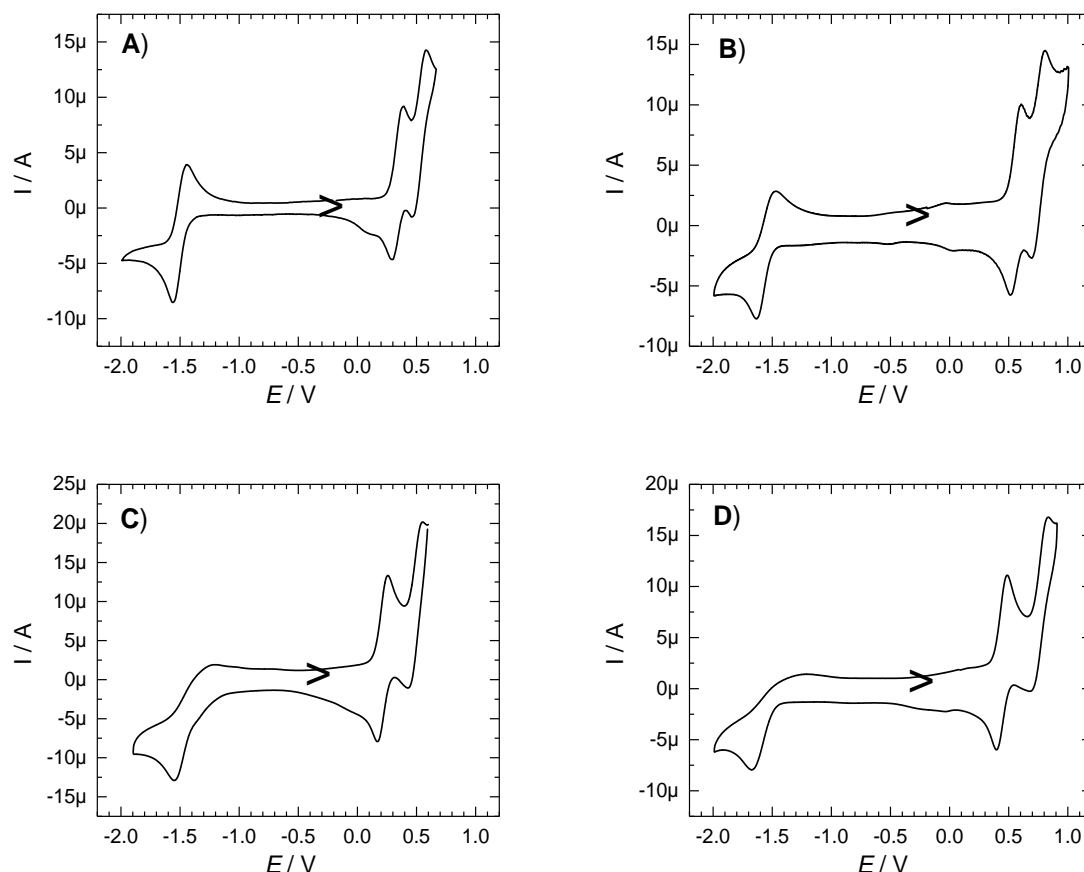


Figure V.8. CV curves of 0.5 mM solutions (+0.1 M TBAP) of **CuL^{bp,OMe}** (A) **CuL^{bp,tBu}** (B) **CuL^{pu,OMe}** (C) and **CuL^{pu,tBu}** (D). $T = 298$ K, vitreous carbon electrode, scan rate: 100 mV/s. Potentials given versus the Fc^+/Fc reference.

Complex **CuL^{pu,OMe}** also showed two quasi-reversible oxidation events at $E_{1/2}^{\text{ox1}} = 0.22$ and $E_{1/2}^{\text{ox2}} = 0.50$ V (**Figure V.8.C**). The oxidation potentials were compared to **CuL^{bp,OMe}** and other copper salens bearing 2-*tert*-butyl-4-methoxyphenolate peripheral rings. **CuL^{pu,OMe}** showed a significantly cathodically shifted first oxidation wave in comparison to **CuL^{bp,OMe}** ($E_{1/2}^{\text{ox1}} = 0.34$ V). The oxidation potential is more within range of values reported for other copper salens complexes with aliphatic linker chains like ethylidene or propylidene ($E_{1/2}^{\text{ox1}} = 0.26$ V).^[329] This suggests that the distortion at the copper ion has a negligible impact on the first oxidation potential. Rather, this is indicative of the stronger electron-donating properties of the aliphatic putrescine linker in **CuL^{pu,OMe}** when compared to the aromatic biphenyl bridge in **CuL^{bp,OMe}**. **CuL^{pu,OMe}** displayed a reduction wave that was nevertheless much less reversible than in the complexes bearing the biphenyl bridge. The difference in behavior between the two series might arise from the flexibility of the putrescine linker that could lead to a slower reorganization after reduction. **CuL^{pu,tBu}** displayed a similar oxidation behavior than its methoxy analogue but the oxidation events were once again anodically shifted (**Figure V.8.D**).

The anodic shifts from the methoxy-substituted complexes to their *tert*-butyl counterpart were highly similar between the two series of complexes. The first oxidations were both shifted by +0.22 V and the second redox events were shifted by +0.22 V from **CuL^{bp,OMe}** to **CuL^{bp,tBu}** and by +0.26 V from **CuL^{pu,OMe}** to **CuL^{pu,tBu}**.

Table V.2. Electrochemical data of the neutral copper(II) salen complexes.^a

complex	$E_{1/2}^{\text{red}}$ (ΔE)	$E_{1/2}^{\text{ox1}}$ (ΔE)	$E_{1/2}^{\text{ox2}}$ (ΔE)	$\Delta E_{1/2}^{\text{ox}}$
CuL^{bp,OMe}	-1.50 (0.11)	0.34 (0.09)	0.53 (0.12)	0.19
CuL^{bp,tBu}	-1.55 (0.17)	0.56 (0.09)	0.75 (0.11)	0.19
CuL^{pu,OMe}	-1.68 ^b	0.22 (0.09)	0.50 (0.10)	0.28
CuL^{pu,tBu}	-1.55 ^b	0.44 (0.09)	0.76 (0.15)	0.22
CuL^{ch,OMe} ^c	N.d.	0.28	0.44	0.16
CuL^{ch,tBu} ^d	N.d.	0.45	0.65	0.20

^aThe potentials are given at 293 K and referenced to the Fc⁺/Fc redox couple (0.19 V vs Ag/AgNO₃ 0.01 M and $\Delta E_p = 0.08$ V under our experimental conditions). In 0.5 mM CH₂Cl₂ solutions (+ 0.1 M TBAP); scan rate: 100mV/s. ^bIrreversible process. The Epc value is given instead. ^cAs reported in reference [76]. ^dAs reported in reference [74].

As was previously detailed in Chapter II, the electrochemical properties of complexes bearing two redox-active phenolate rings can give us some insight on the electronic communication between the two redox centers. Assuming the two oxidation events to be ligand-centered, the difference in oxidation potentials ($\Delta E_{1/2}^{\text{ox}} = E_{1/2}^{\text{ox2}} - E_{1/2}^{\text{ox1}}$) allows us to compare the degree of delocalization of the ligand radical obtained after one electron oxidation. A larger $\Delta E_{1/2}$ is representative of a stronger electronic coupling, with a greater delocalization of the phenoxyl radical. The electrochemical data therefore suggest that the delocalization of the radical, and thus its mixed-valent character, would be the largest in the case of the one-electron oxidized [CuL^{pu,OMe}]⁺.

5. UV-vis-NIR and EPR spectroscopies of the neutral complexes

The absorption spectra of the neutral complexes displayed typical features of copper(II)-salen species in the visible region (**Figure V.9**, black spectra). Metal $d \rightarrow d$ transitions were observed as weak excitations ($\epsilon < 700 \text{ M}^{-1} \cdot \text{cm}^{-1}$) at low energy ($< 16\,000 \text{ cm}^{-1}$). They were observed at 15400 and 15 700 cm^{-1} for the biphenyl complexes **CuL^{bp,OMe}** and **CuL^{bp,tBu}** respectively. Due to the different coordination environment, the transitions were significantly red-shifted for **CuL^{pu,OMe}** and **CuL^{pu,tBu}** with energies of 14 700 and 14 400 cm^{-1} respectively. As expected from their metallic character, they were only barely affected by the electronic properties of the phenolate *para* substituents.

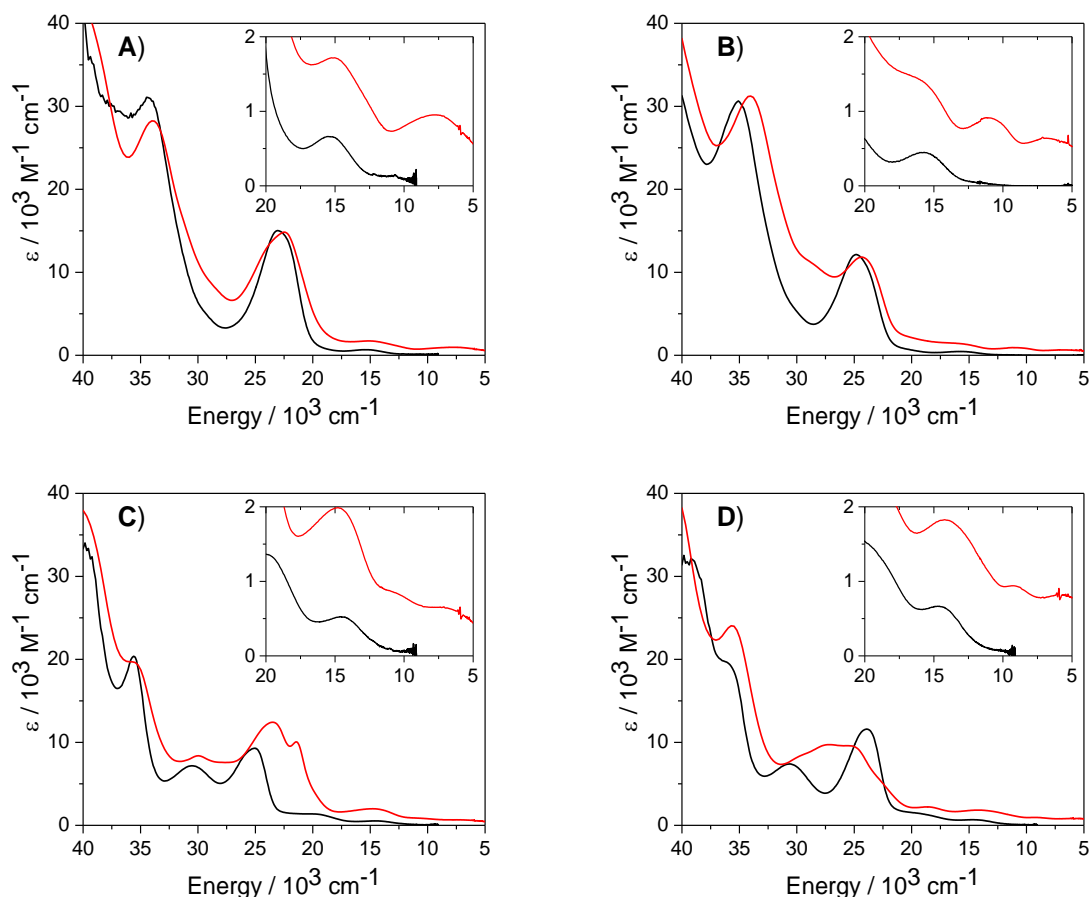


Figure V.9. UV-Vis-NIR spectra of **CuL^{bp,OMe}** (A) **CuL^{bp,tBu}** (B) **CuL^{pu,OMe}** (C) and **CuL^{pu,tBu}** (D). CH₂Cl₂ solutions (+0.1 M TBAP) of neutral complexes (black) and one-electron electrochemical oxidations (red). *T* = 298 K.

All complexes also displayed an intense band ($\epsilon > 9\,000\text{ M}^{-1}\cdot\text{cm}^{-1}$) at higher energies (23 000–26 000 cm^{-1}). Contrary to the $d \rightarrow d$ transitions, a significant blue shift was observed when changing from the methoxyl substituted complexes (**CuL^{bp,OMe}**, **CuL^{pu,OMe}**) to the *tert*-butyl analogues (**CuL^{bp,tBu}**, **CuL^{pu,tBu}**). The difference in energy was +1800 cm^{-1} in the biphenyl complexes and +1200 cm^{-1} in the putrescine series. This notable shift indicated the involvement of ligand orbitals in the electronic transition. Therefore, the bands were attributed to a mix of intraligand and ligand to metal charge transfers (IL/LMCT). The UV-vis-NIR absorption data are reported in **Table V.3**.

Table V.3. UV-vis-NIR data of the copper complexes.^a

complex	λ_{\max} [cm ⁻¹] (ϵ [M ⁻¹ .cm ⁻¹])
CuL^{bp,OMe}	34500 (31100), 23000 (15000), 15400 (700)
CuL^{bp,tBu}	35100 (30 600), 24800 (12100), 5700 (400)
CuL^{pu,OMe}	35500 (18500), 30600 (7400), 23900 (11600), 14700 (700)
CuL^{pu,tBu}	35 600 (20 400), 30 500 (7200), 25 100 (9300), 19400 (1300), 14 400 (520)
[CuL^{bp,OMe}]⁺	34000 (28200), 22500 (14800), 15200 (1700), 7800 (1000)
[CuL^{bp,tBu}]⁺	34000 (31200), 24400 (11800), 11200 (900), 7100 (700)
[CuL^{pu,OMe}]⁺	35500 (19600), 29900 (8400), 23500 (12400), 21500 (10000), 14800 (2000), 7100 (700)
[CuL^{pu,tBu}]⁺	35700 (24000), 27200 (9700), 25200 (9600), 18700 (2200), 14200 (1800), 9400 (900), 5700 (800)

^aIn CH₂Cl₂ solutions containing 0.1 M TBAP. Molar extinction coefficients were calculated from the concentration of complex before electrolysis.

The X-band EPR spectra of the neutral copper(II) salen complexes were also recorded. The spectra of all four complexes displayed characteristic features of axial copper(II) (d^9 , $S = 1/2$) systems. This showed that the complexes were also mononuclear in solution and were isolated spin systems. Their spin Hamiltonian parameters were obtained from spectra simulation and are reported in **Table V.4**. The copper center itself holds a nuclear spin of 3/2 that gives rise to a 4-line hyperfine splitting, which is most apparent in the low-field component (g_{\parallel}) of the axial system. Additional superhyperfine couplings with the two neighboring ¹⁴N nuclei of the coordinating imine groups were also observed on the high-field component (g_{\perp}).

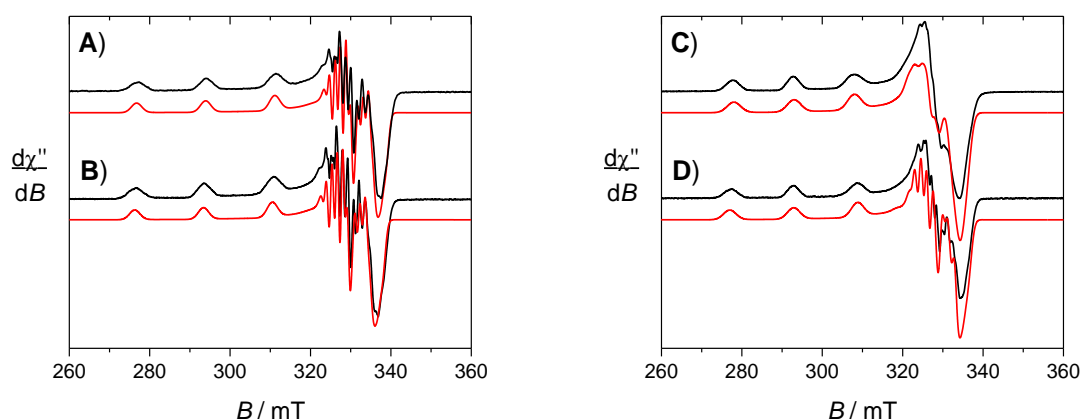


Figure V.10. X-band EPR spectra of the neutral complexes in 0.5 mM CH₂Cl₂ solutions (+ 0.1 M TBAP): **CuL^{bp,OMe}** (A) **CuL^{bp,tBu}** (B) **CuL^{pu,OMe}** (C) and **CuL^{pu,tBu}** (D). Experimental spectra (black) and simulated (red) using parameters given in **Table V.4**. Microwave frequency 9.42 GHz, power 1.1 mW; mod. frequency 100 kHz, amp. 0.3 mT; $T = 100$ K.

Table V.4. Spin Hamiltonian parameters of the neutral complexes.^a

complex	g_{\parallel}, g_{\perp}	A_{\parallel}, A_{\perp} (MHz)	$g_{\parallel}/A_{\parallel}$ (cm)
CuL^{bp,OMe}	2.232, 2.048	533, 50 ^b	125
CuL^{bp,tBu}	2.231, 2.047	536, 49 ^b	125
CuL^{pu,OMe}	2.238, 2.053	498, 48 ^c	135
CuL^{pu,tBu}	2.242, 2.052	470, 51 ^c	143

^aIn CH₂Cl₂ solutions containing 0.1 M TBAP. Values extracted from spectral simulations. ^bAn additional superhyperfine coupling of 38 MHz is observed for two equivalent ¹⁴N nuclei (A_{\perp}). ^cAn additional superhyperfine coupling of 40 MHz is observed for two equivalent ¹⁴N nuclei (A_{\perp}).

The EPR parameters of **CuL^{bp,OMe}** and **CuL^{bp,tBu}** were highly similar within the accuracy of the simulation. This behavior is rather expected in the case of such constrained systems because the phenol *para* substituents are too distant to the copper center to have a significant influence. Nevertheless, the linker itself had a profound effect on the g_{\parallel} and A_{\parallel} tensors. These parameters are known to be correlated to the coordination geometry of the metal ion. Their ratio $g_{\parallel}/A_{\parallel}$ has been used to measure the tetrahedral distortion in four-coordinate copper(II) complexes, where the higher the $g_{\parallel}/A_{\parallel}$ value the larger the distortion is.^[332] Among our four complexes the putrescine complexes presented the largest $g_{\parallel}/A_{\parallel}$ values with 135 and 143 cm for **CuL^{pu,OMe}** and **CuL^{pu,tBu}** respectively, compared to 125 cm for both **CuL^{bp,OMe}** and **CuL^{bp,tBu}**. Therefore, the larger tetrahedral distortion observed in the solid state for the putrescine bridge complexes over the biphenyl species is also respected in frozen solutions.

6. Oxidation protocol and structures of one-electron oxidized complexes

Mono-oxidized species were generated quantitatively, either by coulometry-controlled bulk electrolysis at +0.4 to 0.6 V at low temperature (233 K) or by chemical oxidation using a slight excess of silver hexafluoroantimonate oxidant on CH₂Cl₂ solutions of the neutral complexes. Both methods afforded the same results, indicated by the appearance of an intense dark color upon oxidation. It is worth noting that [**CuL^{bp,tBu}**]⁺ did not undergo a clean chemical oxidation by the silver hexafluoroantimonate oxidant ($E_{1/2}$ Ag⁺/Ag = 0.65 V vs Fc⁺/Fc in CH₂Cl₂)^[317] due to its high oxidation potential ($E_{1/2}^{\text{ox1}} = 0.56$ V). The chemically generated methoxy substituted cations [**CuL^{bp,OMe}**]⁺(SbF₆⁻) and [**CuL^{pu,OMe}**]⁺(SbF₆⁻) were remarkably stable in solution and they were isolated as single crystals by vapor diffusion of pentane into the concentrated CH₂Cl₂ solutions. All attempts to crystalize the *tert*-butyl derivatives only afforded crystals of the starting neutral complexes, which is attributed to the lower stability of the radicals due to the lower ligand electron-density.

The copper ion in [**CuL^{bp,OMe}**]⁺(SbF₆⁻) is a symmetry center making the opposite Cu-O and Cu-N bonds equivalent, with coordination bond distances of 1.926 and 1.965 Å respectively (**Table V.1**). Two oxygens from methoxy *para* substituents of neighboring complexes are also interacting from the axial positions with the copper center. They are located at 2.763 Å above and below the mean square plane, forming a structure best represented as an elongated octahedral complex with strong Jahn-Teller distortion (**Figure V.11.A**). This environment is unusual for mono-oxidized copper salen complexes which are usually four-coordinate and not involved in intermolecular interactions. The dihedral angle between the two aromatic rings of

the biphenyl linker is of 56° , which is closely similar to the structure of both the neutral precursor $\text{CuL}^{\text{bp,OMe}}$ and the free ligand. However, the τ_4 index (0.21) is significantly smaller in $[\text{CuL}^{\text{bp,OMe}}]^+$ compared to the neutral complex, which indicates a decreased tetrahedral distortion in the tetradentate ligand after oxidation. This effect was also observed for ethylene and propylene bridged copper complexes.

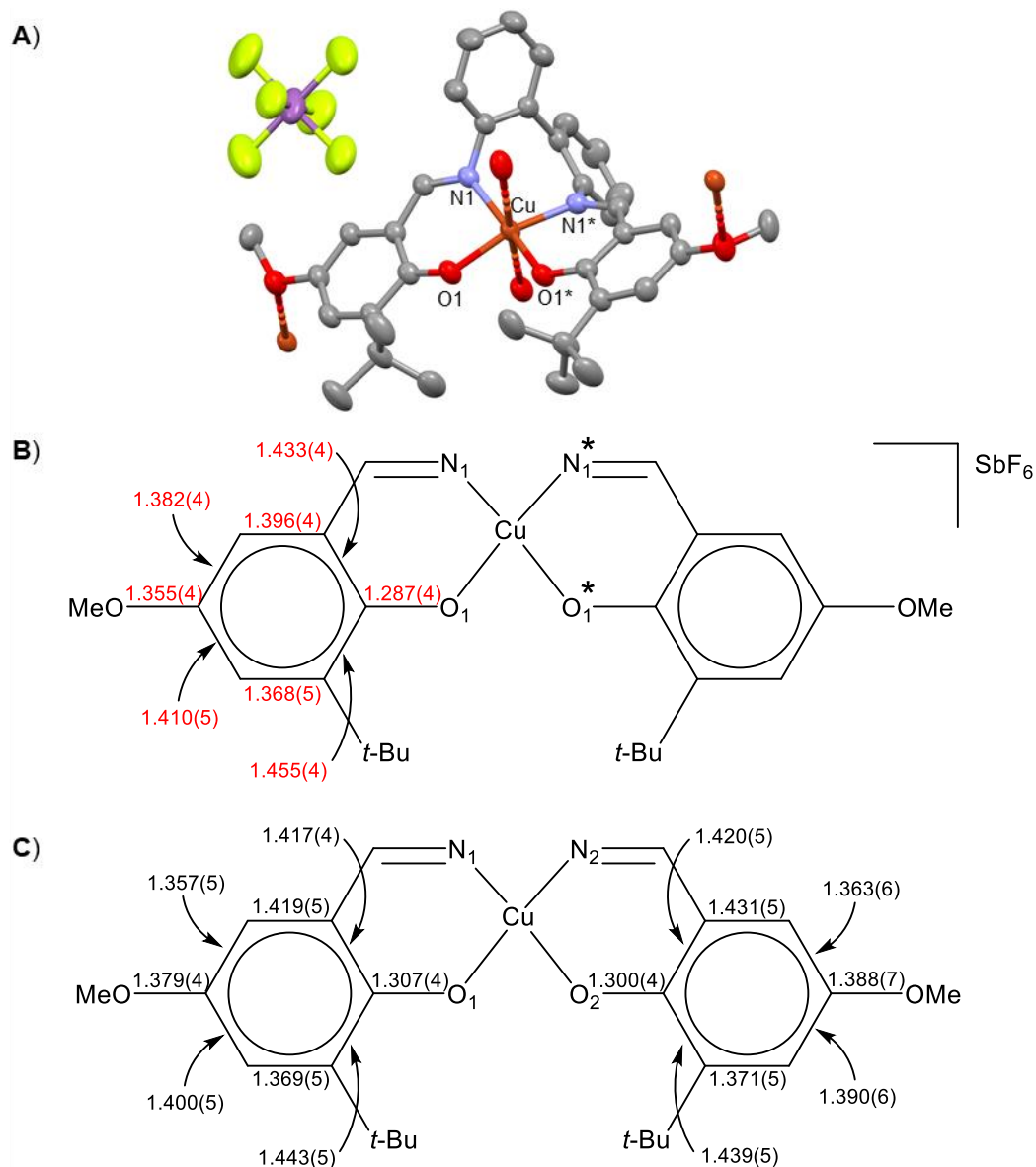


Figure V.11. Structural analysis of $[\text{CuL}^{\text{bp,OMe}}]^+$: X-ray structure (A), phenolic bond distances in $[\text{CuL}^{\text{bp,OMe}}]^+$ (B) and comparison with the neutral precursor $\text{CuL}^{\text{pu,OMe}}$ (C). The bond distances are given in Å. For (A), the intermolecular short contacts between the copper ions and the methoxy oxygen atoms are highlighted (hydrogens are omitted for clarity).

The coordination sphere was expanded after oxidation when compared to the neutral complex, with longer Cu-O (1.926 Å vs 1.895 and 1.820 Å) and Cu-N bonds (1.965 Å vs 1.946 and 1.953 Å). This demonstrates the weaker donating properties of the ligand after oxidation and is consistent with the formation of a phenoxyl radical species, rather than a high-valent Cu(III) ion. The phenolic C-O bond in the peripheral rings are also slightly shortened after oxidation (1.287 Å vs 1.307 and 1.301 Å) and a quinoidal distribution of the bond distances was observed

(**Figure V.11.B**), which is reminiscent of methoxyphenoxyl radicals. From the symmetric nature of the cation, the electronic hole of the phenoxyl radical appears to be delocalized over both peripheral rings. $[\text{CuL}^{\text{bp,OMe}}]^+$ can thus be best described as a copper(II)(phenoxyl)(phenolate) mixed-valent species, at least in the solid state.

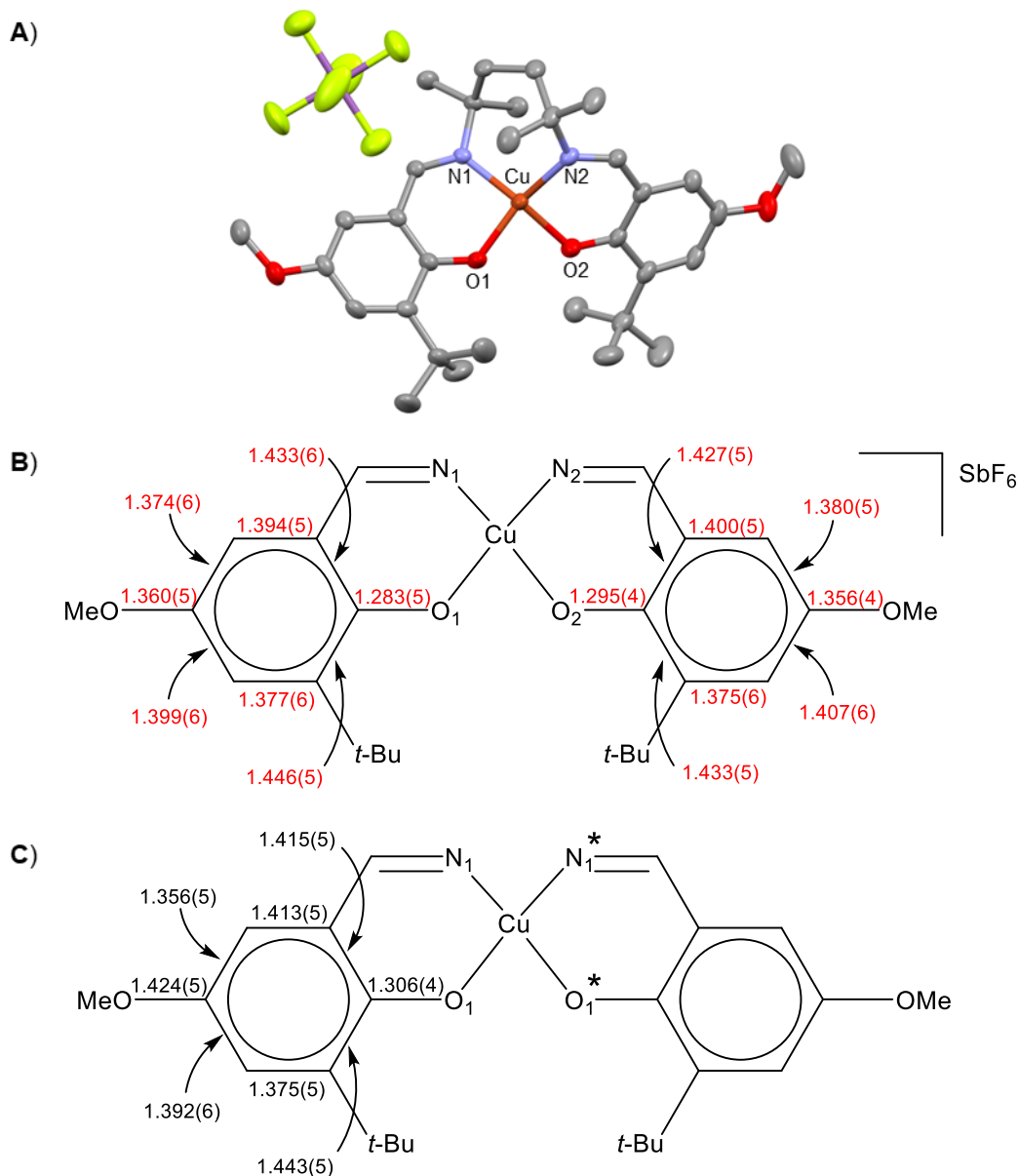


Figure V.12. Structural analysis of $[\text{CuL}^{\text{pu,OMe}}]^+$: X-ray structure (hydrogens omitted for clarity) (**A**), phenolic bond distances in $[\text{CuL}^{\text{pu,OMe}}]^+$ (**B**) and comparison with the neutral precursor $\text{CuL}^{\text{pu,OMe}}$ (**C**). The bond distances are given in Å.

$[\text{CuL}^{\text{pu,OMe}}]^+$ showed a mostly symmetrical coordination sphere within the resolution limits of the structure, with Cu-O1, Cu-O2, Cu-N1 and Cu-N2 bond lengths of 1.911(3), 1.904(3), 1.957(3) and 1.954(3) Å respectively (**Table V.1**). Once again, those results show a small expansion of the coordination sphere after oxidation that is consistent with the formation of a phenoxyl radical. Similarly to $[\text{CuL}^{\text{bp,OMe}}]^+$, a characteristic quinoid bond distribution was observed within both peripheral rings, with shortened C-O and C_{para}-O_{methoxy} phenolic bonds (**Figure V.12.B**). $[\text{CuL}^{\text{pu,OMe}}]^+$ was therefore also described as a mixed-valent species in the

solid state. The τ_4 index remained relatively large in the cation (0.43) but was again smaller than in the neutral complex $\text{CuL}^{\text{pu,OMe}}$ (0.46). This suggests that the decrease in distortion observed after oxidation of $\text{CuL}^{\text{bp,OMe}}$ is likely not the result of the weak axial ligations of the neighboring methoxy groups.

7. EPR and magnetic measurements of the cations

Chemical oxidation of the neutral copper(II) salen complexes to their respective cations was accompanied by a quenching of the EPR copper signatures. In some instances, a sharp signal centered around $g \approx 2.03$ was observed but integration of the signals in each case proved it to be trace contaminants and not the major species. The g value indicated that the signature likely corresponds to over-oxidized radical byproducts. As introduced in Chapter I, the EPR silence observed in one-electron oxidized copper-salen species can be interpreted by different electronic structures:

- (i) From a metal-centered oxidation, forming a Cu(III) center (d^8 , $S = 0$) as a closed-shell cation (singlet).
- (ii) From a ligand-centered oxidation, with anti-ferromagnetic coupling between the spins of the phenoxyl radical and of the copper(II) center (broken-symmetry singlet, BSS).
- (iii) From a ligand-centered oxidation, with a strong ferromagnetic coupling (triplet), exhibiting zero-field splitting larger than the X-band energy ($\approx 0.3 \text{ cm}^{-1}$).

The formation of a high-valent Cu(III) ion appears as the least probable based on the crystal structure observed in cations $[\text{CuL}^{\text{bp,OMe}}]^+$ and $[\text{CuL}^{\text{pu,OMe}}]^+$. The electronic structure of the cations was further investigated by solution magnetic measurements using the Evans method.^[333] Chemically generated $[\text{CuL}^{\text{bp,OMe}}]^+$, $[\text{CuL}^{\text{pu,OMe}}]^+$ and $[\text{CuL}^{\text{pu,tBu}}]^+$ had a magnetic susceptibility of $\mu_{\text{eff}} = 2.65$, 2.61 and 2.92 corresponding to a respective number of unpaired electrons of 1.83, 1.80 and 2.09 that confirmed the radical nature of the cations. These results also pointed towards the population of a triplet state (iii) which is the electronic structure proposed for most copper radical salen species (Chap I.1.3.3.).

8. UV-vis-NIR investigation of the cations

Contrary to their neutral precursors, the radical cations displayed remarkable NIR features ($< 11\,000 \text{ cm}^{-1}$) in their absorption spectra (red spectra, **Figure V.9**). The spectra of all four complexes were found to be temperature independent in the 233-300 K range. This showed that the Cu(II)-phenoxyl triplet ground state of the cations was significantly lower in energy than the closed-shell singlet solution. This confirmed that the Cu(III)-phenolate species cannot be populated at room temperature and thus that no valence tautomerism is expected in the cations.

A single clearly defined NIR band was observed for $[\text{CuL}^{\text{bp,OMe}}]^+$ and $[\text{CuL}^{\text{bp,tBu}}]^+$ at $7800 \text{ (} 1000 \text{ M}^{-1}.\text{cm}^{-1} \text{)}$ and $7200 \text{ cm}^{-1} \text{ (} 700 \text{ M}^{-1}.\text{cm}^{-1} \text{)}$ respectively. The oxidized complexes of the putrescine series displayed a less defined NIR signature with two bands or shoulders (**Figure V.9**). The nature of the transitions was investigated using TD-DFT calculations and the band of lowest energy was systematically assigned as a phenolate to phenoxyl inter-valence charge transfer (see section 8.). To gain further insight on the delocalization of the phenoxyl radicals, we deconvoluted the NIR signature of the cations to conduct a Marcus-Hush analysis of the band shape parameters of the IVCT bands. The experimental bandwidth was

systematically larger than the theoretical value (calc. $\Delta\nu_{1/2}$, equation (1)), indicating a partial localization of the phenoxyl radical. The electronic coupling H_{AB} of the systems were also calculated according to the Hush equation (2).

The H_{AB} values of the cations ranged from 1080 to 1670 cm^{-1} , which is comparable to a series of copper radical salen complexes using a cyclohexyl bridge.^[87] The $2H_{AB}/\lambda$ ratios of the four cations all fell in a short range of low values from 0.35 to 0.43, which supports the assignment of the cations as class II mixed-valent species. When comparing to the cyclohexyl-bridged species, both ϵ_{max} and H_{AB} values are overall smaller (Table V.5), suggesting a less probable electron transfer when there is a larger metal distortion. The $2H_{AB}/\lambda$ of the oxidized copper salen complexes $[\text{CuL}^{\text{ch,OMe}}]^+$ and $[\text{CuL}^{\text{ch,tBu}}]^+$ were also calculated based on the data given in reference^[87] (Table V.5). Both $[\text{CuL}^{\text{ch,OMe}}]^+$ and $[\text{CuL}^{\text{ch,tBu}}]^+$ presented larger $2H_{AB}/\lambda$ values (0.51 and 0.81 respectively) depicting a larger delocalization of the radical.

Table V.5. Band shape analysis of the inter-valence transition of the mono-oxidized complexes.^a

complex	$\lambda = \nu_{\text{max}}$ [cm^{-1}]	ϵ_{max} [$\text{M}^{-1}.\text{cm}^{-1}$]	calc. $\Delta\nu_{1/2}$ [cm^{-1}]	$\Delta\nu_{1/2}$ [cm^{-1}]	H_{AB} [cm^{-1}]	$2H_{AB}/\lambda$
$[\text{CuL}^{\text{bp,OMe}}]^+$	7840	872	4255	6525	1670 ^b	0.43
$[\text{CuL}^{\text{bp,tBu}}]^+$	6630	630	3915	6345	1285 ^b	0.39
$[\text{CuL}^{\text{pu,OMe}}]^+$	7180	623	4072	5460	1240 ^c	0.35
$[\text{CuL}^{\text{pu,tBu}}]^+$	5715	642	3633	5040	1080 ^c	0.38
$[\text{CuL}^{\text{ch,OMe}}]^+{}^d$	7800	1400	4200	6200	2000	0.51 ^e
$[\text{CuL}^{\text{ch,tBu}}]^+{}^d$	5700	2900	3600	5600	2300	0.81 ^e

^aElectrochemically generated in CH_2Cl_2 solutions containing 0.1 M TBAP. ^bWith $r_{\text{CT}} = r_{\text{O1-O2}}$ distance (2.609 Å) from X-ray structure of $[\text{CuL}^{\text{bp,OMe}}]^+$. ^cWith $r_{\text{CT}} = r_{\text{O1-O2}}$ distance (2.597 Å) from X-ray structure of $[\text{CuL}^{\text{pu,OMe}}]^+$. ^dAs reported in reference^[87]. ^eCalculated from data given in reference^[87].

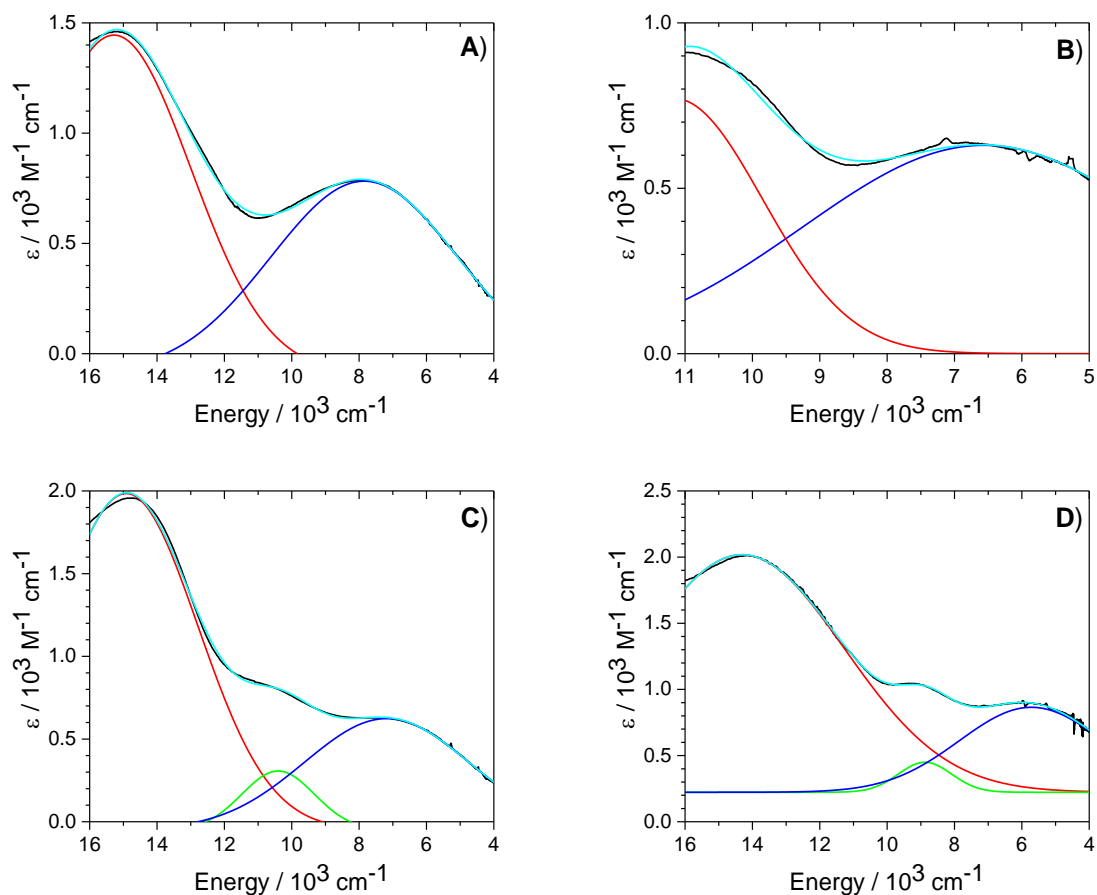


Figure V.13. Deconvolution of the low energy region of the absorption spectrum of $[\text{CuL}^{\text{bp,OMe}}]^+$ (A) $[\text{CuL}^{\text{bp,tBu}}]^+$ (B), $[\text{CuL}^{\text{pu,OMe}}]^+$ (C) and $[\text{CuL}^{\text{pu,tBu}}]^+$ (D). Experimental spectra (black) and sum of the subspectra (cyan). The deconvoluted IVCT transitions of interest are depicted in blue.

9. Theoretical calculations

The four complexes were also investigated by DFT. Based on previous research from our group, the B3LYP functional has shown to be one of the most reliable to depict the electronic structure of oxidized copper salen complexes. A polarizable continuum model was used for the CH_2Cl_2 solvent medium that was used to experimentally characterize our complexes. The structures of the neutral copper(II) bis(phenolate) complexes were reasonably well predicted with a faithful coordination sphere within 0.02 \AA of the crystal structures (**Table V.6**).

Table V.6. Crystallographic and theoretical coordination distances in the neutral complexes (Å).

complex	bonds	crystal. ^a	Doublet ^b
CuL^{bp,OMe}	Cu-O	1.895(3) / 1.880(3)	1.901 / 1.901
	Cu-N	1.946(5) / 1.953(4)	1.939 / 1.939
CuL^{bp,tBu}	Cu-O	1.885(2) / 1.894(2)	1.905 / 1.905
	Cu-N	1.959(3) / 1.951(3)	1.961 / 1.961
CuL^{pu,OMe}	Cu-O	1.892(2) / 1.892(2)	1.902 / 1.902
	Cu-N	1.972(3) / 1.972(3)	1.940 / 1.940
CuL^{pu,tBu}	Cu-O	1.896(1) / 1.896(1)	1.906 / 1.906
	Cu-N	1.958(1) / 1.958(1)	1.962 / 1.962

^aFrom the respective crystallographic structures. ^bFrom B3LYP/6-31 g*/SCRF(CH₂Cl₂) calculations.

The SOMO of the four complexes were developed over both peripheral rings (**Figure V.14.A**). This is consistent with an electron removal on the phenolate moieties to afford phenoxyl radical species upon oxidation. The LUMO were heavily centered on the copper ion and supported a metal-centered reduction (**Figure V.14.B**). This result further supported the assignment of the Cu(II)/Cu(I) redox couple for the reduction event observed around -1.6 V in CV experiments (see section 4.).

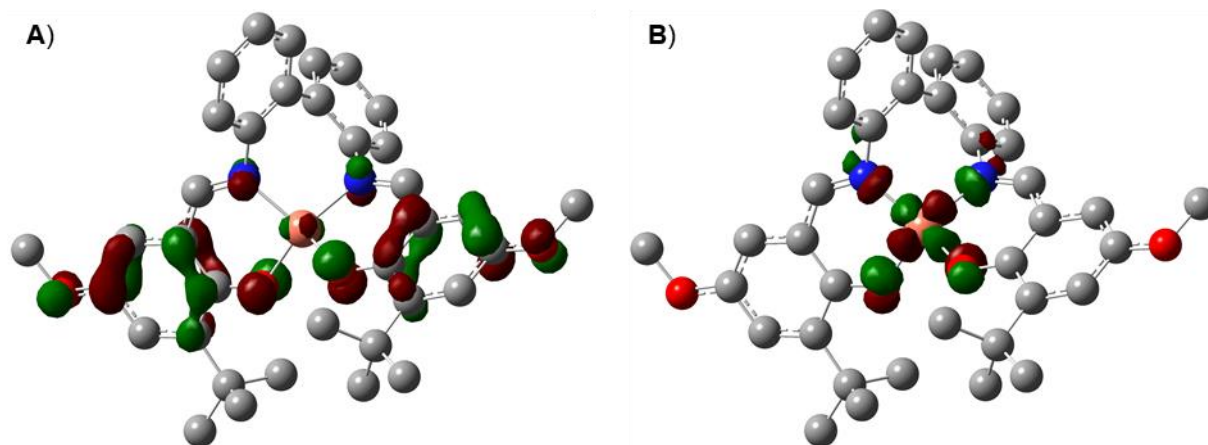
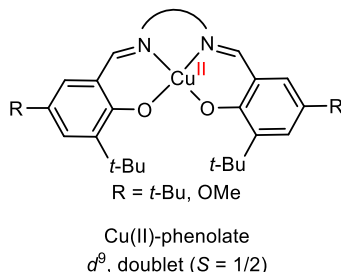


Figure V.14. Frontier orbitals of neutral complex **CuL^{bp,OMe}**: α -SOMO (**A**) and β -LUMO (**B**). From B3LYP/6-31G*/SCRF(CH₂Cl₂) calculation, isoval = 0.05. The hydrogen atoms are omitted for clarity. All four neutral complexes displayed similar frontier orbitals.

Chapter V. Distorted copper salen complexes

For the cations, we considered the three different electronic structures presented previously to rationalize the EPR silence observed after oxidation: a closed-shell singlet (Cu(III)-phenolate complex), a triplet (ferromagnetically coupled Cu(II)-phenoxyl species) and a broken-symmetry singlet (BSS) state (antiferromagnetically coupled Cu(II)-phenoxyl complex).

Neutral:



Cations:

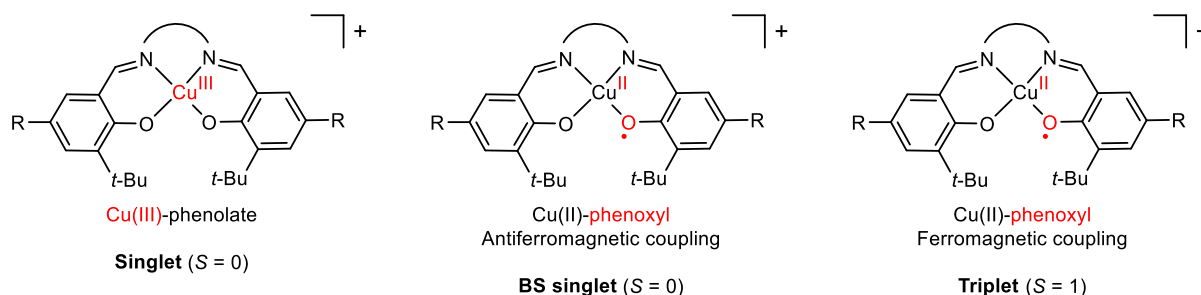


Figure V.15. Different electronic structures of the neutral and one-electron oxidized copper salen complexes.

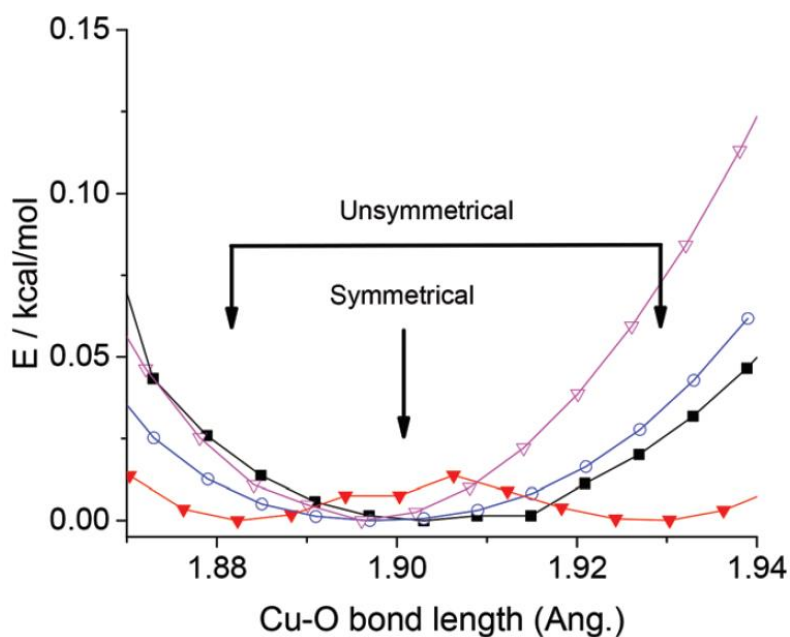
As can be expected from a Cu(III) species, the optimized closed-shell singlet presented a contracted coordination sphere in comparison with the neutral precursor (-0.02 to -0.04 Å, **Table V.7**). These results contrast with the expansion of the coordination sphere observed experimentally in $[\text{CuL}^{\text{bp,OMe}}]^+$ and $[\text{CuL}^{\text{pu,OMe}}]^+$ and further discredit the Cu(III) high-valent form as a possible electronic structure for the cations. In the case of the triplet Cu(II)-radical solution, two distinct geometries were optimized. $[\text{CuL}^{\text{bp,OMe}}]^+$, $[\text{CuL}^{\text{bp,tBu}}]^+$ and $[\text{CuL}^{\text{pu,tBu}}]^+$ were calculated with a symmetrical coordination sphere with Cu-O bonds ranging from 1.897 to 1.903 Å, which is in relatively good agreement with the symmetric crystal structure of $[\text{CuL}^{\text{bp,OMe}}]^+$ (**Table V.7**). In the case of $[\text{CuL}^{\text{pu,OMe}}]^+$, we were able to converge structures having either a symmetric coordination, with Cu-O bonds of 1.900 Å, or a dissymmetric geometry, with Cu-O bonds of 1.884 and 1.928 Å.

Table V.7. Crystallographic and theoretical coordination distances in the cations (\AA).

complex	bonds	crystal. ^a	Triplet ^b	Singlet ^b
$[\text{CuL}^{\text{bp,OMe}}]^+$	Cu-O	1.926(2) / 1.926(2)	1.897 / 1.898	1.871 / 1.871
	Cu-N	1.965(3) / 1.965(3)	1.933 / 1.933	1.892 / 1.892
$[\text{CuL}^{\text{bp,tBu}}]^+$	Cu-O		1.896 / 1.896	1.856 / 1.856
	Cu-N		1.933 / 1.933	1.881 / 1.881
$[\text{CuL}^{\text{pu,OMe}}]^+$	Cu-O	1.892(2) / 1.892(2)	1.883 / 1.928	1.882 / 1.882
	Cu-N	1.972(3) / 1.972(3)	1.946 / 1.962	1.920 / 1.920
$[\text{CuL}^{\text{pu,tBu}}]^+$	Cu-O		1.903 / 1.903	1.869 / 1.869
	Cu-N		1.953 / 1.953	1.910 / 1.910

^a From the respective crystallographic structures. ^b From B3LYP/6-31G*/SCRF calculations.

To gain further insight into this specific desymmetrization of the structure for $[\text{CuL}^{\text{pu,OMe}}]^+$, we conducted relaxed potential energy surface (PES) scans for the four cations. In this case, the relaxed scans consisted in fixing a Cu-O bond at different bond lengths and reoptimizing the structures at each step. Three energy minima were found for $[\text{CuL}^{\text{pu,OMe}}]^+$, which corresponded to the symmetric and dissymmetric structures. The dissymmetric structures presented the lowest energies but the energy gap was extremely small between each of the 3 minima, within $0.02 \text{ kcal.mol}^{-1}$ (7 cm^{-1}). No dissymmetric structure could be identified in the frame of the PES for the other cations.

**Figure V.16.** SCF energy as a function of the Cu-O bond length (\AA) from relaxed PES scans in the triplet Cu(II)-radical states for the four cations.

The radical character of the triplet states was confirmed by the analysis of their spin density plots (**Figure V.17**). In each cation, the electron density is spread out over both the copper ion and the peripheral phenolic rings. The symmetric species $[\text{CuL}^{\text{bp,OMe}}]^+$, $[\text{CuL}^{\text{bp,tBu}}]^+$ and $[\text{CuL}^{\text{pu,tBu}}]^+$ presented spin density over both peripheral rings, whereas dissymmetric $[\text{CuL}^{\text{pu,OMe}}]^+$ showed a localization of the radical on a single phenoxyl ring (**Figure V.17.C**). This behavior is further supported by the fact that $[\text{CuL}^{\text{pu,OMe}}]^+$ presents the only asymmetrical SOMO among the four different cations.

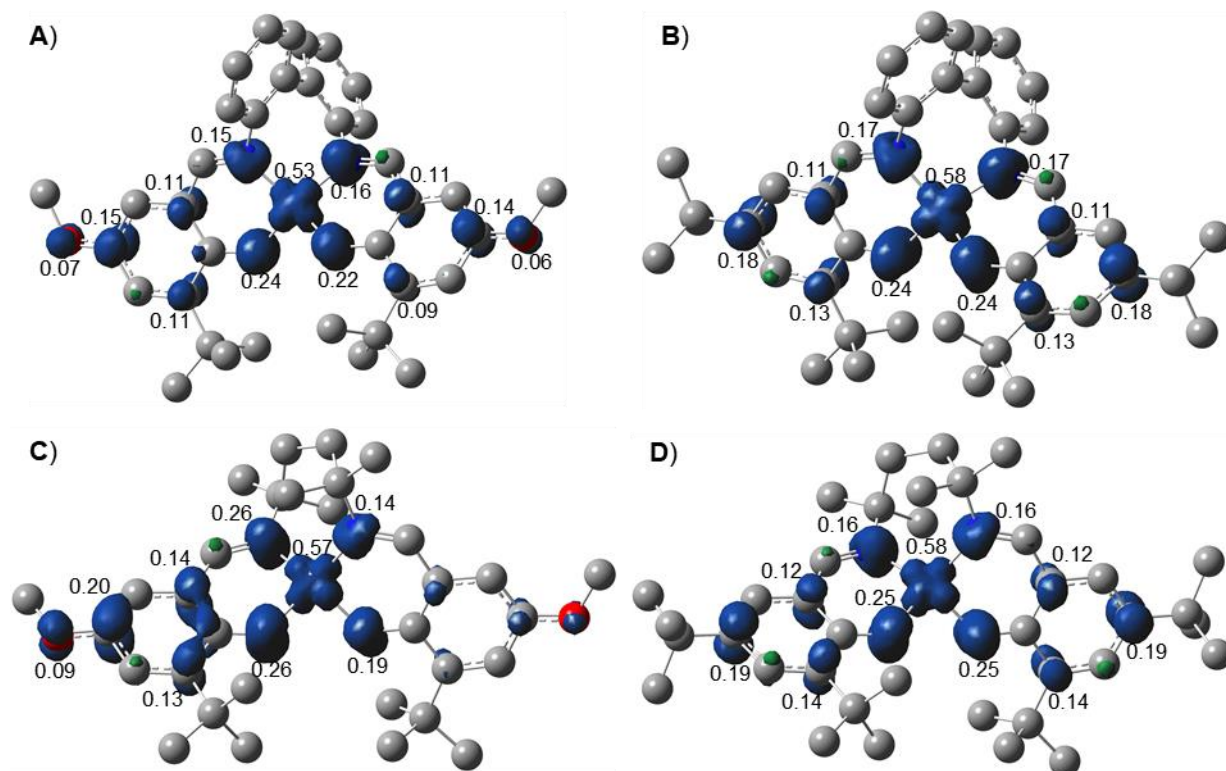


Figure V.17. Spin density plots (including the main Mulliken spin populations) of $[\text{CuL}^{\text{bp,OMe}}]^+$ (A), $[\text{CuL}^{\text{bp,tBu}}]^+$ (B), $[\text{CuL}^{\text{pu,OMe}}]^+$ (C) and $[\text{CuL}^{\text{pu,tBu}}]^+$ (D). From B3LYP/6-31G*/SCRF(CH_2Cl_2) calculations, isoval = 0.005. The hydrogen atoms are omitted for clarity.

The broken symmetry singlets were also converged but proved to be of significantly higher energy than the ferromagnetically coupled triplet species (**Table V.8**). As discussed previously, Evans method NMR experiments showed the presence of two unpaired electrons for each chemically oxidized complex at 298 K. This is consistent with the energetic analysis that presents the ferromagnetically coupled Cu(II)-phenoxyl triplet solution as the unambiguous ground state *in-silico* (**Table V.8**).

Table V.8. Energetic analysis of the electronic structure of the cations.^a

complex	Triplet (cm ⁻¹)	BS singlet (cm ⁻¹) ^b	Singlet (cm ⁻¹) ^b	$\langle S^2 \rangle_{\text{triplet}}$	$\langle S^2 \rangle_{\text{BSS}}$	J (cm ⁻¹) ^c
[CuL ^{bp,OMe}] ⁺	0	+1910	+4720	2.0175	0.9831	+1850
[CuL ^{bp,tBu}] ⁺	0	+2760	+3670	2.0224	0.9464	+2560
[CuL ^{pu,OMe}] ⁺	0	+450	+4300	2.0167	1.0087	+450
[CuL ^{pu,tBu}] ⁺	0	+1680	+4060	2.0216	0.9480	+1560

^aFrom B3LYP/6-31G*/SCRF(CH₂Cl₂) calculations. ^bRelative energies to the triplet state of lowest energy. ^cCalculated according to the Yamaguchi formula: $J = -(E_{\text{triplet}} - E_{\text{BSS}}) / (\langle S^2 \rangle_{\text{triplet}} - \langle S^2 \rangle_{\text{BSS}})$ where BSS = broken-symmetry singlet.

The magnetic couplings J were calculated from the Yamaguchi formula.^[287] The symmetric cations [CuL^{bp,OMe}]⁺, [CuL^{bp,tBu}]⁺ and [CuL^{pu,tBu}]⁺ had the largest coupling values in the range +1560 cm⁻¹ to +2650 cm⁻¹. These large values are consistent with the experimental observation of a triplet at 298 K through the Evan's method. When the radical was localized on a single ring in [CuL^{pu,OMe}]⁺, its electronic coupling with the copper center was significantly smaller at +450 cm⁻¹. This can be explained by the longer Cu-O coordination bond to the phenoxyl ring (1.928 Å) in comparison to the symmetric cations (Cu-O bonds = 1.897-1.903 Å). These results show that the orbital overlap between the d_{x²-y²}, holding the copper(II) single electron, and the phenoxyl π system is still insufficient to promote an antiferromagnetic coupling, despite the highly distorted geometry of the complexes.

Based on the Cu(II)-radical triplet solution, the spectroscopic properties of the cations were investigated using TD-DFT calculations. For each complex the lowest energy band corresponded to a β -HOMO \rightarrow β -LUMO transition that was assigned as an IVCT transition involving ligand radical orbitals.

Table V.9. Low-energy transitions from the TD-DFT investigation of the cations.^a

complex	main transitions	assignment	calcd.	exp.	f_{osc}
[CuL ^{bp,OMe}] ⁺	β -HOMO \rightarrow β -LUMO	LLCT (IVCT)	4719	7840	0.1134
	β -HOMO-1 \rightarrow β -LUMO	LLCT	8850		0.0191
	β -HOMO-1 \rightarrow β -LUMO+1	LMCT	11 628		0.0428
[CuL ^{bp,tBu}] ⁺	β -HOMO \rightarrow β -LUMO	LLCT (IVCT)	4771	6630	0.1084
	β -HOMO-1 \rightarrow β -LUMO	LLCT	7321		0.0292
	β -HOMO-1 \rightarrow β -LUMO+1	LMCT	11 173		0.0283
[CuL ^{pu,OMe}] ⁺	β -HOMO \rightarrow β -LUMO	LLCT (ICVT)	4615	7180	0.1046
	β -HOMO-1 \rightarrow β -LUMO+1	LMCT	13 661		0.123
[CuL ^{pu,tBu}] ⁺	β -HOMO \rightarrow β -LUMO	LLCT (ICVT)	4572	5715	0.1008
	β -HOMO-1 \rightarrow β -LUMO+1	LMCT	13 405		0.0802

^aBLYP/TZVP/SCRF(CH₂Cl₂) calculations. Structures optimized in B3LYP/6-31G*/SCRF(CH₂Cl₂) conditions.

It is important to note that we obtained a significant discrepancy between the experimental transitions and the theoretical energies of excitations. This inconsistency could be related to the initial optimization of the triplet states that showed a more compact coordination sphere when compared to the crystal structures of $[\text{CuL}^{\text{bp,OMe}}]^+$ and $[\text{CuL}^{\text{pu,OMe}}]^+$ (Table V.7). Different standard functionals with varying Hartree Fock exchange coefficients were tested, both for structural optimizations and for the TD-DFT calculations. The TD-DFT results closest to the experimental NIR spectra were found when using the B3LYP functional to optimize the structures of the cations (B3LYP/6-31G*/SCRF(CH_2Cl_2)) and the BLYP functional in the TD-DFT calculations (BLYP/TVZP/SCRF(CH_2Cl_2)). Nevertheless, the transitions of lowest energy were consistently shown to involve orbitals heavily located over the phenolic peripheral rings of the ligand (Figure V.18). The nature of the donor and acceptor orbitals was unchanged no matter which functionals were used nor which cation was investigated. The assignment of these transitions as phenolate to phenoxyl IVCT transitions was therefore not further questioned.

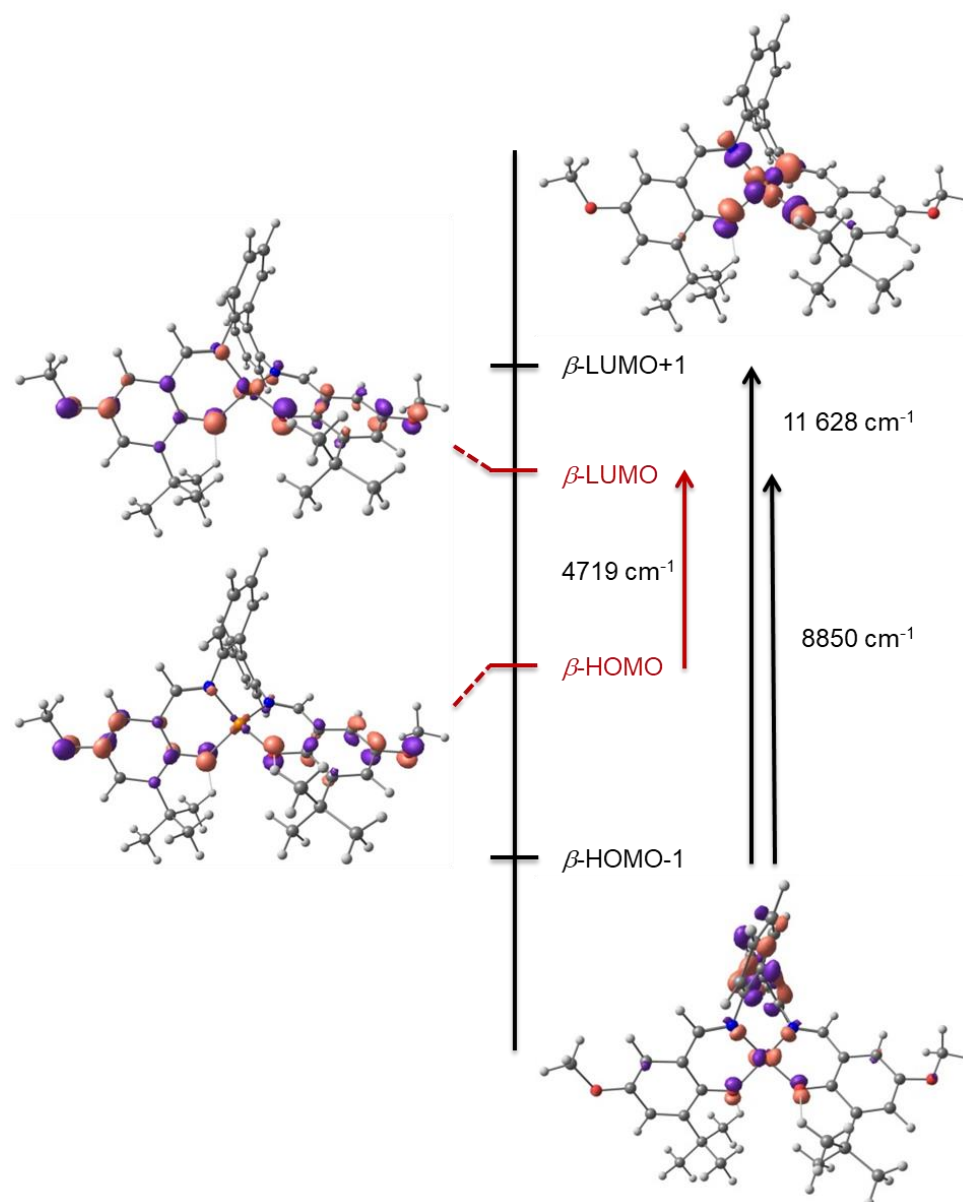


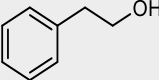
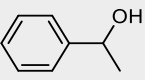
Figure V.18. Low-energy transitions from the TD-DFT of the $[\text{CuL}^{\text{bp,OMe}}]^+$ Cu(II)(phenoxyl) triplet (BLYP/TZVP/SCRF(CH_2Cl_2)).

10. Catalysis

To better probe the reactivity of these new distorted Cu(II)-phenoxyl complexes as mimics of galactose oxidase, we investigated their activity towards the aerobic oxidation of different alcohols. The Thomas group has previously optimized experimental conditions to test the catalytic activity of copper salen complexes,^[334] using 0.08 mol% catalyst with 0.60 M alcohol substrate in CH₂Cl₂ solutions at 298 K under 1 atmosphere of O₂. 1.2 equivalent (0.72 M) of potassium *tert*-butoxide is used in heterogeneous conditions as a strong base to facilitate deprotonation of the alcohol substrates. The different aldehyde products were quantified using aliquots dissolved in CDCl₃ to analyze in ¹H NMR. As discussed previously, the cation [CuL^{bp,tBu}]⁺ could not be cleanly generated chemically due to the high oxidation potential of the neutral precursor. Its catalytic properties were therefore not investigated.

Benzyl alcohol has been the historic standard reagent to test molecular models of galactose oxidase since the first reports of catalytic alcohol oxidation by oxidized copper salens by Stack *et al.* in the late 1990s.^[68,69] We conducted preliminary catalytic trials on benzyl alcohol but our distorted copper complexes did not present a superior reactivity when compared to the reference planar complex [CuL^{ch,tBu}]⁺. We thus extended the scope of our alcohol substrates to include the unactivated primary alcohol 2-phenylethanol (**Table V.10**). No oxidation of 2-phenylethanol was observed in the absence of a catalyst. In the presence of free copper in the form of a Cu(OAc)₂ salt, a catalytic activity is recorded at 7 turnover numbers (TON) after 1h and up to 18 TON after 3 h. The TONs appeared to reach a plateau after 6h at 40 and eventually decreased after 24 h to 37. This behavior was observed for other complexes as well and was hypothesized to be the result of overoxidation of the aldehyde product to a carboxylic acid. Different attempts were made to characterize and quantify side-products of the catalysis in ¹H NMR but all were unfruitful. We therefore limited our analysis to aliquots collected at 1 and 3 hours of reaction.

Table V.10. Turnover numbers (TON) for the catalytic aerobic oxidation of alcohols.^{a,b}

complex	2-phenylethanol		1-phenylethanol ^c	
	1h	3h	1h	3h
CuL ^{bp,OMe}	15(5)	29(12)	318(30)	280(30)
CuL ^{pu,OMe}	34(4)	58(8)	371(10)	329(30)
CuL ^{pu,tBu}	12(7)	38(15)	326(15)	229(15)
[CuL ^{bp,OMe}] ⁺	24(1)	36(1)	233(30)	163(30)
[CuL ^{pu,OMe}] ⁺	28(4)	57(7)	353(30)	317(30)
[CuL ^{pu,tBu}] ⁺	26(4)	33(1)	354(40)	269(40)
[CuL ^{ch,tBu}] ⁺	12(1)	23(1)	422(20)	441(10)
Cu(OAc) ₂	7(2)	18(8)	0(10)	10(5)

^aReaction: 0.60 M alcohol in CH₂Cl₂, 0.72 M tBuOK, 0.08 mol% catalyst, 1 atm O₂, *T* = 298 K. Standards deviation for 3 assays are given in brackets. ^bNo catalytic activity was observed for 1-phenyl-2-propanol. ^cCorrected from background oxidation in the absence of copper.

The TONs improved significantly when the distorted salen catalysts were used, with 24, 28 and 26 TONs after 1 h and up to 36, 57 and 33 TONs after 3 h for [CuL^{bp,OMe}]⁺, [CuL^{pu,OMe}]⁺ and [CuL^{pu,tBu}]⁺ respectively. The neutral precursors CuL^{bp,OMe}, CuL^{pu,OMe} and CuL^{pu,tBu} also showed a catalytic activity. They generally presented lower TONs after 1 h, but showed essentially the same activity than the cations after 6h. This suggests an induction period where the neutral precursors are able to form a reactive radical, as was reported by Stack *et al.* with their catalysts.^[68] For reference, the activity of [CuL^{ch,tBu}]⁺ was also investigated and the cation presented a lower activity with 23 TONs after 3h.

Wild type galactose oxidase is able to oxidize a wide range of primary alcohols into aldehydes but is not active towards secondary alcohols. Thus, to test the selectivity of the distorted complexes, we investigated the oxidation of an activated secondary alcohol, 1-phenylethanol. The substrate was readily oxidized even in the absence of catalysts, with 570 TONs after 3h (with a standard deviation of 24 for 3 assays). After accounting for the background oxidation, the conversion of 1-phenylethanol appeared to not be impacted by the presence of free copper. A non-negligible increase in activity was observed in the presence of the copper complexes with additional 163, 317 and 269 TONs after 3 h for [CuL^{bp,OMe}]⁺, [CuL^{pu,OMe}]⁺ and [CuL^{pu,tBu}]⁺ respectively. The neutral precursors showed essentially similar TONs than the cations, even at 1 hour of catalysis, that possibly point towards a shorter induction time in the presence of the 1-phenylethanol substrate. In the same conditions, [CuL^{ch,tBu}]⁺ presented significantly larger TONs with 441 after 3 h. These results might indicate a better selectivity of the catalysts towards primary alcohols with an increased tetrahedral distortion of the copper ion. We further expanded our screening of substrates towards the unactivated secondary alcohol 1-phenyl-2-propanol but we did not observe any reactivity.

11. Conclusion

We developed a new series of four salen complexes with a highly distorted copper center by using two different salen linkers. The rigid biphenyl bridge was utilized for the constraints of the steric clash from the ortho position of its two aromatic rings to enforce a tetrahedral distortion. The putrescine spacer was used as an elongated and flexible bridge akin to other salen ligands previously reported using elongated n-alkyl bridges. The distorted environment coupled with the donating properties of the phenolic *para* substituents provided unique electrochemical properties where four different redox states were shown to be stable at the CV time-scale. The putative reduced copper(I) and two-electron oxidized Cu(II)-bis(phenoxy) states were not isolated but the neutral complexes and one-electron oxidized species were thoroughly characterized. The cations were defined as copper(II) phenoxy radical species with strong ferromagnetic coupling. Their IVCT transition was modulated depending on the phenolic *para* substituents, whereby the tert-butyl group leads to weaker excitation energies. A complete band shape analysis of the transition also provided an estimation of the mixed-valence electronic coupling H_{AB} and they were assigned as class II species in the Robin-Day classification of mixed-valent systems. The four copper(II) radical complexes presented a significantly smaller H_{AB} coupling than those reported for complexes with less distorted copper centers. The electronic communication between the two redox active phenolic rings is highly affected by the overlap between donor and acceptor orbitals and that electronic properties of the ligand are not the only factor to impact the electronic coupling in mixed-valent systems. These results underline the intricate possibilities to modulate the electronic structure of such complex systems bearing multiple redox-active centers.

Finally, these distorted copper salen complexes were shown to have a non-negligible increase in catalytic activity and selectivity towards the oxidation of an unactivated primary alcohol substrate in 2-phenylethanol. Most of the catalytic assays of copper(II)-phenoxy complexes have focused on activated alcohols, specifically benzyl alcohol derivatives, and have often used co-oxidants, such as TEMPO or TBHP,^[335] to increase catalytic performances. This work has demonstrated that the catalytic scope of copper salen complexes could be expanded towards more inert substrates. Thus, these distorted salen complexes might be interesting candidates to develop as catalysts for more challenging chemical reactions. One prime example would be the oxidative cleavage of the lignin biopolymer, which is a key element in the use of the biomass as an attractive alternative energy supply to standard carbon-based sources.^[336]

Chapter VI.

Conclusion and perspectives

1. General conclusion	207
2. Perspectives.....	209
2.1. Nickel complexes	209
2.2. Manganese complexes.....	211
2.3. Chromium complexes.....	213
2.4. Distorted copper salen complexes	215

1. General conclusion

Metal complexes bearing redox-active ligands have been extensively studied for their interesting electronic structures and their propensity to catalyze polyelectronic reactions using abundant metal centers. Salen ligands, bearing a bis-imine bis-phenoxide chelating pattern, have been one of the most popular classes of compound studied for its redox non-innocence. Nevertheless, they still present some limited coordination properties. They have shown to stabilize unusual high-valent metal centers, such as Cu(III) (Chap I.1.3.3.), but these reports remain scarce. In general, they are also poorly suited to form stable dioxidized species and a threshold remains to reach reactions involving more than two electrons. Finally, salen ligands tend to not easily accommodate low-valent, electron-rich metal centers. For example, no persistent Cu(I)-salens are known in the biomimicry of galactose oxidase.

To overcome these limitations, we focused our efforts on the introduction of *N*-Heterocyclic carbenes (NHCs) in our ligand design. NHCs are known in organometallic catalysis to form stable complexes with electron-rich metal ions (Chap I.2.3.). Recently, they have also been reported in high-valent metal complexes, including Cu(III), Co(IV) species and more. Hence, we designed and synthesized an original redox-active framework bearing two NHC units and two pro-radical phenolate centers. This new ligand, labelled **L^{C2O2}**, was developed as a C₂O₂ chelating framework, analogue to the N₂O₂ donor set of salen ligands. The binding and electronic properties of the ligand was investigated in complexes of different metal centers.

Group 10 (M = Ni, Pd, Pt) metal complexes were developed to investigate the electronic properties of the ligand in the formation of oxidized complexes. By a combination of crystallographic, spectroscopic and theoretical investigations, we assessed that the oxidations of the complexes were ligand-centered and formed phenoxyl radicals. The ligand showed to be highly electron-rich and allowed us to reach two-electron oxidized, bis(phenoxyl) complexes. This type of oxidized species remains scarce in the literature of redox-active ligands. We also developed and characterized the first Ni(III) complex with NHC donors by introduction of exogenous pyridine ligands.

The **L^{C2O2}** ligand was also investigated in context of the development of metal complexes with nitride (N³⁻) ligands. Transition metal-nitrides have been studied as molecular models of nitrogenase for the fixation of N₂ and as N-atom transfer reagents in amination reactions. Recently, oxidized manganese and chromium nitride salen complexes have shown tunable reactivity depending on the location of the electronic hole after oxidation. Thus, we looked to develop manganese and chromium complexes with our **L^{C2O2}** ligand to form electron-rich metal-nitride compounds.

The manganese nitride complex of the **L^{C2O2}** ligand proved to be unstable. It was shown to readily degrade in successive intramolecular nitride insertions on the carbenic center of both NHC units. The overall degradation formed a peculiar N-inserted organic salt with three fused rings with a central triazone pattern. On the opposite, the chromium nitride complex of the **L^{C2O2}** ligand proved to be inert to nitride-NHC couplings and was thoroughly characterized. The one-electron oxidized product was also obtained at low temperature but readily evolved in standard conditions.

Chapter VI. Conclusion and perspectives

In a parallel work, we also developed new types of sterically hindered salen ligands to form distorted copper salen complexes. Oxidized copper salen complexes have been developed as molecular models of galactose oxidase for the aerobic oxidation of primary alcohols. Our copper salen complexes showed an intermediate geometry, between a square planar and a tetrahedral coordination. This structural organization was proposed to enhance the turnover between the reduced and oxidized states of the copper catalyst and thus enhance reactivity. The distorted structure in our copper salen catalysts showed to be effective for the oxidation of more inert alcohol substrates when compared with standard copper salen species that display mostly planar geometries.

2. Perspectives

2.1. Nickel complexes

The NiL^{C2O2} complex and its $[\text{NiL}^{\text{C2O2}}]^+$ cation were investigated in the aerobic oxidation of alcohols but showed limited reactivity. Nonetheless, $\text{Ni}(\text{NHC})$ catalysts have been used in a number of cross-coupling reactions. Hence, we propose to probe the reactivity of different nickel species in standard C-C or C-N bond formation reactions.

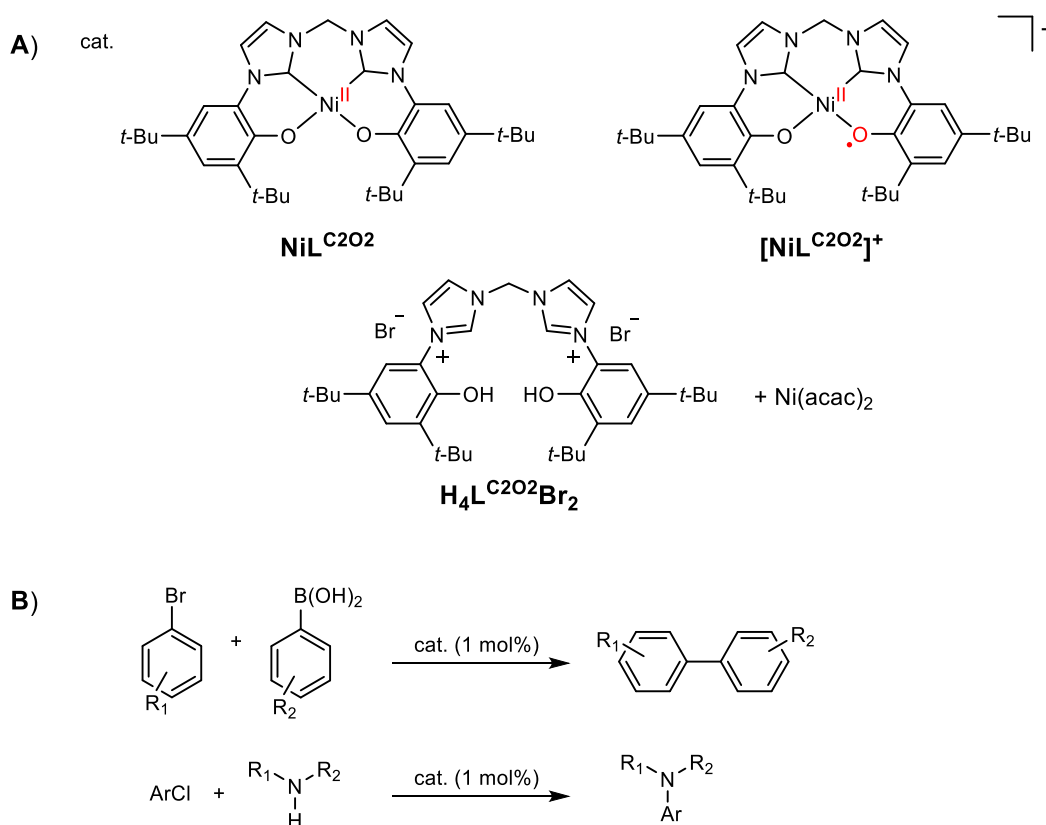


Figure VI.1. Perspectives for the investigation of nickel L^{C2O2} species in catalytic cross-coupling reactions: nickel catalyst systems (**A**) and standard trial reactions based on reference ^[148](**B**).

We also developed a series of bidentate LCOR^{R} NHC-phenolate ligands with *tert*-butyl or methoxy phenolate *para*-substituents. Neutral nickel(II) homoleptic complexes and their respective cations have been isolated and their characterization is underway (**Figure VI.2**). We speculate that the bidentate chelating pattern should present a more adequate coordination to facilitate ligand exchange with substrates in catalytic reactions. Furthermore, the study of different *t*-Bu or OMe-substituted complexes, in their different oxidation states, should give us some insight into the relationship between their electronic structure and their reactive properties.

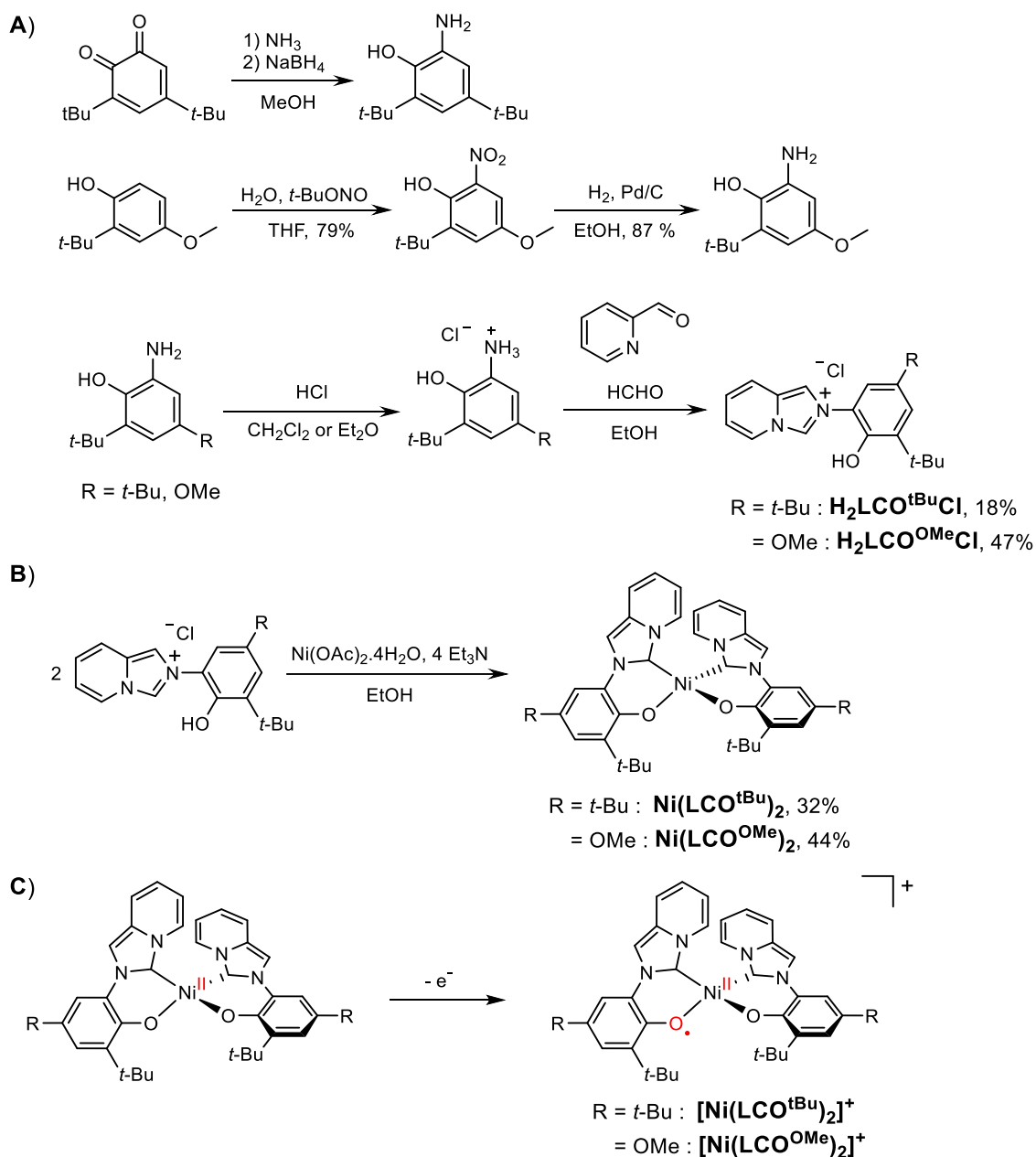


Figure VI.2. Development of nickel species with bidentate NHC-phenolate ligands: synthesis of the imidazolium proligands $\text{H}_2\text{LCO}^{\text{R}}\text{Cl}$ (A), the nickel complexes $\text{Ni}(\text{LCO}^{\text{R}})_2$ (B) and their respective cations (C).

2.2. Manganese complexes

The manganese nitride complex $\text{Mn}^{\text{V}}\text{L}^{\text{C2O2}}(\text{N})$ appeared to degrade through intramolecular nitride-NHC reductive couplings to afford a purely organic triazonium compound. The exact degradation mechanism remains unclear as we were not able to thoroughly characterize manganese intermediate species in the reaction. Manganese species could not be detected using traditional X-band EPR, either in perpendicular or parallel modes. Hence, we propose to use high-field high-frequency EPR (HF-EPR) spectroscopy to characterize the putative manganese products of the degradation of $\text{MnL}^{\text{C2O2}}(\text{N})$ (**Figure VI.3.A**).^[337,338] We will also investigate the transition states of the theoretical nitride-NHC coupling reactions we detailed in Chapter III. This will complete our theoretical analysis of the proposed mechanism for the evolution of $\text{MnL}^{\text{C2O2}}(\text{N})$ with some insight into its kinetic limitations.

We also plan to follow the photoactivation of the $\text{Mn}^{\text{III}}\text{L}^{\text{C2O2}}(\text{N}_3)$ azide precursor by low-temperature X-band EPR. The Meyer group were able to prove the existence of a transient Co(IV)-nitride species by irradiation of a frozen EPR sample of a cobalt-azido precursor.^[154] Hence, we plan to spectroscopically characterize the transient $\text{Mn}^{\text{V}}\text{L}^{\text{C2O2}}(\text{N})$ complex in a similar fashion (**Figure VI.3.B**).

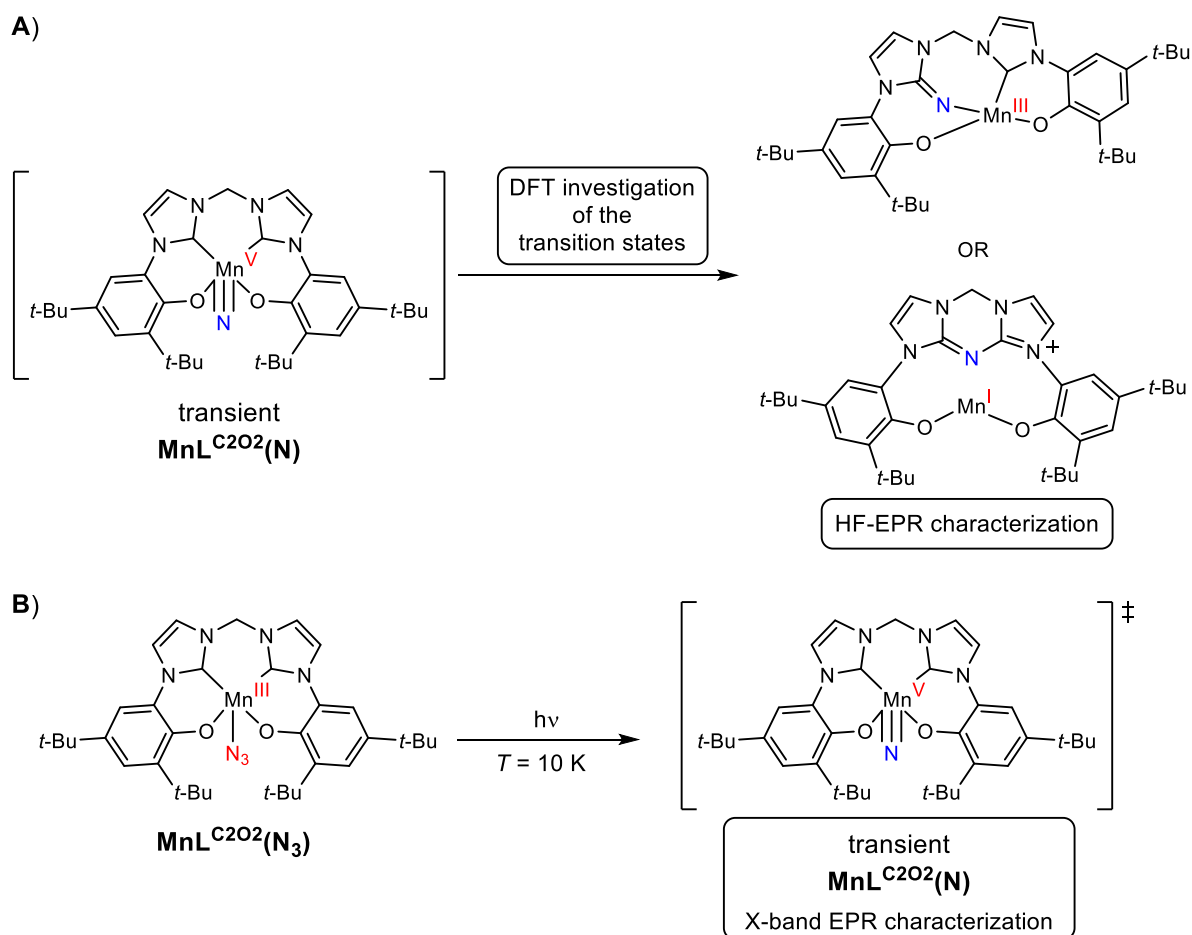


Figure VI.3. Proposed investigation in the evolution of the transient $\text{MnL}^{\text{C2O2}}(\text{N})$ nitride complex: Investigation on the manganese degradation products in high-field high-frequency EPR and theoretical calculations (**A**). Characterization of $\text{Mn}^{\text{V}}\text{L}^{\text{C2O2}}(\text{N})$ by frozen solution EPR analysis of the photoactivation of the $\text{Mn}^{\text{III}}\text{L}^{\text{C2O2}}(\text{N}_3)$ precursor (**B**).

We will also continue our research on the oxidation of ammonia using the $\text{Mn}^{\text{III}}\text{L}^{\text{C2O2}}\text{Br}$ complex. Our first efforts will focus on chemical oxidation trials to verify the formation of N_2 and other derivative products. We will also investigate the evolution of the $\text{Mn}^{\text{III}}\text{L}^{\text{C2O2}}$ catalyst and verify the formation of N-inserted products to obtain some mechanistic insights (**Figure VI.4**). Indeed, formation of a nitride intermediate in the ammonia oxidation mechanism should lead to the same degradation pathway we observed while attempting to isolate the $\text{MnL}^{\text{C2O2}}(\text{N})$ complex. On the opposite, alternating pathways through hydrazido intermediates might be able to form N_2 molecules without degradation of the manganese catalyst.

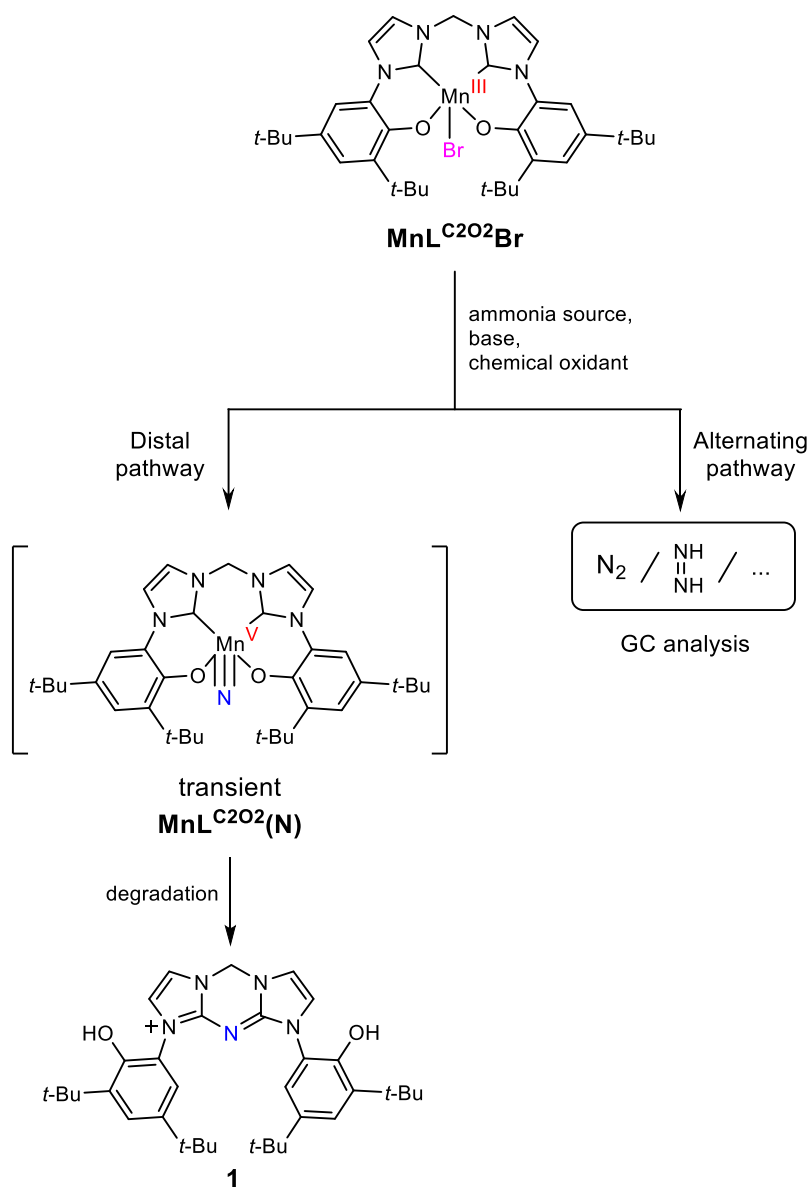


Figure VI.4. Investigation of the possible ammonia oxidation reactivities of the $\text{MnL}^{\text{C2O2}}\text{Br}$ complex using chemical oxidation.

2.3. Chromium complexes

We will continue our characterization on the nature of the oxidation products of $\text{CrL}^{\text{C2O2}}(\text{N})$ at room temperature. We will further probe the possibility of homocoupling reactivity using isotopic labelling experiments with ^{15}N labelled nitride complex $\text{CrL}^{\text{C2O2}}(^{15}\text{N})$. The room temperature chemical oxidation of $\text{CrL}^{\text{C2O2}}(^{15}\text{N})$ will be activated by exogenous ligands and the formation of $^{15}\text{N}_2$ gas will be monitored by gas chromatography-mass spectrometry (GC-MS, **Figure VI.5.A**). The nature of the oxo complex $\text{CrL}^{\text{C2O2}}(\text{O})$ and its formation mechanism from the nitride complex $\text{CrL}^{\text{C2O2}}(\text{N})$ could also be investigated using isotopically labelled $^{18}\text{O}_2$ or $\text{H}_2(^{18}\text{O})$ and mass spectrometry experiments (**Figure VI.5.B**). We finally plan to separately prepare the oxo $\text{CrL}^{\text{C2O2}}(\text{O})$ complex for further characterization.

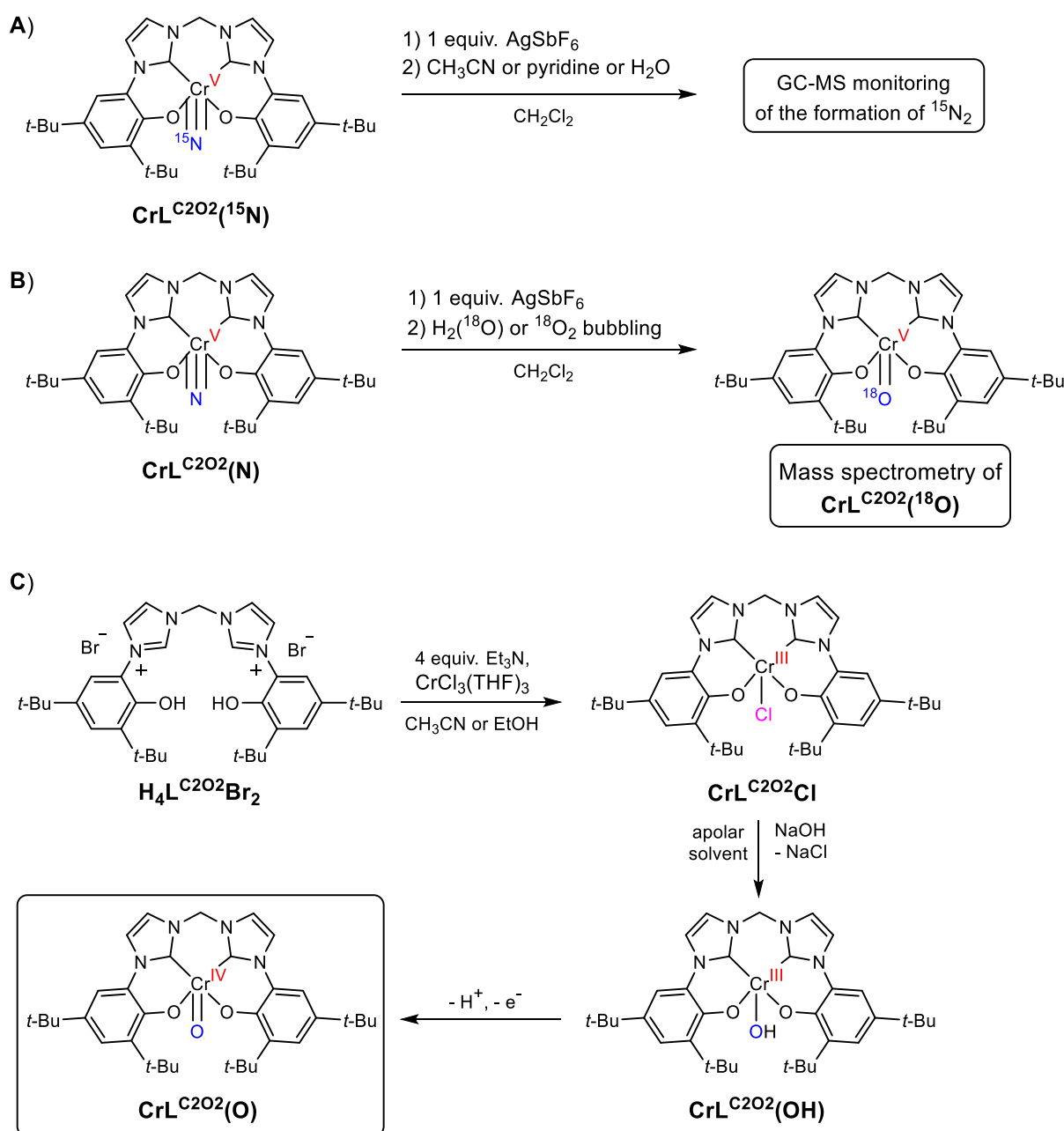


Figure VI.5. Investigation perspectives for the room temperature oxidation products of the $\text{CrL}^{\text{C2O2}}(\text{N})$ complex: Study of homocoupling reactivity (A) and formation of the oxo $\text{CrL}^{\text{C2O2}}(\text{O})$ complex (B) in isotopic labelling experiments. Proposed synthesis for the oxo compound (C).

Chapter VI. Conclusion and perspectives

Finally, the reactivity of the nucleophilic $\text{CrL}^{\text{C2O2}}(\text{N})$ complex and the $[\text{CrL}^{\text{C2O2}}(\text{N})]^+$ cation will be tested with different electrophilic substrates, including tris(pentafluorophenyl)borane, the trityl cation, or electron-poor olefins (**Figure VI.6.A**). In a long-term perspective, the $\text{CrL}^{\text{C2O2}}(\text{N})$ complex could also be tested as a molecular catalyst in N_2 reduction and in ammonia oxidation experiments (**Figure VI.6.B**).

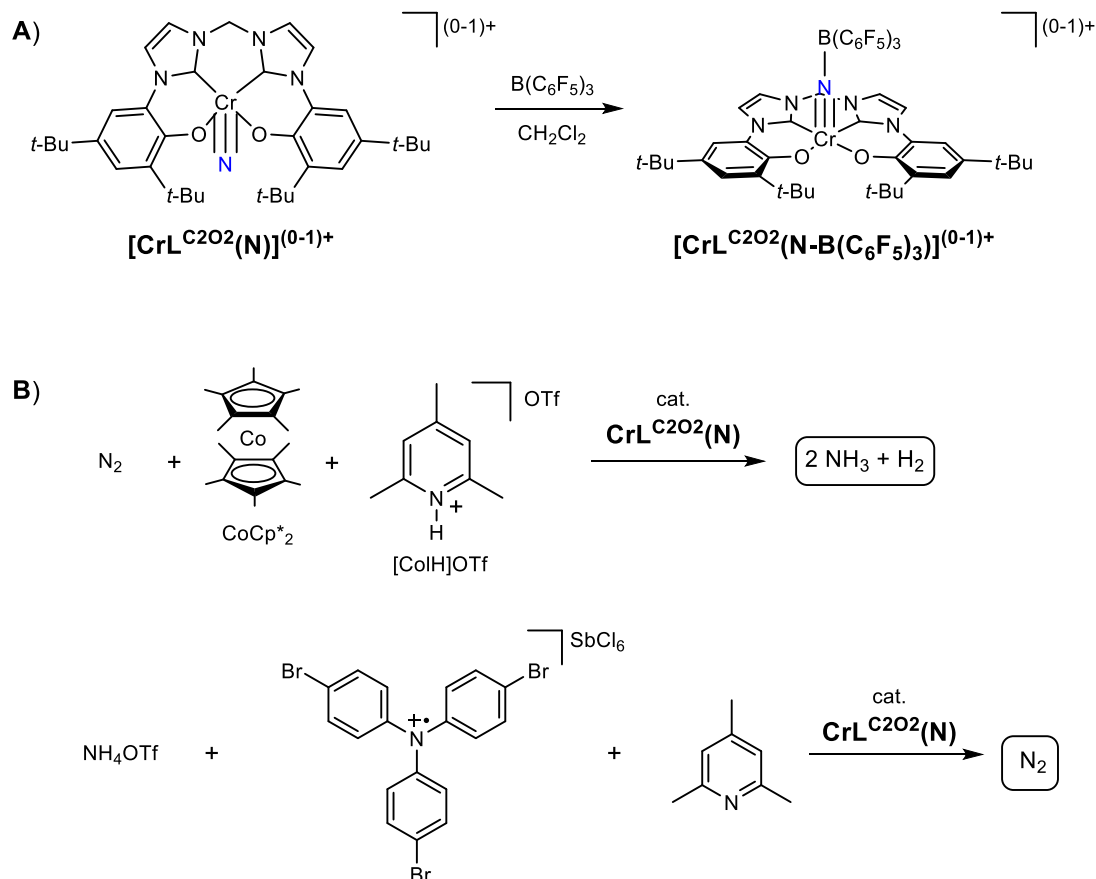


Figure VI.6. Perspectives for the reactivity of the nitridochromium complexes: nucleophilic reaction on electrophilic substrates (**A**) and $\text{CrL}^{\text{C2O2}}(\text{N})$ catalyst in N_2 reduction and ammonia oxidation, based on references ^[189] and ^[304] respectively (**B**).

2.4. Distorted salen copper complexes

The distorted copper salen complexes showed some unique stability for the reduced copper(I) oxidation state on the CV time-scale. Hence, we plan to isolate and characterize the reduced complexes to present the first report of persistent Cu(I)-salen species as mimics of the reduced form of the galactose oxidase. Preliminary reduction attempts were unsuccessful, either by chemical reduction using decamethyl cobaltocene or bulk electrolysis experiments.

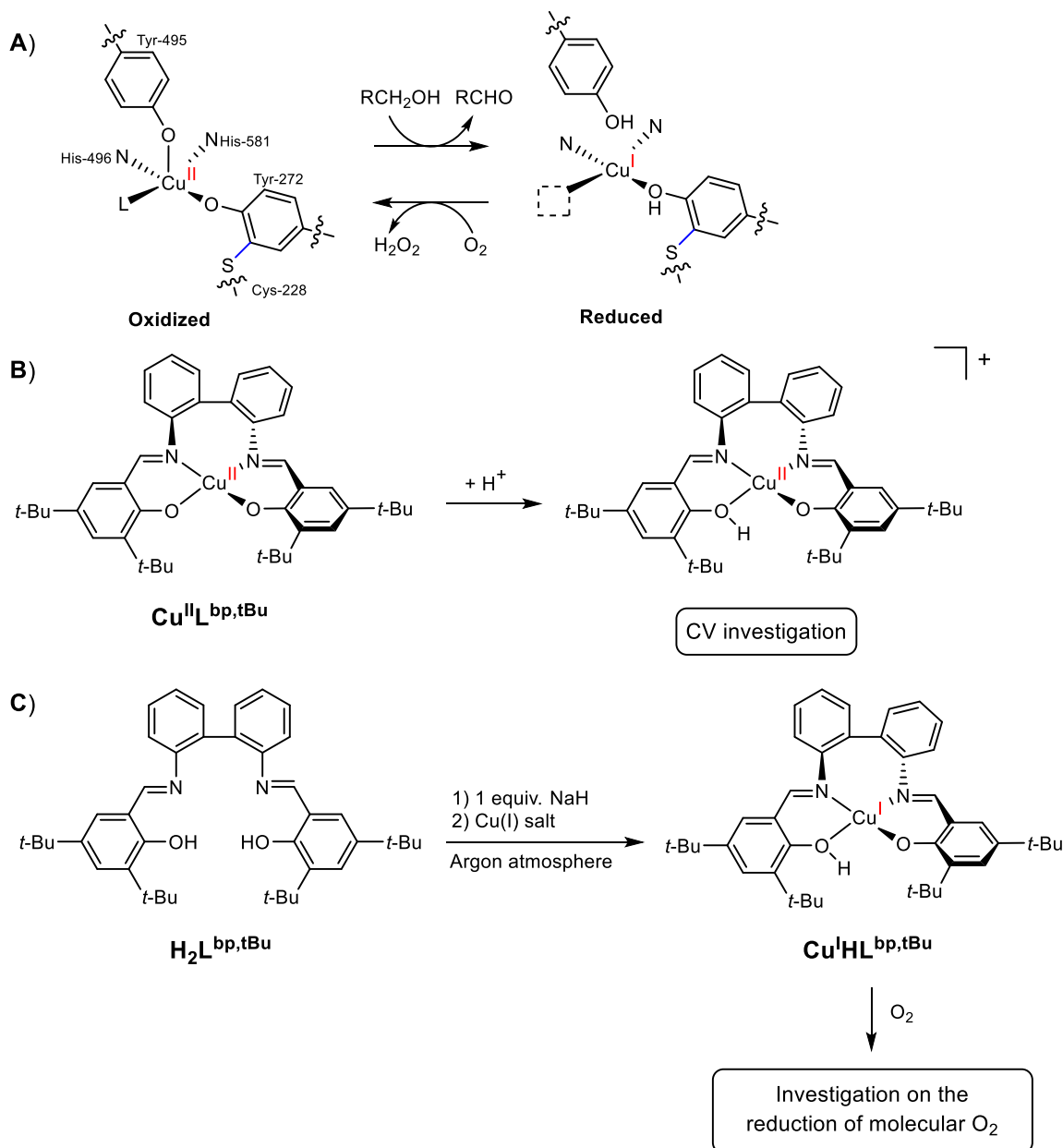


Figure VI.7. Biomimicry of the reduced form of galactose oxidase using distorted copper salen complexes: active forms of GOase (**A**). Investigation on the protonation of a copper(II) salen complex and its impact on the electrochemical properties of the complex (**B**). Proposed general synthesis to obtain a neutral Cu(I)-phenolate-phenol complex (**C**).

Chapter VI. Conclusion and perspectives

To further stabilize the copper(I) ion, we propose to keep a phenol arm in the salen ligand. We hypothesize that the soft phenol donor should help accommodate the Cu(I) center, whilst also affording a more stable neutral complex. The resulting species would also be a more relevant model for the reduced form of the GOase, that presents tyrosine amino acids under their protonated forms (**Figure VI.7.A**).

We plan to study the protonation of the Cu(II)-salen complex and its impact on the electrochemical properties of the Cu(II)/Cu(I) redox couple (**Figure VI.7.B**). We also propose to directly prepare the Cu(I)-phenolate-phenol complex using a Cu(I) metallic salt (**Figure VI.7.C**). If successfully obtained, the Cu(I)-phenolate-phenol complex could represent a major finding to model the activity of GOase to reduce molecular oxygen.

Chapter VII.

Experimental section

1. Methods	219
1.1. Electron paramagnetic resonance (EPR) spectroscopy	219
1.2. Nuclear magnetic resonance (NMR) spectroscopy	219
1.3. Mass spectrometry (MS)	219
1.4. Microanalysis	219
1.5. Electrochemistry	219
1.6. Ultraviolet-visible and near-infrared spectroscopy (UV-vis-NIR)	219
1.7. Crystal structure analysis	220
1.8. Computational details	226
1.9. Catalysis (Chapter V)	227
 2. Synthesis	 228
2.1. Chapter II	228
2.2. Chapter III	232
2.3. Chapter IV	234
2.4. Chapter V	235

1. Methods

1.1. Electron paramagnetic resonance (EPR) spectroscopy

X-Band EPR spectra were recorded on a BRUKER EMX Plus spectrometer controlled with Xenon software and equipped with a Bruker teslameter. A Bruker nitrogen flow cryostat connected to a high sensitivity resonant cavity was used for 100 K measurements and a Bruker Helium flow cryostat was used for 4 K experiments. Samples for X-band measurements were placed in 4 mm outer-diameter sample tubes with sample volumes of 200 μL . The EPR spectra were simulated by using the Easyspin package in Matlab.^[339]

1.2. Nuclear magnetic resonance (NMR) spectroscopy

At Université Grenoble Alpes, ^1H NMR and spectra were recorded using an Avance III 400 or an Avance III 500 Bruker spectrometer at 293 K. $^{13}\text{C}\{^1\text{H}\}$ spectra were recorded on a BRUKER AM 300 at 293 K at 300 MHz. At Simon Fraser University, ^1H and $^{13}\text{C}\{^1\text{H}\}$ NMR spectra were recorded using Avance III 400, Avance III 500 or Avance III 600_QNP Bruker spectrometers at 293 K. Chemical shifts are quoted relative to tetramethylsilane (TMS).

1.3. Mass spectrometry (MS)

ESI mass spectra were collected on a Bruker maXis Impact at Simon Fraser University, or on a POLARIS-Q (ThermoFisher) in Université Grenoble Alpes. High resolution mass spectra were recorded on a Waters Xevo G2-S QToF apparatus.

1.4. Microanalysis

Microanalysis were performed with a C,H,N analyzer constructed by the Service Central d'Analyse de Vernaison (SCA CNRS, France).

1.5. Electrochemistry

Cyclic voltammetry (CV) curves were recorded on a CHI 620 potentiostat in a standard three-electrode cell under argon atmosphere. The electrolytic medium is anhydrous CH_2Cl_2 containing 0.1 M tetra-*n*-butylammonium perchlorate (TBAP) as supporting electrolyte. The cell volume is 8 mL, with both the counter and reference electrodes being compartmentalized to avoid diffusion of the analyte at the platinum wire or in the AgNO_3/Ag (0.01 M) compartment (in CH_3CN + TBAP 0.1 M). All the potentials given in the text are referred to the regular Fc^+/Fc redox couple used as external reference. A vitreous carbon disc electrode (5 mm diameter) polished with 1 mm diamond paste was used as working electrode. Electrolysis was performed at 233 K (using liquid nitrogen/ethanol baths) with a Biologic SP300 potentiostat by using a carbon foam working electrode and was monitored by coulometry and rotating-disk electrode voltammetry. The integrity of the oxidized products was also accessed by recording CV curves after the oxidations and ensuring that they match with that of the unoxidized sample.

1.6. Ultraviolet-visible and near-infrared spectroscopy (UV-vis-NIR)

At Université Grenoble Alpes, UV-vis-NIR spectra were recorded on a Perkin–Elmer Lambda 1050 with Hellma quartz cells of 1.000 mm path length. Low temperature spectra (253 K) were

recorded using a temperature controller unit set at 253 K and the quartz cell was kept under a heavy flow of argon gas to prevent fogging of the cell walls. UV-vis spectra were recorded on a Cary Varian 50 spectrophotometer with quartz cells of 1.000 cm path length. 233 K UV-vis spectra were obtained using a Hellma low temperature immersion probe (1.000 cm path length quartz cell). The temperature was controlled with a Lauda RK8 KS cryostat.

At Simon Fraser University, UV-vis-NIR spectra were recorded on a Cary 5000 spectrophotometer with a custom-designed immersion fiber-optic probe with variable path-length (1 and 10 mm; Hellma, Inc.). In low-temperature experiments, constant temperatures were maintained with an electronically controlled cold well (FTS – Multi Cool).

1.7. Crystal structure analysis

Single crystals were coated with a parafin mixture, picked up with nylon loops and mounted in the nitrogen cold stream of an Enraf–Nonius–Bruker diffractometer equipped with an APEX II detector. Mo-K α radiation ($\lambda = 0.71073 \text{ \AA}$) from a Mo target high brilliance micro X-ray source equipped with INCOATEC Montel optics was used. In the case of **Ni(LCO^{tBu})₂** (Chapter II), **H₂L^{pu,tBu}** and **[CuL^{bp,OMe}]⁺** (Chapter V), suitable crystals were mounted in the nitrogen cold stream of a Bruker-AXS-enraf-nonius KappaCCD equipped with graphite-monochromated Cu K α radiation ($\lambda = 1.54184 \text{ \AA}$). Final cell constants were obtained from refinement using the whole data. Refinement of the structures were performed by Dr. Christian Philouze from the Département de Chimie Moléculaire, Université Grenoble Alpes, France. The data was integrated and corrected for Lorentz and polarization factor using the EVAL14^[340] software. Final cell parameters were obtained post-refining the whole data. The data was then reintegrated and corrected for absorption using the SADABS^[341] program and finally merged with the software XPREP.^[342] The structures were solved by charge flipping methods and refined using subsequent difference Fourier techniques. The SHELX-2016 and SHELXL-2013 programs^[343] implemented in the Olex2 software^[344] were used for the refinements. All non-hydrogen atoms were anisotropically refined and hydrogen atoms were placed at calculated positions and refined as riding atoms with isotropic displacement parameters.

In the case of **PdL^{C202}** (Chapter II),^[274] when refining the Pd atom anisotropically, one could note very high electronic density residues. That is the reason why we were obliged to refine the Pd atom anharmonically with the use of Jana.^[345] Using this, the highest negative calculated residual density shrunk from $-2.576 \text{ e} \cdot \text{\AA}^{-3}$ to $-1.23 \text{ e} \cdot \text{\AA}^{-3}$ and the positive calculated residual density from $1.245 \text{ e} \cdot \text{\AA}^{-3}$ to $0.96 \text{ e} \cdot \text{\AA}^{-3}$ leading to a better fit of the experimental data which resulted in an improvement of the R factor from 5.55% to 4.10%.

Diffraction data for single crystals of **MnL^{C202}Br** and **MnL^{C202}(N₃)** (Chapter III) were collected at the University of British Columbia (Canada) by Dr. Brian Patrick on a Bruker X8 Apex II diffractometer with graphite monochromated Mo-K α radiation ($\lambda = 0.71073 \text{ \AA}$) at 296 K. Data were integrated using the Bruker SAINT software package^[346] and absorption corrections were performed using the multiscan technique (SADABS).^[341] The structures were solved by Dr. Nicholas Hein using the SHELX software^[343] implemented by Olex2.^[344] All non-hydrogen atoms were anisotropically refined and hydrogen atoms were placed at calculated positions and refined as riding atoms with isotropic displacement parameters.

Chapter VII. Experimental section

Table VII.1. Crystal data and structure refinement for **NiL^{C2O2}**, **PdL^{C2O2}**, **PtL^{C2O2}** and **[NiL^{C2O2}]⁺**.

Compound	NiL^{C2O2}	PdL^{C2O2}	PtL^{C2O2}	[NiL^{C2O2}]⁺
CCDC number	1886568	1897863	1886567	1886569
Formula	C ₃₅ H ₄₆ N ₄ NiO ₂	C ₃₅ H ₄₆ N ₄ O ₂ Pd	C ₃₅ H ₄₆ N ₄ O ₂ Pt	2(F ₃ Sb _{0.5}), C ₃₅ H ₄₆ N ₄ NiO ₂ , C _{0.25} H _{0.5} Cl _{0.5}
<i>F_w</i> [g.mol ⁻¹]	613.47	661.16	749.85	870.45
<i>T</i> [K]	200	200	200	200
Morphology	needle	needle	needle	needle
Color	yellow	colourless	colourless	black
Crystal size [mm]	0.14 x 0.2 x 0.3	0.14 x 0.16 x 0.3	0.14 x 0.2 x 0.34	0.16 x 18 x 0.3
Crystal system	orthorhombic	orthorhombic	orthorhombic	orthorhombic
Space group	-P 2n 2ab	-P 2n 2ab	-P 2n 2ab	-P 2ac 2n
<i>a</i> [Å]	18.233(4)	18.459(4)	18.443(4)	12.3564(11)
<i>b</i> [Å]	26.234(5)	25.895(5)	25.939(5)	36.487(4)
<i>c</i> [Å]	6.8713(14)	6.9722(14)	6.9859(14)	17.323(6)
α [°]	90	90	90	90
β [°]	90	90	90	90
γ [°]	90	90	90	90
Unit-cell volume [Å ³]	3286.7(11)	3332.7(12)	3341.9(12)	7810(3)
<i>Z</i>	4	4	4	8
<i>D_x</i> [g.cm ⁻³]	1.240	1.3178	1.490	1.481
μ [mm ⁻¹]	0.626	0.592	4.234	1.272
<i>F</i> (000)	1312	1384	1512	3548
Radiation	MoK α (λ = 0.71073)	MoK α (λ = 0.71073)	MoK α (λ = 0.71073)	MoK α (λ = 0.71073)
Θ range for data collection/°	2.721 to 27.499	1.35 to 27.506	3.141 to 27.500	2.024 to 24.999
Index ranges	-22 ≤ <i>h</i> ≤ 23	-23 ≤ <i>h</i> ≤ 23	-20 ≤ <i>h</i> ≤ 23	-14 ≤ <i>h</i> ≤ 14
	-32 ≤ <i>k</i> ≤ 34	-33 ≤ <i>k</i> ≤ 28	-33 ≤ <i>k</i> ≤ 33	-43 ≤ <i>k</i> ≤ 43
	-8 ≤ <i>l</i> ≤ 8	-8 ≤ <i>l</i> ≤ 9	-9 ≤ <i>l</i> ≤ 8	-20 ≤ <i>l</i> ≤ 16
Total reflections	18688	26580	17982	45105
Unique reflections	3770	3764	3747	6967
Used reflections	3053 (<i>I</i> > 2σ(<i>I</i>))	2704 (<i>I</i> > 3σ(<i>I</i>))	2584 (<i>I</i> > 2σ(<i>I</i>))	4129 (<i>I</i> > 2σ(<i>I</i>))
Refined parameters	228	236	228	521
<i>R</i> _{int} .	0.0377	0.0736	0.0696	0.1164
<i>R</i> ₁	0.0425	0.0429	0.0518	0.0842
<i>R</i> (<i>w</i>) ^a	0.1043	0.0486	0.1038	0.1591
Goodness of fit <i>S</i>	1.192	2.09	1.153	1.055
$\Delta\rho_{\min}/\Delta\rho_{\max}$ (e·Å ⁻³)	-0.584/0.299	-1.23/0.96	-1.896/1.919	-1.036/1.476

^aBased on *F*² where *w* = 1/[*s*²(*Fo*²)+(0.0505*P*)²+1.6390*P*] where *P*=(*Fo*²+2*Fc*²)/3 for **NiL^{C2O2}***w* = 1/[*s*²(*Fo*²)+(0.0001*P*)²] where *P*=(*Fo*²+2*Fc*²)/3 for **PdL^{C2O2}***w* = 1/[*s*²(*Fo*²)+(0.0001*P*)²+39.7330*P*] where *P*=(*Fo*²+2*Fc*²)/3 for **PtL^{C2O2}***w* = 1/[*s*²(*Fo*²)+(0.0636*P*)²+52.3532*P*] where *P*=(*Fo*²+2*Fc*²)/3 for **[NiL^{C2O2}]⁺**

Table VII.2. Crystal data and structure refinement for **MnL^{C2O2}Br**, **MnL^{C2O2}(N₃)** and **1**.

Compound	MnL^{C2O2}Br	MnL^{C2O2}(N₃)	1
CCDC number	-	-	-
Formula	C ₃₅ H ₄₆ BrMnN ₄ O ₂	C ₃₅ H ₄₆ MnN ₇ O ₂	Cl, C ₃₅ H ₄₈ N ₅ O ₂ , H ₂ O, CH ₂ Cl ₂ , C ₂ H ₃ N
<i>F_w</i> [g.mol ⁻¹]	689.61	651.73	750.23
<i>T</i> [K]	296(2)	273(2)	210
Morphology	needle	blade	prism
Color	brown	red	yellow
Crystal size [mm]	0.1 x 0.1 x 1	0.04 x 0.07 x 0.37	0.11 x 0.21 x 0.22
Crystal system	monoclinic	monoclinic	triclinic
Space group	-C 2yc	-P 2yn	-P 1
<i>a</i> [Å]	30.477(2)	15.6595(7)	8.1811(16)
<i>b</i> [Å]	15.0603(11)	9.0777(5)	13.290(3)
<i>c</i> [Å]	20.2126(14)	25.7615(13)	20.518(4)
α [°]	90	90	96.27(3)
β [°]	122.3273(18)	90.347(2)	96.47(3)
γ [°]	90	90	106.01(3)
Unit-cell volume [Å ³]	7839.5(10)	3662.0(3)	2107.6(8)
<i>Z</i>	8	4	2
<i>D_x</i> [g.cm ⁻³]	1.169	1.182	1.182
μ [mm ⁻¹]	1.387	0.399	0.258
<i>F</i> (000)	2880	1384	800
Radiation	MoK α (λ = 0.71073)	MoK α (λ = 0.71073)	MoK α (λ = 0.71073)
Θ range for data collection/°	1.581 to 28.737	1.526 to 22.533	2.392 to 24.997
Index ranges	-41 \leq <i>h</i> \leq 41	-16 \leq <i>h</i> \leq 16	-16 \leq <i>h</i> \leq 16
	-20 \leq <i>k</i> \leq 20	-9 \leq <i>k</i> \leq 9	-9 \leq <i>k</i> \leq 9
	-27 \leq <i>l</i> \leq 27	-27 \leq <i>l</i> \leq 27	-27 \leq <i>l</i> \leq 27
Total reflections	165068	29267	33145
Unique reflections	10145	4778	7349
Used reflections	7774 (<i>I</i> > 2 σ (<i>I</i>))	3777 (<i>I</i> > 2 σ (<i>I</i>))	5498 (<i>I</i> > 2 σ (<i>I</i>))
Refined parameters	400	418	553
<i>R</i> _{int} .	0.0721	0.0583	0.0719
<i>R</i> ₁	0.0382	0.0353	0.0750
<i>R</i> (<i>w</i>) ^a	0.0866	0.1044	0.1960
Goodness of fit <i>S</i>	1.043	0.861	1.112
$\Delta\rho_{\min}/\Delta\rho_{\max}$ (e·Å ⁻³)	-1.555/1.399	-0.307/0.249	-0.572/0.512

^aBased on F^2 where $w = 1/[s^2(\text{Fo}^2) + (0.0389\text{P})^2 + 14.4630\text{P}]$ where $\text{P} = (\text{Fo}^2 + 2\text{Fc}^2)/3$ for **MnL^{C2O2}Br**
 $w = 1/[s^2(\text{Fo}^2) + (0.1000\text{P})^2]$ where $\text{P} = (\text{Fo}^2 + 2\text{Fc}^2)/3$ for **MnL^{C2O2}(N₃)**
 $w = 1/[s^2(\text{Fo}^2) + (0.1062\text{P})^2 + 2.1078\text{P}]$ where $\text{P} = (\text{Fo}^2 + 2\text{Fc}^2)/3$ for **1**

Table VII.3. Crystal data and structure refinement for **CrL^{C202}(N)**, **CrL^{C202}(¹⁵N)**.

Compound	CrL^{C202}(N)	CrL^{C202}(¹⁵N)
CCDC number	-	-
Formula	C ₃₅ H ₄₆ CrN ₅ O ₂	C ₃₅ H ₄₆ Cr ¹⁵ NN ₄ O ₂
<i>F_w</i> [g.mol ⁻¹]	620.784	621.781
<i>T</i> [K]	296.15	200
Morphology	prism	cube
Color	orange	orange
Crystal size [mm]	0.14 x 0.33 x 0.45	0.3 x 0.3 x 0.4
Crystal system	monoclinic	monoclinic
Space group	-P 2ybc	-P 2ybc
<i>a</i> [Å]	15.7083(10)	15.826(3)
<i>b</i> [Å]	12.5593(9)	12.651(3)
<i>c</i> [Å]	16.5802(11)	16.605(3)
α [°]	90	90
β [°]	96.353(2)	96.10(3)
γ [°]	90	90
Unit-cell volume [Å ³]	3250.9(4)	3305.6(12)
<i>Z</i>	4	4
<i>D_x</i> [g.cm ⁻³]	1.268	1.247
μ [mm ⁻¹]	0.391	0.384
<i>F</i> (000)	1325.782	1324
Radiation	MoK α (λ = 0.71073)	MoK α (λ = 0.71073)
Θ range for data collection/°	2.04 to 30.59 -22 \leq <i>h</i> \leq 22	2.476 to 29.999 -22 \leq <i>h</i> \leq 22
Index ranges	-17 \leq <i>k</i> \leq 17 -23 \leq <i>l</i> \leq 23	-15 \leq <i>k</i> \leq 17 -23 \leq <i>l</i> \leq 23
Total reflections	93546	43486
Unique reflections	9981	9481
Used reflections	8454 (<i>I</i> > 2 σ (<i>I</i>))	7609 (<i>I</i> > 2 σ (<i>I</i>))
Refined parameters	400	431
<i>R</i> _{int} .	0.0392	0.0494
<i>R</i> ₁	0.0349	0.0490
<i>R</i> (<i>w</i>) ^a	0.1227	0.1284
Goodness of fit <i>S</i>	1.0690	1.098
$\Delta\rho_{\min}/\Delta\rho_{\max}$ (e·Å ⁻³)	-0.4959/0.7229	-0.722/0.614

^aBased on *F*² where $w = 1/[s^2(\text{Fo}^2) + (0.1\text{P})^2]$ where $\text{P} = (\text{Fo}^2 + 2\text{Fc}^2)/3$ for **CrL^{C202}N** $w = 1/[s^2(\text{Fo}^2) + (0.0640\text{P})^2 + 2.5043\text{P}]$ where $\text{P} = (\text{Fo}^2 + 2\text{Fc}^2)/3$ for **CrL^{C202}(¹⁵N)** $w = 1/[s^2(\text{Fo}^2) + (0.2000\text{P})^2]$ where $\text{P} = (\text{Fo}^2 + 2\text{Fc}^2)/3$ for **[3CrL^{C202}(μ -N)₂]⁺**

Table VII.4. Crystal data and structure refinement for **H₂L^{bp,OMe}**, **H₂L^{pu,tBu}**, **CuL^{bp,tBu}** and **CuL^{pu,tBu}**.

Compound	H₂L^{bp,OMe}	H₂L^{pu,tBu}	CuL^{bp,tBu}	CuL^{pu,tBu}
CCDC number	2014605	2014609	2014606	2014604
Formula	C ₃₆ H ₄₀ N ₂ O ₄	2(C ₁₉ H ₃₀ NO)	C ₄₂ H ₅₀ CuN ₂ O ₂ , C _{2.5} H ₆	C ₁₉ H ₂₉ Cu _{0.5} NO
<i>F_w</i> [g.mol ⁻¹]	564.70	576.88	714.45	319.20
<i>T</i> [K]	200	200	200	200
Morphology	plate	needle	plate	block
Color	orange	yellow	black	orange
Crystal size [mm]	0.2 x 0.3 x 0.33	0.16 x 0.24 x 0.71	0.1 x 0.26 x 0.41	0.26 x 0.3 x 0.42
Crystal system	monoclinic	triclinic	tetragonal	monoclinic
Space group	-C 2yc	-P 1	-I 4ad	-C 2yc
<i>a</i> [Å]	22.432(5)	10.267(2)	22.352(3)	17.661(4)
<i>b</i> [Å]	11.329(2)	11.826(2)	22.352(3)	16.537(3)
<i>c</i> [Å]	13.480(3)	15.541(3)	33.005(7)	13.206(3)
α [°]	90	76.67(3)	90	90
β [°]	117.10(3)	83.43(3)	90	101.07(3)
γ [°]	90	80.89(3)	90	90
Unit-cell volume [Å ³]	3049.7(13)	1807.0(7)	16489(6)	3785.2(14)
<i>Z</i>	4	2	16	8
<i>D_x</i> [g.cm ⁻³]	1.230	1.060	1.151	1.120
μ [mm ⁻¹]	0.080	0.488	0.566	0.608
<i>F</i> (000)	1208	636	6112	1380
Radiation	MoK α (λ = 0.71073)	CuK α (λ = 1.54178)	MoK α (λ = 0.71073)	MoK α (λ = 0.71073)
Θ range for data collection/°	2.361 to 29.999	3.878 to 68.006	2.468 to 27.499	2.463 to 29.998
Index ranges	-31 $\leq h \leq$ 25	-12 $\leq h \leq$ 11	-12 $\leq h \leq$ 11	-24 $\leq h \leq$ 24
	-15 $\leq k \leq$ 14	-14 $\leq k \leq$ 14	-14 $\leq k \leq$ 14	-21 $\leq k \leq$ 23
	-18 $\leq l \leq$ 18	-18 $\leq l \leq$ 18	-18 $\leq l \leq$ 18	-18 $\leq l \leq$ 18
Total reflections	17098	34614	53484	22919
Unique reflections	4398	6303	9388	5485
Used reflections	3342 (<i>I</i> > 2 σ (<i>I</i>))	5198 (<i>I</i> > 2 σ (<i>I</i>))	5520 (<i>I</i> > 2 σ (<i>I</i>))	4467 (<i>I</i> > 2 σ (<i>I</i>))
Refined parameters	195	459	474	234
<i>R</i> _{int} .	0.0593	0.0296	0.0897	0.0397
<i>R</i> ₁	0.0537	0.0437	0.0593	0.0372
<i>R</i> (<i>w</i>) ^a	0.1320	0.1179	0.1434	0.0814
Goodness of fit <i>S</i>	1.084	1.037	1.086	1.155
$\Delta\rho_{\min}/\Delta\rho_{\max}$ (e·Å ⁻³)	-0.271/0.333	-0.234/0.209	-0.472/0.627	-0.411/0.327

^aBased on *F*² where $w = 1/[s^2(\text{Fo}^2) + (0.0640\text{P})^2 + 2.2407\text{P}]$ where $\text{P} = (\text{Fo}^2 + 2\text{Fc}^2)/3$ for **H₂L^{bp,OMe}**
 $w = 1/[s^2(\text{Fo}^2) + (0.0679\text{P})^2 + 0.5145\text{P}]$ where $\text{P} = (\text{Fo}^2 + 2\text{Fc}^2)/3$ for **H₂L^{pu,tBu}**
 $w = 1/[s^2(\text{Fo}^2) + (0.0732\text{P})^2 + 25.7279\text{P}]$ where $\text{P} = (\text{Fo}^2 + 2\text{Fc}^2)/3$ for **CuL^{bp,tBu}**
 $w = 1/[s^2(\text{Fo}^2) + (0.0271\text{P})^2 + 3.3252\text{P}]$ where $\text{P} = (\text{Fo}^2 + 2\text{Fc}^2)/3$ for **CuL^{pu,tBu}**

Chapter VII. Experimental section

Table VII.5. Crystal data and structure refinement for **CuL^{bp,OMe}**, **CuL^{bp,OMe}**, **[CuL^{bp,OMe}]⁺** and **[CuL^{pu,OMe}]⁺**.

Compound	CuL^{bp,OMe}	CuL^{pu,OMe}	[CuL^{bp,OMe}]⁺	[CuL^{pu,OMe}]⁺
CCDC number	2014610	2014603	2014608	2014607
Formula	C ₃₆ H ₃₈ CuN ₂ O ₄ , C _{0.16} H _{0.32} Cl _{0.32}	C ₃₂ H ₄₆ CuN ₂ O ₄	C ₃₆ H ₃₈ CuN ₂ O ₄ , SbF ₆ , 0.36(CH ₂ Cl ₂)	F ₆ Sb, C ₃₂ H ₄₆ CuN ₂ O ₄ , 0.98(CH ₂ Cl ₂)
<i>F_w</i> [g.mol ⁻¹]	639.60	586.25	892.28	905.01
<i>T</i> [K]	200	200	200	200
Morphology	needle	needle	needle	needle
Color	black	green	black	black
Crystal size [mm]	0.13 x 0.14 x 0.42	0.18 x 0.2 x 0.3	0.1 x 0.16 x 0.7	0.1 x 0.12 x 0.43
Crystal system	rhombohedral	trigonal	orthorhombic	triclinic
Space group	-P 3*	-R 3 2" c	-C 2bc 2	-P 1
<i>a</i> [Å]	21.012(2)	29.373(4)	22.840(5)	11.027(2)
<i>b</i> [Å]	21.012(2)	29.373(4)	25.399(5)	13.071(3)
<i>c</i> [Å]	21.012(2)	20.654(4)	16.261(3)	14.287(3)
α [°]	115.759(17)	90	90	108.75(3)
β [°]	115.759(17)	90	90	92.22(3)
γ [°]	115.759(17)	120	90	91.99(3)
Unit-cell volume [Å ³]	4814(2)	15433(5)	9433(3)	1946.1(8)
<i>Z</i>	6	18	8	2
<i>D_x</i> [g.cm ⁻³]	1.324	1.135	1.257	1.544
μ [mm ⁻¹]	0.748	0.670	5.959	1.440
<i>F</i> (000)	2014	5634	3592	918
Radiation	MoK α (λ = 0.71073)	MoK α (λ = 0.71073)	CuK α (λ = 1.54178)	MoK α (λ = 0.71073)
Θ range for data collection/°	2.841 to 27.497	2.337 to 24.999	3.763 to 67.994	2.448 to 30.000
Index ranges	-26 ≤ <i>h</i> ≤ 25	-33 ≤ <i>h</i> ≤ 34	-27 ≤ <i>h</i> ≤ 27	-15 ≤ <i>h</i> ≤ 15
	-25 ≤ <i>k</i> ≤ 23	-33 ≤ <i>k</i> ≤ 34	-30 ≤ <i>k</i> ≤ 30	-18 ≤ <i>k</i> ≤ 18
	-27 ≤ <i>l</i> ≤ 27	-21 ≤ <i>l</i> ≤ 24	-19 ≤ <i>l</i> ≤ 18	-20 ≤ <i>l</i> ≤ 20
Total reflections	29196	30288	41090	39588
Unique reflections	7300	3013	4385	11332
Used reflections	4660 (<i>I</i> > 2 σ (<i>I</i>))	2269 (<i>I</i> > 2 σ (<i>I</i>))	3638 (<i>I</i> > 2 σ (<i>I</i>))	8611 (<i>I</i> > 2 σ (<i>I</i>))
Refined parameters	429	183	327	492
<i>R</i> _{int}	0.0780	0.0814	0.0457	0.0643
<i>R</i> ₁	0.0562	0.0684	0.0571	0.0603
<i>R</i> (<i>w</i>) ^a	0.1054	0.1861	0.1801	0.1230
Goodness of fit <i>S</i>	1.091	1.139	1.125	1.152
$\Delta\rho_{\min}/\Delta\rho_{\max}$ (e·Å ⁻³)	-0.559/0.394	-1.192/0.668	-1.413/0.840	-1.054/0.920

^aBased on *F*² where *w* = 1/[*s*²(*Fo*²)+(0.0349*P*)²+4.6650*P*] where *P*=(*Fo*²+2*Fc*²)/3 for **CuL^{bp,OMe}**
w = 1/[*s*²(*Fo*²)+(0.1481*P*)²+15.6062*P*] where *P*=(*Fo*²+2*Fc*²)/3 for **CuL^{pu,OMe}**
w = 1/[*s*²(*Fo*²)+(0.1280*P*)²+10.6247*P*] where *P*=(*Fo*²+2*Fc*²)/3 for **[CuL^{bp,OMe}]⁺**
w = 1/[*s*²(*Fo*²)+(0.0270*P*)²+4.8368*P*] where *P*=(*Fo*²+2*Fc*²)/3 for **[CuL^{pu,OMe}]⁺**

Chapter VII. Experimental section

1.8. Computational details

- Chapter II

Calculations of these parts were performed by Pr. Fabrice Thomas from the Département de Chimie Moléculaire, Université Grenoble Alpes, France.

Full geometry optimizations were performed with the Gaussian 9 program,^[347] by using the B3LYP,^[348,349] B3LYP-D3,^[350] or CAM-B3LYP^[351] functionals. The 6-31G* basis set^[352] was used for the C, H, N, and O atoms. For the metal ion in $[\text{NiL}^{\text{C2O2}}]^+$, we tested both the 6-31G* basis set and a pseudo-potential based on the LANL2Dz basis set.^[353] For $[\text{PdL}^{\text{C2O2}}]^+$ and $[\text{PtL}^{\text{C2O2}}]^+$, we used only the pseudopotential for the metal center. Frequency calculations were systematically performed in order to ensure that the optimized structure corresponds to a minimum and not a saddle point. Optical properties were computed by using time-dependent density functional theory (TD-DFT)^[354] with the same basis set as for optimization. The solvent was taken in account by using a polarized continuum model (PCM).^[355] The 30 lowest energy excited states were calculated. The calculations of the EPR parameters of $[\text{NiL}^{\text{C2O2}}]^+$ were carried out using the ORCA program package.^[356] The EPR parameters were computed using the B3LYP functional with D3 dispersion correction with Becke–Johnson damping. The Def2-TZVP basis set^[357,358] was used for all atoms except the metal. A softer basis set (“CP(PPP)”) ^[359] was used for the metal ion. The integration grid was Grid 6 in the orca convention, with a special radial integration accuracy set to 5.67 for the metal ion. A complete mean field approach was used to calculate the SOC, with Coulomb terms via RI. The magnetic exchanges were calculated by using the Yamaguchi approach.^[287]

- Chapter III and IV

Full geometry optimizations were performed with the Gaussian 16 program,^[360] by using the BP86^[361] or B3LYP^[348,349] functionals and a polarizable continuum model (CH_2Cl_2).^[355] The 6-31G* basis set^[352] was used for all atoms. Frequency calculations were systematically performed in order to ensure that the optimized structure corresponds to a minimum and not a saddle point. Single point and natural bond orbital calculations^[293,362] were performed using the B3LYP, B3LYP-D3, CAMB3LYP, BP86 or B3P86 functionals and a polarizable continuum model (CH_2Cl_2).^[355] The TZVP basis set^[359] was used for all atoms. Optical properties were computed by using time-dependent DFT (TD-DFT).^[354] The magnetic exchanges were calculated by using the Yamaguchi approach.^[287]

- Chapter V

Calculations of these parts were performed by Pr. Fabrice Thomas from the Département de Chimie Moléculaire, Université Grenoble Alpes, France.

Full geometry optimizations were performed with the Gaussian 9 program,^[347] by using the B3LYP^[348,349] functional and a polarizable continuum model (CH_2Cl_2).^[355] The 6-31G* basis set^[352] was used for all atoms. Frequency calculations were systematically performed in order to ensure that the optimized structure corresponds to a minimum and not a saddle point. Optical properties were computed by using time-dependent DFT (TD-DFT),^[354] with the optimized structures and using the BLYP functional,^[348,349] together with the TZVP basis set,^[359] which

proved to better reproduce the experimental spectra. The solvent was again taken in account by using a polarized continuum model (PCM).^[355] The 30 lowest energy excited states were calculated. The magnetic exchanges were calculated by using the Yamaguchi approach.^[287]

1.9. Catalysis (Chapter V)

- Salen catalysts

0.6 mmol of an alcohol substrate and 0.72 mmol of potassium *tert*-butoxide (solid form) were introduced to a glass tube. 1 mL of 0.48 mM solution of the copper catalysts (prepared from stock solutions in degassed CH₂Cl₂) were added and the tube was immediately sealed with a septum and purged with oxygen using a syringe (3-time purge). The mixture was shaken at room temperature and aliquots of 30 μ L were taken after 1 and 3 h. The tube is purged once with oxygen after the aliquots were collected before continuing the catalysis. The aliquots were directly dissolved in CDCl₃ (300 μ L) for immediate ¹H NMR analysis. The NMR data analysis was conducted with the MestReNova software (version 12.0.0-20080). Auto phase and auto baseline corrections were made and the α protons of the alcohol substrates were normalized for the integration. The protons of the alcohol substrates and their oxidized products were selected as follow for integration in ¹H NMR (500 MHz, CDCl₃):

Benzyl alcohol: δ 4.70 ppm (s, 2H, α -CH₂), benzaldehyde: δ 10.03 ppm (s, 1H, O=CH);

2-Phenylethanol: δ 3.85 ppm (t, 2H, α -CH₂), 2-phenylacetaldehyde: δ 10.02 ppm (s, 1H, O=CH);

1-Phenylethanol: δ 4.91 ppm (q, 1H, α -CH), acetophenone: δ 2.61 ppm (s, 3H, CH₃).

- Blank with the Cu(OAc)₂ salt

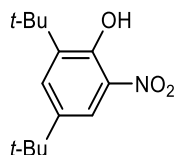
0.6 mmol of an alcohol substrate and 0.72 mmol of potassium *tert*-butoxide (solid form) were introduced to a glass tube. 9.6–9.8 mg of Cu(OAc)₂·H₂O (0.48–0.49 μ mol) were added, then suspended in 1 mL of degassed CH₂Cl₂. The catalysis was then conducted using the same procedure as for the salen catalysts.

- Background

0.6 mmol of an alcohol substrate and 0.72 mmol of potassium *tert*-butoxide (solid form) were introduced to a glass tube. 1 mL of degassed CH₂Cl₂ were added and the catalysis was then conducted using the same procedure as for the salen catalysts.

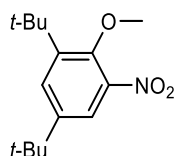
2. Synthesis

2.1. Chapter II

- Synthesis of the $H_4L^{C2O2}Br_2$ proligand2,4-di-*tert*-butyl-6-nitro-phenol

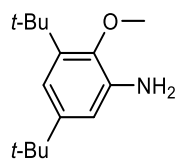
65% nitric acid (3.5 mL, 50.2 mmol) was added dropwise to a solution of 2,4-di-*tert*-butylphenol (10.08 g, 48.9 mmol) in acetic acid (100 mL) and cooled down with an ice/water bath. The red mixture was stirred for 2h, then quenched with addition of 60 mL of H₂O and saturated NaHCO₃ solution until pH 5 was reached. The resulting red precipitate was collected and rinsed with water, solubilized in 250 mL of CH₂Cl₂, and washed with 150 mL of H₂O and 150 mL of brine (2 times), dried over Na₂SO₄ and evaporated to obtain 2,4-di-*tert*-butyl-6-nitrophenol as an orange solid (12.26 g, 99%).

¹H NMR (400 MHz, CDCl₃) δ 1.32 (s, 9H, *t*-Bu), 1.45 (s, 9H, *t*-Bu), 7.64 (s, 1H, aryl-H), 7.96 (s, 1H, aryl-H), 11.45 (s, 1H, OH). ¹³C NMR (500 MHz, CDCl₃) δ 29.53, 31.25, 34.66, 35.87, 119.00, 132.73, 133.81, 140.00, 142.10, 153.15. MS (HRMS): *m/z* = 250.14 [M – H][–]. Anal. Calcd. for C₁₄H₂₁NO₃: C, 66.89; H, 8.44; N, 5.57. Found: C, 66.01; H, 9.05; N, 5.38.

1,5-di-*tert*-butyl-2-methoxy-3-nitro-benzene

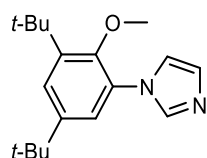
Potassium carbonate (13.482 g, 97.5 mmol) and iodomethane (29 g, 204 mmol) were added to a solution of 2,4-di-*tert*-butyl-6-nitrophenol (12.26 g, 48.8 mmol) in acetone (210 mL). The mixture was heated at 70 °C and stirred for 20 h, then the potassium carbonate was filtered. The crude mixture was evaporated then resolubilized in 250 mL of CH₂Cl₂, washed with 150 mL of H₂O and 150 mL of brine (2 times), dried over Na₂SO₄ and evaporated to obtain 1,5-di-*tert*-butyl-2-methoxy-3-nitrobenzene as an orange oil (12.42 g, 96%).

¹H NMR (400 MHz, CDCl₃) δ 1.32 (s, 9H, *t*-Bu), 1.41 (s, 9H, *t*-Bu), 3.79 (s, 3H, O–CH₃), 7.55 (d, 1H, aryl-H, 2.50 Hz), 7.59 (d, 1H, aryl-H, 2.5 Hz). ¹³C NMR (500 MHz, CDCl₃) δ 30.67, 31.32, 34.90, 35.95, 61.43, 120.49, 128.64, 143.93, 144.55, 145.90, 150.96. MS (HRMS): *m/z* = 266.18 [M + H]⁺. Anal. Calcd. for C₁₅H₂₃NO₃: C, 67.88; H, 8.75; N, 5.28. Found: C, 68.13; H, 8.97; N, 5.17.

3,5-di-*tert*-butyl-2-methoxy-aniline

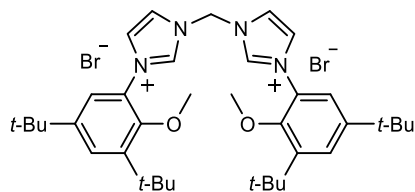
1,5-di-*tert*-butyl-2-methoxy-3-nitro-benzene (12.42 g, 46.8 mmol) was solubilized in ethanol (200 mL) and palladium on charcoal (10 wt. %, 1.25 g, 1.17 mmol) was added. The mixture was vigorously stirred under H₂ atmosphere for 3 days at room temperature. The catalyst was then filtered over celite, and the filtrate evaporated, affording 3,5-di-*tert*-butyl-2-methoxyaniline as an orange solid (10.83 g, 98%).

¹H NMR (400 MHz, CDCl₃) δ 1.27 (s, 9H, *t*-Bu), 1.39 (s, 9H, *t*-Bu), 3.60 (s, 2H, NH₂), 3.79 (s, 3H, O-CH₃), 6.67 (s, 1H, aryl-H), 6.76 (s, 1H, aryl-H). ¹³C NMR (500 MHz, CDCl₃) δ 31.25, 31.64, 34.58, 35.34, 59.20, 112.36, 114.50, 139.73, 142.02, 144.82, 146.41. MS (HRMS): *m/z* = 236.30 [M + H]⁺. Anal. Calcd. for C₁₅H₂₅NO: C, 76.53; H, 10.73; N, 5.95. Found: C, 76.63; H, 10.76; N, 4.94.

1-(3,5-di-*tert*-butyl-2-methoxy-phenyl)imidazole

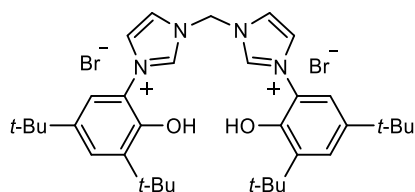
Glyoxal in H₂O (10 wt. %, 0.52 mL, 4.55 mmol) was added to a solution of 3,5-di-*tert*-butyl-2-methoxy-aniline (1.06 g, 4.51 mmol) in ethanol (25 mL). The mixture was stirred overnight at room temperature before adding ammonium chloride (482 mg, 9.01 mmol) and formaldehyde (37 wt. % in H₂O, 0.68 mL, 9.13 mmol). The mixture was heated to reflux for 2 h, and phosphoric acid (85 wt. % in H₂O, 0.74 mL, 10.8 mmol) was added. The mixture was maintained at reflux for a further 12 h. The crude mixture was then evaporated and treated with a potassium hydroxide solution (40% in water) until pH 9 is reached. The aqueous phase was extracted with CH₂Cl₂ (3 × 30 mL), and the combined organic phases were washed with H₂O (50 mL) and brine (2 × 50 mL), dried over Na₂SO₄, and evaporated. The crude brown solid was purified on silica chromatography with a pentane/ethyl acetate 40/60 eluent affording 1-(3,5-di-*tert*-butyl-2-methoxy-phenyl)imidazole as a pale white solid (788 mg, 61%).

¹H NMR (400 MHz, CDCl₃) δ 1.32 (s, 9H, *t*-Bu), 1.41 (s, 9H, *t*-Bu), 3.20 (s, 3H, O-CH₃), 7.11 (d, 1H, aryl-H, 2.36 Hz), 7.22 (s, 1H, aryl-H), 7.23 (s, 1H, aryl-H), 7.37 (d, 1H, aryl-H, 2.32 Hz), 7.76 (s, 1H, aryl-H). ¹³C NMR (500 MHz, CDCl₃) δ 30.78, 31.51, 34.77, 35.66, 59.72, 120.42, 121.60, 123.95, 129.72, 130.52, 137.71, 143.74, 146.58, 151.07. MS (HRMS): *m/z* = 287.21 [M + H]⁺. Anal. Calcd. for C₁₈H₂₆N₂O: C, 75.47; H, 9.17; N, 9.78. Found: C, 74.20; H, 9.86; N, 9.78.

1,1'-methylenebis(3-(3,5-di-*tert*-butyl-2-methoxyphenyl)-1*H*-imidazol-3-ium) bromide

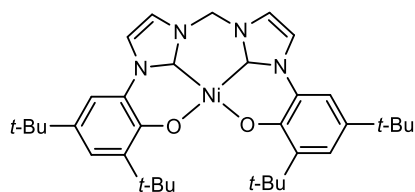
A mixture of dibromomethane (1.0 mL, 14 mmol) and of 1-(3,5-di-*tert*-butyl-2-methoxyphenyl)imidazole (103.1 mg, 0.36 mmol) was sealed in a tube and stirred overnight at 100 °C. The resulting white precipitate was collected and washed with cold acetone affording 1,1'-methylenebis(3-(3,5-di-*tert*-butyl-2-methoxyphenyl)-1*H*-imidazol-3-ium) bromide as a white solid (88.0 mg, 65%).

^1H NMR (400 MHz, DMSO- d_6) δ 1.31 (s, 18H, *t*-Bu), 1.42 (s, 18H, *t*-Bu), 3.35 (s, 6H, O-CH₃), 6.90 (s, 2H, CH₂), 7.47 (d, 2H, aryl-H, 2.00 Hz) 7.54 (d, 2H, aryl-H, 2.08 Hz), 8.26 (s, 2H, aryl-H) 8.34 (s, 2H, aryl-H), 9.96 (s, 2H, aryl-H). ^{13}C NMR (500 MHz, DMSO- d_6) δ 30.51, 30.97, 34.62, 35.27, 58.72, 61.04, 121.95, 122.62, 124.10, 125.86, 128.20, 139.04, 143.57, 146.81, 150.21. MS (HRMS): m/z = 293.21 [$M - 2\text{Br}$] $^{2+}$. Anal. Calcd. for C₃₇H₅₄N₄O₂.2Br: C, 59.51; H, 7.30; N, 7.50. Found: C, 59.30; H, 7.71; N, 7.21.

Proligand **H₄L^{C202}Br₂**

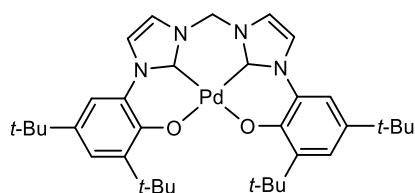
Boron tribromide (0.36 mL, 3.54 mmol) was added dropwise to a suspension of 1,1'-methylenebis(3-(3,5-di-*tert*-butyl-2-methoxyphenyl)-1*H*-imidazol-3-ium) bromide (434.2 mg, 0.58 mmol) in dry CH₂Cl₂ (15 mL) under argon atmosphere. The solution was stirred overnight then quenched by successive additions and evaporations of methanol (4 × 20 mL). The resulting white solid was collected and washed with cold acetone to afford proligand **H₄L^{C202}Br₂** as a white solid (377.6 mg, 90%).

^1H NMR (400 MHz, DMSO- d_6) δ 1.29 (s, 18H, *t*-Bu), 1.42 (s, 18H, *t*-Bu), 6.93 (s, 2H, CH₂), 7.32 (d, 2H, aryl-H, 2.40 Hz) 7.45 (d, 2H, aryl-H, 2.35 Hz), 8.14 (t, 2H, aryl-H, 1.77 Hz) 8.27 (t, 2H, aryl-H, 1.72 Hz), 9.19 (s, 2H, aryl-H), 9.89 (s, 2H, aryl-H). ^{13}C NMR (500 MHz, DMSO- d_6) δ 29.54, 31.10, 34.22, 35.19, 58.08, 121.09, 122.28, 124.37, 124.92, 125.58, 139.10, 139.81, 142.67, 146.94. MS (HRMS): m/z = 279.20 [$M - 2\text{Br}$] $^{2+}$. Anal. Calcd for C₃₅H₅₀N₄O₂.2Br: C, 58.49; H, 7.03; N, 7.80. Found: C, 57.31; H, 7.26; N, 7.23.

- Synthesis of the group 10 complexesComplex **NiL**^{C2O2}

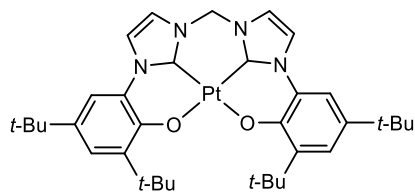
Triethylamine (0.12 mL, 0.86 mmol) was added to a solution of **H₄L^{C2O2}Br₂** (80.1 mg, 0.111 mmol) and nickel(II) acetate tetrahydrate (28.6 mg, 0.115 mmol) in methanol (10 mL) under argon atmosphere. The mixture was heated at 55 °C and stirred overnight. The precipitated solid was collected and washed with methanol to afford **NiL^{C2O2}** as a pale yellow powder (49.7 mg, 73%).

¹H NMR (400 MHz, DMSO-*d*₆) δ 1.29 (s, 18H, *t*-Bu), 1.43 (s, 18H, *t*-Bu), 6.13 (s, 2H, CH₂), 7.00 (d, 2H, aryl-H), 7.39 (d, 2H, aryl-H, 2.04 Hz), 7.74 (s, 2H, aryl-H, 1.96 Hz), 8.34 (s, 2H, aryl-H, 2.04 Hz). ¹³C NMR (500 MHz, DMSO-*d*₆) δ 30.16, 31.68, 33.82, 35.61, 60.44, 111.88, 118.11, 119.96, 121.45, 124.27, 133.21, 138.77, 152.09, 153.65. MS (HRMS): *m/z* = 612.30 [NiL]⁺. Anal. Calcd. for C₃₅H₄₆NiN₄O₂ · 1/3 CH₃OH: C, 67.99; H, 7.64; N, 8.98. Found: C, 67.56; H, 7.81; N, 9.13. Crystals suitable for X-Ray diffraction were obtained by slow evaporation of a concentrated methanol solution of **NiL^{C2O2}**, affording yellow crystals.

Complex **PdL**^{C2O2}

Triethylamine (65 μL, 0.46 mmol) was added to a solution of **H₄L^{C2O2}Br₂** (81.5 mg, 0.113 mmol) and palladium(II) acetate (25.6 mg, 0.115 mmol) in methanol (10 mL) under argon atmosphere. The mixture was heated at 60 °C and stirred for 4 h. The precipitated solid was collected and washed with methanol to afford **PdL^{C2O2}** as a pale gray powder (42.5 mg, 57%).

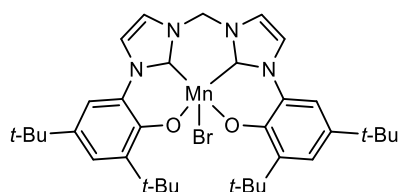
¹H NMR (400 MHz, DMSO-*d*₆) δ 1.30 (s, 18H, *t*-Bu), 1.48 (s, 18H, *t*-Bu), 6.33 (s, 2H, CH₂), 7.08 (d, 2H, aryl-H, 1.60 Hz), 7.40 (s, 2H, aryl-H), 7.81 (d, 2H, aryl-H, 1.64 Hz), 8.39 (d, 2H, aryl-H, 1.84 Hz). ¹³C NMR (500 MHz, DMSO-*d*₆) δ 29.90, 31.69, 33.83, 35.77, 62.15, 113.51, 118.07, 120.79, 121.25, 125.04, 132.98, 139.61, 153.84, 154.52. MS (HRMS): *m/z* = 661.27 [PdL + H]⁺. Anal. Calcd. for C₃₅H₄₆N₄O₂Pd: C, 63.57; H, 7.03; N, 8.47. Found: C, 63.18; H, 6.84; N, 8.03. Crystals suitable for X-Ray diffraction were obtained by slow evaporation of a concentrated dimethylformamide solution of **PdL^{C2O2}**, affording colorless crystals.

Complex **PtL^{C2O2}**

Triethylamine (0.06 mL, 0.43 mmol) was added to a solution of **H4L^{C2O2}Br₂** (76.0 mg, 0.106 mmol) and cis-dichlorobis(dimethyl sulfoxide)-platinum(II) (48.8 mg, 0.116 mmol) in ethanol (12 mL) under argon atmosphere. The mixture was heated under reflux at 100 °C and stirred for 5 h then overnight at 60 °C. The precipitated solid was collected and washed with cold ethanol to afford **PtL^{C2O2}** as a pale white powder (58.0 mg, 73%).

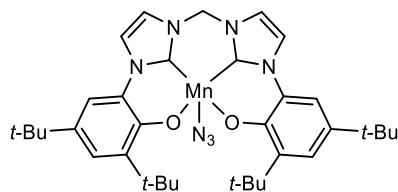
¹H NMR (400 MHz, DMSO-d₆) δ 1.30 (s, 18H, *t*-Bu), 1.48 (s, 18H, *t*-Bu), 6.28 (s, 2H, CH₂), 7.11 (s, 2H, aryl-H) 7.43 (s, 2H, aryl-H), 7.68 (s, 2H, aryl-H) 8.37 (s, 2H, aryl-H). ¹³C NMR (500 MHz, DMSO-d₆) δ 29.94, 31.66, 33.90, 35.88, 62.07, 113.24, 116.74, 120.46, 120.87, 125.34, 134.29, 139.50, 140.04, 151.76. MS (HRMS): *m/z* = 749.33 [PtL]⁺. Anal. Calcd. for C₃₅H₄₆N₄O₂Pt. 1/3 CH₃OH: C, 55.80; H, 6.27; N, 7.37. Found: C, 55.40; H, 6.64; N, 7.39. Crystals suitable for X-Ray diffraction were obtained by slow evaporation of a concentrated dimethylsulfoxide solution of **PtL^{C2O2}**, affording colorless crystals.

2.2. Chapter III

- Mn^{III}L^{C2O2} precursorsComplex **MnL^{C2O2}Br**

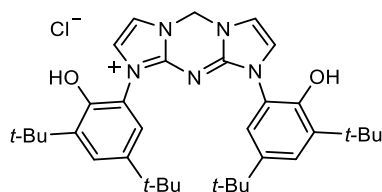
The proligand **H4L^{C2O2}Br₂** (152 mg, 212 μmol) was suspended in a solution of manganese(II) acetate tetrahydrate (52.1 mg, 213 μmol) in dry acetonitrile (25 mL). Triethylamine (120 μL, 0.86 mmol) was added and the resulting mixture was stirred at 80 °C for 3 h. The solution gradually homogenized as it took a brown color. It was then evaporated and the crude product was solubilized in toluene, then filtered over celite. The filtrate was evaporated and dried under high vacuum overnight to afford **MnL^{C2O2}Br** as a brown solid (147 mg, 98%).

MS (HRMS): *m/z* = 609.29 [MnL - Br]⁺. Crystals suitable for X-Ray diffraction were obtained by slow evaporation of a concentrated dichloromethane solution of **MnL^{C2O2}Br**, affording dark brown crystals.

Complex **MnL^{C2O2}(N₃)**

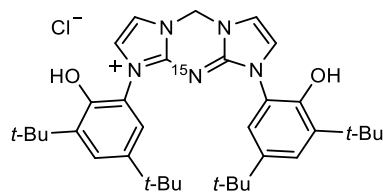
MnL^{C2O2}Br (135 mg, 196 μmol) was solubilized in a solution acetonitrile (8 mL) and H_2O (1.5 mL). A solution of sodium azide 1 M in H_2O (215 μL , 215 μmol) was added dropwise and the mixture was stirred at room temperature for 1 h. A large spatula of sodium sulfate was added and the volatiles were removed under vacuum. The crude product was solubilized in dichloromethane and filtered over celite. The filtrate was evaporated to afford **MnL^{C2O2}(N₃)** as a brown solid (122 mg, 95%).

IR: $\nu(\text{N}_3) = 2040 \text{ cm}^{-1}$. ESI-MS: $m/z = 609.30 [\text{MnL} - \text{N}_3]^+$. Crystals suitable for X-Ray diffraction were obtained by slow evaporation of a concentrated acetonitrile solution of **MnL^{C2O2}(N₃)**, affording brown crystals.

- N-inserted products**1.Cl**

A solution of **MnL^{C2O2}Br** (102.8 mg, 149 μmol) in dichloromethane (8 mL) was added dropwise to **Mn(salen)(N)** (50.4 mg, 150 μmol) suspended in dichloromethane (5 mL). A brown precipitate formed instantly and the solution was stirred under air for 2 h. The precipitate was eliminated by filtration and the brown filtrate was evaporated. The crude mixture was solubilized in 20 mL of diethyl ether. The organic phase was washed three times by a 10% hydrochloric acid H_2O solution, then three times by a saturated H_2O solution of tetrasodium EDTA, followed by two times with H_2O and one final time with brine. The organic phase was dried over Na_2SO_4 and evaporated. The resulting pale brown solid was solubilized in acetonitrile and washed 5 times with hexanes. Finally, the acetonitrile solution was evaporated and dried under high vacuum overnight, affording **1.Cl** as a beige powder (42.3 mg, 47%).

^1H NMR (600 MHz, CDCl_3) δ 1.25 (s, 18H, *t*-Bu), 1.29 (s, 18H, *t*-Bu), 6.52 (s, 2H, CH_2), 6.89 (s, 2H, aryl-H), 6.91 (s, 2H, aryl-H), 7.32 (d, $J = 2.2 \text{ Hz}$, 2H, aryl-H), 8.72 (s, 2H, aryl-H). MS (HRMS): $m/z = 570.38 [\text{M} - \text{Cl}]^+$.

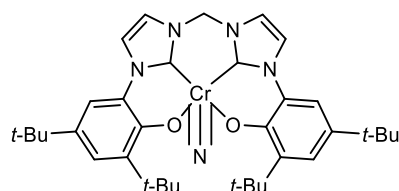
1(¹⁵N).Cl

A solution of **MnL^{C202}Br** (101.7 mg, 147 μ mol) in dichloromethane (7 mL) was added dropwise to **Mn(salen)(¹⁵N)** (50.0 mg, 149 μ mol) suspended in dichloromethane (4 mL). A brown precipitate formed instantly and the solution was stirred under air for 3 h. The precipitate was eliminated by filtration and the filtrate was evaporated. The crude mixture was solubilized in diethyl ether. The organic phase was washed three times by a 10% hydrochloric acid H₂O solution, then three times by a saturated H₂O solution of tetrasodium EDTA, followed by two times with H₂O and one final time with brine. The organic phase is dried over Na₂SO₄ and evaporated. The resulting pale brown solid was solubilized in acetonitrile and washed 5 times with hexanes. Finally, the acetonitrile solution was evaporated and dried under high vacuum overnight, affording **1(¹⁵N).Cl** as a beige powder (50.0 mg, 56%).

MS (HRMS): $m/z = 571.38$ $[M - Cl]^+$. Crystals suitable for X-Ray diffraction were obtained by slow evaporation of a CH₂Cl₂/CH₃CN (1:1 v/v) solution of **1(¹⁵N).Cl** affording colorless crystals.

2.3. Chapter IV

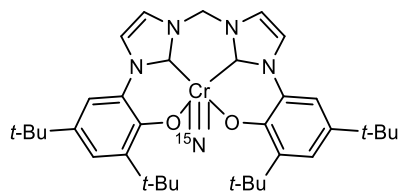
The synthesis of the Cr(V)-nitride complexes were adapted from a procedure developed by Birk and Bendix.^[204]

Complex CrL^{C202}(N)

A solution of CrCl₃(THF)₃ (219.1 mg, 585 μ mol) was prepared in dry acetonitrile (5 mL) under N₂ atmosphere in a glovebox. The solution was then added on **Mn(salen)(N)** (193.4 mg, 577 μ mol) under strong stirring. The purple solution immediately turned brown and a brown precipitate formed. The mixture was stirred under air at room temperature for 1 h then was filtered over celite to afford a yellow-brown solution of $[N\equiv Cr]^{2+}$ complex.

The solution containing the $[N\equiv Cr]^{2+}$ complex was then added dropwise to an ethanol solution (40 mL) of **H₄L^{C202}Br₂** (376.0 mg, 523 μ mol) and Et₃N (300 μ L, 2.15 mmol) stirred at 60°C. The resulting mixture was stirred under reflux under air overnight then evaporated. The orange-brown crude solid was suspended in cold methanol, collected and washed with cold methanol to afford **CrL^{C202}(N)** as a bright orange powder (127.6 mg, 39%).

IR: $\nu(N\equiv Cr) = 1025$ cm⁻¹. ESI-MS: $m/z = 621.32$ $[CrL + H]^+$. Crystals suitable for X-Ray diffraction were obtained by slow evaporation of a concentrated solution of **CrL^{C202}(N)** in a concentrated dichloromethane/acetonitrile solvent system, affording bright orange crystals.

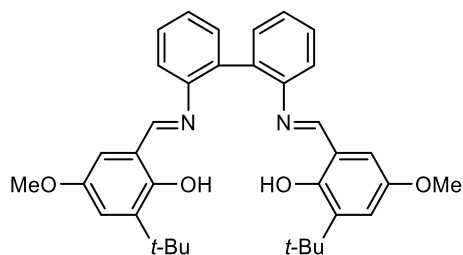
Complex **CrL**^{C2O2}(¹⁵N)

A solution of $\text{CrCl}_3(\text{THF})_3$ (105.5 mg, 273 μmol) was prepared in dry acetonitrile (2.1 mL) under N_2 atmosphere in a glovebox. The solution was then added on **Mn(salen)**(¹⁵N) (98.0 mg, 291 μmol) under strong stirring. The purple solution immediately turned brown and a brown precipitate formed. The mixture was stirred under air at room temperature for 1 h then was filtered over celite to afford a yellow-brown solution of $[\text{N}\equiv\text{Cr}]^{2+}$ complex.

The solution containing the $[\text{N}\equiv\text{Cr}]^{2+}$ complex was then added dropwise to an ethanol solution (23 mL) of **H₄L**^{C2O2}**Br₂** (189.7 mg, 264 μmol) and Et_3N (162 μL , 1.16 mmol) stirred at room temperature. The resulting mixture was stirred under reflux under air overnight then evaporated. The orange brown crude solid was suspended in cold methanol, collected and washed with cold methanol to afford **CrL**^{C2O2}(¹⁵N) as a bright orange powder (57.5 mg, 35%).

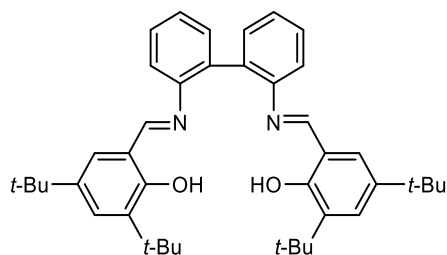
IR: $\nu(^{15}\text{N}\equiv\text{Cr}) = 998 \text{ cm}^{-1}$. MS (HRMS): $m/z = 622.31 [\text{CrL} + \text{H}]^+$. Crystals suitable for X-Ray diffraction were obtained by slow evaporation of a concentrated methanol solution of **CrL**^{C2O2}(¹⁵N), affording bright orange crystals.

2.4. Chapter V

- Salen ligands**H₂L**^{bp,OMe}

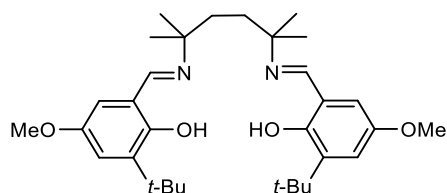
To a solution of 3-(*tert*-butyl)-2-hydroxy-5-methoxybenzaldehyde (659 mg, 3.17 mmol) in ethanol (5 mL) was added a solution of 2,2'-biphenyldiamine (290 mg, 1.57 mmol) in ethanol (5 mL). The solution was stirred and heated under reflux under anaerobic conditions over 3 days, forming an orange precipitate. After concentration, the solution was cooled in a freezer overnight, filtrated, washed with cold ethanol and dried under vacuum affording **H₂L**^{bp,OMe} as an orange powder (712 mg, 80%).

¹H NMR (400 MHz, CDCl_3): $\delta = 1.35$ (s, 18H, *t*-Bu); 3.64 (s, 6H, O-CH₃); 6.15 (s, 2H, aryl-H); 6.88 (s, 2H, aryl-H); 7.15 (s, 2H, aryl-H); 7.38 (s, 2H, aryl-H); 7.45 (dd, $J = 24.3, 6.4$ Hz, 4H, 2 aryl-H); 8.25 (s, 2H, N=CH). ¹³C NMR (300 MHz, CDCl_3): $\delta = 29.20; 34.91; 55.35; 111.09; 117.99; 118.72; 119.12; 126.67; 129.12; 130.89; 134.62; 138.80; 147.86; 151.14; 154.70; 163.42$. MS (HRMS): $m/z = 565.30 [\text{M} + \text{H}]^+$. Anal. Calcd. for $\text{C}_{36}\text{H}_{40}\text{N}_2\text{O}_4$: C, 76.55; H, 7.15; N, 4.96. Found: C, 75.72; H, 7.30; N, 4.66.

H₂L^{bp,tBu}

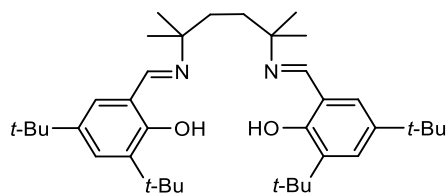
To a solution of 3,5-(di-*tert*-butyl)-2-hydroxybenzaldehyde (679 mg, 2.90 mmol) in methanol (4 mL) was added a solution of 2,2'-biphenyldiamine (267 mg, 1.45 mmol) in methanol (6 mL). The solution was stirred and heated under reflux for 16 hours, forming an orange precipitate. After concentration, the solution was cooled in freezer overnight, filtrated, washed with cold methanol and dried in vacuum affording **H₂L^{bp,tBu}** as an orange powder (670 mg, 75%).

¹H RMN (400 MHz, CDCl₃): δ = 1.26 (s, 18H, *t*-Bu); 1.37 (s, 18H, *t*-Bu); 7.04–7.03 (d, *J* = 2.1 Hz, 2H, aryl-H); 7.21–7.20 (d, *J* = 6.2 Hz, 2H, aryl-H); 7.31 (d, *J* = 2.1 Hz, 2H, aryl-H); 7.36–7.35 (d, *J* = 5.6 Hz, 2H, aryl-H); 7.46–7.38 (m, 4H, aryl-H); 8.55 (s, 2H, N=CH); 13.02 (s, 2H). ¹³C NMR (300 MHz, CDCl₃): δ = 29.32; 31.42; 34.04; 34.98; 117.94; 118.37; 126.45; 126.71; 127.49; 128.84; 130.71; 134.97; 136.46; 139.93; 147.44; 158.01; 163.70. MS (HRMS): *m/z* = 617.41 [M + H]⁺. Anal. Calcd. for C₄₂H₅₂N₂O₂: C, 81.76; H, 8.51; N, 4.54. Found: C, 80.30; H, 8.69; N, 3.89.

H₂L^{pu,OMe}

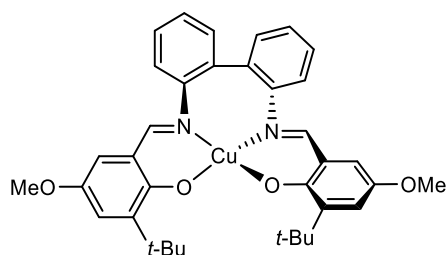
To a solution of 3-(*tert*-butyl)-2-hydroxy-5-methoxybenzaldehyde (812 mg, 3.90 mmol) in ethanol (4 mL) was added a solution of 2,5-dimethylhexane-2,5-diamine (280 mg, 1.94 mmol) in ethanol (4 mL). The solution was stirred and heated for reflux under air for 4 hours, forming an orange precipitate. After concentration, the solution was cooled in freezer overnight, filtered, washed with cold ethanol and dried in vacuum affording **H₂L^{pu,OMe}** as an orange powder (643 mg, 63%).

¹H NMR (400 MHz, CDCl₃): δ = 1.30 (s, 12H, CH₃); 1.43 (s, 18H, *t*-Bu); 1.63 (s, 4H, CH₂); 3.76 (s, 6H, O–CH₃); 6.60 (d, *J* = 3.0 Hz, 2H, aryl-H); 6.96 (d, *J* = 3.0 Hz, 2H, aryl-H); 8.27 (s, 2H, N=CH); 14.20 (s, 2H, OH). ¹³C NMR (300 MHz, CDCl₃): δ = 27.16; 29.28; 34.98; 37.61; 55.84; 59.12; 111.58; 117.99; 137.07; 151.00; 155.46; 160.74. MS (HRMS): *m/z* = 525.36 [M + H]⁺. Anal. Calcd. for C₃₂H₄₈N₂O₄: C, 73.23; H, 9.24; N, 5.34. Found: C, 73.08; H, 9.34; N, 5.24.

H₂L^{pu,tBu}

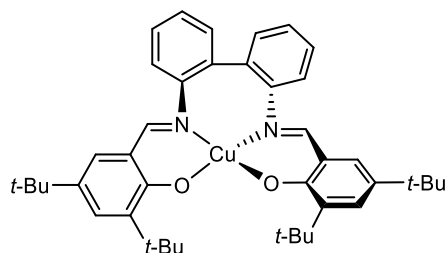
To a solution of 3,5-(di-*tert*-butyl)-2-hydroxybenzaldehyde (443 mg, 1.89 mmol) in ethanol (4 mL) was added a solution of 2,5-dimethylhexane-2,5-diamine (136 mg, 0.94 mmol) in ethanol (4 mL). The solution was stirred and heated to reflux for 4 hours, forming a bright yellow precipitate. The precipitate was filtered, washed with ethanol and dried under vacuum at 45 °C, affording **H₂L^{pu,tBu}** as a yellow powder (517 mg, 95%).

¹H NMR (400 MHz, CDCl₃): δ = 1.31–1.30 (2s, 30H, CH₃ and *t*-Bu); 1.45 (s, 18H, *t*-Bu); 1.62 (s, 4H, CH₂); 7.09 (s, 2H, aryl-H); 7.36 (s, 2H, aryl-H); 8.31 (s, 2H, N=CH); 14.46 (s, 2H, OH). ¹³C NMR (300 MHz, CDCl₃): δ = 27.12; 29.46; 31.53; 34.13; 35.05; 37.73; 59.00; 117.90; 125.97; 126.60; 136.78; 139.64; 158.69; 161.24. MS (HRMS): *m/z* = 577.47 [M + H]⁺. Anal. Calcd. for C₃₈H₆₀N₂O₂: C, 79.10; H, 10.50; N, 4.86. Found: C, 79.24; H, 10.36; N, 4.98.

- Copper complexes**CuL^{bp,OMe}**

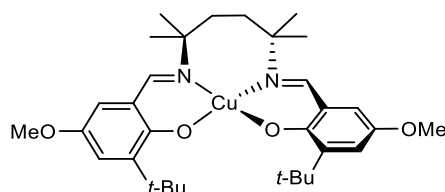
To a solution of ligand **H₂L^{bp,OMe}** (206 mg, 0.36 mmol) in dichloromethane (10 mL) was added a Cu(OAc)₂·H₂O solution (75 mg, 0.376 mmol) in methanol (10 mL) and Et₃N (102 μL, 0.732 mmol). The solution was stirred and heated to reflux for 2 h, then concentrated and cooled in freezer overnight, forming dark green thin crystals. The crystals were collected, washed with cold methanol and dried under vacuum, affording **CuL^{bp,OMe}** (179 mg, 78%).

MS (HRMS): *m/z* = 626.22 [M + H]⁺. Anal. Calcd. for C₃₆H₃₈CuN₂O₄: C, 69.03; H, 6.13; N, 4.47. Found: C, 67.03; H, 6.16; N, 4.49. Crystals suitable for X-Ray diffraction were obtained by vapor diffusion of pentane in a concentrated solution of **CuL^{bp,OMe}** in dichloromethane, affording dark green crystals.

CuL^{bp,tBu}

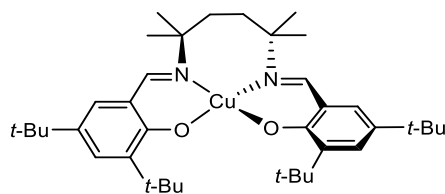
To a solution of ligand **H₂L^{bp,tBu}** (100 mg, 0.162 mmol) in dichloromethane (5 mL) was added a Cu(OAc)₂·H₂O solution (37 mg, 0.185 mmol) in methanol (5 mL) and Et₃N (52 μL, 0.37 mmol). The solution was stirred and heated to reflux for 2 h, then concentrated and cooled in freezer overnight, forming a dark green precipitate. The precipitate was collected washed with cold methanol and dried in vacuum affording **CuL^{bp,tBu}** as a dark green powder (90 mg, 85%).

ESI-MS: *m/z*: 678.33 [M + H]⁺. Anal. Calcd. for C₃₆H₃₈CuN₂O₄: C, 74.36; H, 7.43; N, 4.13. Found: C, 72.10; H, 7.54; N, 4.10. Crystals suitable for X-Ray diffraction were obtained by slow evaporation of a pentane solution of **CuL^{bp,tBu}**, affording dark green crystals.

CuL^{pu,OMe}

To a solution of ligand **H₂L^{pu,OMe}** (94 mg, 0.179 mmol, 1 eq.) in dichloromethane (6 mL) was added a Cu(OAc)₂·H₂O solution (46 mg, 0.23 mmol) in methanol (2 mL) and Et₃N (50 μL, 0.36 mmol). The solution was stirred and heated to reflux for 2 h, forming a dark brown precipitate. The solution was concentrated and cooled in freezer overnight. The precipitate was collected, washed with cold methanol and dried in vacuum, affording **CuL^{pu,OMe}** as a brown powder (89 mg, 85%).

MS (HRMS): *m/z* = 586.28 [M + H]⁺. Anal. Calcd. for C₃₂H₄₆CuN₂O₄: C, 65.54; H, 7.92; N, 4.78. Found: C, 64.55; H, 7.64; N, 4.54. Crystals suitable for X-Ray diffraction were obtained by slow evaporation of an acetone solution of **CuL^{pu,OMe}** affording dark brown crystals.

CuL^{pu,tBu}

To a solution of ligand **H₂L^{pu,tBu}** (222 mg, 0.38 mmol) in dichloromethane (8 mL) was added a Cu(OAc)₂·H₂O solution (88 mg, 0.441 mmol) in methanol (15 mL) and Et₃N (120 μL, 0.86 mmol). The solution was stirred and heated to reflux for 2 h, forming a dark brown precipitate. The solution was concentrated and cooled in freezer overnight. The precipitate was then collected, washed with cold methanol and dried in vacuum, affording **CuL^{pu,tBu}** as a dark brown powder (219 mg, 89%).

MS (HRMS): $m/z = 638.39$ [M + H]⁺. Anal. Calcd. for C₃₈H₅₈CuN₂O₂: C, 71.47; H, 9.17; N, 4.39. Found: C, 71.55; H, 9.22; N, 4.07. Crystals suitable for X-ray diffraction were obtained by slow evaporation of a concentrated acetone solution of **CuL^{pu,tBu}** to afford needle-like brown crystals.

References

- [1] M. Gomberg, *J. Am. Chem. Soc.* **1900**, 22, 757–771.
- [2] P. K. Maurya, in *Animal Biotechnology*, Elsevier, **2014**, pp. 177–191.
- [3] W. B. Jensen, *J. Chem. Educ.* **1984**, 61, 191.
- [4] F. Paneth, W. Hofeditz, *Ber. dtsh. Chem. Ges. A/B* **1929**, 62, 1335–1347.
- [5] M. S. Kharasch, F. R. Mayo, *J. Am. Chem. Soc.* **1933**, 55, 2468–2496.
- [6] J. Andersson, M. Westman, M. Sahlin, B.-M. Sjöberg, *J. Biol. Chem.* **2000**, 275, 19449–19455.
- [7] L. R. F. Backman, M. A. Funk, C. D. Dawson, Catherine. L. Drennan, *Crit. Rev. Biochem. Mol. Biol.* **2017**, 52, 674–695.
- [8] K. D. Miner, T. D. Pfister, P. Hosseinzadeh, N. Karaduman, L. J. Donald, P. C. Loewen, Y. Lu, A. Ivancich, *Biochemistry* **2014**, 53, 3781–3789.
- [9] J. Rittle, M. T. Green, *Science* **2010**, 330, 933–937.
- [10] P. R. Ortiz de Montellano, *Chem. Rev.* **2010**, 110, 932–948.
- [11] A. Ehrenberg, P. Reichard, *J. Biol. Chem.* **1972**, 247, 3485–3488.
- [12] J. W. Whittaker, *Chem. Rev.* **2003**, 103, 2347–2364.
- [13] M. M. Whittaker, J. W. Whittaker, *J. Biol. Chem.* **1988**, 263, 6074–6080.
- [14] N. Ito, S. E. V. Phillips, C. Stevens, Z. B. Ogel, M. J. McPherson, J. N. Keen, K. D. S. Yadav, P. F. Knowles, *Nature* **1991**, 350, 87–90.
- [15] A. J. Baron, C. Stevens, C. Wilmot, K. D. Seneviratne, V. Blakeley, D. M. Dooley, S. E. Phillips, P. F. Knowles, M. J. McPherson, *J. Biol. Chem.* **1994**, 269, 25095–25105.
- [16] M. M. Whittaker, P. J. Kersten, D. Cullen, J. W. Whittaker, *J. Biol. Chem.* **1999**, 274, 36226–36232.
- [17] P. Kersten, D. Cullen, *Fungal Genet. Biol.* **2014**, 72, 124–130.
- [18] M. S. Rogers, A. J. Baron, M. J. McPherson, P. F. Knowles, D. M. Dooley, *J. Am. Chem. Soc.* **2000**, 122, 990–991.
- [19] M. A. Halcrow, L. M. LindyChia, X. Liu, E. J. L. McInnes, L. J. Yellowlees, F. E. Mabbs, I. J. Scowen, M. McPartlin, J. E. Davies, *J. Chem. Soc., Dalton Trans.* **1999**, 1753–1762.
- [20] M. M. Whittaker, W. R. Duncan, J. W. Whittaker, *Inorg. Chem.* **1996**, 35, 382–386.
- [21] S. Itoh, S. Takayama, R. Arakawa, A. Furuta, M. Komatsu, A. Ishida, S. Takamuku, S. Fukuzumi, *Inorg. Chem.* **1997**, 36, 1407–1416.
- [22] J. A. Halfen, B. A. Jazdzewski, S. Mahapatra, L. M. Berreau, E. C. Wilkinson, L. Que, W. B. Tolman, *J. Am. Chem. Soc.* **1997**, 119, 8217–8227.
- [23] J. A. Moulijn, P. W. N. M. van Leeuwen, R. A. van Santen, in *Studies in Surface Science and Catalysis*, Elsevier, **1993**, pp. 3–21.
- [24] Chr. K. Jørgensen, *Coord. Chem. Rev.* **1966**, 1, 164–178.
- [25] M. R. Ringenberg, T. B. Rauchfuss, *Eur. J. Inorg. Chem.* **2012**, 2012, 490–495.

References

- [26] P. J. Chirik, K. Wieghardt, *Science* **2010**, 327, 794–795.
- [27] J. M. Hoyt, V. A. Schmidt, A. M. Tondreau, P. J. Chirik, *Science* **2015**, 349, 960–963.
- [28] K. T. Sylvester, P. J. Chirik, *J. Am. Chem. Soc.* **2009**, 131, 8772–8774.
- [29] K. Wang, E. I. Stiefel, *Science* **2001**, 291, 106–109.
- [30] D. J. Harrison, N. Nguyen, A. J. Lough, U. Fekl, *J. Am. Chem. Soc.* **2006**, 128, 11026–11027.
- [31] L. Dang, M. F. Shibl, X. Yang, A. Alak, D. J. Harrison, U. Fekl, E. N. Brothers, M. B. Hall, *J. Am. Chem. Soc.* **2012**, 134, 4481–4484.
- [32] C. A. Grapperhaus, K. Ouch, M. S. Mashuta, *J. Am. Chem. Soc.* **2009**, 131, 64–65.
- [33] K. Ouch, M. S. Mashuta, C. A. Grapperhaus, *Inorg. Chem.* **2011**, 50, 9904–9914.
- [34] E. N. Jacobsen, W. Zhang, A. R. Muci, J. R. Ecker, L. Deng, *J. Am. Chem. Soc.* **1991**, 113, 7063–7064.
- [35] P. Pfeiffer, E. Breith, E. Lübbe, T. Tsumaki, *Justus Liebigs Ann. Chem.* **1933**, 503, 84–130.
- [36] L. E. Martinez, J. L. Leighton, D. H. Carsten, E. N. Jacobsen, *J. Am. Chem. Soc.* **1995**, 117, 5897–5898.
- [37] B. Saito, T. Katsuki, *Tetrahedron Lett.* **2001**, 42, 3873–3876.
- [38] S. E. Schaus, J. Brånalt, E. N. Jacobsen, *J. Org. Chem.* **1998**, 63, 403–405.
- [39] Y. Tamura, T. Uchida, T. Katsuki, *Tetrahedron Lett.* **2003**, 44, 3301–3303.
- [40] A. Watanabe, T. Uchida, K. Ito, T. Katsuki, *Tetrahedron Lett.* **2002**, 43, 4481–4485.
- [41] Z. Li, K. R. Conser, E. N. Jacobsen, *J. Am. Chem. Soc.* **1993**, 115, 5326–5327.
- [42] Y. N. Belokon', M. North, T. Parsons, *Org. Lett.* **2000**, 2, 1617–1619.
- [43] E. F. DiMauro, M. C. Kozlowski, *Org. Lett.* **2001**, 3, 3053–3056.
- [44] P. G. Cozzi, *Angew. Chem. Int. Ed.* **2003**, 42, 2895–2898.
- [45] S. K. Edulji, S. T. Nguyen, *Organometallics* **2003**, 22, 3374–3381.
- [46] J. A. Miller, W. Jin, S. T. Nguyen, *Angew. Chem.* **2002**, 114, 3077–3080.
- [47] M. S. Sigman, E. N. Jacobsen, *J. Am. Chem. Soc.* **1998**, 120, 5315–5316.
- [48] T. Linker, *Angew. Chem. Int. Ed. Engl.* **1997**, 36, 2060–2062.
- [49] D. Ager, in *Comprehensive Chirality*, Elsevier, **2012**, pp. 104–128.
- [50] C. H. Senanayake, F. E. Roberts, L. M. DiMichele, K. M. Ryan, J. Liu, L. E. Fredenburgh, B. S. Foster, A. W. Douglas, R. D. Larsen, T. R. Verhoeven, P. J. Reider, *Tetrahedron Lett.* **1995**, 36, 3993–3996.
- [51] C. H. Senanayake, G. B. Smith, K. M. Ryan, L. E. Fredenburgh, J. Liu, F. E. Roberts, D. L. Hughes, R. D. Larsen, T. R. Verhoeven, P. J. Reider, *Tetrahedron Lett.* **1996**, 37, 3271–3274.
- [52] D. L. Hughes, G. B. Smith, J. Liu, G. C. Dezeny, C. H. Senanayake, R. D. Larsen, T. R. Verhoeven, P. J. Reider, *J. Org. Chem.* **1997**, 62, 2222–2229.
- [53] J. E. Lynch, W.-B. Choi, H. R. O. Churchill, R. P. Volante, R. A. Reamer, R. G. Ball, *J. Org. Chem.* **1997**, 62, 9223–9228.

References

- [54] M. Tokunaga, J. F. Larrow, F. Kakiuchi, E. N. Jacobsen, *Science* **1997**, 277, 936–938.
- [55] S. Kemper, P. Hrobárik, M. Kaupp, N. E. Schlörer, *J. Am. Chem. Soc.* **2009**, 131, 4172–4173.
- [56] A. Kochem, H. Kanso, B. Baptiste, H. Arora, C. Philouze, O. Jarjayes, H. Vezin, D. Luneau, M. Orio, F. Thomas, *Inorg. Chem.* **2012**, 51, 10557–10571.
- [57] T. Kurahashi, H. Fujii, *Inorg. Chem.* **2013**, 52, 3908–3919.
- [58] J. F. Larrow, E. N. Jacobsen, in *Organometallics in Process Chemistry*, Springer Berlin Heidelberg, Berlin, Heidelberg, **2004**, pp. 123–152.
- [59] X.-L. Hou, B.-F. Li, L.-X. Dai, *Tetrahedron Asymmetry* **1999**, 10, 2319–2326.
- [60] R. Pummerer, F. Frankfurter, *Ber. Dtsch. Chem. Ges.* **1914**, 47, 1472–1493.
- [61] C. D. Cook, R. C. Woodworth, *J. Am. Chem. Soc.* **1953**, 75, 6242–6244.
- [62] E. Müller, K. Ley, *Chem. Ber.* **1954**, 87, 922–934.
- [63] E. R. Altwicker, *Chem. Rev.* **1967**, 67, 475–531.
- [64] D. E. Williams, *Mol. Phys.* **1969**, 16, 145–151.
- [65] V. W. Manner, T. F. Markle, J. H. Freudenthal, J. P. Roth, J. M. Mayer, *Chem. Commun.* **2008**, 256–258.
- [66] F. G. Bordwell, J. Cheng, *J. Am. Chem. Soc.* **1991**, 113, 1736–1743.
- [67] R. D. Webster, *Electrochem. commun.* **2003**, 5, 6–11.
- [68] Y. Wang, J. L. DuBois, B. Hedman, K. O. Hodgson, T. D. P. Stack, *Science* **1998**, 279, 537–540.
- [69] Y. Wang, T. D. P. Stack, *J. Am. Chem. Soc.* **1996**, 118, 13097–13098.
- [70] B. A. Jazdzewski, A. M. Reynolds, P. L. Holland, V. G. Young, S. Kaderli, A. D. Zuberbühler, W. B. Tolman, *J. Biol. Inorg. Chem.* **2003**, 8, 381–393.
- [71] T. E. King, H. S. Mason, M. Morrison, *Oxidases and Related Redox Systems: Proceedings of the Third International Symposium on Oxidases and Related Redox Systems, Held in the State University of New York at Albany, USA*, Pergamon Press, Oxford, New York, **1982**.
- [72] M. Melník, M. Kabešová, *J. Coord. Chem.* **2000**, 50, 323–338.
- [73] F. C. Anson, T. J. Collins, T. G. Richmond, B. D. Santarsiero, J. E. Toth, B. G. R. T. Treco, *J. Am. Chem. Soc.* **1987**, 109, 2974–2979.
- [74] R. C. Pratt, T. D. P. Stack, *J. Am. Chem. Soc.* **2003**, 125, 8716–8717.
- [75] T. Storr, P. Verma, R. C. Pratt, E. C. Wasinger, Y. Shimazaki, T. D. P. Stack, *J. Am. Chem. Soc.* **2008**, 130, 15448–15459.
- [76] M. Orio, O. Jarjayes, H. Kanso, C. Philouze, F. Neese, F. Thomas, *Angew. Chem. Int. Ed.* **2010**, 49, 4989–4992.
- [77] A. Dei, D. Gatteschi, L. Pardi, A. L. Barra, L. C. Brunel, *Chem. Phys. Lett.* **1990**, 175, 589–592.
- [78] P. Sharrock, M. Melník, *Can. J. Chem.* **1985**, 63, 52–56.
- [79] M. Orio, O. Jarjayes, H. Kanso, C. Philouze, F. Neese, F. Thomas, *Angew. Chem. Int. Ed.* **2010**, 49, 4989–4992.

References

- [80] K. Asami, A. Takashina, M. Kobayashi, S. Iwatsuki, T. Yajima, A. Kochem, M. van Gastel, F. Tani, T. Kohzuma, F. Thomas, Y. Shimazaki, *Dalton Trans.* **2014**, 43, 2283–2293.
- [81] A. Kochem, O. Jarjayes, B. Baptiste, C. Philouze, H. Vezin, K. Tsukidate, F. Tani, M. Orio, Y. Shimazaki, F. Thomas, *Chem. Eur. J.* **2012**, 18, 1068–1072.
- [82] M. B. Robin, P. Day, in *Advances in Inorganic Chemistry and Radiochemistry*, Elsevier, **1968**, pp. 247–422.
- [83] R. A. Marcus, *J. Chem. Phys.* **1956**, 24, 966–978.
- [84] N. S. Hush, in *Progress in Inorganic Chemistry*, John Wiley & Sons, Inc., Hoboken, NJ, USA, **2007**, pp. 391–444.
- [85] B. S. Brunschwig, C. Creutz, N. Sutin, *Chem. Soc. Rev.* **2002**, 31, 168–184.
- [86] R. Kunert, C. Philouze, F. Berthiol, O. Jarjayes, T. Storr, F. Thomas, *Dalton Trans.* **2020**, 49, 12990–13002.
- [87] R. C. Pratt, C. T. Lyons, E. C. Wasinger, T. D. P. Stack, *J. Am. Chem. Soc.* **2012**, 134, 7367–7377.
- [88] T. K. Paine, T. Weyhermüller, K. Wieghardt, P. Chaudhuri, *Dalton Trans.* **2004**, 2092–2101.
- [89] C. Mukherjee, T. Weyhermüller, E. Bothe, P. Chaudhuri, *Inorg. Chem.* **2008**, 47, 11620–11632.
- [90] A. Kochem, J. K. Molloy, G. Gellon, N. Leconte, C. Philouze, F. Berthiol, O. Jarjayes, F. Thomas, *Chem. Eur. J.* **2017**, 23, 13929–13940.
- [91] L. Lecarme, A. Kochem, L. Chiang, J. Moutet, F. Berthiol, C. Philouze, N. Leconte, T. Storr, F. Thomas, *Inorg. Chem.* **2018**, 57, 9708–9719.
- [92] F. Thomas, G. Gellon, I. Gautier-Luneau, E. Saint-Aman, J.-L. Pierre, *Angew. Chem. Int. Ed.* **2002**, 41, 3047–3050.
- [93] P. Chaudhuri, M. Hess, T. Weyhermüller, K. Wieghardt, *Angew. Chem. Int. Ed.* **1999**, 38, 1095–1098.
- [94] B. De Castro, C. Freire, *Inorg. Chem.* **1990**, 29, 5113–5119.
- [95] C. Freire, B. de Castro, *J. Chem. Soc., Dalton Trans.* **1998**, 1491–1498.
- [96] O. Rotthaus, O. Jarjayes, F. Thomas, C. Philouze, C. Perez Del Valle, E. Saint-Aman, J.-L. Pierre, *Chem. Eur. J.* **2006**, 12, 2293–2302.
- [97] O. Rotthaus, O. Jarjayes, C. Perez Del Valle, C. Philouze, F. Thomas, *Chem. Commun.* **2007**, 4462–4464.
- [98] F. Thomas, *Dalton Trans.* **2016**, 45, 10866–10877.
- [99] Y. Shimazaki, F. Tani, K. Fukui, Y. Naruta, O. Yamauchi, *J. Am. Chem. Soc.* **2003**, 125, 10512–10513.
- [100] T. Storr, E. C. Wasinger, R. C. Pratt, T. D. P. Stack, *Angew. Chem. Int. Ed.* **2007**, 46, 5198–5201.
- [101] Y. Shimazaki, T. Yajima, F. Tani, S. Karasawa, K. Fukui, Y. Naruta, O. Yamauchi, *J. Am. Chem. Soc.* **2007**, 129, 2559–2568.
- [102] L. Chiang, A. Kochem, O. Jarjayes, T. J. Dunn, H. Vezin, M. Sakaguchi, T. Ogura, M. Orio, Y. Shimazaki, F. Thomas, T. Storr, *Chem. Eur. J.* **2012**, 18, 14117–14127.

References

- [103] L. Chiang, K. Herasymchuk, F. Thomas, T. Storr, *Inorg. Chem.* **2015**, *54*, 5970–5980.
- [104] T. Kurahashi, H. Fujii, *J. Am. Chem. Soc.* **2011**, *133*, 8307–8316.
- [105] S. Aono, M. Nakagaki, T. Kurahashi, H. Fujii, S. Sakaki, *J. Chem. Theory Comput.* **2014**, *10*, 1062–1073.
- [106] R. M. Clarke, T. Storr, *J. Am. Chem. Soc.* **2016**, *138*, 15299–15302.
- [107] J.-B. Dumas, E.-M. Péligot, *Ann. Chim. Phys.* **1835**, *58*, 5–74.
- [108] H. W. Wanzlick, *Angew. Chem. Int. Ed. Engl.* **1962**, *1*, 75–80.
- [109] H.-W. Wanzlick, H.-J. Schönherr, *Angew. Chem. Int. Ed. Engl.* **1968**, *7*, 141–142.
- [110] K. Öfele, *J. Organomet. Chem.* **1968**, *12*, P42–P43.
- [111] A. J. Arduengo, R. L. Harlow, M. Kline, *J. Am. Chem. Soc.* **1991**, *113*, 361–363.
- [112] R. Hoffmann, *J. Am. Chem. Soc.* **1968**, *90*, 1475–1485.
- [113] J. Chatt, L. A. Duncanson, *J. Chem. Soc.* **1953**, 2939.
- [114] C. A. Tolman, *Chem. Rev.* **1977**, *77*, 313–348.
- [115] H. V. Huynh, *Chem. Rev.* **2018**, *118*, 9457–9492.
- [116] D. Bourissou, O. Guerret, F. P. Gabbaï, G. Bertrand, *Chem. Rev.* **2000**, *100*, 39–92.
- [117] P. de Frémont, N. Marion, S. P. Nolan, *Coord. Chem. Rev.* **2009**, *253*, 862–892.
- [118] S. P. Nolan, in *N-Heterocyclic Carbenes: Effective Tools for Organometallic Synthesis*, Wiley-VCH, Weinheim, **2014**.
- [119] N. Marion, S. Díez-González, S. P. Nolan, *Angew. Chem. Int. Ed.* **2007**, *46*, 2988–3000.
- [120] V. Nair, S. Bindu, V. Sreekumar, *Angew. Chem. Int. Ed.* **2004**, *43*, 5130–5135.
- [121] L. Benhamou, E. Chardon, G. Lavigne, S. Bellemin-Laponnaz, V. César, *Chem. Rev.* **2011**, *111*, 2705–2733.
- [122] A. Fürstner, M. Alcarazo, V. César, C. W. Lehmann, *Chem. Commun.* **2006**, 2176–2178.
- [123] A. Fürstner, M. Alcarazo, V. César, H. Krause, in *Organic Syntheses*, John Wiley & Sons, Inc., Hoboken, NJ, USA, **2008**, pp. 34–44.
- [124] J. Iglesias-Sigüenza, A. Ros, E. Díez, M. Alcarazo, E. Álvarez, R. Fernández, J. M. Lassaletta, *Dalton Trans.* **2009**, 7113–7120.
- [125] A. J. Aduengo, *Preparation of 1,3-Disubstituted Imidazolium Salts*, **1991**, 5,077.414.
- [126] M. B. Andrus, C. Song, J. Zhang, *Org. Lett.* **2002**, *4*, 2079–2082.
- [127] N. Hadei, E. A. B. Kantchev, C. J. O’Brien, M. G. Organ, *Org. Lett.* **2005**, *7*, 3805–3807.
- [128] V. P. W. Böhm, C. W. K. Gstöttmayr, T. Weskamp, W. A. Herrmann, *Angew. Chem. Int. Ed.* **2001**, *40*, 3387–3389.
- [129] M. Henrion, V. Ritleng, M. J. Chetcuti, *ACS Catal.* **2015**, *5*, 1283–1302.
- [130] E. Peris, *Chem. Rev.* **2018**, *118*, 9988–10031.
- [131] A. G. Tennyson, V. M. Lynch, C. W. Bielawski, *J. Am. Chem. Soc.* **2010**, *132*, 9420–9429.
- [132] M. Süßner, H. Plenio, *Angew. Chem. Int. Ed.* **2005**, *44*, 6885–6888.
- [133] H. Aihara, T. Matsuo, H. Kawaguchi, *Chem. Commun.* **2003**, 2204–2205.

References

- [134] A. W. Waltman, R. H. Grubbs, *Organometallics* **2004**, 23, 3105–3107.
- [135] T. R. T. R. Younkin, E. F. Connor, J. I. Henderson, S. K. Friedrich, R. H. Grubbs, D. A. Bansleben, *Science* **2000**, 287, 460–462.
- [136] S. Matsui, M. Mitani, J. Saito, Y. Tohi, H. Makio, N. Matsukawa, Y. Takagi, K. Tsuru, M. Nitabaru, T. Nakano, H. Tanaka, N. Kashiwa, T. Fujita, *J. Am. Chem. Soc.* **2001**, 123, 6847–6856.
- [137] H. Ren, P. Yao, S. Xu, H. Song, B. Wang, *J. Organomet. Chem.* **2007**, 692, 2092–2098.
- [138] A. El-Batta, A. Waltman, R. H. Grubbs, *J. Organomet. Chem.* **2011**, 696, 2477–2481.
- [139] M. Liu, J. C. Namyslo, M. Nieger, M. Polamo, A. Schmidt, *Beilstein J. Org. Chem.* **2016**, 12, 2673–2681.
- [140] D. Yang, Y. Tang, H. Song, B. Wang, *Organometallics* **2015**, 34, 2012–2017.
- [141] S. Bellemin-Laponnaz, R. Welter, L. Brelot, S. Dagorne, *J. Organomet. Chem.* **2009**, 694, 604–606.
- [142] C. Romain, B. Heinrich, S. B. Laponnaz, S. Dagorne, *Chem. Commun.* **2012**, 48, 2213–2215.
- [143] C. C. Quadri, E. Le Roux, *Dalton Trans.* **2014**, 43, 4242–4246.
- [144] E. Borré, G. Dahm, A. Aliprandi, M. Mauro, S. Dagorne, S. Bellemin-Laponnaz, *Organometallics* **2014**, 33, 4374–4384.
- [145] C. Romain, S. Choua, J.-P. Collin, M. Heinrich, C. Bailly, L. Karmazin-Brelot, S. Bellemin-Laponnaz, S. Dagorne, *Inorg. Chem.* **2014**, 53, 7371–7376.
- [146] C. F. Harris, M. B. Bayless, N. P. van Leest, Q. J. Bruch, B. N. Livesay, J. Bacsá, K. I. Hardcastle, M. P. Shores, B. de Bruin, J. D. Soper, *Inorg. Chem.* **2017**, 56, 12421–12435.
- [147] C. Gandara, C. Philouze, O. Jarjays, F. Thomas, *Inorganica Chim. Acta* **2018**, 482, 561–566.
- [148] M. Nirmala, G. Prakash, R. Ramachandran, P. Viswanathamurthi, J. G. Malecki, W. Linert, *J. Mol. Catal. A Chem.* **2015**, 397, 56–67.
- [149] K. Li, G. Cheng, C. Ma, X. Guan, W.-M. Kwok, Y. Chen, W. Lu, C.-M. Che, *Chem. Sci.* **2013**, 4, 2630–2644.
- [150] R. Lalrempuia, J. Underhaug, K. W. Törnroos, E. Le Roux, *Chem. Commun.* **2019**, 55, 7227–7230.
- [151] R. Taakili, C. Barthes, A. Goëffon, C. Lepetit, C. Duhayon, D. A. Valyaev, Y. Canac, *Inorg. Chem.* **2020**, 59, 7082–7096.
- [152] Y. Zhuang, Y. Qian, D. Tu, Y. Li, J. Liu, L. Shen, D. Wu, *Eur. J. Inorg. Chem.* **2021**, 34, 3443–3447.
- [153] M. Käß, J. Hohenberger, M. Adelhardt, E. M. Zolnhofer, S. Mossin, F. W. Heinemann, J. Sutter, K. Meyer, *Inorg. Chem.* **2014**, 53, 2460–2470.
- [154] E. M. Zolnhofer, M. Käß, M. M. Khusniyarov, F. W. Heinemann, L. Maron, M. van Gastel, E. Bill, K. Meyer, *J. Am. Chem. Soc.* **2014**, 136, 15072–15078.
- [155] Z. S. Ghavami, M. R. Anneser, F. Kaiser, P. J. Altmann, B. J. Hofmann, J. F. Schlagintweit, G. Grivani, F. E. Kühn, *Chem. Sci.* **2018**, 9, 8307–8314.
- [156] R. R. Eady, *Chem. Rev.* **1996**, 96, 3013–3030.
- [157] B. J. Hales, *Adv. Inorg. Biochem.* **1990**, 8, 165–198.

References

- [158] O. Einsle, F. A. Tezcan, S. L. A. Andrade, B. Schmid, M. Yoshida, J. B. Howard, D. C. Rees, *Science* **2002**, 297, 1696–1700.
- [159] D. Sippel, O. Einsle, *Nat. Chem. Biol.* **2017**, 13, 956–960.
- [160] R. N. F. Thorneley, D. J. Lowe, *Biochem.* **1984**, 224, 887–894.
- [161] R. N. F. Thorneley, D. J. Lowe, *J. Biol. Inorg. Chem.* **1996**, 1, 576–580.
- [162] D. Lukoyanov, N. Khadka, Z.-Y. Yang, D. R. Dean, L. C. Seefeldt, B. M. Hoffman, *J. Am. Chem. Soc.* **2016**, 138, 1320–1327.
- [163] D. Lukoyanov, B. M. Barney, D. R. Dean, L. C. Seefeldt, B. M. Hoffman, *Proc. Natl. Acad. Sci. U.S.A.* **2007**, 104, 1451–1455.
- [164] M. J. Dilworth, R. R. Eady, *Biochem.* **1991**, 277, 465–468.
- [165] D. J. Lowe, R. N. F. Thorneley, J. R. Postgate, in *Advances in Nitrogen Fixation Research*, Springer Netherlands, Dordrecht, **1984**, pp. 133–138.
- [166] J. Rittle, J. C. Peters, *J. Am. Chem. Soc.* **2016**, 138, 4243–4248.
- [167] A. D. Allen, C. V. Senoff, *Chem. Commun. (London)* **1965**, 621–622.
- [168] F. Bottomley, S. C. Nyburg, *Chem. Commun. (London)* **1966**, 897–898.
- [169] K. Komori, H. Oshita, Y. Mizobe, M. Hidai, *J. Am. Chem. Soc.* **1989**, 111, 1939–1940.
- [170] J. O. Dzięgielewski, R. Grzybek, *Polyhedron* **1990**, 9, 645–651.
- [171] A. E. Shilov, *J. Mol. Catal.* **1987**, 41, 221–234.
- [172] C. R. Dickson, A. J. Nozik, *J. Am. Chem. Soc.* **1978**, 100, 8007–8009.
- [173] K. Tanaka, Y. Hozumi, T. Tanaka, *Chem. Lett.* **1982**, 11, 1203–1206.
- [174] D. V. Yandulov, R. R. Schrock, *Science* **2003**, 301, 76–78.
- [175] M. D. Fryzuk, S. A. Johnson, *Coord. Chem. Rev.* **2000**, 200–202, 379–409.
- [176] F. Mus, A. B. Alleman, N. Pence, L. C. Seefeldt, J. W. Peters, *Metallomics* **2018**, 10, 523–538.
- [177] J. S. Anderson, J. Rittle, J. C. Peters, *Nature* **2013**, 501, 84–87.
- [178] S. E. Creutz, J. C. Peters, *J. Am. Chem. Soc.* **2014**, 136, 1105–1115.
- [179] T. J. Del Castillo, N. B. Thompson, J. C. Peters, *J. Am. Chem. Soc.* **2016**, 138, 5341–5350.
- [180] J. A. Wiig, Y. Hu, C. C. Lee, M. W. Ribbe, *Science* **2012**, 337, 1672–1675.
- [181] T. Spatzal, M. Aksoyoglu, L. Zhang, S. L. A. Andrade, E. Schleicher, S. Weber, D. C. Rees, O. Einsle, *Science* **2011**, 334, 940.
- [182] K. M. Lancaster, M. Roemelt, P. Ettenhuber, Y. Hu, M. W. Ribbe, F. Neese, U. Bergmann, S. DeBeer, *Science* **2011**, 334, 974–977.
- [183] K. M. Lancaster, Y. Hu, U. Bergmann, M. W. Ribbe, S. DeBeer, *J. Am. Chem. Soc.* **2013**, 135, 610–612.
- [184] K. Arashiba, Y. Miyake, Y. Nishibayashi, *Nat. Chem.* **2011**, 3, 120–125.
- [185] K. Arashiba, K. Sasaki, S. Kuriyama, Y. Miyake, H. Nakanishi, Y. Nishibayashi, *Organometallics* **2012**, 31, 2035–2041.

References

- [186] S. Kuriyama, K. Arashiba, K. Nakajima, H. Tanaka, N. Kamaru, K. Yoshizawa, Y. Nishibayashi, *J. Am. Chem. Soc.* **2014**, *136*, 9719–9731.
- [187] H. Tanaka, K. Arashiba, S. Kuriyama, A. Sasada, K. Nakajima, K. Yoshizawa, Y. Nishibayashi, *Nat. Commun.* **2014**, *5*, 3737 (1–11).
- [188] S. Kuriyama, K. Arashiba, K. Nakajima, H. Tanaka, K. Yoshizawa, Y. Nishibayashi, *Chem. Sci.* **2015**, *6*, 3940–3951.
- [189] A. Eizawa, K. Arashiba, H. Tanaka, S. Kuriyama, Y. Matsuo, K. Nakajima, K. Yoshizawa, Y. Nishibayashi, *Nat. Commun.* **2017**, *8*, 14874 (1–12).
- [190] Y. Ashida, K. Arashiba, K. Nakajima, Y. Nishibayashi, *Nature* **2019**, *568*, 536–540.
- [191] I. Pappas, P. J. Chirik, *J. Am. Chem. Soc.* **2016**, *138*, 13379–13389.
- [192] B. A. MacKay, M. D. Fryzuk, *Chem. Rev.* **2004**, *104*, 385–402.
- [193] K. Dehnicke, J. Strähle, *Angew. Chem. Int. Ed. Engl.* **1981**, *20*, 413–426.
- [194] K. Dehnicke, J. Strähle, *Angew. Chem. Int. Ed. Engl.* **1992**, *31*, 955–978.
- [195] J. M. Smith, in *Progress in Inorganic Chemistry*, John Wiley & Sons, Inc., Hoboken, New Jersey, **2014**, pp. 417–470.
- [196] J. Schöffel, A. Yu. Rogachev, S. DeBeer George, P. Burger, *Angew. Chem. Int. Ed.* **2009**, *48*, 4734–4738.
- [197] B. L. Tran, M. Pink, X. Gao, H. Park, D. J. Mindiola, *J. Am. Chem. Soc.* **2010**, *132*, 1458–1459.
- [198] K. Meyer, J. Bendix, N. Metzler-Nolte, T. Weyhermüller, K. Wieghardt, *J. Am. Chem. Soc.* **1998**, *120*, 7260–7270.
- [199] G. Izzet, E. Ishow, J. Delaire, C. Afonso, J.-C. Tabet, A. Proust, *Inorg. Chem.* **2009**, *48*, 11865–11870.
- [200] Y.-F. Song, J. F. Berry, E. Bill, E. Bothe, T. Weyhermüller, K. Wieghardt, *Inorg. Chem.* **2007**, *46*, 2208–2219.
- [201] J. Du Bois, J. Hong, E. M. Carreira, M. W. Day, *J. Am. Chem. Soc.* **1996**, *118*, 915–916.
- [202] C. J. Chang, W. B. Connick, D. W. Low, M. W. Day, H. B. Gray, *Inorg. Chem.* **1998**, *37*, 3107–3110.
- [203] G. Golubkov, Z. Gross, *J. Am. Chem. Soc.* **2005**, *127*, 3258–3259.
- [204] T. Birk, J. Bendix, *Inorg. Chem.* **2003**, *42*, 7608–7615.
- [205] B. L. Tran, M. Singhal, H. Park, O. P. Lam, M. Pink, J. Krzystek, A. Ozarowski, J. Telser, K. Meyer, D. J. Mindiola, *Angew. Chem. Int. Ed.* **2010**, *49*, 9871–9875.
- [206] A. S. Veige, L. M. Slaughter, E. B. Lobkovsky, P. T. Wolczanski, N. Matsunaga, S. A. Decker, T. R. Cundari, *Inorg. Chem.* **2003**, *42*, 6204–6224.
- [207] D. J. Mindiola, C. C. Cummins, *Angew. Chem. Int. Ed.* **1998**, *37*, 945–947.
- [208] G. K. B. Clentsmith, V. M. E. Bates, P. B. Hitchcock, F. G. N. Cloke, *J. Am. Chem. Soc.* **1999**, *121*, 10444–10445.
- [209] A. Duatti, A. Marchi, R. Pasqualini, *J. Chem. Soc., Dalton Trans.* **1990**, 3729–3733.
- [210] M. J. Abrams, C. Qin, S. N. Shaikh, J. Zubietta, *Inorganica Chim. Acta* **1990**, *176*, 11–13.

References

- [211] J. R. Dilworth, P. Jobanputra, J. R. Miller, S. J. Parrott, Q. Chen, J. Zubieta, *Polyhedron* **1993**, *12*, 513–522.
- [212] D. Watanabe, S. Gondo, H. Seino, Y. Mizobe, *Organometallics* **2007**, *26*, 4909–4920.
- [213] K. H. Horn, N. Böres, N. Lehnert, K. Mersmann, C. Näther, G. Peters, F. Tuczek, *Inorg. Chem.* **2005**, *44*, 3016–3030.
- [214] L. Bonomo, E. Solari, R. Scopelliti, C. Floriani, *Angew. Chem.* **2001**, *113*, 2597–2599.
- [215] K. Dehnicke, J. Strähle, *Angew. Chem. Int. Ed. Engl.* **1992**, *31*, 955–978.
- [216] M. G. Fickes, A. L. Odom, C. C. Cummins, *Chem. Commun.* **1997**, 1993.
- [217] A. L. Odom, C. C. Cummins, J. D. Protasiewicz, *J. Am. Chem. Soc.* **1995**, *117*, 6613–6614.
- [218] L. N. Grant, B. Pinter, T. Kurogi, M. E. Carroll, G. Wu, B. C. Manor, P. J. Carroll, D. J. Mindiola, *Chem. Sci.* **2017**, *8*, 1209–1224.
- [219] Ju Chang Kim, Byung Min Lee, I. S. Jong, *Polyhedron* **1995**, *14*, 2145–2149.
- [220] T. J. Crevier, B. K. Bennett, J. D. Soper, J. A. Bowman, A. Dehestani, D. A. Hrovat, S. Lovell, W. Kaminsky, J. M. Mayer, *J. Am. Chem. Soc.* **2001**, *123*, 1059–1071.
- [221] R. W. Marshman, P. A. Shapley, *J. Am. Chem. Soc.* **1990**, *112*, 8369–8378.
- [222] K. R. Powell, P. J. Perez, L. Luan, S. G. Feng, P. S. White, M. Brookhart, J. L. Templeton, *Organometallics* **1994**, *13*, 1851–1864.
- [223] J. C. Kim, W. S. Rees, V. L. Goedken, *Inorg. Chem.* **1995**, *34*, 2483–2486.
- [224] U. Abram, A. Voigt, R. Kirmse, *Polyhedron* **2000**, *19*, 1741–1748.
- [225] A. Walstrom, H. Fan, M. Pink, K. G. Caulton, *Inorganica Chim. Acta* **2010**, *363*, 633–636.
- [226] W.-H. Leung, E. Y. Y. Chan, T. C. Y. Lai, W.-T. Wong, *J. Chem. Soc., Dalton Trans.* **2000**, 51–56.
- [227] J. Bendix, C. Anthon, M. Schau-Magnussen, T. Brock-Nannestad, J. Vibenholt, M. Rehman, S. P. A. Sauer, *Angew. Chem. Int. Ed.* **2011**, *50*, 4480–4483.
- [228] S. Ritter, U. Abram, *Inorganica Chim. Acta* **1995**, *231*, 245–248.
- [229] U. Abram, E. Schulz Lang, S. Abram, J. Wegmann, J. R. Dilworth, R. Kirmse, J. D. Woollins, *J. Chem. Soc., Dalton Trans.* **1997**, 623–630.
- [230] L. H. Doerrer, A. J. Graham, M. L. H. Green, *J. Chem. Soc., Dalton Trans.* **1998**, 3941–3946.
- [231] J. Strähle, *Angew. Chem.* **1989**, *101*, 957–957.
- [232] F. Refosco, F. Tisato, A. Moresco, G. Bandoli, *J. Chem. Soc., Dalton Trans.* **1995**, 3475–3482.
- [233] J. F. Berry, *Comments Inorg. Chem.* **2009**, *30*, 28–66.
- [234] D. Sieh, J. Schöffel, P. Burger, *Dalton Trans.* **2011**, *40*, 9512–9524.
- [235] C. C. Hojilla Atienza, A. C. Bowman, E. Lobkovsky, P. J. Chirik, *J. Am. Chem. Soc.* **2010**, *132*, 16343–16345.
- [236] V. Vreeken, M. A. Siegler, B. de Bruin, J. N. H. Reek, M. Lutz, J. I. van der Vlugt, *Angew. Chem.* **2015**, *127*, 7161–7165.

References

- [237] N. B. Thompson, M. T. Green, J. C. Peters, *J. Am. Chem. Soc.* **2017**, *139*, 15312–15315.
- [238] J. J. Scepaniak, M. D. Fulton, R. P. Bontchev, E. N. Duesler, M. L. Kirk, J. M. Smith, *J. Am. Chem. Soc.* **2008**, *130*, 10515–10517.
- [239] J. J. Scepaniak, R. P. Bontchev, D. L. Johnson, J. M. Smith, *Angew. Chem. Int. Ed.* **2011**, *50*, 6630–6633.
- [240] J. J. Scepaniak, C. G. Margarit, J. N. Harvey, J. M. Smith, *Inorg. Chem.* **2011**, *50*, 9508–9517.
- [241] G. Sabenya, L. Lázaro, I. Gamba, V. Martin-Diaconescu, E. Andris, T. Weyhermüller, F. Neese, J. Roithova, E. Bill, J. Lloret-Fillol, M. Costas, *J. Am. Chem. Soc.* **2017**, *139*, 9168–9177.
- [242] C.-M. Che, H.-W. Lam, W.-F. Tong, T.-F. Lai, T.-C. Lau, *J. Chem. Soc., Chem. Commun.* **1989**, 1883–1884.
- [243] D. W. Pipes, M. Bakir, S. E. Vitols, D. J. Hodgson, T. J. Meyer, *J. Am. Chem. Soc.* **1990**, *112*, 5507–5514.
- [244] D. C. Ware, H. Taube, *Inorg. Chem.* **1991**, *30*, 4605–4610.
- [245] K. D. Demadis, T. J. Meyer, P. S. White, *Inorg. Chem.* **1997**, *36*, 5678–5679.
- [246] G. M. Coia, K. D. Demadis, T. J. Meyer, *Inorg. Chem.* **2000**, *39*, 2212–2223.
- [247] E.-S. El-Samanody, K. D. Demadis, T. J. Meyer, P. S. White, *Inorg. Chem.* **2001**, *40*, 3677–3686.
- [248] B. Askevold, J. T. Nieto, S. Tussupbayev, M. Diefenbach, E. Herdtweck, M. C. Holthausen, S. Schneider, *Nat. Chem.* **2011**, *3*, 532–537.
- [249] S. N. Brown, *J. Am. Chem. Soc.* **1999**, *121*, 9752–9753.
- [250] A. G. Maestri, K. S. Cherry, J. J. Toboni, S. N. Brown, *J. Am. Chem. Soc.* **2001**, *123*, 7459–7460.
- [251] M. H. V. Huynh, D. L. Jameson, T. J. Meyer, *Inorg. Chem.* **2001**, *40*, 5062–5063.
- [252] B. K. Bennett, E. Saganic, S. Lovell, W. Kaminsky, A. Samuel, J. M. Mayer, *Inorg. Chem.* **2003**, *42*, 4127–4134.
- [253] G.-S. Fang, J.-S. Huang, N. Zhu, C.-M. Che, *Eur. J. Inorg. Chem.* **2004**, *2004*, 1341–1348.
- [254] Yi, T. C. H. Lam, Y.-K. Sau, Q.-F. Zhang, I. D. Williams, W.-H. Leung, *Inorg. Chem.* **2007**, *46*, 7193–7198.
- [255] F. S. Schendzielorz, M. Finger, C. Volkmann, C. Würtele, S. Schneider, *Angew. Chem. Int. Ed.* **2016**, *55*, 11417–11420.
- [256] J. D. Bois, C. S. Tomooka, J. Hong, E. M. Carreira, M. W. Day, *Angew. Chem. Int. Ed. Engl.* **1997**, *36*, 1645–1647.
- [257] J. Du Bois, C. S. Tomooka, J. Hong, E. M. Carreira, *Acc. Chem. Res.* **1997**, *30*, 364–372.
- [258] C. P. Lenges, M. Brookhart, *J. Am. Chem. Soc.* **1997**, *119*, 3165–3166.
- [259] C.-M. Ho, T.-C. Lau, H.-L. Kwong, W.-T. Wong, *J. Chem. Soc., Dalton Trans.* **1999**, 2411–2414.
- [260] S. Minakata, M. Nishimura, T. Takahashi, Y. Oderaotoshi, M. Komatsu, *Tetrahedron Lett.* **2001**, *42*, 9019–9022.

References

- [261] M. Nishimura, S. Minakata, T. Takahashi, Y. Oderaotoshi, M. Komatsu, *J. Org. Chem.* **2002**, *67*, 2101–2110.
- [262] A. Gunay, K. H. Theopold, *Chem. Rev.* **2010**, *110*, 1060–1081.
- [263] A. S. Borovik, *Chem. Soc. Rev.* **2011**, *40*, 1870.
- [264] J. T. Groves, T. Takahashi, *J. Am. Chem. Soc.* **1983**, *105*, 2073–2074.
- [265] L. A. Bottomley, F. L. Neely, *J. Am. Chem. Soc.* **1988**, *110*, 6748–6752.
- [266] J. Du Bois, J. Hong, E. M. Carreira, M. W. Day, *J. Am. Chem. Soc.* **1996**, *118*, 915–916.
- [267] F. R. Pérez, J. Belmar, Y. Moreno, R. Baggio, O. Peña, *New J. Chem.* **2005**, *29*, 283–287.
- [268] S. K.-Y. Leung, J.-S. Huang, J.-L. Liang, C.-M. Che, Z.-Y. Zhou, *Angew. Chem. Int. Ed.* **2003**, *42*, 340–343.
- [269] W.-L. Man, W. W. Y. Lam, S.-M. Yiu, T.-C. Lau, S.-M. Peng, *J. Am. Chem. Soc.* **2004**, *126*, 15336–15337.
- [270] S.-M. Yiu, W. W. Y. Lam, C.-M. Ho, T.-C. Lau, *J. Am. Chem. Soc.* **2007**, *129*, 803–809.
- [271] M. G. Scheibel, B. Askevold, F. W. Heinemann, E. J. Reijerse, B. de Bruin, S. Schneider, *Nat. Chem.* **2012**, *4*, 552–558.
- [272] J. Abbenseth, M. Finger, C. Würtele, M. Kasanmascheff, S. Schneider, *Inorg. Chem. Front.* **2016**, *3*, 469–477.
- [273] R. M. Clarke, T. Storr, *J. Am. Chem. Soc.* **2016**, *138*, 15299–15302.
- [274] R. Kunert, C. Philouze, O. Jarjays, F. Thomas, *Inorg. Chem.* **2019**, *58*, 8030–8044.
- [275] J. A. Bellow, S. A. Stoian, J. van Tol, A. Ozarowski, R. L. Lord, S. Groysman, *J. Am. Chem. Soc.* **2016**, *138*, 5531–5534.
- [276] S. Li, Z. Wang, T. S. A. Hor, J. Zhao, *Dalton Trans.* **2012**, *41*, 1454–1456.
- [277] Y. Shimazaki, T. D. P. Stack, T. Storr, *Inorg. Chem.* **2009**, *48*, 8383–8392.
- [278] D. A. Pratt, R. P. Pesavento, W. A. van der Donk, *Org. Lett.* **2005**, *7*, 2735–2738.
- [279] D. M. D'Alessandro, F. R. Keene, *Chem. Soc. Rev.* **2006**, *35*, 424–440.
- [280] N. V. Vugman, M. L. N. Grillo, V. K. Jain, *Chem. Phys. Lett.* **1988**, *147*, 241–245.
- [281] J. Luo, N. P. Rath, L. M. Mirica, *Organometallics* **2013**, *32*, 3343–3353.
- [282] F. Tang, S. V. Park, N. P. Rath, L. M. Mirica, *Dalton Trans.* **2018**, *47*, 1151–1158.
- [283] T. V. O'Halloran, M. M. Roberts, S. J. Lippard, *J. Am. Chem. Soc.* **1984**, *106*, 6427–6428.
- [284] P. J. Alonso, R. Alcalá, R. Usón, J. Forniés, *J. Phys. Chem. Solids* **1991**, *52*, 975–978.
- [285] R. Ojha, J. F. Boas, G. B. Deacon, P. C. Junk, A. M. Bond, *J. Inorg. Biochem.* **2016**, *162*, 194–200.
- [286] T. J. Dunn, M. I. Webb, K. Hazin, P. Verma, E. C. Wasinger, Y. Shimazaki, T. Storr, *Dalton Trans.* **2013**, *42*, 3950–3956.
- [287] T. Soda, Y. Kitagawa, T. Onishi, Y. Takano, Y. Shigeta, H. Nagao, Y. Yoshioka, K. Yamaguchi, *Chem. Phys. Lett.* **2000**, *319*, 223–230.
- [288] K. Ray, T. Petrenko, K. Wieghardt, F. Neese, *Dalton Trans.* **2007**, 1552–1566.

References

- [289] B. De Castro, C. Freire, *Inorg. Chem.* **1990**, 29, 5113–5119.
- [290] T. Maekawa, H. Sekizawa, K. Itami, *Angew. Chem. Int. Ed.* **2011**, 50, 7022–7026.
- [291] R. M. Clarke, T. Storr, *J. Am. Chem. Soc.* **2016**, 138, 15299–15302.
- [292] V. M. Chernyshev, E. A. Denisova, D. B. Eremin, V. P. Ananikov, *Chem. Sci.* **2020**, 11, 6957–6977.
- [293] F. Weinhold, C. R. Landis, E. D. Glendening, *Int. Rev. Phys. Chem.* **2016**, 35, 399–440.
- [294] F. Weinhold, C. R. Landis, in *Discovering Chemistry with Natural Bond Orbitals*, Wiley, Hoboken, NJ, **2012**, pp. 96–105.
- [295] A. E. Reed, R. B. Weinstock, F. Weinhold, *J. Chem. Phys.* **1985**, 83, 735–746.
- [296] M. Keilwerth, J. Hohenberger, F. W. Heinemann, J. Sutter, A. Scheurer, H. Fang, E. Bill, F. Neese, S. Ye, K. Meyer, *J. Am. Chem. Soc.* **2019**, 141, 17217–17235.
- [297] M. Keilwerth, L. Grunwald, W. Mao, F. W. Heinemann, J. Sutter, E. Bill, K. Meyer, *J. Am. Chem. Soc.* **2021**, 143, 1458–1465.
- [298] B. J. Cook, S. I. Johnson, G. M. Chambers, W. Kaminsky, R. M. Bullock, *Chem. Commun.* **2019**, 55, 14058–14061.
- [299] W. Ahlgren, *J. Press. Vessel Technol.* **2012**, 134, 054504(1–3).
- [300] J. J. Warren, T. A. Tronic, J. M. Mayer, *Chem. Rev.* **2010**, 110, 6961–7001.
- [301] N. M. Adli, H. Zhang, S. Mukherjee, G. Wu, *J. Electrochem. Soc.* **2018**, 165, J3130–J3147.
- [302] S. Mukherjee, S. V. Devaguptapu, A. Sviripa, C. R. F. Lund, G. Wu, *Appl. Catal. B.* **2018**, 226, 162–181.
- [303] F. Habibzadeh, S. L. Miller, T. W. Hamann, M. R. Smith, *Proc. Natl. Acad. Sci. U.S.A.* **2019**, 116, 2849–2853.
- [304] K. Nakajima, H. Toda, K. Sakata, Y. Nishibayashi, *Nat. Chem.* **2019**, 11, 702–709.
- [305] M. D. Zott, J. C. Peters, *J. Am. Chem. Soc.* **2021**, 143, 7612–7616.
- [306] H. Toda, K. Kuroki, R. Kanega, S. Kuriyama, K. Nakajima, Y. Himeda, K. Sakata, Y. Nishibayashi, *ChemPlusChem* **2021**, cplu.202100349.
- [307] M. D. Zott, P. Garrido-Barros, J. C. Peters, *ACS Catal.* **2019**, 9, 10101–10108.
- [308] L. Tao, T. A. Stich, A. V. Soldatova, B. M. Tebo, T. G. Spiro, W. H. Casey, R. D. Britt, *J. Biol. Inorg. Chem.* **2018**, 23, 1093–1104.
- [309] A. Sokolowski, E. Bothe, E. Bill, T. Weyhermüller, K. Wieghardt, *Chem. Commun.* **1996**, 1671–1672.
- [310] J. Müller, A. Kikuchi, E. Bill, T. Weyhermüller, P. Hildebrandt, L. Ould-Moussa, K. Wieghardt, *Inorganica Chimica Acta* **2000**, 297, 265–277.
- [311] D. Martelino, *Modulating Electronic Structure and Reactivity of Cr Nitride Complexes via Oxidation*, Thesis for Master of Science Degree in Chemistry, Simon Fraser University, **2020**.
- [312] J. Bendix, *J. Am. Chem. Soc.* **2003**, 125, 13348–13349.
- [313] J. Bendix, T. Birk, T. Weyhermüller, *Dalton Trans.* **2005**, 2737–2741.
- [314] J. Bendix, S. R. Wilson, T. Prussak-Wieckowska, *Acta Crystallogr. C Struct.* **1998**, 54, 923–925.

References

- [315] C. M. Che, J. X. Ma, W. T. Wong, T. F. Lai, C. K. Poon, *Inorg. Chem.* **1988**, 27, 2547–2548.
- [316] N. Azuma, T. Ozawa, S. Tsuboyama, *J. Chem. Soc., Dalton Trans.* **1994**, 2609–2613.
- [317] N. G. Connelly, W. E. Geiger, *Chem. Rev.* **1996**, 96, 877–910.
- [318] J. S. McIndoe, K. L. Vikse, *J Mass Spectrom* **2019**, 54, 466–479.
- [319] K. Srinivasan, J. K. Kochi, *Inorg. Chem.* **1985**, 24, 4671–4679.
- [320] R. S. Drago, in *Physical Methods for Chemists*, W.B. Saunders Company, Philadelphia, **1977**, pp. 390–392.
- [321] M. Orio, C. Philouze, O. Jarjayes, F. Neese, F. Thomas, *Inorg. Chem.* **2010**, 49, 646–658.
- [322] B. Bleaney, K. D. Bowers, *Proc. R. Soc. Lond. A* **1952**, 214, 451–465.
- [323] Y. Hirao, H. Ino, A. Ito, K. Tanaka, T. Kato, *J. Phys. Chem. A* **2006**, 110, 4866–4872.
- [324] R. A. Sheldon, *Catalysis Today* **2015**, 247, 4–13.
- [325] J. Wang, L. Guo, W. Ruan, Z. Zhu, *Chin. J. Appl. Chem.* **2014**, 31, 303–309.
- [326] T. P. Cheeseman, D. Hall, T. N. Waters, *J. Chem. Soc. A* **1966**, 1396–1406.
- [327] L. Yang, D. R. Powell, R. P. Houser, *Dalton Trans.* **2007**, 955–964.
- [328] F. Thomas, O. Jarjayes, C. Duboc, C. Philouze, E. Saint-Aman, J.-L. Pierre, *Dalton Trans.* **2004**, 2662–2669.
- [329] H. Kanso, R. M. Clarke, A. Kochem, H. Arora, C. Philouze, O. Jarjayes, T. Storr, F. Thomas, *Inorg. Chem.* **2020**, 59, 5133–5148.
- [330] L. C. Nathan, J. E. Koehne, J. M. Gilmore, K. A. Hannibal, W. E. Dewhirst, T. D. Mai, *Polyhedron* **2003**, 22, 887–894.
- [331] G. S. Patterson, R. H. Holm, *Bioinorg. Chem.* **1975**, 4, 257–275.
- [332] H. Yokoi, A. W. Addison, *Inorg. Chem.* **1977**, 16, 1341–1349.
- [333] D. F. Evans, *J. Chem. Soc.* **1959**, 2003–2005.
- [334] A. Kochem, J. K. Molloy, G. Gellon, N. Leconte, C. Philouze, F. Berthiol, O. Jarjayes, F. Thomas, *Chem. Eur. J.* **2017**, 23, 13929–13940.
- [335] V. B. Arion, S. Platzer, P. Raptá, P. Machata, M. Breza, D. Vegh, L. Dunsch, J. Telser, S. Shova, T. C. O. Mac Leod, A. J. L. Pombeiro, *Inorg. Chem.* **2013**, 52, 7524–7540.
- [336] J. C. Chan, M. Paice, X. Zhang, *ChemCatChem* **2020**, 12, 401–425.
- [337] J. Limburg, J. S. Vrettos, R. H. Crabtree, G. W. Brudvig, J. C. de Paula, A. Hassan, A.-L. Barra, C. Duboc-Toia, M.-N. Collomb, *Inorg. Chem.* **2001**, 40, 1698–1703.
- [338] C. Mantel, C. Baffert, I. Romero, A. Deronzier, J. Pécaut, M.-N. Collomb, C. Duboc, *Inorg. Chem.* **2004**, 43, 6455–6463.
- [339] S. Stoll, A. Schweiger, *Journal of Magnetic Resonance* **2006**, 178, 42–55.
- [340] A. J. M. Duisenberg, L. M. J. Kroon-Batenburg, A. M. M. Schreurs, *J. Appl. Crystallogr.* **2003**, 36, 220–229.
- [341] SADABS, Version 2008/1. G. M. Sheldrick, University of Gottingen, Gottingen, Germany, **2006**.

References

- [342] XPREP Version 2008/2. G. M. Sheldrick, Bruker AXS Inc., Madison, Wisconsin, USA, **2008**.
- [343] G. M. Sheldrick, *Acta Crystallogr. A* **2008**, *64*, 112–122.
- [344] O. V. Dolomanov, L. J. Bourhis, R. J. Gildea, J. A. K. Howard, H. Puschmann, *J. Appl. Crystallogr.* **2009**, *42*, 339–341.
- [345] V. Petříček, M. Dušek, L. Palatinus, *Z. Kristallogr. Cryst. Mater.* **2014**, *229*, 345–352.
- [346] SAINT, Version 7.03A., Bruker AXS Inc., Madison, Wisconsin, USA, **2003**.
- [347] Gaussian 09, Revision D.01. M. J. Frisch, G. W. Trucks, H. B. Schlegel, G. E. Scuseria, M. A. Robb, J. R. Cheeseman, G. Scalmani, V. Barone, G. A. Petersson, H. Nakatsuji, X. Li, M. Caricato, A. Marenich, J. Bloino, B. G. Janesko, R. Gomperts, B. Mennucci, H. P. Hratchian, J. V. Ortiz, A. F. Izmaylov, J. L. Sonnenberg, D. Williams-Young, F. Ding, F. Lipparini, F. Egidi, J. Goings, B. Peng, A. Petrone, T. Henderson, D. Ranasinghe, V. G. Zakrzewski, J. Gao, N. Rega, G. Zheng, W. Liang, M. Hada, M. Ehara, K. Toyota, R. Fukuda, J. Hasegawa, M. Ishida, T. Nakajima, Y. Honda, O. Kitao, H. Nakai, T. Vreven, K. Throssell, J. A. Montgomery, Jr., J. E. Peralta, F. Ogliaro, M. Bearpark, J. J. Heyd, E. Brothers, K. N. Kudin, V. N. Staroverov, T. Keith, R. Kobayashi, J. Normand, K. Raghavachari, A. Rendell, J. C. Burant, S. S. Iyengar, J. Tomasi, M. Cossi, J. M. Millam, M. Klene, C. Adamo, R. Cammi, J. W. Ochterski, R. L. Martin, K. Morokuma, O. Farkas, J. B. Foresman, and D. J. Fox, Gaussian, Inc., Wallingford CT, **2016**.
- [348] C. Lee, W. Yang, R. G. Parr, *Phys. Rev. B* **1988**, *37*, 785–789.
- [349] A. D. Becke, *J. Chem. Phys.* **1993**, *98*, 5648–5652.
- [350] S. Grimme, J. Antony, S. Ehrlich, H. Krieg, *J. Chem. Phys.* **2010**, *132*, 154104.
- [351] T. Yanai, D. P. Tew, N. C. Handy, *Chem. Phys. Lett.* **2004**, *393*, 51–57.
- [352] G. A. Petersson, M. A. Al-Laham, *J. Chem. Phys.* **1991**, *94*, 6081–6090.
- [353] W. R. Wadt, P. J. Hay, *J. Chem. Phys.* **1985**, *82*, 284–298.
- [354] M. E. Casida, in *Recent Advances in Computational Chemistry*, World Scientific, **1995**, pp. 155–192.
- [355] S. Miertuš, E. Scrocco, J. Tomasi, *Chem. Phys.* **1981**, *55*, 117–129.
- [356] F. Neese, *Wiley Interdiscip. Rev. Comput. Mol. Sci.* **2012**, *2*, 73–78.
- [357] F. Weigend, R. Ahlrichs, *Phys. Chem. Chem. Phys.* **2005**, *7*, 3297–3305.
- [358] F. Weigend, *Phys. Chem. Chem. Phys.* **2006**, *8*, 1057–1065.
- [359] A. Schäfer, C. Huber, R. Ahlrichs, *J. Chem. Phys.* **1994**, *100*, 5829–5835.
- [360] Gaussian 16, Revision C.01. M. J. Frisch, G. W. Trucks, H. B. Schlegel, G. E. Scuseria, M. A. Robb, J. R. Cheeseman, G. Scalmani, V. Barone, G. A. Petersson, H. Nakatsuji, X. Li, M. Caricato, A. V. Marenich, J. Bloino, B. G. Janesko, R. Gomperts, B. Mennucci, H. P. Hratchian, J. V. Ortiz, A. F. Izmaylov, J. L. Sonnenberg, D. Williams-Young, F. Ding, F. Lipparini, F. Egidi, J. Goings, B. Peng, A. Petrone, T. Henderson, D. Ranasinghe, V. G. Zakrzewski, J. Gao, N. Rega, G. Zheng, W. Liang, M. Hada, M. Ehara, K. Toyota, R. Fukuda, J. Hasegawa, M. Ishida, T. Nakajima, Y. Honda, O. Kitao, H. Nakai, T. Vreven, K. Throssell, J. A. Montgomery, Jr., J. E. Peralta, F. Ogliaro, M. J. Bearpark, J. J. Heyd, E. N. Brothers, K. N. Kudin, V. N. Staroverov, T. A. Keith, R. Kobayashi, J. Normand, K. Raghavachari, A. P. Rendell, J. C. Burant, S. S. Iyengar, J. Tomasi, M. Cossi, J. M. Millam, M. Klene, C. Adamo, R. Cammi, J. W. Ochterski, R.

References

- L. Martin, K. Morokuma, O. Farkas, J. B. Foresman, and D. J. Fox, Gaussian, Inc., Wallingford CT, **2016**.
- [361] A. D. Becke, *Phys. Rev. A* **1988**, 38, 3098–3100.
- [362] F. Weinhold, *J. Comput. Chem.* **2012**, 33, 2363–2379.

Synthesis, characterization and applications of complexes involving redox-active ligands.

We developed a new type of redox-active ligand, involving two *N*-heterocyclic carbenes and two phenolate units. The strong electron donating properties of the NHC moieties were utilized to stabilize complexes in high oxidation states while the phenolate groups were used as redox-active units.

Group 10 metal complexes were developed. Their oxidation chemistry showed the formation of phenoxyl radicals, reaching up to two-electron oxidized, bis(phenoxyl) complexes. We also report the first Ni(III) complex with NHC donors.

The ligand was also used to develop metal complexes with nitride ligands. The nitridomanganese complex proved to be unstable and degraded in successive intramolecular nitride-NHC reductive couplings. The degradation afforded a peculiar organic salt with three fused rings forming a central triazone pattern. Conversely, the chromium nitride complex could be isolated and thoroughly characterized. The one-electron oxidized product was generated reversibly at low temperature but readily evolved at room temperature.

In a parallel work, we also developed new types of sterically hindered salen ligands to form distorted copper salen complexes as molecular models of galactose oxidase. The copper salen catalysts showed to be effective for the aerobic oxidation of non-activated alcohol substrates.

Key-words: Synthesis, redox-active ligands, *N*-heterocyclic carbenes, radicals, phenoxyl, metal nitride, electronic structure.

Synthèse, caractérisation et applications de complexes comportant des ligands rédox-actifs.

Nous avons développé un nouveau type de ligand rédox-actif, impliquant deux carbènes *N*-hétérocycliques (NHC) connectés à deux unités phénolates. Le fort effet donneur des unités NHC a été utilisé pour stabiliser des complexes dans des états d'oxydation élevés, tandis que les groupes phénolates ont été utilisés comme centres rédox-actifs.

Des complexes métalliques du groupe 10 ont été développés. Leur chimie d'oxydation a montré qu'ils étaient des précurseurs de radicaux phénoxy et qu'il était possible d'accéder à des complexes bis(phénoxy) oxydés à deux électrons. Nous avons également décrit le premier complexe Ni(III) avec des donneurs NHC.

Ce ligand a également été utilisé pour développer des complexes métalliques de nitrure. Le complexe de nitrure de manganèse s'est révélé instable et s'est dégradé par couplages NHC-nitrure successifs. La réaction globale a conduit à un sel organique présentant trois cycles fusionnés correspondant à un motif triazone central. Le complexe de nitrure de chrome a quant à lui été isolé et caractérisé. Le produit oxydé à un électron est généré réversiblement à basse température mais évolue à température ambiante.

Dans un travail parallèle, nous avons également développé de nouveaux ligands salen stériquement encombrés pour former des complexes de cuivre distordus, utilisés comme modèles moléculaires de la galactose oxydase. Les catalyseurs de salen de cuivre se sont révélés efficaces pour l'oxydation aérobie de substrats alcools non-activés.

Mots-clés : Synthèse, ligands rédox-actifs, carbènes *N*-hétérocycliques, radicaux, phénoxy, nitrure métallique, structure électronique.